Measurement of the Higgs boson coupling with tau leptons and search for an additional neutral MSSM Higgs boson with the ATLAS detector

by

Damián Álvarez Piqueras

A thesis dissertation submitted for the degree of

Doctor of Philosophy

Under the supervision of:

Luca Fiorini

VNIVERSITAT DE VALÈNCIA

Departamento de Física Atómica, Molecular y Nuclear
Instituto de Física Corpuscular (IFIC-CSIC)
Programa de Doctorado en Física

March 2018

Informe del director

Luca Fiorini, investigador doctor de la Universidad de Valencia, como director de tesis del estudiante **Damián Álvarez Piqueras**,

CERTIFICA:

que los trabajos aquí detallados han sido realizados por el estudiante en el Instituto de Física Corpuscular bajo su dirección y que el presente texto constituye el trabajo de tesis doctoral por la que el estudiante opta al grado de Doctor en Física por la Universidad de Valencia.

Paterna, a 13 de Marzo de 2018

Firmado: Luca Fiorini

Qué bien vivís!
Qué bien lo pasáis!
Qué envidia me dais!

Agradecimientos Institucionales

Esta tesis ha sido realizada en el Instituto de Física Corpuscular (IFIC), un Centro de Excelencia Severo Ochoa (SEV-2014-0398) situado en Valencia, España.

El IFIC es un centro mixto que pertenece al Consejo Superior de Investigaciones Científicas (CSIC) y a la Universidad de Valencia (UV), dedicado a la investigación en Física Nuclear, de Partículas y de Astropartículas.

VNIVERSITAT DE VALÈNCIA

El trabajo de la tesis se ha realizado en el experimento ATLAS, que pertenece al CERN, la Organización Europea para la Investigación Nuclear situada en Ginebra, Suiza.

Esta colaboración se enmarca dentro del proyecto *Contribuciones al Calorímetro Hadrónico TileCal y al programa de física del experimento ATLAS* del Programa Nacional de Física de Partículas (FPA2009-13234-C04-03, FPA2012-32843, FPA2015-65652-C4-2-R), financiado por el Ministerio de Economía, (Industria) y Competitividad y por el Fondo Europeo de Desarrollo Regional (FEDER) de la Unión Europea (UE).

Abstract

Doctor of Philosophy

Measurement of the Higgs boson coupling with tau leptons and search for an additional neutral MSSM Higgs boson with the ATLAS detector

by Damián Álvarez Piqueras

The aim of this thesis is the search for the Standard Model Higgs boson and for additional heavy MSSM Higgs bosons in the $\tau\tau$ channel with the ATLAS detector of the LHC.

The search for the Higgs boson predicted by the Standard Model is performed using the full integrated luminosity of the Run 1 of the LHC: $4.5\,\text{fb}^{-1}$ of data collected at an energy in the center of mass of 7 TeV and $20.3\,\text{fb}^{-1}$ of data collected at an energy in the center of mass of 8 TeV. The analysis enhances the sensitivity to signal events by implementing a Boosted Decision Tree trained on the signal and background models. The BDT score distribution shows an excess of data over the background expectation, with an observed (expected) statistical significance of $4.5\,\sigma$ ($3.4\,\sigma$), which provides evidence for the direct coupling of the Higgs boson to fermions. The measured signal strength normalized to the Standard Model expectation of $\mu = 1.43^{+0.43}_{-0.37}$ is consistent with the predicted Yukawa coupling strength in the Standard Model.

The search for additional neutral Higgs bosons predicted by the Minimal Supersymmetric extension of the Standard Model is performed using $3.21\,\text{fb}^{-1}$ of data collected during the first year of the Run 2 of the LHC, at an energy in the center of mass of 13 TeV. The data is in good agreement with the background predicted by the Standard Model. Therefore, exclusion limits on the cross-section times branching ratio of the different MSSM production modes and on the $\tan\beta$–m_A space for different MSSM benchmark scenarios are extracted. The most stringent constraints exclude at 95% confidence level $\tan\beta > 7.6$ for $m_A = 200\,\text{GeV}$ in the MSSM $m_h^{\text{mod}+}$ scenario.

Contents

Preface

The Standard Model of particle physics is the framework which describes the behavior of subatomical particles. One of its key foundations is the Higgs mechanism, which implies the existence of a particle called Higgs boson. Despite the growing number of evidences supporting indirectly the Higgs mechanism, the particle physics community was eagerly expecting the construction of the Large Hadron Collider (LHC) at CERN, the latest and more powerful particle accelerator of its kind, which could reach –finally– the range of energies where this particle was expected to be found. The validity of the Standard Model was depending on the discovery for the Higgs boson.

In 2009, after an enormous worldwide collaborative effort, the LHC started to take data from proton-proton collision events at energies never reached before in a controlled experiment. The analysis of the subsequent data led to the discovery of a particle compatible with a Higgs boson, which was announced on the 4^{th} July 2012, forty eight years after it was proposed. The discovery of the Higgs boson, and thus the long-awaited confirmation of the Higgs mechanism, opened a new era in particle physics. Half a century of theoretical predictions depending on the Higgs parameters were waiting to be tested, having as priority the comprehensive analysis of all the properties of the new particle and their comparison with the Standard Model prediction. However, due to the mass at which the Higgs boson was discovered, some features of the theoretical framework are not explained in a fully satisfactory way. Hence, new theories that extend the Standard Model, accounting for these features, are being tested at the LHC.

The study of the coupling of the Higgs boson to tau leptons, its comparison with the theoretical prediction of the Standard Model and the search for an additional Higgs boson decaying to tau leptons, are the main topics of this thesis, which has been done in the *Instituto de Física Corpuscular* (IFIC), a Severo Ochoa research center belonging to the *Consejo Superior de Investigaciones Científicas* (CSIC) and the *Universitat de València* (UV). This work is part of a research performed by the ATLAS Collaboration, an experiment of the *European Organization for Nuclear Research* (CERN).

The first part of the thesis sets up the context, both theoretical and experimental, in which the work of this thesis was done. The description of the theoretical framework of

the Standard Model, including the Higgs mechanism, and the Minimal Supersymmetric extension are presented in **Chapter 1**. **Chapter 2** describes the phenomenological aspects of the collisions at the LHC and the interactions of the Higgs boson, both in terms of production and decay. The experimental setup is given in **Chapter 3**, where the CERN organization, the LHC and the ATLAS Experiment are described. The members of the ATLAS Collaboration have to contribute to the functioning, maintenance and development of the different parts of the experiment. The activities performed as service tasks for the Tile Calorimeter of the ATLAS Experiment are presented in **Chapter 4**.

The second part of this thesis presents the two different analyses performed in the context of the search of a Higgs boson decaying to tau leptons. First of all, the definition, identification and reconstruction of the physics objects which are relevant for the analyses are detailed in **Chapter 5**. **Chapter 6** focuses on the study of the coupling of the Standard Model Higgs boson to tau leptons, using the data of the Run 1 of the LHC. **Chapter 7** extends the search to the high mass range, aiming to find additional Higgs bosons predicted by an extension beyond the Standard Model, namely, different scenarios of the Minimal Supersymmetric Standard Model, using data collected during the first year of Run 2. Finally, **Chapter 8** summarizes the results of both analyses, putting them in the general context of particle physics, and discusses the future prospects of the searches for the next steps of the LHC roadmap.

Chapter 1

Theoretical motivation

This chapter describes the theoretical context of the Higgs boson search. It starts with a brief description of the Standard Model of particle physics (Section 1.1), the theory that predicted the existence of this observable particle and its coupling with tau leptons. However, despite its enormous success, the Standard Model has several limitations, which are described in Section 1.2. Finally, Section 1.3 presents one extension beyond the Standard Model that addresses some of those issues: the Minimal Supersymmetric Standard Model. This theory predicts the existence of additional observable Higgs bosons yet to be discovered, the search of which is one of the topics of this thesis.

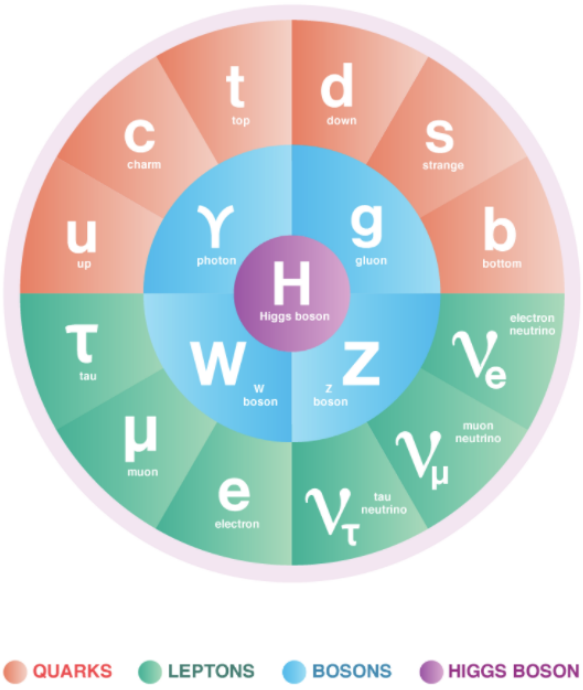

Figure 1.1: The Standard Model of particle physics, sorting the particles by type (quarks, leptons and bosons). Symmetry Magazine [1].

1.1 The Standard Model and the Higgs boson

The Standard Model of particle physics (SM) is the theoretical framework that describes the fundamental particles and their interactions. In this mathematical construction, the particles are defined as excited states of fundamental quantum fields, and the interactions between the fields are considered as the classical forces of nature: electromagnetic, weak and strong. The Standard Model fails to include a quantified gravity interaction that complies with the general relativity and also lacks explanation for several phenomena of nature, but its validity is beyond any reasonable doubt as it has provided confirmed predictions for an enormous number of experimental results. The SM has been very successful in the description of the subatomical world.

Mathematically, the SM is described by a non-abelian gauge[1] quantum field theory (QFT) containing the internal symmetries of the Lie's algebra unitary product group $SU(3)_C \times SU(2)_L \times U(1)_Y$, corresponding to the strong and electroweak forces. However, the electroweak symmetry is broken at low energies, becoming effectively a $SU(3)_C \times U(1)_{\mathrm{Q}}$, which represents the strong and electromagnetic symmetries.

The SM is conventionally expressed using the lagrangian formalism as the integral over all the space of a lagrangian density (Equation 1.1) [2]. The lagrangian density is constructed from several terms describing the fundamental particles and forces.

$$\int L dt = \int \mathcal{L}\left(\phi, \partial_\mu \phi\right)\, d^4x \tag{1.1}$$

where L is the lagrangian of the system and $\mathcal{L}$ is the lagrangian density. By convention, as used in this thesis, the integration is usually implicit and the formulation is given in terms of the lagrangian density.

The particles are described in the lagrangian in terms of fields. Two types of particles can be differentiated, according to one property: the spin. Conceptually, the spin is a property that allows the particles to react to a magnetic field, in a sort of intrinsic angular momentum. The spin-statistics theorem allows to characterize two types of particles, according to their type of spin: **fermions**, which have a semi-integer value for the spin and represent the ordinary matter; and **bosons**, with an integer value for the spin, which are the carriers of the different forces. The observable particles are considered to be excited states of the fundamental fields. Figure 1.1 illustrates the elemental particles of the SM, while a detailed description of their properties is summarized in Table 1.1.

[1] A gauge theory is a type of field theory whose equations of motion (or the lagrangian $\mathcal{L}$, to this effect) are invariant under a continuous group of local transformations of the field, like $\psi \to \psi' = e^{i\lambda(x)}\psi$. If ψ is gauge invariant, $\mathcal{L}(\psi') = \mathcal{L}(\psi)$. See Section 1.1.2.

Particle	Spin	Type	Color	Gen./Force	Name	Symbol	Charge [e]	Mass	
Fermions	1/2	Quarks	RGB	I	Up	u	$+2/3$	2.2 ± 0.6	MeV
				II	Charm	c		1.27 ± 0.03	GeV
				III	Top	t		173.1 ± 0.6	GeV
				I	Down	d	$-1/3$	4.7 ± 0.5	MeV
				II	Strange	s		96 ± 8	MeV
				III	Bottom	b		4.18 ± 0.04	GeV
		Leptons	–	I	Electron	e	-1	$0.511 \pm (3.1 \times 10^{-9})$	MeV
				II	Muon	μ		$105.66 \pm (2.4 \times 10^{-6})$	MeV
				III	Tau	τ		1776.86 ± 0.12	MeV
				I	Electron neutrino	ν_e	0	< 2	eV
				II	Muon neutrino	ν_μ		< 0.19	MeV
				III	Tau neutrino	ν_τ		< 18.2	MeV
Bosons	1	Vector	RGB	Strong	Gluon	g	0	$< 2 \cdot 10^{-4}$ eV	~ 0
			–	Weak	Photon	γ	0	$< 10^{-18}$ eV	~ 0
					Weak	W	± 1	80.385 ± 0.015	GeV
					Zero	Z	0	91.1876 ± 0.0021	GeV
	0	Scalar	–	Higgs field	Higgs	H	0	125.09 ± 0.24	GeV

Table 1.1: General properties of the elemental particles. The electric charge is given in units of the electron charge [e], the *RGB* color charge refers to the convention of {red, green, blue} colors and the *Gen./Force* refers to the *generation* in which the fermions are sorted or the force of which the bosons are carriers, respectively. For the neutrinos, gluon and photon, measured upper limits on their masses are given. The gluon and the photon, however, are expected to be massless [3].

1.1.1 Fermions

Fermions (ψ) are the fundamental particles that form the ordinary matter. They are described mathematically by the Fermi-Dirac statistics, which means that their spin is a semi-integer number and thus, they have to obey the Pauli exclusion principle and the canonical anti-commutation relations.

The fundamental fermions, with a spin of $\frac{1}{2}$, are the solutions to the Dirac equation[2]: $(i\partial\!\!\!/ - m)\psi = 0$, where γ^μ are the *gamma matrices* [4], defined in Appendix A. The fermionic field takes the form of a plane wave [2]:

$$\psi(x) = \int \frac{d^3p}{(2\pi)^3} \frac{1}{\sqrt{2E_p}} \sum_s^2 \left(a^s_{\mathbf{p}} u_s(p) e^{-ipx} + b^{s\dagger}_{\mathbf{p}} v_s(p) e^{ipx} \right) \tag{1.2}$$

where $u_s(p)$ and $v_s(p)$ are spinors[3] with momentum p and spin s; $a^s_{\mathbf{p}}$ and $b^{s\dagger}_{\mathbf{p}}$ are the ladder operators of *creation* and *destruction*, which act as a base for the Fourier transformation of the field. The creation operator raises the field level, creating new excited states, which are conceptually viewed as *particles*. Conversely, the destruction operator de-excites those states, removing particles.

In order to keep the Lorentz invariance, a hermitian conjugate of the fermionic field has to be defined as follows: $\bar{\psi} \equiv \psi^\dagger \gamma^0$, which represents the antimatter particles, a symmetric partner of each fermion with opposite quantum numbers.

The lagrangian term for the free field of the fermions ($\mathcal{L}_f$) can be written, summing over all the types of fermionic fields, as:

$$\mathcal{L}_f = i\bar{\psi}\partial\!\!\!/\psi - m\bar{\psi}\psi \tag{1.3}$$

However, since some interactions are sensitive to the chirality of the particles involved, it is more useful to separate the fermions in their chiral components. For that, a chiral operator is defined as $\gamma^5 \equiv i\gamma^0\gamma^1\gamma^2\gamma^3$. Using this, fermions can be rewritten in terms of their two chiral components: left-handed ψ_L and right-handed ψ_R:

$$\psi = \underbrace{\frac{1-\gamma^5}{2}\psi}_{\psi_L} + \underbrace{\frac{1+\gamma^5}{2}\psi}_{\psi_R} = \psi_L + \psi_R \tag{1.4}$$

Since both components are orthogonal, the scalar product of two fields is:

$$\bar{\psi}\psi = \left(\bar{\psi}_R + \bar{\psi}_L\right)\left(\psi_L + \psi_R\right) = \bar{\psi}_R\psi_L + \bar{\psi}_L\psi_R \tag{1.5}$$

[2]The notation used in this document assumes the natural units convention ($c = \hbar = 1$), Einstein implicit summation ($cx \to c_i x^i \equiv \sum_i^n c_i x^i$) and the Feynman slash notation ($\partial\!\!\!/ = \gamma^\mu \partial_\mu$). In addition, the index convention for three-vector ($i = \{1, 2, 3\}$) and four-vector ($\mu = \{0, 1, 2, 3\}$) is used.

[3]A spinor is a special type of vector field that transforms under rotations by inverting the sign of the associated spin property.

Two types of fermions can be differentiated: **quarks** and **leptons**. The main difference between them is that the quarks carry an additional charge, the *color*, which makes them sensitive to the strong force. The leptons, on the other hand, are color-neutral, thus they cannot interact via that force. Twelve different fundamental fermions are known: six quarks and six leptons. Due to their common properties, they can be further categorized in generations or type.

Quarks and leptons can also be divided in three generations. Fermions of the same type but from different generation differ in the value of their masses. The particles of the *first generation* are the lightest ones while the *second* and *third* generations are heavier copies[4]. The existence of a fourth or further generations is constrained by the measurement of the Z boson decay width [5], though the validity of this result depends on the mass and coupling of the neutrinos with the Z boson and thus, heavier generations cannot be totally ruled out.

Each generation of quarks and leptons is composed of two particles with different electric charge. This allows to further divide fermions in two types: up-type and down-type for quarks, and neutrino-type and electron-type for leptons. The fermions belonging to the same type have the same fundamental[5] quantum numbers, therefore, they interact in the same way.

Quarks

Quarks (ψ_q) are, by definition, fermions which carry a color charge. Color is the fundamental charge of the strong force and can take three different values, which are labelled *red*, *green* and *blue*. The two types of quarks are the up-type, composed of the quarks up (u), charm (c) and top (t), which carry an electric charge[6] of $+\frac{2}{3}$; and the down-type, composed of the quarks down (d), strange (s) and bottom (b), which carry an electric charge of $-\frac{1}{3}$.

Due to a particular property of the strong interaction, *confinement* (explained in Section 1.1.3), color-charged particles cannot be observed as free states in nature. Thus, quarks combine to form color-neutral composite particles, called *hadrons*. The simplest possibilities are *mesons* (a quark-antiquark combination of the same color) and *baryons* (a composite state of three quarks with different colors). The mesons have an integer spin value, hence they behave effectively as bosons. Baryons, on the other hand, have a semi-integer spin and thus, behave as fermions. The ordinary matter is formed by two baryons, the proton (uud) and the neutron (udd).

[4] The mass hierarchy cannot be applied to neutrinos since their masses are still unknown. See Sections 1.1.7 and 1.2.1.

[5] The convention used in this thesis considers the flavor numbers (strangeness, charm, bottomness and topness) as a *defining* feature of several particles (the quarks strange, charm, bottom and top) and not a global property.

[6] The value of the electric charge is given using as reference the charge of the electron, $Q_e = 1.6021766208(98) \cdot 10^{-19}$ C[3], which takes the conventional value of -1.

Leptons

Leptons (ψ_l) are fermions without a color charge and so, they are not sensitive to the strong force. By contrast to the quarks, the two types of leptons also differ in the interactions to which they are sensitive to. The electron-type group of leptons is composed of the electron (e), the muon (μ) and the tau lepton (τ). They carry an electric charge of -1, thus they interact through the weak and electromagnetic forces. Conversely, the neutrino-type group is composed of electrically-neutral particles, and thus, they can only interact through the weak force[7]. Neutrinos are also divided in three generations, which are named according to their electron family correspondent: electron neutrino (ν_e), muon neutrino (ν_μ) and tau neutrino (ν_τ). The lack of electric charge and their extremely small mass make the neutrinos remarkably elusive particles, very hard to detect and characterize. They have been proved to be massive particles but their masses have not been measured yet and only upper limits for the squared mass differences have been set so far (see Sections 1.1.7 and 1.2.1).

1.1.2 Bosons

Bosons are excited states of the fields that describe the fundamental forces in the SM, for which they act as *carriers* (mediators). The fundamental interactions are the *strong* force, responsible for the nuclear cohesion in atoms; and the *electroweak* force (EW), which, at low energies, breaks into two different interactions: the classical electromagnetic force, responsible for the atom cohesion, and the weak force, responsible for radioactivity and nuclear decay.

Bosons have to obey the canonical commutation relations and they are described by the Bose-Einstein statistics, which means that their spin value is an integer number. In addition, some compound particles with an integer spin (as mesons) can behave effectively as force carriers under certain circumstances.

Two types of boson fields can be defined: **scalar fields**, solution to the Klein-Gordon equation ($-\partial_t^2\phi + \nabla^2\phi = m^2\phi$), which have the form [2]:

$$\phi(x) = \int \frac{d^3p}{(2\pi)^3}\frac{1}{\sqrt{2E_p}}\left(a_{\mathbf{p}}e^{-ipx} + b^\dagger_{\mathbf{p}}e^{ipx}\right) \tag{1.6}$$

and **vectorial fields**, solution to the Proca equation ($\partial_\mu\partial^\nu A^\mu = m^2 A^\mu$) [2]:

$$A_\mu(x) = \int \frac{d^3p}{(2\pi)^3}\frac{1}{\sqrt{2E_p}}\sum_r^3\left(a^r_{\mathbf{p}}\xi^r_\mu(p)e^{-ipx} + b^{r\dagger}_{\mathbf{p}}\xi^{r\star}_\mu(p)e^{ipx}\right) \tag{1.7}$$

where the ξ^r_μ terms represent the possible polarization states, r, of the vector particles.

[7] As the weak force is a chiral interaction, only left-handed neutrinos are able to interact with it. Right-handed neutrinos do not interact with any known quantum force. See Section 1.2.1.

The Yang-Mills theory [6] is a non-abelian gauge field theory based on the internal continuous symmetries of the Special Unitary group of Lie algebra, $SU(N)$. The $SU(N)$ is a group within the Lie algebra of $N \times N$ unitary matrices with determinant 1 and with $N^2 - 1$ generators. The generators represent the different forms in which the boson particles associated with each field can exist. Moreover, since the Noether currents are conserved, each of the continuous symmetries (each interaction) has a conserved quantity associated, a *charge*.

The bosonic fields contribute to the SM lagrangian with several terms: the free propagation, the self-interaction and the interaction with other fields. The free propagation term and the self interaction are usually jointly labelled as the kinematic term, which is described by the strength tensor field $F^a_{\mu\nu}$ of a generic non-abelian bosonic field A^a_μ:

$$F^a_{\mu\nu} \equiv \partial_\mu A^a_\nu - \partial_\nu A^a_\mu + g f^a_{bc} A^b_\mu A^c_\nu \tag{1.8}$$

In this equation, g is the coupling constant, a parameter that measures the strength of the force, related to the charge associated with the field; and f^a_{bc} is the structure constant, a mathematical object in Lie algebra that is defined after the commutator of two generators of the group, in the way: $[T_a, T_b] = i f^c_{ab} T_c$. The cross derivatives correspond to the free propagator, and the last term, which contains two instances of the field, describes its self-interaction.

The contribution of the kinematic term to the lagrangian is, then:

$$\mathcal{L}_{\text{kin}} = -\frac{1}{4} F^a_{\mu\nu} F^{\mu\nu}_a \tag{1.9}$$

In addition to the kinematic term, the gauge fields can interact with other objects, in particular, with the fermion fields. This interaction must conserve the gauge invariance, which states that its dynamics cannot be changed by a infinitesimal rotation of the gauge field, of the form $e^{i\lambda(x)}$. However, the standard derivative does not conserve the invariance for these rotations ($\partial_\mu \psi' \neq \partial_\mu \psi$), as:

$$\psi \to \psi' = e^{i g T_a A^a_\mu} \psi \tag{1.10}$$

$$\partial_\mu \psi \to \partial_\mu \psi' = \partial_\mu \psi + i g T_a A^a_\mu \tag{1.11}$$

In order to recover the gauge invariance, a new differential operator, the *covariant derivative*, has to be defined, following the rules of parallel transport from differential geometry and using the gauge field A^a_μ as the connection:

$$\partial_\mu \to D_\mu \equiv \partial_\mu - i g T_a A^a_\mu \tag{1.12}$$

By substituting the derivative of Equation 1.11 by the covariant derivative defined in Equation 1.12, the gauge invariance is recovered in the lagrangian, $D_\mu \psi' = D_\mu \psi$.

The two fundamental forces, the strong force (described by Quantum Chromodynamics) and the Electroweak interaction, are described in the SM using bosonic fields, which give rise to a set of fundamental bosons.

1.1.3 Quantum Chromodynamics

In the context of the Standard Model, the strong force is described by a quantum field theory known as Quantum Chromodynamics (QCD). The charge of the QCD interaction is called *color*, which has three possible values (labelled *red*, *green* and *blue*) and its fundamental boson is the *gluon*, labelled as g^a or simply g. Gluons are massless and electrically neutral gauge bosons which carry a combination of color-anticolor charge, allowing them to self-interact and interact with the quarks. Eight independent color-anticolor combinations are possible, which correspond to eight different types of gluons. The two main properties of the QCD force are *asymptotic freedom* and *confinement*.

Asymptotic freedom is the feature that makes QCD interaction weaker as the energy increases or distance decreases. When interacting with QCD objects, the anti-screening effect[8] created by fluctuating pairs of gluon-antigluon near the object enhances the strength of the charge. Since the *effective* charge seems bigger as the distance grows, the *bare* charge in the short distance has to be smaller. This feature make the quarks and gluons inside the hadrons effectively free particles for short range interactions.

Confinement, on the other hand, is a postulate of QCD driven by observations, stating that color-charged particles cannot exist isolated in nature. Since the fundamental particles, quarks and gluons, are color-charged, only composite particles, the hadrons, can be detected. The mechanism behind this feature is that the QCD force grows with distance and so, when two quarks are separated due to an energetic event, the potential energy due to the QCD binding grows rapidly between the moving quarks, to the point that spontaneously generates pairs of quark-antiquark. These quarks bond with the original ones, maintaining the color neutralness of the observable objects while reducing their kinematic energy. The process repeats successively, transforming the initial kinematic energy of the disrupted quarks in a cascade of hadrons that moves along their initial direction. This feature, which takes the name of *hadronization*, and is crucial in understanding high energy collider physics such as the LHC.

The mathematical description of QCD is a non-abelian Yang-Mills gauge theory that corresponds to the $SU(3)_C$ sector of the SM. The free term of the interaction is described by a strength tensor field $G^a_{\mu\nu}$ constructed from the gluon fields, G^a_μ:

[8] The *screening* effect is the reduction of the measured valued of a central charge due to the influence of nearby objects. This effect is observed in atoms, where orbital electrons reduce the effective charge of the atomic nucleus. On the other hand, when the nearby objects *enhance* the central charge, the effect is labelled as *anti-screening effect*.

$$G^a_{\mu\nu} \equiv \partial_\mu G^a_\nu - \partial_\nu G^a_\mu + g_s f^a_{bc} G^b_\mu G^c_\nu \tag{1.13}$$

where the non-abelian index a refers to the color charge; g_s is the strong coupling constant; and f^a_{bc} is the structure constant, which is the result of the commutator of the generators of the group: $[T_a, T_b] = i f^c_{ab} T_c$. In $SU(3)$, there are eight different generators which take the form of the Gell-Mann matrices divided by two (T_a, defined in Appendix A) and correspond to the number of gluons.

In addition to the kinematic term (which includes the self-interaction), the interaction of QCD with fermions has to be described. However, the $SU(3)$ symmetry group requires the definition of a 3-dimension object, a *triplet* of quarks, ψ_Q, a color-neutral object that is constructed by combining three quarks, each of them carrying a different color charge.

$$\psi_Q \equiv \begin{pmatrix} \psi_{\text{red}} \\ \psi_{\text{green}} \\ \psi_{\text{blue}} \end{pmatrix} \tag{1.14}$$

The triplet of fermions and its derivative transform under the $SU(3)$ group as:

$$\psi_Q \to \psi'_Q = e^{i g_s T_a G^a_\mu} \psi_Q \tag{1.15}$$

$$\partial_\mu \psi_Q \to \partial_\mu \psi'_Q = \partial_\mu \psi_Q + i g_s T_a G^a_\mu \tag{1.16}$$

which leads to the covariant derivative being defined as:

$$\partial_\mu \to D_\mu \equiv \partial_\mu - i g_s T_a G^a_\mu \tag{1.17}$$

Finally, the lagrangian of the QCD interaction, $\mathcal{L}_{\text{QCD}}$, is constructed by the kinematic term of the gluon fields, which includes the free propagator of gluons and their self-interaction; and the fermionic term, with the covariant derivative accounting for the presence of the gluon fields and the fermion masses[9].

$$\mathcal{L}_{\text{QCD}} = i\bar{\psi}_Q \left(\not{D}_\mu - m \right) \psi_Q - \frac{1}{4} G^a_{\mu\nu} G^{\mu\nu}_a \tag{1.18}$$

1.1.4 The Electroweak Theory

In addition to the strong force, two different forces can be observed at low energies: the electromagnetic force, an infinite-range interaction responsible for the cohesion of the atoms; and the weak force, a short-range interaction responsible for various nuclear decays. In the early developments of particle physics, both forces were described as independent interactions, since the observed features of each one were clearly distinct.

[9] Since the QCD interaction respects the chiral symmetry, the mass terms do not violate the gauge symmetry. Thus, they can appear explicitly in the lagrangian.

The electromagnetic interaction was a classical force and the weak force was known as Fermi's interaction [7], an effective short-range mechanism which described the interaction between 4 fermions without a mediator (Figure 1.2 (a)).

This model started to change when the electromagnetic force was successfully quantized by Schwinger, Tomonaga, Feynman and Dyson, which lead to the birth of the Quantum Electrodynamics (QED) [8–14]. The electromagnetic force was described as an interaction of two fermions with the mediation of a boson, the photon (γ). QED was gauge invariant (not dependent on the choice of parameters) and overall, renormalizable (all the infinities in the formulation could be successfully eliminated), hence it could be tested in experiments. These crucial features made the physics community wonder if the gauge symmetry was indeed a fundamental symmetry of nature and so, great efforts were made to describe the other forces in a gauge-invariant formalism. However, the attempts to describe the weak theory respecting the gauge invariant condition failed because of its short range, but also because its quantum description was not renormalizable –the infinities could not be removed.

To overcome this, Schwinger proposed [15] a description of the weak interaction analogue to the electromagnetic force: the weak force would not be a short-range interaction of four fermions but a long-range interaction of two fermions mediated by a charged vector boson, which was called $W^{\pm}$, for Weak (Figure 1.2 (b)). The similarities between QED and the weak force, and the root of the gauge invariance, led to the belief that both interactions could be unified as a single fundamental force. Many attempts were done in the following years with little success, though small advances were achieved. The main one was the idea that the P-symmetry violation (difference in behavior of chiral components), a characteristic of the weak force, could be achieved by a Vector-Axial theory (V-A theory) [16, 17], in which QED would play the vectorial role.

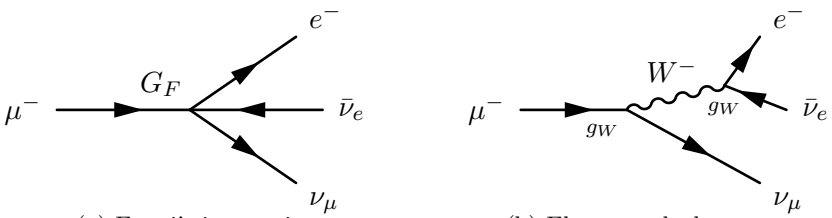

(a) Fermi's interaction (b) Electroweak theory

Figure 1.2: Feynman diagrams for the muon decay as (a) a Fermi's interaction, without a propagator and (b) a Yang-Mills theory mediated by a W^- boson. The strength of the interaction vertex is proportional to G_F in (a) and to g_W^2 in (b).

In 1961, Sheldon Glashow proposed a $SU(2) \times U(1)$ Yang-Mills theory [18] to unify both interactions. The proposal defined two fields, B_μ and W_μ^a, with four fundamental bosons, B and W^i. The observable features, including the vector bosons $W^{\pm}$ and Z, were not fundamental, but a linear combination of both fields which a mixing angle, θ_W. Nonetheless, the model had several crucial flaws and was ignored at the time.

Firstly, it predicted the existence of new phenomena for which there was no evidence at the time: neutral conserving-flavor currents mediated by a neutral massive vector boson different from the photon. Secondly, its renormalizability, the main concern of QFT theories, was unclear. And finally, and more important, the experimental results showed that the weak interactions had an extremely short range, which was strong evidence of the existence of a massive, charged, weak boson. This was a problem because chiral Yang-Mills theories, being gauge invariant, did not allow the addition of a mass term. Three years after Glashow's paper, Abdus Salam and John Ward arrived to the same model independently [19], but neither they had answered the problem of the mediator mass.

The solution came from a different field: the physics of condensed matter. The work in superconductivity had led to the establishment of the Goldstone theorem [20], that stated that scalar bosons (Goldstone bosons) arise from the breaking of global continuous symmetries. If the symmetry is *spontaneously* broken (by picking a particular gauge choice), massless Goldstone bosons arise. However, in some circumstances, these predicted bosons had not been observed. The models trying to employ the spontaneous symmetry breaking (SSB) encountered the same problem.

The idea was given by Philip Anderson, who pointed out [21] in 1963 that in a degenerated state within a gauge potential, the massless Goldstone bosons could combine with the massless propagators of the gauge field to become massive bosons. The Goldstone bosons would not appear as observables and the massless vector bosons of the field would acquire a mass, solving both issues. In superconductivity, this happens when photons interact with the electromagnetic potential in a superconducting electron gas: the massless photons become massive plasmons, while no Goldstone boson appears. He pointed out that this was an exception of the Goldstone theorem[10] and that it could be applied to particle physics, if it was implemented in a relativistic frame.

In the summer of 1964, three groups of physicist developed independently a mechanism to give mass to gauge bosons in the QFT framework, based on the SSB, by adding a new scalar field: François Englert and Robert Brout in August 1964 [22], Peter Higgs in October 1964 [23, 24] and Gerald Guralnik, Carl Hagen and Tom Kibble in November 1964 [25], giving birth to the Brout-Englert-Higgs mechanism[11], more commonly known by the name of the latter, the **Higgs mechanism**. Peter Higgs was the only one to remark explicitly a consequence of the addition of the new scalar field: a new scalar boson could be observed, which could be used as an experimental test for the mechanism. In a latter paper [27], he also developed the dynamics of this new boson. In 1967, Kibble,

[10] Actually, the feature he mentioned as an exception is the application of Goldstone theorem with local symmetries, not global ones.

[11] Also known as the ABEGHHK'tH mechanism, for Anderson, Brout, Englert, Guralnik, Hagen, Higgs, Kibble and 't Hooft, as named by Peter Higgs [26].

who had also continued working in the mechanism, adapting it to the $SU(2)$ formalism, proved that one of the EW bosons would remain massless [28].

Later that same year, Steven Weinberg united the SSB mechanism and Glashow's $SU(2) \times U(1)$ theory, having as result *A model of Leptons* [29], the paper where the **Electroweak theory** was introduced. The model finally had an explanation for the masses of all the gauge bosons and predicted several features, which could be tested experimentally. However, it still lacked a crucial point: the renormalizability of the theory. This last step was provided by Gerard 't Hooft in 1972 [30, 31], who proved that all Yang-Mills theories are renormalizable.

Only after the work of 't Hooft, QFT, the SSB, the Higgs mechanism and the model of Electroweak interactions drew the attention of the physics community. The first success came shortly after, when the Gargamelle experiment at CERN proved the existence of one of the EWT predictions [32, 33], observing elastic collisions of neutrinos with electrons and hadrons. In 1979, Glashow, Weinberg and Salam shared the 1979 Nobel Prize for the Electroweak theory. In 1999, 't Hooft and his supervisor, Martinus J.G. Veltman, were also awarded the Nobel Prize in Physics.

However, the EWT still lacked direct experimental confirmation of the existence of the vector and Higgs bosons, which had to wait until the development of technologies to reach the required energy. The $W^{\pm}$ bosons were first observed in 1982 in the UA1 [34] and UA2 [35] experiments of the Super Proton Synchrotron (SPS) at CERN, and the Z boson, in the same experiments [36, 37], in 1983. The confirmation of the Higgs mechanism had to wait for newer generations of particle colliders: the Large Electron-Positron Collider (LEP, 1989-2000) at CERN; and the Tevatron (1987-2011) at Fermilab, were only able to set up exclusion limits [38, 39] on the mass of the Higgs boson. Finally, in 2012, the LHC experiments, ATLAS [40] and CMS [41], independently observed a massive scalar neutral particle, compatible with the Higgs boson (Figure 1.3), which gave the 2013 Nobel Prize in Physics to F. Englert and P. Higgs.

It is fundamental for this thesis to notice that the Higgs mechanism also addresses another significant issue of the SM: the masses of the fermions, as also developed in Weinberg's paper [29]. In the same way as the weak bosons, the masses of the fermions could not be described in the SM lagrangian as explicit mass terms, since that approach would break the gauge invariance. However, when introducing the SSB mechanism in the interaction between the Higgs field and the fermions (Yukawa interaction), fermionic mass terms arise, the value of which is proportional to the coupling of the fermion to the Higgs boson.

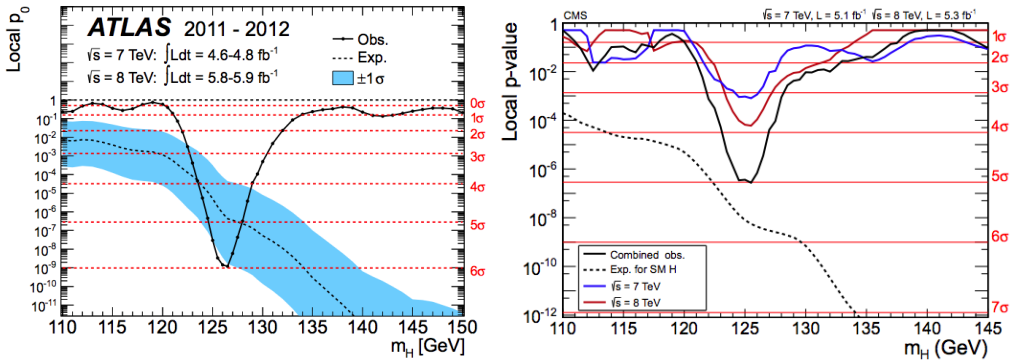

(a) ATLAS (b) CMS

Figure 1.3: Statistical significance plots of the 2012 discovery of the Higgs boson. The figures show a $5\,\sigma$ excess compatible with a scalar neutral boson with spin $s \neq 1$ for the (a) ATLAS Experiment [40] and (b) CMS Experiment [41].

Mathematical formulation of the Electroweak Theory

The Electroweak interaction has distinct features such as the chiral asymmetry, the fact that the electromagnetic and weak forces are distinct at low energies and the fact that its gauge bosons are massive particles. The EWT corresponds to the $SU(2)_L \times U(1)_Y$ sector of the SM and is formulated using two different fields (W^a_μ for $SU(2)_L$ and B_μ for $U(1)_Y$, respectively), along with their associated bosons and charges. At low energies, the Higgs field breaks the unification using the spontaneous symmetry breaking mechanism, thus recovering the electrodynamic symmetry $U(1)_Q$ of the electromagnetic field (A_μ) and the observable bosons (the massless photon γ and the massive $W^\pm$ and Z).

$$\underbrace{SU(2)_L \times U(1)_Y}_{\text{EWT}} \xrightarrow{SSB} \underbrace{U(1)_Q}_{\text{EM}} \tag{1.19}$$

The $SU(2)_L$ sector is described by the strength tensor field $W^a_{\mu\nu}$, constructed from the non-abelian field W^a_μ:

$$W^a_{\mu\nu} \equiv \partial_\mu W^a_\nu - \partial_\nu W^a_\mu + g_W f^a_{bc} W^b_\mu A^c_\nu \tag{1.20}$$

where the parameter g_W corresponds to the coupling constant of the W^a_μ field and the structure constant f^a_{bc} is defined after the commutator of the generators of $SU(2)$, which take the form of the Pauli matrices divided by two, (τ_a, defined in Appendix A) in the way $[\tau_a, \tau_b] = i f^c_{ab} \tau_c$. This field is the responsible for the chiral asymmetry and thus, it only interacts with left-handed fermions, ψ_L, defined in Equation 1.4. The associated charge of this field is the third component of the weak isospin (I_3) and the three generators of $SU(2)$ correspond to the fundamental bosons W^i, where $i = \{1, 2, 3\}$. The third term, which contains g_W, f^a_{bc} and two instances of W^a_μ, represents the self-coupling of the field.

The $U(1)_Y$ sector is described by the strength tensor field $B_{\mu\nu}$, constructed with the abelian field B_μ:

$$B_{\mu\nu} \equiv \partial_\mu B_\nu - \partial_\nu B_\mu \tag{1.21}$$

The coupling constant associated to this field is g_B, the interaction is mediated by only one boson, B, and the charge associated is the weak hypercharge (Y), commonly abbreviated simply as *hypercharge*. The hypercharge is defined as a combination of the electromagnetic charge (Q) and weak isospin (I_3), with the relation:

$$Y \equiv 2\,(Q - I_3) \tag{1.22}$$

The kinematic term of the EWT, which includes the free propagator of both fields and the self-coupling of the non-abelian W^a_μ, is constructed as:

$$\mathcal{L}_{\text{EW-kin}} = -\frac{1}{4} W^a_{\mu\nu} W^{\mu\nu}_a - \frac{1}{4} B^{\mu\nu} B_{\mu\nu} \tag{1.23}$$

The interaction with fermions depends on the chiral properties and the structure of the symmetry group, hence it is different for each field. This different behavior is represented by the values of the charges associated to each field, which are summarized in Table 1.2.

Interaction		**Left chirality - ψ_L**				**Right chirality - ψ_R**			
		Quarks		Leptons		Quarks		Leptons	
Charge	Group	u-type	d-type	ν-type	e-type	u-type	d-type	ν-type	e-type
Weak Isospin (I_3)	$SU(2)_L$	+1/2	-1/2	+1/2	-1/2	0	0	0	0
Hypercharge (Y)	$U(1)_Y$	+1/3	+1/3	-1	-1	+4/3	-2/3	0	-2
EM Charge (Q)	$U(1)_Q$	+2/3	-1/3	0	-1	+2/3	-1/3	0	-1

Table 1.2: Values of the electroweak charges (weak isospin I_3, hypercharge Y, electromagnetic charge Q) for the different fermions, according to their type and chirality.

Regarding the chiral properties, the B_μ field interacts with fermions of both chiralities indistinctly, while the W^a_μ field only interacts with left-handed fermions. In other words, left-handed fermions (ψ_L) are able to interact with both fields, B_μ and W^a_μ, while right-handed fermions (ψ_R) are only sensitive to B_μ. As can be observed in Table 1.2, the right-handed fermions are neutral for the weak isospin I_3 and thus, to the W^a_μ field. Moreover, the right-handed neutrino particles are also neutral for the hypercharge, making them insensitive to B_μ too.

Regarding the structure of the different symmetry groups, the W_μ^a field, associated to $SU(2)_L$, requires that the fermions are constructed using a $SU(2)$ doublet of isospin, a two-dimension object whose components have opposite weak isospin and same hypercharge. Hence, the doublet transforms as a whole under $U(1)_Y$ but each component is different for $SU(2)$. Considering also the chiral requirements –only left-handed fermions transform under $SU(2)$– the doublet has to be composed of left-handed fermions: an u-type and its respective d-type of the same generation. Under these conditions, six doublets of left-handed fermions can be defined:

$$L_q \equiv P_L \begin{pmatrix} \psi_u \\ \psi_d \end{pmatrix} = \begin{pmatrix} \psi_u \\ \psi_d \end{pmatrix}_L = \left\{ \begin{pmatrix} u \\ d \end{pmatrix}_L, \begin{pmatrix} c \\ s \end{pmatrix}_L, \begin{pmatrix} t \\ b \end{pmatrix}_L \right\} \tag{1.24}$$

$$L_l \equiv P_L \begin{pmatrix} \psi_\nu \\ \psi_e \end{pmatrix} = \begin{pmatrix} \psi_\nu \\ \psi_e \end{pmatrix}_L = \left\{ \begin{pmatrix} \nu_e \\ e \end{pmatrix}_L, \begin{pmatrix} \nu_\mu \\ \mu \end{pmatrix}_L, \begin{pmatrix} \nu_\tau \\ \tau \end{pmatrix}_L \right\}$$

The right-handed fermions (except neutrinos) only transform under $U(1)$ and thus, they have to be defined using a $U(1)$ object, a singlet. Nine singlets need to be defined[12]:

$$R \equiv P_R\, \psi = \psi_R = \begin{cases} u_R,\ c_R,\ t_R,\ d_R,\ s_R,\ b_R \\ e_R,\ \mu_R,\ \tau_R \end{cases} \tag{1.25}$$

The transformation of the doublets and singlets of fermions, and their derivatives, under the EW group is:

$$\text{for } L: \qquad \partial_\mu L \to \partial_\mu L' = \partial_\mu L + i g_B Y B_\mu + i g_W \tau_a W_\mu^a \tag{1.26}$$

$$\text{for } R: \qquad \partial_\mu R \to \partial_\mu R' = \partial_\mu R + i g_B Y B_\mu \tag{1.27}$$

which makes the covariant derivative be defined as:

$$\text{for } L: \qquad \partial_\mu \to D_\mu \equiv \partial_\mu - i g_B Y B_\mu - i g_W \tau_a W_\mu^a \tag{1.28}$$

$$\text{for } R: \qquad \partial_\mu \to D_\mu \equiv \partial_\mu - i g_B Y B_\mu \tag{1.29}$$

The lagrangian of the Electroweak interaction ($\mathcal{L}_{\text{EW}}$), before the symmetry breaking, is constructed using the kinematic terms from both fields (Equation 1.23) and the interaction between the fields and the fermions, which is described using the chiral doublet-singlet formulation.

$$\mathcal{L}_{\text{EW}} = \underbrace{i\bar{L}\left(\not{D}_\mu\right) L + i\bar{R}\left(\not{D}_\mu\right) R}_{i\bar{\psi}\not{D}_\mu\psi} - \frac{1}{4} W_{\mu\nu}^a W_a^{\mu\nu} - \frac{1}{4} B_{\mu\nu} B^{\mu\nu} \tag{1.30}$$

[12] Since only left-handed neutrinos interact, there is no need for right-handed neutrinos (ν_R) in the theory. However, the theory seems to be incomplete, see Sections 1.1.7 and 1.2.1.

1.1.5 The Higgs mechanism

As described in previous section, the observable gauge bosons, $W^{\pm}$ and Z, are massive and thus, their masses have to be included in the lagrangian. Since the EW theory is not chiral invariant, the mass terms could not be included explicitly, as they would break the gauge invariance of the SM lagrangian. The solution [23] is the addition of a new complex scalar field ϕ, commonly named the *Higgs field*, with the form of a $SU(2)$ doublet:

$$\phi(x) = \frac{1}{\sqrt{2}} \begin{pmatrix} \phi^{(+)} \\ \phi^{(0)} \end{pmatrix} = \frac{1}{\sqrt{2}} \begin{pmatrix} \phi_3 + i\,\phi_4 \\ \phi_1 + i\,\phi_2 \end{pmatrix} \tag{1.31}$$

The lagrangian associated with this field is composed of the potential created by the field ($V(\phi)$) and the kinematic term ($\left|\partial_\mu \phi\right|^2$), which includes the free propagator of the field and the interaction with the weak fields. Since this interaction breaks the gauge invariance of the Higgs derivative, the covariant derivative has to be defined as:

$$\partial_\mu \rightarrow D_\mu \equiv \partial_\mu - i g_W \tau_a W_\mu^a - i g_B Y B_\mu \tag{1.32}$$

which leads to the Higgs mechanism lagrangian, $\mathcal{L}_{\mathrm{H}}$:

$$\mathcal{L}_H = \left|D_\mu \phi\right|^2 - V(\phi) \tag{1.33}$$

The potential energy of the field, $V(\phi)$, is constructed ad-hoc to make use of the mechanism of spontaneous symmetry breaking, which requires a degenerated vacuum state and a local maximum. These conditions can be achieved by a certain type of function, analogue to the bi-quadratic function ($y = x^4 - x^2$), whose shape in the plane (Figure 1.4) shows the required properties.

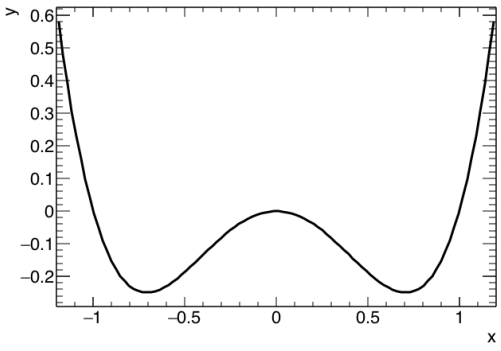

Figure 1.4: Graphic representation of the bi-quadratic function $y = x^4 - x^2$ in the range $[-1.5, 1.5]$. The function has a local maximum for $\phi = 0$ and two minima, located at $\pm\frac{1}{\sqrt{2}}$.

The simplest way in which the Higgs potential can be constructed is:

$$V(\phi) \equiv \lambda(\phi^\dagger \phi)^2 - \mu^2(\phi^\dagger \phi) \tag{1.34}$$

In this definition, the potential depends of two parameters: λ, for the quartic term; and μ^2, for the quadratic term. The λ parameter is defined positive[13], as the potential has to be bounded from below (i.e. when $\phi \to +\infty$, $V(\phi) \to +\infty$). The sign of the quadratic term, on the other hand, has to be defined negative for the function to develop the minima. With a negative sign[14] for μ^2, the potential acquires the *Mexican hat* shape, shown in Figure 1.5.

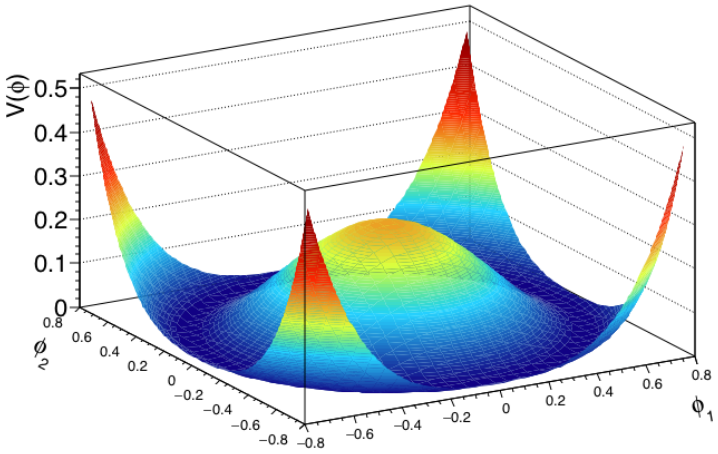

Figure 1.5: Graphic representation of the Higgs potential function, $V(\phi)$, showing the local maximum at $\phi = 0$ and the degenerated minima at $|\phi| = 1$.

In order to expand the Higgs field, the real ground state of the field has to be found. The ground state of a field is the expected value of the field in the vacuum (vev) and corresponds to the minimum of the potential, which is usually zero. For the Higgs field, however, this value (denoted by v) depends on the relation between the μ^2 and λ parameters, as:

$$\langle\phi\rangle_0 = \frac{1}{\sqrt{2}}\sqrt{\frac{\mu^2}{\lambda}} \equiv \frac{v}{\sqrt{2}} \tag{1.35}$$

Physically, this feature means that the vacuum does not have a null Higgs field, but some residual potential energy remains. The transition between the vacuum and the Higgs minimum is the responsible for the spontaneous symmetry breaking mechanism, which results in massive weak bosons.

Since the lagrangian is gauge invariant, the Higgs field can be described from its minimum without loss of generality by applying a gauge transformation, which conserves

[13]The simplest way to make the potential display a local maximum requires a positive λ and a negative value of μ^2. However, λ and μ^2 relate to the minimum of the field and thus, their value can be constrained at higher orders by measuring the Yukawa couplings of Higgs boson to fermions and the masses of the vector and Higgs bosons. It could happen that the measured value does not fit the required conditions, which would lead to some fundamental problems (see Section 1.2.2).

[14]This convention assumes $\mu^2 > 0$ with $\mu \in \mathbb{R}$, and lets the negative sign of the quadratic term be established by functionality, by analogy with the bi-quadratic function. Other conventions obtain the sign by defining a complex μ^2 parameter: $\mu^2 < 0$ with $\mu \equiv i\epsilon$

the number of degrees of freedom. For this, it is useful to describe the field (Equation 1.31) using a exponential decomposition [42]:

$$\phi(x) = \frac{1}{\sqrt{2}} e^{i\tau_a \theta^a(x)/f} \begin{pmatrix} 0 \\ \rho(x) \end{pmatrix} \tag{1.36}$$

where $\theta^a(x)$ and $\rho(x)$ are real fields, τ_a corresponds to the generators of $SU(2)$ and f is a unit normalization constant, which will be identified with the scale of the system, v [43]. θ^a contains three of the four degrees of freedom of the Higgs doublet, while ρ conserves the remaining one, in a sort of *module* of the field.

The vacuum symmetry can be broken now by expanding the Higgs field in a particular set of coordinates. In order to get physical observables, this position has to be the minimum of the field, v. Thus, a new real field h can be defined by a translation:

$$h(x) \equiv \rho(x) - \langle\phi\rangle_0 = \rho(x) - v \tag{1.37}$$

However, as the minimum is degenerated, there are infinite points of the space satisfying this condition. By choosing one particular point to develop the Higgs field, the symmetry is broken. The easiest way to do so is the *unitary gauge*, in which the degrees of freedom are minimized. For the Higgs field, it means setting all θ^a to 0 (which is analogous to setting $\phi_3 = \phi_4 = \phi_2 = 0$ in the cartesian definition). After the gauge fixing and the translation to the minimum, the Higgs field becomes [44]:

$$\phi(x) = \frac{1}{\sqrt{2}} \begin{pmatrix} 0 \\ v + h(x) \end{pmatrix} \tag{1.38}$$

Developing the Higgs lagrangian (Equation 1.33) using this form for the Higgs field results in mass terms for the gauge bosons [4]:

$$\begin{aligned} \mathcal{L}_H = & \frac{1}{2} \left(\partial_\mu h\right) \left(\partial^\mu h\right) + \frac{1}{2} \left(2\mu^2\right) h^2 \\ & + \frac{1}{2} \left(\frac{g_W^2 v^2}{4}\right) \left(W_\mu^1 W^{1\mu} + W_\mu^2 W^{2\mu}\right) \\ & + \frac{1}{8} v^2 \left(g_W W_\mu^3 - g_B B_\mu\right) \left(g_W W^{3\mu} - g_B B^\mu\right) \\ & + \mathcal{O}(h^2) \end{aligned} \tag{1.39}$$

where the term $\mathcal{O}(3)$ refers to the higher orders of the lagrangian, which contains the couplings of the Higgs with the vector bosons and the self-coupling of the Higgs boson.

In QFT, the quadratic term is interpreted as the mass term of the particle associated to the field. However, in Equation 1.39, these mass terms are not linearly independent, thus

they cannot be true observables of the interaction. In order to obtain the physical bosons, the fields have to be rewritten in a different representation, combining the fundamental ones in such way that their mass terms are totally independent. The new fields[15] A_μ, W_μ and Z_μ, relate to the fundamental ones W^i_μ and B_μ, as:

$$W^\pm_\mu = \frac{1}{\sqrt{2}}\left(W^1_\mu \mp i\, W^2_\mu\right) \tag{1.40}$$

$$Z_\mu = \cos(\theta_{W_\mu})\, W^3 - \sin(\theta_{W_\mu}) B_\mu \tag{1.41}$$

$$A_\mu = \cos(\theta_{W_\mu})\, B \quad + \sin(\theta_{W_\mu}) W^3_\mu \tag{1.42}$$

where the parameter θ_W is the *Weinberg angle* [18], that is defined in terms of the coupling constants of the fundamental fields:

$$\tan\theta_W \equiv \frac{g_B}{g_W} \tag{1.43}$$

The coupling constants, in turn, are related to the electric charge (e) as:

$$\frac{g_W\, g_B}{\sqrt{g_W^2 + g_B^2}} \equiv e \tag{1.44}$$

After the rotation, Equation 1.39 becomes:

$$\begin{aligned}\mathcal{L}_H(\mathcal{O}(h^2)) = {} & \frac{1}{2}\left(\partial_\mu h\right)\left(\partial^\mu h\right) + \frac{1}{2}\underbrace{\left(2\mu^2\right)}_{m_H^2} h^2 \\ & + \frac{1}{2}\underbrace{\left(\frac{g_W^2 v^2}{4}\right)}_{m_{W+}^2} W^+_\mu W^{+\mu} + \frac{1}{2}\underbrace{\left(\frac{g_W^2 v^2}{4}\right)}_{m_{W-}^2} W^-_\mu W^{-\mu} \\ & + \frac{1}{2}\underbrace{\left(\frac{g_W^2 v^2}{4\cdot\cos\theta_W}\right)}_{m_Z^2} Z_\mu Z^\mu + \underbrace{0}_{m_\gamma^2}\cdot A_\mu A^\mu\end{aligned} \tag{1.45}$$

In this representation, each of the new fields has an independent mass term, which is an observable physical object: a massive boson. For the electromagnetic field, A_μ, no mass term remains[16], and so, the boson associated with the A_μ field, the photon (γ), is massless. Hence, by means of a non-zero Higgs field, the masses of the different bosons, $m_{W^\pm}$, m_Z, m_γ and m_H arise in a gauge invariant lagrangian.

The value of the masses of the different gauge bosons matched with their theoretical expectations [34–37], which had been obtained from the Fermi constant (G_F) and the

[15] The electromagnetic field and its associated boson, the photon, are denoted by A_μ, specially in the lagrangian formulation. However, due to historic reasons, when the photon is mentioned as a standalone particle, it is usually labelled as γ.

[16] As one of the degrees of freedom of the Higgs field is used for the own Higgs particle, one of the generators remains unbroken, which results in a massless boson, the photon.

EW coupling constants, g_W and g_B. However, no prediction could be obtained for the Higgs boson mass as its value depends solely on one free parameter of the theory, μ^2 and hence, it could only be measured experimentally. After the Higgs boson was discovered, the value of its mass was set[17] at $m_H \sim 125\,\text{GeV}$.

The measured values of the different masses and the EWT parameters v and θ_W, are shown below [3]:

$$\sin^2\theta_W = \frac{g_B^2}{g_W^2 + g_B^2} = 0.23129(5) \pm 0.000022$$
$$v = \left(\sqrt{\sqrt{2}\,G_F}\right)^{-1} = (246.2196 \pm 0.0005)\,\text{GeV}$$

$$m_\gamma = 0$$
$$m_W \equiv \frac{v \cdot g_W}{2} = (80.385 \pm 0.015)\,\text{GeV}$$
$$m_Z \equiv \frac{v}{2}\sqrt{g_W^2 + {g_B}^2} = (91.1876 \pm 0.0021)\,\text{GeV}$$

$$m_H \equiv 2\mu^2 = \sqrt{2\lambda v^2} = 125.09 \pm 0.21\,(\text{stat.}) \pm 0.11\,(\text{syst.})\,\text{GeV} \tag{1.46}$$

1.1.6 The Yukawa interaction

In addition to the EW fields, the Higgs field can also interact with the fermions. The interaction between a scalar field (ϕ) and a Dirac field (ψ) –which is called *Yukawa interaction*– results in the appearance of the mass terms of the fermion particles in the lagrangian, in a way such that the gauge invariance is preserved.

The description of the masses of the fermions as Dirac masses (Equation 1.47) is not allowed in the EW lagrangian since they contain crossed $\psi_R - \psi_L$ terms which would break the gauge invariance due to the chiral asymmetry of the EWT.

$$\mathcal{L}_{\text{mass}} = -m\,\bar{\psi}\psi = -m\,(\bar{\psi}_L\psi_R + \bar{\psi}_R\psi_L) \tag{1.47}$$

The Yukawa interaction, formulated in the $SU(2)_L \times U(1)_Y$ framework, gives a mechanism to derive the mass terms in a gauge invariant way (Equation 1.48) by adding the scalar Higgs doublet.

$$\mathcal{L}_{\text{Y}} = -i\,\lambda_f\,\bar{L}\,\phi\,R_f - i\,\lambda_f\,\bar{R_f}\,\phi\,L = -i\,\lambda_f\,(\bar{L}\phi R_f + \bar{R_f}\phi L) \tag{1.48}$$

where the $SU(2)$ formulation of doublets and singlets is used. The λ_f terms are the coupling constants of the Higgs field to the respective fermion R_f.

[17] This value comes from the combination of the Higgs boson mass measurement of the ATLAS and CMS experiments [3, 45], yielding a value for the mass of the observed particle of $m_H = 125.09 \pm 0.21(\text{stat.}) \pm 0.11\ (\text{syst})\,\text{GeV}$.

If the symmetry of the Higgs scalar doublet is spontaneously broken in the form of Equation 1.38, a mass term for the down-type component of the fermion doublet appears. This would work for the lepton sector, as the neutrino-type is considered to be massless in the SM lagrangian, but it fails for up-type quarks, which also require a mass.

However, the Higgs field can be written in a second representation, the *charge-conjugated* of the $SU(2)$ framework, ϕ^c:

$$\phi^c \equiv i\sigma_2\phi^* = \begin{pmatrix} \phi^{(0)*} \\ -\phi^{(-)} \end{pmatrix} \xrightarrow{SSB} \frac{1}{\sqrt{2}} \begin{pmatrix} -(v+h(x)) \\ 0 \end{pmatrix} \tag{1.49}$$

where the σ_2 is the second Pauli matrix, generator of $SU(2)$. The Higgs field written in this form has the symmetry-breaking term as the upper component of the doublet and thus, it couples with the up-type quarks to provide them with a mass term.

Hence, the Yukawa lagrangian becomes:

$$\begin{aligned} \mathcal{L}_{\mathrm{Y}} &= -i\,\lambda_e\,(\bar{\nu}\;\bar{e})_L\,\phi\,e_R \;- i\,\lambda_d\,\left(\bar{u}\;\bar{d}\right)_L\phi\,d_R \;- i\,\lambda_u\,\left(\bar{u}\;\bar{d}\right)_L\phi^c\,u_R \\ &= -i\,\lambda_f\,(\bar{L}\phi R_f + \bar{R}\phi L) - i\,\lambda_f\,(\bar{L}\phi^c R_f + \bar{R}\phi^c L) \\ &= -i\,\lambda_f\,(\bar{L}\phi R_f + \bar{L}\phi^c R_f) + h.c. \end{aligned} \tag{1.50}$$

where the *h.c.* term refers to the *hermitian conjugated* and it is used to simplify the notation of the equation. In this case, it avoids the explicit formulation of the symmetrical terms $\bar{R}\cdot L$. After picking the gauge, by arranging the chiralities, the lagrangian simplifies to:

$$\mathcal{L}_{\mathrm{Y}} = \frac{-\lambda_f\,(v+h)}{\sqrt{2}}\,\left(\bar{\psi}_R\,\psi_L + \psi_L\,\bar{\psi}_R\right) \tag{1.51}$$

and thus, the mass terms of the fermions are defined as:

$$m_f \equiv \lambda_f \frac{v}{\sqrt{2}} \tag{1.52}$$

Equation 1.52 leads to the conclusion that the strength of the coupling of the Higgs field to a particular fermion is proportional to the mass of the fermion ($\lambda_f \propto m_f$), i.e. heavier fermions have stronger coupling to the Higgs boson.

The measurement the coupling of Higgs boson to the τ lepton and its comparison to the SM prediction are the main goals of the analysis described in Chapter 6.

1.1.7 Flavor mixing

A fundamental step has been omitted in the development of Equation 1.50. Regarding the quarks, in that equation, the interactions do not occur uniquely between the same type of quarks (e.g. $\bar{d}d$) but mixed-flavor interactions happen too (e.g. $\bar{d}c$). The λ_f parameters are, in fact, λ_{ij}, where $i = \{u, c, t\}$ and $j = \{d, s, b\}$. The coupling parameters of the

different couplings can be combined to form a 3×3 matrix that, due to the mixed terms, is not diagonal.

This matrix is called the *mass basis* of the SM and it can be diagonalized to determine the mass-eigenstates, which are the truly observables of the theory, in comparison to the flavor-eigenstates, which are the fundamental basis (*flavor basis*) of the EW interaction. When the mass matrix is diagonalized, Equation 1.50 can be obtained, but with modified fermion states, $\widetilde{\psi}_f$, which are a linear combination of the flavor ones.

If the whole EW interaction is rewritten as a matrix in terms of the mass-eigenstates, $\widetilde{\psi}_f$, the interaction loses its diagonality, thus allowing interactions where generation, in addition to type, can be changed. The matrix of the coupling constants of the EWT for the quark sector is called the Cabibbo-Kobayashi-Maskawa (CKM matrix) [46, 47].

A relevant feature of the CKM matrix is that it can be parametrized using only three angles and a complex phase. The appearance of this phase results in the violation of the charge and parity symmetries of the weak interactions (CP-symmetry), as the interaction parameters would not be invariant under a conjugation of the matrix. Although this is one of the sources of CP-violation in the SM, its small effect cannot fully account for the observed amount of CP-violation in nature.

An analogous matrix could be constructed for leptons, but since these mixings are proportional to the mass of the particles, due to the extremely low mass of the neutrino particles, the lepton mixing is greatly suppressed. However, neutrinos experience an additional process with a similar structure, although its origin is completely different.

Since the neutrinos are neutral for the electromagnetic and QCD interactions, their wave functions can exist in a superpositon state for long periods. In this state, the neutrinos experience an effect called *oscillation*, where the particle flavor is alternating between the three possible generations [48, 49]. Thus, in the same way as the quarks, the observable mass-eigenstates (ν_1, ν_2 and ν_3) are composed of a linear combination of the flavor-eigenstates (ν_e, ν_μ and ν_τ), a feature that was discovered using neutrinos produced in the Sun [50] and atmospheric reactions [51]. In both cases, the number of observed neutrinos of one specific flavor was smaller than expected, due to the fact that some of them changed their flavor to the other generations.

The parameters that regulate the oscillations between the generations are combined in the Pontecorvo-Maki-Nakagawa-Sakata matrix (PMNS matrix). An important consequence of this effect is that only massive particles can oscillate and thus, even though their masses have not been measured yet, the neutrinos must be massive particles. The relative strength of the couplings of both matrices, CKM and PMNS, is shown graphically in Figure 1.6 while the complete values are described in Appendix A.

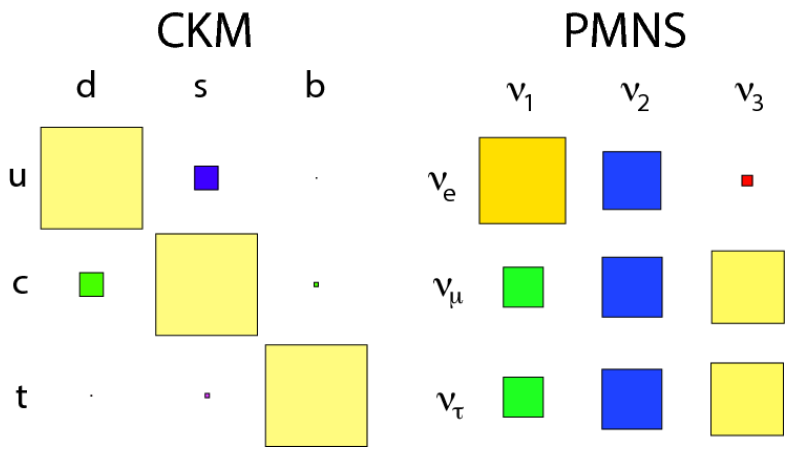

Figure 1.6: Relative sizes of (a) the CKM matrix elements for quark mixing and (b) the PMNS matrix (right) for neutrino mixing. The area of the squares represents the square of the matrix elements [52].

1.1.8 The Standard Model lagrangian

The complete SM lagrangian is written by combining the different sectors described in the previous sections (Equations 1.18, 1.30, 1.33 and 1.50). The formulation is composed of the kinematic terms of the different bosonic fields (the gluon field and the two fields of EWT); the kinematic term of the fermion fields, corrected by its interaction with the bosonic fields in the form of the covariant derivative; the Higgs mechanism, composed of its covariant kinematic term and the Higgs potential; and finally, the Yukawa interaction of fermions with the Higgs boson. In addition, the experimental value of the nineteen free parameters of the SM, shown in Table 1.3.

$$\mathcal{L}_{\text{SM}} = \underbrace{-\frac{1}{4}F^a_{\mu\nu}F^{\mu\nu}_a}_{\text{Free bosons}} + \underbrace{i\,\psi \not{D} \psi}_{\text{Fermion term}} \underbrace{+ i\,\lambda_f\left(\bar{L}\phi R_f + \bar{L}\phi^c R_f\right) + h.c.}_{\text{Yukawa Interaction}} + \underbrace{\left|D_\mu \phi\right|^2 - V\left(\phi\right)}_{\text{Higgs mechanism}} \tag{1.53}$$

where:

$$\begin{aligned} F^a_{\mu\nu}F^{\mu\nu}_a &\equiv G^a_{\mu\nu}G^{\mu\nu}_a + W^a_{\mu\nu}W^{\mu\nu}_a + B_{\mu\nu}B^{\mu\nu} \\ i\bar{\psi}\not{D}\psi &\equiv i\bar{\psi}\gamma^\mu\left(\partial_\mu - g_s T_a G^a_\mu - g_W T_a W^a_\mu - g_B Y B_\mu\right)\psi \\ D_\mu\phi &\equiv \left(\partial_\mu - ig_W T_a W^a_\mu - ig_B B_\mu\right)\phi \\ V(\phi) &\equiv \lambda(\phi^\dagger\phi)^2 - \mu^2(\phi^\dagger\phi) \end{aligned}$$

Name	**Symbol**	**Value**	
Up quark mass	m_u	$2.2^{+0.6}_{-0.4}$	MeV
Charm quark mass	m_c	1.27 ± 0.03	GeV
Top quark mass	m_t	173.1 ± 0.6	GeV
Down quark mass	m_d	$4.7^{+0.5}_{-0.4}$	MeV
Strange quark mass	m_s	96^{+8}_{-4}	MeV
Bottom quark mass	m_b	$4.18^{+0.04}_{-0.03}$	GeV
Electron mass	m_e	$0.511 \pm (0.31 \cdot 10^{-8})$	MeV
Muon mass	m_μ	$105.66 \pm (0.24 \cdot 10^{-5})$	MeV
Tau mass	m_τ	1776.86 ± 0.12	MeV
CKM I-II mixing angle	θ_{12}	$(13.01 \pm 0.03)^\circ$	
CKM II-III mixing angle	θ_{23}	$(2.35 \pm 0.09)^\circ$	
CKM I-III mixing angle	θ_{13}	$(0.20 \pm 0.04)^\circ$	
CKM CP-violating phase	δ_{CKM}	$(70 \pm 3)^\circ$	
$U(1)_Y$ gauge coupling	g_B	0.34970 ± 0.00019	
$SU(2)_L$ gauge coupling	g_W	0.65295 ± 0.00012	
$SU(3)_C$ gauge coupling	$\alpha_s(m_Z)$	0.1182 ± 0.0012	
QCD vacuum angle	θ_{QCD}	$< 10^{-10}$	~ 0
Higgs v.e.v.	v	$246 \pm (6 \cdot 10^{-5})$	GeV
Higgs boson mass	m_H	125.09 ± 0.24	GeV

Table 1.3: Experimental value of the 19 free parameters of the Standard Model [3].

1.2 Current issues with the Standard Model

The SM is an impressive breakthrough in particle physics. Not only it provides a natural order for the known particles (from simple electrons to complex hadrons), but it was also able to predict the existence of unknown particles, such as the charm quark and the $W^\pm$, Z and Higgs bosons. Furthermore, the accuracy in the precision of the value of some interaction parameters is astonishing: the measured value for the electromagnetic coupling constant α_{EM} matches with the theoretical prediction with a precision up to the 10^{-12} [3]. The validity of the SM at the current energies is confirmed beyond any reasonable doubt.

However, it can be said that the theory is not *complete*, as it lacks explanation for several natural phenomena and it includes too many empirical parameters (up to 19 parameters that cannot be predicted, only measured). Moreover, the explanation that the SM provides for other phenomena is not convincing enough for part of the scientific community as its unnaturalness could be evidence of a hidden mechanism. Given these issues, it is hypothesized that the SM might be an *effective* theory, while there is a deeper,

simpler and more complete description of the subatomic world.

The list of issues of the SM can be divided according to experimental phenomena for which the SM has no explanation and features where the explanation provided by the SM is not fully satisfactory.

1.2.1 Incompleteness

Gravity The gravitational force is not included in the SM since, up to now, no quantum description of it has been achieved. Although several attempts are currently being developed (loop quantum gravity, string theory,...) so far none of them has been able to provide a satisfactory result. Gravity is 10^{-32} times weaker than the weak force [3] and so, its effects in the subatomic world are totally negligible within the current experimental accuracy. The inclusion of gravity in the SM would require the connection of quantum physics and general relativity, one of the main goals of the theoretical physics in the last century.

Neutrino masses and right-handed neutrinos Since the neutrinos do not interact with the Higgs boson, they are described as massless fermions in the current SM lagrangian. However, experimental observations, such as the neutrino oscillation [50, 51], have undoubtedly proved that they are massive particles. So far, only upper limits for their masses have been obtained[18]: $m(\nu_e) < 2\,\text{eV}$, $m(\nu_\mu) < 0.19\,\text{MeV}$ and $m(\nu_\tau) < 18.2\,\text{MeV}$ [3]. Hence, the true value of the neutrino masses, their hierarchy, and their inclusion in the SM lagrangian are pending issues.

The existence of the mass of the neutrinos leads to a second issue. The EWT is a chiral theory that violates parity maximally, hence only left-handed neutrinos are required in its formulation. However, since the neutrinos are massive particles, their right-chirality particles have to exist in nature but as they have no known interaction, they cannot be included in the current SM. Several hypothesis, as the *seesaw* mechanism [53–58], have been proposed to describe these *sterile* neutrinos but so far there is little evidence supporting any of them.

Dark Matter and Dark Energy Dark Matter is a type of matter which does not interact electromagnetically, only its gravitational effects have been inferred, as from the shape of galaxies or their rotation speed. No known particle of the SM can explain the features and abundance of the dark matter and thus, there is no explanation for it within the SM. Several extensions of the SM, as SUSY, include candidate particles for the Dark Matter, though no evidence of them has been found yet.

[18] The limits are given as flavor states for simplicity but, as explained in Section 1.1.7, the true observables are the mass-eigenstates ν_1, ν_2 and ν_3.

The Dark Energy is the name given to the unknown force responsible of the accelerated expansion of the universe. There is wide evidence for this phenomenon, which accounts for 73% of the energy of the universe, but so far no successful explanation has been given. Some of the models, like a scalar field responsible for the expansion, could be included in the SM, but currently no advance has been achieved on this issue.

Matter-antimatter asymmetry The Dirac equation predicted that each particle has a partner with opposite quantum numbers, e.g. $e^- \to e^+$, which forms the antimatter. Since only matter appears at large scale in the universe but particle and antiparticle are created/annihilated in pairs, there has to be some asymmetric process that discriminates between matter and antimatter, to account for the disappearance of antimatter. The EWT indeed violates the CP-symmetry, which provides a mechanism for the matter-antimatter asymmetry, however, it can only account for a fraction several order of magnitudes smaller than the observed asymmetry. New sources of CP-violations, or further mechanisms, are necessary to successfully account for this asymmetry.

Vacuum Stability of the Standard Model In Equation 1.34, the Higgs field was defined ad-hoc with a positive quartic term ($\lambda > 0$) and a negative quadratic term ($\mu^2 < 0$) to ensure the stability of the Higgs potential when $\phi \to \infty$ and the presence of the local maximum. The relation between λ and μ defines the vacuum expectation value, but their values are constrained by high order corrections of the Yukawa interaction, dominated by the coupling with the top quark, since its mass is several orders of magnitude larger than the rest of the masses. These corrections can modify the general shape of the Higgs potential, leading to a second local minimum or to a global minimum ($V \to -\infty$ when $\phi \to \infty$), as shown in Figure 1.7. A new global minimum would make the current ground state meta-stable, or even unstable, thus requiring a new mechanism.

Due to the extremely short life-time of the top quark, there is a big uncertainty in the value of its mass, even bigger than on the Higgs boson mass. The current value of m_t places the potential in the meta-stable region, while its uncertainty can reach up to the stability region and, though unlikely, the instability region too, as can be observed in Figure 1.8. Since the uncertainty on the value of m_t will decrease in the following years, with more data from the LHC, the final shape would be constrained and it will be clear if the SM needs a new mechanism to avoid the instability.

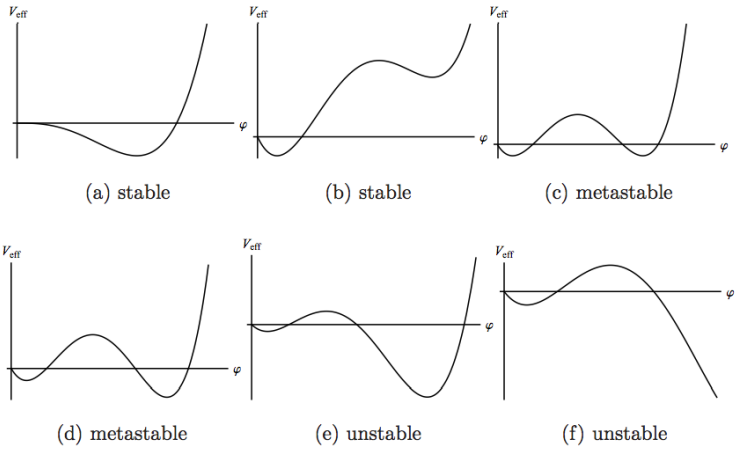

Figure 1.7: Shape of the configurations for the Higgs potential, depending of different values of λ. The first minimum of each distribution is the original EW vacuum. [59].

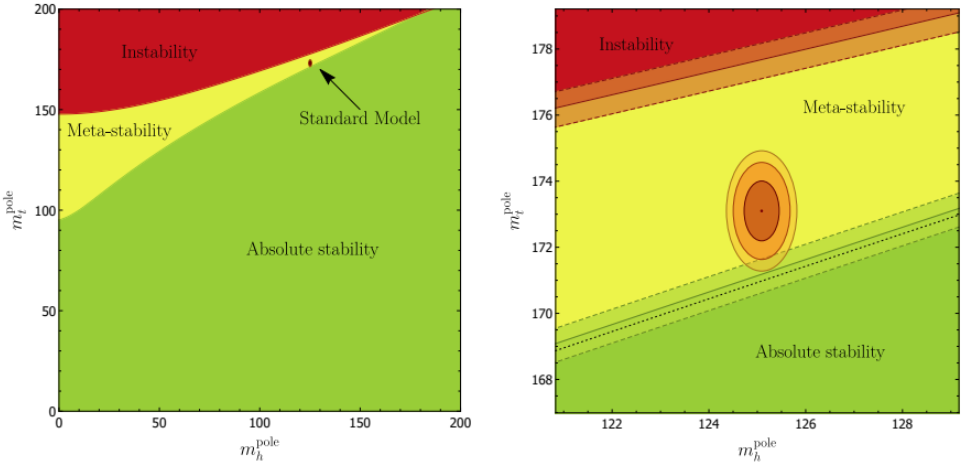

Figure 1.8: Regions of absolute stability, meta-stability and instability of the SM vacuum in the $m_t - m_H$ plane. The zoom plot (right) shows the boundary limits of the measured top and Higgs masses ($\pm 1, 2, 3\,\sigma$) [60] (2017).

1.2.2 Naturalness

The Standard Model, in its current form, has several features which raise concern among the physics community. The main controversies are related to the *naturalness* principle, which states that the numerical factors in each of the terms of the lagrangian formula have to be of about the same order of magnitude. The naturalness principle is not a requirement of the scientific method, neither physical nor mathematical, since it is not a "first principle", but rather an heuristic precept, as is the Occam's razor [61]. However, historically, non-natural theories have been proved to be incomplete and later corrected by a more profound theory. Hence, having a model with several naturalness issues raises concern as it could point to the need for a new mechanism. The naturalness principle lies at the base of the hierarchy and fine-tuning problems.

An example of a naturalness issue in the SM is the *Strong CP problem*. It has been discussed in previous sections that the EWT clearly violates the CP-symmetry, however, this phenomenon has not been observed in the QCD interaction despite the fact that, mathematically, the QCD theory can incorporate sources of CP violation. The extremely low values of the required parameter (QCD vacuum angle, θ_{QCD}) to suppress the CP-violation in the QCD lagrangian without any mechanism to account for this suppression is a source of naturalness concern.

Naturalness in the Higgs mechanism

However, the mechanism which raises more concerns about naturalness is, actually, the Higgs mechanism, specially after the mass of its boson was measured.

In the subatomic world, the observable masses of the particles are different from the *bare* mass of their theoretical formulation, since the observable value is affected by radiative corrections. The theoretical formulation of their masses (as shown in Equation 1.46) is usually derived at first order of perturbative calculation, however, to get a more precise value fine contribution of different processes affecting the measure have to be taken into account. These contributions have to be computed up to the next scale of energy, where their effects become negligible.

Regarding the Higgs boson mass, the relation between the observable mass (*obs*) and the value of the model (*bare*) is given in Equation 1.54 [62]:

$$m_H^2[\text{obs}] = m_H^2[\text{bare}] + \Delta m_H^2 \tag{1.54}$$

where Δm_H^2 represents the radiative corrections, defined as [62]:

$$\Delta m_H^2 \equiv \left(\frac{1}{16\pi^2}\, g^2 + \frac{1}{16\pi^2}\, \lambda - \frac{3}{8\pi^2}\, \lambda_f^2 + \cdots \right) \Lambda_{\text{UV}}^2 \tag{1.55}$$

where the terms represent the different types of couplings of the Higgs boson. Among them, g is a generic coupling constant for the EW bosons fields, λ is the self-coupling constant of the Higgs boson, λ_f is the Yukawa coupling constant of the Higgs to fermions and Λ is the large-scale (UV) cutoff parameter. Since the Yukawa coupling parameter depends on the mass of the fermions and the top quark mass is several orders of magnitude higher than the other quarks, the fermionic term is dominated by the top loop. As can be seen, fermions and bosons contribute with opposite sign (Figure 1.9).

The problem arises when computing the radiative corrections for the Higgs boson. In this case, the next relevant scale of energy is the Planck scale. This means that the cutoff parameter has to be set to the Planck mass, which has an incredibly high value ($m_{\text{P}} \sim 1.220910(29) \cdot 10^{19}\,\text{GeV}$) [3]. Since the Higgs boson mass was found to be in the order of $m_H[\text{obs}] \sim 125\,\text{GeV}$, the difference between both scales is 17 orders of magnitude (*hierarchy problem*). In the absence of any other mechanism or new physics

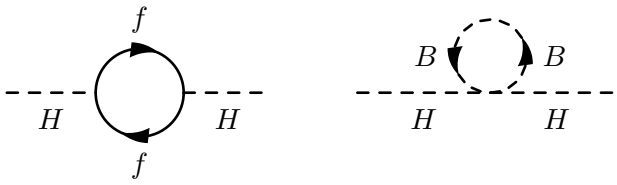

(a) Fermionic loop (b) Bosonic loop

Figure 1.9: First order radiative correction for the Higgs boson corresponding to (a) a fermionic loop and (b) a bosonic loop.

before the Planck scale, the only way in which the computation of radiative radiations up to 10^{19} GeV can lead to such a small value of the observable mass is an extremely precise cancellation between the fermionic terms (negative contributions) and bosonic terms (positive contributions). In other words, the factors of the corrections have to be extremely *fine-tuned*, in an unnatural way, to accommodate the experimental result.

In order to release the SM from the naturalness concerns, several models have been proposed but none of them have shown convincing evidence so far. An example is the Composite Higgs model [63], where the discovered Higgs boson is not considered a fundamental particle but rather a bound state arising from an unknown interaction that breaks the EW symmetry. In this model, the cutoff would be set at the binding energy of the new force, softening the natural concerns. Other models, preserving the standard Higgs particle, propose a new undetected interaction before the Planck scale that do not couple with the Higgs boson, naturally avoiding the radiative corrections.

One beyond the Standard Model theory that provides a solution to the mentioned issues is Supersymmetry, which can be implemented in different ways, the simplest one being the Minimum Supersymmetric Standard Model. The Supersymmetry models introduce a new symmetry between fermions and bosons providing a natural mechanism to address the hierarchy problem. The analysis described in Chapter 7 aims to discover one of the predictions of the Minimum Supersymmetric Standard Model: the existence of additional Higgs bosons.

1.3 SUSY, MSSM and new Higgs bosons

The fine-tuning problems of the Standard Model have been known since its early development and so, many hypotheses have been proposed to address them. One of the most promising models is Supersymmetry (SUSY), as it extends the symmetries of the Standard Model, solving the different issues and providing a Dark Matter candidate.

SUSY [64] states that fermions and bosons are not independent objects but different flavors of a more fundamental field. Following this symmetry, each fermion of the SM

has a bosonic partner, the *sfermion*, which carries an integer spin[19], and conversely, each boson has a fermionic partner, called *bosino*, which carries a semi-integer spin. Both objects belong to a *multiplet* with the same quantum numbers (except the spin). However, since no superpartner has been detected so far, this symmetry must be broken at the current scale of energy in nature and thus, only the ordinary fermions and bosons would be detected, pushing the existence of the superpartners to a higher energy scale. The SUSY theory implies the addition of a big set of new, undiscovered, observable particles, along with more free parameters in the theoretical formulation, namely the masses of the new particles and the coupling constants of the interactions. The behavior of the new fields can give a reasonable explanation to some of the current issues of the SM.

As stated in Section 1.2.2, for the radiative corrections to give rise to such a small mass for the Higgs boson (compared to the Planck mass), a fine-tuned cancellation must happen between the bosonic and fermionic loops. However, if SUSY holds, the contribution to the radiative corrections of the superpartners (Figure 1.10) would naturally cancel the divergence. This happens because the superpartners contribute with a similar order of magnitude but with opposite sign than their respective partners. Since the contributions are canceled by terms of the same order, the mechanism does not need a fermion-boson fine-tuning.

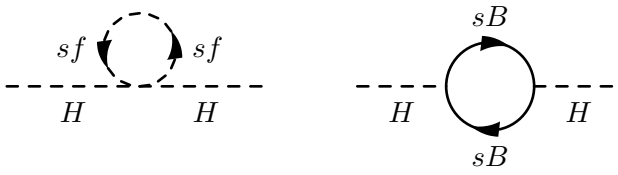

(a) sfermion loop (b) bosino loop

Figure 1.10: First order radiative correction for the Higgs boson corresponding to a sfermion loop (a) and a bosino loop (b). These corrections are the opposite to those in Figure 1.9

The mathematical formulation of the SUSY lagrangian is far from the scope of this thesis, but for the purpose of illustrating how the issue of radiative corrections is addressed, the lagrangian can be approximated, at first order, as:

$$\mathcal{L} = \mathcal{L}_{\text{SUSY}} + \mathcal{L}_{\text{soft}} \tag{1.56}$$

where $\mathcal{L}_{\text{SUSY}}$ contains all the SUSY terms and interactions that preserve the symmetry and $\mathcal{L}_{\text{soft}}$ describes the supersymmetry-broken mass terms, whose scale of energy would be around m_{soft}. The radiative corrections of the Higgs boson, up the next scale of energy, would be, then:

[19]The conditions imposed by the SUSY symmetry requires the partner of the fermion to be an scalar (s-fermion), thus, its spin must exactly 0.

$$\Delta m_H^2 = m_{\text{soft}}^2 \left[\frac{\lambda}{16\pi^2} \ln\left(\frac{\Lambda_{\text{UV}}}{m_{\text{soft}}}\right) + \cdots \right] \tag{1.57}$$

where the different contributions to the radiative corrections have been simplified as a generic λ term. As it can be seen, the quadratic divergences have been eliminated and the corrections now run as a logarithmic term, which avoids the divergence.

Another consequence of the SUSY models could be the unification of the three forces into one, in a so-called Grand Unified Theory (GUT). The unification of the weak and electromagnetic forces was a milestone in this path, but achieving the same with the strong force is problematic since the QCD and the EW theories do not seem to converge in the SM. If SUSY interactions are added, the running couplings of the forces could be modified in such a way that they converge at a large energy scale, thus providing a natural mechanism for the unification, as shown in Figure 1.11.

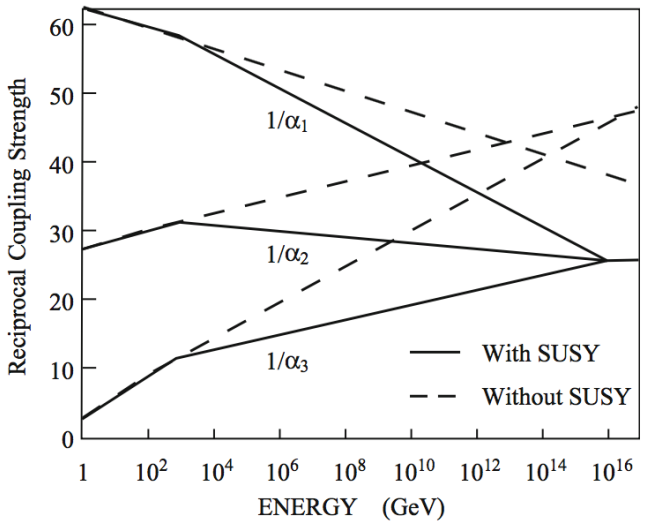

Figure 1.11: Running value of the coupling constants for $U(1)$ (α_1), $SU(2)$ (α_2), and $SU(3)$ (α_3) interactions with and without SUSY particles. The coupling constants converge only if SUSY is added. In this example, the SUSY symmetry is broken around ~ 1 TeV [42].

Since SUSY is a general framework which depends on many unknown parameters, it can be implemented in different forms. The simplest model that realizes SUSY is called the Minimal Supersymmetric Standard Model.

1.3.1 The Minimal Supersymmetric Standard Model

The Minimal Supersymmetric Standard Model (MSSM) [64–69] is the simplest way in which SUSY can be implemented while being compatible with the current observations. The aim is to add the minimal amount of new parameters, particles and interactions, while keeping all the current symmetries and observables of the SM.

The general postulate of SUSY models is the symmetry between fermions and bosons, along with a mechanism to explain why it is broken at low energies. As explained

before, the symmetry states that each ordinary particle has a supersymmetric partner with the same quantum numbers except for the spin, which would be of the opposite kind (integer/semi-integer). Table 1.4 summarizes the symmetry between the ordinary particles and their superpartners. The Higgs boson sector in the SM, however, has four additional particles, not present in the current SM. These additional bosons are a requirement of the MSSM and their motivation and mechanism is explained in Section 1.3.2.

SM particle ($R = +1$)				**Superpartner** ($R = -1$)			
Type	Spin	Particle	Symbol	Symbol	Particle	Spin	Type
Fermions	1/2	Quark	ψ_f	$\widetilde{\psi}_f$	Squark	0	Sfermions
		Lepton	ψ_l	$\widetilde{\psi}_l$	Slepton		
Bosons	1	Gluon	g	$\widetilde{g}$	Gluino	1/2	Bosinos
		W	W^i	$\widetilde{W}$	Wino		
		B	B	$\widetilde{B}$	Bino		
	0	Higgs	h, $\boldsymbol{H}$, $\boldsymbol{H^{\pm}}$, $\boldsymbol{A}$	$\widetilde{h}$, $\widetilde{H}$, $\widetilde{H}^{\pm}$, $\widetilde{A}$	Higgsinos		

Table 1.4: Relations between the SM particles and their superpartners, before the EW symmetry-breaking, according to the MSSM. In the MSSM, the ordinary SM sector of the Higgs mechanism requires four additional Higgs bosons (H, A and $H^{\pm}$, marked in bold), in addition to the SM one h. These five bosons have their correspondent supersymmetric partner, the higgsinos.

This simple approach, however, would allow certain interactions which have not been observed in the SM. In particular, due to the addition of new terms, SUSY models could allow processes where the baryon (B) and lepton (L) numbers are not conserved[20]. So far, all observed processes in nature conserve both particle numbers, B and L, and by extension, $B - L$. Since processes violating these numbers have not been observed[21], a new symmetry has to be added to the MSSM to suppress the $B - L$ violating processes: the *R-parity*. The operator of the R-parity, which is discrete, is defined, for each particle in a interaction as:

$$P_R = (-1)^{3(B-L)-2s} \tag{1.58}$$

where s stands for the spin of the particle, and B and L are the baryon and lepton numbers, respectively. The SM particles are defined as having $P_R = 1$ while the superparticles have $P_R = -1$. For the R-parity to be conserved, the combined P_R has to

[20]The baryon (lepton) number is defined as 1 for each baryon (lepton) in a given state, and -1 for each anti-baryon (anti-lepton). Another number, more global, is the difference between both numbers, $B - L$.

[21]If these processes were allowed, the proton would not be stable and then, it will eventually decay, which has not been observed. The lower limit to the mean lifetime of the proton has been set in 2016 to $\tau_p > 5.8 \cdot 10^{29}$ years [3].

be positive. SUSY models conserving the R-parity have one additional consequence: the lightest supersymmetric particle (LSP) is stable, thus all decay chains of heavier SUSY particles end in the LSP. If the LSP is, in addition, electrically neutral, it would be a candidate for the composition of the Dark Matter. Multiple searches looking for a LSP are being performed, but no evidence of its existence has been observed so far [3].

The addition of an unique fermionic superpartner for the Higgs boson (named *higgsino*) has also several implications. The first one is that a chiral anomaly would appear, which is the generation of low mass-states due to the non-conservation of a chiral current. These states have not been observed in the Higgs sector, so a mechanism to suppress them must be present. The second one is that the suppression of the flavor-changing neutral currents, which are not observed in nature either, is not granted. And finally, the third consequence relates to the ratio between the neutral (G_N) and charged (G_c) currents in the EWT. As for the current energies reached, this ratio, denoted as ρ, seems to be of the order of the unit [3], which would not be the case if an unique higgsino is introduced.

$$\rho = \frac{G_N}{G_c} = \frac{m_W^2}{m_Z^2 \cos\theta_W} = 1.00037 \pm 0.00023 \tag{1.59}$$

The simplest solution which avoids these issues, recovering the observations of the SM, is the addition of a second Higgs field doublet in the ordinary part of the SM.

1.3.2 The Two-Higgs-Doublet Model in the MSSM

The Two-Higgs-Doublet model (2HDM) is an extension of the SM that postulates the existence of a second $SU(2)$ Higgs field doublet [70, 71]. The 2HDM hypothesis is more general than SUSY, several models beyond the SM include the addition of a second Higgs doublet without adding other SUSY features. However, for the MSSM, a second Higgs doublet is a requirement, as it is the simplest mechanism in which the MSSM can be implemented being compatible with the current experimental results.

The MSSM implements a specific case of 2HDM, called Type-II [72, 73], in which one of the doublets couples with up-type quarks (ϕ_u) while the second one couples with down-type quarks and leptons (ϕ_d). The two Higgs doublets are defined as [62]:

$$\phi_d \equiv \begin{pmatrix} \phi^{(+)} \\ \phi^{(0)} \end{pmatrix} \qquad \phi_u \equiv \begin{pmatrix} \phi^{(0)*} \\ -\phi^{(-)} \end{pmatrix} \tag{1.60}$$

The total amount of degrees of freedom of the pair of doublets is eight. As in the SM, three of them are taken by the vector bosons in the spontaneous breaking of the symmetry and thus, the remaining five arise as massive observable bosons. One of them is a neutral

light scalar boson denoted by h, analogous to the SM[22] . In addition, the MSSM Higgs mechanism adds a second neutral heavier scalar boson, H; a neutral pseudo-scalar boson[23], A; and a pair of charged bosons, $H^{\pm}$. As shown in Table 1.4, despite being a postulate of the MSSM, these new particles are conventional bosons of the SM, not supersymmetric partners. Hence, each of the five bosons would have, in addition, their own fermionic partner, the *higgsinos*:

$$\underbrace{\left(h,\, H,\, A,\, H^{\pm}\right)}_{\text{ordinary}} \longrightarrow \underbrace{\left(\widetilde{h},\, \widetilde{H},\, \widetilde{A},\, \widetilde{H}^{\pm}\right)}_{\text{supersymmetric}} \tag{1.61}$$

The masses of these additional particles are free parameters of the theory and so, they could lie at any value of mass. Assuming the MSSM principles, the simplest approach would be a scenario where the masses of the Higgs bosons are of the same order of magnitude. This would make these particles observable by the LHC experiments, thus allowing an experimental test of the MSSM and SUSY.

1.3.3 Mathematical formulation of the Higgs sector in the MSSM

The simplified Higgs potential can be described as [62]:

$$\begin{aligned} V(\phi_d, \phi_u) = {} & \mu_u^2(\phi_u^\dagger \phi_u) + \mu_d^2(\phi_d^\dagger \phi_d) - \mu^2(\varepsilon_{ij}\phi_d^i \phi_u^j + h.c.) \\ & + \frac{g_W^2 + g_B^2}{8}(\phi_d^\dagger \phi_d - \phi_u^\dagger \phi_u) + \frac{g_W^2}{2}\left|\phi_d^\dagger \phi_u\right|^2 \end{aligned} \tag{1.62}$$

where $\varepsilon = 0$ if $i = j$ and $\varepsilon_{du} = -\varepsilon_{ud} = 1$. To ensure the vacuum stability, the potential has to be bound from below and thus, the following condition has to be ensured: $\mu_d^2 + \mu_u^2 > 2\mu^2$. The requirement for the spontaneous symmetry breaking becomes: $\mu^4 > \mu_u^2\mu_d^2$, and the symmetry is spontaneously broken by the choice of the non-zero vacuum at:

$$\langle \phi_d \rangle = \frac{1}{\sqrt{2}}\begin{pmatrix} 0 \\ v_d \end{pmatrix} \qquad \langle \phi_u \rangle = \frac{1}{\sqrt{2}}\begin{pmatrix} v_u \\ 0 \end{pmatrix} \tag{1.63}$$

The vacuum expectation value of the SM, v, is recovered by:

$$v^2 \equiv v_d^2 + v_u^2 \tag{1.64}$$

The relation of both expectation values defines a fundamental value in the description of the MSSM:

$$\tan\beta \equiv \frac{v_u}{v_d} \tag{1.65}$$

[22]The current convention in the MSSM framework, and used in this thesis, is to assume that the Higgs boson discovered at $m_h \sim 125\,\text{GeV}$ is the lightest Higgs boson proposed by the MSSM Higgs mechanism, h. The scenario where the discovered particle is the heavier H is much less favorable, though not totally ruled out, as its mass limit is $m_H > 92.8\,\text{GeV}$ [3].

[23]A pseudo-scalar is a type of scalar whose wave-function changes sign under a parity operator.

The value of v is related to the masses of the vector bosons defined in Equation 1.46. The $W^{\pm}$ mass relation holds as in the SM, but the Z boson mass relation is modified, becoming dependent on the $\tan\beta$ parameter.

$$m_W \equiv \frac{v \cdot g_w}{2} \qquad\qquad m_Z \equiv \frac{\mu_d^2\,\mu_u^2 \cdot \tan^2\beta}{\tan^2\beta - 1} \tag{1.66}$$

The Yukawa couplings of the different Higgs bosons to the quarks are also modified with respect to the SM, and can be expressed as a correction of the coupling of the SM boson, depending on $\tan\beta$ and a second angle, α, defined in Equation 1.67. The corrections, in units of the coupling of the SM, are given in Table 1.5. The measure of these couplings is a powerful tool to discriminate experimentally between the SM and MSSM.

$$\tan 2\alpha \equiv \frac{m_A^2 + m_Z^2}{m_A^2 - m_Z^2}\tan 2\beta \qquad \text{with:} \quad \alpha \in [-\frac{\pi}{2}, 0] \tag{1.67}$$

$\boldsymbol{\lambda_{ij}/\lambda_{\mathrm{SM}}}$	$\boldsymbol{\lambda_{VV}}$	$\boldsymbol{\lambda_{uu}}$	$\boldsymbol{\lambda_{dd,ll}}$
h	$\sin(\beta-\alpha)$	$\cos\alpha/\sin\beta$	$-\sin\alpha/\cos\beta$
H	$\cos(\beta-\alpha)$	$\sin\alpha/\sin\beta$	$\cos\alpha/\cos\beta$
A	0	$\cot\beta$	$\tan\beta$

Table 1.5: Relation of the Yukawa coupling parameters (λ_{ii}) with the respect to the SM coupling (λ_{SM}) for the neutral MSSM Higgs bosons (h, H, and A) to the vector bosons (λ_{VV}), and to the different fermions, split in u-type (only quarks, λ_{uu}) and d-type (quarks and electron-type, $\lambda_{dd,ll}$) as a function of the angles α and β.

Similarly, the formulation of the masses of the five Higgs bosons can be obtained at tree level as:

$$\begin{aligned} m_A^2 &= \frac{2\mu^2}{\sin 2\beta} \\ m_{H^{\pm}}^2 &= m_A^2 + m_W^2 \\ m_{H,h}^2 &= \frac{1}{2}\left[m_A^2 + m_Z^2 \pm \sqrt{\left(m_A^2 + m_Z^2\right)^2 - 4m_Z^2 m_A^2 \cos^2 2\beta}\right] \end{aligned} \tag{1.68}$$

As previous relations state, the masses of the Higgs bosons at lowest order depend only on two free unknown parameters, which are conventionally chosen to be $\boldsymbol{\tan\beta}$ and $\boldsymbol{m_A}$. Furthermore, these relations impose several constrains on the values of the masses, namely:

$$\begin{aligned} m_{H^{\pm}}^2 &> m_W^2 \\ m_H &\geq \max(m_A, m_Z) \geq \min(m_A, m_Z)\cos 2\beta \\ m_H^2 + m_h^2 &> m_A^2 + m_Z^2 \end{aligned} \tag{1.69}$$

Relations as Equation 1.68 are valid only at tree level. However, when high-order corrections are included, several additional parameters such as the stop mixing parameter

($X_t \equiv A_t - \mu \cot\beta$, which depends on the soft SUSY-breaking Higgs-stop coupling A_t), or the average scale of SUSY ($m_{\text{SUSY}} \equiv \sqrt{m_{\tilde{t}_1} m_{\tilde{t}_2}}$, average scale of the stop masses) also appear in the computations. At higher orders, the corrections on the Higgs mass become [62]:

$$\Delta m_h^2 \approx \frac{3m_t^4}{2\pi^2 v^2}\left[\ln\frac{m_{\text{SUSY}}^2}{m_t^2} + \frac{X_t^2}{m_{\text{SUSY}}^2}\left(1 - \frac{X_t^2}{12\, m_{\text{SUSY}}^2}\right)\right] \tag{1.70}$$

As a huge number of free parameters is impractical for the experimental test, an usual procedure is to manually set the high-order parameters to a particular value, aiming to focus on specific MSSM phenomenologies (called *scenarios)*, and then set experimental limits on the $\tan\beta$ and m_A parameters for these specific scenarios.

A description of the most relevant scenarios for this thesis is covered in Section 2.3.1, but for illustration purposes a particular one will be shown here. Setting the condition, among others, that the h boson has the maximum value of its allowed range, a particular scenario, called m_h^{max}, is defined. In this scenario, the phase-space of the values for the masses, depending on $\tan\beta$ and m_A, can be computed, and is shown in Figure 1.12.

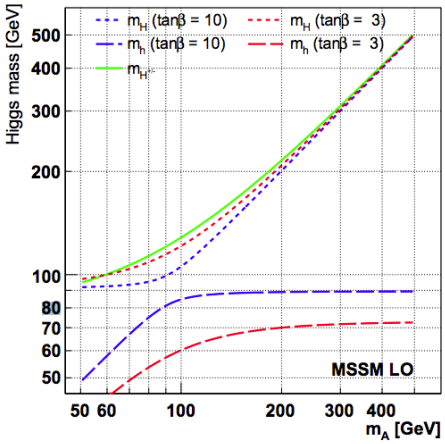

Figure 1.12: Masses of the different MSSM Higgs bosons at tree level as a function of m_A for two values of $\tan\beta$ in the m_h^{max} scenario. [74].

Several observations can be drawn from Figure 1.12: in the limit of large m_A, $m_H \approx m_{H^\pm} \approx m_A$, while m_h remains stable at a low value, as $\alpha \approx \beta - \pi/2$. Although the mass of the Higgs boson was a free parameter in the SM, in the MSSM it is constrained from above: at tree level $m_h < m_Z$, which is disproved by the observations. However, if the radiative corrections are added, the limit is pushed to $m_h < 135\,\text{GeV}$ [64], which can accommodate to the observed mass of the Higgs boson.

The search for the additional neutral bosons of the MSSM, H/A, is one of the aims of this thesis. The search is done in several MSSM scenarios, aiming for topologies where the differences with respect to the SM are enhanced.

Chapter 2

Phenomenology of the pp collisions and the Higgs boson at the LHC

This chapter describes the phenomenology of the physics related to this thesis. It starts in Section 2.1 with a brief explanation of the pp collisions at the LHC. Then, the phenomenology of the production and decay of the Higgs boson at the LHC, according to the SM is given in Section 2.2. The MSSM, however, introduces several modifications to these parameters and thus, these corrections are covered in Section 2.3, which also includes a brief description of the different MSSM benchmark scenarios under study.

2.1 Phenomenology of the proton-proton collisions

The LHC accelerates and collides beams of protons to achieve the necessary energy in the center of mass (e.c.m.) to generate the processes of interest. When two protons collide, they usually scatter elastically due to the repulsion of their positive charge. Only in a small fraction of cases the interaction is inelastic, resulting in the production of new particles. Protons, unlike electrons, are hadrons, composite particles formed by three valence quarks (namely uud) that are bound together by a continuous exchange of gluons. Within the proton, gluons are transformed continuously in pairs of quark-antiquark, which forms the *sea of quarks*.

The physics of the pp collisions is modeled by the QCD theory. The main event comes from the *hard scattering* of the protons at high energy, and it can be described using a perturbative approximation of QCD, assuming asymptotic freedom. However, the collisions are dominated by the *soft scattering*, radiation of low energy interactions. The estimation of the soft scattering is more difficult to describe, as QCD perturbative theory cannot be used and so, it has to be parametrized from data.

The entities that are effectively involved in the collisions, either the quarks (from valence or sea) or the gluons, are called *partons*. Since they are bound within the proton,

they carry part of its energy in a dynamic way. In order to model the collisions, the fraction of the proton energy each parton carries at the moment of the impact has to be known. Since this value cannot be exactly computed, it is estimated using probability distributions called Parton Distribution Functions (PDFs). Different PDF schemes, such as CTEQ [75], MSTW [76] and NNPDF [77], have been developed and tested at different energy regimes. Figure 2.1 shows two examples of the MSTW PDF with its uncertainty for two values of the momentum interchange, Q^2.

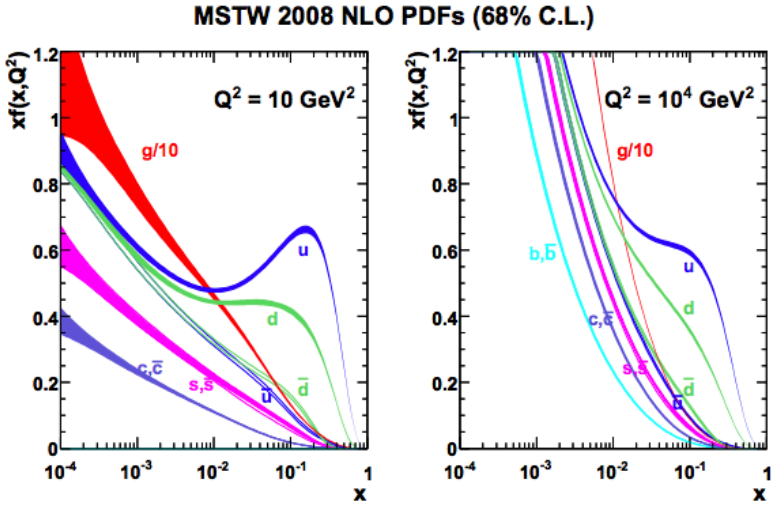

Figure 2.1: MSTW 2008 Parton Distribution Function at NLO for $Q^2 = 10\,\mathrm{GeV}^2$ and $Q^2 = 10^4\,\mathrm{GeV}^2$ [76].

The cross-section of the pp collisions, $\sigma\,(pp \to X)$, is given by the QCD factorization theorem [78]:

$$\sigma\,(pp \to X) = \sum_{i,j} \int\int f_i\left(x_1, \mu_F^2\right)\, f_j\left(x_2, \mu_F^2\right)\, \hat{\sigma}_{ij\to X}\left(s\, x_1\, x_2, \mu_R^2, \mu_F^2\right)\, dx_1\, dx_2 \quad (2.1)$$

where the x_1 and x_2 variables are the fraction of the total momentum that the partons i,j carry, providing an effective e.c.m. $\hat{s} = s\, x_1\, x_2$, and the variables μ_R^2 and μ_F^2 are the renormalization and factorization factors respectively, which are obtained by truncating the strong coupling constant. Finally, the variables f_i and f_j are the parton densities, obtained from PDFs for a momentum transfer of $Q^2 = (p_1 - p_2)^2$, where p_1 and p_2 are the momenta of the respective incoming partons.

The partial cross-sections, $\hat{\sigma}_{ij\to X}$, can be computed through the QCD lagrangian in the perturbative method, up to Leading Order (LO), or adding further corrections to next orders, (NLO, NNLO,...). However, the physical process does not end here: the partons involved in the collision can irradiate soft-gluons (parton shower) which later will hadronize, forming a cascade of particles. An accurate theoretical modeling of these effects is not possible and thus, their simulation is constrained using experimental data.

Additionally, several interactions can happen simultaneously to the main collision event, due to the recombination of the rest of partons of the proton. These secondary collisions form the *underlying event* (UE). A schematic diagram of the whole process is shown in Figure 2.2.

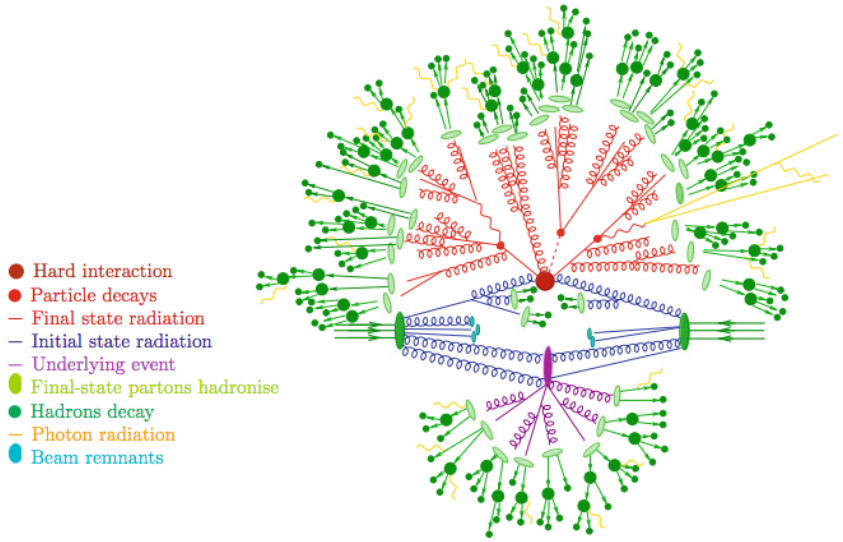

Figure 2.2: Schematic diagram of a proton-proton collision. The hard interaction (big red blob) is followed by the decay of both top quarks and the Higgs boson (small red blobs). Additional hard QCD radiation is produced (red) and a secondary interaction (the underlying event) takes place (purple blob) before the final-state partons hadronize (light green blobs) and hadrons decay (dark green blobs). Photon radiation occurs at any stage (yellow) [79].

The proton-proton collisions in the accelerators have a specific topology, thus it is useful to define an appropriated system of coordinates for their study. By convention, the direction of the beam is considered to be the z-axis of the system while the x and y axis form the transverse plane. In this system of coordinates, the momentum of the incoming beam particles is essentially pointing in the z-axis direction, $p = p_z$ and therefore approximately 0 in the transverse plane $p_{\mathrm{T}} = 0$.

However, since the detectors (and ATLAS in particular) have a cylindrical symmetry, it is more useful to define a set of cylindrical coordinates, with the origin in the interaction point. The cylindrical coordinates are (ϕ, θ, z) where ϕ is the azimuthal angle in the transverse plane to the beam, defined within $\phi \in [-\pi, \pi]$; and θ is the polar angle.

An additional variable can be defined, the *rapidity*:

$$y = \frac{1}{2} \ln \left(\frac{E + p_z}{E - p_z} \right) \tag{2.2}$$

which is interesting because the difference of rapidity between two objects $(y_1 - y_2)$ is invariant under boosts along the z-axis.

Another typical convention of the high energy physics is that the mass of the particle is negligible compared to its momentum, $p \gg m$, which yields $E^2 = m^2 + p^2 \approx p^2 \rightarrow E \approx p$.

The condition is usually true due to the high energy of the collisions in the center of mass, compared with the relatively small mass of the particles produced.

In the limit $p \gg m$, the rapidity can be approximated by the *pseudorapidity* variable, η, defined as:

$$\eta \equiv -\ln\left(\tan\frac{\theta}{2}\right) \tag{2.3}$$

which only requires the polar direction of the particle to be defined.

Finally, another useful parameter can be defined: ΔR, which is the distance in the $\phi - \eta$ plane of two objects, as:

$$\Delta R \equiv \sqrt{(\Delta\eta)^2 + (\Delta\phi)^2} \tag{2.4}$$

2.2 Phenomenology of the Higgs boson in the SM

2.2.1 Higgs boson production

At the LHC, neutral Higgs bosons can be produced in several different processes and thus, the computation of its production in the different modes has been performed with great accuracy [80]. The cross-section of the Higgs boson for different production modes as a function of e.c.m. is shown Figure 2.3, whereas the values of the cross-section for the most relevant modes for this thesis are summarized in Table 2.1.

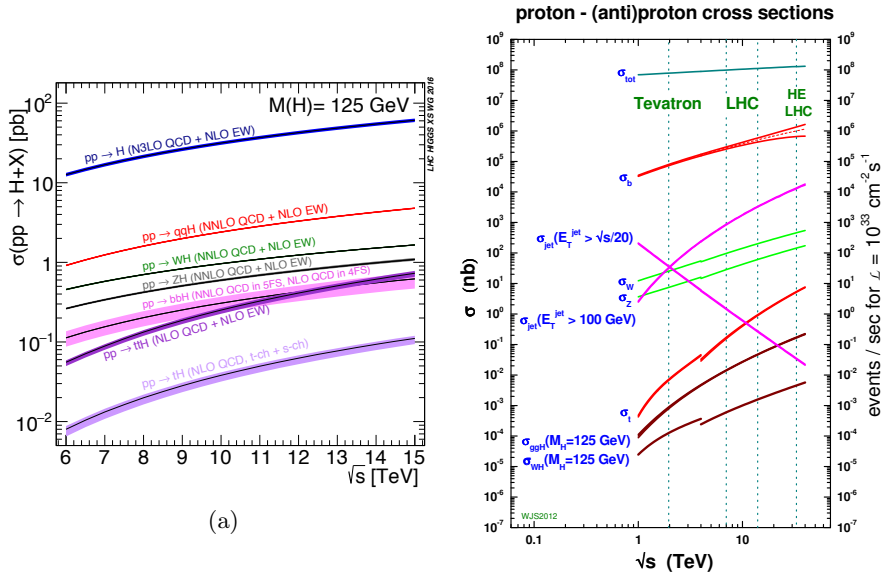

(a) (b)

Figure 2.3: Cross-sections for different Higgs boson production processes as a function of center-of-mass energies in (a) the LHC range ($7 - 13$ TeV) and (b) the most relevant hadron colliders, for a Higgs boson with a mass of $m_H = 125$ GeV [81].

The dominant Higgs production process at the LHC is the **gluon fusion**, labelled as ggF or ***ggH*** (Figure 2.4), an interaction of gluons mediated by a triangular loop of quarks. Since the Yukawa coupling of the Higgs boson with fermions depends on the mass of the fermion (as shown in Equation 1.52) the top quark loop dominates the process. The ggH is the most abundant production mode of the SM Higgs boson at the LHC, being responsible of approximately the 85% of the Higgs bosons produced. Its cross-section has been computed with perturbative expansion in QCD at N3LO and in EW at NLO [81].

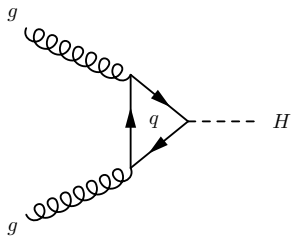

Figure 2.4: Feynman diagram for the gluon fusion process (ggH) at lowest order, showing the production of a Higgs boson via a fermion loop.

The second most abundant production mode at LHC is the **vector boson fusion** [82], **VBF** (Figure 2.5), where two vector bosons ($W^{\pm}$ or Z) fuse to produce a Higgs boson. Despite having a cross-section ten times lower than ggH at LHC, this process is particularly important thanks to the behavior of the two outgoing quarks, which hadronize forming two observable energetic jets back-to-back in the beam direction. The strong tendency of these jets to be forward-backward directed is a clear signature of the process, in contrast to other jet-production mechanisms and so, it serves for background suppression. The current computation of the cross-section includes NNLO QCD corrections and NLO EW corrections [81].

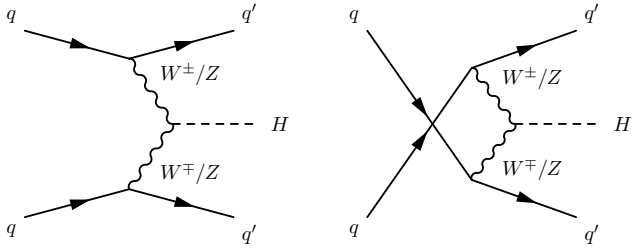

(a) VBF t-channel (b) VBF u-channel

Figure 2.5: Feynman diagrams for the Vector Boson Fusion process of a Higgs boson with two jets at leading order for the (a) t- and (b) u- channels.

Another process is the **vector boson associated production**, ***VH*** (Figure 2.6), also called Higgs-strahlung. In this process, the collision of a quark-antiquark pair produces an energetic vector boson, $W^{\pm}$ or Z, that irradiates a Higgs boson. The VH production mode cross-section is smaller than ggH or VBF production modes. The cross-sections are computed up to NNLO for the QCD corrections plus NLO EW corrections [81].

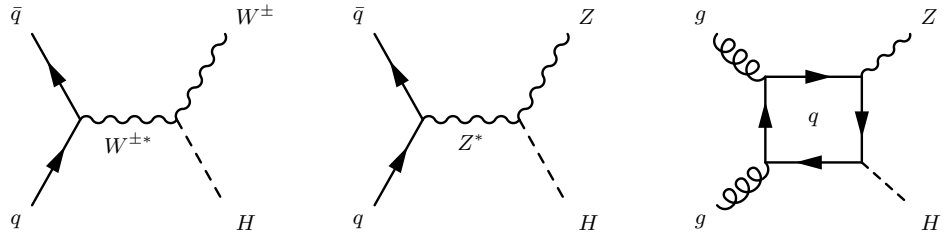

(a) WH process (b) ZH process (c) ZH via t-loop

Figure 2.6: Feynman diagrams for the vector boson associated production process (VH) at leading order for (a) the W boson and (b) the Z boson (b). Diagram (c) correspond to a gluon fusion via top quark loop which contributes to the ZH mode.

Additional production modes of the Higgs boson at LHC are the **associated production with heavy fermions**, namely with top quarks (ttH) and bottom quarks (***bbH***), the latter shown in Figure 2.7. However, these modes have neither a significant SM cross-section at LHC nor a clear signature, and due to the huge amount of b-quark background from QCD processes, their identification is troublesome. Therefore, the contribution of these production modes for the SM analysis described in Chapter 6 was found to be negligible and is not taken into account. The MSSM analysis, however, takes advantage of the enhanced coupling of the b-quarks to the Higgs boson for large $\tan\beta$ values and thus, the bbH mode is studied as a significant (even dominant) source of additional Higgs bosons. The corrections to the bbH in the MSSM are described in Section 2.3. The cross-section for the ttH modes are computed at NLO QCD and NLO EW accuracy, whereas for bbH modes they are computed at NNLO for the 5-flavor scheme[1] (5FS) and NLO for the 4-flavor scheme (4S) [81].

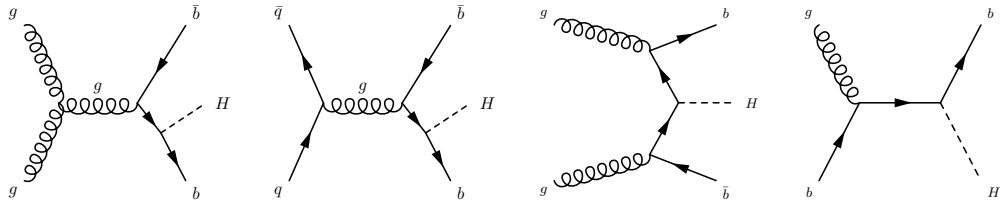

(a) 4FS (b) 4FS (c) 4FS (d) 5FS

Figure 2.7: Feynman diagrams for the b-associated production process at leading order in the four-flavor scheme (a,b,c) and the five-flavor scheme (d).

A summary of the theoretical cross-sections for the described production modes assuming $m_h = 125\,\text{GeV}$ is shown in Table 2.1. Additional modes, such as tH, the cross-section of which is several orders of magnitude smaller, are not shown.

[1] In order to model the proton, different approaches are considered: the four-flavour schemes (4FS) are phenomenologies that model the proton by including the 4 lightest quarks: u, d, c, and s; while the five-flavour schemes (5FS) are the ones that include a fifth quark in the proton model: the b.

Mode		Cross-section [pb]		
		7 TeV	8 TeV	13 TeV
	ggH	16.85	21.42	48.58
	VBF	1.241	1.601	3.782
VH	WH	0.577	0.703	1.373
VH	ZH	0.339	0.421	0.884
	ttH	0.089	0.133	0.507
	bbH	0.155	0.202	0.488
Total		19.251	24.480	55.614

Table 2.1: Approximated theoretical cross-sections for the main production modes of a Higgs boson with a mass of $m_H = 125\,\text{GeV}$ at the different e.c.m. operation values of the LHC during Run 1 and Run 2. An extended table with the respective uncertainties is available in Ref. [81].

2.2.2 Higgs boson decay

The Higgs boson is a particle with a short life time ($\sim 10^{-22}\,\text{s}$) [3]. Hence, its direct observation is infeasible and the searches have to look for the signatures of its decay. Each of the decay modes has a different topology as well as different branching ratios (BR). In the SM, the couplings of the Higgs boson to the different particles depend, in the last instance, on the Higgs boson mass, a free parameter of the theory which can only be measured experimentally. Hence, the estimation of the BR of the different decay channels had to be done as a function of the Higgs boson mass, as Figure 2.8 shows.

After the measurement of the Higgs boson mass, the theoretical values of the BR of the different channels are set in the SM, as summarized in Table 2.2, for a Higgs boson with a mass of $m_H = 125\,\text{GeV}$. Hence, the dominant decay of the Higgs boson is the bb channel, with a BR of $\sim 58\%$; the WW channel is second in order of probability (BR of $\sim 21\%$), followed by the gg channel (BR of $\sim 8\%$) and the $\tau\tau$ channel, with a BR of $\sim 6.3\%$.

This thesis studied the Higgs boson decay into a pair of τ leptons, denoted as the $H \to \tau\tau$ channel[2], whose Feynman diagram is shown in Figure 2.9. The $H \to \tau\tau$ is a very sensitive fermionic channel despite its relatively low branching ratio because its final state provides a clear signature (high energetic τ leptons), while the more abundant $H \to bb$ channel suffers from significant backgrounds at the LHC.

[2]The formally correct label is $H \to \tau^+\tau^-$ but for notation simplicity the signs in the fermionic decays are omitted. In the same way, the decays to quarks should be formally denoted as $H \to q\bar{q}$, but the bar of the anti-quark is also dropped.

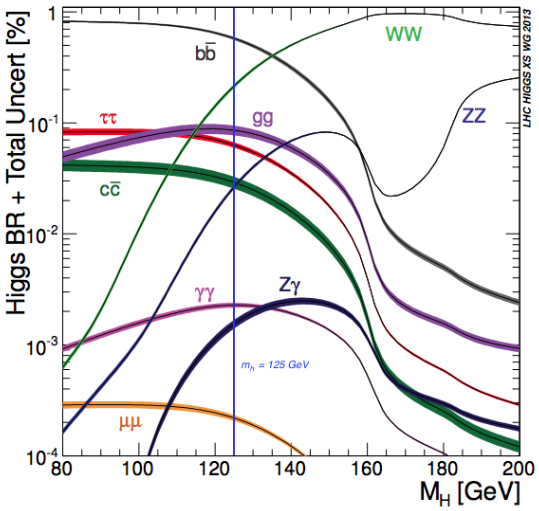

Figure 2.8: SM Higgs boson branching ratios for each of the decay channels, as a function of the Higgs boson mass M_H. The blue line marks the position of the discovered Higgs boson, at $M_H = 125\,\text{GeV}$ [83].

Decay channel	**BR**
$H \to b\bar{b}$	58.24 %
$H \to W^+W^-$	21.37 %
$H \to gg$	8.19 %
$H \to \tau^+\tau^-$	6.27 %
$H \to c\bar{c}$	2.89 %
$H \to ZZ$	2.62 %
$H \to \gamma\gamma$	0.227 %
Total Γ_H	4.09 MeV

Table 2.2: Partial branching ratios in the SM of the main decay channels to the total width (Γ_H) of a Higgs boson with a mass of $m_H = 125\,\text{GeV}$. Complete table with the respective uncertainties is available in Ref. [81].

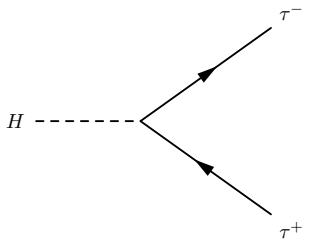

Figure 2.9: Feynman diagram for the $H \to \tau\tau$ decay at tree level.

2.2.3 The τ decay

The τ lepton is an unstable particle with a mean life time of $\sim 10^{-13}\,\text{s}$ [3] and thus, a decay length of $87.03\,\mu\text{m}$. Therefore, its decaying vertex is usually close to the production one. The τ decays via the electroweak interaction, converting into a ν_τ and emitting other fermions, mediated by a $W^\pm$ in the process, as shown in Figure 2.10.

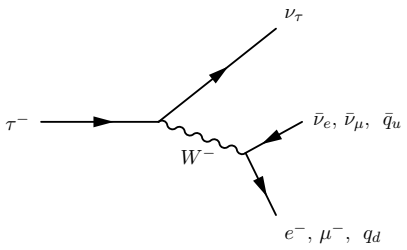

Figure 2.10: Feynman diagram for the decay of a τ^- particle, mediated by a W^- boson at tree level. The W^- can decay as pairs of electron/electron-neutrino, muon/muon-neutrino or d-type quark/u-type antiquark.

The decay of the τ lepton can produce a quark-antiquark pair, which is labelled the *hadronic* decay; or a lepton-neutrino pair (μ/ν_μ or e/ν_e), denoted as the *leptonic*

decay. These two types of decay have a completely different topology since the quark pair hadronizes, causing a cascade of hadronic particles (jet), while the lepton pair results in the emission of a highly energetic lepton and an invisible neutrino.

The different τ decays allow to categorize the final states of $H \to \tau\tau$ events, hence three possible final states are defined: the fully leptonic channel ($\tau_{\text{lep}}\tau_{\text{lep}}$), where *lep* stands for either e or μ; the fully hadronic channel ($\tau_{\text{had}}\tau_{\text{had}}$), where both τ decays are hadronic; and the semi-leptonic decay, with one τ of each type of decay. Table 2.3 shows the partial branching ratios of the different τ decays (a) and the relative proportion of the different $H \to \tau\tau$ final states (b).

Decay channel	**BR**
$\tau \to \nu_\tau\, e\, \nu_e$	17.8 %
$\tau \to \nu_\tau\, \mu\, \nu_\mu$	17.4 %
$\tau \to \nu_\tau$+hadrons	64.8 %

(a) τ decay

Decay channel	**BR**
$H \to \tau_{\text{lep}}\tau_{\text{lep}}$	12.4 %
$H \to \tau_{\text{lep}}\tau_{\text{had}}$	45.6 %
$H \to \tau_{\text{had}}\tau_{\text{had}}$	42.0 %

(b) $H \to \tau\tau$ decay

Table 2.3: Approximated partial branching ratios of the main decay channels of the τ lepton (a) and the relative proportion of the $H \to \tau\tau$ decay modes (b). The full table of decays for the τ with their respective experimental uncertainties is available in Ref. [3].

2.3 Phenomenology of the MSSM

The MSSM is an extension of the SM which includes a new set of particles and a new symmetry. Due to the theoretical requirements covered in Section 1.3, a second Higgs doublet must be added in the SM sector, which results in five observable Higgs bosons: h, H, A and $H^{\pm}$. The most common interpretation of the Higgs boson discovered at $\sim 125\,\text{GeV}$ in the MSSM context is to assume that it corresponds to the lightest boson of the MSSM, h, which is favored by data. This assumption constrains the phase-space of the MSSM parameters, as it sets the value of m_h as:

$$m_h = 125 \pm 3\,\text{GeV} \tag{2.5}$$

with a theoretical uncertainty of $\pm 3\,\text{GeV}$ due to the unknown effect of higher-order corrections [83]. The converse interpretation, where the discovered boson is the heavy H, is constrained by $m_H > 92.8\,\text{GeV}$ [3]. This thesis assumes the former interpretation, therefore the MSSM analysis is focused on the search of the heavy bosons A and H.

The MSSM modifies the relations of the masses and couplings of the Higgs particles with respect to the SM. At tree level, the correction to the masses can be written to depend uniquely on m_A and $\tan\beta$ parameters, while the corrections to the Yukawa couplings can be written in terms of the angles α and β. By construction (Equation 1.67), at leading

order, α is defined negative while $\tan\beta$ is defined positive, hence $\beta > \alpha$. Among the MSSM couplings parameters (Table 1.5), the parameters of interest for the purpose of this thesis are the couplings of the different neutral Higgs bosons to down-type fermions (namely to b quarks and τ leptons) [64]:

$$\lambda(H \to bb, \tau\tau) \propto \frac{\cos\alpha}{\cos\beta} = \frac{\cos\alpha}{\sin\beta}\tan\beta \tag{2.6}$$

$$\lambda(A \to bb, \tau\tau) \propto \tan\beta \tag{2.7}$$

As seen in previous relations, the coupling of both heavy Higgs bosons depends, directly and proportionally, on the value of the free parameter $\tan\beta$. Hence, for large values of $\tan\beta$, the coupling of these Higgs bosons to d-type fermions (*down*-type quarks and electron-type leptons) is enhanced with respect to the SM. On the other hand, the coupling to the u-type quarks is suppressed. Conversely, for low values of $\tan\beta$ ($\tan\beta < 1$), this behavior is reversed: the coupling to u-fermions is enhanced while the coupling to d-fermions is suppressed. This scenario, however, is not favored by experimental observation of the top quark coupling.

The enhanced coupling to down-type fermions is essential in the MSSM analysis. The difference with respect to the SM can be turned as an advantage, not only as a way to discriminate between SM and MSSM, but also to open new ways to detect the Higgs particles using mechanisms that were not favored in the SM. With a large $\tan\beta$, the $H \to \tau\tau$ and $H \to bb$ channels would be enhanced with respect to the SM. In addition, the associated production of the Higgs boson with b-quarks (bbH mode) (Figure 2.7) would be enhanced too, thus increasing significantly the overall production cross-section.

A large $\tan\beta$ would also affect the ggH mode, as the Higgs boson production in this mode happens through a fermionic loop. In the SM, the coupling of the Higgs boson with fermions depends on the mass of the fermion and therefore, due to its enormous mass, the top quark loop dominates completely the production, rendering all other contributions not significant. In the MSSM, a large value of $\tan\beta$ would enhance the b-quark loops (even dominating over the t-loop), hence augmenting its contribution. Also, the p_{T} distribution of Higgs bosons produced by a b-loop is softer than for a t-loop.

The $\tan\beta$ enhancement of the coupling of d-type leptons to the Higgs boson constrains the upper values of $\tan\beta$, while the lower bound is linked to the mass value of the discovered Higgs boson and the stability of the Yukawa coupling to top quarks. Within those limits, multiple scenarios can be drawn, after setting appropriately the higher-order parameters. The different scenarios have specific phenomenologies and will be used to interpret the results of the $H/A \to \tau\tau$ analysis.

2.3.1 MSSM benchmark scenarios

This section covers some of the benchmark scenarios of the MSSM framework, which are tested in the analysis described in Chapter 7. The exclusion limits on the $\tan\beta$–m_A phase space for the different scenarios are shown in Figure 2.11 [84] as of 2013. Further descriptions, which include the mathematical formulation and the exact values for the parameters of the models, can be found in [74, 83–86].

The m_h^{max} scenario

The m_h^{max} scenario, mentioned in Section 1.3.3 as an example, was originally defined to give conservative exclusion bounds on $\tan\beta$ for the LEP searches, by aiming for the heaviest-possible light Higgs boson h. The value of X_t was chosen to maximize m_h at large values of m_A for a given value of $\tan\beta$. The discovery of the Higgs boson at $m_h \sim 125\,\text{GeV}$ constrained significantly the phase parameter of the m_h^{max} scenario, as the compatibility of the predicted values with the mass of the observed signal can be achieved only in a relatively small region of the parameter space, in particular for rather low values of $\tan\beta$ ($\tan\beta < 10$).

The m_h^{mod} scenario

The m_h^{mod} scenario is a modification of the m_h^{max}, reducing the contribution of the stop mixing parameter (X_t/m_{SUSY}) to make the value of m_h more adjusted to the experimental value of the discovered particle, rather than to maximize it. This can be done for different signs of X_t, thus two variants of this scenario are established: $m_h^{\text{mod+}}$ and $m_h^{\text{mod-}}$.

The hMSSM scenario

The hMSSM describes the MSSM sector assuming the validity of the tree-level parameters and setting m_h as exactly the observed value measured by the ATLAS and CMS experiments, i.e. $m_h \sim 125\,\text{GeV}$. In addition to this, the scenario also supposes that the corrections to the matrix mass are only affected by the leading logarithmic terms arising from top and stop loops. Finally, it assumes that the masses of the rest of SUSY particles is high enough to escape detection at the LHC, neglecting their effect on the Higgs sector.

Under the hMSSM assumptions, it is possible to determine the production cross-sections and the decay branching ratios of all the MSSM Higgs bosons, as function of m_A and $\tan\beta$.

The light stop scenario

The measured value of the lightest Higgs boson mass may only be achieved in the MSSM by relatively large radiative contributions from the top-stop sector, which can only be

obtained if the mixing parameter X_t in the stop sector is larger than the average stop mass. The dependence of m_h on the stop mass scale is logarithmic and allows for values of m_{SUSY} below the TeV scale, which are still possible if X_t is close to the value that maximizes the lightest Higgs boson mass. A large value of X_t and a relatively low value of m_{SUSY} necessarily lead to the presence of a light stop ($m_{\tilde{t}} \approx 325\,\text{GeV}$), which defines the *light stop scenario*. The light stop would contribute negatively to the *ggH* cross-section, effect which is accounted to be of the order of $\sim 8\%$.

The light stau scenario

While light stops may lead to a large modification of the gluon fusion rate with a relative minor effect on the di-photon rate, it has been shown that light staus, in the presence of large mixing, may lead to important modifications of the di-photon decay width of the lightest Higgs boson. Large mixing in the stau sector may happen naturally for large values of $\tan\beta$, for which the mixing parameter $X_\tau = A_\tau - \mu \tan\beta$ becomes large. This choice leads to a light stau particle and defines the *light stau* scenario, whose main phenomenological feature is an enhanced di-photon branching ratio.

The tauphobic scenario

In addition to the loop effects on the Higgs vertices described in the previous sections, the propagator-type corrections involving the mixing between the two CP-even Higgs bosons of the MSSM can have an important impact. This type of corrections can lead to relevant modifications of the Higgs couplings to down-type fermions and a light value for the mass of the stau particle, thus defining the *tauphobic* scenario.

2.3.2 Summary plots

The different results obtained by the analyses can be combined to draw the excluded phase-space of the MSSM parameters in different scenarios. Two different approaches are shown here, which display the results of different analyses by the end of Run 1.

First, Figure 2.12 shows a summary plot of the results of the $H/A \to \tau\tau$ [87, 88] and $H^\pm \to \tau\nu$ [89, 90] analyses in both, ATLAS and CMS experiments, for the search for neutral and charged Higgs bosons decaying to τ leptons, in the $m_h^{\text{mod}+}$ scenario, in the mass range $60 - 1000\,\text{GeV}$. In addition, Figure 2.13 shows a summary plot of the results of different search channels, including $H/A \to \tau\tau$, within the ATLAS Experiment, for the search for neutral Higgs bosons, in the hMSSM scenario, in the mass range $200 - 500\,\text{GeV}$.

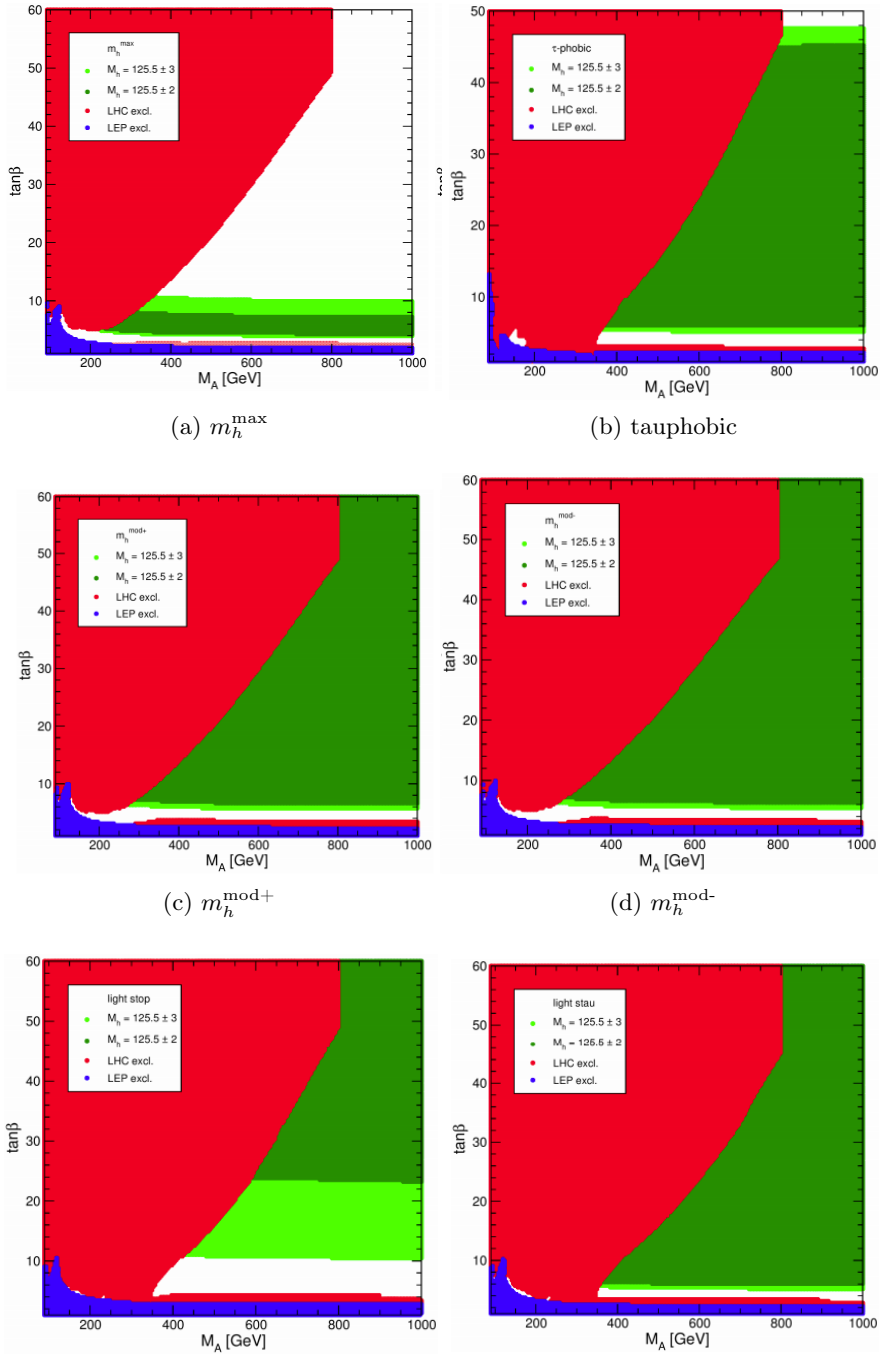

(a) $m_h^{\max}$ (b) tauphobic

(c) $m_h^{\text{mod+}}$ (d) $m_h^{\text{mod-}}$

(e) light stop (f) light stau

Figure 2.11: Regions of the m_A and $\tan\beta$ plane excluded for the different MSSM benchmark scenarios from the direct Higgs searches at LEP and LHC as of 2013. The dark (light) green zone corresponds to the excluded area for which $m_h = 125.5 \pm 2(3)\,\text{GeV}$. Reproduced from [74, 83].

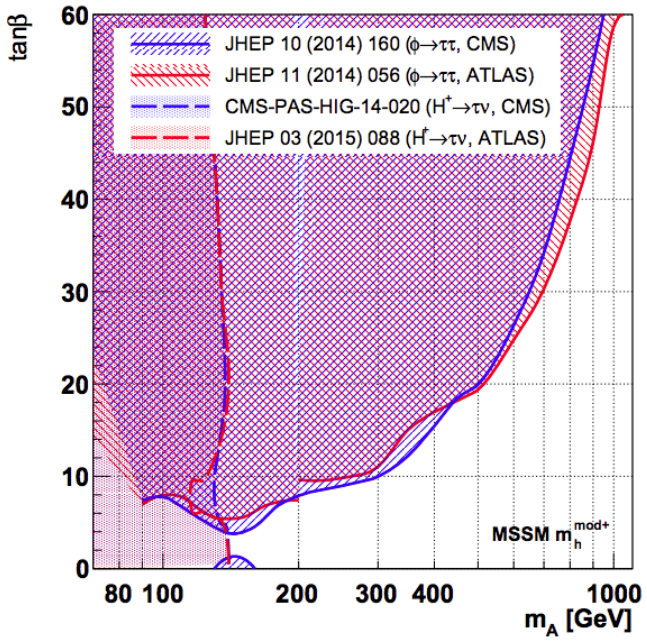

Figure 2.12: Regions of the m_A–$\tan\beta$ plane in the $m_h^{\text{mod}+}$ scenario excluded by the ATLAS and CMS Experiments based ons searches for Higgs bosons decaying to $\tau\tau$ (neutral) or $\tau\nu$ (charged) [74].

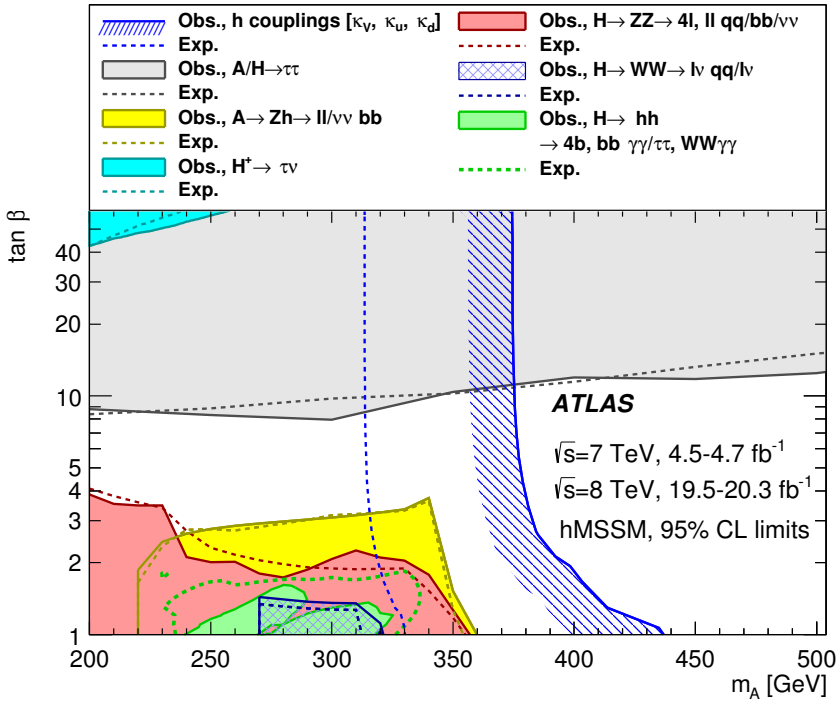

Figure 2.13: Regions of the m_A–$\tan\beta$ plane excluded by the combination of different search channels, including the $H/A \to \tau\tau$, in the ATLAS Experiment, for the search for neutral Higgs bosons, in the hMSSM scenario [91].

Chapter 3

The ATLAS experiment at the CERN Large Hadron Collider

This chapter describes the experimental setup which was used in the analyses of this thesis. The analyses were performed with the data collected by the ATLAS Experiment (Section 3.4), a particle detector placed at one of the collision points of the Large Hadron Collider (Section 3.2), situated within the facilities of the CERN laboratory (Section 3.1) in Geneva, Switzerland.

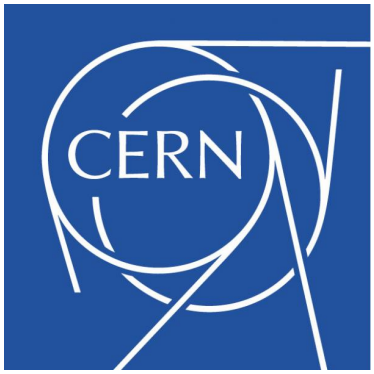

3.1 The CERN laboratory

CERN is the French acronym for the European Organization for Nuclear Research[1], a laboratory situated on the French-Swiss border near Geneva, Switzerland (Figure 3.1). The institution was founded in 1954 by 12 European countries after the events of World War II, with the aim of stimulating the European science, namely the nuclear and atomic fields. Currently, the CERN organization has expanded its borders and now it is supported

[1] In 1952, a provisional institution called *Conseil Européen pour la Recherche Nucléaire* was founded which, two years later, changed to the *European Organization for Nuclear Research*. The old acronym, however, was conserved.

by 22 member states and the additional collaboration of observer states and institutions around the globe.

Figure 3.1: Aerial view of the Meyrin CERN site in 2012 [92].

CERN has provided the physical space and logistics for a numerous group of experiments since its foundation. The experiments are run by collaborations, composed of CERN and a number of institutes and universities from all around the world, while CERN maintains the responsibility of the experimental site, construction and management of the machines.

The fields in which CERN is involved cover a wide range of areas, not only in the scientific department (both theoretical and experimental), but also in engineering and computing fields. Regarding physics, the main subject is particle physics, to which the landmark machines of CERN, such as the LHC, belong. Besides, it has also important contributions to nuclear physics, plasma physics and cosmology. In the engineering department, the CERN experiments have contributed to expand the knowledge of a wide range of technical applications like electronics, cryogenics, superconducting materials and construction techniques.

Since its foundation, the CERN experiments have made several breakthroughs in the field of fundamental physics, especially by the use of particle accelerators. The bubble chamber Gargamelle led to the discovery of the neutral currents in 1973 [32, 33]; in 1983, the UA1 and UA2 experiments placed on the SPS collider, discovered the $W^{\pm}$ and Z bosons [34–37]; the direct CP-violation was confirmed by the NA48 experiment in 1999 [93], supporting the observation made by the NA31 experiment in 1998 [94] and 1993 [95]; and finally, in 2012, the LHC experiments, ATLAS and CMS, observed [40, 41] a scalar neutral massive particle with the expected features of a Higgs boson.

3.2 The Large Hadron Collider

The Large Hadron Collider (LHC) is the largest and most powerful particle collider in the world, the last member of the generation of particle colliders at CERN. It is in function

since 2008 and it is planned to continue working until after 2030, with different upgrade phases.

The LHC is a synchrotron collider which works by accelerating and colliding beams of protons, p, as well as heavy ions, namely ionized lead ($^{208}_{82}$Pb) and Xenon ($^{129}_{54}$Xe), though only the pp collisions are covered in this thesis. The LHC is placed in the underground tunnel used by the previous accelerator, the Large Electron Positron collider (LEP). The LEP/LHC tunnel, which is situated in the west side of the city of Geneva (Switzerland), is a ring with a circumference of 26.7 km and a depth varying between 45 and 170 m. Its layout is shown in Figure 3.2.

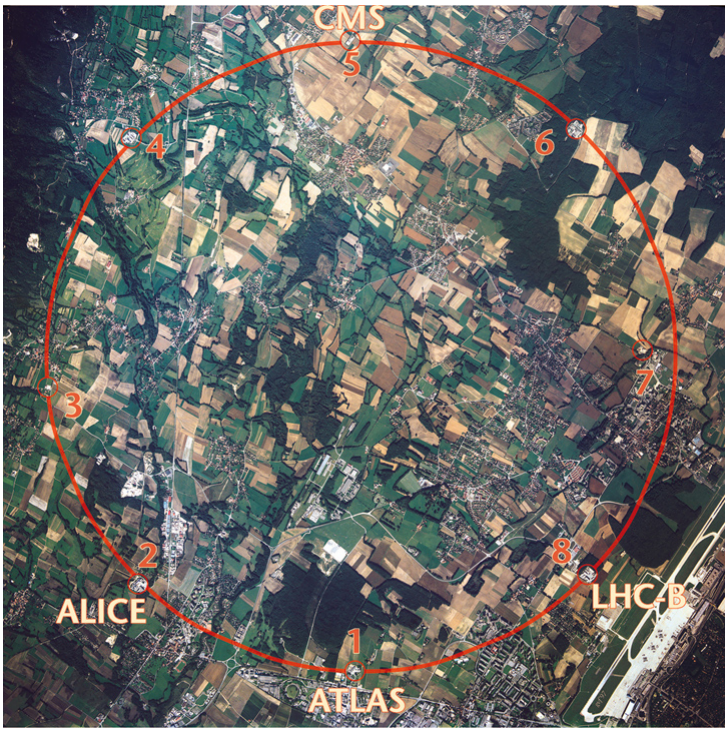

Figure 3.2: Aerial view of the surface over the LEP/LHC tunnel in 1994, showing the location of its four experiments and the CERN laboratory, which can be seen under the ATLAS label. The Geneva International Airport appears on the right of the photo [96].

The LHC is composed [97–100] of two adjacent parallel beam lines (or beam pipes), separated by 194 mm and that intersect at four points, where experiments are placed. The accelerator is composed of eight 2.45 km long arcs and eight 528 m long insertions. An insertion consists of a long straight section plus two transition regions (dispersion suppressors). The exact layout of the straight section depends on its specific use: physics (beam collisions), injection, beam dumping or beam cleaning. The arcs consist of a regular lattice structure which contains 23 arc cells, 106.9 m long. In turn, the arc cells are made of two symmetrical half-cells, composed of a long cryostat, a short straight section assembly and three 14.3 m long dipole magnets (Figure 3.3).

In total, the LHC contains 16 radio-frequency cavities, used for the acceleration of the beam, and 9593 magnets, of different kind, which were able to generate a magnetic

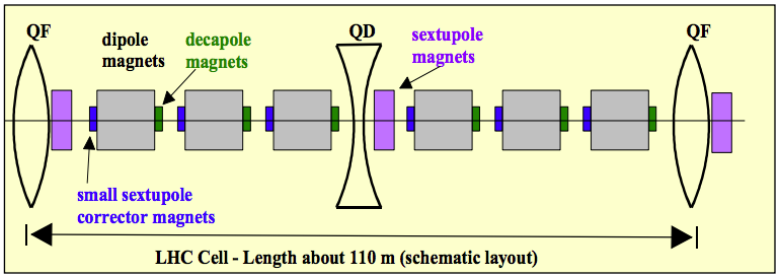

Figure 3.3: Schematic layout of a LHC half-cell arc, showing the dipoles, quadrupoles, sextupoles and decapoles [100].

field with a strength of 8.3 T for the design beam energy of 7 TeV. The main function of the 1232 main dipoles is the bending of the beam direction. Additional 392 main quadrupoles are used for collimation purposes. Higher-order multipoles, such as sextupoles or decapoles, are used for corrections of smaller imperfections in the field geometry and fine-corrections of the beam direction. A diagram of the cross-section of a dipole and a quadrupole is shown in Figure 3.4.

In order to provide the required electrical current (up to 12.4 kA) while avoiding a huge energy consumption of the coils, the magnets have to be *superconductors*, which is achieved by cooling them with liquid helium to 1.9 K. The magnets have also a security system for magnet quenches (sudden loss of superconducting conditions), as well as a safe extraction of the beam, both in controlled and emergency cases.

3.2.1 Roadmap of the LHC

The roadmap of the LHC program is summarized in Figure 3.5. The program is divided in several periods of data-taking called *Runs*, separated by consolidation periods, called *Long Shutdowns* (LS), where the accelerator (and the detectors) undergo repairing and upgrading works. Figure 3.6 shows a forecast of the instantaneous and integrated luminosity for the roadmap of the LHC.

The first phase of the LHC is **Run 1**, spanning from 2011 to 2013, followed by the Long Shutdown 1 (**LS1**) during 2013 and 2014; the second phase is **Run 2**, from 2015 to 2018, which will be followed by the **LS2** (2019-2020); and finally, the last phase is Run 3, which is planned to span from 2021 to 2023. In 2024, the LHC is expected to enter into the LS3, to prepare the machine for its Phase II, the High-Luminosity LHC (HL-LHC) [101], a significant upgrade to achieve higher luminosity conditions. The working parameters of the LHC (energy, luminosity, intensity, bunch spacing,...) change for each Run. Its design values, as well as the working values for the Runs 1 and 2 of the LHC, are summarized in Table 3.1.

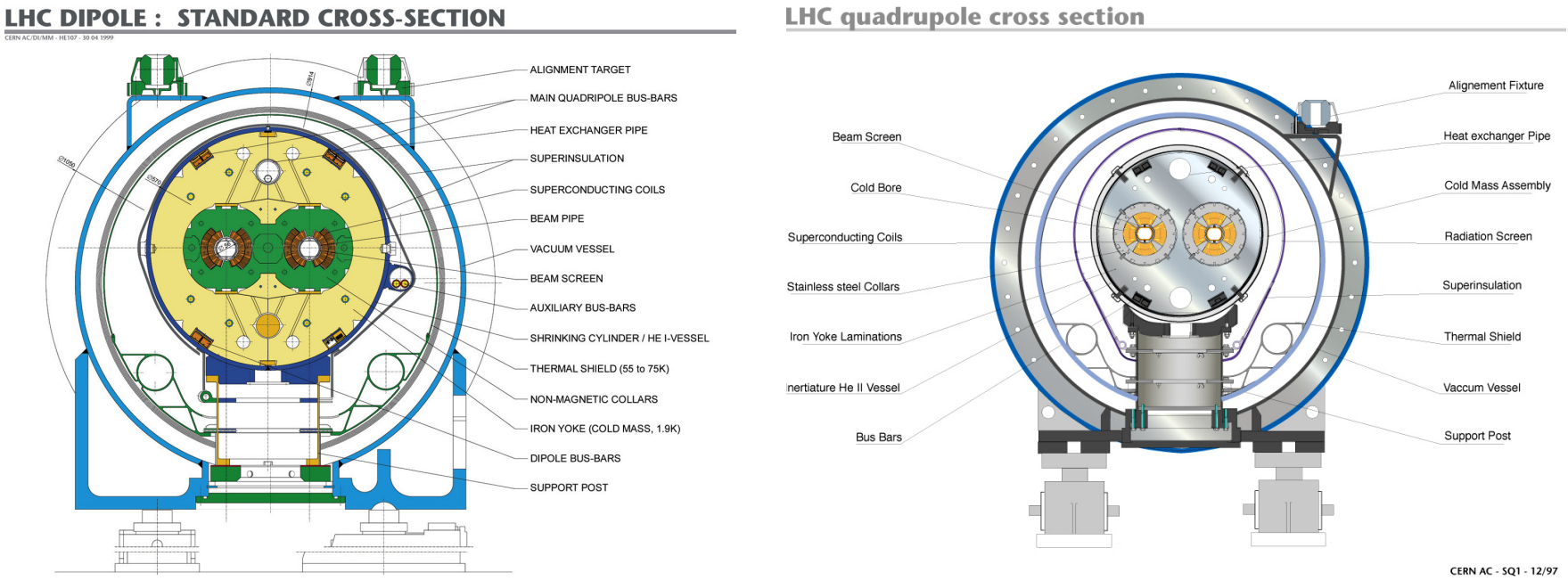

(a) Dipole

(b) Quadrupole

Figure 3.4: Diagram of the cross-section of (a) a dipole and (b) a quadrupole of the LHC [100].

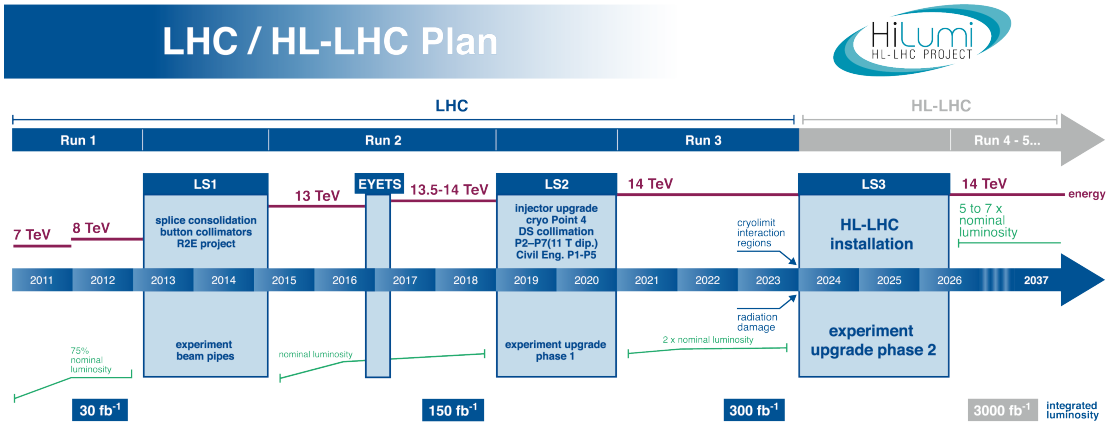

Figure 3.5: Roadmap of the LHC program showing the Runs and the Long Shutdowns (LS), spanning from the machine start in 2011 to the beginning of the next phase, the HL-LHC [102].

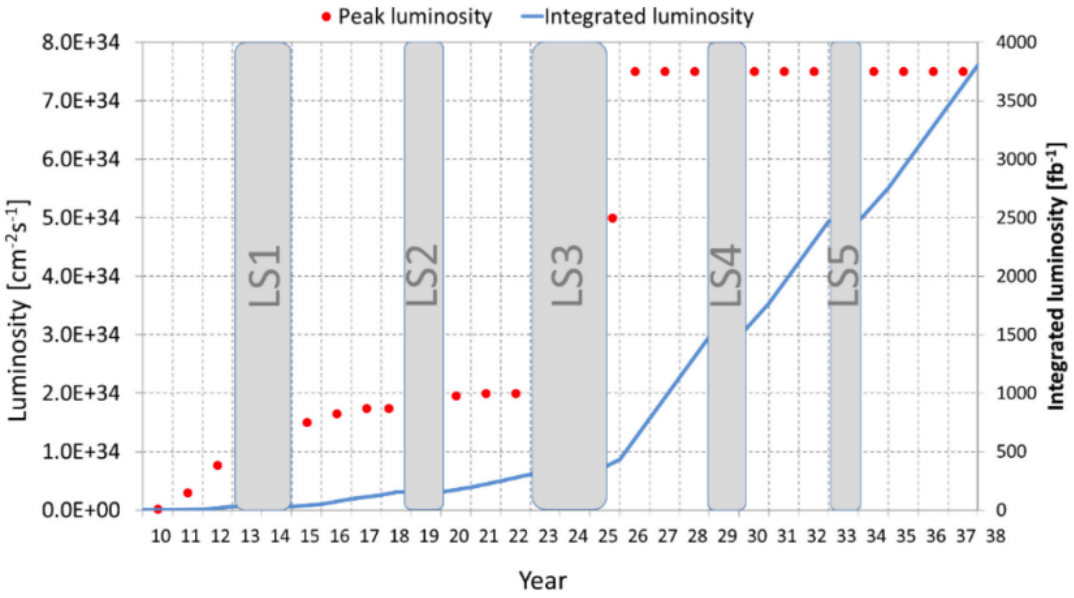

Figure 3.6: Simplified scheme for instantaneous luminosity (red dots) and integrated luminosity (blue line) in the LHC and HL-LHC programs [101].

3.2.2 LHC Accelerator Complex and the LHC experiments

The acceleration of protons up to the energies required for the collisions is done at the LHC in several stages, which employs different machines. The whole ensemble is called the LHC Accelerator Complex (Figure 3.7). The protons are obtained from ionized hydrogen and accelerated to 50 MeV in the Linear Accelerator 2 (LINAC2). The beam of protons passes from LINAC2 to the Proton Synchrotron Booster, which accelerates them to 1.4 GeV. After that, they are transferred to the Proton Synchrotron (PS), which pushes their energy to 26 GeV and then, they are sent to the Super Proton Synchrotron (SPS). The SPS is used to accelerate the packs of protons to the injection energy of

			Run 1		Run 2	
Parameter	**Unit**	**Design**	2011	2012	2015	2016
Beam energy	TeV	7	3.5	4.0	6.5	6.5
Energy at center of mass	TeV	14	7.0	8.0	13	13
# of particles per bunch	$\times 10^{11}$	1.15	1.45	1.6	1.2	1.15
# of bunches per fill		2808	1380	1380	2240	2220
Peak Luminosity	$\times 10^{34}$ cm^{-2}s^{-1}	1	0.35	0.77	0.5	1.4
Bunch-spacing	ns	25	75 / 50	50	25	25
Amplitude function β^*	m	0.55	1.5 / 1	0.6	0.8	0.4
Emittance ϵ	μm	3.75	2.3	2.5	3.5	2.0
Initial avg. collisions per bunch-crossing		26	17	37	18	52

Table 3.1: Summary of the LHC operation parameters for the pp collisions during Run 1 (years 2011 and 2012) [103] and Run 2 (years 2015 and 2016) [104].

450 GeV, ready to be transferred to the LHC. The SPS injects bunches of protons in each direction, in series called *trains*. The LHC, then, performs the final acceleration of the trains of protons, and it squeezes the bunches, increasing the proton density (i.e. the instantaneous luminosity), and adjusts the beams position, triggering the collisions at the crossing points (Figure 3.8).

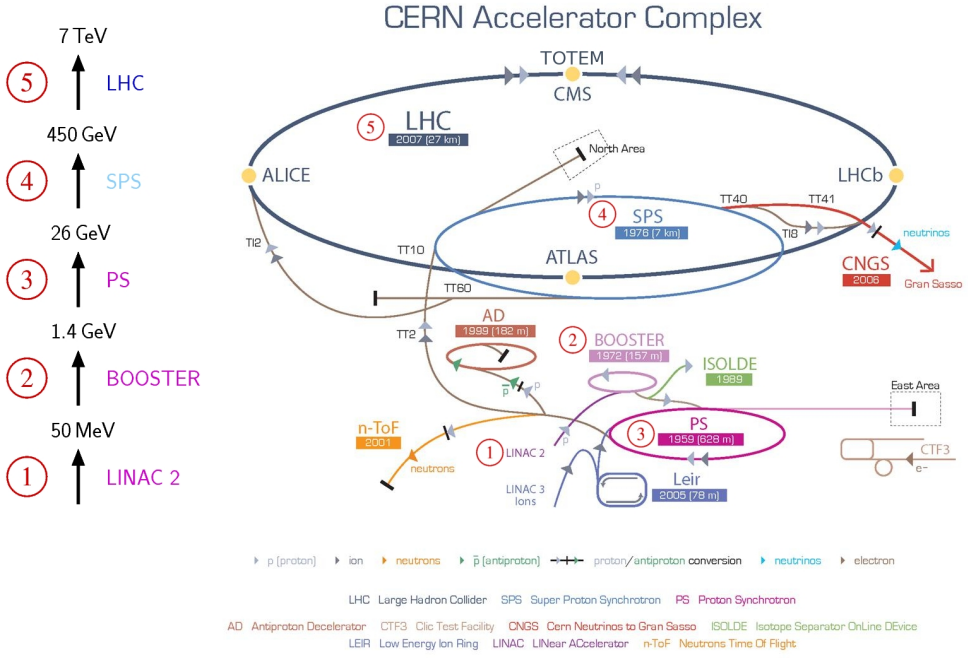

Figure 3.7: Diagram of the full accelerator complex at CERN, including the LINAC2, Booster, PS, SPS and LHC accelerators [105].

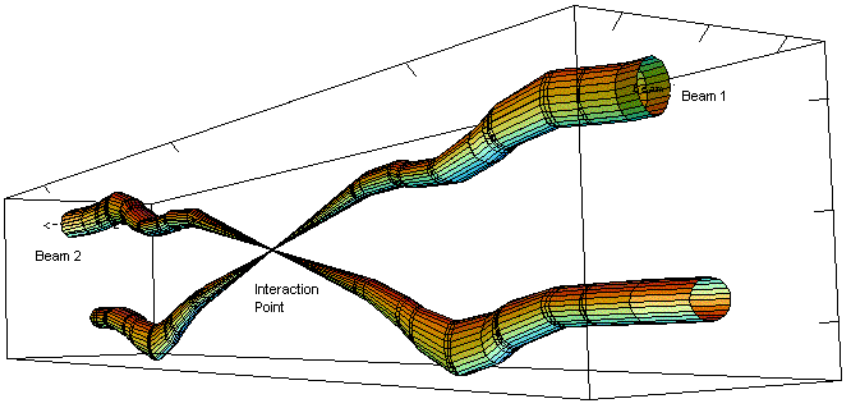

Figure 3.8: Simulation of the squeezing of the beam that happens at each of the interaction points of the LHC for triggering the collisions [106].

The two beams cross in four different points, where the physics experiments are placed. Figure 3.2 shows the position of the four experiments around the LHC ring. In addition, the experiment logo and a schematic diagram of each the four detectors is shown in Figure 3.9.

In Point 1, the closest to the Meyrin site of the CERN laboratory, stands the ATLAS experiment (A Toroidal LHC ApparatuS). The CMS experiment (Compact Muon Solenoid) is installed in Point 5, near the village of Cessy, which is at the opposite site of the ring with respect to ATLAS. ATLAS and CMS are two akin detectors. While they are structurally different, they are both multi-purpose, with the aim of searching for the Higgs boson, performing precision studies of the SM and discovering new physics beyond the SM.

The ALICE detector (A Large Ion Collider Experiment) is located in Point 2, near the village of Saint Genis-Pouilly. ALICE is a detector whose focus is the analysis of the heavy-ion collisions to investigate the physics of dense matter and the QCD interaction in the quark-gluon plasma. And finally, the LHCb detector (LHC-beauty) is located in Point 8, near the village of Ferney-Voltaire. The LHCb Experiment studies the physics of the B-mesons and CP-violation.

3.2.3 Luminosity delivered

The first injection of protons took place on 10^{th} September 2008, but a few days later an electrical fault occurred in Sector $3-4$ resulting in mechanical damage, releasing the cooling helium, as well as losing the vacuum and cryogenic conditions [107]. Up to 700 m of magnets were damaged and the LHC roadmap had to be reconsidered.

It took one year to recover the functioning of the LHC after the incident and thus, the first collisions at injection energy were obtained on 23^{rd} November 2009. The LHC was designed to run at an energy in the center of mass (e.c.m. or $\sqrt{s}$) of 14 TeV, however, due to significant concerns about the safety of the magnets after the incident,

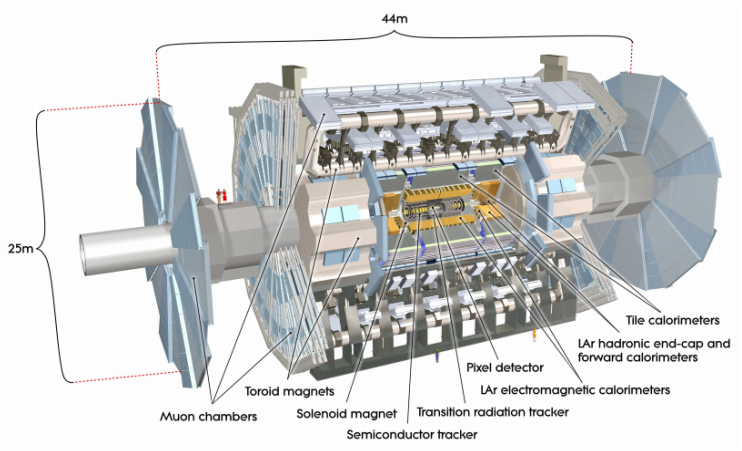

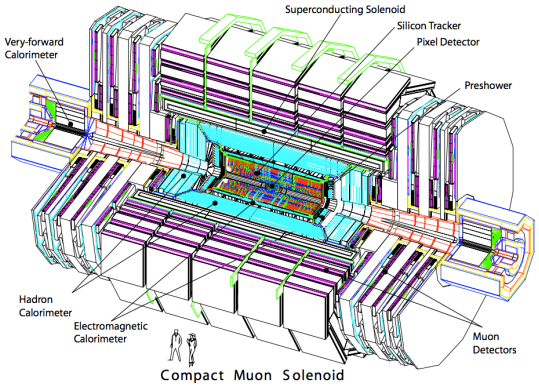

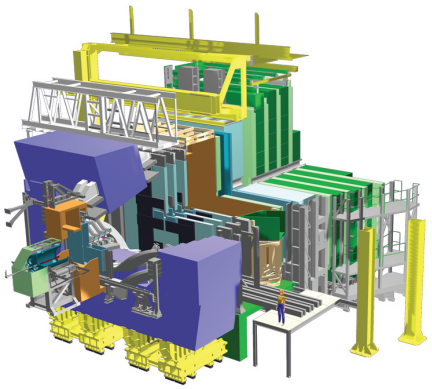

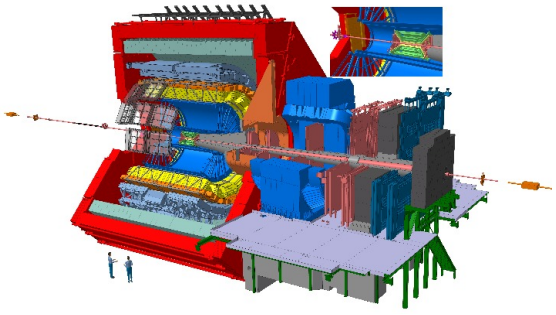

Figure 3.9: Logos and schematic diagrams of the four different experiments at LHC. CERN Document Server.

that milestone was postponed for Run 2. Run 1 started officially on 30$^{\text{th}}$ March 2010 with an e.c.m of 7 TeV, though the instantaneous luminosity achieved was small. In 2011, the collisions continued at 7 TeV, collecting 5.46 fb^{-1} of integrated luminosity. After running all the year without further incidents, the e.c.m. was raised to 8 TeV in 2012, collecting 22.8 fb^{-1} of data. On 11$^{\text{th}}$ February 2013, the LHC was stopped and Run 1 was finalized. Figure 3.10 (a) shows the integrated luminosity of Run 1 as a function of time, while (b) shows the distribution of the average number of collisions per bunch crossing.

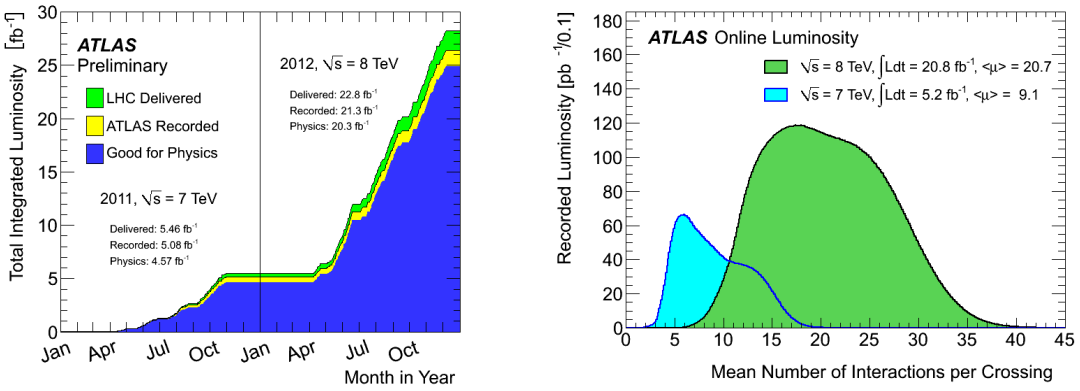

(a) Cumulative luminosity

(b) Average collisions per bunch-crossing

Figure 3.10: Cumulative luminosity as a function of time for Run 1 (a) and average number of collisions per bunch crossing (b). In (a) the luminosity delivered by LHC appears in green, the value recorded by ATLAS in yellow and the luminosity certified to be of good quality is drawn in blue [108].

The LS1 spanned for one year and half while the LHC and the detectors were repaired and upgraded. Even after the consolidation works, it was not considered safe enough for the magnets to be powered up to the design current of the LHC and thus, the Run 2 e.c.m. was risen only to 13 TeV. In addition, the bunch spacing was reduced from 50 ns to 25 ns, greatly enhancing the instantaneous luminosity, to the point that, during 2016, it surpassed the designed value of $10^{34}\,\text{cm}^{-2}\,\text{s}^{-1}$ of the LHC. Run 2 continues during the years 2017 and 2018 until the LS2. The total integrated luminosity collected so far in the Run 2, at $\sqrt{s} = 13\,\text{TeV}$ was 3.21 fb^{-1} during 2015 and 36.1 fb^{-1} during 2016. Figure 3.11 (a) compares the luminosity collected during the different years of both Run 1 and Run 2. In (b), the distribution of average collisions per bunch crossing in Run 2 is shown.

During LS2 the machine will be upgraded to deliver collisions at $\sqrt{s} = 14\,\text{TeV}$, expecting to record around 300 fb^{-1} of integrated luminosity during Run 3. For the next stage, the Phase-II, the HL-LHC is expected to provide up to 3000 fb^{-1} of integrated luminosity.

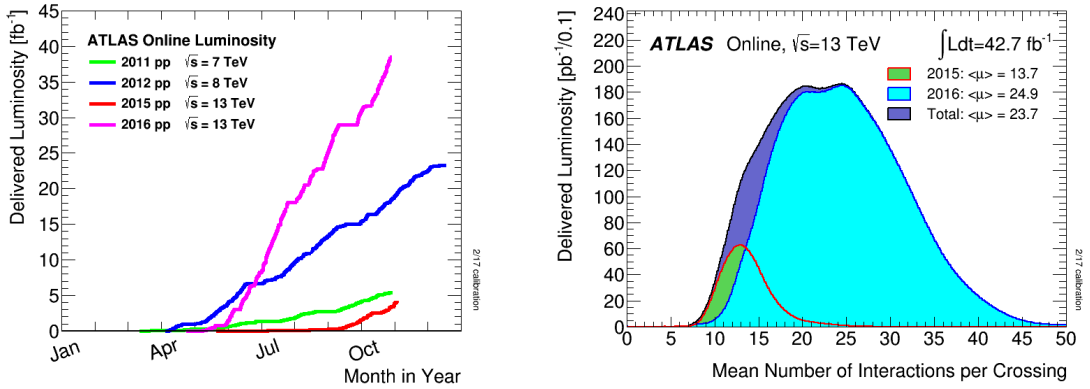

(a) Cumulative luminosity (b) Average collisions per bunch-crossing

Figure 3.11: Cumulative luminosity as a function of time for Run 2 (a) and average number of collisions per bunch crossing (b). In (a), the values are shown for Run 1 (green for 2011 and blue for 2012 data) and for Run 2 (red for 2015 and pink for 2016).

3.3 The LHC Computing Grid

The field o fcomputing is a crucial part of the CERN past and present history. The communication needs between scientists led to the invention of the World Wide Web (www) by Tim Berners-Lee in 1989 [109], one of the biggest technological milestones in history. The current need for storage and management of a huge amount of data, the *Big Data* problem, led to the development of the Worldwide LHC Computing Grid (WLCG), usually referred simply as *GRID*. The GRID is a huge network of interconnected computer centers around the world, which allows the storage and access of the data recorded by the LHC experiments, as well as providing distributed computing services for the analysis of these data.

The WLCG is composed of three levels, or *Tiers*, numbered 0, 1, and 2 respectively, whose hierarchy is shown in Figure 3.12. Each Tier is made up of several computer centers and provides a specific set of services. Tier-0 is the CERN Data Center, the heart of the network. All of the data from the LHC passes through this central hub, but it provides less than 20% of the GRID's total computing capacity. It also distributes the raw data and the reconstructed output to Tier-1, and reprocesses data when the LHC is not running. Tier-1 consists of 13 computer centers large enough to store LHC data. They provide round-the-clock support for the GRID and are responsible for storing a proportional share of raw and reconstructed data, as well as performing large-scale reprocessing and storing the corresponding output; distributing data to Tier-2; and storing a share of the simulated data that the Tier-2 produces. Tier-2 are typically universities and other scientific institutes (around 155 sites around the world) that can store sufficient data and provide adequate computing power for specific analysis tasks. They handle a proportional share of the production and reconstruction of simulated events.

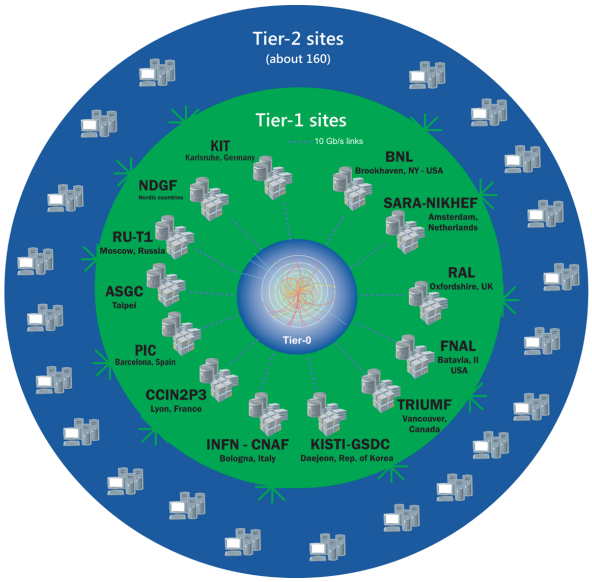

Figure 3.12: Diagram of the Tier hierarchy of the GRID, showing the Tier-0 (CERN Computer Center) in the center layer, the 13 Tier-1 sites in the green layer and the Tier-2 sites in the blue outer layer [110].

3.4 The ATLAS detector

The ATLAS experiment is a multi-purpose detector whose main objective is the search for the Higgs boson, as well as for new physics at the TeV scale. The detector is a cylinder of 25 m of diameter and 44 m of length, built underground around the collision point 1 of the LHC, which is the closest to the Meyrin site of CERN. It was built, and it is currently run, by the *ATLAS Collaboration*, an association of research groups from 182 different institutions of 38 countries all over the world. The Collaboration was in charge of the design and construction of the detector, and it has now the responsibility for its correct functioning and management, as well as providing for a framework for the analysis of the collected data.

ATLAS is composed of several layers of subsystems, each of them focusing on a different objective. In particular, they are specialized in identifying and measuring the properties of different kind of particles (and their decay products) generated by the collisions. The general characteristics of the ATLAS detector are [112]:

- Fast detection and processing, to cope with the high-frequency collisions.
- Radiation-resistant electronics and sensor elements, to avoid radiation damage.
- High detector granularity, to discriminate the signals of interest in a dense environment.
- Full coverage in the azimuthal angle and large acceptance in pseudorapidity (defined in Equation 2.4).

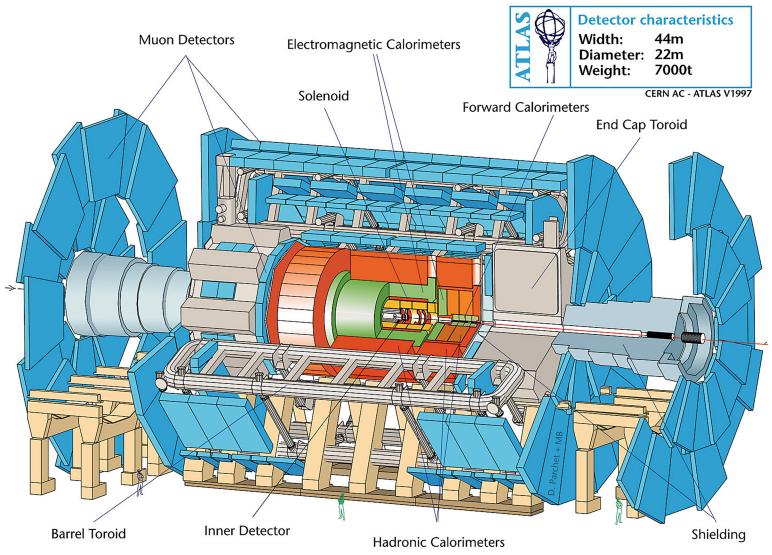

Figure 3.13: Diagram of the ATLAS detector with its main components [111].

- Good charged-particles momentum resolution and reconstruction efficiency, especially in the inner tracker.
- Good vertex reconstruction accuracy, both for primary and secondary vertices.
- Excellent electromagnetic calorimetry for electron and photon identification and energy measurement.
- Full-coverage hadronic calorimetry for accurate jet and missing transverse energy measurements.
- Good muon identification and momentum resolution.
- High efficient triggering of low transverse-momentum objects to achieve an acceptable trigger rate for interesting physics events.

As was described in Section 2.1, in order to parametrize position and coverage of the different elements, a coordinate system (x, y, z) is defined, with the origin in the nominal interaction point (IP). The z-coordinate runs along the beam line while the $x-y$ plane (transverse plane) is the one perpendicular to the beam direction. The positive x-axis is defined as pointing to the center of the LHC ring, the positive y-axis is defined as pointing upwards and the positive z-axis is defined pointing towards the Leman Lake, on the east side.

However, as ATLAS has a cylindrical symmetry, it is more useful to define a set of cylindrical coordinates, with the origin in the IP. The cylindrical coordinates are (ϕ, η, z) where ϕ is the azimuthal angle in the transverse plane to the beam, defined within $\phi \in [-\pi, \pi]$; and η is the *pseudorapidity*, which is a parameter related to the polar angle, θ.

The angular distance in the $\phi - \eta$ plane is measured in terms of ΔR. The mathematical definitions of η and ΔR were shown in Equation 2.4.

The main subsystems of the ATLAS detector are described in the following sections. Three main sub-detectors can be defined: the Inner Detector, the Calorimeters (Electromagnetic and Hadronic) and the Muon Spectrometer. The comparison of the coverage and resolution of the different sub-detectors is given in Table 3.2. An illustration of the measurement principles of each sub-detector is shown in Figure 3.14. Additional systems, which are crucial for the functioning of the detector, are the Magnet system, the Trigger and Data Acquisition system and the Forward detectors.

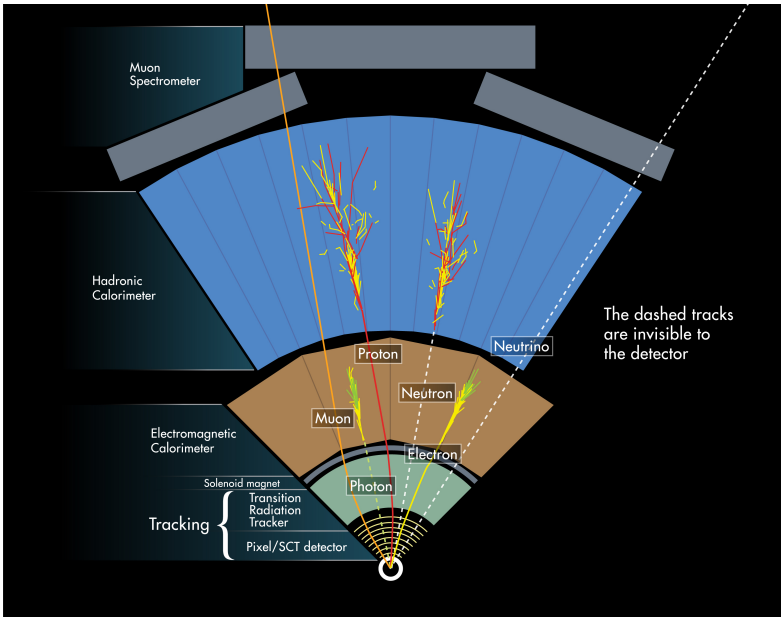

Figure 3.14: Diagram of the response of each sub-detector of ATLAS to the behavior of the different particles [113].

		η coverage	
Sub-detector	**Resolution**	Measurement	Trigger
Tracking	$\sigma_{p_T}/p_T = 0.05\% \, p_T \oplus 1\%$	$[-2.5, +2.5]$	-
EM Calorimetry	$\sigma_E/E = 10\%/\sqrt{E} \oplus 0.7\%$	$[-3.2, +3.2]$	$[-2.5, +2.5]$
Hadronic Forward	$\sigma_E/E = 100\%/\sqrt{E} \oplus 10\%$	$[\pm 3.1, \pm 4.9]$	$[\pm 3.1, \pm 4.9]$
Hadronic Barrel and end-cap	$\sigma_E/E = 50\%/\sqrt{E} \oplus 3\%$	$[-3.2, +3.2]$	$[-3.2, +3.2]$
Muon Spectrometer	$\sigma_{p_T}/p_T = 10\%$ at $p_T = 1$ TeV	$[-2.7, +2, 7]$	$[-2.4, +2.4]$

Table 3.2: Resolution and coverage of the different ATLAS sub-detectors. The units for E and p_T are GeV [112].

3.4.1 The Inner Detector

The Inner Detector (ID) is the innermost part of ATLAS and acts as a tracking device. It is designed to provide hermetic and robust pattern recognition, excellent momentum resolution and both primary and secondary vertex measurements for charged tracks within $|\eta| < 2.5$. It also provides electron identification over $|\eta| < 2.0$. In addition, the ID is immersed in a 2 T magnetic field generated by the central solenoid which curves the direction of the charged particles going through it, thus providing valuable information about their charge and momentum. Its layout is shown in Figure 3.15.

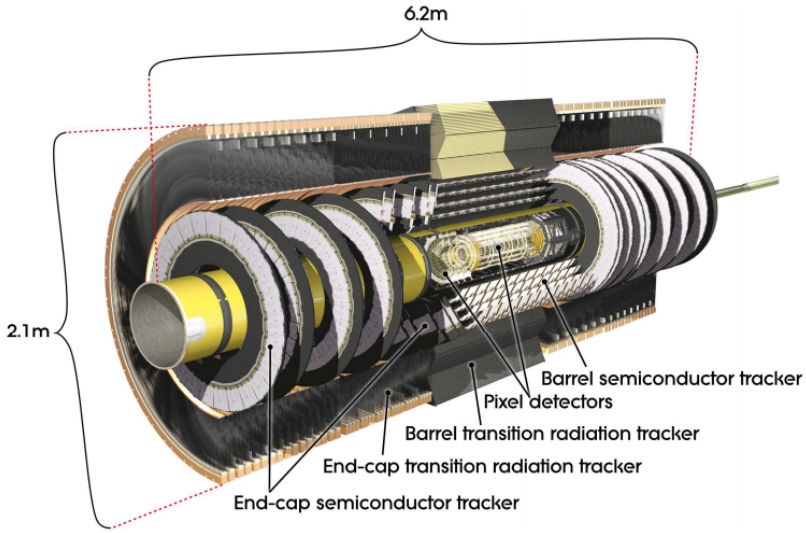

Figure 3.15: Diagram showing in detail the Inner Detector and its components as built in 2008 [112].

The ID is contained in a cylindrical envelope with a length of 5.30 m and of radius of 1.2 m, within the central solenoid magnet. It consists of three independent but complementary sub-detectors.

The innermost part is the **Pixel detector**, a detector with high-resolution pattern recognition capabilities that uses discrete space-points from silicon pixel layers. The Pixel detector is made of strips of silicon sensors arranged on three concentric cylinders around the beam pipe (barrel) and another three disks in each end-cap. Each of the 1744 sensors contains 46 080 channels (from 47 232 pixels) and thus, it has approximately 80.4 million read-out channels distributed in three layers around the beam pipe.

In order to improve the performance of the ATLAS detector in the tracking, during the LS1 a new layer was added to the Pixel subsystem, the **Insertable B-layer (IBL)** [114]. The IBL is a single cylindrical detector layer placed between the Pixel detector and the new[2] beam pipe, encircling it, as can be seen in Figure 3.16. The IBL adds around 6 million pixels and was designed to improve the quality of impact parameter

[2]The old beam pipe had to be substituted by a new one, much thinner and smaller, in order to make space for the new detector.

reconstruction and the precision of the track reconstruction. In addition, it was designed to provide a more robust structure to stand the radiation effects from the collisions.

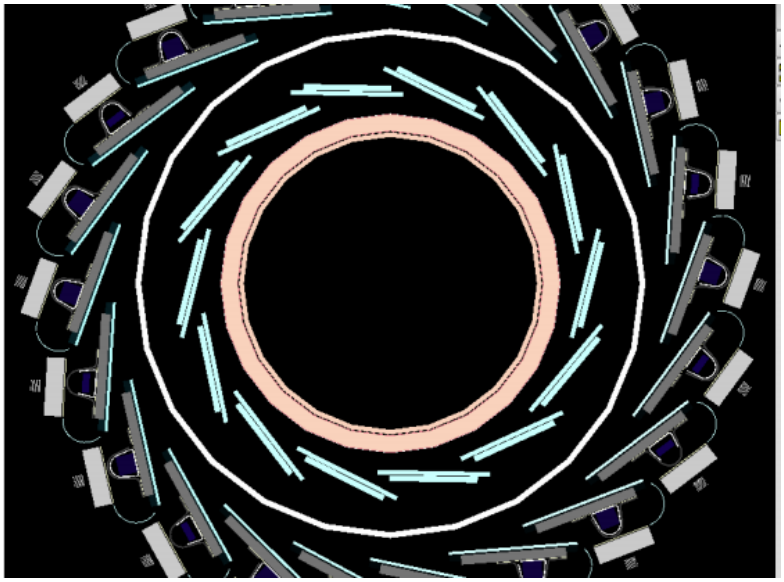

Figure 3.16: Diagram showing the placement of the Insertable B-Layer within the Inner Detector. The IBL is the light blue set of pixels, which is placed surrounding the beam pipe (red) and within the inner layer of the Pixel detector (dark gray-blue) [114].

The next component is the **Silicon Tracker (SCT)**, which is formed by stereo pairs of silicon microstrip layers with two differentiated regions. One is the barrel region, where the SCT is placed as concentric cylinders around the beam axis, surrounding the Pixel detector. In the end-caps, on each side of the Pixel, the SCT is made of several disks perpendicular to the beam axis. In general, one of the strips of the pair is placed parallel (perpendicular) to the beam pipe, while the second one is placed forming a small angle, thus allowing a 3D measurement. The total number of read-out channels of the SCT is approximately 6.3 million from 15 912 sensors distributed in four layers around the beam pipe.

The outermost part of the ID is the **Transition Radiation Tracker (TRT)**, which is formed by layers of gaseous straw tube elements interleaved with transition radiation material. The latter provides electron identification on top of continuous tracking, to enhance the pattern recognition and improve the momentum resolution over $|\eta| < 2.0$. It is read-out by around 350 000 electronic channels.

3.4.2 The Calorimeter system

The calorimetry requirements of the ATLAS detector are fulfilled by two different sub-detectors, the Liquid Argon Calorimeter (LAr) and the Tile Calorimeter (TileCal), which jointly cover the region $|\eta| < 4.9$. Whereas TileCal is fully an hadronic calorimeter, the LAr calorimeter comprises a set of detectors: the Electromagnetic LAr (EM LAr), the LAr hadronic end-caps and the LAr forward calorimeter. An overview of the full calorimeter

Sub-detector		R (mm)	$\lvert z\rvert$ (mm)	**Precision** (μm)
Beam pipe		[25, 29] with IBL	-	-
		[29, 36] original	-	-
ID		[0, 1150]	[0, 3512]	-
IBL	Overall	[31, 40]	[0, 332]	-
Pixel	Overall	[45.5, 242]	[0, 3092]	-
	Barrel	[50.5, 122.5]	[0, 400.5]	10 ($R-\phi$) 115 (z)
	End-cap	[88.8, 149.6]	[0, 650]	10 ($R-\phi$) 115 (z)
SCT	Overall	[255, 549] (barrel)	[0, 805]	-
		[251, 610] (end-cap)	[810, 2797]	-
	Barrel	[299, 514]	[0, 749]	17 ($R-\phi$) 580 (z)
	End-cap	[275, 560]	[0, 2735	10 ($R-\phi$) 580 (R)
TRT	Overall	[554, 1082] (barrel)	[0, 780]	130
		[617, 1106] (end-cap)	[810, 2744]	-
	Barrel	[563, 1066]	[0, 712]	-
	End-cap	[644, 1004]	[0, 2710]	-

Table 3.3: Main parameters of the Inner Detector system including the IBL [112, 114].

system of ATLAS, showing all of these components is shown in Figure 3.17, while a summary of the η coverage and the number of channels of each of the sub-detectors is given in Table 3.4. An brief overview of the LAr systems will be covered in this section while the description of the Tile Calorimeter will be given in a dedicated section (Section 3.4.3), since a part of the studies of this thesis is related to this sub-detector.

3.4.2.1 The Liquid Argon calorimeter

The **LAr EM calorimeter** is a lead-liquid argon detector whose main purpose is the detection and measure of energy deposits left by the decay of electromagnetic-driven particles, such as electrons and photons. It consists of accordion-shaped kapton electrodes and lead absorber plates. As Figure 3.18 shows, it is divided in two main parts, the barrel region ($|\eta| < 1.475$) and the end-caps ($1.375 < |\eta| < 3.2$). The barrel part is located surrounding the central solenoid, in which the ID is placed. The barrel calorimeter consists of two identical halves, separated by a small gap (4 mm) at $z = 0$, whereas each end-cap calorimeter is mechanically divided into two coaxial wheels: an outer wheel covering the region $1.375 < |\eta| < 2.5$, and an inner wheel, covering the region $2.5 < |\eta| < 3.2$. Over the region devoted to precision physics (coverage of the precision ID tracking, $|\eta| < 2.5$), the

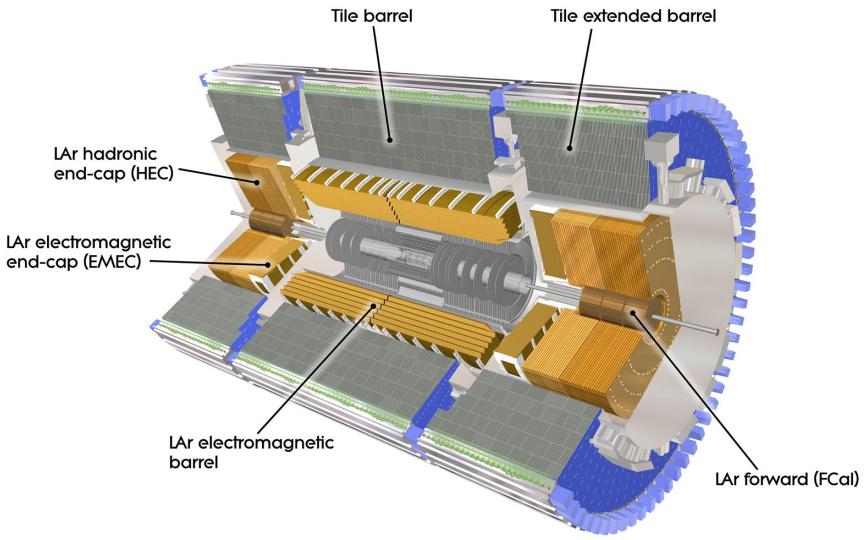

Figure 3.17: Diagram showing the Calorimeter system of the ATLAS detector. The LAr calorimeter system, the closest to the beam pipe, that includes the EM part, the hadronic end-caps and the forward detector, is drawn in orange color. The Tile Calorimeter is situated in the outer part of the cylinder and is drawn in blue color [112].

Sub-detector		η	**Channels**
LAr EM Barrel	Presampler	$\lvert\eta\rvert < 1.52$	7808
	Calorimeter	$\lvert\eta\rvert < 1.475$	101 760
LAr EM End-cap	Presampler	$1.5 < \lvert\eta\rvert < 1.8$	1536
	Calorimeter	$1.375 < \lvert\eta\rvert < 3.2$	62 208
HEC		$1.5 < \lvert\eta\rvert < 3.2$	5632
FCal		$3.1 < \lvert\eta\rvert < 4.9$	3524
TileCal	Long Barrel	$\lvert\eta\rvert < 1$	5760
	Extended Barrel	$0.8 < \lvert\eta\rvert < 1.7$	4092

Table 3.4: η coverage and number of channels of the Calorimeter system in ATLAS, including all the LAr subsystems (EM, HEC, FCal) and the Tile Calorimeter [112].

EM calorimeter is segmented in three sections in depth. For the end-cap inner wheel, the calorimeter is segmented in two sections in depth and has a coarser lateral granularity than for the rest of the acceptance. In the region of $|\eta| < 1.8$, a presampler detector is used to correct for the energy lost by electrons and photons upstream of the calorimeter. The presampler consists of an active LAr layer of thickness 1.1 cm in the barrel region and 0.5 cm in the end-cap region.

The LAr detector includes also two hadronic end-cap detectors, the **Hadronic End-cap Calorimeters (HEC)**. They consist of two independent wheels per end-cap,

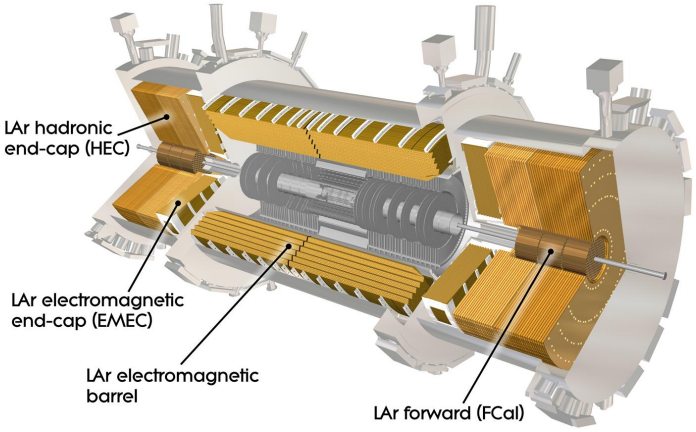

Figure 3.18: Diagram showing the structure of the ATLAS LAr system, including the Electromagnetic barrel (EM LAr) and endcaps (EMEC), the LAr hadronic endcaps (HEC) and the LAr Forward detector (FCal). The Inner Detector is shown in gray inside the EM LAr barrel. [115].

located directly behind the end-cap electromagnetic calorimeter and sharing the same cryostats. Each wheel is built from 32 identical wedge-shaped modules, assembled with fixtures at the periphery and at the central core. Each wheel is divided into two segments in depth, for a total of four layers per end-cap. To reduce the drop in material density at the transition between the end-cap and the forward calorimeter (around $|\eta| = 3.1$), the HEC extends out to $|\eta| = 3.2$, thereby overlapping with the forward calorimeter. Similarly it also overlaps with TileCal ($|\eta| < 1.7$) by extending to $|\eta| = 1.5$.

Finally, the **Forward Calorimeter (FCal)** is a calorimeter placed in the forward region (high η) at each side of the ID. It is placed inside the LAr End-cap calorimeters, surrounding the beam pipe, as can be observed in Figure 3.18. The FCal consists of three modules in each end-cap: the first, made of copper, is optimized for electromagnetic measurements, while the other two, made of tungsten, measure predominantly the energy of hadronic interactions. Each module consists of a metal matrix, with regularly spaced longitudinal channels. The channels are filled with the electrode structure consisting of concentric rods and tubes parallel to the beam axis. The FCal is integrated into the end-cap cryostats, as this provides clear benefits in terms of uniformity of the calorimetric coverage as well as reduced radiation background levels in the muon spectrometer.

3.4.3 The Tile Calorimeter detector

3.4.3.1 Hardware structure

The Tile Calorimeter (TileCal) [116] is a hadronic sampling detector that uses steel as absorber and tiles of plastic scintillator as active medium. Its main purpose is the

absorption of the hadronic particles produced in the collisions and the measurement of their energy.

As Figure 3.17 shows, TileCal is placed surrounding the LAr system, in the region $|\eta| < 1.7$. The detector is divided in two parts: a central barrel, named *Long Barrel* (LB), which covers the region $|\eta| < 1.0$, and two Extended Barrels (EB), which cover the region $0.8 < |\eta| < 1.7$. Each barrel is a cylinder with an inner radius of 2.28 m and an outer radius of 4.25 m. The Long Barrel has a length of 5.8 m while the Extended Barrels have a length of 2.6 m. The read-out of the Long Barrel is divided in two parts, symmetric with respect to the z-axis. The parts, both Long and Extended, that point to the east, i.e. which have $[z > 0, \eta > 0]$, are labelled side-A; conversely, the other two sections, with $\eta < 0$, are named side-C. This makes the TileCal read-out divided in four partitions, labelled EBA, LBA, LBC, and EBC.

However, the TileCal is not totally hermetic, as there is a 0.6 m gap between the Long Barrel and the Extended Barrels, which is needed for the Inner Detector and Liquid Argon Calorimeter services. A stepped calorimeter structure is placed in the gap region, which tries to maximize the active material in this region while leaving enough space for cables and services. The special cells covering the region between $1.0 < |\eta| < 1.6$, are called gap scintillators ($1.0 < |\eta| < 1.2$) and crack scintillators ($1.2 < |\eta| < 1.6$).

Each partition is divided in the transverse plane in 64 wedge-shaped modules starting at $\phi = 0$ (Figure 3.19). Each of the modules is composed of a steel structure with interlaced plastic tiles of scintillator material. The light produced in the scintillators is collected at the two edges of each tile using wavelength-shifting fibers. The fibers are grouped together and coupled to the read-out photomutipliers (PMTs), which are housed at the outer edge of each module. The read-out divides the module structure in three differentiated layers in the longitudinal plane: A, BC and D. The fiber grouping is used to define a three-dimensional cell structure which has dimensions $\Delta\eta \times \Delta\phi = 0.1 \times 0.1$ in the first two layers and 0.2×0.1 in the last layer (Figure 3.20). Each of the modules of TileCal are read by 36–45 PMTs, depending on the position of the modules. In total, TileCal is read-out by approximately 10 000 read-out channels.

3.4.3.2 Read-out electronics

The major tasks of the read-out electronics (Figure 3.21) are to process the information of the calorimeter and to provide it to the first level (L1) of the trigger system (see Section 3.4.7) organized by trigger towers of size $\Delta\eta \times \Delta\phi = 0.1 \times 0.1$, as well as to supply the energy deposit in each calorimeter cell for L1-triggered beam crossings. The dynamic range to be covered goes from a maximum of 3 TeV down to a lower limit of 10 MeV, limited by the electronic noise. The system is divided in a front-end electronics,

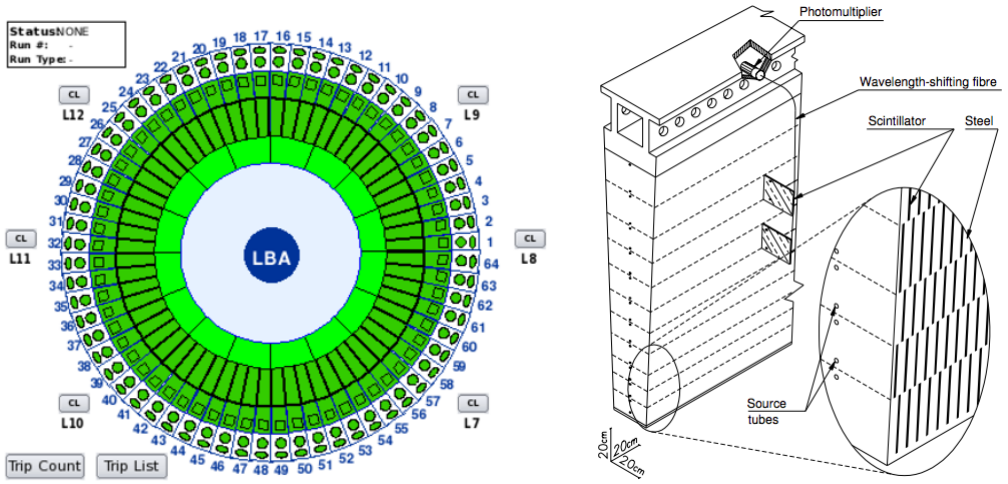

(a) (b)

Figure 3.19: Diagrams showing (a) the division of the LBA partition of TileCal in the 64 transverse modules and (b) the mechanical assembly structure of one of those modules [112].

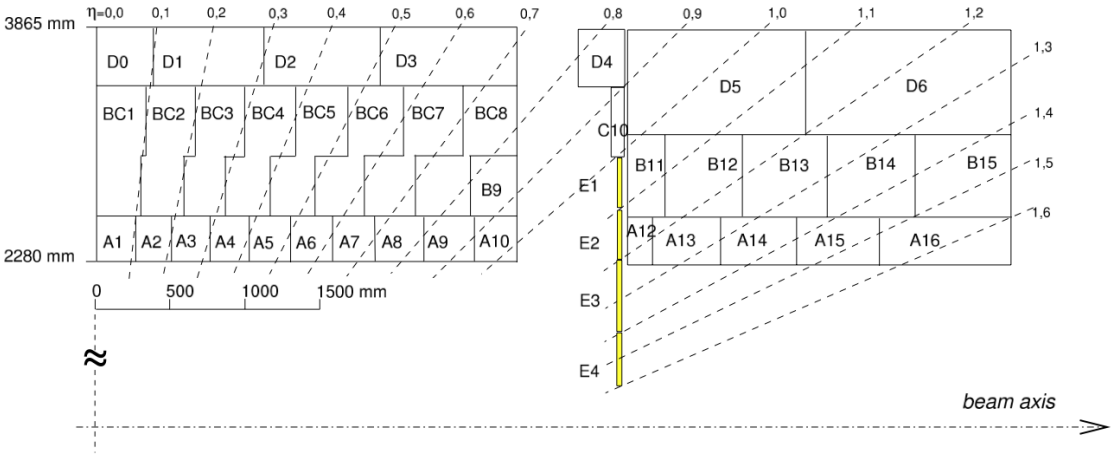

Figure 3.20: Longitudinal cut of the Tile Calorimeter, showing the cell structure of the LBA and EBA partitions [112].

which is placed within the detector, and the back-end electronics, which is placed in the service cavern, away from the detector.

The front-end electronics performs the read-out of the PMTs, the devices converting the light emitted by the scintillators into electric current. This analogous information is then sent to the so-called 3-in-1 cards, which provide unipolar signal shaping to yield a pulse width of 50 ns and two linear outputs to achieve the overall 10 bit dynamic range required. The signal is divided in two gains: high and low gain (HG and LG), scaled by a factor of 64. The full scale on the LG channel corresponds to 800 pC and the PMT gain is adjusted to provide approximately 1 pC/GeV. The 3-in-1 card also produces the analogue signals for the L1 trigger.

The digitizer system samples the incoming data from the 3-in-1 cards every 25 ns,

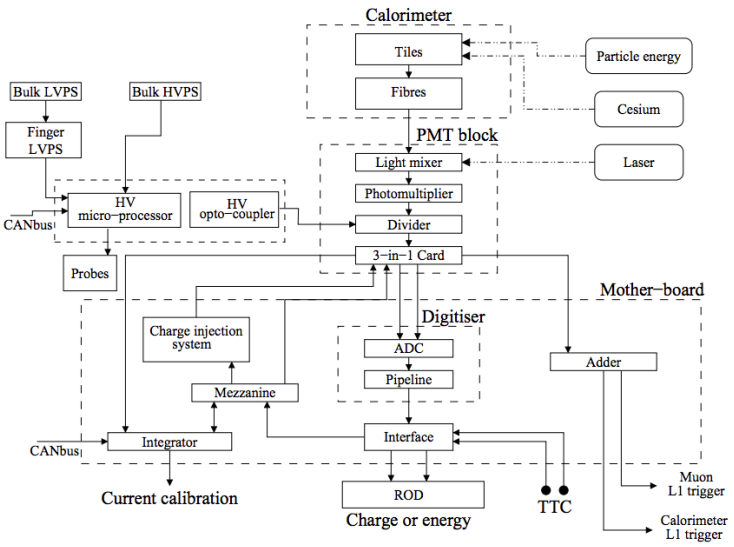

Figure 3.21: Block diagram of the TileCal front-end electronics [112].

using two dedicated 10 bit analog-to-digital converters (ADC), one for each gain, and stores the information in a fixed-length pipeline, while waiting for a L1 trigger accept decision signal (L1A). Each digitizer services up to six PMT channels. Each triggered event is recorded over an extended time frame, with a programmable length of up to 16 time samples. In normal data-taking mode, following a L1A signal, **7 samples** are kept, centered at the peak of the pulse.

The interface board receives and distributes the Timing, Trigger and Control (TTC) signals, collects and formats data from the digitizer cards, and transmits the digitized data via an optical link. It also performs cyclic redundancy checks on the input and output datastreams. There is one interface board per pair of drawers. A system of four linked motherboards form the base of the read-out system processing the signals. Each motherboard also contains circuitry which generates a precise reference voltage used by the 3-in-1 cards for charge injection and integrator calibration. The adders cards in these motherboards receive the analogue trigger outputs from up to six 3-in-1 cards, which are connected to form trigger towers and send them to the L1 trigger system.

The back-end system electronics is housed in the main services cavern (USA15), located 70 m away from the detector. It contains three different subsystems: the read-out driver system (ROD), which constitutes the core of the back-end, the TTC system, and the L1 trigger receiver. The back-end system reads the data from the front-end electronics, and digitally processes it before transmitting it to the data acquisition system at a L1 trigger rate of up to 100 kHz for the physics data-taking mode and at a 10 kHz rate for the calibration mode. The RODs are responsible for receiving, digitally processing, and formatting the data. They also perform the energy reconstruction using the *Optimal Filtering* algorithm, which is described in Chapter 4.

In order to estimate the energy from the measured signal, the detector has to be properly and continuously calibrated, to accurately compensate for the variation of the response. The calibration is done with three independent systems, which address the different steps from the measurement of the deposits in the tiles to the signal pulse in the read-out.

The first step is the electronic processing of the signal, which is calibrated with the *Charge injection system*. The behavior of the electronics is characterized by injecting a known programmable charge directly into the 3-in-1 cards, and monitoring the response of the electronics.

The second step is the conversion of light into an electron current in the PMT. The response is calibrated using a *Laser system* which injects a well known light pulse (532 nm) to each PMT, which corresponds to the typical wavelength of the light produced by particles crossing the detector. The Laser system also helps to monitor the timing of the read-out.

The last step is the light-related system, composed of the light-reacting scintillator and the fibers that transport the light to the PMTs. The *Cesium system* is sensitive to the behavior of the scintillators and fibers. A source of radioactive ^{137}Cs is circulated through a system of steel tubes crossing each cell of TileCal. The light emitted by the decay of the Cesium is well known (662 keV γ-rays with an activity of around 330 MBq/g) which allows to characterize the response of the scintillator, fibers and PMTs.

The factor of conversion of energy to ADC-counts is specific for each cell, however, with typical values about 1.05 pC/GeV. In HG, the charge range $0 - 12.5$ pC is digitized to 1024 ADC-counts, which yields a conversion factor of 1 GeV = 85.932 ADC-counts. For the cells D0−D4 and C10, the conversion is sensibly different: 1 GeV $\sim$ 71.61 ADC-counts while for the E cells, the factor is 1 GeV $\sim$ 57.22 ADC-counts. For LG, the values are scaled by a factor of 64.

3.4.4 The Muon Spectrometer

The Muon Spectrometer forms the outermost part of the ATLAS detector and is designed to detect muons exiting the barrel and end-cap calorimeters and to measure their momentum in the pseudorapidity range $|\eta| < 2.7$. It is also designed to trigger on these particles in the region $|\eta| < 2.4$. It is based on the magnetic deflection of muon trajectory by the large superconducting air-core toroid magnets and it is instrumented with separate trigger and high-precision tracking chambers. Over the range $|\eta| < 1.4$, magnetic bending is provided by the large barrel toroid. For $1.6 < |\eta| < 2.7$, muon tracks are bent by two smaller end-cap magnets inserted into both ends of the barrel toroid. Over $1.4 < |\eta| < 1.6$, usually referred to as the transition region, magnetic deflection is provided by a combination of barrel and end-cap fields. Its structure is shown in

Figure 3.22 and a summary of the η coverage and the amount of channels is shown in Table 3.5.

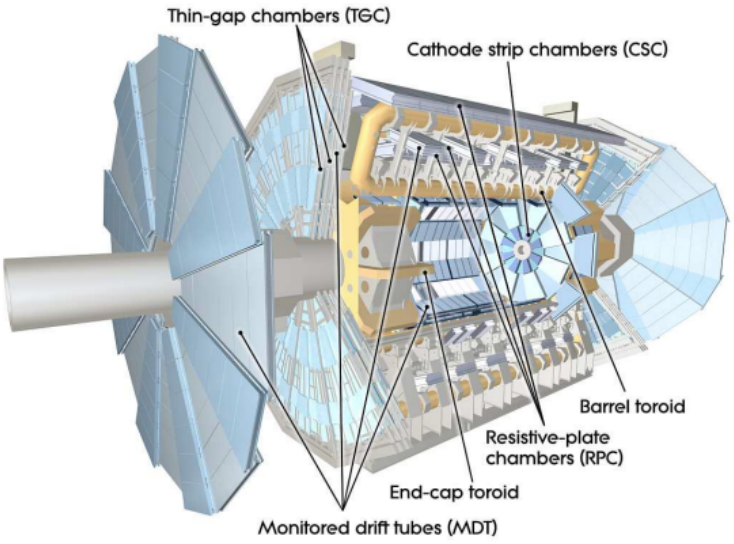

Figure 3.22: Diagram showing the structure of the ATLAS Muon Spectrometer [112].

Sub-detector		η	**Channels**
MDT	General	$\lvert\eta\rvert < 2.0$	354 000
	External wheels	$\lvert\eta\rvert < 2.7$	
CSC		$2.0 < \lvert\eta\rvert < 2.7$	31 000
RPC		$\lvert\eta\rvert < 1.05$	373 000
TGC		$1.05 < \lvert\eta\rvert < 2.4$	318 000

Table 3.5: η coverage and number of channels of the Muon Spectrometer system in ATLAS [112].

Over most of the covered η-range, a precision measurement of the track coordinates is performed by **Monitored Drift Tubes (MDT)**. The mechanical isolation in the drift tubes of each sense wire from its neighbors guarantees a robust and reliable operation. The higher granularity **Cathode Strip Chambers (CSC)**, which are multiwire proportional chambers with cathodes segmented into strips, are used in the innermost plane over $2.0 < |\eta| < 2.7$, to withstand the demanding rate and background conditions. The stringent requirements on the relative alignment of the muon chamber layers are met by the combination of precision mechanical-assembly techniques, optical alignment systems both within and between muon chambers and in-situ measurements with cosmic muons.

Triggers are provided by the **Resistive Plate Chambers (RPC)** in the barrel and the **Thin Gap Chambers (TGC)** in the end-cap regions. The trigger chambers for the muon spectrometer serve a threefold purpose: provide bunch-crossing identification, provide well-defined p_{T} thresholds, and measure the muon coordinate in the direction

orthogonal to that determined by the precision-tracking chambers. During the LS1, the last missing chambers in the transition region between the barrel and end-caps ($1.0 < |\eta| < 1.4$) were added, completing the MS to its initial design specifications [117].

3.4.5 The Magnet system

ATLAS features a unique hybrid system of four large superconducting magnets, whose purpose is the bending of charged particles within the detector, in order to provide the measurement of their momenta and charge.

The magnet system is composed of one solenoid and three sets of toroids (one barrel and two end-caps) as Figure 3.23 shows. The solenoid is placed surrounding the ID, aligned with the beam axis, and it provides an axial magnetic field of 2 T for the ID. The toroid is composed of a barrel structure and two end-caps. The barrel toroid has eight coils encased in individual racetrack-shaped, stainless-steel vacuum vessels, which are placed along the longitudinal plane of the ATLAS detector, in a symmetric structure in the transverse plane. The coils are situated surrounding the Tile Calorimeter and within the Muon Spectrometer. The toroid end-caps consist of a single cold mass built up from eight flat, square, coil units and eight keystone wedges, bolted and glued together into a rigid structure to withstand the Lorentz forces. The barrel toroid generates a magnetic field of 3.9 T while the end-caps generate it at 4.1 T. The toroids and the solenoid all have to be cooled to 4.5 K to reach the superconducting state.

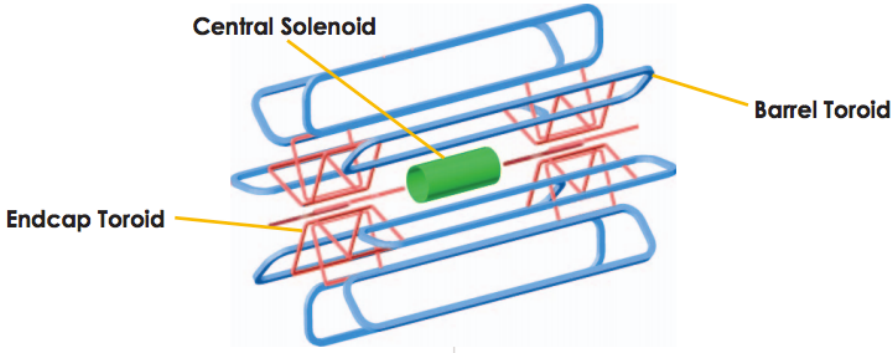

Figure 3.23: Diagram showing the structure of the Magnet system in ATLAS. The green cylinder in the middle is the central solenoid, which is placed between the Liquid Argon and the Inner Detector. The blue lines represent the toroids, both in the barrel and the end-caps. The toroids are placed surrounding the Tile Calorimeter [118].

3.4.6 The Forward detectors

Several detector systems (Figure 3.24) are placed in the forward region. The main function of **LUCID** (LUminosity measurement using Cerenkov Integrating Detector) is to determine the luminosity delivered to ATLAS. It lies at ± 17 m from the interaction point, detects inelastic pp scattering in the forward direction and is the main online

luminosity monitor for ATLAS. Another forward detector is **ALFA** (Absolute Luminosity For ATLAS). It lies at ±240 m and consists of scintillating fiber trackers located inside moving Roman pots, which are designed to approach as close as 1 mm to the beam.

A third system, called the Zero-Degree Calorimeter (**ZDC**), which plays a key role in determining the centrality of heavy-ion collisions, is located at ±140 m from the interaction point, just beyond the point where the common straight-section vacuum-pipe divides back into two independent beam pipes. The ZDC modules consist of layers of alternating quartz rods and tungsten plates, and measure neutral particles at pseudorapidities $|\eta| \geq 8.2$. During Run 1, the detector was used also to provide a luminosity measurement, however, the quartz rods which comprise the active calorimeter components were found to be less radiation hard than required for exposure to high intensity *pp* operation and thus, it was decided to use it only during heavy ion runs and low luminosity *pp* runs [119].

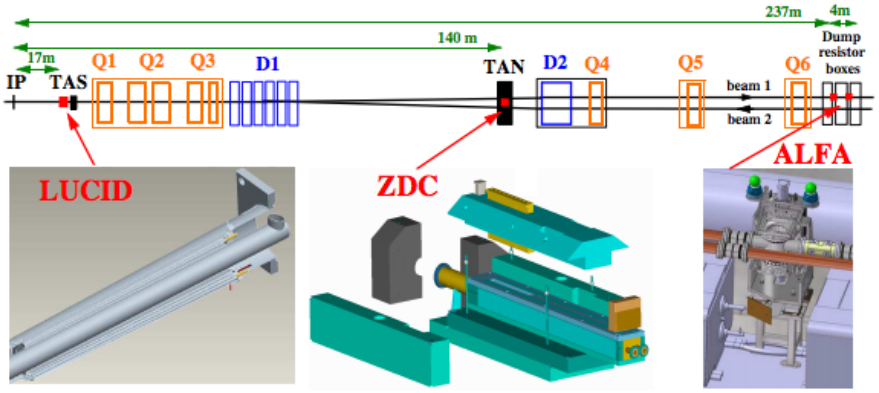

Figure 3.24: Diagram showing the position of the ATLAS Forward detectors with respect to the interaction point (IP) [112].

3.4.7 The Trigger and Data Acquisition systems

The Trigger and Data Acquisition systems [112, 120], labelled TDAQ, are the logic that controls which events should be permanently stored for a later analysis. In the LHC, the proton bunches can interact as frequently as each 25 ns, which translates to 40 million bunch-crossings every second (40 MHz). The computing system is unable to cope with the amount of data produced if all these collisions were to be stored, so an accurate selection of physically-interesting events is crucial. The system has to comply with two conditions: it has to be complex enough to decide which events are interesting while avoiding keeping the detector in a non-recording state (*busy*) for long time.

During Run 1 the trigger system was composed of three distinct levels: L1, L2, and the Event Filter (EF) (Figure 3.25). The L2 and EF are labelled together as the High-Level Trigger (HLT). Each trigger level refines the decisions made at the previous level and, where necessary, applies additional selection criteria. The data acquisition system receives and buffers the event data from the detector-specific read-out electronics,

at the L1 trigger accept rate. The first level uses a limited amount of the total detector information to make a decision in less than 2.5 μs, thus reducing the rate to about 100 kHz. The two higher levels access more detector information for a final rate of up to 200 Hz, with an event size of approximately 1.3 MB. The final rate was gradually increased up to 600 Hz by the end of Run 1.

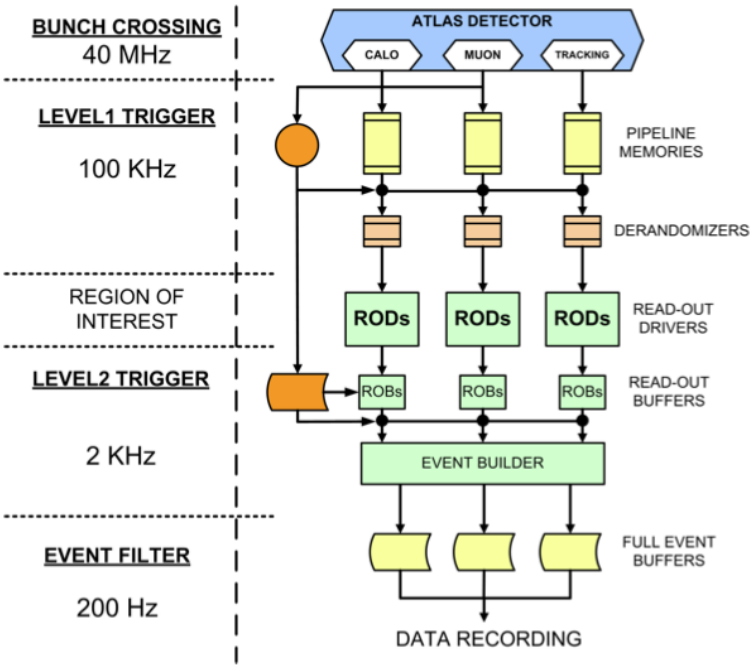

Figure 3.25: Diagram of the trigger levels in the ATLAS Data Acquisition System showing the structure of L1, L2 and Event Filter [112].

As the Run 2 peak luminosity was expected to surpass the nominal value of the LHC, the trigger was redesigned and upgraded to accommodate for an increase by a factor of 5 of the trigger rates. The L2 and the Event Filter were fully combined in the High-Level Trigger, which reduced the impact of bottlenecks in the processing. The bandwidth limits were increased, and the final output rate of data to storage was raised to 1.5 kHz at peak luminosity.

The Data Acquisition system (DAQ) receives and buffers the event data from the detector specific read-out electronics at the L1 trigger rate. The requested data is transmitted to the L2 trigger and for those events fulfilling the L2 selection criteria event-building is performed. The assembled events are then moved by the Data Acquisition system to the event filter, and the events selected there are moved to permanent event storage. In addition to controlling the movement of data down the trigger selection chain, the DAQ system also provides infrastructure for the configuration, control and monitoring of the ATLAS detector during data-taking.

The Level 1 Trigger

The Level 1 of the ATLAS trigger searches for signatures from high-p_{T} muons, electrons/photons, jets, and τ leptons decaying into hadrons. The information flow of the L1 trigger is shown in Figure 3.26. It also selects events with large missing transverse energy ($E_{\mathrm{T}}^{\mathrm{miss}}$) and large total transverse energy (ΣE_{T}). The L1 trigger uses reduced-granularity information from a subset of detectors: the RPC and TGC from the MS for high-p_{T} muons, and all the calorimeter subsystems.

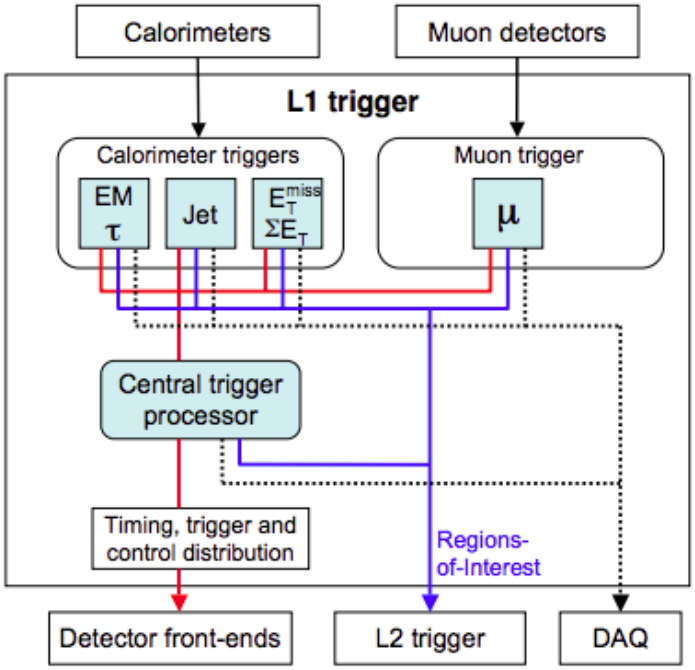

Figure 3.26: Block diagram of the L1 trigger. The overall L1 accept decision is made by the central trigger processor, taking input from calorimeter and muon trigger results. The paths to the detector front-ends, L2 trigger, and data acquisition system are shown from left to right in red, blue and black, respectively [112].

The L1 Calorimeter Trigger (L1Calo) aims at identifying high-E_{T} objects such as electrons and photons, jets, and τ leptons decaying into hadrons, as well as events with large $E_{\mathrm{T}}^{\mathrm{miss}}$ and large ΣE_{T}. A trigger on the scalar sum of only jet transverse energies is also available. For the electron/photon and τ triggers, isolation can be required. The information for each bunch-crossing used in the L1 trigger decision is the multiplicity of hits for 4 to 16 programmable E_{T} thresholds per object type.

The L1 muon trigger is based on signals in the muon trigger chambers: RPC's in the barrel and TGC's in the end-caps. The trigger searches for patterns of hits consistent with high-p_{T} muons originating from the interaction region. The logic provides six independently-programmable p_{T} thresholds. The information for each bunch-crossing used in the L1 trigger decision is the multiplicity of muons for each of these thresholds. Muons are not double-counted across them.

The overall L1 accept decision (L1A) is made by the Central Trigger Processor (CTP), which combines the information for different object types. Trigger menus can be programmed with up to 256 distinct items, each item being a combination of requirements on the input data. The trigger decision, together with the LHC clock and other signals, are distributed to the detector front-end and read-out systems via the TTC system, using an optical-broadcast network. While the L1A is based only on the multiplicity of trigger objects (or flags indicating which thresholds were passed, for global quantities), information about the geometric location of trigger objects is retained in the muon and calorimeter trigger processors. Upon the event being accepted by the L1 trigger, this information is sent as Regions of Interest (RoI) to the L2 trigger, where it is used to seed the selection performed by the HLT.

While the trigger decision is being formed, the information for all detector channels has to be retained in pipeline memories, which are intended to be as short as possible. The L1 latency, which is the time from the proton-proton collision until the L1 trigger decision, must therefore be kept as short as possible. The design of the trigger and front-end systems requires the L1 latency to be less than $2.5\,\mu$s, with a target latency of $2.0\,\mu$s, leaving $0.5\,\mu$s contingency. About $1\,\mu$s of this time is accounted for cable-propagation delays alone.

The High-Level Trigger and the Data Acquisition systems

The main components of the data acquisition system/High-Level Trigger (DAQ/HLT) are: read-out, L2 trigger, event-building, event filter, configuration, control and monitoring. The flow of events from the detector to mass storage starts with the selection of events by the L1 trigger. During the latency of the L1 trigger selection, the event data are buffered in memories located within the detector-specific front-end electronics. Upon selection by the L1 trigger, the event data is transferred to the DAQ/HLT system over 1574 read-out links (ROL's), having first transited through the detector-specific ROD's. The 1574 event fragments are received into the 1574 Read-out Buffers (ROB's) contained in the read-out system (ROS) units where they are temporarily stored and provided, on request, to the subsequent stages of the DAQ/HLT system.

For every selected event, the L1 trigger subsystems (calorimeter, muon, and CTP) also provide the RoI information to the RoI builder where it is assembled into a single data structure and forwarded to the L2. Using the RoI information, requests for event data are made to the appropriate ROS's and a final result, accept or reject, is given to the Data Flow Manager (DFM). The sequence of data requests is determined by the type of RoI identified by the L1 trigger and the configuration of the L2 trigger processing, i.e. the order of items in the trigger menu and the order of the algorithms per trigger item.

The DFM marshals the events during the event-building. For those events which were found not to fulfill any of the L2 selection criteria, the DFM informs all the ROS's to expunge the associated event data from their respective ROB's. Each event which has been selected by the L2 trigger is assigned by the DFM to an event-building node, which builds a single event-data structure, the *event*. The full event structure is sent to the Event Filter for further analysis. Upon completing the building of an event, the ROS expunges the associated data from the respective ROB's.

The EF, in addition to the selection, classifies the selected events according to a predetermined set of streams and the result of this classification is added to the event structure. Selected events are subsequently sent to the output nodes of the DAQ/HLT system. Conversely, those events not fulfilling any of the EF selection criteria are expunged from the system. The accepted events are stored in its local file system according to the classification performed by the EF. The event files are subsequently transferred to the central data-recording facility of CERN.

3.4.8 Data Quality

The quality and consistency of the reconstruction of each event depends on the performance of the detector at data-taking. However, the different sub-detectors may undergo under several issues that may compromise the validity of a certain event, or series of events. Examples of these issues are data-recording while the magnets are off, increase of the electronic noise in some channels, loss of read-out coverage of parts of the detectors, etc.

In order to avoid using problematic data in the analyses, the datasets have to pass several layers of checks set by the groups responsible of each sub-detector and the groups dedicated to the reconstruction of physics objects, both during data-taking and after the reconstruction of data. These filters remove the compromised events and provide a list (called Good Run List, *GRL*) of luminosity blocks (lumi-blocks) which are labelled as data *Good for Physics*. The lumi-blocks are the smallest periods of continuous data taking with constant instantaneous luminosity (usually lasting about 1 min) in which the datasets are divided. Preliminary GRL are released during data taking to allow for a fast physics analysis, but new GRLs are provided each time a reprocessing is performed. These reprocessings implement a more accurate calibration and recover part of the previously discarded data. The summary of the good quality data collected during Runs 1 and 2 is shown in Figure 3.27.

ATLAS 2011 p–p run

Inner Tracking			Calorimeters				Muon Detectors				Magnets	
Pixel	SCT	TRT	LAr EM	LAr HAD	LAr FWD	Tile	MDT	RPC	CSC	TGC	Solenoid	Toroid
99.8	99.6	99.2	97.5	99.2	99.5	99.2	99.4	98.8	99.4	99.1	99.8	99.3

Luminosity weighted relative detector uptime and good quality data delivery during 2011 stable beams in pp collisions at $\sqrt{s}$=7 TeV between March 13th and October 30th (in %), after the summer 2011 reprocessing campaign

(a) Run 1 - year 2011

ATLAS p-p run: April-December 2012

Inner Tracker			Calorimeters		Muon Spectrometer				Magnets	
Pixel	SCT	TRT	LAr	Tile	MDT	RPC	CSC	TGC	Solenoid	Toroid
99.9	99.1	99.8	99.1	99.6	99.6	99.8	100.	99.6	99.8	99.5

All good for physics: 95.5%

Luminosity weighted relative detector uptime and good quality data delivery during 2012 stable beams in pp collisions at $\sqrt{s}$=8 TeV between April 4th and December 6th (in %) – corresponding to 21.3 fb^{-1} of recorded data.

(b) Run 1 - year 2012

ATLAS pp 25ns run: August-November 2015

Inner Tracker			Calorimeters		Muon Spectrometer				Magnets	
Pixel	SCT	TRT	LAr	Tile	MDT	RPC	CSC	TGC	Solenoid	Toroid
93.5	99.4	98.3	99.4	100	100	100	100	100	100	97.8

All Good for physics: 87.1% (3.2 fb^{-1})

Luminosity weighted relative detector uptime and good data quality (DQ) efficiencies (in %) during stable beam in pp collisions with 25ns bunch spacing at $\sqrt{s}$=13 TeV between August-November 2015, corresponding to an integrated luminosity of 3.7 fb^{-1}. The lower DQ efficiency in the Pixel detector is due to the IBL being turned off for two runs, corresponding to 0.2 fb^{-1}. Analyses that don't rely on the IBL can use those runs and thus use 3.4 fb^{-1} with a corresponding DQ efficiency of 93.1%.

(c) Run 2 - year 2015

ATLAS pp 25ns run: April-October 2016

Inner Tracker			Calorimeters		Muon Spectrometer				Magnets		Trigger
Pixel	SCT	TRT	LAr	Tile	MDT	RPC	CSC	TGC	Solenoid	Toroid	L1
98.9	99.9	99.7	99.3	98.9	99.8	99.8	99.9	99.9	99.1	97.2	98.3

Good for physics: 93-95% (33.3-33.9 fb^{-1})

Luminosity weighted relative detector uptime and good data quality efficiencies (in %) during stable beam in pp collisions with 25ns bunch spacing at $\sqrt{s}$=13 TeV between April-October 2016, corresponding to an integrated luminosity of 35.9 fb^{-1}. The toroid magnet was off for some runs, leading to a loss of 0.7 fb^{-1}. Analyses that don't require the toroid magnet can use that data.

(d) Run 2 - year 2016

Figure 3.27: Luminosity-weighted relative fraction of good quality data delivery by the various components of the ATLAS detector [121].

Chapter 4

Enhancement of the Pulse Simulator

Contributions to the data-taking and the Phase-II upgrade of the Tile Calorimeter sub-detector were performed in the scope of this thesis. This chapter describes the enhancement of the *Pulse Simulator* (PS), a tool used for simulating the read-out output of the Tile Calorimeter. The work improved the out-of-time pile-up simulation, by implementing configurable pile-up conditions and gain switching.

The enhancement of the Pulse Simulator for the HL-LHC conditions is the main objective of this chapter. First, the signal reconstruction process of the TileCal is detailed in Section 4.1. The description and current possibilities of the PS are covered in Section 4.2. The improvement obtained for the tool are shown in Section 4.3. Finally, further potential improvements are proposed in Section 4.4.

4.1 Signal reconstruction in the Tile Calorimeter

The Tile Calorimeter was described in Section 3.4.3, detailing its hardware structure and read-out mechanism. Particles crossing the detector leave a light signal which is collected by PMTs. If the event is selected by the L1 trigger, seven equally spaced time samples are retained for each PMT signal, spanning from −75 ns to +75 ns with respect to the time of the trigger signal. Using this information, the detected pulse can be reconstructed thanks to the knowledge of the pulse shape. Although this shape is slightly different depending on the type of particle crossing the scintillators and the amount of energy deposited, an average pulse shape is used to reconstruct the depositions [122], which is shown in Figure 4.1.

In order to reconstruct the pulse, three parameters have to be obtained: the **amplitude**, the **pedestal** and the **phase**. The pedestal is defined as the baseline of the signal, and its typical values are between 30 and 60 ADC-counts (Figure 4.2). The phase is the time difference between the peak of the pulse and its expected time of arrival, produced by a particle coming from the interaction point. Its value is measured with respect to the central sample and is estimated independently for each channel.

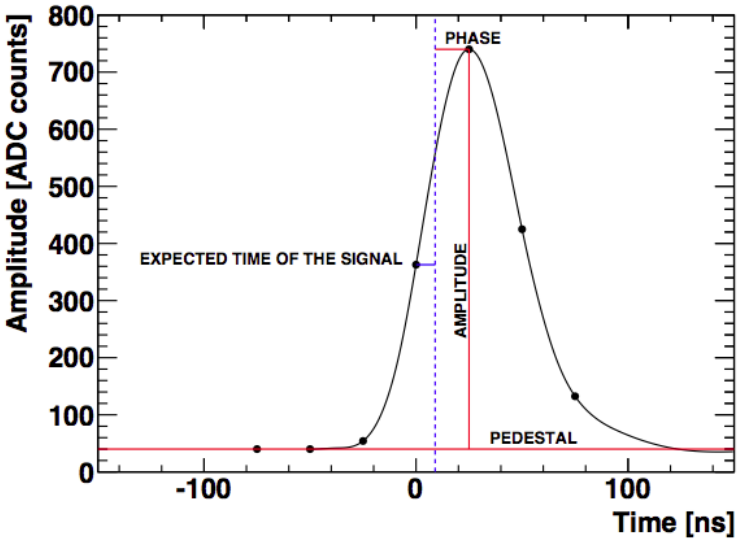

Figure 4.1: Pulse shape with the definition of amplitude, reconstructed phase and pedestal. The points represent the seven samples transmitted to the ROD [122].

The amplitude of the pulse is the main parameter of the reconstruction, as its value is proportional to the energy deposited in the detector. The pulse amplitude is defined as the measured value after subtracting the pedestal.

The pulse produced by the TileCal front-end can be expressed by:

$$S_i(t) = A\, g(t_i - \tau) + p \quad \text{for} \qquad i = 0, \ldots, 6 \tag{4.1}$$

where $g(t)$ represents the normalized pulse shape as a function of the time t, A is the amplitude of the signal, τ is the relative phase and p is the pedestal.

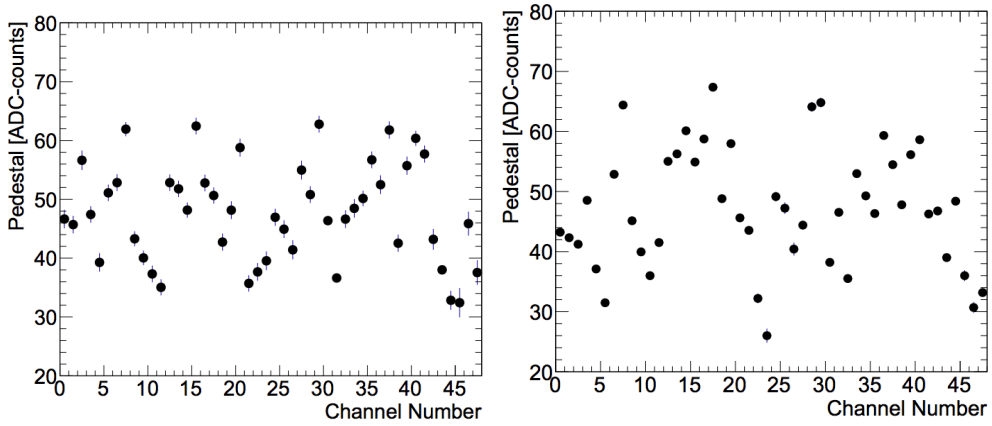

(a) High gain (b) Low gain

Figure 4.2: Mean value and RMS of the pedestal as a function of channel ID for module LBA01 in a recent pedestal data-taking for (a) high gain and (b) low gain [122].

However, two sources of noise can distort the amplitude measurement: electronic noise and pile-up. The electronic noise are small fluctuations of the samples around their

expected value, intrinsic to the electronics. The variations of the pedestal (as the ones shown in Figure 4.2) are mainly due to the electronic noise and their contribution is more significant in high gain samples. The electronic noise was studied during the test beams and the commissioning period, and its dispersion is currently parametrized using a double gaussian distribution.

The so-called pile-up noise is the contribution to the measurement of the pulse of energy deposited by uncorrelated events produced close in time or position to the collision that triggered the event. The contribution of pile-up depends strongly on the conditions of the LHC collisions. Namely, the number of interactions per bunch-crossing (μ) depends on the instantaneous luminosity and the energy in the center of mass of the LHC.

In particular, during the 2011 data-taking , at $\sqrt{s} = 7\,\text{TeV}$, the average μ was $\langle\mu\rangle = 9.1$; for the 2012 data-taking, at $\sqrt{s} = 8\,\text{TeV}$, it was $\langle\mu\rangle = 20.7$. During Run 2 the energy in the center of mass was raised to 13 TeV and the value was $\langle\mu\rangle = 13.7$ during the 2015 data-taking, and $\langle\mu\rangle = 24.9$ for the 2016 data-taking. The distributions of the number of collisions per bunch-crossing during Run 1 and Run 2 were shown in Figures 3.10 and 3.11. Due to its dependencies, the out-of-time pile-up contribution is expected to increase further in the following years. For Run 3, the average value is forecasted to be $\langle\mu\rangle \sim 60$, while for the Phase-II upgrade of the LHC, it can achieve $\langle\mu\rangle \sim 200$ [101, 123].

In addition, another relevant parameter that relates the pile-up to the signal reconstruction is the bunch-spacing. During Run 1, the LHC bunch-spacing was 50 ns while for Run 2, it was reduced to the design value of 25 ns. The TileCal signals are sampled every 25 ns, and therefore the change in the bunch-spacing had a great impact on the reconstruction of the signal.

The aim of the reconstruction algorithms is to compute the properties of the received pulse, while minimizing the contribution of noise. The default algorithm used in TileCal is the Optimal Filtering (OF) [122, 124, 125] which is implemented in the ROD boards for the reconstruction to be performed in real time.

The OF algorithm calculates the amplitude A, the phase τ and the pedestal p, by means of a weighted sum of the digitized samples (S_i), using weights (a_i, b_i and c_i) that minimize the contribution of the noise and estimate the pedestal. The approach used to estimate the pedestal defines two forms of the algorithm: OF1 and OF2, which are implemented in the TileCal RODs. The difference between them is that OF1 estimates the pedestal from the first sample or gets it from a database, while OF2 calculates it as an another parameter of the reconstruction. During the data-taking of Run 1, the energy reconstruction was done with OF2, while for the Run 2, OF1 was selected.

As an example, the relation between the weights and the parameters in OF2 is:

$$A = \sum_{i=0}^{6} a_i S_i \qquad A\tau = \sum_{i=0}^{6} b_i S_i \qquad p = \sum_{i=0}^{6} c_i S_i \tag{4.2}$$

The weights are calculated using a set of equations extracted from the noise auto-correlation matrix and contour conditions on a_i, b_i and c_i. The values of the weights and the noise auto-correlation matrix were obtained during the test beam and commissioning phases. The differences between channels were found to be negligible. During these periods, it was found that the samples were weakly correlated and thus, the noise auto-correlation matrix was assumed to be unitary for Run 1. For Run 2, however, the algorithm implemented the noise auto-correlation matrix. Finally, the final weights were computed from -100 ns to $+100$ ns in steps of 0.1 ns, stored in the database and downloaded to the ROD boards at the beginning of Run 2.

4.2 The Pulse Simulator tool

The Pulse Simulator is an Athena[1] algorithm designed to simulate the output from the Tile Calorimeter front-end electronics and RODs. It generates accurate simulation of the samples in order to test:

- the different reconstruction algorithms,
- the accuracy of the reconstruction algorithms,
- the effects in the reconstruction related to different kinds of pulse shape imperfection.
- the effect of electronic and pile-up noise in the pulse reconstruction.

The Pulse Simulator reproduces the digital response of the detector by using simulated pulses as input. The pulses can be fully configured, starting from a template pulse shape which was obtained from test-beam data. The configuration is done by modifying certain parameters such as the timing of the peak and the amplitude.

Using the input analogue pulse, the response of the detector is simulated for a given PMT. The program digitizes the signal by reproducing the digital samples that the front-end electronics provides and adds a simulated electronic noise. Like for the Tile Calorimeter read-out, seven samples are stored as output of the simulator for each signal, and they are used as input to the standard energy reconstruction algorithms.

The Pulse Simulator works in a bi-gain mode, thus two copies of each sample are saved, one for high gain (HG) and one for low gain (LG) respectively. Since no gain switch is implemented, the low gain values are obtained by dividing the high gain result by a factor of 64. In addition, simulated electronic noise is added to the output.

[1] Athena is the offline reconstruction framework in the ATLAS Experiment.

The configurable options of the Pulse Simulator are:

- For the main in-time pulse:
  - Define a fixed pulse amplitude or take it randomly from an input distribution (Figure 4.3 (a)).
  - Add gaussian fluctuations of programmable mean and RMS values.
  - Define a time offset for the main pulse with respect to the center of the read-out window.
- Add a secondary pulse to simulate "out-of-time" signal:
  - Define a fixed pulse amplitude or take it randomly from an input distribution (Figure 4.3 (b)).
  - Define the time offset for the secondary pulse.
  - Set the probability of an event to be affected by the secondary pulse (**pile-up fraction**).
- Add electronic noise by:
  - defining fixed parameters of the double gaussian noises,
  - or retrieving channel-specific parameter values of the electronic noise from the TileCal database.
- Set the pedestal value of the ADC samples:
  - from custom values,
  - or retrieving channel-specific pedestal values from the TileCal database.

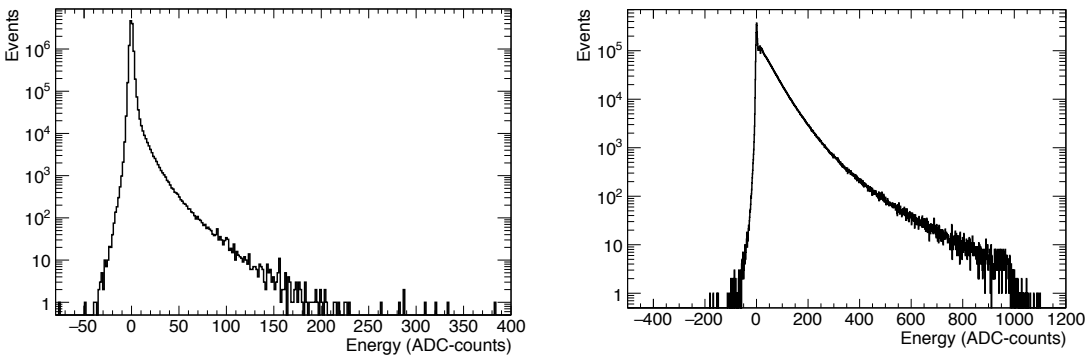

(a) For in-time pulse

(b) For out-of-time pile-up

Figure 4.3: Template amplitude distributions for the simulation of the (a) in-time and (b) out-of-time pulses. The out-of-time amplitudes were obtained from a minimum bias sample for the E4 cell for $\mu = 40$.

Simulation of out-of-time pile-up

Originally, the PS simulates the out-of-time pile-up by adding a secondary pulse shifted in time from the main one. The sensitivity of each cell to the pile-up depends on its position and structure, therefore each cell has to be simulated independently. The amplitude of the pile-up pulse was taken from a specific energy distribution obtained for a particular cell[2] (A12−A14, B11−B15, D4−D6, C10, E1−E4) and for a specific pile-up value ($\mu = \{10, 20, 40\}$). An example of these distributions is shown in Figure 4.3 (b) for $\mu = 40$ in the E4 cell.

The pulses are then added in their respective time-positions and the seven read-out samples of the TileCal are simulated. An example of the full time-range of the simulator, displaying the position of the in-time pulse (in black) and an enhanced out-of-time pile-up pulse (in blue) is shown in Figure 4.4 (a). In (b), the distribution shows the sampling of the signal, with the seven measures performed at their respective time values. The measurement of each sample collects the energy deposited from both pulses (in-time and out-of-time), which distorts the correct reconstruction of the in-time signal.

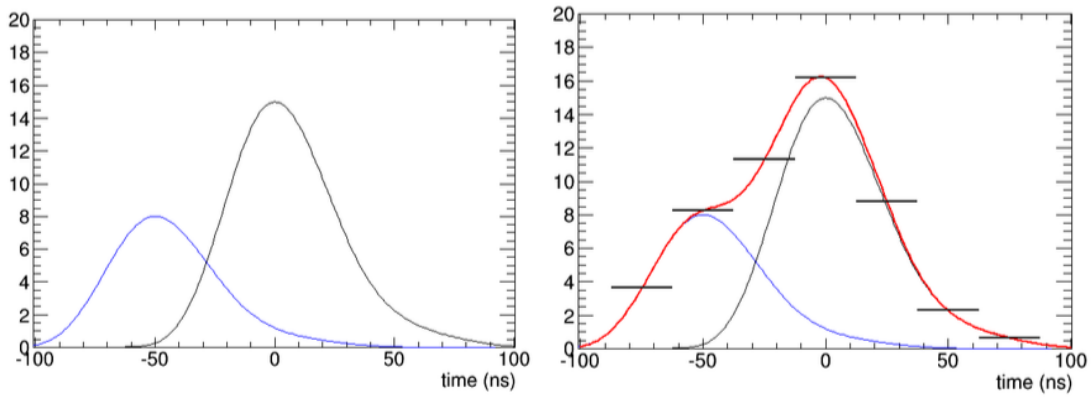

(a) (b)

Figure 4.4: Simulated full time of the collision range [−75 ns, +75 ns] showing the primary in-time pulse (black) and a secondary pile-up pulse (blue). In (b), the sum of both pulses is shown on top (red) while the measured value of the seven samples is shown as black horizontal lines at the seven time stamps. The unit of the y-axis is ADC-counts.

4.3 Enhancement of the Pulse Simulator of HL-LHC

4.3.1 Simulation of high pile-up conditions

Initially, the pile-up simulation of the PS was very limited, because it only allowed to add a single pulse at a fixed time stamp, only three pile-up values could be simulated and the template energy distribution of the pulse was available only for a few specific cells. In order to adapt the PS to the conditions of the HL-LHC, with an expected average

[2]The map of the cells in the Tile Calorimeter is shown in Figure 3.20 in Section 3.4.3.

number of collisions per bunch-crossing of the order of $\langle\mu\rangle \sim 200$ and a bunch-spacing of 25 ns, the pile-up simulation procedure was completely re-implemented.

The single "out-of-time" pulse method was replaced by a new multi-pulse system. A new option allows to select a desired bunch-spacing for the simulation (25 ns, 50 ns or 75 ns), and then additional pulses are simulated at the corresponding time stamps of the bunch-crossings, e.g. if the bunch-spacing is set to 50 ns, three pulses are generated at −50 ns, 0 ns and +50 ns (Figure 4.5 (a)), for a bunch-spacing of 75 ns, the pulses are generated at −75 ns, 0 ns and +75 ns (Figure 4.5 (b)), finally, if it is set to 25 ns, the pulses are generated for each of the bunch-crossings, as shown in (Figure 4.5 (c)).

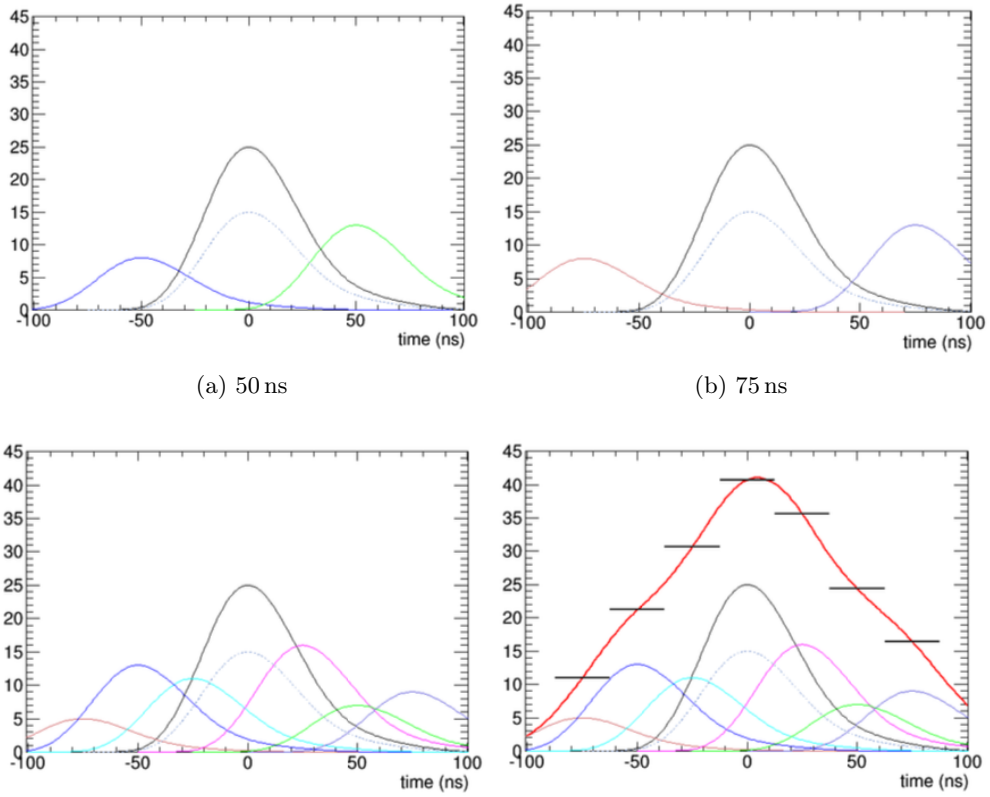

(a) 50 ns (b) 75 ns

(c) 25 ns (d) Total sum for 25 ns

Figure 4.5: Simulated full time of the collision range [−75 ns, +75 ns] showing the primary in-time pulse at $t = 0$ ns and the secondary pile-up pulses, for a bunch-spacing of (a) 50 ns, (b) 75 ns and (c) 25 ns. For $t = 0$ ns, a secondary pile-up pulse is added to the main in-time pulse. In (d), the total pulse, which is the sum of the contributions of all the pulses, is shown in a thick red line, along with the measured value of the seven samples, shown as black horizontal lines in the seven time stamps. The amplitude of the pile-up pulses has been randomly sampled from a template distribution and the unit of the y-axis is ADC-counts.

The amplitude of each of the pile-up pulses is randomly sampled from the minimum bias energy distribution of the selected cell, therefore each of the extra pulses has a different amplitude. The pile-up pulses are still controlled by the "Pile-up fraction" option, which could be used to set the pile-up contribution to a fixed value.

A comparison of the results of the PS with and without pile-up is shown below. The study was done generating 100.000 pulses of the E4 cell for a bunch-spacing of 25 ns, a pile-up value of $\mu = 40$ and a pile-up-fraction of 1. For simplicity, the amplitude of the in-time pulse was sampled from a flat distribution (Figure 4.6), though the value was fluctuated with gaussian variations of 1%. Thus, an almost flat distribution was the expected output of the energy reconstruction, whereas deviations from it show the effect of pile-up. In addition, no time offset was selected, setting the in-time pulse to be centered exactly at $t = 0$ ns.

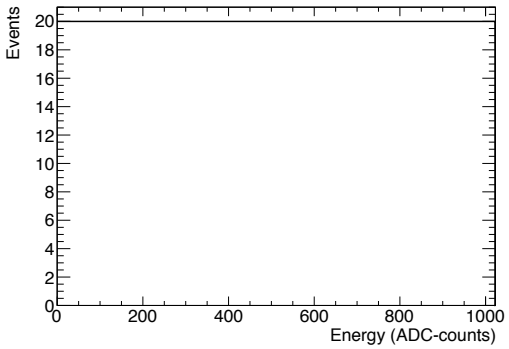

Figure 4.6: Energy template for an in-time pulse showing a flat distribution. Each value of the amplitude has the same probability of being selected in the sampling.

Figure 4.7 shows the seven HG samples returned by the simulator in a study (a) without pile-up and (b) with a pile-up of $\mu = 40$. The effect of the pile-up is visible as an increase of the mean value of the measurement and the width of the distribution. This is especially clear in the first and last two samples, where the in-time pulse has a small contribution. In the central samples, which measure the peak of the in-time pulse, a second effect is seen, as the distribution is not flat any more (it develops a tail, rather than a sharp end) and is shifted towards higher values.

Figure 4.8 shows the reconstructed amplitude of the study in HG, obtained by the OF1 algorithm using as input the seven samples of Figure 4.7. The effect of the pile-up in the reconstruction is visible in two features: first, deviations from a flat distribution; secondly, a sharp peak appears at a value of 0, which corresponds to events in which two or more samples saturate the gain. These events are not reconstructed due to a feature of the reconstruction algorithm, and therefore are assigned a conventional value of 0. This feature is present in HG as consequence of the bi-gain reconstruction of the PS, which was addressed in the works described in Section 4.3.2.

A further improvement in the pulse simulation was considered. The pulses defined in the current version of the PS were defined only in the range [−75 ns, +75 ns], since they were aimed for the original bunch-spacing of 50 ns, where pulses outside the read-out window did not have a significant effect. However, with a bunch-spacing of 25 ns, the

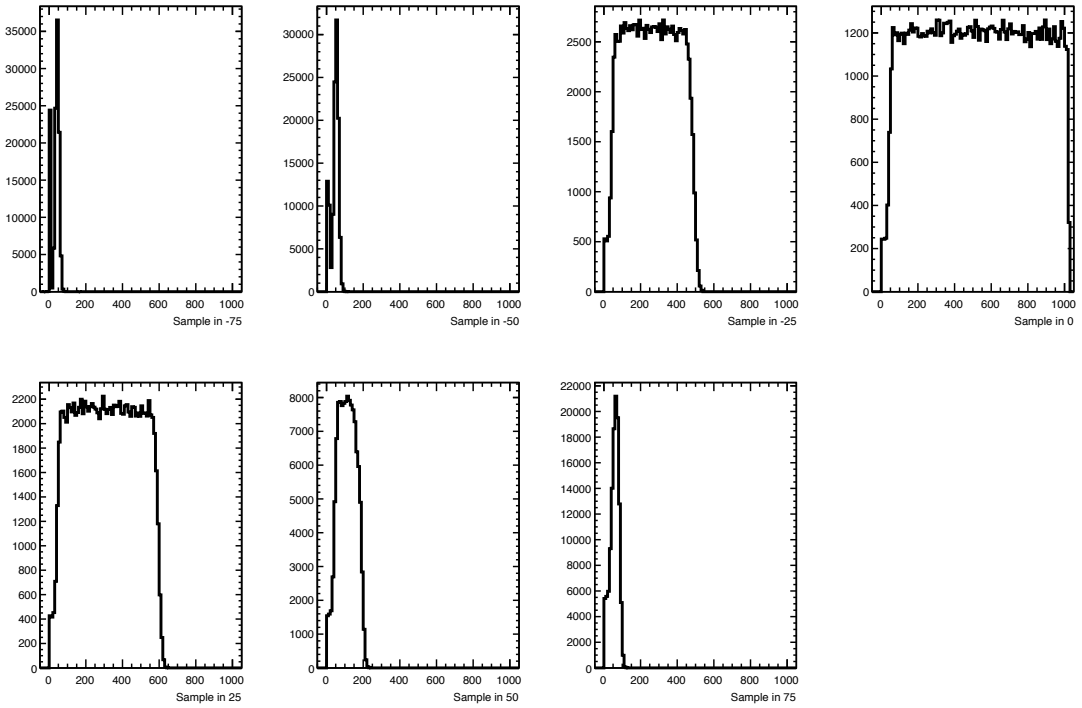

(a) $\mu = 0$

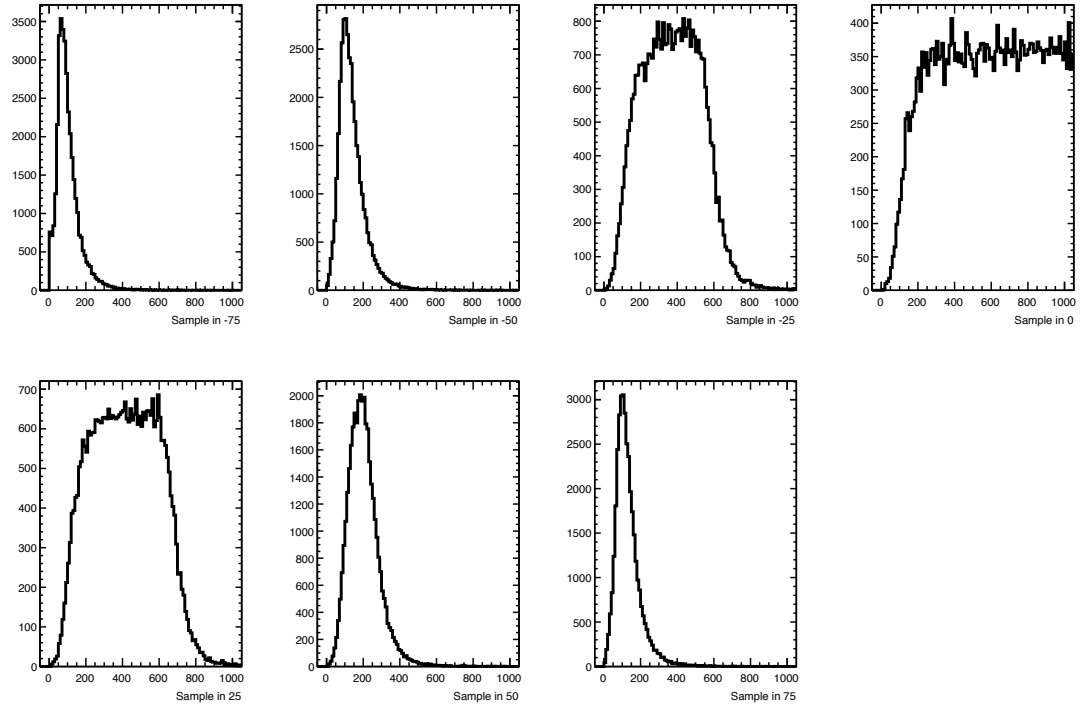

(b) $\mu = 40$

Figure 4.7: Distribution of the seven HG samples as output of the Pulse Simulator for the E4 cell, comparing a study (a) without pile-up and (b) with a pile-up of μ =40. In the output of (b), an increase of the measured value can observed, as the effect of the pile-up. The pulses are sorted chronologically starting with -75 ns, with the in-time pulse ($t = 0$) the standalone one on the right. The distributions are histograms where the x-axis shows the amplitude of each sample in ADC-counts.

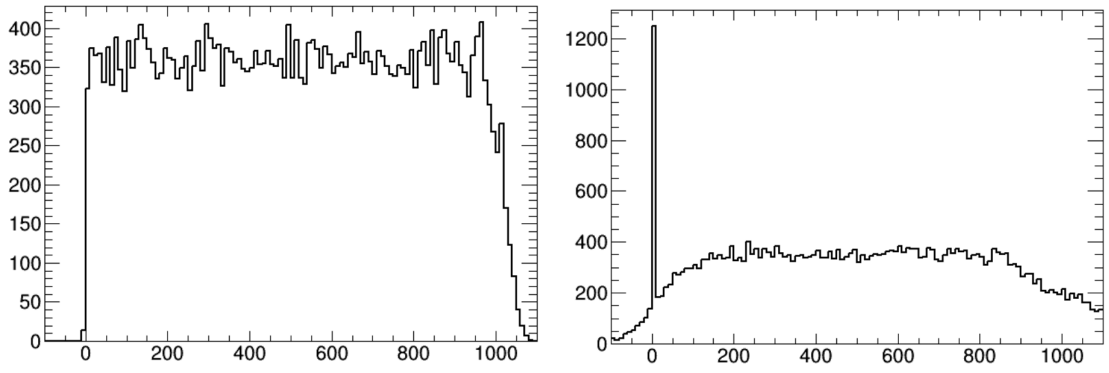

(a) $\mu = 0$ (b) $\mu = 40$

Figure 4.8: Comparison of the energy distributions in high gain in a pile-up study with (a) $\mu = 0$ and (b) $\mu = 40$. The impact of the pile-up is visible in two features: the worsening of the squareness of the distribution and the peak at 0, which corresponds to saturated events. The distributions are histograms where the x-axis shows the amplitude of each sample in ADC-counts

seven read-out samples could be affected by pulses outside the time-range but whose tails fall in the time window.

In addition, the template pulse shape is computed and available for the range -75 ns to $+130$ ns (Figure 4.9). The shape has a significant feature, since for $t > 100$ ns the pulse amplitude becomes negative. The pulse enters in a setback phase, before returning to 0, and thus the remote pulses would contribute negatively, an effect which has to be taken into account in the simulation. The estimated duration of the setback phase is approximately around 1 μs.

By using the full pulse shape and extending the time window to ± 300 ns, the contribution of the tails of pulses can be included in the computation of the measurement of each sample, as it is shown in Figure 4.10. Since the pulse is not symmetric and has a long tail after the peak, the measurement of a sample is affected by contributions of previous bunch-crossings.

The enhanced simulation of out-of-time pulses, containing the customizable bunch-spacing, the full pulse-shape and the extended time-range, was implemented, tested and added to the Pulse Simulator.

4.3.2 Implementing a mono-gain switch

In the previous state, the PS used a bi-gain system: for each event, two copies of each sample are stored, one in high gain (HG) and a second one in low gain (LG). The LG was obtained simply by dividing the amplitude of each HG sample by a factor of 64, for all the events in the study. In addition, the remaining variables (such as the amplitude or the energy) were also computed for each of the gains.

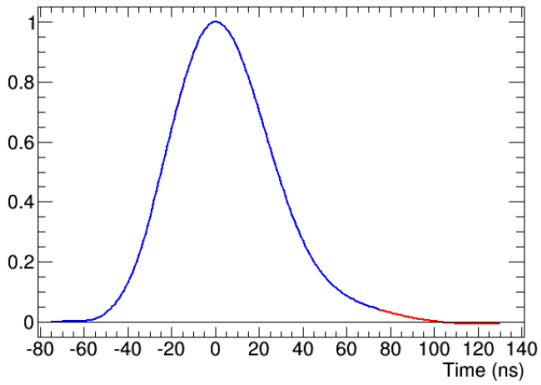

Figure 4.9: Full shape of the pulse used for the in-time and out-of-time pile-up distributions. The original shape was defined in the range [−75 ns to +75 ns] and is shown in blue, while the full shape is defined in the range [−75 ns to +130 ns] and adds the red tail, which goes to negative values for $t > 100$ ns.

This system did not reproduce the real behavior of the detector and led to several issues, like when the energy of the pulse is high enough to saturate at least two samples. For highly sensitive cells, this can happen very often, leading to an unnatural peak at 0 due to a feature of the HG reconstruction, as is seen in Figure 4.8 (b) and in Figure 4.11 (a). On the other hand, the LG reconstruction was performed for all amplitudes, and thus it was filled with events with a very low amplitude, overloading the LG output with non-interesting low energetic events (Figure 4.11 (b)).

However, these issues can be avoided by replication of the mono-gain switching of TileCal. In this mode, the samples are first calculated in HG. Then, if any sample reaches the value of 1023 ADC-counts, the event is set to be saturated in HG and stored in LG instead. The logic that decides in which gain the event is stored is called *gain switch*. Hence, in the mono-gain system, instead of two copies for each sample, only one instance is stored, plus one bit stating if the event has been saved in LG or HG. The energy, amplitude and the rest of parameters, are computed only once for each pulse.

4.3.3 Improvements of the energy templates

The out-of-time pile-up simulation relies on template energy distributions used to randomly sample the amplitude of each of the additional pulses. The available templates were obtained from the reconstruction of a simulated minimum bias sample for several specific cells, with different values of $\langle\mu\rangle$. However, this introduces a bias since the templates are *reconstructed* energies. A particularly relevant effect is the overestimation of the electronic noise. The PS adds the electronic noise in the pulse simulation, however, the template from which the amplitude of the pile-up pulse is sampled already carries the effects of the electronic noise, which results in a double counting of this feature.

The effect of the electronic noise can be observed in the templates shown in Figure 4.3 as the distributions extend to *negative* values of the amplitude, a feature that is

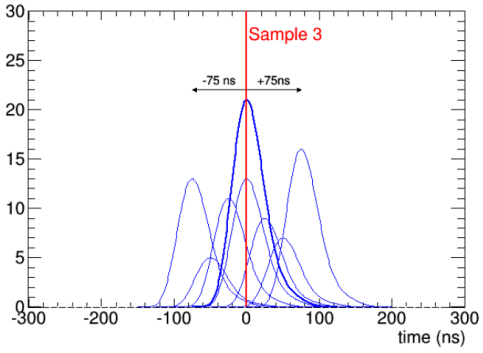

(a) Central sample - original

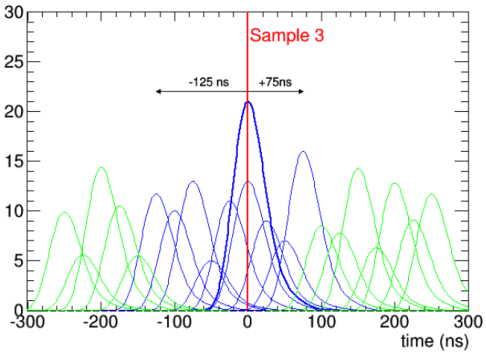

(b) Central sample - new

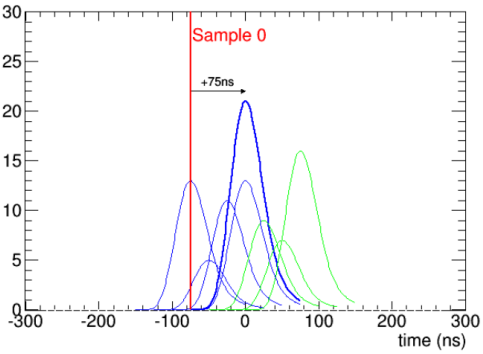

(c) First sample - original

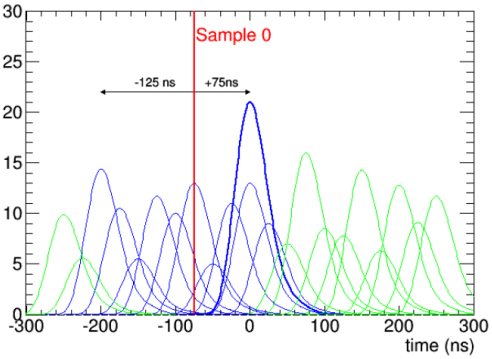

(d) First sample - new

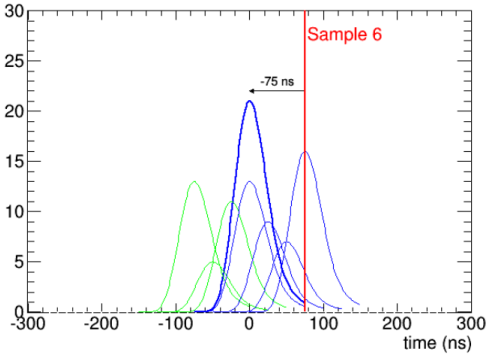

(e) Last sample - original

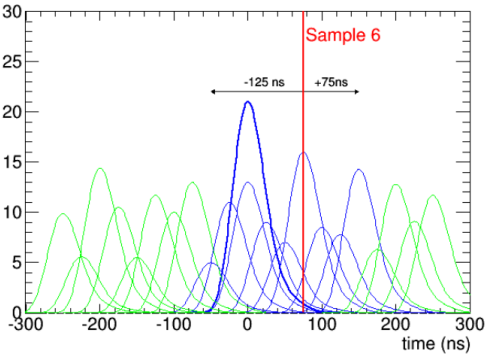

(f) Last sample - new

Figure 4.10: Extended full time of the collision range [−300 ns, +300 ns], showing the pulse distribution and the sum for the original version (only seven pile-up pulses) and the new version (all the pulses in the available interval) for a study with a bunch-spacing of 25 ns. The pulses are drawn in green, but the specific ones which enter in the computation of particular sample are shown in blue. For each computed sample (marking its position with a vertical red line), black arrows show the extent of the range where pulses are accounted: from −125 ns to +75 ns. The first sample can be greatly affected by the remaining energy of previous bunch-crossings.

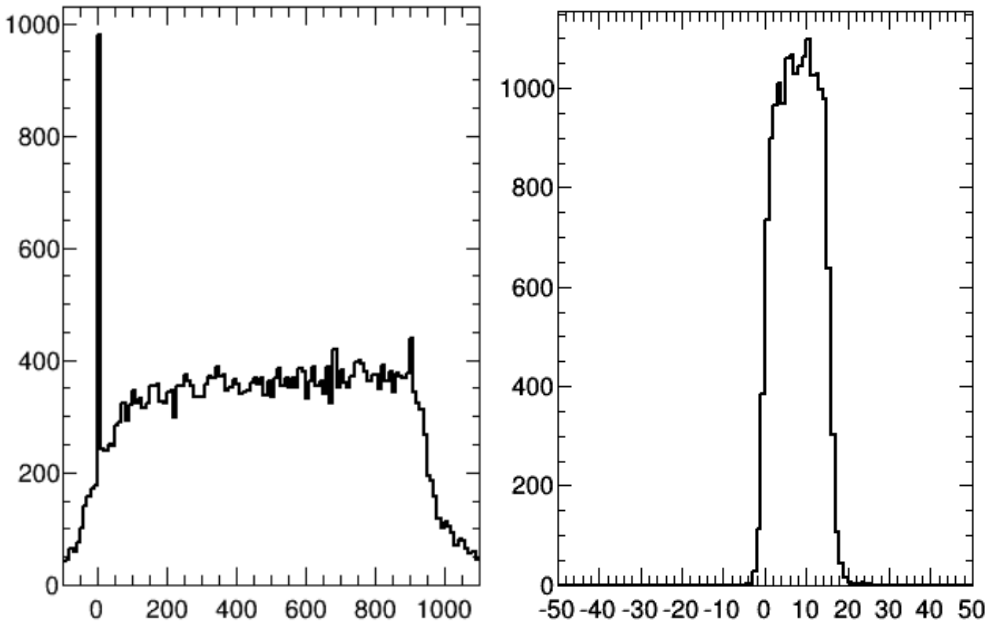

(a) Rec. amplitude in HG (b) Rec. amplitude in LG

Figure 4.11: Reconstructed amplitude of a pulse in (a) high gain and (b) low gain, for the old version of the Pulse Simulator. In the HG mode (a), the events which are saturated in HG (ADC-counts $>$ 1023) are misreconstructed with an amplitude of 0, leading to a peak of non-reconstructed events. On the other hand, all events of the study are also computed in LG, which results in a overload of very low energetic events, visible in the LG output (b). The units of measure of the x-axis are ADC-counts.

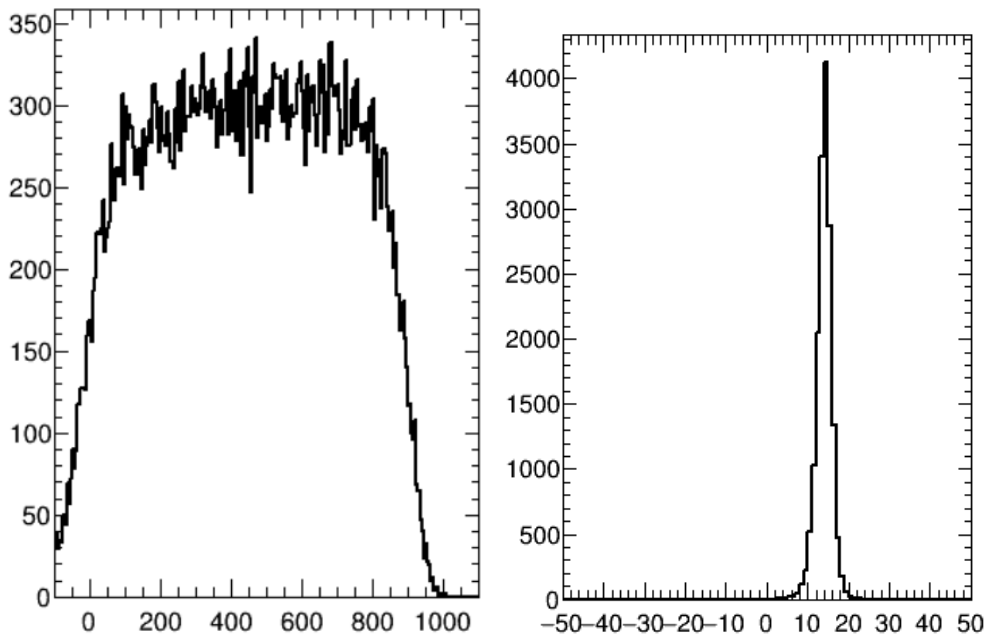

(a) Rec. amplitude HG (b) Rec. amplitude LG

Figure 4.12: Reconstructed amplitude of a pulse in (a) high gain and (b) low gain, for the new version of the Pulse Simulator, showing the impact of the implementation of the gain switch. In (a), the events which are saturated in HG (ADC-counts $>$ 1023) are now removed from HG and computed as LG. On the other hand, the LG is now computed only for the events that have saturated HG, thus removing the majority of non-interesting low energy events. The units of measure of the x-axis is ADC-counts.

due to the fluctuations of the electronic noise. The negative amplitude is relevant since it is then possible that the out-of-time pulses are simulated with a negative amplitude, and therefore they would contribute negatively to the read-out samples. This is an unphysical behavior which should be avoided in the PS.

In order to fix it, a different approach was used. Instead of taking a reconstructed template energy, which carries a reconstruction bias, the template of energy was taken from Monte Carlo simulation. For this, a sample of simulated *Hits* of 1 million collisions was used. The *Hits* sample is obtained from the simulation of the detector response using the GEANT 4 program [126]. The GEANT 4 detector simulation program replicates the behavior of the particle interactions and the energy loss inside the detector. The deposited energy inside the detector can be obtained by integrating the energy loss in the time range of [−5 ns, +20 ns] from the trigger signal for the Tile Calorimeter, as shown in (Figure 4.13).

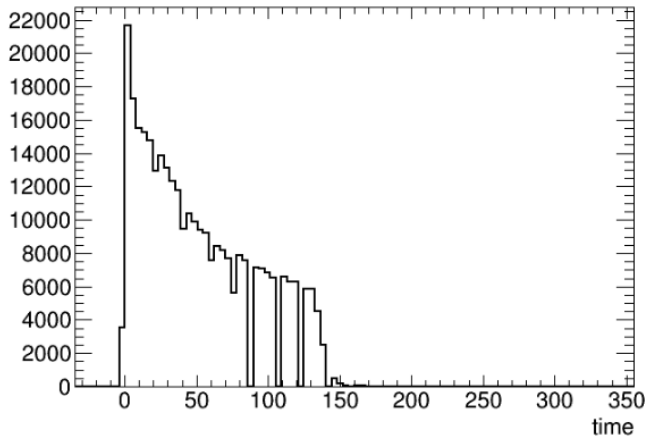

Figure 4.13: Distribution of *hits* in the detector as a function of time in the E4 cell. The integration in the time range [−5 ns, +20 ns] gives the deposited energy.

The resulting distribution is the template energy, which were obtained for each of the cells of the detector and are shown in Figure 4.14. Finally, in Figure 4.15, a comparison between the old and the new templates is shown for some example cells. As the new distributions are not affected by the reconstruction bias or electronic noise, they end sharply at 0 and do not have negative amplitude values.

Simulation of arbitrary values of pile-up

The template energy distributions obtained can be considered to be the energy deposited by a single *pp* collision, which is the same to say that they are distributions for a $\mu = 1$. If assumed that the pile-up can be described by overlapping $\mu = 1$ distributions, the templates could be use to simulate any desired value of μ. This would allow to access the high pile-up conditions expected for the coming Runs, such as simulating values of, for example, $\mu = 140$ or even $\mu = 200$.

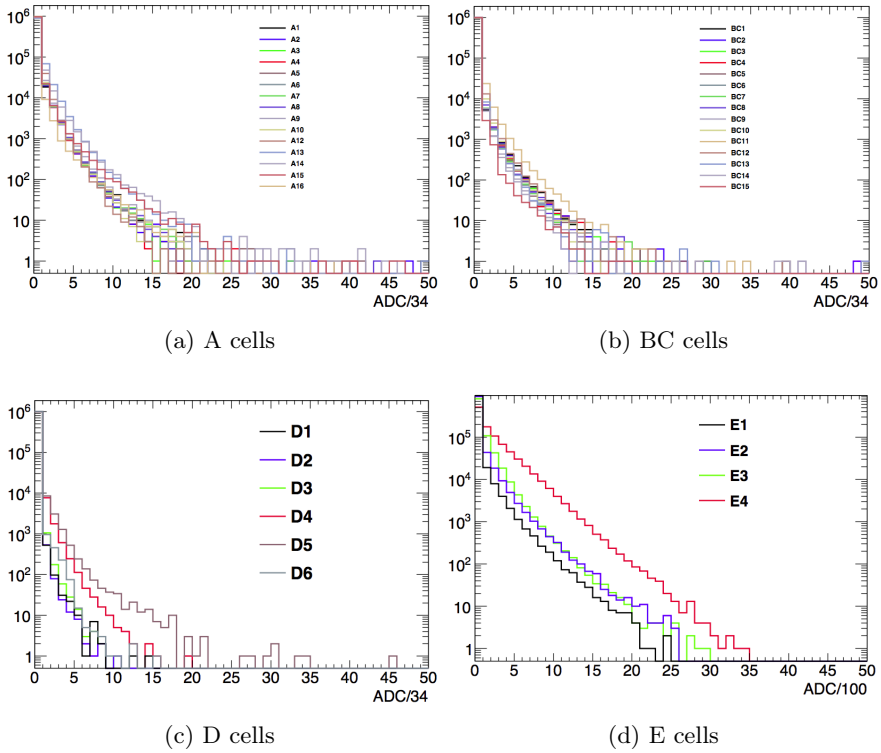

(a) A cells (b) BC cells

(c) D cells (d) E cells

Figure 4.14: Template energy distributions obtained from *Hits* for the different cells in the detector. The units of measure of the x-axis is ADC-counts, divided by the conversion factor.

In order to allow a customized μ in the PS, the simulation of the out-of-time pulses was completely modified, for which a new option, desired μ, was added. In the previous version, a pulse was added in each of the bunch-crossings, obtaining its amplitude from the template distribution for the selected μ. In the new version, this amplitude is obtained from several amplitudes[3] sampled from the μ =1 template energy distribution.

The previous study was repeated using the new templates, and its results can be seen in Figure 4.16. The results are preliminary, since the templates need validation and a fine-tuning, in order to test their agreement with the real data, but these results show that the PS can be used to simulate higher values of pile-up and study high-luminosity conditions.

4.4 Summary

The PS has been greatly upgraded with the implementation of new features that improve its performance and prepare it for the high-luminosity conditions of the Phase-II upgrade.

[3]Experimentally only the *average* number of collisions per bunch-crossing is considered, hence the PS employs a Poisson probability distribution with average value equal to μ. Then for each bunch-crossing it randomly samples the number of collisions from such distribution.

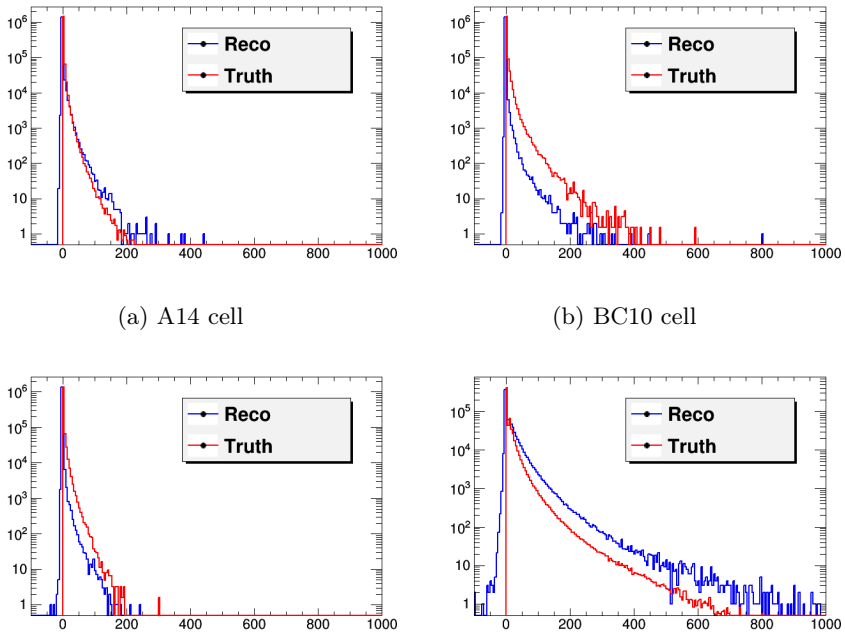

(a) A14 cell (b) BC10 cell

(c) D4 cell (d) E4 cell

Figure 4.15: Comparison of the template energy distribution for the pile-up pulses for different cells for (blue, labelled *reco*) the original template, which used a reconstructed energy and (red, labelled *truth*) the new template, that uses a sample of simulated events to obtain the energy from the *Hits* in the detector. The units of measure of the x-axis of the left plots are ADC-counts.

The enhancement of the out-of-time pulse simulation, updating from only one additional pulse to a customizable bunch-spacing with an arbitrarily-defined number of interactions per bunch-crossing is a great advance that allows for a more versatile simulation of the interference of pile-up pulses with the signal pulse. The implementation of the extended time-window, up to +130 ns, in the pile-up simulation provides a more accurate modeling of the out-of-time pile-up in the measurement of the sample amplitude. However, the measurement of the pulse shape is limited to such a time range and so, it fails to describe the undershoot effect, which affects the value of the pedestals of the subsequent bunch-crossings. A possible improvement of this work would be to measure the complete pulse shape, improving the modeling of the undershoot effect.

In addition, the gain switch implementation improves one deficiency of the PS, namely that it could not reproduce the correct behavior of the detector. This correction allows to study conditions with a high number of saturated samples.

Finally, the change of the energy template is still an open topic. Using truth templates obtained by MC Hits shows clear advantages with respect to the previous reconstructed templates, such as avoiding overestimating the electronic noise and negative amplitude values in the templates. It also allows to simulate any desired number of collisions per bunch-crossing by superposing several $\mu = 1$ amplitudes. This was one of

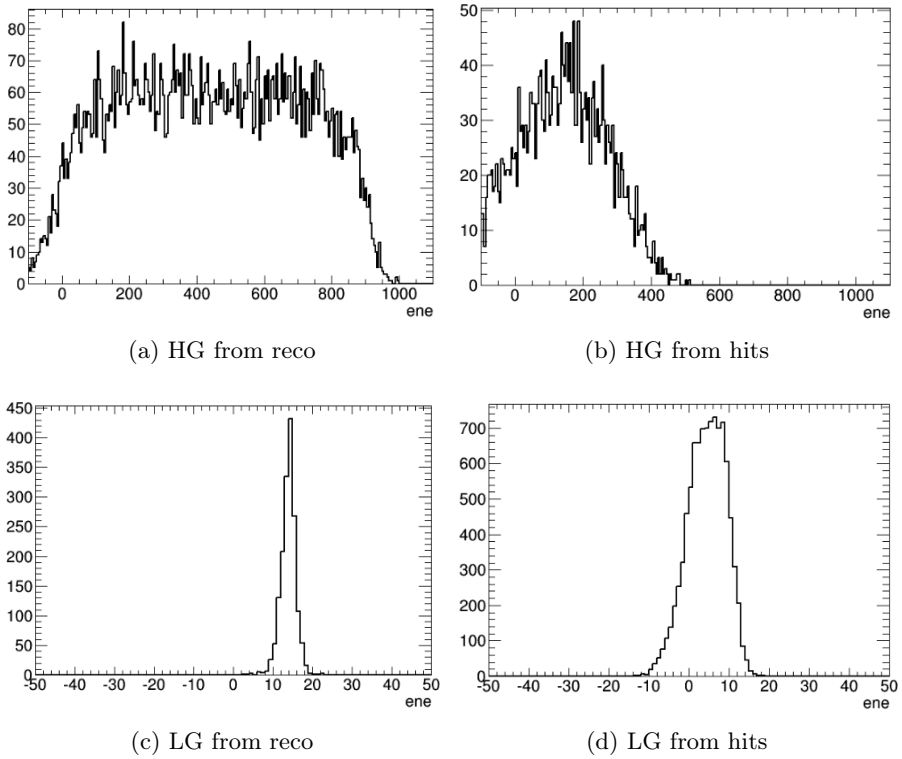

(a) HG from reco (b) HG from hits

(c) LG from reco (d) LG from hits

Figure 4.16: Reconstructed amplitude obtained by the Pulse Simulator, comparing the results using (left) the old template of reconstructed energy and (right) the new template of true energy from Hits, for the E4 cell and for a pile-up of $\mu = 40$. The units of measure of the x-axis is ADC-counts.

the main goals for this tool for the Phase-II upgrade of the LHC. The preliminary results are consistent with the expected behavior of the detector in the conditions where pile-up starts to be significant, but further checks must be done to ensure a correct reproduction of the real data. A proper validation of the energy templates with data is needed. This task is beyond the scope of the work realized for this thesis but it would be a good topic for future developments.

Chapter 5

Object definition

Each event recorded by the ATLAS detector is composed of a set of measurements made by the different sub-detectors, such as energy deposits or hits. In order to analyze the physics of the event, all particles generated in the collision have to be reconstructed from the available raw information. For each kind of particle (electron, μ, τ and jets), several sets of selection criteria with different tightness are defined, and a scan of the whole event is performed, looking for all possible candidates that match the selection. A summary of the criteria for each kind of object is described below.

Due to the presence of undetectable neutrinos, an accurate reconstruction of particles such as the τ can be problematic. Moreover, the invariant mass of the event cannot be fully calculated due to the missing information and so, several approximations and algorithms are developed, both for the reconstruction of the missing momentum and for the mass of the Higgs boson candidate decaying to τ pairs. However, since each analysis has a specific approach for the mass reconstruction, these procedures will be described in the respective analysis chapters.

5.1 Tracking and vertexing

Tracks are reconstructed in the Inner Detector using a sequence of algorithms [127]. The inside-out [128] is the baseline algorithm designed for the efficient reconstruction of primary charged particles, which are defined as the particles with a mean lifetime greater than $3 \cdot 10^{-11}$ s, directly produced in a pp interaction or from the subsequent decays of particles with a shorter lifetime. To reconstruct the tracks, the inside-out algorithm starts from 3-point seeds in the silicon detectors (Pixel + SCT) and adds hits moving away from the interaction point, using a combinatorial Kalman filter. Ambiguities in the track candidates found in the silicon detectors are resolved, and tracks are extended into the TRT. The tracks reconstructed by the inside-out algorithm are required to have a transverse momentum $p_{\mathrm{T}} > 400\,\mathrm{MeV}$.

In a second stage, a track search starts from segments reconstructed in the TRT and extends them inwards by adding silicon hits, which is referred to as back-tracking. Back-tracking is designed to reconstruct secondaries, which are particles produced in the interactions of primaries. Finally, tracks with a TRT segment but no extension into the silicon detectors are referred to as TRT-standalone tracks. Fake tracks can be minimized by tightening the quality requirements on reconstructed tracks. A set of robust requirements is therefore defined by selecting tracks with at least 9 hits in the silicon detectors and exactly zero holes[1] in the Pixel.

The interaction vertices are reconstructed using an iterative vertex finding algorithm, based on the reconstruction of charged-particle tracks in the Inner Detector. The tracks used for the reconstruction need to match the following selection criteria [129]: $p_{\mathrm{T}} > 150\,\mathrm{MeV}$, $d_0 < 4\,\mathrm{mm}$, $\sigma(d_0) < 5\,\mathrm{mm}$ and $\sigma(z_0) < 10\,\mathrm{mm}$, resolution values two times greater than the typical values. Additionally, at least 4 hits in the SCT and at least 6 hits in the SCT and Pixel detectors are required. Vertex seeds are obtained from the z-position along the beamline of the reconstructed tracks. An iterative χ^2 fit is made using the seed and nearby tracks (at least 3), which are weighted according to the χ^2. The tracks incompatible with the vertex by more than 7σ are used to seed a new vertex. This procedure is repeated until no unassociated tracks are left in the event or no additional vertex can be found.

Primary vertices (PV) are found within the beam interaction region and provide information about the number and position of the primary collisions. Secondary vertices are found outside the beam interaction region and are used to identify decays of heavy-flavor and long-lived particles.

5.2 Electrons

Physics channels of prime interest at the LHC are expected to produce electrons with a p_{T} between a few GeV and 5 TeV [130]. Good electron identification is therefore needed over a broad energy range. The standard reconstruction of electrons starts with an electromagnetic tower seed with transverse energy above 3 GeV from the EM calorimeter and a matching track which does not belong to a photon-conversion pair reconstructed in the Inner Detector. The track, after extrapolation to the EM calorimeter, is required to match the cluster within a broad $\Delta\eta \times \Delta\phi$ window of 0.05×0.10. The ratio of the energy of the cluster to the momentum of the track (E/p) is required to be lower than 10. Approximately 93% of true isolated electrons, with $E_{\mathrm{T}} > 20\,\mathrm{GeV}$ and $|\eta| < 2.5$, are selected as electron candidates. Candidates found in the transition region between the end-cap and barrel calorimeters ($1.37 < |\eta| < 1.52$) are not considered.

[1] Expected hits along a track path which are not present.

Various identification techniques, such as a simple cut-based or a more advanced likelihood discriminant, can be applied to the reconstructed electron candidates, combining calorimeter and track quantities and the TRT information to discriminate jets and background electrons from the signal electrons. The standard cut-based identification of high-p_{T} electrons is based on cuts which can all be applied independently. These cuts have been optimized in up to seven bins in η and up to six bins in p_{T}. Three reference sets of cuts have been defined [131], with different tightness: loose, medium and tight. In addition to the cut-based identification, default for Run 1 analyses, several multivariate techniques have been developed for Run 2, such as a discriminant called H-matrix, a Boosted Decision Tree, a neural network and a likelihood discriminant, this one being used in the analysis of Chapter 7. The detailed description of these methods can be found in Ref. [130].

5.3 Muons

ATLAS employs a variety of strategies for identifying and reconstructing muons [130]. The direct approach is to reconstruct *standalone* muons by finding tracks in the Muon Spectrometer and then extrapolating these to the beam line. *Combined* muons are found by matching standalone muons to nearby Inner Detector tracks and then combining the measurements from the two systems. Tagged muons are found by extrapolating Inner Detector tracks to the Muon Spectrometer detectors and searching for nearby hits. Two different sets of algorithms are available, each of them including a framework for each of the strategies: the Staco [132] and Muid [133].

The standalone algorithms first build track segments in each of the three muon stations and then link the segments to form tracks. The Staco-family algorithm that finds the spectrometer tracks and extrapolates them to the beam line is called Muonboy [132]. On the Muid side, Moore [134] is used to find the tracks, and the first stage of Muid performs the inward extrapolation. Standalone algorithms have the advantage of slightly greater $|\eta|$ coverage (up to 2.7 compared to 2.5 for the ID) but they have holes in the coverage at $|\eta| \sim 0$ and ~ 1.2. Also, low-p_{T} muons may not arrive to the outermost stations, hindering their reconstruction.

For the combined muons, both families pair MS tracks with ID tracks to identify muons by using a χ^2 match. Staco does a statistical combination of the inner and outer track vectors to obtain the combined track while Muid does a partial refit, it does not directly use the measurements from the inner track, but starts from the inner track and adds the measurements from the outer track.

The spectrometer tagging algorithms, MuTag [132] and MuGirl [135], propagate all ID tracks with sufficient momentum out to the first station of the MS and search for nearby segments. MuTag defines a tag χ^2 using the difference between any nearby

segment and its prediction from the extrapolated track. MuGirl uses an artificial neural network as a discriminant. In either case, if a segment is sufficiently close to the predicted track position, then the ID track is tagged as corresponding to a muon. MuGirl considers all inner-detector tracks and redoes segment finding in the region around the track. MuTag only makes use of inner-detector tracks and muon-spectrometer segments not used by Staco. Thus MuTag serves only to supplement Staco while MuGirl attempts to reconstruct all muons.

For Run 2, the muon reconstruction runs a unified chain, with simplified steering and configuration [136], grouping the muons in four different categories: standalone, combined, segment-tagged, and calorimeter-tagged. In addition, four efficiency working points are defined [137]: loose, medium (only for combined and standalone muons), tight (only for medium combined muons with at least two stations of the MS), and high-p_{T} (for combined muons with at least 3 stations of the MS).

5.4 Jets

As explained in Section 1.1.3, the quarks can only be observed as compound states with no color-charge. When a quark is produced in one of the collision events, the strong force generates pairs of particles that conserve the color neutralness of the final object, in a process called hadronization. This shower of particles is called *jet*.

Jets are reconstructed in the detector [130] from deposits of energy in the form of clusters in the calorimeters. The objects are reconstructed using the anti-k_t algorithm [138] with topological cell clusters (Topoclusters) [112] within $\Delta R = 0.4$. Topoclusters represent an attempt to reconstruct three-dimensional energy depositions in the calorimeter, using as seed cells with an energy above $4\,\sigma$ of the noise, and iteratively adding any cell with energy $> 2\,\sigma$, and a boundary layer of cells. After the initial clusters are formed, they are analyzed for local signal maxima by a splitting algorithm.

The topoclusters are first reconstructed at the EM scale, which is defined as the calibrated energy scale for electromagnetic particles [139]. In a second step, the probability that a topocluster is generated by an electromagnetic shower is computed using local cell and cluster level information, which is called cluster classification, and is performed based on the cell energy density and the longitudinal shower depth of the clusters. A hadronic calibrations is applied to the Topoclusters based on their classification probability. Calibrated topoclusters are referred to as Local Cluster Weighted topocluster.

Jets are calibrated to truth-particle level using a factorized, sequential scheme, consisting of several steps. The first step is an additive offset pile-up correction to remove the effect of additional energy from pile-up particles inside the jet, which is used to reduce pile-up fluctuations from one event to the next. The next step is the application of a multiplicative Jet Energy Scale (JES) correction derived from MC events. The goal

of this correction is to restore the jet response to that of truth particle jets in QCD di-jet events. The last step is a residual in-situ correction that is only applied to jets in data. This residual correction, computed as the ratio of MC to data jet energy response, improves the agreement of the energy response of jets in data and MC, reducing the JES systematic uncertainty. For the SM $H \to \tau\tau$ analysis, the jets were formed starting from Local Cluster Weighted topoclusters, while for the MSSM $H/A \to \tau\tau$ analysis, the jets were formed from EM calibrated clusters.

However, jets can originate from primary vertex collisions as well as from nearby collisions. In order to reduce the contamination of non primary vertex jets, a Jet Vertex Fraction condition (JVF) [140] is applied. The JVF is defined as the ratio between the sum of the transverse momentum of the tracks in the jet associated to the PV and the sum of the transverse momentum of the tracks associated to any vertex in the event. Due to the requirement of tracks, this cut can only be applied on jets within the coverage of the ID ($|\eta| < 2.5$). The threshold is optimized for each dataset (7 and 8 TeV) since they have different pile-up conditions. For the 7 TeV data, jets are required to have a JVF ratio > 0.75. For 8 TeV dataset, with higher average pile-up, the cut is relaxed to JVF > 0.5 and applied only to jets with $p_{\mathrm{T}} > 50$ GeV.

For Run 2, the JVF criterion was substituted by the Jet Vertex Tagger (JVT) [141], which is a 2D-likelihood discriminant that uses as inputs a vertex-corrected JVF variable and the ratio of the scalar p_{T}-sum of the tracks associated to the jet, divided by the calibrated jet p_{T}. The condition of the JVT algorithm for the selection of jets was $|\mathrm{JVT}| > 0.64$, applied only to jets with $p_{\mathrm{T}} < 50$ GeV and $|\eta| < 2.4$.

A special scan of the jet candidates is done to identify the ones produced by the hadronization of a b-quark, which are referred as b-jets. The identification uses three features of the b-physics [130], such that the b-hadrons retain about 70% of the original b-quark momentum, its mass is relatively high and they have a long lifetime which results in a displaced secondary vertex. Such vertices can be identified inclusively by measuring the impact parameters of the tracks from the b-hadron decay products. These tracks tend to have rather large impact parameters (d_0, z_0) which can be distinguished from tracks stemming from the PV. In addition, the semi-leptonic decays of b-hadrons can be used by tagging the lepton in the jet, since the lepton will have a relatively large transverse momentum and a large momentum relative to the jet axis.

Various b-tagging algorithms [142] have been developed in ATLAS to achieve high b-tagging efficiencies while keeping the misidentification efficiency for c and light-flavor jets (u, d, s, g jets) at very low levels. They range from relatively simple algorithms based on impact parameters (as IP3D) and secondary vertices (SV1) to a more refined algorithm exploiting the topology of weak b- and c-hadron decays (JetFitter) [143, 144]. The most discriminating variables resulting from these algorithms are combined in artificial neural

networks, and output weight probabilities are evaluated separately for b, c, and light-flavor jets. Finally, multivariate tagging algorithms based on these probabilities are used to further enhance the tagging performance. One of these is the MV1 algorithm, which is calibrated for a fixed value of efficiency. A 70% efficiency working point is used in this analysis [143, 144]. The corresponding light-quark jet misidentification probability is 0.1-1%, depending on the jet's p_{T} and η.

In Run 2, the algorithms for the reconstruction of b-jets were updated [145] to include the information of the IBL and improve their performance. In particular the MV1 algorithm was upgraded to the MV2, which has multiple implementations. The one which was used in the physics analyses was the MV2c20 algorithm, which is defined as the output of such a BDT with the training performed by assigning b-jets as signal and a mixture of 80% light-flavor jets and 20% c-jets as background. A working point that corresponds to an average efficiency of 70% for b-jets in $t\bar{t}$ simulated events is chosen. The misidentification rates for c-jets, τ-jets and jets initiated by light quarks or gluons for the same working point and in the same sample of simulated $t\bar{t}$ events are approximately 10%, 4% and 0.2% respectively.

5.5 Tau leptons

The two types of τ decay, τ_{lep} and τ_{had}, have been introduced in Section 2.2.3. They have completely different topologies and thus, their reconstruction follow different strategies.

In the case of the τ_{lep} decay, the τ object is not reconstructed as such, the analyses employ directly the final state objects: the light leptons and the missing energy, thus using the reconstruction of these objects.

The hadronic-decaying taus (τ_{had}), however, are reconstructed [146] as standalone objects. The reconstruction begins using jets reconstructed with the anti-k_t algorithm with $\Delta R = 0.4$ using topoclusters calibrated with a local hadronic calibration (LC). Additional requirements are $E_{\mathrm{T}} > 10\,\mathrm{GeV}$ and $|\eta| < 2.5$. The τ production vertex is identified from the reconstructed primary vertex candidates in the event. This vertex is used to determine the τ_{had} direction, to associate tracks, and to build the coordinate system in which identification variables and impact parameters are calculated.

This is done by a tau vertex association algorithm that uses as input all tau candidate tracks (with $p_{\mathrm{T}} > 1\,\mathrm{GeV}$ and satisfying the ID requirements) in a cone $\Delta R < 0.2$ around the jet seed direction. The p_{T} of these tracks is summed and the primary vertex candidate to which the largest fraction of the p_{T} sum is matched is chosen as the tau vertex. The τ charge is determined from the sum of the charges of its associated tracks. Only candidates with 1 or 3-tracks (prongs) and with a charge of ± 1 are selected as τ_{had} candidates. Additional criteria applied on the τ_{had} candidates include $p_{\mathrm{T}} > 20\,\mathrm{GeV}$.

The identification of τ from jets is done by Boosted Decision Trees, trained separately for 1 and 3-prong τ_{had}, using the simulated $Z/\gamma^* \to \tau^+\tau^-$ process for signal and di-jet process for background. The BDT is built by a set of variables related to the topology and energy of the cluster, which for Run 2 includes the reconstruction of π^0 inside the τ_{had} cone (in Run 1, this was done using a separated algorithm). The BDT employs three working points, labelled "tight", "medium" and "loose" [147], corresponding to different identification efficiencies: 45%, 55% and 60% for 1-prong taus and 30%, 40% and 50%, for 3-prong taus, respectively. The requirements on the BDT score are chosen such that the resulting efficiency is independent of the true τ_{had} p_{T}. The probability to misidentify a jet with $p_{\text{T}} > 20\,\text{GeV}$ as a τ_{had} candidate is typically 1–2%.

Dedicated criteria to separate τ_{had} candidates from misidentified electrons are also applied with a selection efficiency for true τ_{had} decays of 95%. For Run 2, the electron identification uses the likelihood discriminator built for ATLAS electron reconstruction, which is based on the shower shape information from the calorimeter measurements as well as on reconstructed hits in the tracking detector, including information from transition radiation in the TRT.

After the reconstruction step, the energy of tau candidates is calibrated at the LC scale, which mostly corrects for the calorimeter non-compensation and for the energy deposited in dead material or outside the topoclusters. The tau energy scale (TES) consists of two additional corrections which calibrate the tau energy back to the true visible energy: first, the energy contribution originating from pileup interactions is subtracted and then, a second correction is applied to account for effects such as decay products not reaching the calorimeter, not depositing enough energy to create topoclusters, or not detected within $\Delta R = 0.2$ of the reconstructed candidate.

5.6 Overlap removal

The reconstruction processes of the different objects are applied independently and thus, same detector traces, such as energy deposits, can be reconstructed simultaneously as different candidates. To avoid this ambiguity, an *Overlap Removal* procedure (OLR) is performed, which sets the priority of the reconstruction processes. The OLR algorithms looks for overlap conflicts in objects that are not separated geometrically ($\Delta R < 0.2$) and solve each of them by selecting the reconstruction which ranks higher in this order:

$$\mu \to e \to \tau \to \text{jet}$$

5.7 Missing transverse energy

Due to the purely weak interaction of neutrinos, they cannot be detected by ATLAS sub-detectors. However, since momentum has to be conserved and it has to be close to zero in the plane transverse to the beam, it is possible to compute the missing transverse momentum, labelled as $E_{\mathrm{T}}^{\mathrm{miss}}$, as the module of the difference with respect to zero of the vectorial sum of the transverse momentum of all reconstructed objects involved in the event. A good reconstruction of the $E_{\mathrm{T}}^{\mathrm{miss}}$ is crucial for the $H \to \tau\tau$ analyses, due to the presence of several neutrinos (two, three or four, depending on the final state) in the expected signal events.

The $E_{\mathrm{T}}^{\mathrm{miss}}$ is reconstructed [148–150] using the energy deposits in the calorimeter cells calibrated according to the reconstructed physics objects (e, γ, τ_{had}, jets and μ) with which they are associated, and the energy from calorimeter cells and tracks not associated with any physics objects (which is called the *soft-term*), as,

$$\vec{E}_{\mathrm{T}}^{\mathrm{miss}} = -\sum \vec{p}_{\mathrm{T}}^{\,e} - \sum \vec{p}_{\mathrm{T}}^{\,\gamma} - \sum \vec{p}_{\mathrm{T}}^{\,\mu} - \sum \vec{p}_{\mathrm{T}}^{\,\tau_{\mathrm{had}}} - \sum \vec{p}_{\mathrm{T}}^{\,\mathrm{jet}} - \sum \vec{p}_{\mathrm{T}}^{\,\mathrm{soft}} \tag{5.1}$$

$$E_{\mathrm{T}}^{\mathrm{miss}} = \left| \vec{E}_{\mathrm{T}}^{\mathrm{miss}} \right| \tag{5.2}$$

The reconstruction of the soft-term can be done with several algorithms. The Calorimeter Soft Term (CST) uses energy deposits in the calorimeter which are not matched to high-p_{T} physics objects. The Soft-Term Vertex-Fraction (STVF) algorithm uses CST as a base, suppressing pile-up effects by scaling the soft term by the fraction of scalar-summed track p_{T} not associated with high-p_{T} physics objects matched to the PV. In addition, the JVF requirement is applied to jets, in order to suppress contribution from pile-up. Finally, the Track Soft Term (TST) algorithm calculates the soft-term by using ID tracks that are not associated with high-p_{T} physics objects and applying the JVF selection requirement to jets.

During Run 1, the $E_{\mathrm{T}}^{\mathrm{miss}}$ soft-term was reconstructed using the STVF algorithm, while TST was the method used for Run 2, as it is more robust against pile-up.

A second definition of the $E_{\mathrm{T}}^{\mathrm{miss}}$, called $E_{\mathrm{T}}^{\mathrm{miss,HPTO}}$ is also used in this thesis. $E_{\mathrm{T}}^{\mathrm{miss,HPTO}}$ is built using only the high p_{T} objects selected by the analysis. This variable is used to discriminate specific topologies, such as decays with no neutrinos involved, because the $E_{\mathrm{T}}^{\mathrm{miss}}$ and $E_{\mathrm{T}}^{\mathrm{miss,HPTO}}$ are highly correlated for events with neutrinos, while they are not for events without neutrinos. The $E_{\mathrm{T}}^{\mathrm{miss,HPTO}}$ can also be used in the reconstruction of the invariant mass of the system, thus allowing for studies of this specific topology.

Complementary, the total transverse momentum, labelled ΣE_{T}, is calculated from the scalar sum of the transverse momenta of the different objects and the soft-term.

$$\Sigma E_{\mathrm{T}} = \sum p_{\mathrm{T}}^{e} + \sum p_{\mathrm{T}}^{\gamma} + \sum p_{\mathrm{T}}^{\tau_{\mathrm{had}}} + \sum p_{\mathrm{T}}^{\mu} + \sum p_{\mathrm{T}}^{\mathrm{jet}} + \sum p_{\mathrm{T}}^{\mathrm{soft}} \tag{5.3}$$

Chapter 6

Search for the SM Higgs boson in the $\tau_{\text{lep}}\tau_{\text{lep}}$ channel

6.1 Introduction

This chapter describes the search for the Standard Model Higgs boson decaying to a pair of τ leptons ($H \to \tau\tau$) in the fully-leptonic channel, which was performed using the data collected by the ATLAS Experiment during the Run 1 of the LHC. Preliminary results using the 2011 data were published as a paper in the Journal of High Energy Physics in June 2012 [151]. Ensuing results with the 2012 data were made public in preliminary results in November 2012 (2011 and partly 2012 data)[152], November 2013 (full 2012 data) [153] and October 2014 (with 2011 and full 2012 data) [154]. Finally, a paper with the full luminosity of Run 1 (2011+2012 data) and a re-optimized analysis, including consistency cross-checks, was published in April 2015 in the Journal of High Energy Physics [155], which incorporates the work of this thesis.

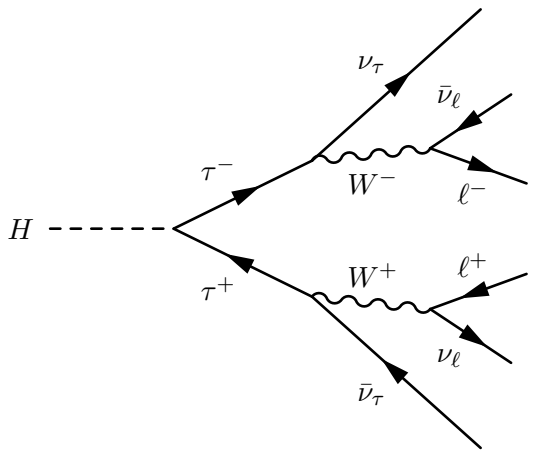

Figure 6.1: Feynman diagram for the decay of a Higgs boson in the $\tau_{\text{lep}}\tau_{\text{lep}}$ channel. The Higgs boson decays into a pair of τ particles which, in turn, decay leptonically, to light leptons ($\ell \equiv \mu, e$) and corresponding neutrinos.

The $H \to \tau\tau$ analysis consists of the search for evidence of a particle compatible with the SM Higgs boson, by looking for a statistically significant excess of signal-like events over the background expectation in a set of di-τ events. The strategy of the analysis and the definition of the different channels is described in Section 6.2. Since the di-τ events contain neutrinos, the invariant mass of the event cannot be analytically reconstructed. Therefore, several approximations and algorithms are developed to provide a estimation of the invariant mass of the di-τ system, which are described in Section 6.3.

Signal-like events are separated from the known backgrounds by exploiting their different kinematics. The background model is validated in dedicated control regions (CR) for the main backgrounds, where one specific background is dominating and no relevant signal is expected. Where possible, the backgrounds are modeled using data-driven methods. Signal is modeled according to the expected properties of the Higgs boson predicted by the SM for a mass of $m_H = 125\,\text{GeV}$. The main backgrounds are deduced from the theoretical expectations of particle production in pp collisions, and their subsequent decays, for a specific energy of center of mass ($\sqrt{s} = 7\,\text{TeV}$ for collisions collected during 2011 and $\sqrt{s} = 8\,\text{TeV}$ for the data collected in 2012)[1]. The full signal and background model is described in Section 6.4.

Due to the low cross-section of the Higgs boson production, the ratio of signal to background events has to be enhanced. Therefore a strict, but efficient background rejection is crucial to the study. The main event selection of the analysis is described in Section 6.5. In addition, the dataset is divided in two categories, VBF and Boosted, optimized for different topologies of the signal events.

The procedure used in previous results of this analysis [152] was a cut-based method, but for the results presented in this thesis, a MultiVariate (MVA) approach is implemented, namely, a Boosted Decision Tree (BDT) algorithm. The MVA algorithms have to be properly optimized and they may suffer from systematic bias, but in return they provide a better background rejection/signal efficiency ratio, compared to a sequential cut-based methodology. Since the cut-based approach was not expected to provide a clear evidence for the $H \to \tau\tau$ decay during Run 1, the MVA proved to be a useful technique to increase the sensitivity of the analysis.

In principle, the MVA had to be optimized individually for the 7 TeV and 8 TeV datasets, but due to the reduced statistics of the MC samples used for the $\sqrt{s} = 7\,\text{TeV}$ data analysis, there were not sufficient MC statistics for a proper BDT training. Hence, it was decided that the MVA would be optimized only with the 8 TeV dataset and applied to both datasets (7 and 8 TeV). The description of the MVA optimization and studies are covered in Section 6.7.

[1] As both years had different e.c.m., the datasets can be addressed indistinctly by the year: 2011/2012 or the e.c.m.: 7 TeV/8 TeV.

While the analysis was being optimized, a blinding of the data of the signal regions for the sensitive variables ($m_{\tau\tau}$ invariant mass and BDT Score) was applied: the data could not be shown in the signal region. The analysis underwent scrupulous quality checks for the accuracy and robustness of the background estimation and the stability of the MVA algorithm. Only after it was considered that the analysis satisfied the current ATLAS standards, the signal region was allowed to be unblinded and the final results were extracted. The results of the MVA analysis of the $\tau_{\text{lep}}\tau_{\text{lep}}$ channel at 8 TeV are shown in Section 6.8. A brief review of the other two channels as well as the additional searches of the $H \to \tau\tau$ analysis are shown in Section 6.9.

The resulting signal regions distributions were analyzed using a maximum-likelihood fit on the data to the background expectation distribution and leaving free-floating the signal estimation, which gives the value of the strength of the measured signal normalized to the Standard Model expectation, as described in Section 6.10.4. The measured value of the signal strength, its comparison with the SM prediction for different production modes and the compatibility studies between the cut-based and the MVA approaches are covered in Section 6.11.

6.2 Channels

As described in Section 2.2.3, the τ particles can decay in two different ways: hadronically or leptonically. Hence, the $H \to \tau\tau$ decay can be separated in three possible final states: fully-leptonic ($\tau_{\text{lep}}\tau_{\text{lep}}$), semi-leptonic ($\tau_{\text{lep}}\tau_{\text{had}}$) and fully-hadronic ($\tau_{\text{had}}\tau_{\text{had}}$). The work performed in this thesis focused on the $\tau_{\text{lep}}\tau_{\text{lep}}$ channel and therefore, the information described in this chapter corresponds mainly to this channel. In addition, a brief description of the $\tau_{\text{lep}}\tau_{\text{had}}$ and $\tau_{\text{had}}\tau_{\text{had}}$ channels is given in Section 6.9. The results of the analysis include the details of the $\tau_{\text{lep}}\tau_{\text{lep}}$ channel and the final combination of the three channels.

The division in the aforementioned channels aims at optimizing the analysis by exploiting the different decay topologies of the τ particles. However, the combination of the three channels required a common baseline and harmonized criteria. Thus, a compromise was achieved to minimize the channel specific criteria while keeping a good sensitivity in the different channels The separation in channels is done by the event selection criteria, described in Section 6.5. The three channels are defined to be orthogonal among them, so the combination can be performed without suffering from correlations.

In the $\tau_{\text{lep}}\tau_{\text{lep}}$ channel, a second division can be performed attending to the flavor of the leptons present in the event. If the two leptons are of the same type, i.e. two electrons (ee) or two muons ($\mu\mu$), the event is labeled as *same flavor* (SF) channel. If the leptons are different ($e\mu$), the event is labeled as *different flavor* (DF) channel. This

division is useful for the optimization of the event selection because several processes couple differently to the SF or DF channels, e.g. the Z boson can only decay to SF events.

6.3 Reconstruction of the di-τ invariant mass

The $H \to \tau\tau$ analysis aims at discriminating $\tau\tau$ decays of Higgs bosons from a background of $\tau\tau$ events coming from other decays, in particular from the Z boson. The main discriminant between these processes is the invariant mass of the decaying object, hence a precise reconstruction of the kinematics of the di-τ system is needed. In the $\tau_{\text{lep}}\tau_{\text{lep}}$ channel in particular, both τ decay leptonically and so, the final state contains 2 light leptons and 4 neutrinos.

Since the mass of the leptons is small in comparison to m_h, they are effectively behaving as massless particles. The neutrinos are, however, more problematic: since they cannot be identified separately, only described collectively by the $E_{\text{T}}^{\text{miss}}$, the computation of the invariant mass is challenging. Several algorithms have been developed to handle the contribution of the neutrinos to the invariant mass, providing different approximations, which are useful for different parts of the physics analysis.

Visible mass The simplest mass variable is the *visible* mass, $m_{\tau\tau}^{\text{vis}}$, which is computed using only the visible decay products of the τ and thus, in the $\tau_{\text{lep}}\tau_{\text{lep}}$ channel it is equal to the invariant mass of the di-lepton system, called m_{ll}. The value of m_{ll} is not close to the expected Higgs boson mass, but is a very useful variable to discriminate $Z \to ll$ events from the signal.

Transverse mass A second approach is the *transverse* mass [156], m_{T}, which is a partial reconstruction of the invariant mass but limited to the transverse plane, where constrains on the missing energy can be set. The transverse mass provides a better separation from the QCD multi-jet backgrounds with fake τ signatures, however, not fully accounting for the neutrino momenta biases and it broadens the reconstructed distribution, therefore leading to a significantly reduced sensitivity in searches and measurements.The transverse mass is used in the $\tau_{\text{lep}}\tau_{\text{had}}$ channel, defined as:

$$m_{\text{T}} = \sqrt{2p_{\text{T}}^{l} E_{\text{T}}^{\text{miss}} \cdot (1 - \cos(\Delta\phi))} \tag{6.1}$$

where $\Delta\phi$ is the azimuthal separation between the lepton and the $E_{\text{T}}^{\text{miss}}$.

Collinear mass A third approach is the *collinear* mass, which will be referred to as $m_{\tau\tau}$. This mass is obtained following the *collinear approximation* [130, 156–158], which assumes that the τ are boosted and thus, the neutrinos and the light leptons are produced collinearly to the τ direction. This approximation constrains the system and reduces

the number of unknown variables of the event, which now depends on the fraction of the τ momentum carried away by the visible products of the decay (labelled as x). The approximation is generally valid since the Higgs boson is much more massive than the τ and thus, the τ are produced highly boosted. However, its computation cannot be performed for back-to-back τ, since the equation system becomes degenerate, so constraints on the $\Delta\phi_{\tau\tau}$ have to be applied. This approach gives a fairly good mass resolution but it is limited to a boosted topology and the tail of the distribution complicates the separation between the Z and the Higgs bosons.

The $m_{\tau\tau}$ is computed as:

$$m_{\tau\tau} \equiv \frac{m_{ll}}{\sqrt{x_1 \cdot x_2}} \tag{6.2}$$

where x_1 and x_2 denote the momentum fraction carried by the visible decays of the τ (p_l^{vis}), and are defined as:

$$x_{1,2} \equiv \frac{p_{1,2}^{\text{vis}}}{p_{1,2}^{\text{vis}} + p_{1,2}^{\text{miss}}} \tag{6.3}$$

The collinear approximation is also useful for defining the p_{T} of the Higgs candidate, $p_{\text{T}}^{\tau\tau}$, which is computed as:

$$p_x^{\tau\tau} \equiv \frac{p_x^{l1}}{x_1} + \frac{p_x^{l2}}{x_2} \qquad\qquad p_y^{\tau\tau} \equiv \frac{p_y^{l1}}{x_1} + \frac{p_y^{l2}}{x_2} \tag{6.4}$$

$$p_{\text{T}}^{\tau\tau} \equiv \sqrt{(p_x^{\tau\tau})^2 + \left(p_y^{\tau\tau}\right)^2} \tag{6.5}$$

From the $m_{\tau\tau}$, a second definition can be derived, the $m_{\tau\tau}^{\text{HPTO}}$, which is the collinear mass reconstruction using as input the missing E_{T} computed only with high p_{T} objects, $E_{\text{T}}^{\text{miss,HPTO}}$, which is used for certain studies.

Missing Mass Calculator The last approach for computing the invariant mass used in the analysis is the Missing Mass Calculator (MMC or $m_{\tau\tau}^{\text{MMC}}$) [156]. This algorithm uses a scan of the possible angular positions of the neutrinos to give the most likely value for the invariant mass. The MMC technique does not suffer from the limitations of the collinear approximation, so it can be applied to all event topologies. However, the technique assumes all the neutrinos of the event come from the Higgs decay, which makes the algorithm dependent on the resolution and purity of the $E_{\text{T}}^{\text{miss}}$ of the event.

The MMC algorithm works by solving an underconstrained system of equations with the assumption that the orientations of the neutrinos and other decay products are consistent with the mass and decay kinematics of a τ lepton. The full reconstruction of the event topology requires solving for 6 to 8 unknowns, depending on the specific decay

of each of the taus: the three components of the invisible momentum carried away by the neutrino system for each of the two τ in the event and the invariant mass of the neutrino pairs from each leptonic τ decay. However, only 4 constraints can be derived from the event: the invariant mass of the two τ decay systems must be the mass of the τ particle and the sum of the components of the neutrinos must match the $E_{\text{T}}^{\text{miss}}$ value (module and direction).

With the available information, the equation system cannot be exactly solved. However, not all solutions are equally likely. Additional knowledge of τ decay kinematics can be used to distinguish more likely solutions. An example of this information is the ΔR between the neutrino and the visible products of the τ decay. If the polarization effects are neglected, the distribution of $\Delta R(\tau_{vis}, \nu)$ is independent of the mother particle of the τ and thus, probability density functions (PDFs) can be derived using samples of $Z/\gamma^* \to \tau^+\tau^-$ at different momenta for 1-prong and 3-prong τ_{had}, and for leptonic decays. The PDFs are incorporated to a properly defined global event likelihood to provide additional constraints and obtain a better estimator. The $E_{\text{T}}^{\text{miss}}$ resolution is also used as a input for the estimation, which greatly improves the reconstruction by taking into account the effect of the detector in the measurement of the $E_{\text{T}}^{\text{miss}}$.

With this information, the value of the invariant mass is computed for all the points in the phase-space of the possible neutrino configurations, with an estimation of its probability. The most probable value is used as the final estimator of the di-τ mass, $m_{\tau\tau}^{\text{MMC}}$.

6.4 Data samples and signal and background modeling

6.4.1 Data samples

All the data used in this analysis corresponds to the Run 1 of LHC, before the Long Shutdown (LS1). Only data from the years 2011 (at $\sqrt{s} = 7\,\text{TeV}$) and 2012 (at $\sqrt{s} = 8\,\text{TeV}$) were considered, as the integrated luminosity collected in 2010 is negligible compared to subsequent years.
The data analyzed in this search amounted to:

- An integrated luminosity of $\mathcal{L} = \quad 4.5\,\text{fb}^{-1}$ at $\sqrt{s} = 7\,\text{TeV}$ in 2011.
- An integrated luminosity of $\mathcal{L} = \ 20.3\,\text{fb}^{-1}$ at $\sqrt{s} = 8\,\text{TeV}$ in 2012.

6.4.2 Signal processes

The main production modes of the Higgs boson in pp colliders have been described in Section 2.2.1 and are shown in Figure 6.2. The $H \to \tau\tau$ analysis in the SM focuses mainly in the vector boson fusion (VBF) and the gluon fusion (ggH), with a secondary

contribution of the vector boson-associated production (VH). Additional sources of signal as fermion-associated production with t-quarks (ttH) or b-quarks (bbH) were found to be negligible in this search. The samples used in this analysis, with their respective cross-sections, are summarized in Table 6.1.

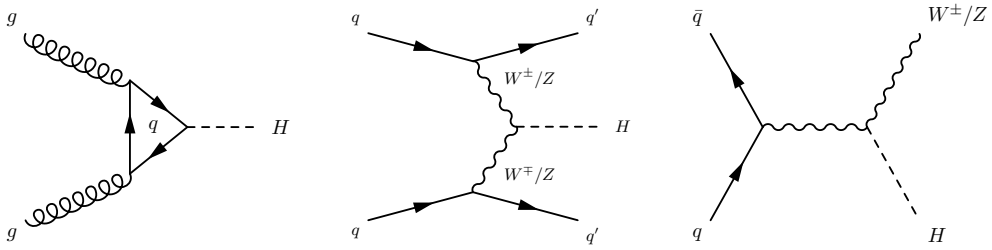

(a) ggH (b) VBF (c) VH

Figure 6.2: Main production modes of a Higgs boson considered in the SM analysis, including (a) gluon fusion process (ggH) (b) Vector boson fusion process (VBF) and (c) Vector-associated production (VH)

Mode		**$\sigma\times$ BR** [pb]	**MC generator**	**Order**	
	ggH	1.22	POWHEG [159–162] + PYTHIA8 [169]	NNLO+NNLL	[83, 163–168]
	VBF	0.100	POWHEG + PYTHIA8	(N)NLO	[83, 170–172]
VH	WH	0.0445	PYTHIA8	NNLO	[83, 173]
VH	ZH	0.0262	PYTHIA8	NNLO	[83, 173]

Table 6.1: Monte Carlo generators used to model the signal at $\sqrt{s} = 8\,\text{TeV}$. The cross-sections times branching fractions ($\sigma\times$BR) used for the normalization of some processes are included in the last column together with the perturbative order of the QCD calculation. The $H \to \tau\tau$ SM branching ratio is included.

The VBF is an important production mode because its signature (two high energetic forward jets in addition to the Higgs boson's products) provides additional information to separate the signal from the background. The POWHEG VBF samples do not include the NLO electroweak corrections, that are known to be non-negligible, but a systematic is added to take into account this effect.

The ggH production mode is the dominant mode at LHC. The effect of the finite quark mass of the bottom and top-quark in the loops is considered in the 8 TeV samples. A reweight of the $p_{\text{T}}^{\tau\tau}$ variable was needed in order to match the behavior predicted by the HRes2.1 program [174, 175]. The reweighting is performed separately for events with no more than one jet at particle level and for events with two or more jets. In the latter case, the Higgs boson p_{T} spectrum is reweighted to match the MINLO HJJ predictions [176] so that the jet multiplicities are in agreement with (N)NLO calculations from JETVHETO [177–179].

Additional contribution of signal events generated by the VH process is included for both topologies, WH and ZH, corrected up to NNLO.

6.4.3 Background processes

This section describes the different SM processes which can be a source of background for the search of the $H \to \tau\tau$ decay. The samples used to model each of the contributions are detailed, as well as information regarding their estimation and validation. The information given here corresponds to the $\tau_{\text{lep}}\tau_{\text{lep}}$ channel. The backgrounds are controlled, when possible, using control regions (CR) or validation regions (VR), to prove the consistency of their estimation and the validity of the extrapolation to the signal region (SR). The selection criteria that define the CR and VR are described in Section 6.5.4. Table 6.2 summarizes the MC samples for the different backgrounds used in this analysis, as well as their respective cross-sections.

Background	**$\sigma\times$BR [pb]**	**MC generator**	**Order**	
$W(\to l\nu)$, $(l = e, \mu, \tau)$	36 800	ALPGEN [180]+PYTHIA8	NNLO	[181, 182]
$Z/\gamma^*(\to ll)$,				
$10\,\text{GeV} < m_{ll} < 60\,\text{GeV}$	13 000	ALPGEN+HERWIG [183]	NNLO	[181, 182]
$60\,\text{GeV} < m_{ll} < 2\,\text{TeV}$	3910	ALPGEN+PYTHIA8	NNLO	[181, 182]
VBF $Z/\gamma^*(\to ll)$	1.1	SHERPA [184]	LO	[184]
$t\bar{t}$	253 †	POWHEG + PYTHIA8	NNLO+NNLL	[185–190]
Single top : Wt	22 †	POWHEG + PYTHIA8	NNLO	[191]
Single top : s-channel	5.6†	POWHEG + PYTHIA8	NNLO	[192]
Single top : t-channel	87.8†	AcerMC [193]+PYTHIA 6 [194]	NNLO	[195]
$q\bar{q} \to WW$	54 †	ALPGEN+HERWIG	NLO	[196]
$gg \to WW$	1.4†	GG2WW [197]+HERWIG	NLO	[197]
WZ, ZZ	30 †	HERWIG	NLO	[196]
$H \to WW$	4.7†	same as for $H \to \tau\tau$ signal		

Table 6.2: Monte Carlo generators used to model the signal and the background processes at $\sqrt{s} = 8\,\text{TeV}$. The cross-sections times branching fractions ($\sigma\times$BR) used for the normalization of some processes are included in the last column together with the perturbative order of the QCD calculation. For the W and Z/γ^* background processes, the branching ratios for leptonic decays ($l = e, \mu, \tau$) of the bosons are included. For all other background processes, inclusive cross-sections are quoted (marked with a †).

6.4.3.1 The $Z \to \tau\tau$ process

The main background of this analysis is the Drell-Yan processes, where a Z boson decay into a pair of taus, the $Z/\gamma^* \to \tau^+\tau^-$ process[2]. This process is an *irreducible* background: in the scope of this analysis, the topology of this decay is very similar to the Higgs boson decay, as both particles are neutral bosons. The biggest difference is the invariant mass of the di-τ system: in the Z case it peaks around 91 GeV, while in the Higgs case the

[2]Usually abbreviated as $Z \to \tau\tau$

peak is expected to be around 125 GeV. The reconstructed mass distributions of the two decays overlap (as seen in Figure 6.3), which makes impossible to distinguish both process clearly. Reducing the amount of $Z \to \tau\tau$ background is a crucial step of this analysis, thus an accurate modeling of this background is critical.

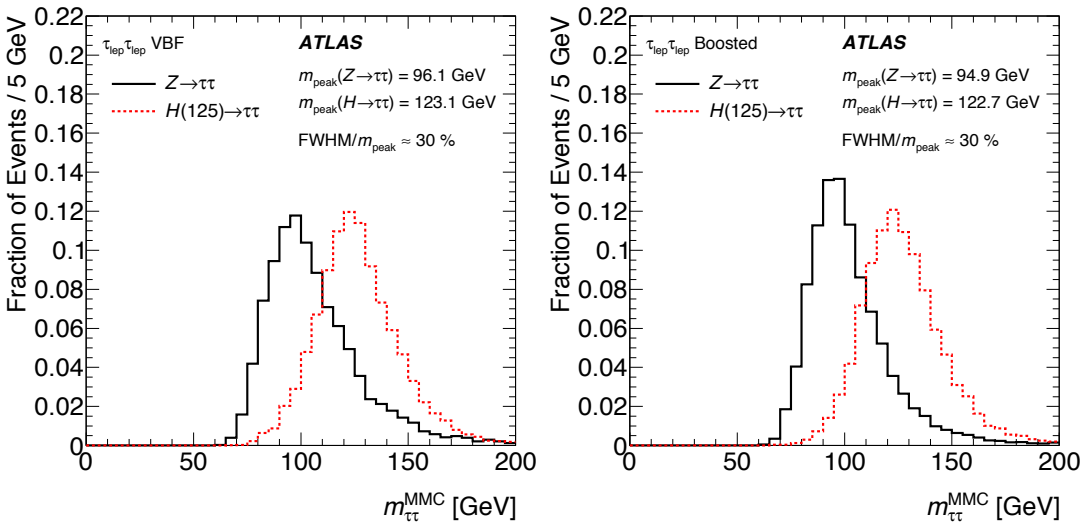

(a) VBF (b) Boosted

Figure 6.3: Reconstructed $m_{\tau\tau}^{\text{MMC}}$ for signal events $H \to \tau\tau$ with $m_H = 125\,\text{GeV}$ and $Z \to \tau\tau$ events in MC simulation and embedding respectively, for events in the (a) the VBF category and (b) the Boosted category of the $\tau_{\text{lep}}\tau_{\text{lep}}$ channel [155].

The ideal approach would be to estimate the $Z \to \tau\tau$ background directly from data in a dedicated region but this method is infeasible due to the difficulty of defining a suitable signal-free region. However, a largely data-driven estimate can be performed by using a sample of $Z \to \mu\mu$ events of data, which is a much more common process and easier to separate from signal and other processes. Except for effects related to the different muon and τ masses, both processes, including additional jets, are kinematically identical assuming lepton universality. In addition, due to the small Higgs coupling to muons, the $Z \to \mu\mu$ process provides a virtually signal-free signature of two isolated, high-energy muons with opposite charge and a di-μ invariant mass close to the Z resonance.

In order to model the $Z \to \tau\tau$ process, the $Z \to \mu\mu$ events are modified using the *embedding* technique [198], which replaces the detector response to the decaying muons with the corresponding information for τ leptons from simulated $Z \to \tau\tau$ decays. These decays are obtained using TAUOLA [199, 200], with the τ kinematics being derived from the kinematics of the original muons (taking into account both the τ-μ mass difference and the τ-τ spin correlation). This substitution results in a $Z \to \tau\tau$ event model where only the well-understood decays of the Z boson and τ leptons, and the detector response to the τ lepton decay products, are obtained from the simulation. All other aspects of the event —including the kinematics of the Z boson and additional jets, the underlying event,

as well as effects from multiple interactions — are directly taken from the data. This is a great advantage, since the $H \to \tau\tau$ analysis relies on an accurate modeling of the $E_{\text{T}}^{\text{miss}}$ and the jet topologies in the event, which are then estimated directly from data.

The embedding contribution is normalized to the MC expectation in an early stage of the selection criteria, requiring only two leptons with opposite charges. The systematic uncertainties arising from the difference between muons and τ leptons, and from the embedding procedure are greatly overcome by the much better modeling of the topology of the analysis. Scrupulous validation of the technique was done and can be found in Ref. [198]. A comparison of the invariant mass reconstruction of $Z \to \tau\tau$ events between $Z \to \tau\tau$ MC and an embedding sample is shown in Figure 6.4.

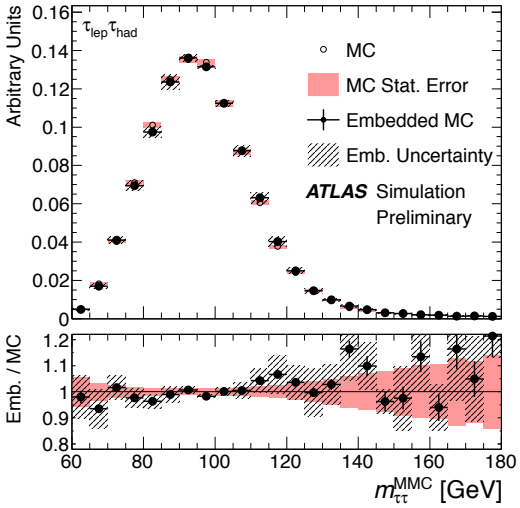

Figure 6.4: Reconstructed $m_{\tau\tau}^{\text{MMC}}$ in the $\tau_{\text{lep}}\tau_{\text{had}}$ channel for simulated $Z \to \tau\tau$ events, compared to the one obtained from simulated $Z \to \mu\mu$ events after the τ embedding. The errors on the ratios represent the statistical uncertainties (points), while the systematic uncertainties are indicated by the hatched bands. The shaded bands represent the statistical uncertainties from the $Z \to \tau\tau$ MC [155].

6.4.3.2 The $Z \to ll$ process

In addition to the $Z \to \tau\tau$ process, the contributions from the other possible leptonic decays of the Z, namely to electrons and muons, have to be taken into account. These decays will be jointly denoted as $Z \to ll$, where $l = e, \mu$. As the τ objects are reconstructed using their visible leptonic decays, $Z \to ll$ events could be identified as $\tau\tau$ events. Only the amount of $E_{\text{T}}^{\text{miss}}$ in the event and the invariant mass of the two leptons can discriminate between the processes, as the $Z \to ll$ decays do not involve neutrinos, contrary to the $Z \to \tau\tau$ or $H \to \tau\tau$ decays. The $Z \to ll$ process plays a relevant role in the same flavor channel, whilst their contribution is negligible in the different flavor channel.

In the $\tau_{\text{lep}}\tau_{\text{lep}}$ channel, with two visible leptons in the final state, the $Z \to ll$ process completely stands over the rest of processes (Figure 6.5). Due to this dominance, the

mass window around the Z peak can be used as a good CR selection for the $Z \to ll$ background. This CR serves to validate the modeling of the $Z \to ll$ background, as well as for deriving a normalization factor to be extrapolated to the SR. In addition, due to discrepancies in the modeling of the $E_{\mathrm{T}}^{\mathrm{miss}}$ distribution, a shape correction factor is derived for the $E_{\mathrm{T}}^{\mathrm{miss}}$ distribution in the Zll CR and applied to the $E_{\mathrm{T}}^{\mathrm{miss}}$ in the SR.

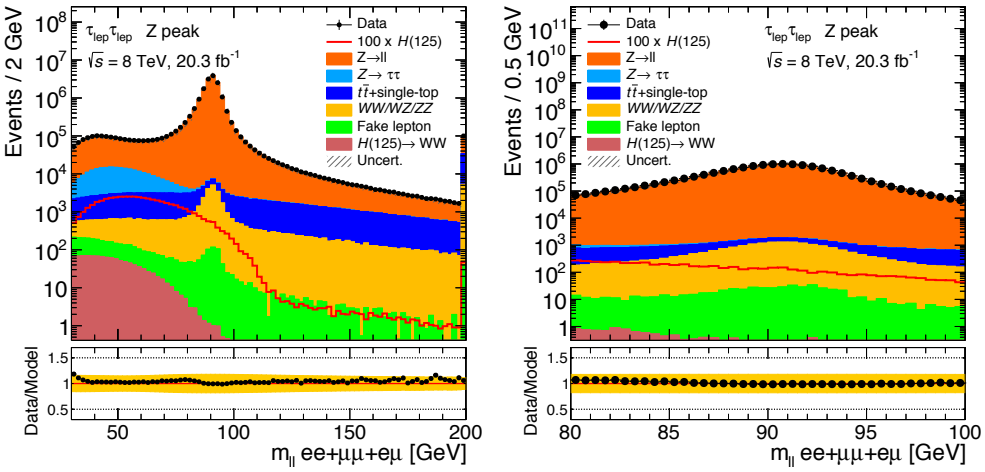

(a) Full range (b) Z peak

Figure 6.5: Distribution of the invariant mass of opposite-sign di-τ events showing the dominance of the $Z \to ll$ background for (a) the extended mass range and (b) the Z peak window.

6.4.3.3 The top quark processes

In addition to the Drell-Yan processes, the top quarks created in the collisions can be a source of background if two leptons are produced via the decay of $W^{\pm}$ bosons, which mediate the decay of the top quark. The contributions of the top backgrounds ($t\bar{t}$ and single-top) are estimated from simulation and are characterized by the presence of high $E_{\mathrm{T}}^{\mathrm{miss}}$ and multiple high-p_{T} jets, as can be seen in Figure 6.6. In the $\tau_{\mathrm{lep}}\tau_{\mathrm{lep}}$ channel, the $t\bar{t}$ background contribution is relevant, while the single-top background (which includes the s-channel, the t-channel and the Wt associated production mode) has a secondary role.

The top quark usually decays to a b-quark, in addition to a $W^{\pm}$ boson. The b-quark hadronizes, forming a jet which can be identified as a b-jet. Hence, this background can be greatly reduced by vetoing the events containing b-tagged jets. Conversely, the requirement of a b-jet defines a CR dominated by $t\bar{t}$ events, which serves to validate the modeling of this background and for deriving a normalization factor for the SR.

6.4.3.4 The di-boson processes

Other processes which can lead to the appearance of two leptons in the event are decay of two weak bosons produced in the pp collisions, such as WW, ZZ and WZ. As these

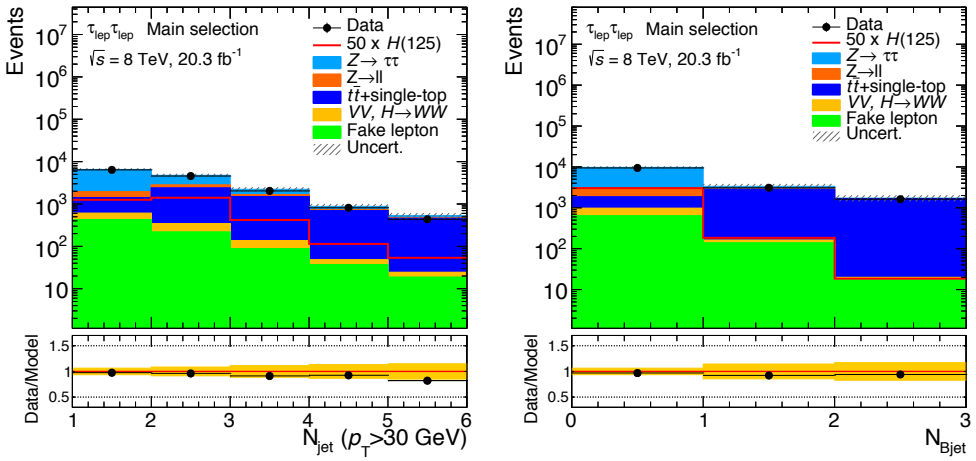

(a) # jets (b) # b-jets

Figure 6.6: Number of (a) jets and (b) b-jets, before categorization, showing the dominance of $t\bar{t}$ background in events with a high number of (b-)jets.

bosons can decay into τ or high energetic leptons, they are a source of di-τ background. However, the cross-section of these events is small and their contribution can be easily estimated with suitable selection criteria. These processes were cross-checked using a VR enriched with WW events.

6.4.3.5 The $H \rightarrow WW$ process

A special case of the di-boson background processes is through the decay of a Higgs boson ($H \rightarrow WW$), where both W decay to leptons. The $H \rightarrow WW$ process was, in fact, one of the final states in which the Higgs boson was first discovered [40] and so, it is considered as a background process in the $H \rightarrow \tau\tau$ analysis (with the SM cross-section), although its relevance is limited. The production modes of the $H \rightarrow WW$ processes are estimated using the same MC generators used for the $H \rightarrow \tau\tau$ signal.

Moreover, since the ATLAS Experiment aims to combine the results of all the Higgs decay modes, their respective analyses have to be orthogonal, for the combination to be done without suffering from event correlations. In order to do that, the $H \rightarrow \tau\tau$ analysis implemented a specific cut to reject the signal and control regions used by the $H \rightarrow WW$ analysis (which implemented the converse requirement). This is done by removing the events with a collinear mass smaller than the Z boson minus 25 GeV, i.e. requiring that the events satisfy $m_{\tau\tau} > m_Z - 25\,\text{GeV} = 66.1876\,\text{GeV}$, as is described in the event selection of Section 6.5.2. As Figure 6.7 shows, this cut was optimized to remove the highest possible amount of events used by the $H \rightarrow WW$ analysis without loss of $H \rightarrow \tau\tau$ signal events.

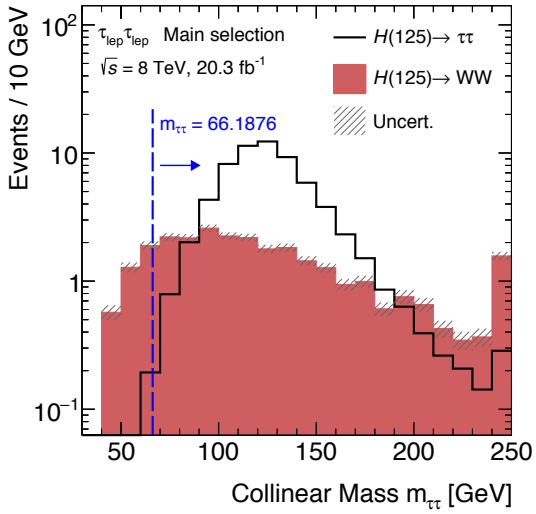

Figure 6.7: Invariant collinear mass of the di-τ system showing the distributions of the $H \to \tau\tau$ and $H \to WW$ processes at the end of the event selection. Both distributions include the three productions modes (VBF, ggH and VH). A cut in $m_{\tau\tau} > 66.1876\,\text{GeV}$ (shown in a vertical blue bar) is implemented to orthogonalize against the $H \to WW$ analysis without affecting the $H \to \tau\tau$ signal.

6.4.3.6 The *Fake* background

The backgrounds described so far were all a source of two *true* taus or light leptons, reconstructed from their decay products by the detector. However, some non-lepton objects can be misidentified, and consequently misreconstructed as leptons, which will be referred to as *fake leptons*. These processes are jointly denoted as *Fakes*, or Fake background, and are of large importance for the analysis. A good understanding and estimation of the fake leptons is critical for the analysis. Their relevance and the extreme difficulty of their modeling via MC techniques led to the development of data-driven methods for their estimation.

Two different types of Fakes can be distinguished: events with one fake lepton whereas the other one is a true lepton, and events where both reconstructed leptons are fake. In the $\tau_{\text{lep}}\tau_{\text{lep}}$ channel, the main type of Fake background is the former, which includes events from W+jets and semi-leptonically decaying $t\bar{t}$ events. In these events a jet is misreconstructed as a lepton (fake lepton) but still contain one true lepton. In this channel, multi-jet and other processes faking both leptons are less relevant. For the estimation, however, all these sources are treated together.

The technique used to estimate the contribution of the Fake background consists of a fit of a template obtained in a dedicated enriched CR, which is defined by inverting the isolation requirements of the lepton of lower p_{T} (sub-leading lepton, labelled p_{T}^{l2}) while keeping all other requirements. The region has a small contribution of true-lepton background processes, which is estimated with MC and subtracted. In addition, the CR

is defined at early stages of the event selection, to neglect the presence of signal. The selection criteria that define the CR are fully described in Section 6.5.4
In order to determine the normalization of the Fakes background in the SR, the p_{T}^{l2} template in the CR is fitted to the distribution in data at the same stage of the event selection. The normalization is determined by minimizing a χ^2 between the total background (including the fake) and the data, based on the binned p_{T}^{l2} distribution.

The same template fit is performed for a validation region, made of events with same-sign charge leptons events (SS) (as opposed to the events with opposite-sign charge events (OS) of the SR), assuming that the isolation is not correlated to the lepton charge. However, the SS region suffers from poor statistics, so in order to increase the number of events, a few selection criteria have to be relaxed. The criteria of the VR are described in Section 6.5.4. By comparing the shapes of SS and OS event distributions, a systematic uncertainty of the shape of the fake background is also derived. The diagram of the Template Fit is shown in Figure 6.8

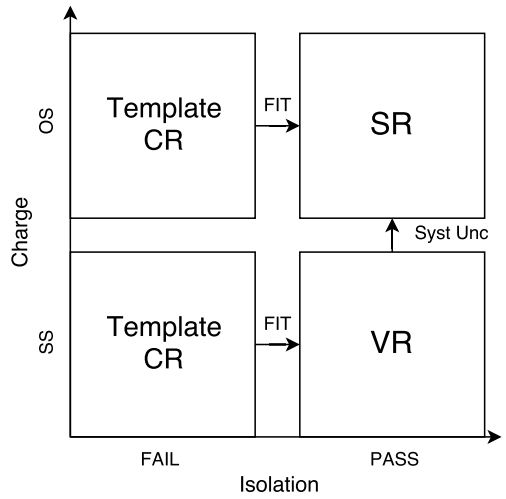

Figure 6.8: Diagram of the phase-spaces of the template fit for the estimation of the Fake background in the $\tau_{\text{lep}}\tau_{\text{lep}}$ channel. Two template fits are performed in the CR (defined by reversing the sub-leading lepton isolation condition): in the region with two OS leptons and in the region with two SS leptons. The fit then is applied to the "pass-isolation" regions, which are the SR (OS) and a VR (SS) which is used to check the validity of the fit to derive the systematic uncertainty related to this method.

However, the distribution of the p_{T} of the leading lepton, p_{T}^{l1}, showed bigger discrepancies between SS and OS in both categories and thus, a reweight is applied to the OS fake control sample. The remaining differences were treated as systematic uncertainties on both normalization and shape. In addition, an extra 50% of the difference between the distributions before and after the reweighting is accounted for as additional systematics.

6.5 Event selection and categorization

In order to enhance the signal over background ratio, a set of selection criteria is defined, whose main purpose is to reject the background events while minimizing the loss in signal events. The cuts are defined and optimized paying attention to the kinematics and the topology of the production and decay of the Higgs boson, according to the Standard Model predictions. The dataset is further divided in two orthogonal categories, VBF and Boosted, focusing in events of two specific topologies. This categorization is harmonized among the three $H \to \tau\tau$ channels: although their exact definition varies slightly, the main aim and cuts are analogous, which helps the combination of the three channels for the final result of the analysis.

The cutflow is divided in a common preselection, the main selection criteria, the categorization, and the final cuts. The preselection, labelled as **event cleaning**, is composed of quality cuts, related to detector performance and aimed to prepare the dataset for the analysis. The **main selection** aims to reduce drastically the number of background event and to enhance the relative fraction of the signal, in order to achieve a good signal over background ratio. The **categorization** is applied next, dividing the data in two categories, VBF and Boosted. Finally, in both categories, a further optimized event selection is performed, to define the signal region (referred to as **full selection**).

The events passing the full selection are used as input to the BDT algorithm (explained in detail in Section 6.7) which returns the final discriminant of the analysis. As mentioned before, a cut-based approach is also studied, which is used as a cross-check to the BDT. Therefore, the cut-based analysis implements a very similar event selection to the BDT analysis, with some particularities, which are described in Section 6.9.4.

6.5.1 Event cleaning

The aim of the initial selection is to increase the purity of the dataset by removing events which are not suitable for physics analysis. The optimized recommendations for the thresholds and conditions come from the ATLAS performance groups, as well as the Data Preparation group for the assessment of the quality of the data events taken by ATLAS.

Other selection criteria aim to reduce the amount of non collision events in the sample, like beam halo events or cosmic rays, which is done by applying compatibility checks with respect to the interaction point (IP). To ensure that the event is a hard scattering pp collision, at least one primary vertex (PV) with at least four associated tracks is required. A set of jet cleaning cuts are applied, to remove events where the reconstruction of jets has been affected by detector issues, such as faulty cells. The impact of all these effects was studied and corrections were applied where necessary. Since these selection criteria can remove a small fraction of true pp collisions or clean events, they have to be applied also on the simulated events.

6.5.2 The $\tau_{\text{lep}}\tau_{\text{lep}}$ selection criteria

The main selection criteria of the analysis aim, first, at selecting di-τ events which are possible candidates of a Higgs boson decay, and second, at reducing the background while enhancing the signal significance. In the $\tau_{\text{lep}}\tau_{\text{lep}}$ channel, the former condition means the selection of events with two leptons, which can be the decay products of two τ.

The selection of di-lepton events is done by requiring that the events have fired a selection of lepton triggers. This requirement is crucial for the analysis as the acceptance of the signal depends greatly on the trigger selection and thus, a complex trigger strategy (single-lepton and di-lepton) was developed to maximize the coverage of the phase-space of the signal. Since the prescale[3] of the triggers changes with the instantaneous luminosity, this strategy had to be optimized for 7 TeV and 8 TeV separately. The trigger selection is sensitive to the p_{T} and the flavor of the leptons involved.

A summary of the triggers used in the $\tau_{\text{lep}}\tau_{\text{lep}}$ channel is reported in Table 6.3. Due to the increasing instantaneous luminosity and the different pile-up conditions, the online p_{T} thresholds had to be raised during data-taking in 2012, compared to the ones in 2011, in addition to more stringent identification requirements. The p_{T} thresholds for the objects in the analysis are usually 2 GeV higher than the trigger requirements, to ensure that the trigger is fully efficient.

$\sqrt{s}$	**Trigger**	**Trigger p_{T}** [GeV]	**Channel**	**Analysis p_{T}** [GeV]	
7 TeV	Single electron	20−22	$e\mu$	$e > 22 - 24$	$\mu > 10$
	Single muon	18	$\mu\mu$	$\mu 1 > 20$	$\mu 2 > 10$
			$e\mu$	$\mu > 20$	$e > 15$
	Di-electron	12/12	ee	$e1 > 15$	$e2 > 15$
8 TeV	Single electron	24	$e\mu$	$e > 26$	$\mu > 10$
			ee	$e1 > 26$	$e2 > 15$
	Di-electron	12/12	ee	$e1 > 15$	$e2 > 15$
	Di-muon	18/8	$\mu\mu$	$\mu 1 > 20$	$\mu 2 > 10$
	$e + \mu$	12/8	$e\mu$	$e > 15$	$\mu > 10$

Table 6.3: Summary of the triggers used to select events in the $\tau_{\text{lep}}\tau_{\text{lep}}$ channel at the two center-of-mass energies, 7 TeV and 8 TeV. The transverse momentum thresholds applied at trigger level and analysis level are listed. When more than one trigger is used, a logical OR is taken and the trigger efficiencies are calculated accordingly.

[3]The trigger prescale is the reduction of the trigger acceptance rate by an established factor. This is done when the acceptance rate of a given trigger surpasses the capacity of the computing power to process the output. To increase the acceptance while keeping an unbiased analysis, it is needed to select events using the lowest unprescaled trigger, which can change with the increase of instantaneous luminosity.

In addition, a tighter selection criteria (with respect to the standard object definition described in Chapter 5) is applied to the leptons objects in the leptonic channels, $\tau_{\text{lep}}\tau_{\text{lep}}$ and $\tau_{\text{lep}}\tau_{\text{had}}$, to require for isolated leptons. Namely, two additional isolation-related variables are defined, the E_{T}-cone ratio and the p_{T}-cone ratio. The E_{T}-cone ratio is a calorimeter-based isolation, defined as the sum of the total transverse energy in the calorimeter in a cone of size $\Delta R = 0.2$ around the electron cluster or the muon track, divided by the E_{T} of the electron cluster or the p_{T} of the muon, respectively. The p_{T}-cone ratio is a track-based isolation, defined as the sum of the p_{T} of tracks within a cone of $\Delta R = 0.4$ around the electron or muon track, divided by the E_{T} of the electron cluster or the muon p_{T} respectively. The definition criteria applied to these variables in the $\tau_{\text{lep}}\tau_{\text{lep}}$ channel, used for the 7 and 8 TeV datasets, are in Table 6.4.

		Electrons		**Muons**	
Variable		7 TeV	8 TeV	7 TeV	8 TeV
p_{T}-cone ratio	$<$	0.08	0.17	0.06	0.18
E_{T}-cone ratio	$<$	0.08	0.09	0.04	0.09

Table 6.4: Summary of isolation requirements applied for the selection of electrons and muons in the $\tau_{\text{lep}}\tau_{\text{lep}}$ channel at 7 TeV and 8 TeV.

The selection criteria were chosen to enhance the signal to background ratio, without having a significant impact on the signal. This was done considering the topologies and kinematics of the decays of the different background processes, compared to the signal topologies. Many different cuts and variables were studied during the optimization processes, trying to maximize the efficiency of the selection. The main selection criteria in the $\tau_{\text{lep}}\tau_{\text{lep}}$ channel are:

1. exactly two isolated light leptons (e or μ) with opposite charge (OS). Events which have a hadronic tau (τ_{had}) with a medium τ-ID are vetoed.
2. the di-lepton invariant mass (m_{ll}) to be within the range $30 - 75$ GeV for the same flavor channel and within the range $30 - 100$ GeV for the different flavor channel. The requirement is tighter in the SF channel to reject the $Z \to ll$ background.
3. high energetic leptons, with $p_{\text{T}}^{l1} + p_{\text{T}}^{l2} > 35$ GeV, to suppress the Fakes background.
4. the event to have at least one jet with $p_{\text{T}} > 40$ GeV to enhance the boosted topology.
5. the event to have for SF events $E_{\text{T}}^{\text{miss}} > 40$ GeV and $E_{\text{T}}^{\text{miss,HPTO}} > 40$ GeV, and for DF events, $E_{\text{T}}^{\text{miss}} > 20$ GeV. Asking for the presence of high energetic neutrinos suppresses the $Z \to ll$ (thus the tighter cut in SF) and multi-jet backgrounds.
6. the collinear approximation: the x_1 and x_2 variables (defined in Section 6.3) are required to be within the range $[0.1, 1.0]$.

7. $\Delta\phi_{ll} < 2.5$, where ϕ refers to the azimuthal angle in the transverse plane. This requirement allows the suppression of $Z \to ll$ and $t\bar{t}$ events.
8. categorization criteria: the dataset is divided in two categories, described in the next section.
9. a veto on events with an identified b-jet, to remove the top background.
10. $m_{\tau\tau} > m_Z - 25\,\text{GeV} = 66.1876\,\text{GeV}$, for orthogonality against the $H \to WW$ search.
11. a physical solution for the MMC mass: $m_{\tau\tau}^{\text{MMC}} > 0$.

6.5.3 Categorization

After the main selection, the dataset is divided in two orthogonal categories. The aim of this division is the optimization of the analysis for two phenomenological scenarios, where a clear signature of the Higgs events could enhance the signal significance. The categories are:

VBF category Optimized for events produced via VBF mode, which are usually accompanied by two energetic jets with a large pseudorapidity separation. Thus, the definition of the category requires events that satisfy the following criteria:

- The event includes at least two jets
- Their transverse momenta satisfies $p_{\text{T}}^{j1} > 40\,\text{GeV}$ and $p_{\text{T}}^{j2} > 30\,\text{GeV}$
- Their angular separation satisfies $\left|\Delta\eta_{jj}\right| > 2.2$

Boosted category Optimized for events produced with a boosted topology. This category aims at collecting events produced via ggH, which is the most abundant source of Higgs bosons. The category will also include a small contribution of events produced via VH mode. The events are required to have a boosted Higgs boson, and thus the selection is:

- Fail the VBF selection
- The transverse momentum of the di-τ system satisfies $p_{\text{T}}^{\tau\tau} > 100\,\text{GeV}$

Events which fail both selections are discarded and not used in the analysis. The preliminary versions of the analysis tried to recover these events by adding two extra categories: with 1-jet and 0-jet, respectively. However, the backgrounds in these categories proved to be difficult to control and the gain in sensitivity was small (less than 10%). The current categories, VBF and Boosted, demonstrated to be sensitive enough for the $H \to \tau\tau$ search.

6.5.4 Control and validation regions

To claim a good understanding of the different backgrounds in the signal region, a good agreement between the model and the data must be achieved in regions where no Higgs signal is expected: control regions (CR) and validation regions (VR).

Control regions

The control regions are used to check the behavior of a particular background and to extract information to be used during the analysis. In particular the CRs are used to derive a normalization factor that is extrapolated to the SR in the fit, as described in Section 6.10.4. A second normalization factor, different from the one used in the statistical framework and that plays no role in the statistical fit, is applied to the distributions for illustration purposes. These pre-fit normalization values are summarized in Table 6.5.

The control regions are defined with the aim to satisfy, when possible, three conditions: a negligible amount of signal events, a dedicated phase-space with clear domination of the particular background to be tested, being orthogonal to the SR, and a selection criteria as similar as possible to the SR. The CRs defined for the analysis are:

Zll CR The $Z \to ll$ background (where $l = e, \mu$) is controlled in a dedicated CR defined for SF events applying the SR selection criteria except that the events must satisfy the following condition: 80 GeV $< m_{ll} <$ 100 GeV, where the $Z \to ll$ background dominates (shown in Figure 6.5).

Top CR The $t\bar{t}$ and single-top backgrounds are controlled in a dedicated CR defined by reversing the b-veto requirement. The CR distribution is dominated by top events with a small contribution of $Z \to \tau\tau$ and Fake events (as shown in Figure 6.6).

Fake-template CR This CR is used to extract the template for the estimation of the Fake background in the SR and thus, it is enriched with multi-jet events with an small contribution from the rest of backgrounds. To define this CR, the isolation requirements of the sub-leading lepton are modified, namely, the E_{T}-cone ratio requirement is dropped and the p_{T}-cone ratio condition is reversed. To neglect the presence of signal, the CR is defined at an early stage of the event selection, by applying the following criteria for each of the two categories:

- Two isolated leptons with opposite charge and veto of hadronic taus
- Di-lepton invariant mass within the range $30 - 75$ GeV for the SF channel and within the range $30 - 100$ GeV for the DF channel
- At least one jet with $p_{\mathrm{T}} > 40$ GeV.
- b-jet veto

- Categorization conditions:
  - VBF: At least two jets and $|\Delta\eta_{jj}| > 2.2$
  - Boosted: No VBF-event and $p_{\text{T}}^{\tau\tau} > 100\,\text{GeV}$

			Dataset	
Control Region	**Category**	**Channel**	7 TeV	8 TeV
Zll CR	VBF	ee	1.12 ± 0.09	0.91 ± 0.16
		$\mu\mu$	1.08 ± 0.07	0.97 ± 0.13
	Boosted	ee	1.09 ± 0.07	0.98 ± 0.10
		$\mu\mu$	1.05 ± 0.05	0.96 ± 0.08
Top CR	VBF	Combined	0.98 ± 0.03	0.99 ± 0.07
	Boosted	Combined	1.08 ± 0.03	1.01 ± 0.05

Table 6.5: Normalization factors for the $Z \to ll$ and $t\bar{t}$ events, derived from their respective CR. Errors are of statistical nature.

Validation regions

Apart from the CR, three validation regions are defined, whose purpose is to check the behavior of one particular background, but they play no role in the statistical analysis. The requirements on the VR are looser than in the CRs and the purity of the background to test is not as strong as in the CRs. However, a good agreement in these regions is also proof of the general consistency of the combined background model. The VRs defined for the analysis are:

Ztt VR Since the main difference between the $H \to \tau\tau$ and the $Z \to \tau\tau$ events is the mass of the resonance, no orthogonal CR close to the SR can be easily defined without a significant contamination from the Higgs signal. However, a VR with a reasonable low contribution from signal can be achieved for the $Z \to \tau\tau$ background. The Ztt VR is defined by looking at low mass events, using the $m_{\tau\tau}^{\text{HPTO}}$ and $E_{\text{T}}^{\text{miss,HPTO}}$ variables, which were shown to correlate inversely with signal. Thus, the Ztt VR is defined by requiring events with $m_{\tau\tau}^{\text{HPTO}} < 100\,\text{GeV}$. The VR is shown in Figure 6.9 (a).

The di-boson VR As described in Section 6.4.3, the modeling of the di-boson background is controlled in a WW enriched region, defined by the following criteria and shown in Figure 6.9 (b):

- OS $e\mu$ events with $m_{ll} > 100\,\text{GeV}$ and $p_{\text{T}}^{l2} > 30\,\text{GeV}$

- veto any jet with $p_{\mathrm{T}} > 30\,\mathrm{GeV}$
- $\cos\left(\Delta\phi(E_{\mathrm{T}}^{\mathrm{miss}}, l_2)\right) < -0.2$

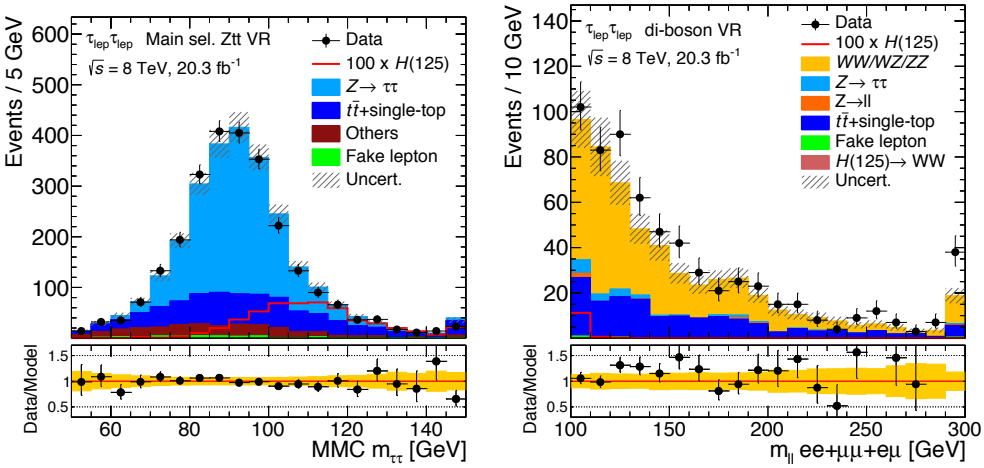

(a) (b)

Figure 6.9: Distribution of (a) $m_{\tau\tau}^{\mathrm{MMC}}$ in the Ztt VR before categorization and (b) m_{ll} in the di-boson VR, as defined in Section 6.5.4. Normalization factors have been applied to top quark and $Z \rightarrow ll$ processes, computed from the respective CRs.

The Fake SS VR As described in Section 6.4.3.6, the Fake background is controlled in a validation region which is defined using the SR criteria but inverting the charge requirement of the leptons, i.e. requiring for same-sign charge leptons, assuming there is no correlation effects between the charge and the isolation of the leptons. However, this definition reduces the statistics of the sample and so, some of the criteria have to be relaxed:

- The E_{T}-cone isolation condition is not applied
- The x_1 and x_2 requirements are dropped
- For the Boosted category, the $p_{\mathrm{T}}^{\tau\tau}$ selection is relaxed to $p_{\mathrm{T}}^{\tau\tau} > 80\,\mathrm{GeV}$

6.6 Control plots of the background modeling

In order to prove the understanding and modeling of the processes involved in the analysis, different variables which describe the kinematics of the events are shown below. The distributions show the p_{T} of both leptons (p_{T}^{l1} and p_{T}^{l2}), the number of jets of the event (# jets), the p_{T} of the most energetic jet (p_{T}^{j1}), the di-lepton mass (m_{ll}), the missing transverse energy ($E_{\mathrm{T}}^{\mathrm{miss}}$) and the sum of the transverse energy (ΣE_{T}).

The distributions are shown at the stage of the main selection and the "first stage" selection. The first stage selection is defined by the selection criteria 1–6, defined in Section 6.5.2. In addition, the distributions of the SRs and CRs are also shown.

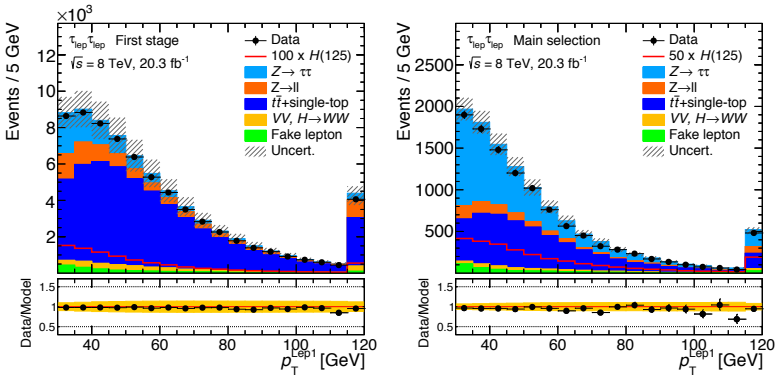

(a) p_{T}^{l1} First stage

(b) p_{T}^{l1} Main selection

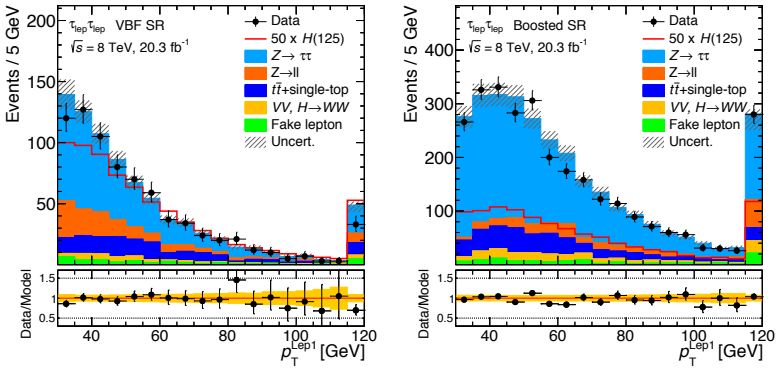

(c) p_{T}^{l1} VBF SR

(d) p_{T}^{l1} Boosted SR

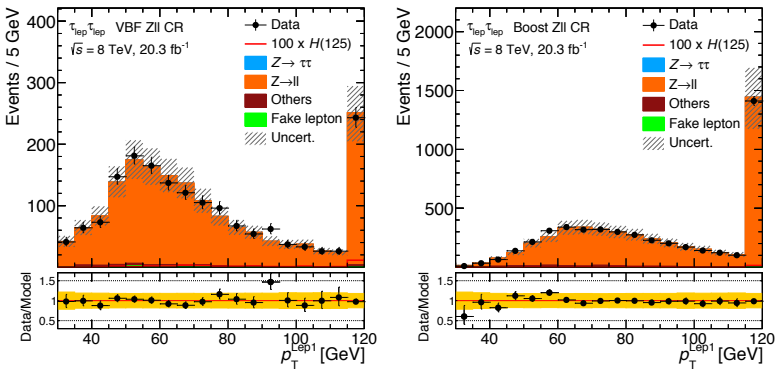

(e) p_{T}^{l1} VBF Zll CR

(f) p_{T}^{l1} Boosted Zll CR

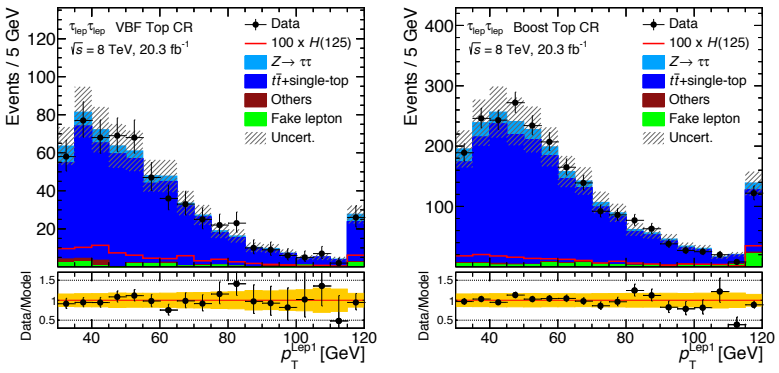

(g) p_{T}^{l1} VBF Top CR

(h) p_{T}^{l1} Boosted Top CR

Figure 6.10: Control plots of the background modeling for the $\tau_{\text{lep}}\tau_{\text{lep}}$ channel. The distributions are shown in two early stages of the event selection and in the SR, the Zll CR and Top CR for the VBF and Boosted categories. The overflow is added, normalization factors are applied and the error band includes the statistic and normalization systematic errors.

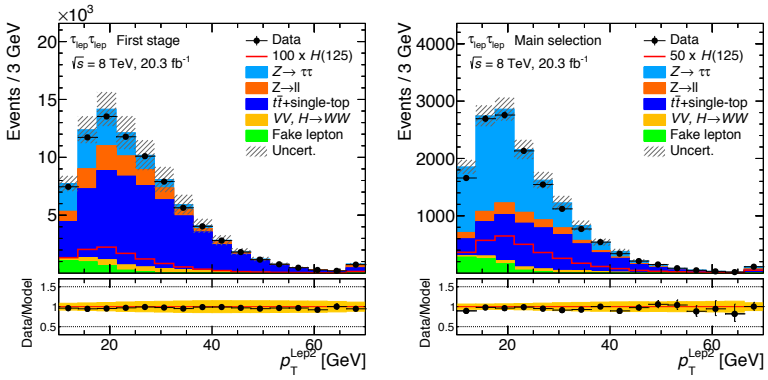

(i) p_{T}^{l2} First stage (j) p_{T}^{l2} Main selection

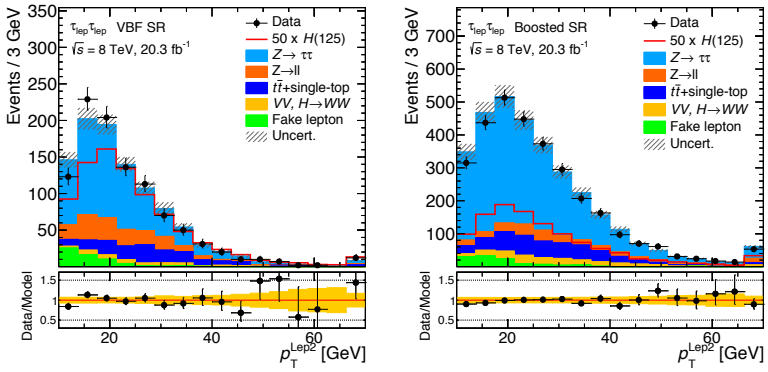

(k) p_{T}^{l2} VBF SR (l) p_{T}^{l2} Boosted SR

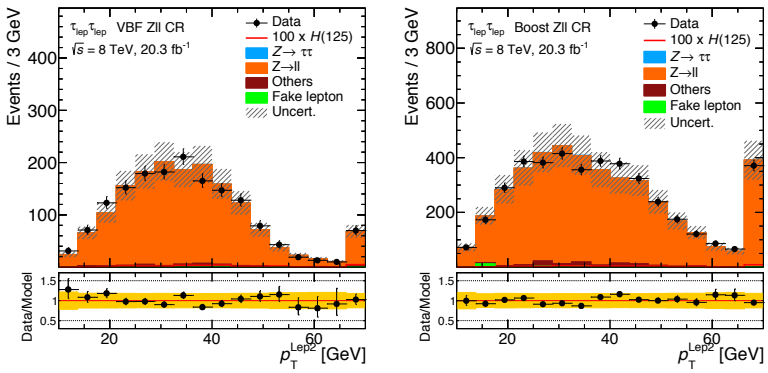

(m) p_{T}^{l2} VBF Zll CR (n) p_{T}^{l2} Boosted Zll CR

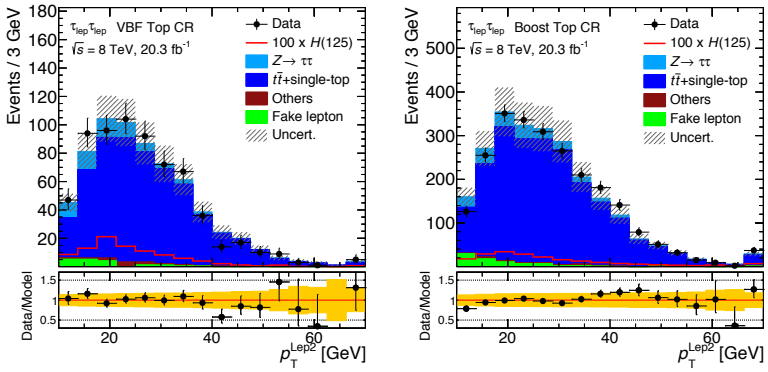

(o) p_{T}^{l2} VBF Top CR (p) p_{T}^{l2} Boosted Top CR

Figure 6.10: Control plots of the background modeling for the $\tau_{\mathrm{lep}}\tau_{\mathrm{lep}}$ channel. The distributions are shown in two early stages of the event selection and in the SR, the Zll CR and Top CR for the VBF and Boosted categories. The overflow is added, normalization factors are applied and the error band includes the statistic and normalization systematic errors.

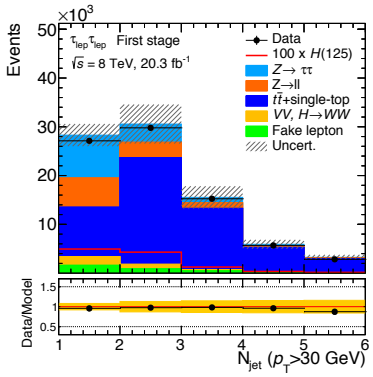

(q) # jets First stage

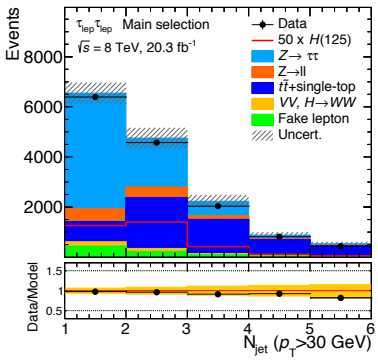

(r) # jets Main selection

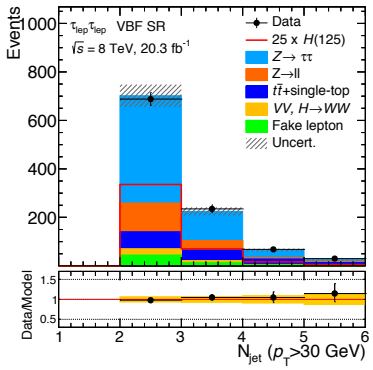

(s) # jets VBF SR

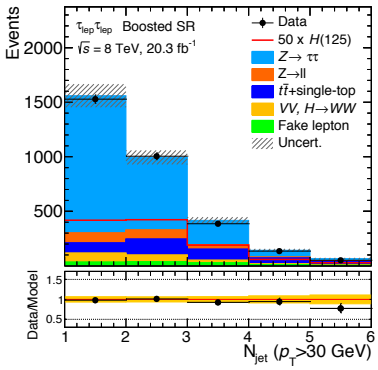

(t) # jets Boosted SR

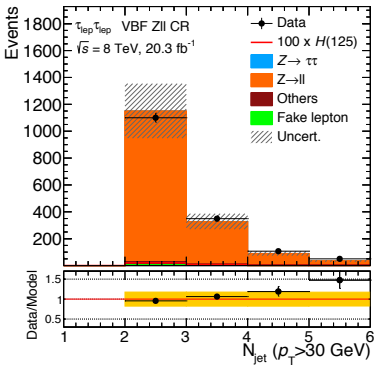

(u) # jets VBF Zll CR

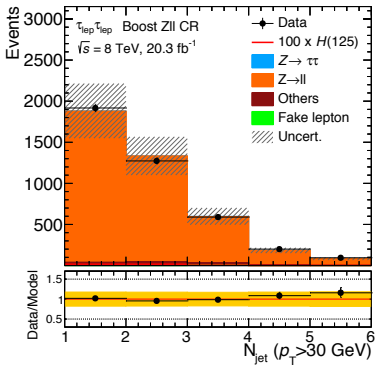

(v) # jets Boosted Zll CR

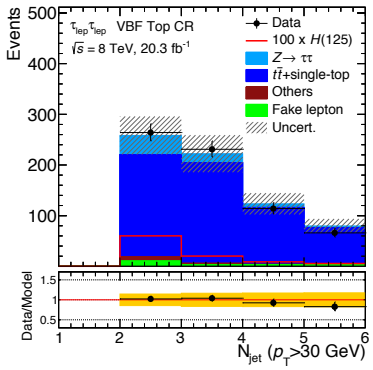

(w) # jets VBF Top CR

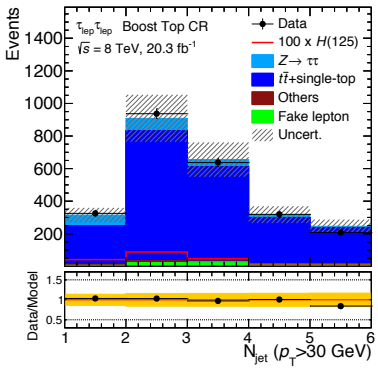

(x) # jets Boosted Top CR

Figure 6.10: Control plots of the background modeling for the $\tau_{\text{lep}}\tau_{\text{lep}}$ channel. The distributions are shown in two early stages of the event selection and in the SR, the Zll CR and Top CR for the VBF and Boosted categories. The overflow is added, normalization factors are applied and the error band includes the statistic and normalization systematic errors.

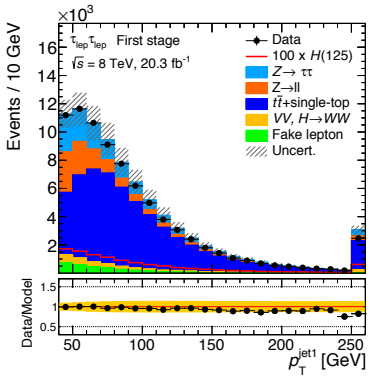

(y) p_{T}^{j1} First stage

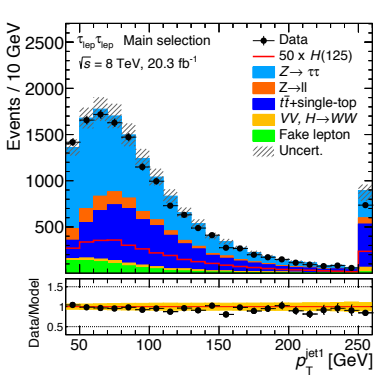

(z) p_{T}^{j1} Main selection

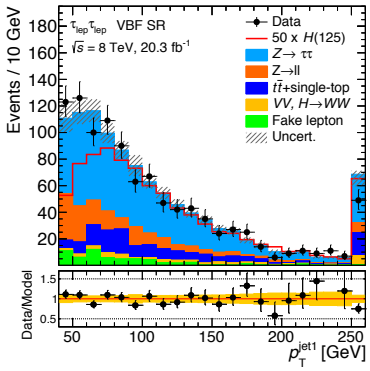

(aa) p_{T}^{j1} VBF SR

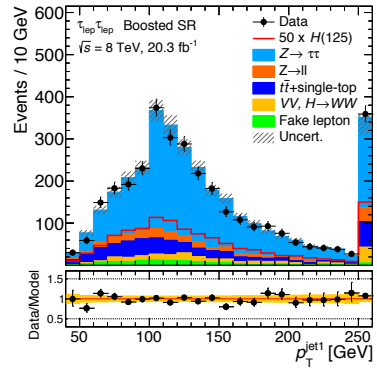

(ab) p_{T}^{j1} Boosted SR

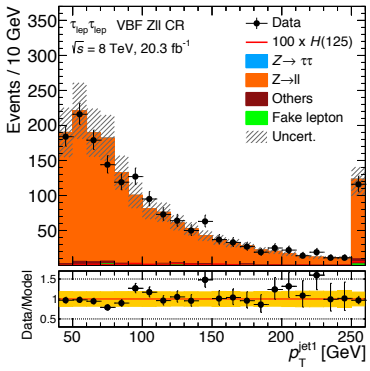

(ac) p_{T}^{j1} VBF Zll CR

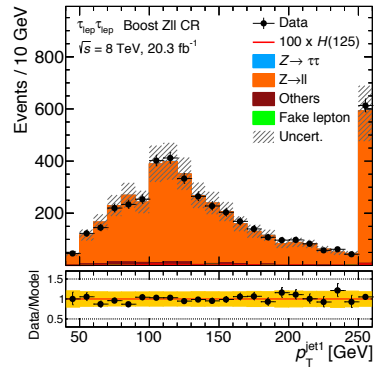

(ad) p_{T}^{j1} Boosted Zll CR

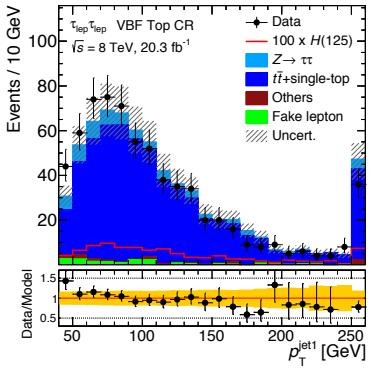

(ae) p_{T}^{j1} VBF Top CR

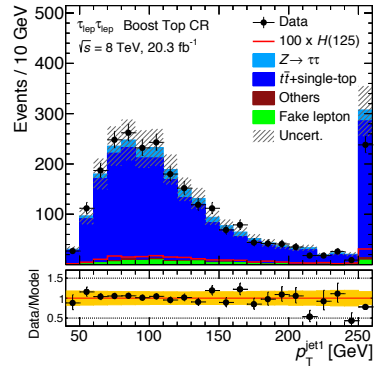

(af) p_{T}^{j1} Boosted Top CR

Figure 6.10: Control plots of the background modeling for the $\tau_{\mathrm{lep}}\tau_{\mathrm{lep}}$ channel. The distributions are shown in two early stages of the event selection and in the SR, the Zll CR and Top CR for the VBF and Boosted categories. The overflow is added, normalization factors are applied and the error band includes the statistic and normalization systematic errors.

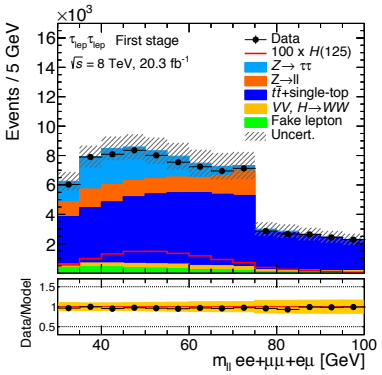

(ag) m_{ll} First stage

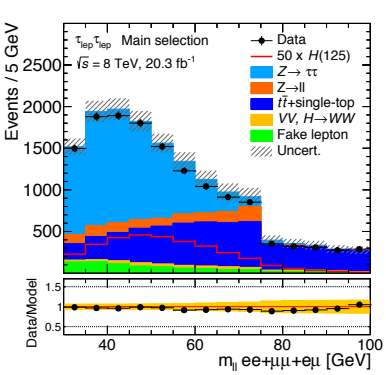

(ah) m_{ll} Main selection

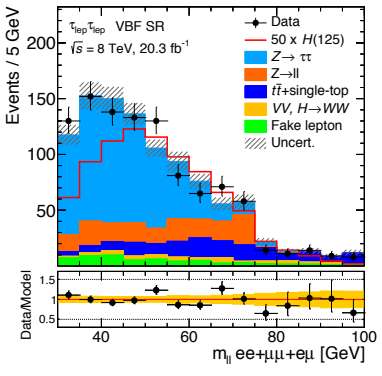

(ai) m_{ll} VBF SR

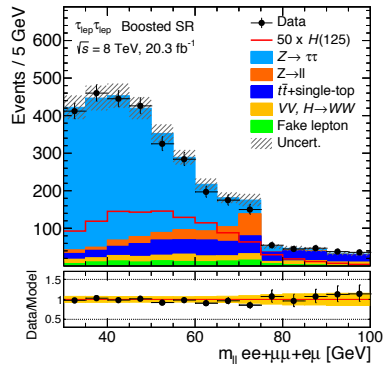

(aj) m_{ll} Boosted SR

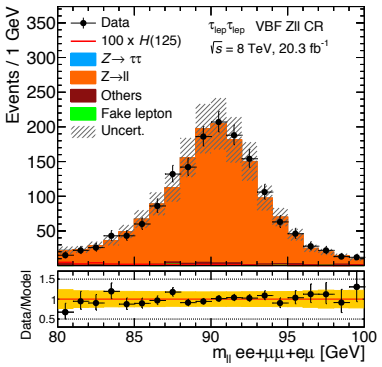

(ak) m_{ll} VBF Zll CR

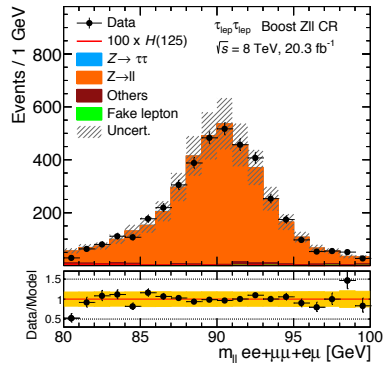

(al) m_{ll} Boosted Zll CR

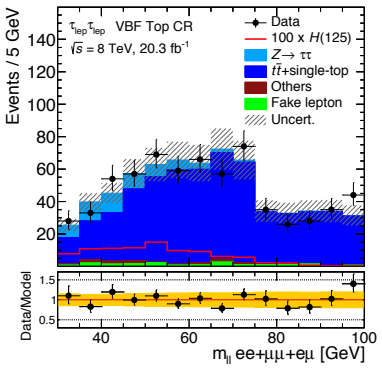

(am) m_{ll} VBF Top CR

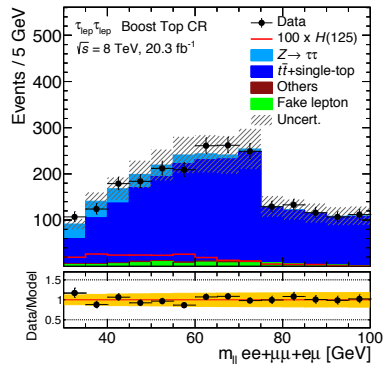

(an) m_{ll} Boosted Top CR

Figure 6.10: Control plots of the background modeling for the $\tau_{\text{lep}}\tau_{\text{lep}}$ channel. The distributions are shown in two early stages of the event selection and in the SR, the Zll CR and Top CR for the VBF and Boosted categories. The overflow is added, normalization factors are applied and the error band includes the statistic and normalization systematic errors.

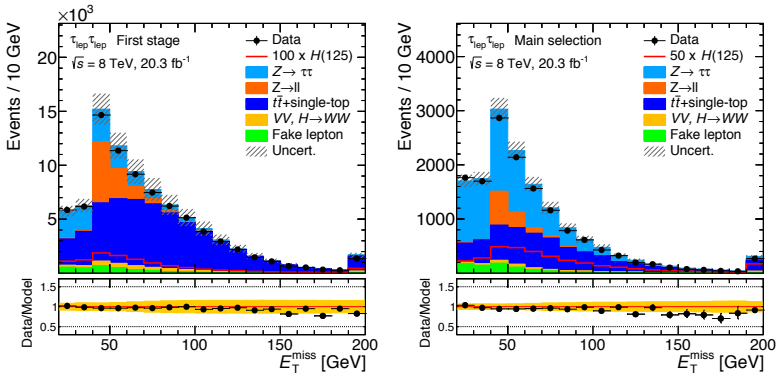

(ao) $E_{\mathrm{T}}^{\mathrm{miss}}$ First stage (ap) $E_{\mathrm{T}}^{\mathrm{miss}}$ Main selection

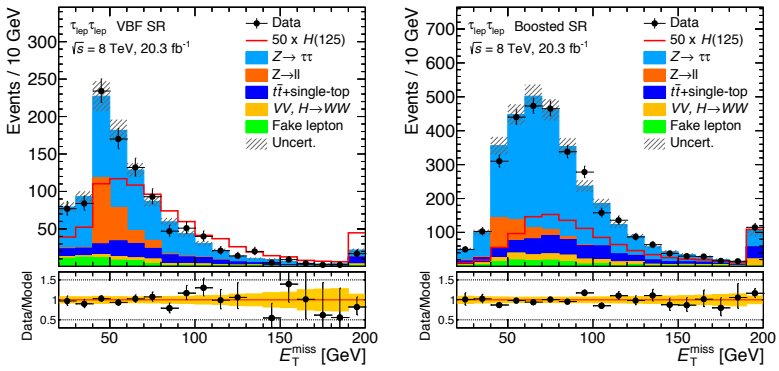

(aq) $E_{\mathrm{T}}^{\mathrm{miss}}$ VBF SR (ar) $E_{\mathrm{T}}^{\mathrm{miss}}$ Boosted SR

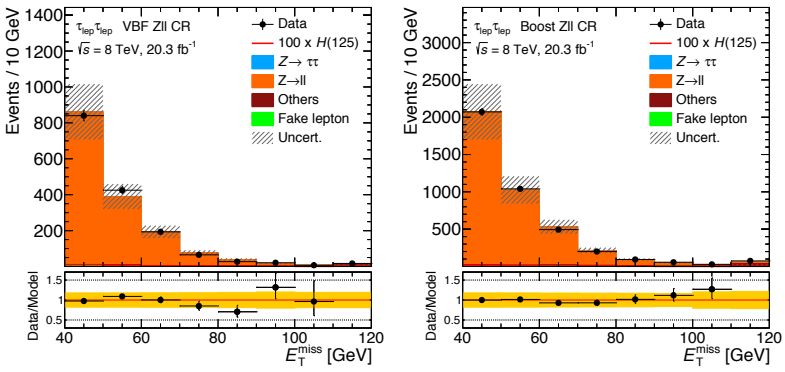

(as) $E_{\mathrm{T}}^{\mathrm{miss}}$ VBF Zll CR (at) $E_{\mathrm{T}}^{\mathrm{miss}}$ Boosted Zll CR

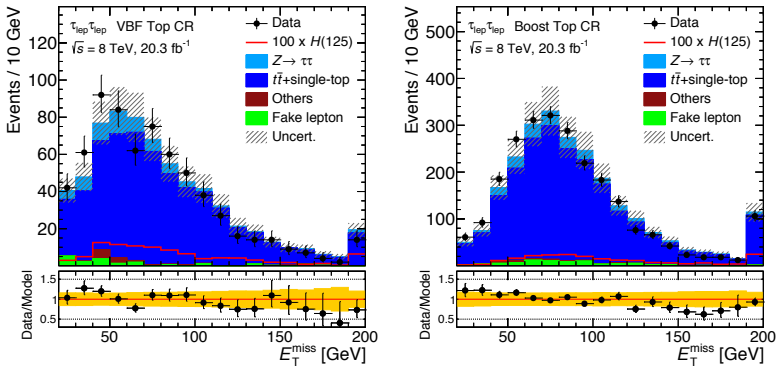

(au) $E_{\mathrm{T}}^{\mathrm{miss}}$ VBF Top CR (av) $E_{\mathrm{T}}^{\mathrm{miss}}$ Boosted Top CR

Figure 6.10: Control plots of the background modeling for the $\tau_{\mathrm{lep}}\tau_{\mathrm{lep}}$ channel. The distributions are shown in two early stages of the event selection and in the SR, the Zll CR and Top CR for the VBF and Boosted categories. The overflow is added, normalization factors are applied and the error band includes the statistic and normalization systematic errors.

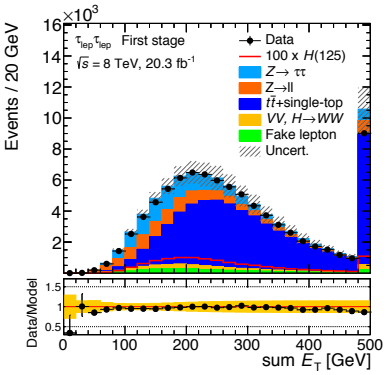

(aw) ΣE_{T} First stage

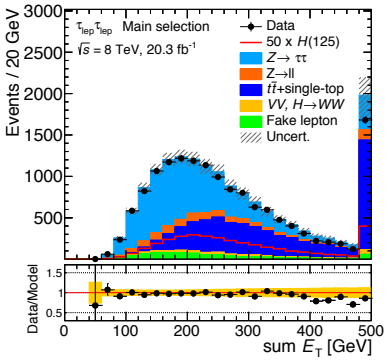

(ax) ΣE_{T} Main selection

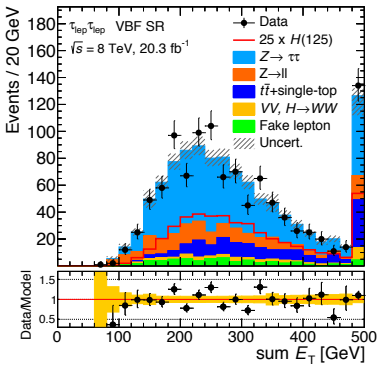

(ay) ΣE_{T} VBF SR

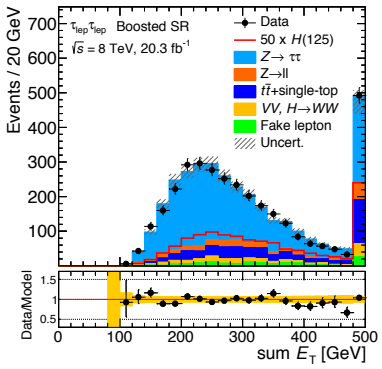

(az) ΣE_{T} Boosted SR

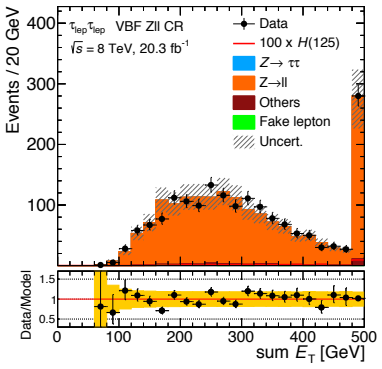

(ba) ΣE_{T} VBF Zll CR

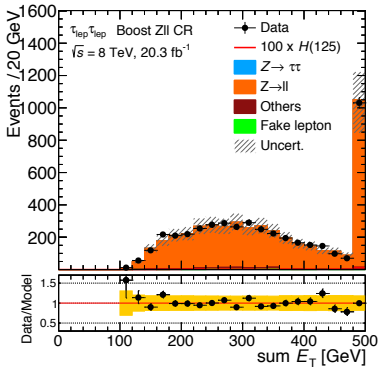

(bb) ΣE_{T} Boosted Zll CR

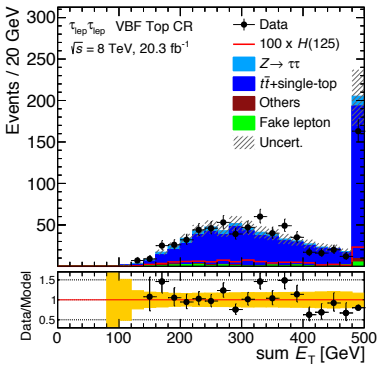

(bc) ΣE_{T} VBF Top CR

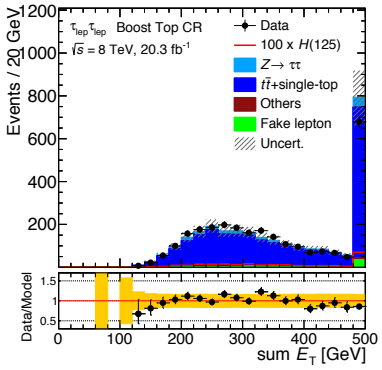

(bd) ΣE_{T} Boosted Top CR

Figure 6.10: Control plots of the background modeling for the $\tau_{\text{lep}}\tau_{\text{lep}}$ channel. The distributions are shown in two early stages of the event selection and in the SR, the Zll CR and Top CR for the VBF and Boosted categories. The overflow is added, normalization factors are applied and the error band includes the statistic and normalization systematic errors.

6.7 Signal discrimination: MultiVariate Analysis

The simplest procedure to enhance the signal over the background events in the final data sample is the cut-based analysis, which applies different selection criteria in a sequential way. These cuts remove events of background-dominated phase-spaces, thus increasing the proportion of signal in the final dataset, but at the cost of losing part of the signal events, which are discarded too. This happens despite the fact that the cut thresholds are optimized by maximizing the background rejection (the amount of background with is removed) while minimizing the signal loss. Furthermore, the cut values are a strict threshold: all events failing a particular cut are removed, no matter how close they are to the threshold or how compatible with signal they are for other selection criteria.

The cut-based approach is simple and effective, but the signal loss affects its sensitivity. An alternative approach which avoids these issues is the MultiVariate Analysis (MVA).

The MVA is a technique which uses the information of several variables at the same time to estimate the compatibility of a data event with certain models that have been learned by a recursive training. In this case, the MVA is used to discriminate the data between signal and background events, and the training is performed using the MC model (and the data-driven estimations) for the signal and background processes. Instead of a binary decision in one variable at a time, the MVAs consider the performance of the event in a set of input variables and then assigns a value (a *score*) of the compatibility of the event with the signal model. Since all the events are kept, the impact of the signal loss is greatly reduced. This advantage is crucial in physics analyses and so, the MVAs are widely used as an alternative approach to the cut-based analyses.

However, the MVAs also have weak points: their computation is slower, their algorithms are more complex (so the control over them is more challenging), and they significantly depend on the training sample used for the optimization, which makes them vulnerable to biases in the selection and leads to further issues, such as overtraining. Systematic errors or additional unknown bias can have a large impact on the final result and thus, the consistency of the results of an MVA has to be carefully checked.

The $H \to \tau\tau$ analysis implements a Boosted Decision Tree –a type of MVA technique– as the main approach. In addition, a simplified cut-based approach is performed, serving as a cross-check of the MVA result.

6.7.1 Boosted Decision Trees

Boosted Decision Trees (BDT)[201, 202] is the name given to a MVA technique that uses trained classification trees to discriminate events. Classification trees differ the standard cut-flow trees in the sense that, after each cut (called *node*), the events which do not pass the threshold are not discarded but keep being evaluated in successive cuts. The BDT is trained against a model of background and signal events where the cut thresholds are optimized to maximize the discrimination power of the classification. Instead of discarding the events that fail one cut, the whole dataset is divided in different phase-spaces (*leafs*), which are assigned a numerical value according to the proportion of signal events that each phase-space contains. This numerical value is called *score* and depends on the weighted signal purity of the leaf. Conceptually, the score represents the compatibility of the event to the selected model. A schematic diagram of a BDT is shown in Figure 6.11.

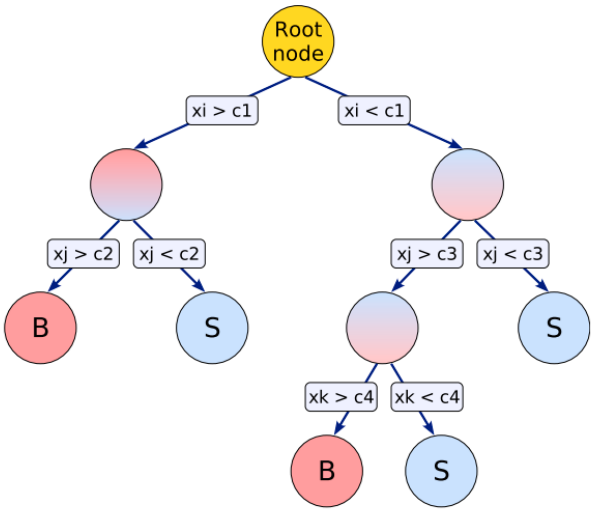

Figure 6.11: Schematic view of a Decision Tree algorithm, showing the division of the initial set in different branches according to the value of a discriminating variable x. The successive splits lead to the final classification of the event between S (signal) or B (background), which are called leaves. The cut thresholds (c) are optimized by training the algorithm against a set of signal and background models [203].

The set of variables used as input of the BDT must be carefully chosen to achieve the highest discrimination power. Using the information provided by the variables in the model sample, the algorithm looks for a threshold in each variable that maximizes a separation function. This separation function can be described by different formulas (Gini Index, Cross Entropy function, Misclassification error,...) although no significant difference in performance is observed [203]. The $H \to \tau\tau$ analysis uses the standard Gini Index [204] which is defined by $G = p \cdot (1 - p)$, where p, the purity of the sample, is defined by $p \equiv n_{sig}/(n_{sig} + n_{bkg})$. The Misclassification error is defined by $\text{MCE} = 1 - \max(p, 1 - p)$, with the same definition of p [203].

A decision tree uses directly the result of one classification. However, this result is very sensitive to statistical fluctuations of the training sample and so, one method to avoid this bias is repeating sequentially the classification tree, assigning a weight to each result according to how it performed with respect to the input model, and then combining all results into a final discriminant. This technique, called *boosting* [205], converts a set of weak learners into a single strong learner and so, it drastically increases the stability and performance of the MVA algorithm.

The machine learning techniques, such as the BDT, improve their performance by using results of a controlled model to optimize the discrimination. After the algorithm is completed and all events of the training have been classified, their score value is compared with their true label and the MCE is computed. Using this information, the tree selection thresholds can be modified so that the MCE is minimized. This can be done in different ways, which defines different types of BDT. The two most common ones are Gradient BDT [206] and Adaptative Boosting (AdaBoost) [202].

AdaBoost weights the data sample by using weights derived from the MCE, so that the events which fail the classification are given more importance in later trees, improving the selection of the events. AdaBoost increases the performance of the selection but it is still sensitive to outliers in the dataset. On the other hand, Gradient Boost uses a log-likelihood binomial as loss function and minimizes it by using a steepest-descent approach. This is done by calculating the current gradient of the loss function and then growing a regression tree whose leaf values are adjusted to match the mean value of the gradient in each of the regions of the tree. Though less powerful than AdaBoost, the Gradient Boost still outperforms the standard decision trees while being robust against outliers and data fluctuations.

This kind of optimization, however, have some vulnerabilities. If the tree selection is performed enough times, the algorithm can become biased to that particular set of data and lose its discrimination power. This effect is called *overtraining* and it is one of the most common issues while dealing with MVAs. The overtraining effect can be avoided by testing the performance of the algorithm in a second unbiased set of model events, not used for the training.

In order to do that, the initial dataset is divided arbitrarily in two parts, a *training sample* and a *test sample*. The MVA is trained using the training sample, but its bias is continuously monitored in the test sample by checking their respective MCE. While the MCE in the training sample always decreases with the number of trainings, eventually reaching zero, the MCE in test sample achieves a minimum before raising again, at which point the MVA is considered to be overtrained, as can be observed in Figure 6.12. The number of iterations used to get the lower MCE in the test sample is the optimal training. However, reducing the size of the training sample to derive a test sample affects the

performance of the training and so, the size of the division of the initial data sample has to be a compromise between achieving a better training and assuring it is unbiased.

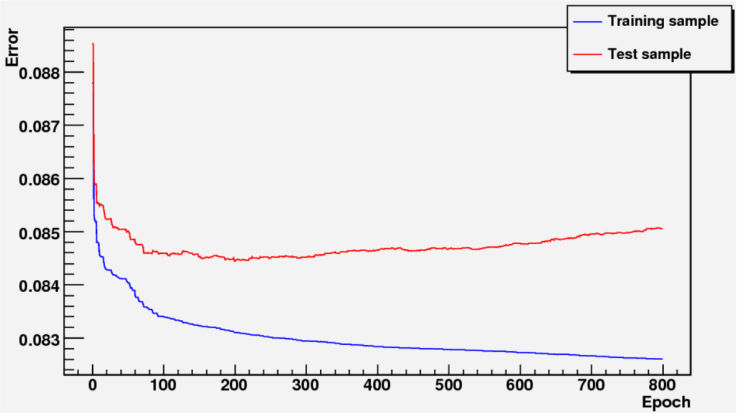

Figure 6.12: Overtraining bias in a MVA algorithm. The figure shows the Misclassification error of a MVA for a training sample (red) and a test sample (blue) with respect to the iteration parameter "epoch". The MCE always gets reduced for the training sample but in the test sample it achieves a minimum at ~ 200 before rising again, showing the overtraining effect.

Another related bias that the BDT can suffer is the size of the phase-spaces. Since the purpose of the training is learning to distinguish the general behavior of a type of event, the final phase-spaces should not be too small, otherwise it will only recognize one specific dynamics. Several conditions to terminate the classification are used to avoid the small-sample bias, as the *Minimum Leaf Size* and the *pruning* of statistically insignificant branches.

Two more properties of the BDT that should be described are *bagging* and *shrinkage*. The term bagging [203] denotes a resampling technique in which a classifier is repeatedly trained using resampled training events such that the combined classifier represents an average of the individual classifiers. Resampling includes the possibility of replacement, which means that the same event is allowed to be (randomly) picked several times from the parent sample. This is equivalent to regarding the training sample as being a representation of the probability density distribution of the parent sample and thus, resampling is implemented by applying random Poisson weights to each event of the parent sample. Shrinkage, on the other hand, is a property of the BDT that establishes the rate of learning of the BDT. A small shrinkage demands more trees to be grown but can significantly improve the accuracy of the prediction in difficult conditions.

The MVA techniques employed in the $H \to \tau\tau$ analysis were performed with the TMVA framework [203] of the ROOT program [207]. In particular, the $\tau_{\text{lep}}\tau_{\text{lep}}$ channel implemented a Gradient BDT. The discriminating variables used in the training as well as the motivation that led to their selection, the optimization parameters, the training procedure of the BDT and the consistency checks performed, are discussed in subsequent sections.

6.7.2 Variables

The selection of the input variables of the BDT is a crucial step in the MVA configuration, as the sensitivity of the algorithm depends greatly on the discrimination information that they provide. However, the complexity of the algorithm and its computing time grow exponentially with the number of variables, becoming more demanding to train and more difficult to control, which can be a limitation. Thus, a careful selection of the variables must be performed to achieve the smallest set which provides the best sensitivity.

The candidate variables must possess a great discrimination power to represent a significant impact in the sensitivity of the BDT algorithm. The discrimination power of the variables comes from the difference of their distribution for background and signal events (as shown for the selected variables in Figures 6.13 and 6.14). The larger the difference in behavior, the more useful it would be for the BDT and thus, studies were performed to identify the variables with the biggest discrimination power. Many variables were tested, trying different approaches, until a small set was selected. However, the discrimination power is not the only feature to take into account when choosing a variable, as the complexity of the BDT algorithm implies that other properties could have a non-negligible effect on the usefulness of the variable. The actual impact of each variable on the BDT was studied in different ways.

As a preliminary requirement, the selected variables must be well modeled. At the stage of the selection where the variables are given as a input of the BDT, the distributions should display a good agreement between the data and the model, in order to claim a good understanding of the processes involved and serve as valid discriminators. The distributions of the variables before entering in the BDT are shown in Figure 6.13 for the VBF category and Figure 6.14 for the Boosted category. Both figures show the agreement between data and background models on the left hand-side and the discrimination power (difference in structure of distribution for signal and background) on the right hand-side.

Besides the qualitative check of the distributions, more quantitative studies are needed. Firstly, the TMVA framework provides a tool which ranks the variables according to their impact in the BDT training (shown in Tables 6.8 and 6.9 in Section 6.7.5). Relevance in the training does not necessarily imply a great impact on the final result, but it is illustrative information on the general performance of the variable, and thus, the rankings were checked for every set.

Secondly, as the variables describing the event are related by physics constraints and conservation laws, some of them might be redundant, as the information they provide can be inferred from other variables. To avoid the inclusion of unnecessary variables, the correlations of all of them were checked, and variables with high values for both models, signal and background, were removed. Figure 6.18 shows the correlation values of the

final set of variables.

Finally, the actual impact of the variables in the final result, not only in the BDT performance, was studied. The statistical analysis was performed, computing the expected statistical sensitivity excluding, one at the time, each of the variables under study. If the loss of significance was non-negligible (more than few percent), the variable was kept.

Since the topology of the events is completely different in each of the categories, independent sets of variables were chosen for them. These sets were optimized focusing on different aspects of the topology of the events, which include different types of variables, objects and approaches: e.g. the VBF category includes 2-jets variables, which are absent in the Boosted category. The only exception is the $m_{\tau\tau}^{\text{MMC}}$, which is used in both categories, as it is the main discriminant of the events and its impact is very significant (in fact the biggest one). The selected variables mainly refer to the invariant masses or angular relations of the objects involved in the event, as these features are the ones which provide the most discriminant information between background and signal.

The variables selected as input of the BDT are enumerated below.

For the **VBF** category:

- $\boldsymbol{m_{\tau\tau}^{\text{MMC}}}$, the $m_{\tau\tau}$ calculated using the Missing Mass Calculator algorithm, defined in Section 6.3.
- $\boldsymbol{\Delta R_{ll}}$, the ΔR separation between the two leptons.
- $\boldsymbol{|\Delta\eta_{jj}|}$, the $\Delta\eta$ separation between the two leading jets.
- $\boldsymbol{\min\left(\Delta\eta_{l1l2,jets}\right)}$, the minimum $\Delta\eta$ separation between the di-lepton system and all jets in the event.
- $\boldsymbol{m_{jj}}$, the invariant mass of the two leading jets.
- $\boldsymbol{C_\eta(l_1) \times C_\eta(l_2)}$, product of the η centrality of the two leptons with respect the two leading jets. The η centrality, C_η, is defined in Equation 6.7.
- $\boldsymbol{\Delta\eta_{j3;jj}}$, the $\Delta\eta$ separation between the third jet (if it exists) with respect to the two leading jets. Events with only two jets are assigned a conventional value of -0.5.

For the **Boosted** category:

- $\boldsymbol{m_{\tau\tau}^{\mathrm{MMC}}}$, the $m_{\tau\tau}$ calculated using the Missing Mass Calculator algorithm, defined in Section 6.3.
- $\boldsymbol{m_{\tau\tau,j1}}$, the invariant mass of the di-τ system and the leading jet.
- $\boldsymbol{C_{\phi}(E_{\mathrm{T}}^{\mathrm{miss}})}$, the ϕ centrality of the $E_{\mathrm{T}}^{\mathrm{miss}}$ object with respect to the two τ of the event, as is defined in Equation 6.6.
- $\boldsymbol{m_{ll}}$, the invariant mass of the two visible leptons.
- $\boldsymbol{\Delta\phi_{ll}}$, the $\Delta\phi$ separation of the two leptons.
- $\boldsymbol{S}$, *sphericity*, variable to describe the spherical isotropy of the event, defined in Equation 6.9.
- $\boldsymbol{p_{\mathrm{T}}^{l1}}$, p_{T} of the leading lepton.
- $\boldsymbol{p_{\mathrm{T}}^{j1}}$, p_{T} of the leading jet.
- $\boldsymbol{E_{\mathrm{T}}^{\mathrm{miss}}/p_{\mathrm{T}}^{l2}}$, ratio of $E_{\mathrm{T}}^{\mathrm{miss}}$ and the p_{T} of the sub-leading lepton.

Though most of the variables have straightforward definitions, some of them need to be described in more detail.

- Object ϕ centrality, $C_{\phi}(\phi_3)$: a variable that quantifies the relative angular position in the ϕ plane of some object (ϕ_3) with respect to other two objects (ϕ_1, ϕ_2) in the transverse plane. It is computed in the following way:

$$A = \frac{\sin(\phi_3 - \phi_1)}{\sin(\phi_2 - \phi_1)} \qquad B = \frac{\sin(\phi_2 - \phi_3)}{\sin(\phi_2 - \phi_1)}$$

$$C_{\phi}(\phi_3) = \frac{A + B}{\sqrt{A^2 + B^2}} \tag{6.6}$$

  where ϕ_1 and ϕ_2 are the ϕ values of the reference objects and ϕ_3 is the ϕ value of the object for which the C_{ϕ} is computed. Thus, the $C_{\phi}(E_{\mathrm{T}}^{\mathrm{miss}})$ variable is defined by taking the τ as the objects labelled 1 and 2, whereas the $E_{\mathrm{T}}^{\mathrm{miss}}$ takes the position of the third object.

- Object η centrality, $C_{\eta}(\eta_3)$: a variable that quantifies the η position of some object (η_3) with respect to other two objects in the event. It is defined as:

$$C_{\eta}(\eta_3) = \exp\left[\frac{-4}{(\eta_1 - \eta_2)^2}\left(\eta_3 - \frac{\eta_1 + \eta_2}{2}\right)^2\right] \tag{6.7}$$

where η_1, η_2 and η_3, are the pseudorapidities of the reference objects and the main object, respectively. Namely, for the $C_\eta(l)$ variables, the reference objects are the two leading jets respectively, and the third object is the lepton from which the centrality is computed. This variable has a value of 1 when the main object is halfway in η between the two jets, $1/e$ when the object is aligned with one of the jets, and $< 1/e$ when the object is not between the jets in η dimension.

- Sphericity: a variable that describes the isotropy of the energy flow in the event [208]. It is based on the quadratic momentum tensor:

$$S^{\alpha\beta} = \frac{\sum_i p_i^\alpha p_i^\beta}{\sum_i |\vec{p_i}^2|}. \tag{6.8}$$

In this equation, α and β are the indices of the tensor. The summation is performed over the momenta of the selected leptons and jets in the event. The sphericity of the event (S) is then defined in terms of the two smallest eigenvalues of this tensor, λ_2 and λ_3,

$$S = \frac{3}{2}(\lambda_2 + \lambda_3). \tag{6.9}$$

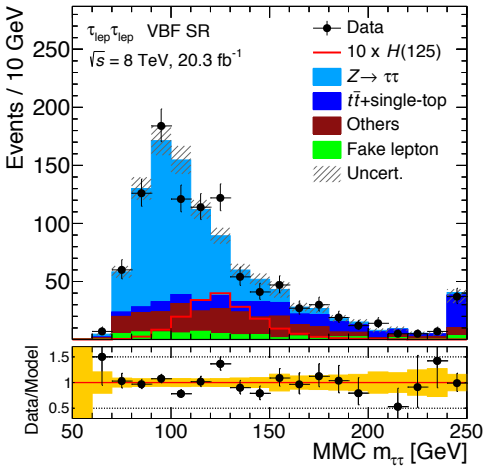

(a) $m_{\tau\tau}^{\text{MMC}}$ SR

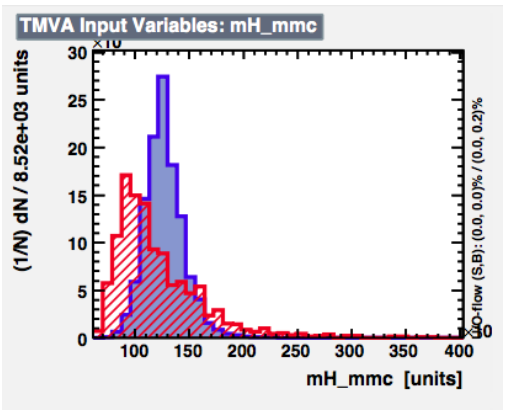

(b) $m_{\tau\tau}^{\text{MMC}}$ discr. power

Figure 6.13: Input variables of the VBF category in the 8 TeV dataset, showing (left) the data/model distribution in the SR and (right) the discrimination power of the variable. The discrimination power normalizes the distribution of signal (blue) to background (red) to compare their different behavior. The variables listed, in order, are: $m_{\tau\tau}^{\text{MMC}}$, ΔR_{ll}, $|\Delta\eta_{jj}|$, $\min(\Delta\eta_{l1l2,jets})$, m_{jj}, $C_\eta(l_1) \times C_\eta(l_2)$ and $\Delta\eta_{j3;jj}$. (Cont.)

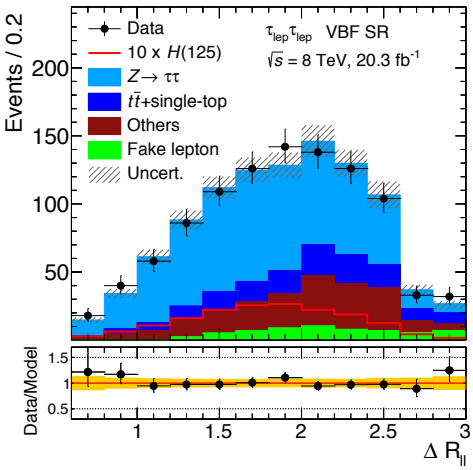

(c) ΔR_{ll} SR

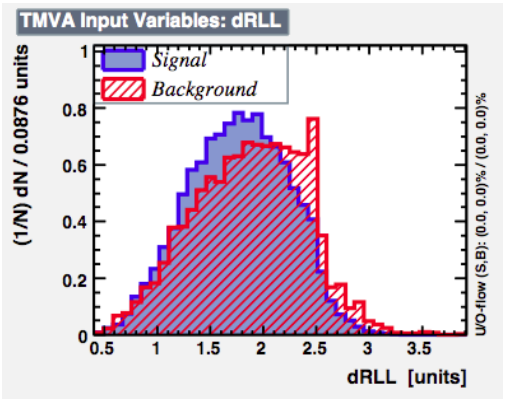

(d) ΔR_{ll} discr. power

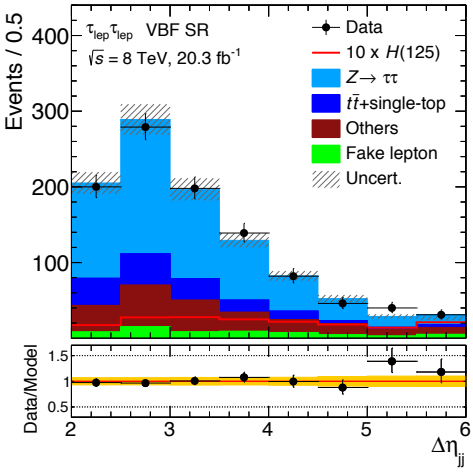

(e) $|\Delta\eta_{jj}|$ SR

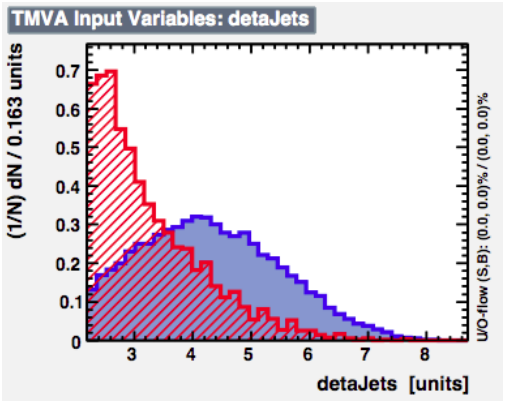

(f) $|\Delta\eta_{jj}|$ discr. power

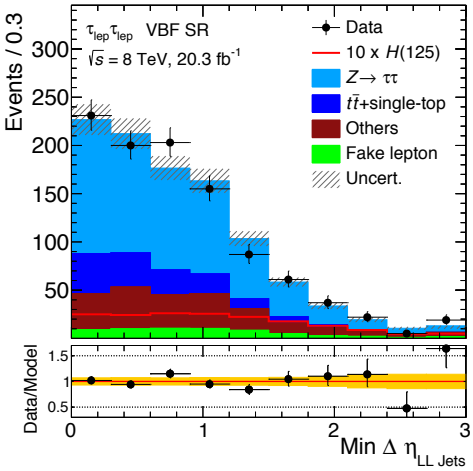

(g) $\min(\Delta\eta_{l1l2,jets})$ model

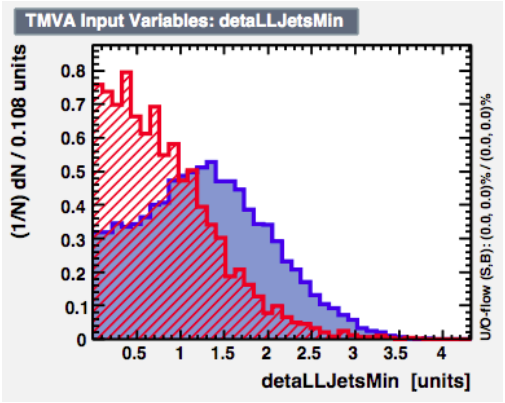

(h) $\min(\Delta\eta_{l1l2,jets})$ discr. power

Figure 6.13: Input variables of the VBF category in the 8 TeV dataset, showing (left) the data/model distribution in the SR and (right) the discrimination power of the variable. The discrimination power normalizes the distribution of signal (blue) to background (red) to compare their different behavior. The variables listed, in order,are: $m_{\tau\tau}^{\mathrm{MMC}}$, ΔR_{ll}, $|\Delta\eta_{jj}|$, $\min(\Delta\eta_{l1l2,jets})$, m_{jj}, $C_\eta(l_1) \times C_\eta(l_2)$ and $\Delta\eta_{j3;jj}$. (Cont.)

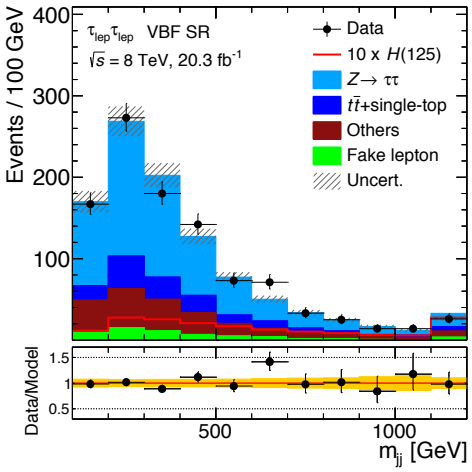

(i) m_{jj} model

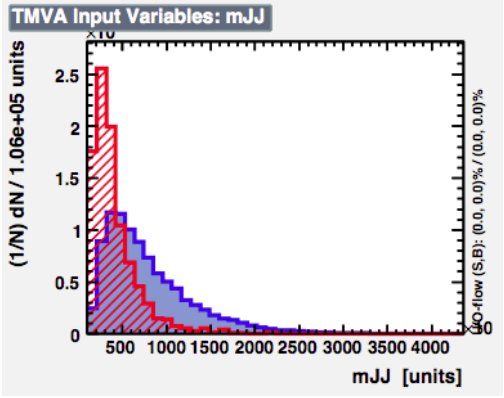

(j) m_{jj} discr. power

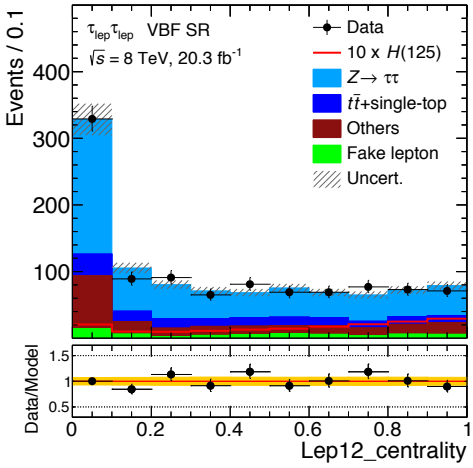

(k) $C_\eta(l_1) \times C_\eta(l_2)$ model

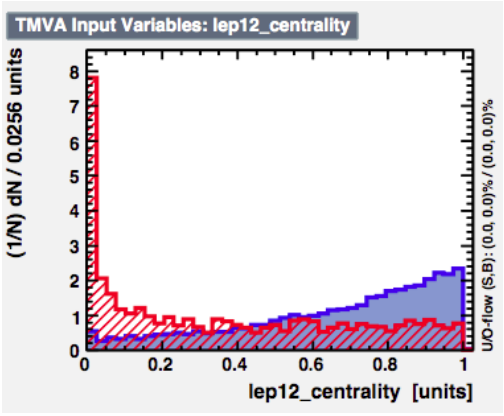

(l) $C_\eta(l_1) \times C_\eta(l_2)$ discr. power

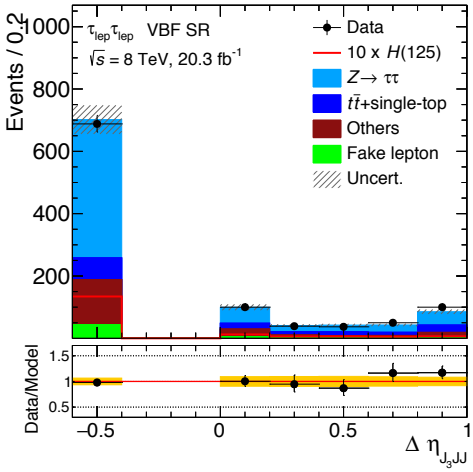

(m) $\Delta\eta_{j3;jj}$ model

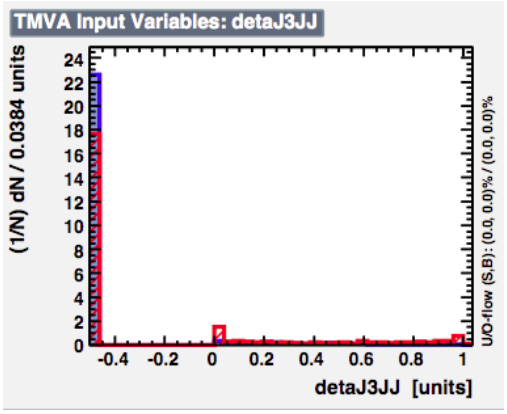

(n) $\Delta\eta_{j3;jj}$ discr. power

Figure 6.13: Input variables of the VBF category in the 8 TeV dataset, showing (left) the data/model distribution in the SR and (right) the discrimination power of the variable. The discrimination power normalizes the distribution of signal (blue) to background (red) to compare their different behavior. The variables listed, in order, are: $m_{\tau\tau}^{\text{MMC}}$, ΔR_{ll}, $|\Delta\eta_{jj}|$, $\min(\Delta\eta_{l1l2,jets})$, m_{jj}, $C_\eta(l_1) \times C_\eta(l_2)$ and $\Delta\eta_{j3;jj}$.

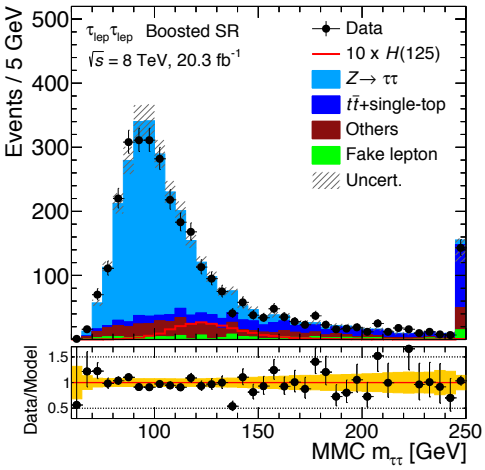

(a) $m_{\tau\tau}^{\text{MMC}}$ model

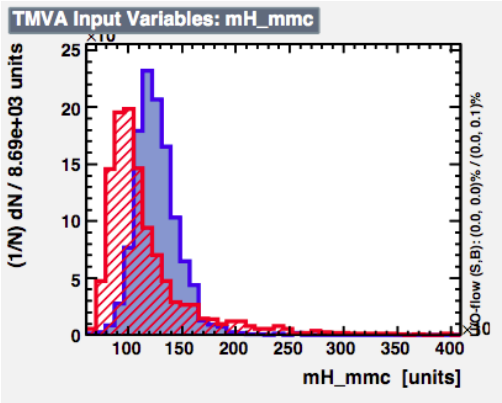

(b) $m_{\tau\tau}^{\text{MMC}}$ discr. power

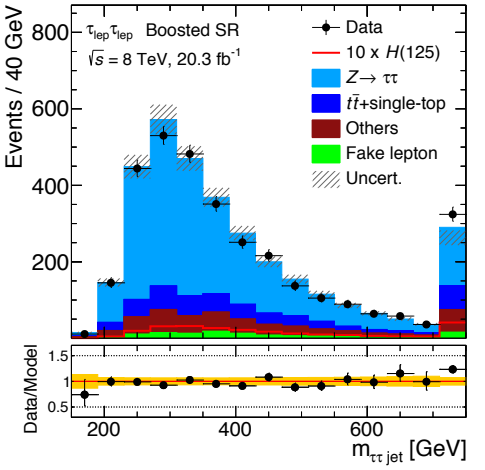

(c) $m_{\tau\tau,j1}$ model

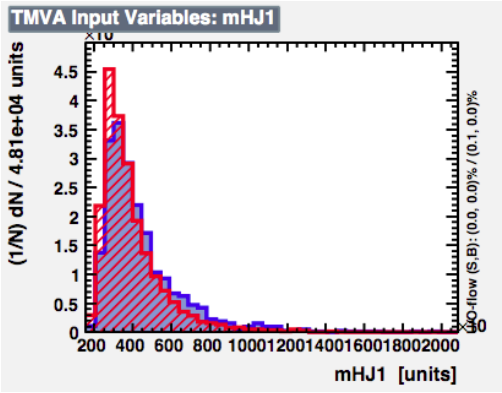

(d) $m_{\tau\tau,j1}$ discr. power

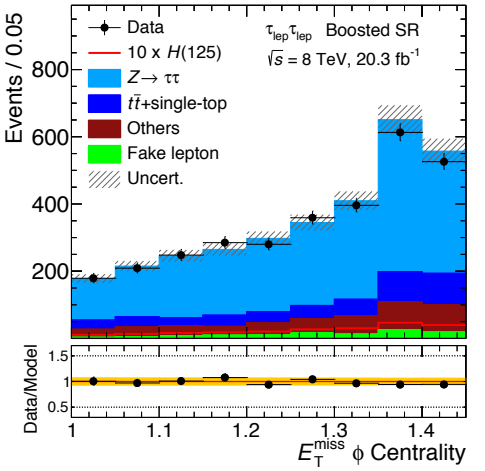

(e) $C_{\phi}(E_{\text{T}}^{\text{miss}})$ model

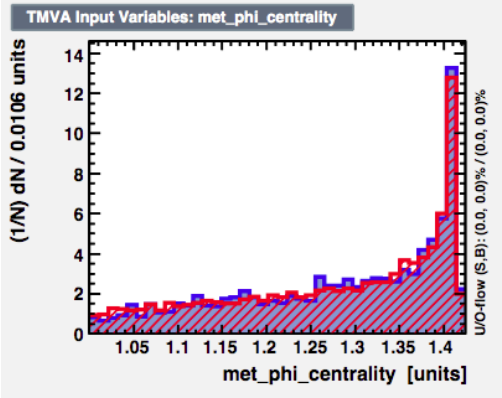

(f) $C_{\phi}(E_{\text{T}}^{\text{miss}})$ discr. power

Figure 6.14: Input variables of the Boosted category in the 8 TeV dataset, showing (left) the data/model distribution in the SR and (right) the discrimination power of the variable. The discrimination power normalizes the distribution of signal (blue) to background (red) to compare their different behavior. The variables listed, in order, are: $m_{\tau\tau}^{\text{MMC}}$, $m_{\tau\tau,j1}$, $C_{\phi}(E_{\text{T}}^{\text{miss}})$, m_{ll}, $\Delta\phi_{ll}$, S, p_{T}^{l1}, p_{T}^{j1} and $E_{\text{T}}^{\text{miss}}/p_{\text{T}}^{l2}$. (Cont.)

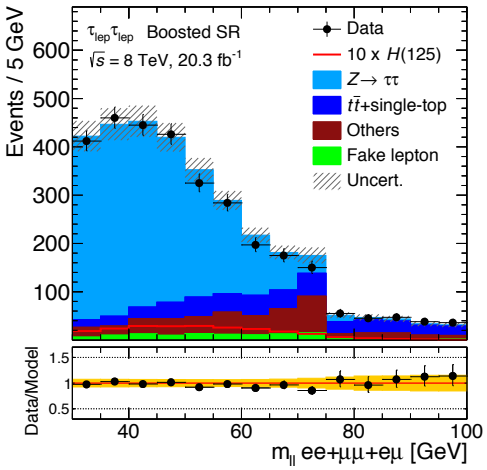

(g) m_{ll} model

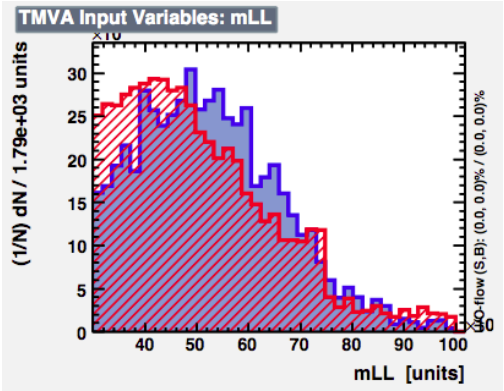

(h) m_{ll} discr. power

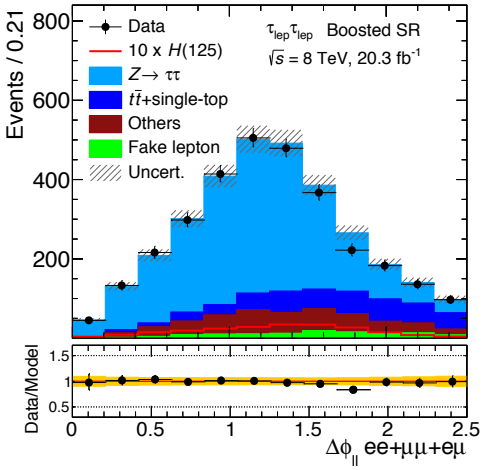

(i) $\Delta\phi_{ll}$ model

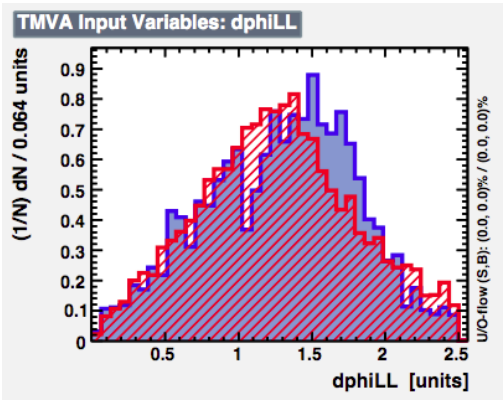

(j) $\Delta\phi_{ll}$ discr. power

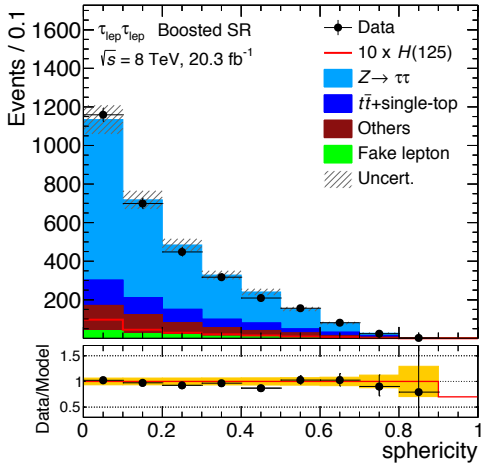

(k) Sphericity model

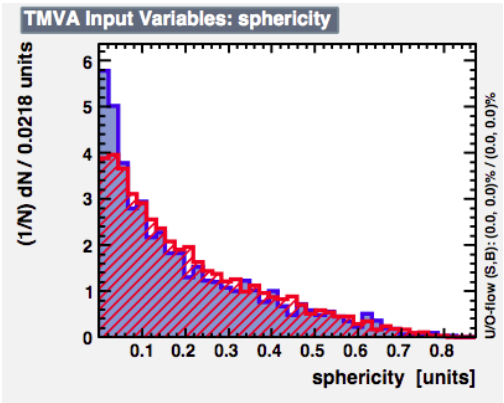

(l) Sphericity discr. power

Figure 6.14: Input variables of the Boosted category in the 8 TeV dataset, showing (left) the data/model distribution in the SR and (right) the discrimination power of the variable. The discrimination power normalizes the distribution of signal (blue) to background (red) to compare their different behavior. The variables listed, in order, are: $m_{\tau\tau}^{\text{MMC}}$, $m_{\tau\tau,j1}$, $C_{\phi}(E_{\text{T}}^{\text{miss}})$, m_{ll}, $\Delta\phi_{ll}$, S, p_{T}^{l1}, p_{T}^{j1} and $E_{\text{T}}^{\text{miss}}/p_{\text{T}}^{l2}$. (Cont.)

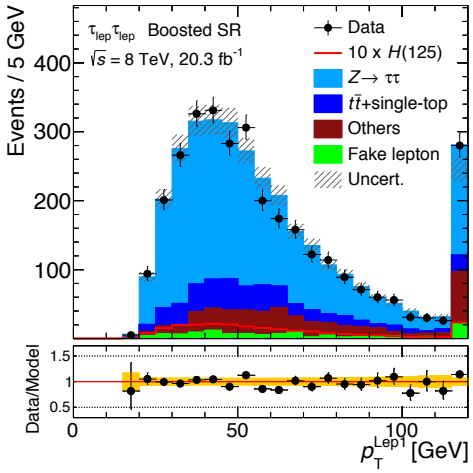

(m) p_{T}^{l1} model

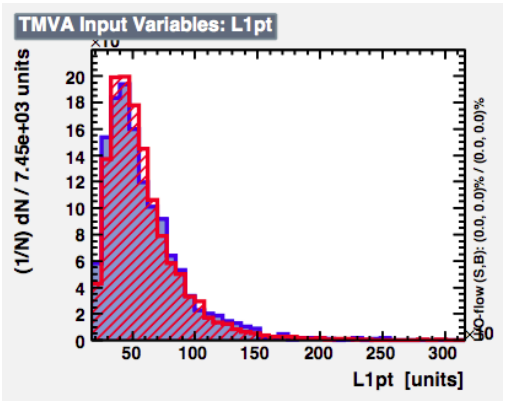

(n) p_{T}^{l1} discr. power

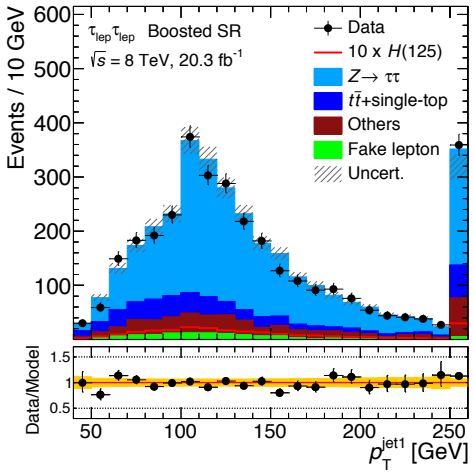

(o) p_{T}^{j1} model

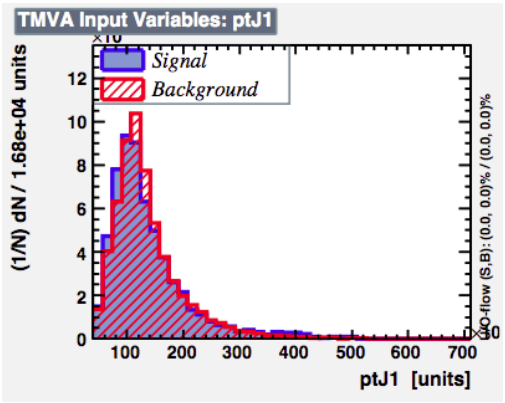

(p) p_{T}^{j1} discr. power

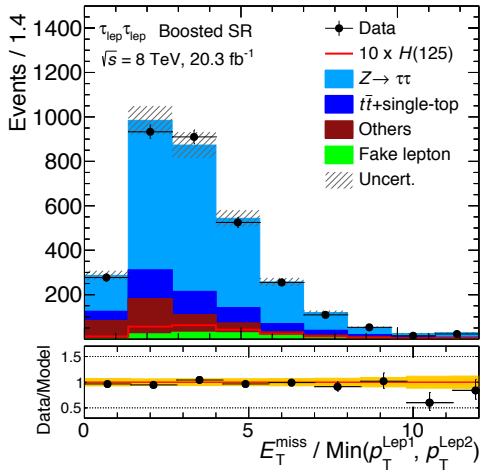

(q) $E_{\mathrm{T}}^{\mathrm{miss}}/p_{\mathrm{T}}^{l2}$ model

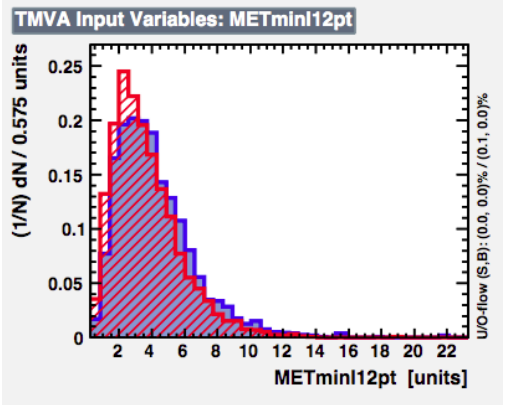

(r) $E_{\mathrm{T}}^{\mathrm{miss}}/p_{\mathrm{T}}^{l2}$ discr. power

Figure 6.14: Input variables of the Boosted category in the 8 TeV dataset, showing (left) the data/model distribution in the SR and (right) the discrimination power of the variable. The discrimination power normalizes the distribution of signal (blue) to background (red) to compare their different behavior. The variables listed, in order, are: $m_{\tau\tau}^{\mathrm{MMC}}$, $m_{\tau\tau,j1}$, $C_\phi(E_{\mathrm{T}}^{\mathrm{miss}})$, m_{ll}, $\Delta\phi_{ll}$, S, p_{T}^{l1}, p_{T}^{j1} and $E_{\mathrm{T}}^{\mathrm{miss}}/p_{\mathrm{T}}^{l2}$.

6.7.3 Optimization of parameters

After the variables have been set, the configuration of the BDT can be fine-tuned to achieve a better performance. Several types of MVAs were tested, such as Neural Networks (MLPNN) or different types of BDT. The performance studies showed that the different algorithms had a similar efficiency, as seen in the ROC curve distribution[4] of Figure 6.15 and thus, due to simplicity, the BDT was chosen over the Neural Network. In addition, the Gradient BDT showed a smoother shape and it raised less concerns about empty bins (bins with 0 events), which were an issue in Adaboost BDT. Hence, the Gradient BDT was chosen as the baseline algorithm for the $\tau_{\text{lep}}\tau_{\text{lep}}$ channel.

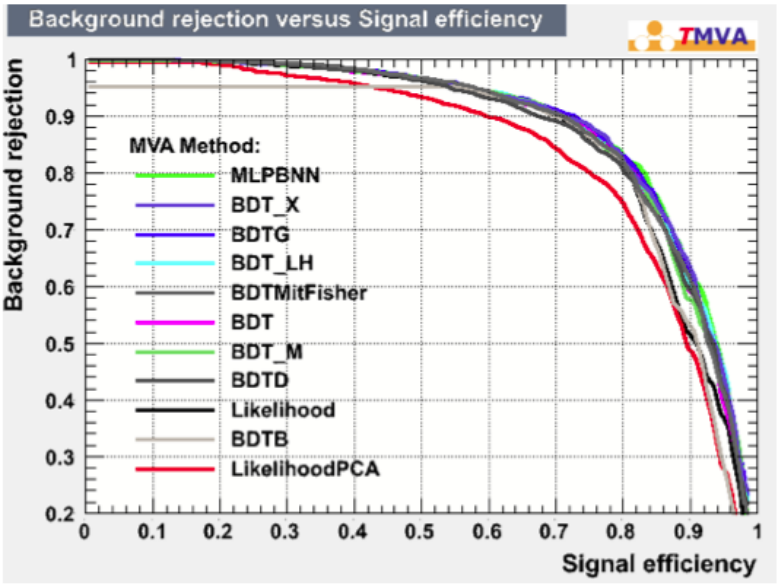

Figure 6.15: ROC curve comparing several types of MVA. The one selected for the VBF category is labelled as "BDT_X" in this figure. As observed, the majority of MVAs have a similar performance.

The Gradient BDT depends on a series of configurable parameters. In order to optimize them, a 2D scan was performed at two of the customizable options of the BDT configuration: the Maximum Depth allowed (*MaxDepth*) and the number of Trees (*nTrees*), checking which combination of them gave the lowest value for the Error Fraction, EF, defined as:

$$\text{EF} = \frac{\sum n_{\text{sig}}^{\text{miss}} + \sum n_{\text{bkg}}^{\text{miss}}}{\sum \text{events}} \tag{6.10}$$

where $n_{\text{sig}}^{\text{miss}}$ and $n_{\text{bkg}}^{\text{miss}}$ are the number of misclassified events in signal and background datasets, respectively.

[4]ROC stands for *Receiver Operation Characteristic*, a fundamental tool for test evaluation. In a ROC curve, the true positive rate is plotted as a function of the false positive rate for different cut-off points of a parameter. The area under the ROC curve is the measure of the performance of the algorithm.

The results of the scan are shown in Figure 6.16. These scans gave a tentative approach for the best configuration numbers. Further tests computing the expected statistical sensitivity for each candidate configuration were performed and the combination of parameters which gave the best performance was chosen.

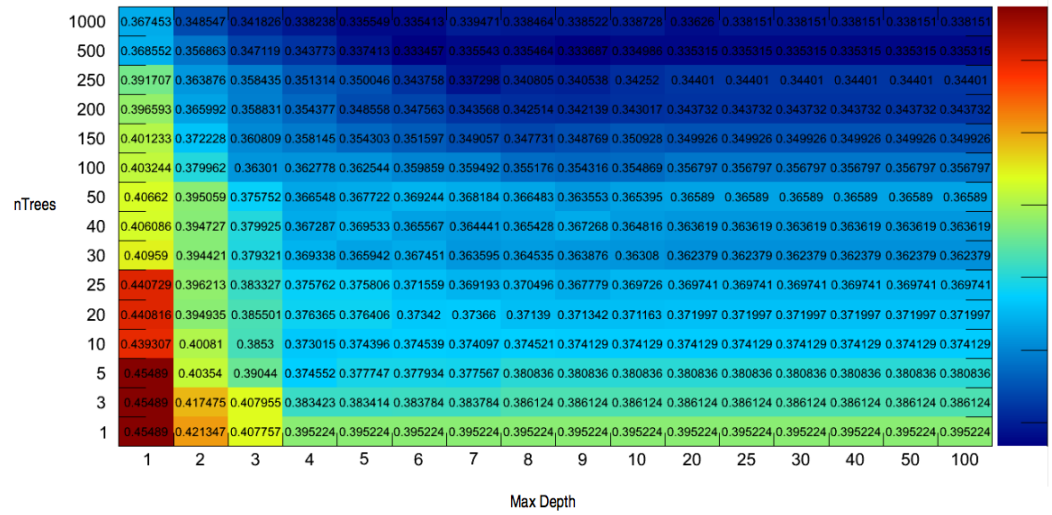

(a) VBF category

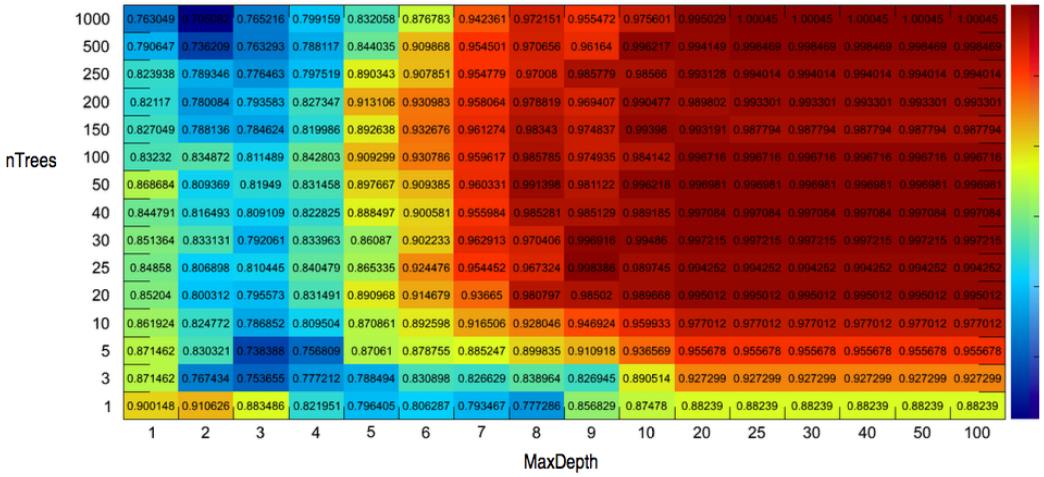

(b) Boosted category

Figure 6.16: 2D scan of BDT parameters, number of Trees (nTrees) and Maximum Depth (MaxDepth), computing the Error Fraction for each configuration in the test sample for (a) VBF category and (b) Boosted category. The red color marks the configuration with higher values for the Error Fraction, while blue color marks the zones with lower error.

The final configuration of both BDTs can be found in Table 6.6.

6.7.4 Training

MVAs, such as the BDTs, are trained in order to improve their performance in discriminating types of events. For that, they have to learn the patterns of the signal and

Option	**VBF**	**Boosted**
Type of MVA	BDT	BDT
Type of Boost	Gradient	Gradient
Number of Trees	250	500
Minimal Node Size	1.3%	5%
Shrinkage	0.05	0.10
Bagged Boost	Yes	Yes
Bagged Sample Fraction	0.5	0.5
Number of Cuts	30	20
Maximum Depth	4	5
Negative Weights	No	No
Node Purity Limit	0.5	0.5
Separation Type	Gini Index	Gini Index
Pruning	No	No

Table 6.6: Configuration parameters of the BDTs for both categories. The general description of each option is given in Section 6.7.1 but a further detailed description can be found in Ref. [203].

background events, which is done by running iteratively the algorithm on datasets of the two models. The difference in distributions of the variables in each of the models allows the BDT to recognize patterns and improve its inner configuration to achieve the best discrimination power. These variables are introduced to the BDT algorithm after the full selection, where the difference in behavior of the variables is enhanced. In addition, the available simulation samples were big enough to allow for a sensitive training of the events. As the topology of the signal events is different in each category (two-jets or boosted events), the BDT training was optimized independently. The final number of events used for the training in each of the categories is summarized in Section 6.7.4.

The signal input in the VBF category was chosen to be only the simulated sample of the VBF production mode, with a mass of $m_H = 125\,\text{GeV}$. Hence, the MVA in this category was specialized to recognize the signature of VBF events. For the training of the Boosted category, only events from the ggH production mode were selected, despite this category also collecting some contribution from VBF and VH modes. The studies performed showed that the MVA worked better with a more homogeneous training sample and thus, only the ggH, which is the dominant mode in this category, was used.

The background training, on the other hand, was identical for the two categories. The samples for the $Z \to \tau\tau$ (embedding), $Z \to ll$, $t\bar{t}$, di-boson and Fakes processes were used, with the corresponding event fractions and after the full selection. The $H \to WW$ process, despite being considered as background, was not included in the training for two reasons: its contribution was expected to be small and its topology would be too similar

to the signal processes, which could interfere with the performance of the MVA.

The Fakes contribution required a special treatment, too. As explained in Section 6.4.3.6, this background is modeled using a weighted data-driven sample from which the contributions of true-lepton backgrounds are estimated by MC and removed. For the BDT, however, only the data events were included in the training, while the MC subtraction was excluded, since the BDT is not prepared to handle efficiently events with a negative weight. This omission could lead to some underperformance in the training but since the contribution of the MC in the Fake background is small, this effect was considered negligible.

In order to optimize the background modeling, different approaches were investigated. The first attempts to do the training aimed for a complex training structure with focus in the discrimination of the irreducible background $Z \to \tau\tau$, with respect to the rest of the processes and thus, two BDT were implemented: one specific to discriminate only the $Z \to \tau\tau$ and a second one to discriminate the rest of backgrounds. A third BDT was constructed, using as input the score of the previous BDTs to get the final BDT score. No significant improvement in the performance of the Gradient BDT was achieved and thus, this approach was dropped in favor of other simpler schemes.

As explained in Section 6.7.1, in order to avoid the overtraining issues in the BDT training, the model sample was divided in a test and a training sub-samples. However, the datasets available for the training were statistically limited and thus, the removal of a significant amount of events for testing purposes would have an impact on the quality of the comparisons between data and predictions. Hence, a test evaluation strategy was developed in such way that, given the limit on the available statistics, all the events could be used for training and testing purposes. This strategy is called cross-validation.

The cross-validation approach is implemented by dividing the initial dataset in two equal subsets using a random number generator. Two identical BDT are defined, with the exact same configuration. The first BDT (BDT1) is trained using the first half of the sample (odd events), while the second one, BDT2, is trained using the second half of the sample (even events). For the test evaluation, the subsets are interchanged: the BDT1, trained with the odd sample, is checked using the even events as test, while the BDT2, which has been trained with the even sample, is tested with the odd events. The evaluation of the BDT score of the data sample follows the same pattern as for the test sample. The cross-validation strategy is illustrated in Figure 6.17.

In this way, each BDT is tested using events which have not been used for its training, avoiding possible biases. The combination of the two unbiased BDTs overcomes the loss of statistics in each BDT.

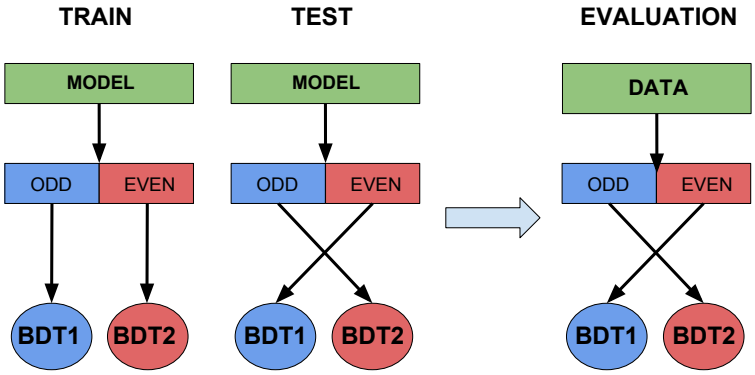

Figure 6.17: Diagram showing the cross-evaluation strategy of a MVA by splitting the dataset in two equal subsets and defining two BDTs which are trained and tested interchanging the subsets. As can be observed, each BDT is trained over one subset, but it is tested over the other subset, thus keeping the algorithm unbiased.

	VBF		**Boosted**	
Type of Event	Train	Test	Train	Test
VBF	25 544	25 994	0	0
ggH	0	0	3371	3385
VH	0	0	0	0
$Z \to \tau\tau$	3596	3731	11 522	11 834
$Z \to ll$	1156	1182	1217	1256
$t\bar{t}$	396	363	1025	1034
di-boson	76	94	403	399
Fakes	242	263	378	389
Total Background	5466	5633	14 545	14 912

Table 6.7: Number of raw (unweighted) events used for the training and test of the BDT1 of each category, for each of the contributions. For BDT2 the numbers are the same, but inverting the training/test samples.

6.7.5 Consistency checks of the BDT

Due to the fragility of the MVA algorithms and their tendency to be biased, they have to be carefully checked, testing the robustness and consistency of their results. In the $H \to \tau\tau$ analysis this was done using the tools provided by the TMVA framework and several of these checks are shown in this section.

A preliminary test to check the usefulness of the variables is the rankings that the TMVA framework provides [203], which show a preliminary review of the impact of each variable in the MVA training. The ranking is given at two different stages: first, a generic ranking is derived, followed by algorithm-specific ranking. The generic ranking

sorts the variables according to their separation power, while the method-specific ranking is computed by counting how often the variables are used to split decision tree nodes, weighting each split occurrence by the separation gain-squared it has achieved and by the number of events in the node.

The rankings obtained in the training of the two BDTs, both generic and method specific, are shown for the VBF category in Table 6.8 and for the Boosted category in Table 6.9.

Rank	Variable	Separation
1	$m_{\tau\tau}^{\text{MMC}}$	0.2607
2	m_{jj}	0.2368
3	$C_\eta(l_1) \times C_\eta(l_2)$	0.2194
4	$\lvert\Delta\eta_{jj}\rvert$	0.2149
5	$\min\left(\Delta\eta_{l1l2,jets}\right)$	0.1214
6	$\Delta\eta_{j3;jj}$	0.06732
7	ΔR_{ll}	0.02152

(a) BDT1 - generic ranking

Rank	Variable	Separation
1	$m_{\tau\tau}^{\text{MMC}}$	0.2363
2	$C_\eta(l_1) \times C_\eta(l_2)$	0.2183
3	m_{jj}	0.1578
4	$\Delta\eta_{j3;jj}$	0.1212
5	$\lvert\Delta\eta_{jj}\rvert$	0.1052
6	ΔR_{ll}	0.1040
7	$\min\left(\Delta\eta_{l1l2,jets}\right)$	0.05713

(b) BDT1 - specific ranking

Rank	Variable	Separation
1	$m_{\tau\tau}^{\text{MMC}}$	0.2589
2	m_{jj}	0.2341
3	$C_\eta(l_1) \times C_\eta(l_2)$	0.2227
4	$\lvert\Delta\eta_{jj}\rvert$	0.2168
5	$\min\left(\Delta\eta_{l1l2,jets}\right)$	0.1236
6	$\Delta\eta_{j3;jj}$	0.04973
7	ΔR_{ll}	0.01917

(c) BDT2 - generic ranking

Rank	Variable	Separation
1	$C_\eta(l_1) \times C_\eta(l_2)$	0.2921
2	$m_{\tau\tau}^{\text{MMC}}$	0.2247
3	m_{jj}	0.1311
4	$\lvert\Delta\eta_{jj}\rvert$	0.1164
5	$\Delta\eta_{j3;jj}$	0.09602
6	ΔR_{ll}	0.07556
7	$\min\left(\Delta\eta_{l1l2,jets}\right)$	0.06412

(d) BDT2 - specific ranking

Table 6.8: Rankings of performance of the different variables in two BDTs of the VBF category. The rankings are shown as given by the TMVA framework.

In Figure 6.18, the correlation matrices of the input variables in the signal and background models are shown for each of the two categories. As explained in Section 6.7.2, a careful selection of the input variables was performed, and as a result of it, a small set of independent variables was chosen, to avoid redundancy of the input information. All the variables with high correlation and no significant improvement on the final sensitivity were removed. Several complex variables, such as $\min\left(\Delta\eta_{l1l2,jets}\right)$, $C_\eta(l_1) \times C_\eta(l_2)$, $\lvert\Delta\eta_{jj}\rvert$ or $E_{\text{T}}^{\text{miss}}/p_{\text{T}}^{l2}$, show relatively high correlations, however, they were kept because they had a positive impact on the final sensitivity.

Rank	Variable	Separation
1	$m_{\tau\tau}^{\text{MMC}}$	0.2891
2	$m_{\tau\tau,j1}$	0.02687
3	m_{ll}	0.02136
4	$E_{\text{T}}^{\text{miss}}/p_{\text{T}}^{l2}$	0.01945
5	$\Delta\phi_{ll}$	0.01937
6	S	0.01368
7	p_{T}^{j1}	0.009035
8	p_{T}^{l1}	0.007318
9	$C_{\phi}(E_{\text{T}}^{\text{miss}})$	0.005253

(a) BDT1 - generic ranking

Rank	Variable	Separation
1	$\Delta\phi_{ll}$	0.1298
2	$C_{\phi}(E_{\text{T}}^{\text{miss}})$	0.1243
3	$m_{\tau\tau}^{\text{MMC}}$	0.1240
4	m_{ll}	0.1162
5	S	0.1152
6	p_{T}^{j1}	0.1060
7	$E_{\text{T}}^{\text{miss}}/p_{\text{T}}^{l2}$	0.09890
8	$m_{\tau\tau,j1}$	0.09294
9	p_{T}^{l1}	0.09285

(b) BDT1 - specific ranking

Rank	Variable	Separation
1	$m_{\tau\tau}^{\text{MMC}}$	0.2932
2	$m_{\tau\tau,j1}$	0.03425
3	m_{ll}	0.03066
4	$E_{\text{T}}^{\text{miss}}/p_{\text{T}}^{l2}$	0.01617
5	$\Delta\phi_{ll}$	0.01600
6	S	0.01051
7	p_{T}^{j1}	0.009600
8	$C_{\phi}(E_{\text{T}}^{\text{miss}})$	0.007787
9	p_{T}^{l1}	0.006549

(c) BDT2 - generic ranking

Rank	Variable	Separation
1	$m_{\tau\tau}^{\text{MMC}}$	0.1297
2	$\Delta\phi_{ll}$	0.1255
3	m_{ll}	0.1229
4	$C_{\phi}(E_{\text{T}}^{\text{miss}})$	0.1177
5	S	0.1154
6	p_{T}^{j1}	0.1041
7	$E_{\text{T}}^{\text{miss}}/p_{\text{T}}^{l2}$	0.09889
8	$m_{\tau\tau,j1}$	0.09424
9	p_{T}^{l1}	0.09165

(d) BDT2 - specific ranking

Table 6.9: Rankings of performance of the different variables in two BDTs of the Boosted category. The rankings are shown as given by the TMVA framework.

In Figure 6.19, the distributions of the training samples for the signal (blue) and background (red) are shown as a binned distribution for the two BDTs of each category. On top of them, the test samples are drawn as dots, with their statistical error. The Kolmogorov-Smirnov test (KS test) is computed for each of the distributions. This compatibility test is used to estimate the level of training bias.

Finally, in Figure 6.20, the ROC curve of both BDTs for each category is shown. As the training and test samples are divided in two equal subsets for the cross-validation, it is expected that both of them have a similar efficiency. The curve for the two BDTs, both for the VBF and Boosted categories, are totally compatible between them. It can also be observed in this plot that the VBF category has a significantly higher area under the curve than the Boosted category.

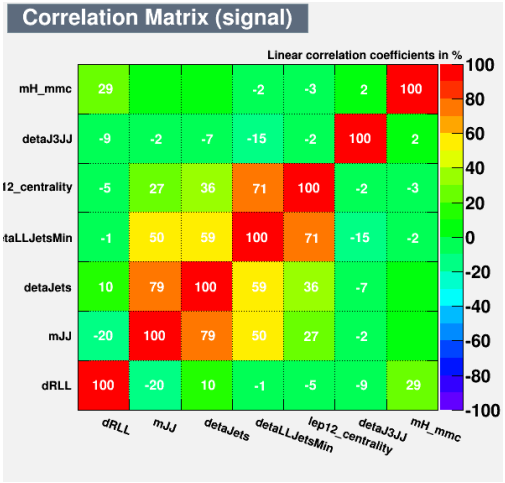

(a) VBF Signal

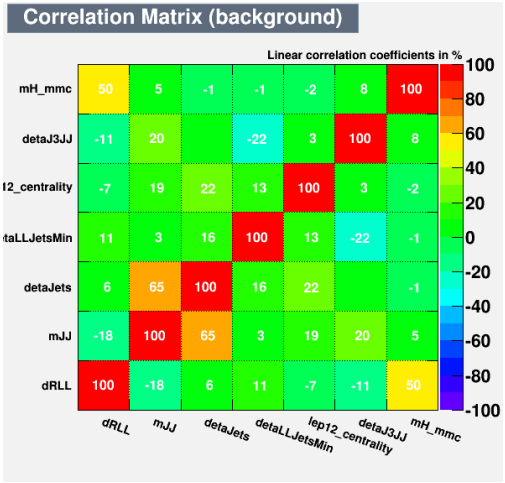

(b) VBF Background

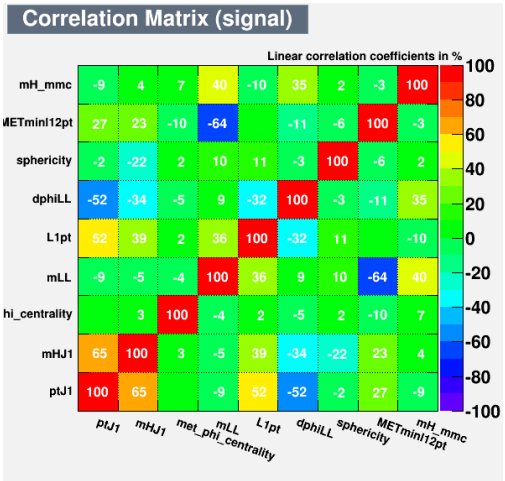

(c) Boosted Signal

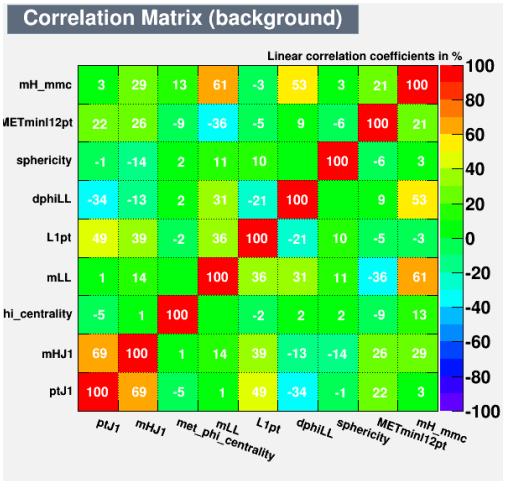

(d) Boosted Background

Figure 6.18: Correlation matrices for signal and background models for the VBF and Boosted categories.

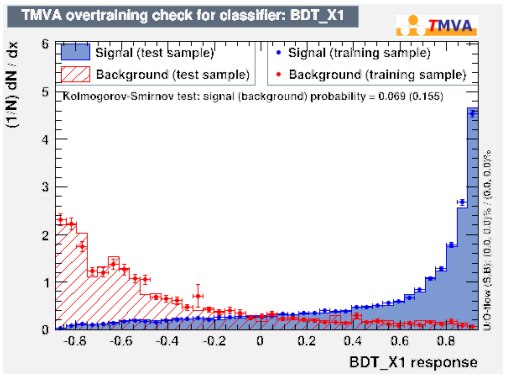

(a) VBF BDT1

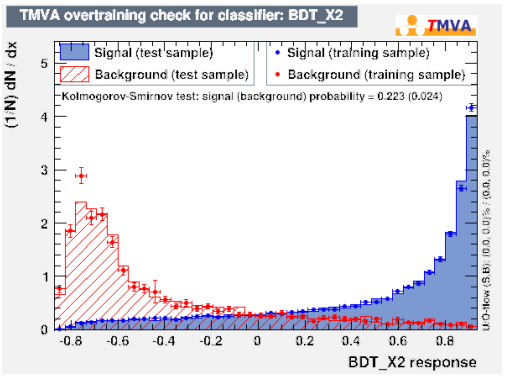

(b) VBF BDT2

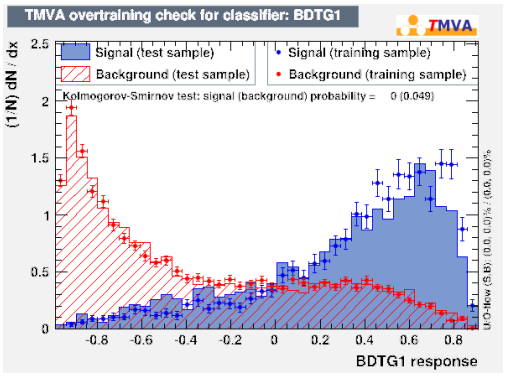

(c) Boosted BDT1

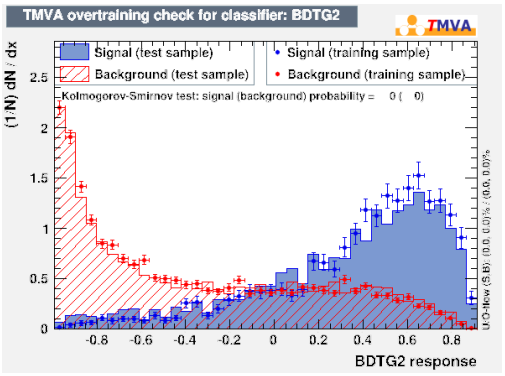

(d) Boosted BDT2

Figure 6.19: Signal and background distribution and Kolmogorov-Smirnov test for the two BDT of the VBF and Boosted categories.

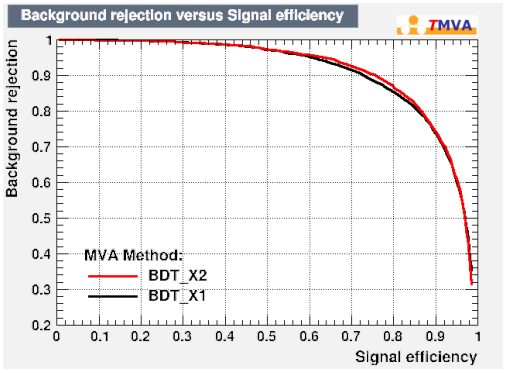

(a) VBF

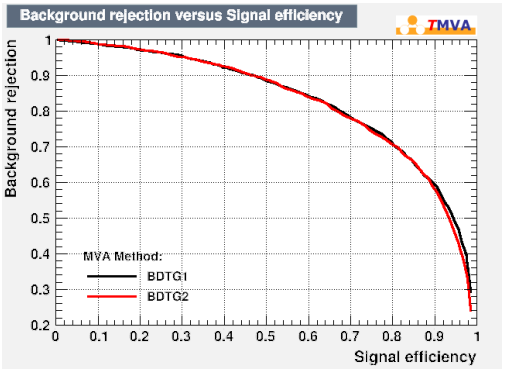

(b) Boosted

Figure 6.20: ROC curve for the two BDT for the (a) VBF and (b) Boosted categories.

6.8 Results of the MVA analysis in the $\tau_{\text{lep}}\tau_{\text{lep}}$ channel

Several input variables are given to the BDT algorithm, which is applied to data to obtain the final discriminant variable: the **BDT Score**. This is done in the two categories for the signal region and the control regions, for 7 TeV and 8 TeV datasets. In the BDT output distributions, the signal is concentrated in the bins with the highest BDT score while the background peaks at low values of the distribution. In addition, due to its importance in the analysis, the $m_{\tau\tau}^{\text{MMC}}$ variable is also shown for each of the categories and regions. The figures shown in this section correspond to the $\tau_{\text{lep}}\tau_{\text{lep}}$ channel for the 8 TeV dataset. The $\tau_{\text{lep}}\tau_{\text{had}}$ and $\tau_{\text{had}}\tau_{\text{had}}$ channels and the 7 TeV dataset are briefly reviewed in Section 6.9.3 while additional distributions can be found in Appendix B.

The results for each category, BDT output and $m_{\tau\tau}^{\text{MMC}}$, are shown in the SR and the two CR, for the VBF category in Figure 6.21 and for the Boosted category in Figure 6.22. The distributions in the CR show a good agreement between the data and the model, thus proving that the backgrounds are well estimated in the analysis. For the BDT output in the SR, any possible excess should be observed in the last bins of the distributions, which are the ones sensitive to the presence of signal. For the $m_{\tau\tau}^{\text{MMC}}$ distribution, the excess should be expected around $m_H = 125$ GeV for the SM Higgs boson.

Moreover, the event yields after the full selection of the $\tau_{\text{lep}}\tau_{\text{lep}}$ channel are shown in Table 6.10. These yields are the prediction of the fit-model, explained in Section 6.10.4, and the observation of data events, which have passed the full selection of each of the categories of the analysis. In addition to the total numbers, the values of the last and second-to-last bin, which are the bins with the highest contribution of signal events, are shown.

The background and signal normalizations and their uncertainties represent the post-fit values. The uncertainties on the total background and total signal represent the full statistical and systematic uncertainty, while the uncertainties on the individual background components represent the full systematic uncertainty.

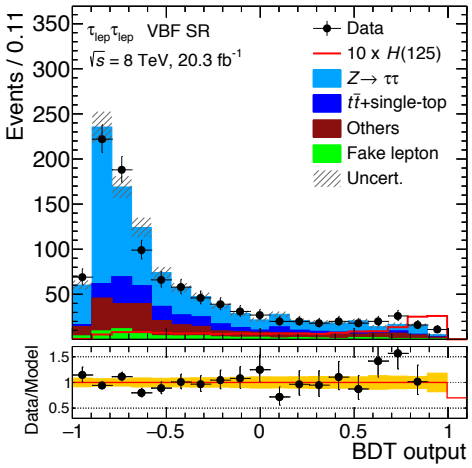

(a) BDT Score SR

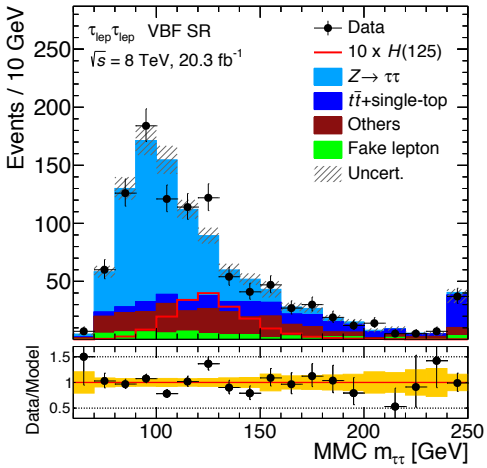

(b) $m_{\tau\tau}^{\text{MMC}}$ SR

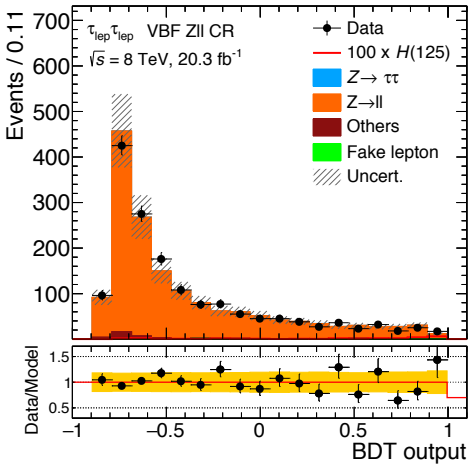

(c) BDT Score Zll CR

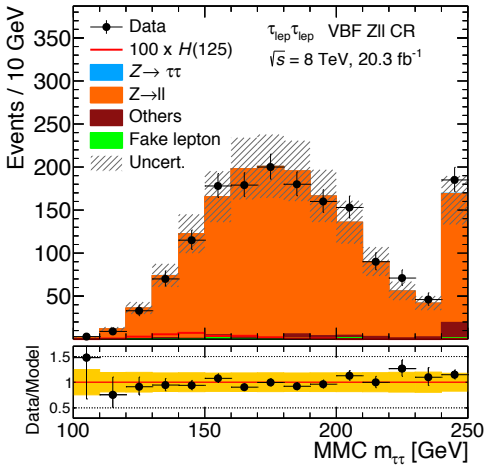

(d) $m_{\tau\tau}^{\text{MMC}}$ Zll CR

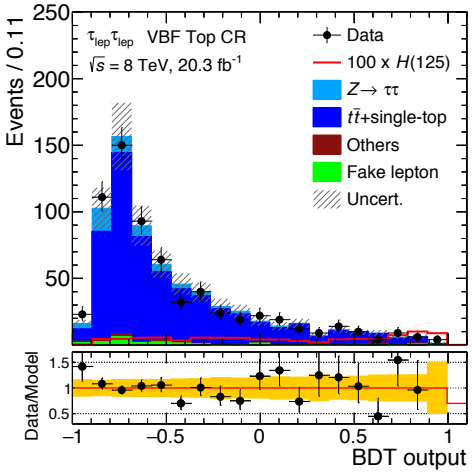

(e) BDT Score Top CR

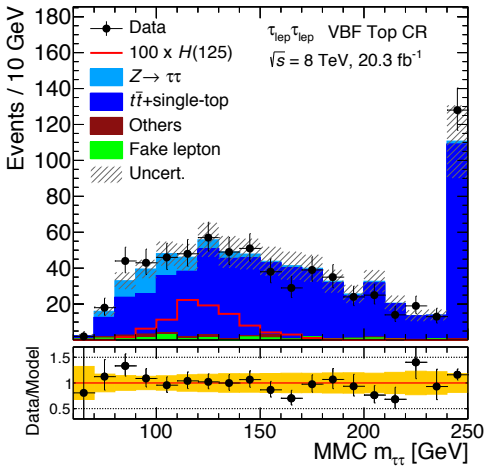

(f) $m_{\tau\tau}^{\text{MMC}}$ Top CR

Figure 6.21: Distributions of the BDT Score and $m_{\tau\tau}^{\text{MMC}}$ distributions in the VBF category of the $\tau_{\text{lep}}\tau_{\text{lep}}$ channel for the (top) signal region, (middle) Zll control region and (bottom) Top control region.

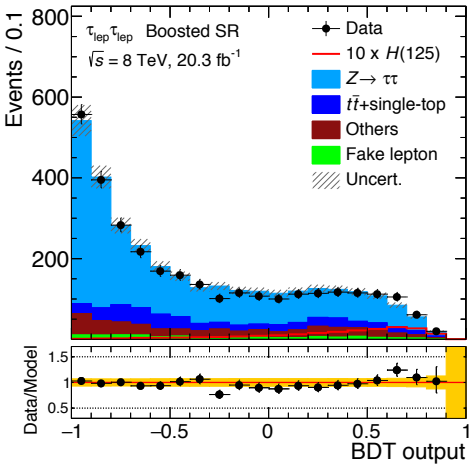

(a) BDT Score SR

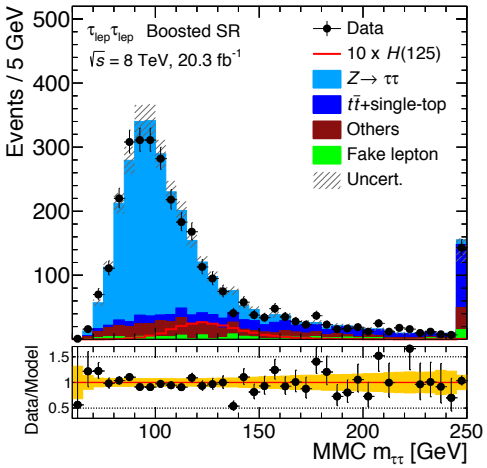

(b) $m_{\tau\tau}^{\text{MMC}}$ SR

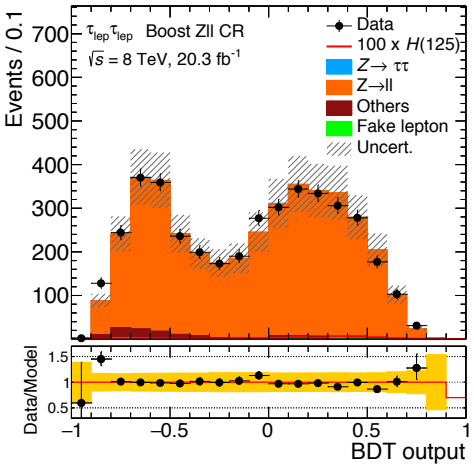

(c) BDT Score Zll CR

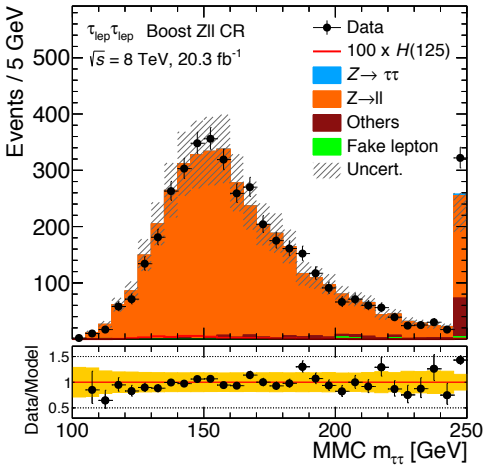

(d) $m_{\tau\tau}^{\text{MMC}}$ Zll CR

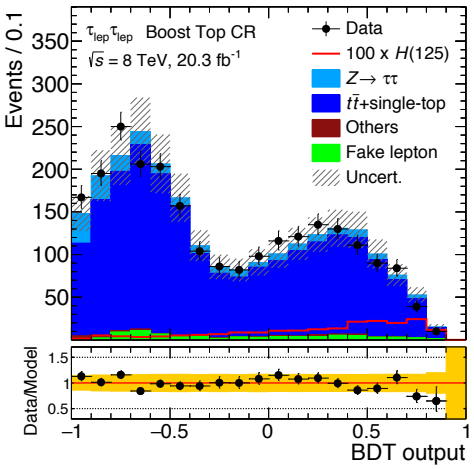

(e) BDT Score Top CR

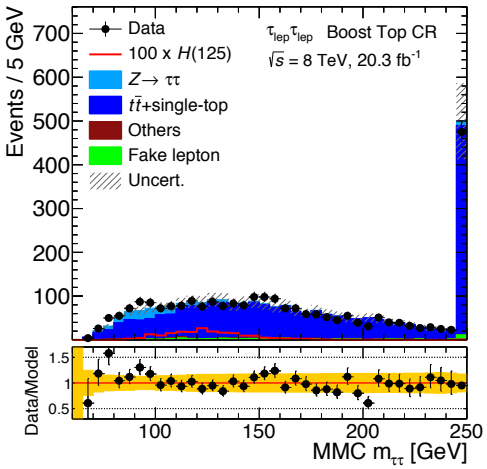

(f) $m_{\tau\tau}^{\text{MMC}}$ Top CR

Figure 6.22: Distributions of the BDT Score and $m_{\tau\tau}^{\text{MMC}}$ distributions in the Boosted category of the $\tau_{\text{lep}}\tau_{\text{lep}}$ channel for the (top) signal region, (middle) Zll control region and (bottom) Top control region.

Process			VBF			Boosted		
			All bins	Second to last bin	Last bin	All bins	Second to last bin	Last bin
Background	$Z \to \tau\tau$		589 ± 24	9.7 ± 1.0	1.99 ± 0.34	2190 ± 80	33.7 ± 2.3	11.3 ± 1.3
	Fake background		57 ± 12	1.2 ± 0.6	0.55 ± 0.35	100 ± 40	2.9 ± 1.3	0.6 ± 0.4
	Top		131 ± 19	0.9 ± 0.4	0.89 ± 0.33	380 ± 50	9.8 ± 2.1	4.3 ± 1.0
	Others		196 ± 17	3.0 ± 0.4	1.7 ± 0.6	400 ± 40	8.3 ± 1.6	2.6 ± 0.7
	$H \to WW$	*ggH*	2.9 ± 0.8	0.12 ± 0.04	0.11 ± 0.04	7.7 ± 2.3	0.43 ± 0.13	0.24 ± 0.08
		VBF	3.4 ± 0.4	0.40 ± 0.06	0.38 ± 0.08	1.65 ± 0.18	0.102 ± 0.017	< 0.1
		WH	< 0.1	< 0.1	< 0.1	0.90 ± 0.10	< 0.1	< 0.1
		ZH	< 0.1	< 0.1	< 0.1	0.59 ± 0.07	< 0.1	< 0.1
Signal	$H \to \tau\tau$	*ggH*	9.8 ± 3.4	0.73 ± 0.26	0.35 ± 0.14	21 ± 8	2.4 ± 0.9	1.3 ± 0.5
		VBF	13.3 ± 4.0	2.7 ± 0.7	3.3 ± 0.9	5.5 ± 1.5	0.95 ± 0.26	0.49 ± 0.13
		WH	0.25 ± 0.07	< 0.1	< 0.1	3.8 ± 1.0	0.44 ± 0.12	0.22 ± 0.06
		ZH	0.14 ± 0.04	< 0.1	< 0.1	2.0 ± 0.5	0.21 ± 0.06	0.113 ± 0.031
Total	Background		980 ± 22	15.4 ± 1.8	5.6 ± 1.4	3080 ± 50	55 ± 4	19.2 ± 2.1
	Signal		24 ± 6	3.5 ± 0.9	3.6 ± 1.0	33 ± 10	4.0 ± 1.2	2.1 ± 0.6
Total Signal+Background			1004 ± 23	19 ± 2	9.2 ± 1.7	3113 ± 51	59 ± 4	21.3 ± 2.2
Observed Data			1014	16	11	3095	61	20

Table 6.10: The predicted post-fit event yields in the $\tau_{\text{lep}}\tau_{\text{lep}}$ channel for the total number of events and for the two highest bins of the BDT distributions for the data taken at 8 TeV. The signal and $H \to WW$ processes are estimated for a Higgs boson with a mass of $m_H = 125$ GeV. The entry labeled as *Others* background covers the $Z \to ll$ and di-boson processes. The background normalizations, signal normalization, and their uncertainties represent the post-fit values. The uncertainties on the total background and total signal represent the full statistical and systematic uncertainty, while the uncertainties on the individual background components represent the full systematic uncertainty only.

6.9 Additional channels of the $H \to \tau\tau$ analysis

Since the final results of the analysis include the combination of all $\tau\tau$ channels, a short description of the $\tau_{\text{lep}}\tau_{\text{had}}$ and $\tau_{\text{had}}\tau_{\text{had}}$ channels is given below.

The $H \to \tau\tau$ analysis was optimized for the dataset taken in 2012, at $\sqrt{s} = 8\,\text{TeV}$. However, it was also applied on the dataset taken in 2011, at $\sqrt{s} = 7\,\text{TeV}$. A brief description of this implementation is given in Section 6.9.3.

Finally, a simplified cut-based analysis was implemented, as a consistency test for the MVA analysis. The details of this analysis are given in Section 6.9.4, while the compatibility of this result with the main MVA result is discussed in Section 6.11.2

6.9.1 The $\tau_{\text{lep}}\tau_{\text{had}}$ channel

The semi-leptonic channel, $\tau_{\text{lep}}\tau_{\text{had}}$, takes advantages of the easy identification of a high energetic lepton and the high proportion of hadronic decaying τ, requiring one τ_{had} candidate and one isolated lepton, passing the p_{T} requirements of Table 6.3 and with OS.

Besides the $Z \to \tau\tau$ process, the main backgrounds in the $\tau_{\text{lep}}\tau_{\text{had}}$ channel are the multi-jet and W+jets, where one jet is misidentified as a τ_{had}. Di-boson, $t\bar{t}$ and $Z \to ll$ are additional backgrounds. The $Z \to \tau\tau$ background is estimated with the embedding technique while the multi-jet and W+jets which both fake τ_{had} are estimated with another data-driven technique called *fake factor* method. The rest of backgrounds are estimated using MC simulations.

The event selection is done by applying a cut in the transverse mass (defined in Section 6.3), rejecting events with $m_{\text{T}} > 70\,\text{GeV}$, to reduce the contribution of W+jets. The $t\bar{t}$ background is suppressed by rejecting events with a b-jet with $p_{\text{T}} > 30\,\text{GeV}$.

The SR and the categorization is done in the same way as in the $\tau_{\text{lep}}\tau_{\text{lep}}$ channel. However, regarding the CRs and VRs there are some differences. As the $Z \to ll$ process is not a relevant background in this channel, there is no dedicated CR for this background. On the other hand, a Top CR, which is used in the global fit, is defined by inverting the b-veto condition and requiring $m_{\text{T}} > 40\,\text{GeV}$, to enhance the top background and suppress the signal contribution. Validation regions with enriched backgrounds are defined for the $Z \to \tau\tau$ process ($m_{\tau\tau}^{\text{MMC}} < 110\,\text{GeV}$ and $m_{\text{T}} < 40\,\text{GeV}$), the W+jets ($m_{\text{T}} > 70\,\text{GeV}$) and the Fakes (SS events). The plot of the W-enriched CR is shown in Figure 6.23.

The BDT defined in the $\tau_{\text{lep}}\tau_{\text{had}}$ channel is a Gradient BDT with the following variables as a input:

- For the VBF category: $m_{\tau\tau}^{\text{MMC}}$, m_{T}, $C_{\phi}(E_{\text{T}}^{\text{miss}})$, $\Delta R(\tau, l)$, m_{jj}, $\eta_{j1} \times \eta j2$, $\left|\eta_{j2} - \eta j1\right|$, $C_{\eta}(l)$, $p_{\text{T}}^{\text{total}}$.
- For the Boosted category: $m_{\tau\tau}^{\text{MMC}}$, m_{T}, $C_{\phi}(E_{\text{T}}^{\text{miss}})$, $\Delta R(\tau, l)$, Σp_{T}, $p_{\text{T}}(\tau)/p_{\text{T}}(l)$.

  where:

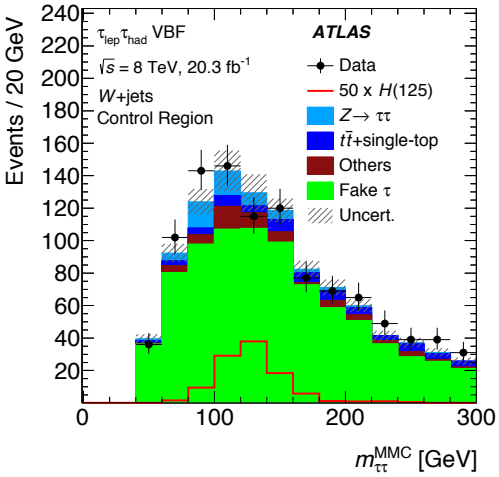

Figure 6.23: Pre-fit distribution of the W-enriched CR of the $\tau_{\text{lep}}\tau_{\text{had}}$ channel for the data collected at 8 TeV. The contributions from a Standard Model Higgs boson with $m_H = 125$ GeV are superimposed, multiplied by a factor of 50. The error band includes statistical and pre-fit systematic uncertainties [155].

$$p_{\text{T}}^{\text{total}} \equiv \left| \vec{p_{\text{T}}^{l}} + \vec{p_{\text{T}}^{\tau_{\text{had}}}} + \vec{p_{\text{T}}^{j1}} + \vec{p_{\text{T}}^{j2}} + \vec{E_{\text{T}}^{\text{miss}}} \right| \tag{6.11}$$

$$\Sigma p_{\text{T}} \equiv p_{\text{T}}^{l} + p_{\text{T}}^{\tau_{\text{had}}} + p_{\text{T}}^{j1} + p_{\text{T}}^{j2} \tag{6.12}$$

Four examples of these variables (two for each category) are shown in Figure 6.24. The event yields of the channel can be found in Appendix B.1.

6.9.2 The $\tau_{\text{had}}\tau_{\text{had}}$ channel

The fully-hadronic channel, $\tau_{\text{had}}\tau_{\text{had}}$, aims at detecting events in which both τ decay hadronically. The hadronic decay of the τ is the most abundant one, thus the $\tau_{\text{had}}\tau_{\text{had}}$ has the advantage of large statistics, similar to the $\tau_{\text{lep}}\tau_{\text{had}}$ channel. On the other hand, its main challenge is the discrimination of the hadronic τ (τ_{had}) from the background of non-τ jets.

Besides the $Z \to \tau\tau$ process, estimated by the embedding technique, the main background of this channel is the QCD multi-jet production in which two jets are misidentified as τ_{had}. This background is estimated using a template extracted from data, with the same selection as the categories but inverting the isolation and charge requirements. Its normalization is determined by a simultaneous fit of the data template and a $Z \to \tau\tau$ template in the $\Delta\eta(\tau_{\text{had}}^1, \tau_{\text{had}}^2)$ distribution. In order to improve the fit and constrain the $Z \to \tau\tau$ and multi-jet processes, a control region called *Rest* is defined by collecting all the events which fail the selection of both categories. Figure 6.25 shows the $\Delta\eta(\tau_{\text{had}}^1, \tau_{\text{had}}^2)$ in the Rest category of the $\tau_{\text{had}}\tau_{\text{had}}$ channel.

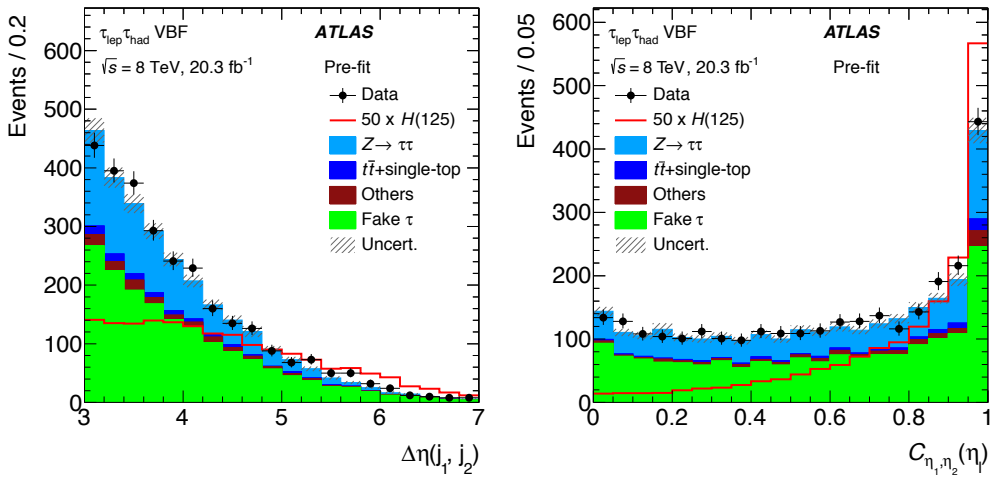

(a) VBF $|\Delta\eta_{jj}|$ (b) VBF $C_\eta(l)$

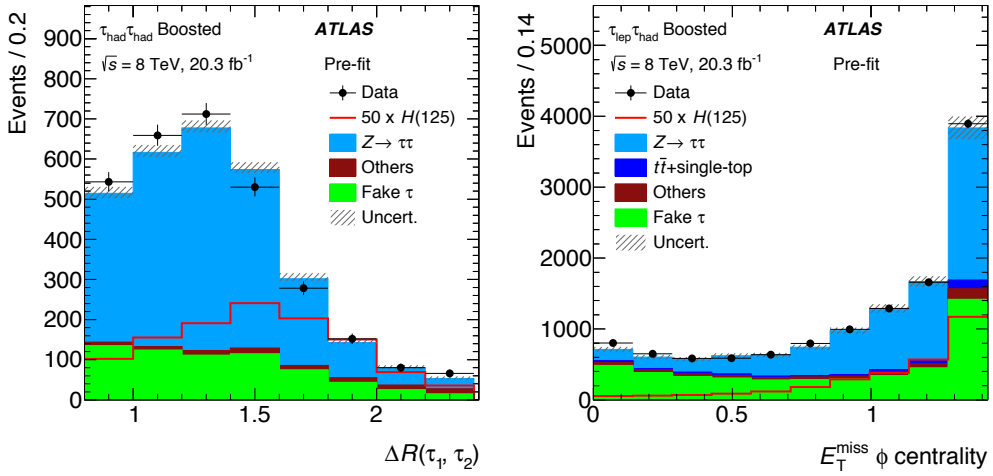

(c) Boosted $\Delta R(\tau_1, \tau_2)$ (d) Boosted $C_\phi(E_{\mathrm{T}}^{\mathrm{miss}})$

Figure 6.24: Pre-fit distributions of several input variables of the BDT of the $\tau_{\mathrm{lep}}\tau_{\mathrm{had}}$ channel for the two categories, VBF (top) and Boosted (bottom), for the data collected at 8 TeV. The contributions from a Standard Model Higgs boson with $m_H = 125$ GeV are superimposed, multiplied by a factor of 50. The error band includes statistical and pre-fit systematic uncertainties [155].

Other background processes in this channel are W+jets (specially $W \to \tau\nu$), di-boson and top, with a real τ and a jet faking the second τ identification. These contributions, however, pay a minor role and are modeled by MC.

The event discrimination in the $\tau_{\mathrm{had}}\tau_{\mathrm{had}}$ relies mainly in the accurate identification of τ_{had}. The event selection is done by requiring two isolated τ_{had} candidates, in which one of them passes the "tight" requirements, while the second one passes the "medium" requirements, as were described in Section 5.5. A veto is applied to events which contain a lepton object, either electron or muon. In addition, the $E_{\mathrm{T}}^{\mathrm{miss}}$ must satisfy the condition $E_{\mathrm{T}}^{\mathrm{miss}} > 20$ GeV and its direction must either be between the two visible τ_{had} candidates in ϕ or within $\Delta\phi < 0.4$ of the nearest τ_{had} candidate.

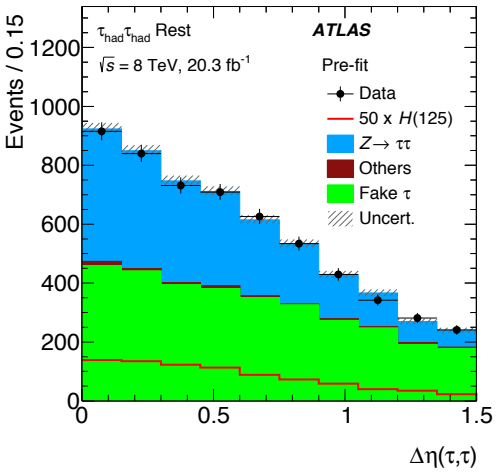

Figure 6.25: Pre-fit distribution of the Rest CR of the $\tau_{\text{had}}\tau_{\text{had}}$ channel for the data collected at 8 TeV. The contributions from a Standard Model Higgs boson with $m_H = 125$ GeV are superimposed, multiplied by a factor of 50. The error band includes statistical and pre-fit systematic uncertainties [155].

The BDT defined in the $\tau_{\text{had}}\tau_{\text{had}}$ channel is an AdaBoost BDT with the following variables as a input:

- For the VBF category: $m_{\tau\tau}^{\text{MMC}}$, $C_\phi(E_{\text{T}}^{\text{miss}})$, $\Delta R(\tau\tau)$, m_{jj}, $\eta_{j1} \times \eta_{j2}$, $|\eta_{j2} - \eta_{j1}|$, $C_\eta(\tau_1)$, $C_\eta(\tau_2)$, p_{T}^{total}.
- For the Boosted category: $m_{\tau\tau}^{\text{MMC}}$, $C_\phi(E_{\text{T}}^{\text{miss}})$, $\Delta R(\tau,\tau)$, $p_{\text{T}}(\tau_1)/p_{\text{T}}(\tau_2)$, Σp_{T}. with Σp_{T} defined as in the $\tau_{\text{lep}}\tau_{\text{had}}$ channel.

Four examples of these variables (two for each category) are shown in Figure 6.26, the event yields of the channel can be found in Appendix B.1.

6.9.3 The 2011 dataset

As explained in Section 6.1, the analysis used the data from 2011 at $\sqrt{s} = 7$ TeV and from 2012 at $\sqrt{s} = 8$ TeV. As the data-taking conditions changed significantly, the optimal approach is to optimize both datasets independently. However, the 7 TeV sample has a reduced statistics, as it collected roughly one fourth of the integrated luminosity of the 8 TeV sample at a smaller center-of-mass energy. This applies as well to the MC samples for the BDT training, where a large dataset is a fundamental requirement.

Thus, the 7 TeV dataset was added, employing the selection criteria and BDT training optimized for the 8 TeV dataset. This addition has a moderated positive impact in the overall $H \to \tau\tau$ analysis, increasing the sensitivity roughly 5%.

The main differences in the object reconstruction and the event selection (especially regarding the trigger requirements) are reviewed in the corresponding sections. In total, 4.5 fb^{-1} of data taken at a e.c.m. of $\sqrt{s} = 7$ TeV were analyzed. The resulting BDT

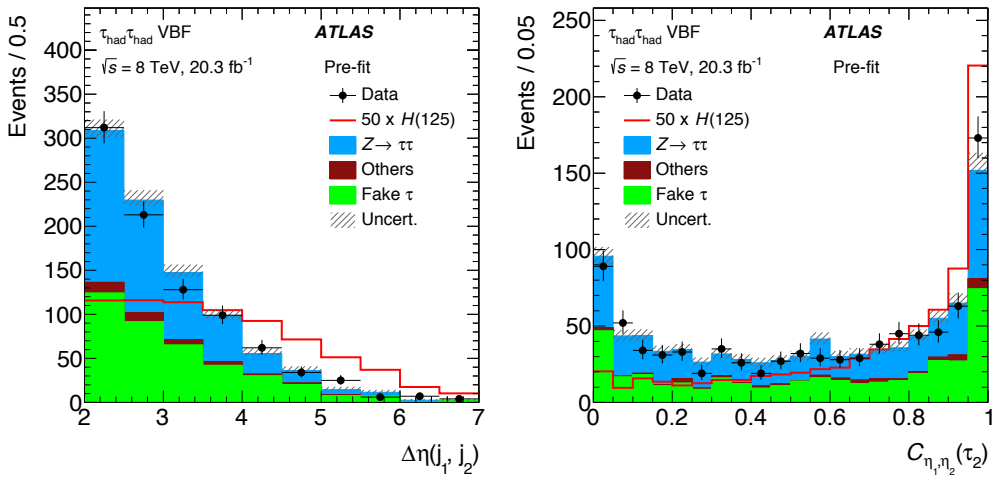

(a) VBF $|\Delta\eta_{jj}|$ (b) VBF $C_\eta(\tau_2)$

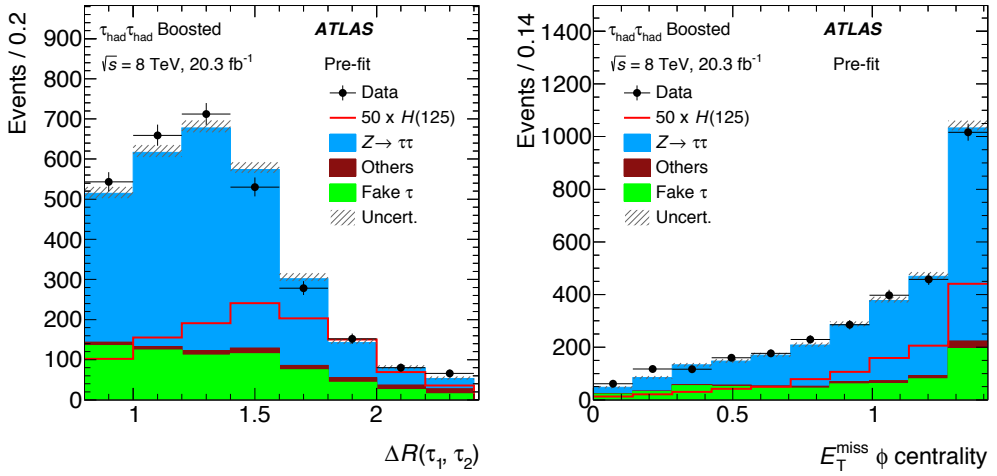

(c) Boosted $\Delta R(\tau_1, \tau_2)$ (d) Boosted $C_\phi(E_{\mathrm{T}}^{\mathrm{miss}})$

Figure 6.26: Pre-fit distributions of several input variables of the BDT of the $\tau_{\mathrm{had}}\tau_{\mathrm{had}}$ channel for the two categories, VBF (top) and Boosted (bottom), for the data collected at 8 TeV. The contributions from a Standard Model Higgs boson with $m_H = 125$ GeV are superimposed, multiplied by a factor of 50. The error band includes statistical and pre-fit systematic uncertainties [155].

Score and the $m_{\tau\tau}^{\mathrm{MMC}}$ plots are shown in Appendix B. The results of this analysis and their combination with the 8 TeV dataset are discussed in Section 6.11.

6.9.4 The cut-based analysis

In order to have a independent check of the MVA result, a second approach for the signal discrimination was performed in parallel to the MVA analysis, following a standard cut-based strategy. This cut-based analysis was developed adapting and updating a previous version of the 7 TeV dataset [151], improving the categorization and fit model. However, as the aim of this study is the cross-check of the MVA algorithm, the cut-based

analysis was not optimized to achieve the maximum sensitivity but to replicate the MVA phase-space. It is expected that the cut-based performs worse that the MVA analysis, but its aim is to study the consistency of both results.

The cut-based analysis employs only the 8 TeV dataset, as the limited statistics of the 7 TeV dataset did not add a significant improvement. The event selection in the cut-based analysis follows the same structure as with the MVA, but it includes some optimization in the definition of the categories. Furthermore, the $\tau_{\text{lep}}\tau_{\text{had}}$ and $\tau_{\text{had}}\tau_{\text{had}}$ channels made a finer categorization, dividing the VBF and Boosted categories into sub-categories. The summary of the event selection of the cut-based analysis is given in Table 6.11

The main difference between the MVA and cut-based analyses is the variable of interest. The MVA analysis uses the BDT Score as the discriminant distribution used in the signal extraction, while in the cut-based analysis the variable with the highest discriminant power was used: the $m_{\tau\tau}^{\text{MMC}}$ invariant mass. Additionally, this variable is sensitive to the value of the Higgs boson mass itself.

The results of the cut-based analysis, the main plots and the discussion of the compatibility with the MVA analysis, are shown in Section 6.11.2. The event yields of the cut-based analysis can be found in Appendix B.

<table>
<tr><th rowspan="2">Channel</th><th colspan="5">Category selection criteria</th></tr>
<tr><th colspan="3">VBF</th><th colspan="2">Boosted</th></tr>
<tr><td>$\tau_{\text{lep}}\tau_{\text{lep}}$</td><td colspan="3">At least two jets with $p_{\text{T}}^{j_1} > 40\,\text{GeV}$ and $p_{\text{T}}^{j_2} > 30\,\text{GeV}$
$|\Delta\eta_{jj}| > 3.0$
$m_{jj} > 400\,\text{GeV}$
b-jet veto for jets with $p_{\text{T}} > 25\,\text{GeV}$
Jet veto: no additional jet with $p_{\text{T}} > 25\,\text{GeV}$ within $|\eta| < 2.4$</td><td colspan="2">Exclude events passing the VBF selection
$p_{\text{T}}^{\tau\tau} > 100\,\text{GeV}$
b-jet veto for jets with $p_{\text{T}} > 25\,\text{GeV}$</td></tr>
<tr><td rowspan="3">$\tau_{\text{lep}}\tau_{\text{had}}$</td><td colspan="3">At least two jets with $p_{\text{T}}^{j_1} > 40\,\text{GeV}$ and $p_{\text{T}}^{j_2} > 30\,\text{GeV}$
$E_{\text{T}}^{\text{miss}} > 20\,\text{GeV}$
$|\Delta\eta_{jj}| > 3.0$ and $\eta(j_1)\cdot\eta(j_2) < 0$
$m_{jj} > 300\,\text{GeV}$
b-jet veto for jets with $p_{\text{T}} > 30\,\text{GeV}$
$\min(\eta_{(j_1)}, \eta_{(j_2)}) < \eta_{(l)}, \eta_{(\tau_{\text{had}})} < \max(\eta_{(\text{j}_1)}, \eta_{(\text{j}_2)})$</td><td colspan="2" rowspan="3">Exclude events passing the VBF selection
$E_{\text{T}}^{\text{miss}} > 20\,\text{GeV}$
$p_{\text{T}}^{\tau\tau} > 100\,\text{GeV}$
$p_{\text{T}}(\tau_{\text{had}}) > 30\,\text{GeV}$ and $p_{\text{T}}^{\text{total}} < 30\,\text{GeV}$
b-jet veto for jets with $p_{\text{T}} > 30\,\text{GeV}$</td></tr>
<tr><td colspan="2">VBF tight</td><td>VBF loose</td></tr>
<tr><td colspan="2">$m_{jj} > 500\,\text{GeV}$, $p_{\text{T}}^{\tau\tau} > 100\,\text{GeV}$
$p_{\text{T}}^{\tau_{\text{had}}} > 30\,\text{GeV}$, $m_{\text{vis}} > 40\,\text{GeV}$</td><td>Non tight VBF</td></tr>
<tr><td rowspan="3">$\tau_{\text{had}}\tau_{\text{had}}$</td><td colspan="4">At least two jets with $p_{\text{T}}^{j_1} > 50\,\text{GeV}$ and $p_{\text{T}}^{j_2} > 30\,\text{GeV}$
$|\Delta\eta(\tau_1,\tau_2)| < 1.5$
$|\Delta\eta_{jj}| > 2.6$ and $m_{j_1,j_2} > 250\,\text{GeV}$
$\min(\eta_{(j_1)}, \eta_{(j_2)}) < \eta_{(\tau_1)}, \eta_{(\tau_2)} < \max(\eta_{(j_1)}, \eta_{(j_2)})$</td><td colspan="2">Exclude events passing the VBF selection
$|\Delta\eta(\tau_1,\tau_2)| < 1.5$
$p_{\text{T}}^{\tau\tau} > 100\,\text{GeV}$</td></tr>
<tr><td>VBF high $p_{\text{T}}^{\tau\tau}$</td><td colspan="2">VBF low $p_{\text{T}}^{\tau\tau}$, tight</td><td>VBF low $p_{\text{T}}^{\tau\tau}$, loose</td><td>Boosted high $p_{\text{T}}^{\tau\tau}$</td><td>Boosted low $p_{\text{T}}^{\tau\tau}$</td></tr>
<tr><td>$\Delta R(\tau_1,\tau_2) < 1.5$
$p_{\text{T}}^{\tau\tau} > 140\,\text{GeV}$</td><td colspan="2">$\left[\Delta R(\tau_1,\tau_2) > 1.5$ or
$p_{\text{T}}^{\tau\tau} < 140\,\text{GeV}\right]$
$m_{jj}[\,\text{GeV}] >$
$(-250\cdot|\Delta\eta_{jj}| + 1550)$</td><td>$\left[\Delta R(\tau_1,\tau_2) > 1.5$ or
$p_{\text{T}}^{\tau\tau} < 140\,\text{GeV}\right]$
$m_{jj}[\,\text{GeV}] <$
$(-250\cdot|\Delta\eta_{jj}| + 1550)$</td><td>$\Delta R(\tau_1,\tau_2) < 1.5$
and
$p_{\text{T}}^{\tau\tau} > 140\,\text{GeV}$</td><td>$\Delta R(\tau_1,\tau_2) > 1.5$
or
$p_{\text{T}}^{\tau\tau} < 140\,\text{GeV}$</td></tr>
</table>

Table 6.11: Selection criteria used to define the VBF and Boosted categories in the cut-based analysis for the three analysis channels.

6.10 Systematic uncertainties and signal extraction method

A careful study of the uncertainties affecting each of the key aspects of the analysis is needed to obtain a precise and consistent result, even more when using a MVA algorithm. The uncertainties are grouped in three categories: theoretical, experimental, and background modeling uncertainties. For all of them, the impacts on the total signal and background yields and on the shape of the BDT output distributions are evaluated. Table 6.12 summarizes the most relevant relative variations that affect the $\tau_{\text{lep}}\tau_{\text{lep}}$ channel in the two categories.

6.10.1 Theoretical uncertainties

The theoretical uncertainties are estimated for the signal and the background contributions which have been modeled by MC simulations (all except $Z \to \tau\tau$ and fake leptons). Uncertainties on the signal cross-sections are assigned from missing higher-order corrections, from uncertainties in the PDFs and from uncertainties in the modeling of the underlying event.

For VBF and *VH* production cross-sections of the Higgs boson signal, the uncertainties due to missing higher-order QCD corrections are estimated by varying the factorization and renormalization scales by factors of two around the nominal scale m_W, as prescribed by the LHC Higgs Cross Section Working Group [80], which results in uncertainties in the range from ±2% to ±4%, depending on the process and the category considered. In addition, a 2% uncertainty related to the inclusion of the NLO EW corrections is applied.

For Higgs boson production via *ggH*, the uncertainties on the cross-sections due to missing higher-order QCD corrections are estimated by varying the renormalization and factorization scales around the central values $\mu_{\text{R}} = \mu_{\text{F}} = \sqrt{m_H^2 + p_{\text{T}}^2}$ in the NLO cross-section calculations of H + 1-jet and H + 2-jet production. In the calculation of the uncertainties, appropriate cuts on the Higgs p_{T} ($p_{\text{T}}^{\tau\tau} > 100\,\text{GeV}$) and on the jet kinematics ($\Delta\eta, p_{\text{T}}$) are applied at parton level for the Boosted and VBF categories, respectively. The resulting uncertainties on the *ggH* contributions are found to be about ±24% in the Boosted category and ±23% in the VBF category. The *ggH* contribution is dominant in the Boosted category, while it is only about 20% of the signal in the VBF category. Since the two categories are exclusive, their anti-correlation is taken into account. The uncertainty on the BDT shape of the *ggH* contribution is evaluated using the MCFM Monte Carlo program [196], which calculates H + 3 jets at LO. Scale variations induce changes of the *ggH* contribution in the highest BDT bin of about ±30%, which are taken into account in the final fit.

Uncertainties related to the simulation of the Underlying Event (UE) and Parton Shower (PS) are estimated by comparing the acceptance from POWHEG+PYTHIA

to POWHEG+HERWIG for both VBF and *ggH* production modes. Differences in the signal yields range from ±1% to ±8% for the VBF and from ±1% to ±9% for *ggH* production, depending on the channel and category. The BDT Score distribution of the POWHEG+PYTHIA and POWHEG+HERWIG samples are compatible with each other within statistical uncertainties.

The PDF uncertainties are estimated by studying the change in the acceptance when using different PDF sets or varying the CT10 PDF set within its uncertainties. The standard VBF POWHEG sample and a MC@NLO [209] *ggH* sample, both generated with the CT10 PDFs, are reweighted to the MSTW2008NLO [76], NNPDF [210] and the CT10 eigen-tunes parameterization. The largest variation in acceptance for each category is used as a constant PDF uncertainty; it varies between approximately ±4.5% and ±6% for *ggH* production and between about ±0.8% and ±1.0% for VBF production. A shape uncertainty is also included to cover any difference between the BDT Score in the default sample and the reweighted ones. The uncertainty on the total cross-section for the VBF, *VH* and *ggH* production modes due to the PDFs is also considered.

Variations in the acceptance for different Monte Carlo generators are also included, comparing POWHEG+HERWIG samples to MC@NLO+HERWIG samples for *ggH*, and to AMC@NLO+HERWIG samples for VBF. The generator modeling uncertainty is around ±2% for *ggH* and ±4% for VBF productions modes.

The theoretical systematic uncertainties on the background predictions taken from the simulation are evaluated by applying the same procedures as used for the signal samples. Uncertainties resulting from the choice of QCD scales, PDF parameterization and underlying event model are estimated.

6.10.2 Experimental uncertainties

The major experimental systematic uncertainties result from uncertainties on efficiencies for triggering, object reconstruction and identification, as well as from uncertainties on the energy scale and resolution of jets, hadronically decaying taus and leptons. In general, the effects resulting from lepton-related uncertainties are smaller than those from jets and taus. In addition, uncertainties on the luminosity affect the number of signal and background events from simulation.

Luminosity uncertainty on the integrated luminosity is ±2.8% for the 8 TeV dataset and ±1.8% for the 7 TeV dataset. It is determined from a calibration of the luminosity scale derived from beam-separation scans performed in 2011 and 2012 using the method described in Ref. [211].

Efficiencies for triggering, reconstructing and identifying electrons, muons, and τ_{had} candidates are measured in data using tag-and-probe techniques. The uncertainties

on the τ_{had} identification efficiency are $\pm$[2–3]% for 1-prong and $\pm$[3–5]% for 3-prong tau decays [146]. The b-jet tagging efficiency has been measured from data using $t\bar{t}$ events, where both top quarks decay to leptons, with a total uncertainty of about $\pm$2% for jets with transverse momenta up to 100 GeV [143, 144]. The MC samples used are corrected for differences in these efficiencies between data and simulation and the associated uncertainties are propagated through the analysis.

Energy scale uncertainties on the Jet Energy Scale (JES) arise from several sources. These include, among others, varied response due to the jet flavor composition (quark- versus gluon-initiated jets), pile-up, η intercalibration, and detector response and modeling of in-situ jet calibration [142, 144]. The impact of the JES uncertainty in this analysis is reduced because many of the background components are estimated using data. The Tau Energy Scale (TES) is obtained by fitting the reconstructed visible mass for $Z \to \tau\tau$ events in data, which can be selected with a satisfactory purity. It is measured with a precision of $\pm[2-4]\%$ [212]. Since systematic uncertainties on the energy scales of all objects affect the reconstructed missing transverse momentum, it is recalculated after each variation is applied. The scale uncertainty on $E_{\text{T}}^{\text{miss}}$ due to the energy in calorimeter cells not associated with physics objects is also taken into account.

Energy resolution systematic uncertainties on the energy resolution of taus, electrons, muons, jets, and $E_{\text{T}}^{\text{miss}}$ affect the final discriminant. The effects resulting from uncertainties on the tau energy resolution (TER) are small. The impact of changes in the amount of material (inactive material in the detector, e.g. support structures), in the hadronic shower model and in the underlying-event tune were studied in the simulation. They result in systematic uncertainties below 1% on the TER . The jet energy resolution (JER) is determined by in-situ measurements, as described in Ref. [213], and affects signal modeling and background components modeled by the simulation. The uncertainty of the resolution on $E_{\text{T}}^{\text{miss}}$ is estimated by evaluating the energy resolution of each of the $E_{\text{T}}^{\text{miss}}$ terms. The largest impact results from the soft term, arising both from the MC modeling of low p_{T} particles and the effects of pile-up. It is evaluated using simulated $Z \to \mu\mu$ events.

6.10.3 Background modeling uncertainties

In the $\tau_{\text{lep}}\tau_{\text{lep}}$ channel, systematic uncertainties on the shape and normalization of the Fake background are estimated by comparing samples of same-sign lepton events that pass and fail the lepton isolation criteria. These uncertainties amount to $\pm$33% ($\pm$20%) at 8 TeV and $\pm$10.5% ($\pm$13%) at 7 TeV for the Boosted (VBF) category. The extrapolation uncertainty for the $Z \to ll$ background is obtained by varying the m_{ll} window that defines the control region for this background, and amounts to about $\pm$6%. The corresponding

extrapolation uncertainty for top quark background sources is $\pm[3-6]\%$, obtained from the differences in event yields in the top-quark control regions when using different MC generators. Neither of these extrapolation uncertainties is significant for the final result. The dominant uncertainties on the normalization of the $t\bar{t}$ background, obtained from the global fit, are the systematic uncertainties on the b-jet tagging efficiency and the JES.

For the embedding method used in the estimation of the $Z \to \tau\tau$ background, the major systematic uncertainties are related to the selection of $Z \to \mu\mu$ events in data and to the subtraction of the muon energy deposits in the calorimeters. The selection uncertainties are estimated by varying the muon isolation criteria in the selection from the nominal value to tighter (p_{T}-cone ratio < 0.06 and E_{T}-cone ratio < 0.04) and looser (no isolation requirements) values. The muon-related cell energies to be subtracted are varied within $\pm 20\%$ ($\pm 30\%$) for the 8 TeV (7 TeV) data. In addition, systematic uncertainties on the corrections for trigger and reconstruction efficiencies are taken into account. All experimental systematic uncertainties relating to the embedded τ decay products (such as TES or identification uncertainties) are applied normally.

An important issue to be studied is the validity of the extrapolation of the information obtained in the CR to the SR. This extrapolation is based on the assumption that the behavior of the background contribution in the SR is the same as in the CR. The assumption has been checked for the different cases, and – where relevant – a systematic uncertainty has been assigned. Additionally, since the normalization is corrected using control regions, the normalization uncertainties are the extrapolation uncertainties.

In the $\tau_{\mathrm{lep}}\tau_{\mathrm{lep}}$ channel, the extrapolation from the Zll control region is checked by varying the m_{ll} window cut used for defining this CR, and evaluating the corresponding normalization change. A systematic uncertainty of 5(3)% is applied for the $Z \to ee$ ($Z \to \mu\mu$) background. For the top background, the extrapolation uncertainty is obtained though the comparison of the CR to SR efficiency between two simulations, namely MC@NLO and POWHEG. The final uncertainty is 4% in the Boosted category and 7% in the VBF category. Additional checks were performed to demonstrate the robustness of the best μ value against a potential shift in the top background normalization in the corresponding CR.

6.10.4 Signal extraction method

The aim of the analysis is to measure a possible excess in data with respect to the background model and study its compatibility with the expected signal of the Higgs boson of the SM. For that, several signal regions are defined, where the backgrounds are reduced via selection cuts and the ratio signal over background is enhanced. The background model is validated using several Control and Validation Regions, where it

	VBF		**Boosted**	
Source/Variation [%]	S	B	S	B
Theoretical				
Higher-order QCD corrections†	$^{+11.3}_{-9.1}$	± 0.2	$^{+19.8}_{-15.3}$	± 0.2
UE/PS	$\pm$ 1.8	< 0.1	$\pm$ 5.9	< 0.1
Generator modeling	$\pm$ 2.3	< 0.1	± 1.2	< 0.1
EW corrections	$\pm$ 1.1	< 0.1	± 0.4	< 0.1
PDF †	$^{+4.5}_{-5.8}$	$\pm$ 0.3	$^{+6.2}_{-8.0}$	$\pm$ 0.2
BR ($H \to \tau\tau$)	$\pm$ 5.7	–	± 5.7	–
Experimental				
Luminosity	$\pm$ 2.8	$\pm$ 0.1	$\pm$ 2.8	± 0.1
Lepton ident. and trigger	$^{+1.4}_{-2.1}$	$^{+1.3}_{-1.7}$	$^{+1.4}_{-2.1}$	$^{+1.1}_{-1.5}$
b-tagging	$\pm$ 1.3	$\pm$ 1.6	$\pm$ 1.6	$\pm$ 1.6
Jet energy scale and resolution†	$^{+8.5}_{-9.1}$	$\pm$ 9.2	$^{+4.7}_{-4.9}$	$^{+3.7}_{-3.0}$
$E_{\text{T}}^{\text{miss}}$ soft scale & resolution	$^{+0.0}_{-0.2}$	$^{+0.0}_{-1.2}$	$^{+0.0}_{-0.1}$	$^{+0.0}_{-1.2}$
Background Model				
Fake background†	–	$\pm$ 1.2	–	$\pm$ 1.2
Embedding†	–	$^{+3.8}_{-4.3}$	–	$^{+6.0}_{-6.5}$
$Z \to ll$ normalization	–	$\pm$ 2.1	–	$\pm$ 0.7

Table 6.12: Impact of systematic uncertainties on the total signal, S, (sum of all production modes) and on the sum of all background estimates, B, in the two categories (VBF and Boosted) of the $\tau_{\text{lep}}\tau_{\text{lep}}$ channel for the analysis of the data collected at $\sqrt{s} = 8\,\text{TeV}$. Uncertainties that affect the shape of the BDT output distribution in a non-negligible way are marked with a †. All values are given before the global fit. The notation UE/PS refers to the underlying event and parton shower modeling.

is proven that the different contributions have a good modeling and their agreement is consistent enough to be extrapolated to the SR.

The signal strength, μ, is the ratio between the number of observed events (sub-index *obs*) divided by the number of events expected (sub-index *exp*) in the SM, which includes the signal. In this case, the signal corresponds to a Higgs boson of $m_H = 125\,\text{GeV}$. Assuming that the number of signal events (N) is given by the Luminosity (L) and the cross-section of the process (σ), as $N = L \cdot \sigma$, the signal strength can be written in terms of the observed and expected cross-sections, as:

$$\mu = \frac{N_{obs}}{N_{exp}} = \frac{L \cdot \sigma_{obs}}{L \cdot \sigma_{SM}} = \frac{\sigma_{obs}}{\sigma_{SM}} \tag{6.13}$$

From this definition, it can be deduced that a value of $\mu = 0$ represents the case where there is no signal observed (a background-only model can reproduce the observed

distribution, which is called the *null-hypothesis*) while a value of $\mu = 1$ represents the case where the data observed behaves exactly as predicted by the SM.

The value of the signal strength is extracted using a maximum-likelihood fit on all the categories simultaneously. The statistical analysis of the data employs a binned profile likelihood function $\mathcal{L}(\mu, \vec{\theta})$, constructed as the product of Poisson probability terms, to estimate μ. The impact of systematic uncertainties on the signal and background expectations is described by nuisance parameters ($\vec{\theta}$ or NP) on the normalization, which are each parametrized by a Gaussian or log-normal constraint. Additionally, the systematics relating to TES, JES or $E_{\mathrm{T}}^{\mathrm{miss}}$ also act as shape NPs in the fit. The expected numbers of signal and background events in each bin are functions of $\vec{\theta}$.

The likelihood is maximized on the BDT Score distribution in the SRs, while the CRs (e.g. Zll and Top in the $\tau_{\mathrm{lep}}\tau_{\mathrm{lep}}$ channel) are used to constraint the normalization of their respective free-floating backgrounds by using a one-bin distribution of the BDT Score in their CR. The $Z \to \tau\tau$ background is constrained directly in the SR, from the part of the spectrum with low BDT Score. The fit scales the distributions of backgrounds (constrained from the CR) and signal within the possible uncertainties to match the observed data. The scaling parameter of the signal distribution is the signal strength.

However, the signal strength alone does not provide all the necessary information to reject the null-hypothesis, as its value could be result of a statistical fluctuation. Thus, a second study is performed, to check the probability that the measured value of the signal strength is the result of a statistical fluctuation rather than a real excess. This check is performed using a test statistic q_μ, constructed according to the profile likelihood ratio as:

$$q_\mu = -2 \ln \left[\mathcal{L}(\mu, \hat{\hat{\vec{\theta}}}) / \mathcal{L}(\hat{\mu}, \hat{\vec{\theta}}) \right] \tag{6.14}$$

where $\hat{\mu}$ and $\hat{\vec{\theta}}$ are the parameters that maximize the likelihood, and $\hat{\hat{\vec{\theta}}}$ are the NP values that maximize the likelihood for a given μ.

The significance of the excess over the null-hypothesis is then calculated as the probability (p_0-value) that a statistical fluctuation of the background, with no signal present, can reproduce the distribution observed in data. This probability is obtained by performing the $q_{\mu=0}$ test (Equation 6.14) in the asymptotic approximation [214] where the p_0 is the asymptotic integral of the probability from the measured value of the q_0 distribution. For convention, the p_0-value is usually expressed in units of standard deviations of the normal distribution (σ).

Nevertheless, the fit depends on the systematic variations that affect the distributions in the SR and thus, their impact on the signal strength has to be investigated. These

effects include how far the NP are pulled away from their pre-fit values by the fit and how well their uncertainties are constrained. In order to estimate these effects, the fit is performed once again for each NP, fixing the value of that parameter shifted up or down by its fitted uncertainty, with all the other parameters allowed to vary. The results are then sorted by the magnitude of the impact and a ranking is obtained.

The number of NPs entering in the fit can be very large, however, many of them do not have a significant impact on the fit. Furthermore, many NP do not behave as shape systematics and only affect the global normalization of the distribution. Hence, in order to reduce the complexity of the fit, the shape variation of this NPs can be neglected and only the variation of the normalization is computed. Furthermore, the normalization systematics are only considered if either of their variation (upward or downward) differs from the nominal yield by more than 0.5%.

Another issue which can be raised comes from the fact that the SR after the full selection has a limited number of events and so, the studies of the impact of the shape NPs can be biased due to the presence of statistical fluctuations. In order to address these two issues, and reduce the number of systematics entering in the fit, several methods are applied: two *prunings* and one *smoothing* procedure.

- **First Pruning**: A χ^2 test between the upward and the downward fluctuated shape variations with respect to the nominal is performed, for each shape systematic NP and for each sample. The shape systematic is retained if the result of the χ^2 test is less than a consistency probability of 0.95, for either of the upwards or downwards fluctuated shape. If neither of them is lower, the shape variation is neglected and thus, its shape NP is not used in the fit. In all cases, however, the normalization uncertainties are kept. This pruning criterion is not applied to those systematic uncertainties that affect the weight of the MC events.

- **Smoothing**: To avoid the statistical fluctuations in the computation of the effect of the systematics, the ratio of variation to nominal (separately for upwards and downwards variations) is smoothed, using the `TH1::Smooth(1)` method [215] of ROOT. The smoothed varied shape is then obtained by multiplying the nominal by the smoothed ratio. The reason for smoothing the ratio rather than the varied shape directly is that the BDT distribution has an intrinsic strong variability and thus, a direct smooth can over-correct the effect.

- **Second Pruning**: In order to remove the shape systematics which are not significant enough for the fit, a second pruning is applied, which is checked individually for each systematic uncertainty of each background sample. The maximum variation significance, $\max_i(S_i)$, computed bin-by-bin, should be at least 10%. The variation

significance is defined as $S_i = |u_i - d_i|/\sigma_i^{tot}$, with u_i (d_i) being the upwards (downwards) variation in bin i for a given background sample, while σ_i^{tot} is the statistical uncertainty for the total background estimation (i.e. for all samples) in bin i. If one variation has a $S_i < 10\%$ for all bins of the distribution, then the shape variation is neglected for this particular background sample.

The BDT Score distribution is extremely sensitive to the bin size, as all the signal is concentrated in very few bins. A coarse binning would reduce the sensitivity due to the addition of more backgrounds events but a too fine binning would increment the statistical error, thus resulting in an increase of fluctuations and a loss of sensitivity. Some studies were performed to search for an optimal binning that maximizes the sensitivity while preventing statistical fluctuations. The optimal binning included a variable-sized structure with finer binning in the last bins, which concentrate the signal-like events, and it was used for the $\tau_{\text{lep}}\tau_{\text{had}}$ and $\tau_{\text{had}}\tau_{\text{had}}$ channels. However, in the $\tau_{\text{lep}}\tau_{\text{lep}}$ channel, the improvement with the variable-sized binning was small and thus, the structure was simplified to the fixed-size.

6.10.5 Fit model tests

The performance of the fit is tested by controlling how the parameters than constrain the fit (nuisance parameters, NP) are affected by the result of the fit with data. This is done for each channel individually and for a combination of all channels, performed using Asimov data[5] for the ranking of the NP and unblinded data for the NP pulls.

The summary of the impact of the most relevant systematic uncertainties for the combined $H \to \tau\tau$ analysis is shown in Figure 6.27. This plot shows the impact of systematic uncertainties on the fitted signal strength parameter $\hat{\mu}$. The systematic uncertainties are listed in decreasing order of their impact on $\hat{\mu}$ on the y-axis. The hatched blue and red boxes show the variations of $\hat{\mu}$ with respect to the total error on μ, σ_{tot}, referring to the top x-axis, when fixing the corresponding individual nuisance parameter θ to its post-fit value $\hat{\theta}$ modified upwards or downwards by its post-fit uncertainty, and repeating the fit. The filled circles, referring to the bottom x-axis, show the pulls of the fitted nuisance parameters, i.e. the deviations of the fitted parameters $\hat{\theta}$ from their nominal values θ_0, normalized to their nominal uncertainties $\Delta\theta$. The black lines show the post-fit uncertainties of the nuisance parameters, relative to their nominal uncertainties, which are indicated by the yellow band.

[5]The median significance of many toy MC experiments can be obtained simply by replacing the ensemble of simulated datasets by a single representative one, the Asimov dataset, defined as the one in which all observed quantities are set equal to their expected values [214].

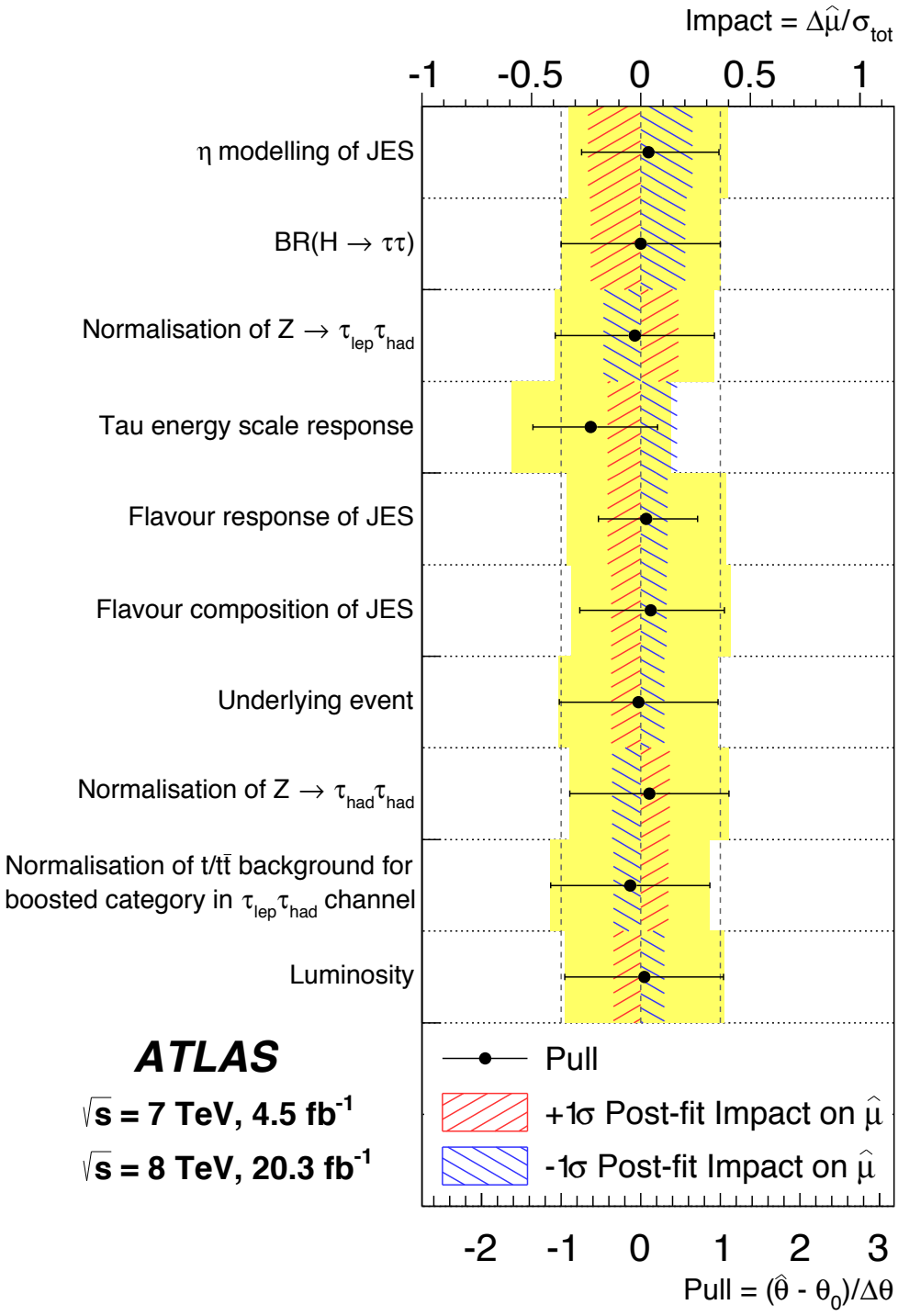

Figure 6.27: Impact of systematic uncertainties on the fitted signal strength parameter $\hat{\mu}$ for the combined fit for all channels and both datasets. The plot is described in the text and in Ref. [155].

6.11 Results of the $H \to \tau\tau$ analysis

This section provides the final result of the $H \to \tau\tau$ analysis in the MVA and cut-based approaches, and the compatibility of both results.

6.11.1 Main MVA analysis

The final discriminating variable was chosen to be the BDT Score, which is obtained by combining the events from the two categories and the three channels. This distribution is fitted to extract the signal strength of the combined $H \to \tau\tau$ analysis for a mass[6] of $m_H = 125.36\,\text{GeV}$. The measured signal strength in the $H \to \tau\tau$ analysis has a value of:

$$\mu = 1.43\,^{+0.27}_{-0.26}\,(\text{stat.})\,^{+0.32}_{-0.25}\,(\text{syst.})\,\pm 0.09\,(\text{theory syst.}) \tag{6.15}$$

The μ values for the different channels independently and split by categories are shown in Figure 6.28.

The systematic uncertainties are split into two groups: the theoretical uncertainties on the inclusive Higgs boson production cross-section and $H \to \tau\tau$ branching ratio (theory syst.), and the rest of systematic uncertainties (syst.) including all experimental effects as well as theoretical uncertainties on the signal region acceptance, such as those due to the QCD scales, the PDF choice, and the underlying event and parton shower. The normalization uncertainties on the $Z \to \tau\tau$ embedded sample are correlated across the categories in each respective channel. The global fit also constrains the normalization for $Z \to \tau\tau$ more strongly than for the $Z \to ll$ and top-quark background components, as the low BDT Score region is dominated by $Z \to \tau\tau$ events. Table 6.13 shows how the different sources of uncertainty affect the μ value.

The significance of the excess for a mass of $m_H = 125.36\,\text{GeV}$ is given by an observed p_0-value of 2.7×10^{-6} which corresponds to a deviation from the background-only hypothesis of $4.5\,\sigma$. For comparison, the expected significance for a SM signal was $3.4\,\sigma$. Table 6.14 shows the observed and expected significance, in terms of σ, for each of the categories and channels independently. This result provides evidence at the level of $4.5\,\sigma$ for the decay of the Higgs boson into τ leptons.

The measurement of the overall signal strength discussed above does not give direct information on the relative contributions of the different production mechanisms. Therefore, the signal strengths of different production processes contributing to the $H \to \tau\tau$ decay mode are determined, exploiting the sensitivity offered by the use of the event

[6]The value of the mass corresponds to the Higgs boson mass measurements of the ATLAS Experiment in the $H \to \gamma\gamma$ and $H \to ZZ \to 4\ell$ decays: $m_H = 125.36 \pm 0.37\,(\text{stat.}) \pm 0.18\,(\text{syst.})\,\text{GeV}$ [216].

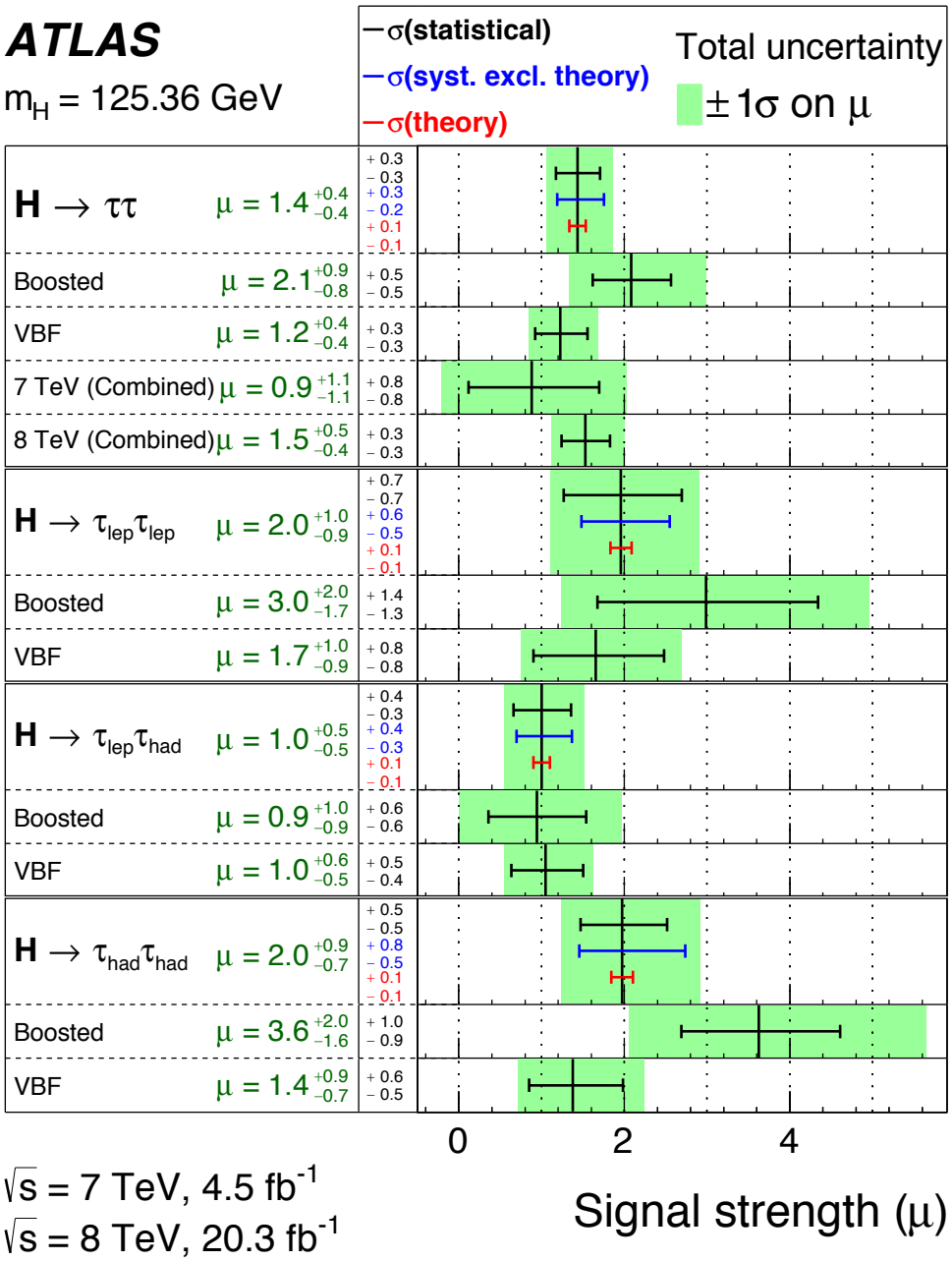

Figure 6.28: Best-fit value for the signal strength μ in the individual channels and their combination for the full ATLAS datasets at $\sqrt{s} = 7\,\text{TeV}$ and $\sqrt{s} = 8\,\text{TeV}$. The total $\pm 1\sigma$ uncertainty is indicated by the shaded green band, with the individual contributions from the statistical uncertainty (top, black), the experimental systematic uncertainty (middle, blue), and the theory uncertainty (bottom, red) on the signal cross-section (from QCD scale, PDF, and branching ratios) shown by the error bars and printed in the central column [155].

Source of Uncertainty	**Uncertainty on μ**
Signal region statistics (data)	$+0.27, -0.26$
Jet energy scale (JES)	$\pm$ 0.13
Tau energy scale (TES)	$\pm$ 0.07
Tau identification (τ-ID)	$\pm$ 0.06
Background normalization	$\pm$ 0.12
Background estimate stat.	$\pm$ 0.10
BR ($H \to \tau\tau$)	$\pm$ 0.08
Parton shower/Underlying event	$\pm$ 0.04
PDF	$\pm$ 0.03

Table 6.13: Important sources of uncertainty on the measured signal-strength parameter μ. The contributions are given as absolute uncertainties on the best-fit value of $\mu = 1.43$. Various sub-components are combined assuming no correlations.

		Significance	
Channel	**Category**	Expected	Observed
$\tau_{\text{lep}}\tau_{\text{lep}}$	VBF	1.15 σ	1.88 σ
	Boosted	0.57 σ	1.72 σ
$\tau_{\text{lep}}\tau_{\text{had}}$	VBF	2.11 σ	2.23 σ
	Boosted	1.11 σ	1.01 σ
$\tau_{\text{had}}\tau_{\text{had}}$	VBF	1.70 σ	2.23 σ
	Boosted	0.82 σ	2.56 σ
$\tau_{\text{lep}}\tau_{\text{lep}}$	VBF+Boosted	1.25 σ	2.40 σ
$\tau_{\text{lep}}\tau_{\text{had}}$	VBF+Boosted	2.33 σ	2.33 σ
$\tau_{\text{had}}\tau_{\text{had}}$	VBF+Boosted	1.99 σ	3.25 σ
$H \to \tau\tau$ analysis combined		**3.43 σ**	**4.54 σ**

Table 6.14: Expected and observed significances of the signal in each channel and category for the combined 7+8 TeV datasets.

categories in the analyses of the three channels. The data are fitted separating the vector-boson-mediated VBF and VH processes from gluon-mediated ggH processes. Two signal strength parameters, $\mu^{\tau\tau}_{\text{ggH}}$ and $\mu^{\tau\tau}_{\text{VBF+VH}}$, which scale the SM-predicted rates to those observed, are introduced, whose best-fit values are:

$$\mu^{\tau\tau}_{\text{ggH}} = 2.0 \pm 0.8\,(\text{stat.})\,^{+1.2}_{-0.8}\,(\text{syst.})\ \pm 0.3\,(\text{theory syst.}) \tag{6.16}$$

$$\mu^{\tau\tau}_{\text{VBF+VH}} = 1.24\,^{+0.49}_{-0.45}\,(\text{stat.})\,^{+0.31}_{-0.29}\,(\text{syst.})\ \pm 0.08\,(\text{theory syst.}) \tag{6.17}$$

which are in agreement with the predictions of the Standard Model. The observed (expected) significances of the $\mu^{\tau\tau}_{\text{ggH}}$ and $\mu^{\tau\tau}_{\text{VBF+VH}}$ signal strengths are $1.74\,\sigma$ $(0.95\,\sigma)$ and $2.25\,\sigma$ $(1.72\,\sigma)$ respectively.

These two values can be represented in a two-dimensional plot [217], showing the 68% and 95% confidence level (CL) contours in the plane of $\mu^{\tau\tau}_{\text{ggH}}$ and $\mu^{\tau\tau}_{\text{VBF+VH}}$, which is shown in Figure 6.29 for $m_H = 125.36\,\text{GeV}$. The best fit value is within the $1\,\sigma$ of the SM expectation.

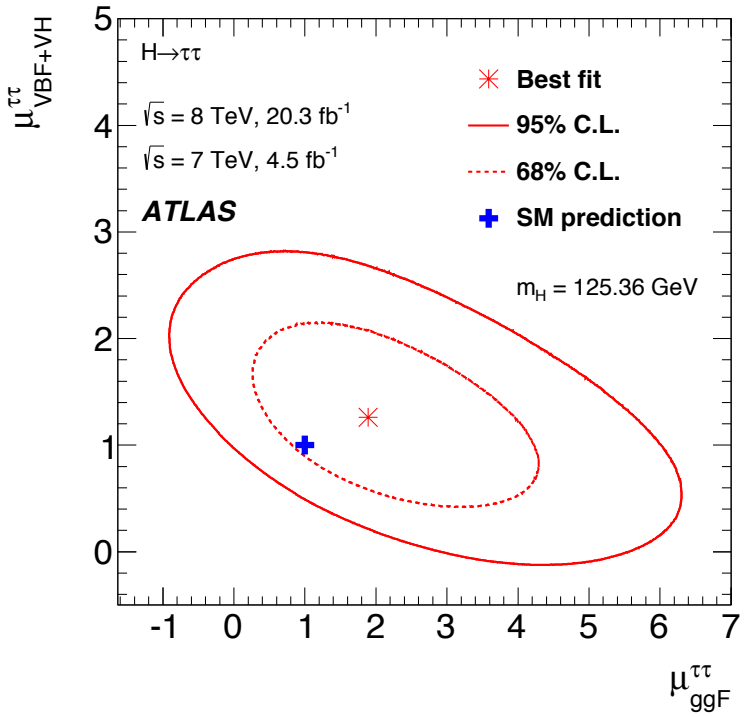

Figure 6.29: Likelihood contours for the combination of all channels in the ($\mu^{\tau\tau}_{\text{ggH}}$, $\mu^{\tau\tau}_{\text{VBF+VH}}$) plane. The signal strength μ is the ratio of the measured signal yield to the Standard Model expectation, for each production mode. The 68% and 95% CL contours are shown as dashed and solid lines respectively, for $m_H = 125.36\,\text{GeV}$. The SM expectation is shown by a filled plus symbol, and the best fit to the data is shown as a star [155].

In addition, the measured cross-section times branching ratio of the $H \to \tau\tau$ process can be calculated by multiplying the theoretical values by the signal strength. The results for the 7 TeV and 8 TeV datasets, as well as the 8 TeV dataset divided according to the

production modes, as in the contour plot (ggH ,VBF+VH) is shown in Table 6.15. The theoretical uncertainties on the inclusive cross-section cancel between μ and the predicted cross-section and thus are not included for the production processes. These include the uncertainties on the inclusive cross-section due to the QCD scale and the PDF choice as well as the uncertainty on the branching ratio $H \to \tau\tau$; however, theoretical uncertainties on the acceptance of the signal regions from the QCD scale and PDF choice are retained, along with the uncertainties due to underlying event, parton shower and the electroweak correction on VBF production.

Dataset		**Measured $\sigma\times$BR** [pb]	**Predicted $\sigma\times$BR** [pb]
7 TeV		$1.0\,^{+0.9}_{-0.8}\,(\text{stat.})\,^{+0.9}_{-0.8}\,(\text{syst.})$	1.09 ± 0.11
8 TeV	Combined	$2.1 \pm 0.4\,(\text{stat.})\,^{+0.5}_{-0.4}\,(\text{syst.})$	1.39 ± 0.14
8 TeV	ggH	$1.7 \pm 1.1\,(\text{stat.})\,^{+1.5}_{-1.1}\,(\text{syst.})$	1.22 ± 0.14
8 TeV	VBF+VH	$0.26 \pm 0.09\,(\text{stat.})\,^{+0.06}_{-0.05}\,(\text{syst.})$	0.17 ± 0.01

Table 6.15: Measured and predicted total cross-section times branching ratio for a Higgs boson with $m_H = 125\,\text{GeV}$, at 7 TeV and at 8 TeV.

The post-fit discriminant plots (BDT Score) of the SR are shown in Figure 6.30 for the two categories of the three channels. The figures include the distributions for the SM prediction ($\mu = 1$) and the best fit ($\mu = 1.4$).

In order to enhance the signal over the background, a different approach is displayed in Figure 6.31. This distribution shows the number of events in bins of $\log_{10}(S/B)$, for all the signal region bins. S/B is the signal-to-background ratio calculated assuming the best fit value of $\mu = 1.4$ for each BDT bin in the signal regions. The expected signal yield for both $\mu = 1$ and the best-fit value $\mu = 1.4$ for $m_H = 125\,\text{GeV}$ are shown on top of the background prediction. The background expectation for the background-only hypothesis, where the signal-strength parameter is fixed to $\mu = 0$, is also shown for comparison.

Due to its relevance as a discriminant variable, the combined $m_{\tau\tau}^{\text{MMC}}$ distribution of the $H \to \tau\tau$ analysis are also shown in Figure 6.32. These plots have also been reweighted to enhance the signal, using a factor of $\ln(1 + S/B)$, where S and B are the expected yields of signal and background in each bin, respectively. The excess of events in these distributions is consistent with the expectation for a SM Higgs boson with $m_H = 125\,\text{GeV}$. Distributions for alternative SM Higgs boson mass hypotheses of $m_H = 110\,\text{GeV}$ and $m_H = 150\,\text{GeV}$ are shown too. The data favor a Higgs boson mass of $m_H = 125\,\text{GeV}$ and are less consistent with the other masses considered.

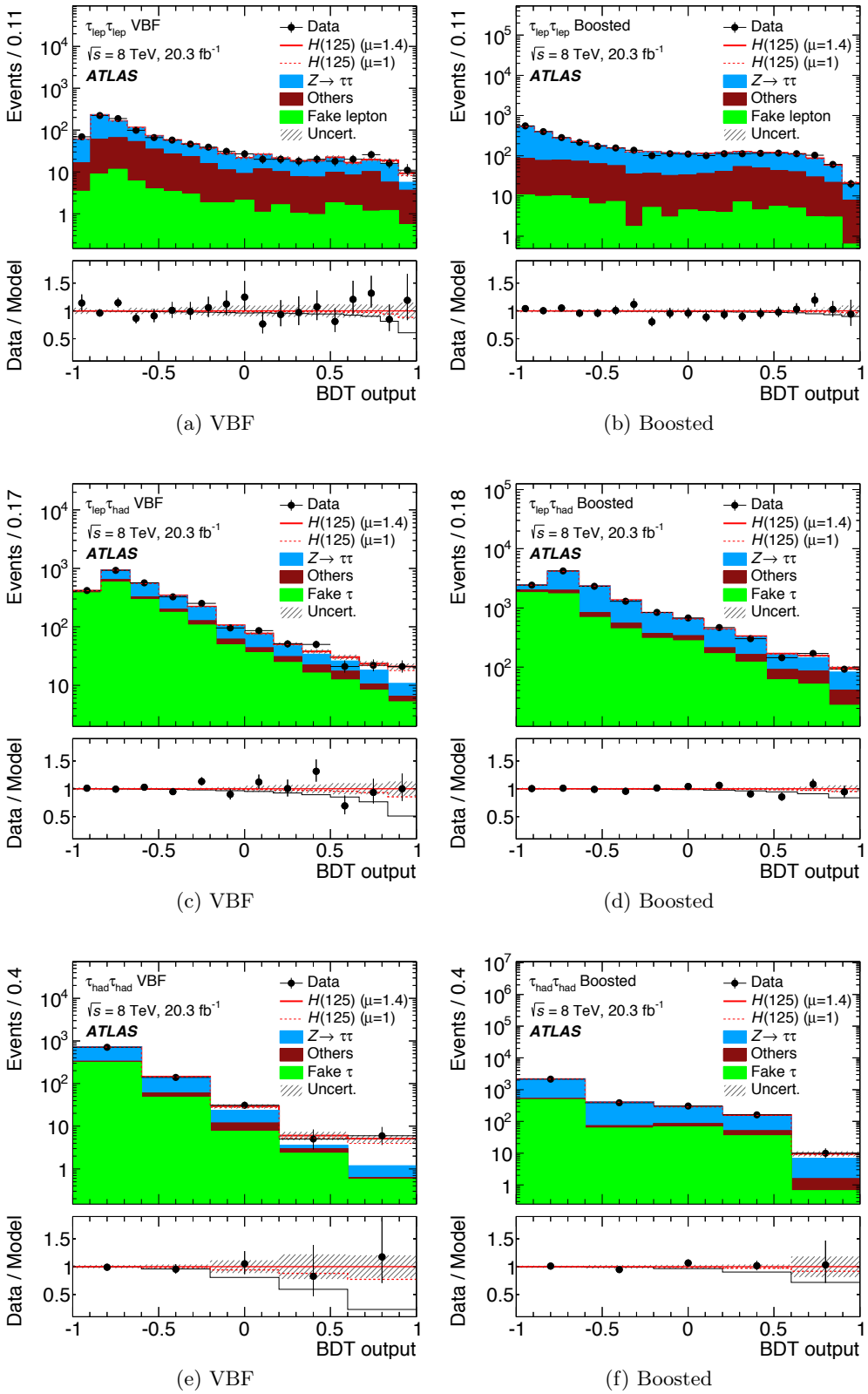

(a) VBF (b) Boosted

(c) VBF (d) Boosted

(e) VBF (f) Boosted

Figure 6.30: BDT Score in the (top) $\tau_{\text{lep}}\tau_{\text{lep}}$, (middle) $\tau_{\text{lep}}\tau_{\text{had}}$ and (bottom) $\tau_{\text{had}}\tau_{\text{had}}$ channels for the two categories, VBF (left) and Boosted (right), for the data collected at 8 TeV. The Higgs boson signal is shown stacked with a signal strength of $\mu = 1$ (dashed line) and $\mu = 1.4$ (solid line). The background predictions are determined in the global fit. The size of the statistical and systematic normalization uncertainties is indicated by the hashed band. The ratios of the data to the model (background plus Higgs boson contributions with $\mu = 1.4$) are shown in the lower panels. The dashed red and the solid black lines represent the changes in the model when $\mu = 1$ or $\mu = 1.4$ are assumed respectively [155].

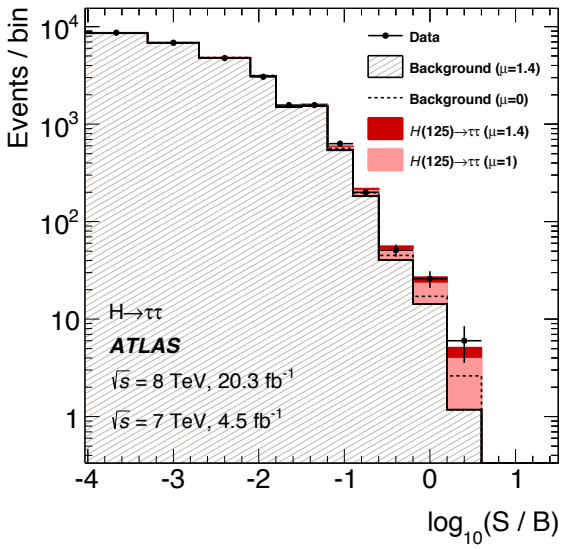

Figure 6.31: Event yields as a function of $\log_{10}(S/B)$, where S and B are the signal and background yields respectively, and are taken from the BDT output bin of each event, assuming a signal strength $\mu = 1.4$. The predicted background is obtained from the global fit (with $\mu = 1.4$), and signal yields are shown for $m_H = 125\,\text{GeV}$ at $\mu = 1$ and $\mu = 1.4$ (the best-fit value). The background-only distribution (dashed line) is obtained from the global fit, with μ fixed at zero [155].

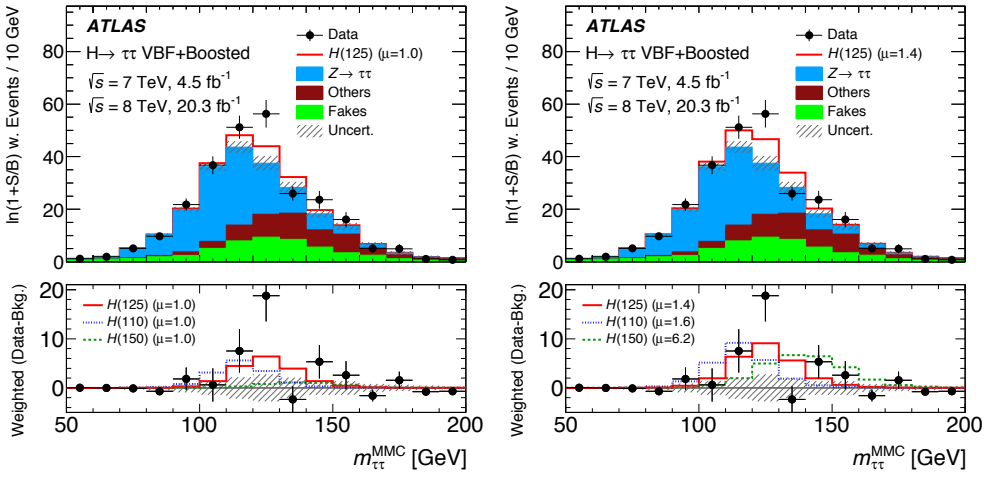

(a) $\mu = 1$ (b) $\mu = 1.4$

Figure 6.32: Distributions of the reconstructed invariant mass $m_{\tau\tau}^{\text{MMC}}$ for all channels, where events are weighted by $\ln(1+S/B)$. S and B are the signal and background predictions for each BDT bin, respectively. The background predictions are obtained from the global fit with the $m_H = 125\,\text{GeV}$ signal hypothesis (signal strength $\mu = 1.4$). The $m_H = 125\,\text{GeV}$ signal is plotted with a solid red line and for comparison signals for $m_H = 110\,\text{GeV}$ (blue) and $m_H = 150\,\text{GeV}$ (green) are also shown. The signal normalizations are taken from fits to data with the corresponding signal mass hypotheses, and the fitted μ values are given in the figure. The signal strengths are shown for the SM expectations in (a), while in (b) the best-fit values are used [155].

6.11.2 Cut-based cross check

As described in Section 6.9.4, a cut-based analysis of the same search was developed, in order to serve as a cross-check for the MVA analysis. The two analyses are performed for the same three channels, with analogous event selection and categories, and they share the same strategy for the estimation of background contributions and systematic uncertainties.

The final results are derived from the combined fit of the distribution of the invariant mass $m_{\tau\tau}^{\text{MMC}}$, combining all categories and channels. This plot is shown in Figure 6.33, where events are weighted by $\ln(1 + S/B)$, based on the signal and background content of their channel and category. An excess of events above the expected SM background is observed in the mass region around 125 GeV.

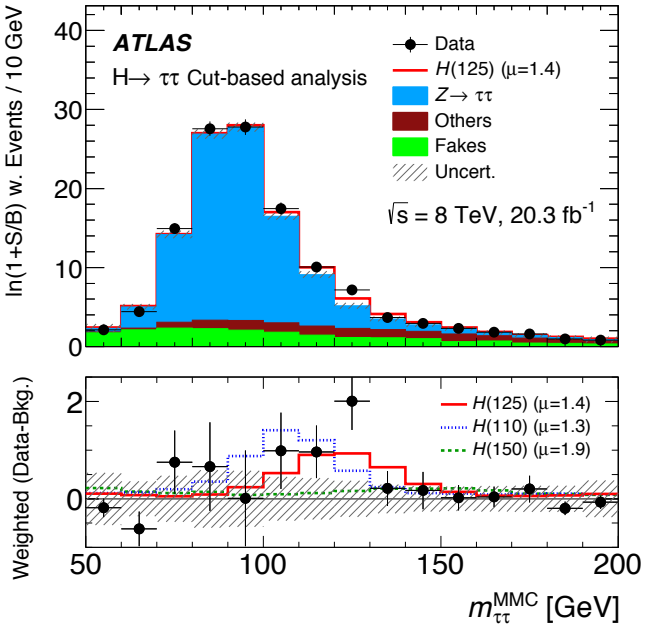

Figure 6.33: Distribution of the invariant mass $m_{\tau\tau}^{\text{MMC}}$ for the sum of all channels in the cut-based analysis for the data collected at $\sqrt{s} = 8\,\text{TeV}$. The events are weighted by a factor of $\ln(1 + S/B)$ based on the signal (S) and background (B) yields in each category. The background predictions are obtained from the global fit with the $m_H = 125\,\text{GeV}$ signal hypothesis (signal strength $\mu = 1.4$). The $m_H = 125\,\text{GeV}$ signal is plotted as a solid red line, and, for comparison, signals for $m_H = 110\,\text{GeV}$ (blue) and $m_H = 150\,\text{GeV}$ (green) are also shown. The signal normalizations are taken from fits to data with the corresponding signal mass hypotheses and the fitted μ values are given in the figure [155].

The signal strengths extracted in the three analysis channels and their combination are given in Table 6.16. For comparison, the results obtained in the MVA analysis for the dataset at $\sqrt{s} = 8\,\text{TeV}$ are also included in Table 6.16. The combined signal strength for $m_H = 125.36\,\text{GeV}$ is:

$$\mu_{\text{cut-based}} = 1.43\ ^{+0.36}_{-0.35}(\text{stat.})\ ^{+0.41}_{-0.33}(\text{syst.})\ \pm 0.10(\text{theory syst.}) \tag{6.18}$$

Channel (8 TeV)	**MVA**	**Cut-based**
$\tau_{\text{lep}}\tau_{\text{lep}}$	$1.9^{+1.0}_{-0.9}$	$3.2^{+1.4}_{-1.3}$
$\tau_{\text{lep}}\tau_{\text{had}}$	$1.1^{+0.6}_{-0.5}$	$0.7^{+0.7}_{-0.6}$
$\tau_{\text{had}}\tau_{\text{had}}$	$1.8^{+0.9}_{-0.7}$	$1.6^{+0.9}_{-0.7}$
Combination 8 TeV	$1.53^{+0.47}_{-0.41}$	$1.43^{+0.55}_{-0.49}$

Table 6.16: Comparison of the fitted values of the signal strength for the different channels at $\sqrt{s} = 8\,\text{TeV}$ for the multivariate and cut-based analyses, measured at $m_H = 125.36\,\text{GeV}$. The results for the combinations of all channels are also given. The total uncertainties (statistical and systematic) are quoted.

Good agreement between the results of the two analyses is found for the individual channels as well as for their combination. To further quantify the level of agreement, the correlation ρ and the uncertainties on the differences between the μ values obtained, i.e. $\Delta\mu \pm \delta(\Delta\mu)$, were evaluated using the so-called jack knife technique [218, 219]. Using this method, the correlation between the μ values obtained in the two analyses is found to be between 0.55 and 0.75 for each of the three analysis channels. The results of the analyses are found to be fully compatible, with deviations $\Delta\mu/\delta(\Delta\mu)$ below 1 for all analysis channels as well as for the combined result.

Given the mass sensitivity of the cut-based analysis, a two-dimensional likelihood fit for the signal strength μ and the mass m_H is performed. The mass points are tested in steps of 5 GeV in the range between 100 GeV and 150 GeV. The best fit value is found at $\mu = 1.4$ and $m_H = 125\,\text{GeV}$. The result is shown in the (m_H, μ) plane in Figure 6.34, together with the 68% and 95% CL contours. This result indicates that the observation is compatible with the decay of a SM Higgs boson with a mass of 125 GeV.

The probability p_0 of obtaining a result at least as signal-like as the observed if no signal were present, is shown as a function of the mass in Figure 6.35 for the cut-based analysis for the combined dataset at $\sqrt{s} = 8\,\text{TeV}$. The observed p_0-values show a shallow minimum around 125 GeV, corresponding to a significance of $3.2\,\sigma$. The expected significance for the cut-based analysis is superimposed on the figure and reaches a significance of $2.5\,\sigma$ at $m_H = 125.36\,\text{GeV}$. These numbers have to be compared to the results of the MVA shown in previous section: $4.5\,\sigma$ (observed) and $3.3\,\sigma$ (expected), which are also shown in the figure.

As it can be observed in Figure 6.35, the results of the MVA and cut-based analyses show a compatible excess. As expected, the MVA analysis sensitivity is significantly higher and thus, the confidence in the exclusion of the null-hypothesis is stronger. Table 6.17 shows a direct comparison of the most relevant results of the MVA and cut-based analyses, where it can be observed that the results are fully compatible between them within the error and are also compatible with the SM hypothesis ($\mu = 1$).

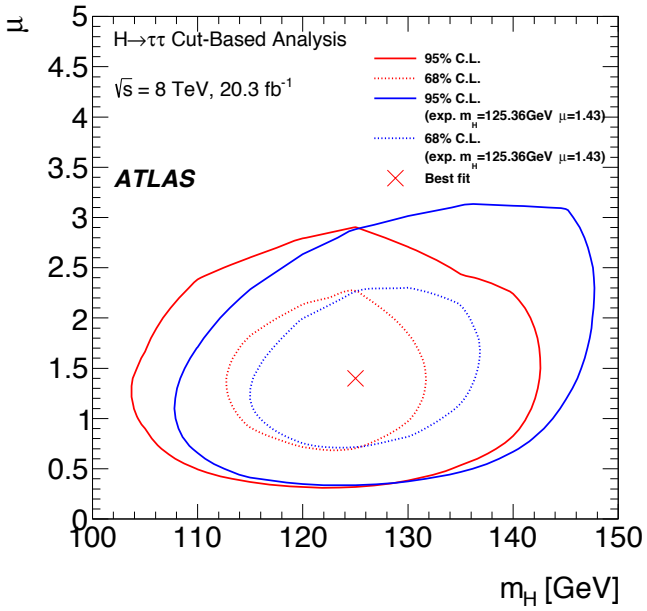

Figure 6.34: Two-dimensional likelihood fit in the (m_H, μ) plane for the cut-based analysis for the data taken at $\sqrt{s} = 8\,\text{TeV}$. The signal strength μ is the ratio of the measured signal yield to the Standard Model expectation. The 68% and 95% CL contours are shown as dashed and solid red lines respectively. The best-fit value is indicated as a red cross. The dashed and solid blue lines correspond to the expected 68% and 95% CL contours for $m_H = 125.36\,\text{GeV}$ and $\mu = 1.43$ [155].

	Signal strength μ	
Channel	MVA	Cut-based
$\tau_{\text{lep}}\tau_{\text{lep}}$	$1.9^{+1.0}_{-0.9}$	$3.2^{+1.4}_{-1.3}$
$\tau_{\text{lep}}\tau_{\text{had}}$	$1.1^{+0.6}_{-0.5}$	$0.7^{+0.7}_{-0.6}$
$\tau_{\text{had}}\tau_{\text{had}}$	$1.8^{+0.9}_{-0.7}$	$1.6^{+0.9}_{-0.7}$
$H \to \tau\tau$ analysis	$1.53^{+0.47}_{-0.41}$	$1.43^{+0.55}_{-0.49}$
Observed significance	$4.5\,\sigma$	$3.2\,\sigma$
Expected significance	$3.3\,\sigma$	$2.5\,\sigma$

Table 6.17: Comparison of the main results of the MVA and cut-based analysis. The results are shown for the three channels independently and the full combination. The signal strength value corresponds to a SM Higgs boson signal measured at $m_H = 125.36\,\text{GeV}$ and is given with the total error.

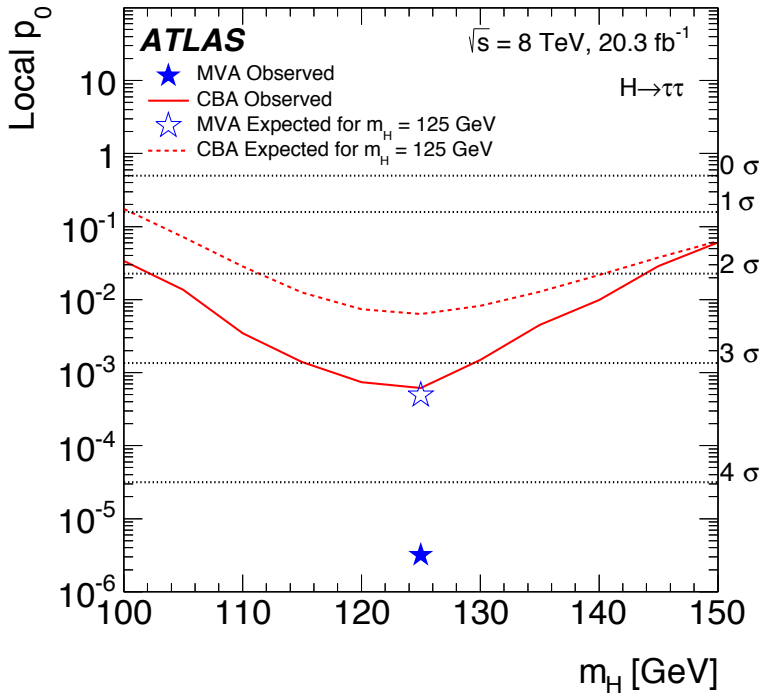

Figure 6.35: Observed (solid red) and expected (dashed red) p_0-values as a function of m_H for the combination of all channels in the cut-based analysis for the data taken at $\sqrt{s} = 8\,\text{TeV}$. The expected p_0-values are given for the background-only hypothesis. The corresponding observed and expected p_0-values for the MVA are indicated for $m_H = 125\,\text{GeV}$ by a full and open star respectively. The axis labels on the right hand side and the dotted lines display the significance in units of Gaussian standard deviations [155].

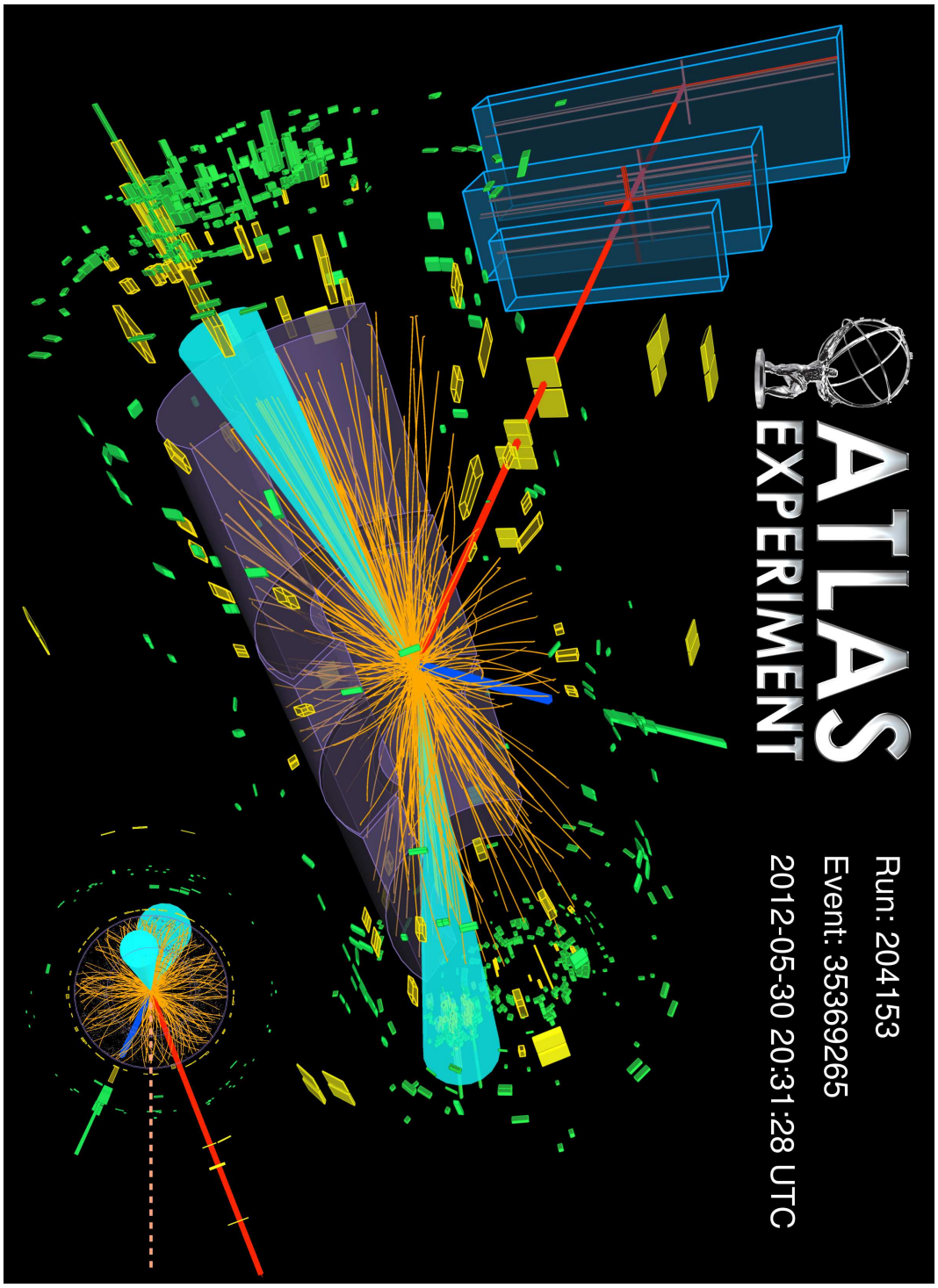

Figure 6.36: Display of an event selected by the $\tau_{\text{lep}}\tau_{\text{lep}}$ channel in the VBF category, where one τ candidate decays to a muon (red track) and the other to an electron (blue track). The $E_{\text{T}}^{\text{miss}}$ direction is represented by an approximately horizontal dashed line in the $R-\phi$ view. The two VBF jets are marked with turquoise cones. The main characteristics of the event are: $p_{\text{T}}^{\mu} = 53\,\text{GeV}$, $p_{\text{T}}^{e} = 34\,\text{GeV}$, $E_{\text{T}}^{\text{miss}} = 102\,\text{GeV}$, $m_{jj} = 1.04\,\text{TeV}$ and the invariant mass is $m_{\tau\tau}^{\text{MMC}} = 127\,\text{GeV}$. The BDT Score of this event is 0.95 (in the range $[-1, 1]$). The S/B ratio in the BDT Score bin of this event is 0.6 [155].

Chapter 7

Search for additional neutral MSSM Higgs bosons H/A in the $\tau_{\text{had}}\tau_{\text{had}}$ channel

7.1 Introduction

The second analysis presented in this thesis corresponds to the search for additional neutral Higgs bosons decaying in the $\tau\tau$ channel, as predicted by the Minimal Supersymmetric Standard Model (MSSM). If MSSM holds true, three neutral bosons can be discovered at the LHC: h, H and A. Different scenarios try to adapt the properties of the already discovered Higgs boson to the MSSM framework, where the most common assumption is that the lightest MSSM boson, h, is the SM Higgs boson[1], which leaves the other two bosons: the heavier H and the pseudo-scalar A, to be found. The MSSM framework enhances the coupling of d-type fermions to the Higgs bosons for large values of $\tan\beta$, therefore, the τ decay of a new Higgs boson as well as the bbH production mode are enhanced, which makes the $\tau\tau$ channel of great interest for the search for new physics during Run 2 of the LHC.

This analysis uses the framework developed for the SM $H \to \tau\tau$ analysis described in Chapter 6 and extends the search to the higher range of masses up to 1.2 TeV, using the data collected during the first year of Run 2, which accounts for 3.21 fb^{-1} of data taken at $\sqrt{s} = 13\,\text{TeV}$. A previous result of this analysis was published using the data of Run 1 [87]. Preliminary results of the Run 2 analysis were published as a CONF note in December 2015 [220]. Finally, an updated version, including a search of the heavy Z' decaying to a pair of τ, was published in the European Physical Journal C in November 2016 [221].

[1] As described in Section 1.3.2, the scenario where the particle discovered in 2012 is the heavier H is much less favorable, though not totally ruled out, as its mass limit is $m_H > 92.8\,\text{GeV}$ [3].

The search for the additional neutral MSSM Higgs bosons decaying to a $\tau\tau$ pair (abbreviated as $H/A \to \tau\tau$) is divided according to the τ decay, following the conventions described in Section 2.2.3. The analysis is thus split in two channels: the semi-leptonic ($\tau_{\text{lep}}\tau_{\text{had}}$) and the fully-hadronic ($\tau_{\text{had}}\tau_{\text{had}}$). Due to the small sensitivity at high-mass, the fully-leptonic channel ($\tau_{\text{lep}}\tau_{\text{lep}}$) is not included at this stage, although it may be considered for future improvements. The work of this thesis are mainly focused on the $\tau_{\text{had}}\tau_{\text{had}}$ channel, in addition to several multi-channel studies.

Two categories (b-tag, b-veto) are defined to take advantage of the different topologies of the signal production modes. The signal is enhanced by performing a cut-based analysis and the signal strength is extracted by fitting a background and signal model on a discriminant variable, chosen to be the total transverse mass, $m_{\text{T}}^{\text{tot}}$. The signal is simulated using several MSSM scenarios and the scan is performed in the range of masses from 200 GeV to 1.2 TeV. No significant excess over the background model is observed and therefore, exclusion limits are extracted for the cross-section of the production modes and for the different scenarios in terms of m_A and $\tan\beta$. The analysis optimization was partially blinded, allowing only a very small part of the data to be visible, while the full signal region was only unblinded after the analysis selection criteria and methodology were finalized.

7.2 Mass discriminant

The final result of the search is extracted using a binned likelihood fit on a discriminant variable, which is related to the kinematics of the di-τ event. However, since at least two neutrinos are involved in the τ final state (three in the $\tau_{\text{lep}}\tau_{\text{had}}$ channel), the invariant mass cannot be computed directly from the visible products of the decay and the missing transverse energy ($E_{\text{T}}^{\text{miss}}$), thus different estimation methods were tested. One method was the Missing Mass Calculator (MMC), defined in Section 6.3, which was optimized for the high mass range, as described in Section 7.2.2. Other tested variables are the MOSAIC mass and the total transverse mass, defined below. An investigation was performed to study the performance of each approach, which is described in Section 7.2.3. As a result of this study, the total transverse mass was finally chosen as the final discriminant of the analysis.

7.2.1 Definitions

Total transverse mass, $m_{\text{T}}^{\text{tot}}$

The total transverse mass, $m_{\text{T}}^{\text{tot}}$, is defined as the quadratic sum of the transverse masses computed between the different objects involved in the Higgs boson decay.

$$m_{\mathrm{T}}^{\mathrm{tot}} = \sqrt{m_{\mathrm{T}}^2\left(\tau_{\mathrm{had}}^{(1)}, \tau_{\mathrm{had}}^{(2)}\right) + m_{\mathrm{T}}^2\left(\tau_{\mathrm{had}}^{(1)}, E_{\mathrm{T}}^{\mathrm{miss}}\right) + m_{\mathrm{T}}^2\left(\tau_{\mathrm{had}}^{(2)}, E_{\mathrm{T}}^{\mathrm{miss}}\right)} \tag{7.1}$$

where m_{T}, the transverse mass between two objects, is defined as:

$$m_{\mathrm{T}}(1,2) = \sqrt{2\ p_{\mathrm{T}}^{(1)}\ p_{\mathrm{T}}^{(2)}\ \left(1 - \cos(\Delta\phi_{12})\right)} \tag{7.2}$$

MMC

The mass computed through the Missing Mass Calculator algorithm (MMC, or $m_{\tau\tau}^{\mathrm{MMC}}$) was defined in Section 6.3, but its implementation had to be adapted to the $H/A \to \tau\tau$ analysis. This is because firstly, the definitions for the $E_{\mathrm{T}}^{\mathrm{miss}}$ (one of the main inputs) were updated for the Run 2 of the LHC, and secondly, the standard MMC gave results compatible with the SM Higgs boson, which is a low-mass particle, while the $H/A \to \tau\tau$ analysis targets to a wide and high range of masses, from 200 GeV to 1.2 TeV. The optimization studies of the MMC are part of the work of this thesis and are summarized in Section 7.2.2.

MOSAIC

A second approach for the reconstruction of the di-τ mass is MOSAIC, that stands for Matrix-element Oriented SAmplIng Calculator. This algorithm is based on the visible energy fraction and an invariant mass of the missing energy system. It is a similar technique to the MMC, as it also uses probability density functions, but it performs the scan using a Markov Chain Monte Carlo instead of a grid point system. Its likelihood function is based on elements of the amplitude matrix of the τ lepton decay and the di-τ resonance, assuming spin and CP. For the hadronic τ decay mode, MOSAIC assumes which hadrons were produced: such as the π, ρ or a_1 mesons, computing the helicity. For the leptonic decay, MOSAIC uses the full matrix element of tau leptonic decay.

7.2.2 MMC optimization

The MMC algorithm provides a value of the invariant mass of the di-τ system as a result of a likelihood scan of the possible angular positions of the neutrinos produced in the two τ decays. Although the angular positions of the neutrinos cannot be mathematically solved, as the system is underconstrained, the different configurations are not equally probable. Using additional information of the τ decays in the form of Probability Density Functions (PDFs), which have obtained by data in control regions, a probable solution can be estimated.

The computation of the MMC depends greatly on the $E_{\mathrm{T}}^{\mathrm{miss}}$ variable, as it is one of the main inputs in the reconstruction of the τ decays. As explained in Chapter 5, the reconstructions of the missing energy ($E_{\mathrm{T}}^{\mathrm{miss}}$) and the sum of all detected energy in

the transverse plane (ΣE_{T}) were updated for the Run 2. This affects particularly the soft-term, which collects the energy deposited in the calorimeter not associated with any physics object. The soft-term reconstruction method used in Run 1 was the STFV, while the new standard computation for Run 2 is the TST, which employs a track-based reconstruction. The comparison in the reconstruction of the $E_{\text{T}}^{\text{miss}}$ and ΣE_{T} variables by the two algorithms is shown in Figure 7.1.

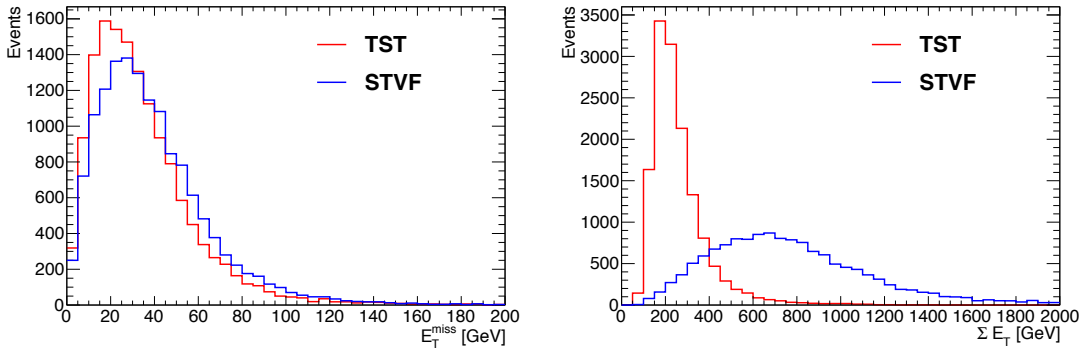

(a) $E_{\text{T}}^{\text{miss}}$ (b) ΣE_{T}

Figure 7.1: Comparison of the distribution of the sum of (a) missing energy in the transverse plane ($E_{\text{T}}^{\text{miss}}$) and (b) detected energy in the transverse plane (ΣE_{T}), by the STVF (blue) and TST (red) algorithms.

In addition, the MMC algorithm depends greatly on the $E_{\text{T}}^{\text{miss}}$ variable, not only in value but also in accuracy, since the measurement of the $E_{\text{T}}^{\text{miss}}$ of the event is affected by the detector resolution, which has a big impact on the result of the algorithm. The effect of the detector resolution on the reconstruction of the MMC is shown in Figure 7.2. In order to account for the detector resolution effect, the $E_{\text{T}}^{\text{miss}}$ resolution is parametrized as a function of $\sqrt{\Sigma E_{\text{T}}}$. An additional likelihood constructed using this information is added into the likelihood of the MMC algorithm, as is described in Ref. [156]. Since the algorithm was originally optimized for a signal in the range $110 - 150\,\text{GeV}$, the parametrization had to be revisited to aim for the reconstruction of a high-mass Higgs boson. This section describes the optimization performed for the $\tau_{\text{had}}\tau_{\text{had}}$ channel.

The $E_{\text{T}}^{\text{miss}}$ resolution is studied by analyzing the deviation of its reconstructed value over the true value as a function of the ΣE_{T}. This deviation, $\Delta E_{\text{T}}^{\text{miss}}$, defined as

$$\Delta E_{\text{T}}^{\text{miss}} \equiv E_{\text{T}}^{\text{miss}}[\text{reco}] - E_{\text{T}}^{\text{miss}}[\text{truth}] \tag{7.3}$$

is calculated for each event in a certain range of ΣE_{T}. The resulting distribution is fitted with a gaussian function to obtain the standard deviation (σ of the gaussian) for the range of ΣE_{T} studied. The parametrization is performed independently for events with jets (with $p_{\text{T}} > 25\,\text{GeV}$) and events with no jets, as the presence of jets affects the resolution. The ranges of $\sqrt{\Sigma E_{\text{T}}}$ are selected maximizing the number of slices while

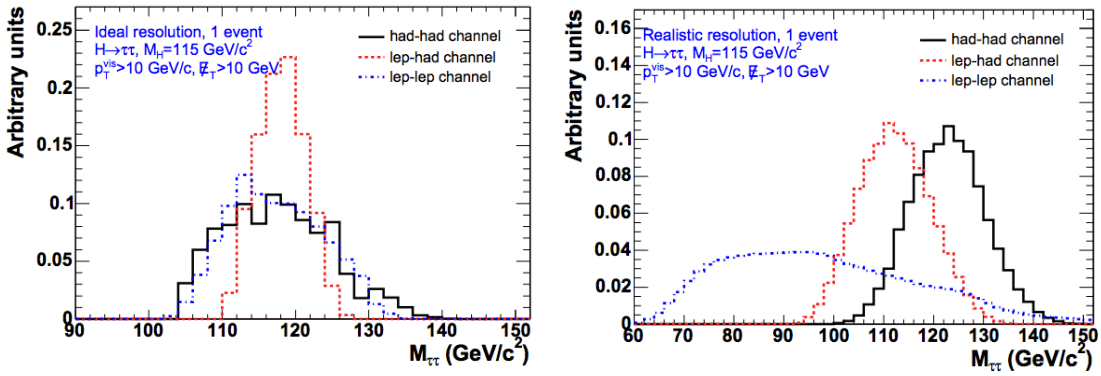

(a) Ideal resolution (b) Reconstruction with detector resolution

Figure 7.2: Comparison of the MMC normalized reconstruction in (a) the ideal resolution case and (b) taking into detector resolution in the reconstruction of the $E_{\mathrm{T}}^{\mathrm{miss}}$. The effect is particularly visible in the $\tau_{\mathrm{lep}}\tau_{\mathrm{lep}}$ channel [156].

keeping the statistical fluctuations low. Quality requirements such a minimum number of events in a slice are applied before the fit. This procedure is done for different mass points of the ggH signal samples ranging from 200 GeV to 1400 GeV, after a simplified $H \to \tau\tau$ selection criteria. Examples of this parametrization are given in Figure 7.3 and Figure 7.4 for events with and without jets, respectively, for the mass point of $m_H = 600\,\mathrm{GeV}$.

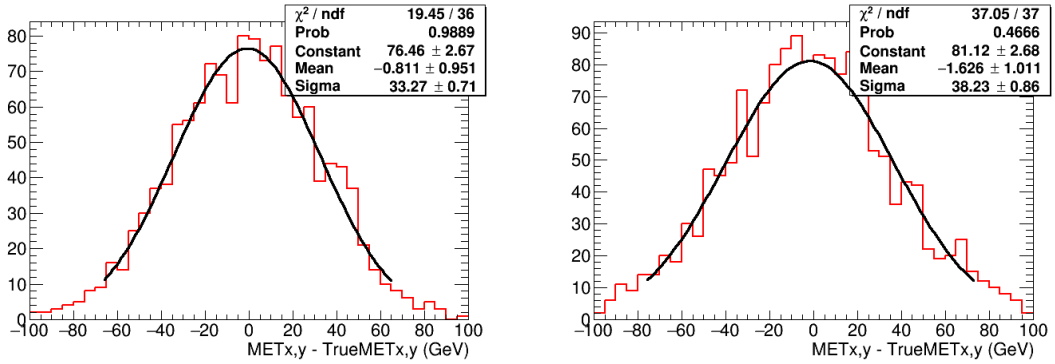

(a) $\sqrt{\Sigma E_{\mathrm{T}}} \in [32, 34]\ \sqrt{\mathrm{GeV}}$ (b) $\sqrt{\Sigma E_{\mathrm{T}}} \in [36, 38]\ \sqrt{\mathrm{GeV}}$

Figure 7.3: Two examples of slices of $\sqrt{\Sigma E_{\mathrm{T}}}$ for a sample of ggH with $m_H = 600\,\mathrm{GeV}$ for events with jets, showing the distributions of deviations of the $E_{\mathrm{T}}^{\mathrm{miss}}$ reconstruction ($\Delta E_{\mathrm{T}}^{\mathrm{miss}} \equiv E_{\mathrm{T}}^{\mathrm{miss}}[\mathrm{reco}] - E_{\mathrm{T}}^{\mathrm{miss}}[\mathrm{truth}]$) and its gaussian fit. The sigma of the gaussian (shown in the legend of each distribution) is the parameter of interest.

In order to study the dependence of the $E_{\mathrm{T}}^{\mathrm{miss}}$ resolution with $\sqrt{\Sigma E_{\mathrm{T}}}$, the σ of the gaussian distributions of each of the ΣE_{T} slices are shown as a function of $\sqrt{\Sigma E_{\mathrm{T}}}$. The resulting distribution is fitted, in turn, with a linear function, where the parameter of interest for the study is the slope of the function. This is done independently for each of the mass points and for the two topologies (with or without jets). An example of this fit in shown in Figure 7.5 for (a) events with jets and (b) events without jets, for the mass point of $m_H = 600\,\mathrm{GeV}$.

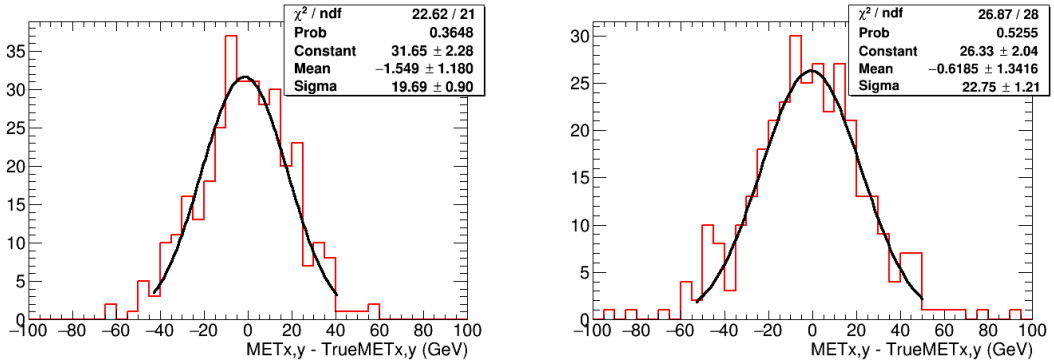

(a) $\sqrt{\Sigma E_{\text{T}}} \in [23, 25]\ \sqrt{\text{GeV}}$ (b) $\sqrt{\Sigma E_{\text{T}}} \in [25, 27]\ \sqrt{\text{GeV}}$

Figure 7.4: Two examples of slices of $\sqrt{\Sigma E_{\text{T}}}$ for a sample of ggH with $m_H = 600\,\text{GeV}$ for events without jets, showing the distributions of deviations of the $E_{\text{T}}^{\text{miss}}$ reconstruction ($\Delta E_{\text{T}}^{\text{miss}} \equiv E_{\text{T}}^{\text{miss}}[\text{reco}] - E_{\text{T}}^{\text{miss}}[\text{truth}]$) and its gaussian fit. The sigma of the gaussian (shown in the legend of each distribution) is the parameter of interest.

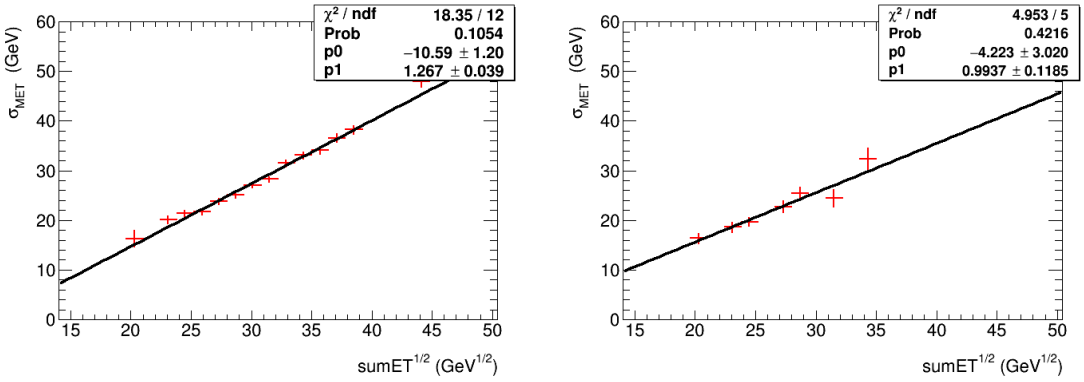

(a) events with jets (b) events without jets

Figure 7.5: Linear fit on the dependence of the $E_{\text{T}}^{\text{miss}}$ resolution (σ_{MET}) with $\sqrt{\Sigma E_{\text{T}}}$ for a sample of ggH with $m_H = 600\,\text{GeV}$ for events (a) with jets and (b) without jets. The σ of the gaussian fits of Figures 7.3 and 7.4 are included in their respective topology.

The compatibility of the results of the linear fits of the different mass point has been studied and thus, the fits of all mass points are shown together in Figure 7.6 and numerically in Table 7.1. The results in both topologies are consistent within uncertainty, although in the case of events with jets (subfigure (a)) this consistency is worse. The disagreement is not big enough to affect the results of this study, but further investigations could be done to improve the stability of the fit for events of this topology.

Since the fit values of the different mass points are considered to be compatible within uncertainty for the range studied, there is no need to provide a different calibration for each of the possible mass points. Hence, the MMC algorithm was optimized for a generic high-mass setup, with no mass-dependent optimization. In order to provide a combined calibration, the events for all the different mass points are merged and only one parametrization for jet topology is performed. The results of the linear fit of the $E_{\text{T}}^{\text{miss}}$

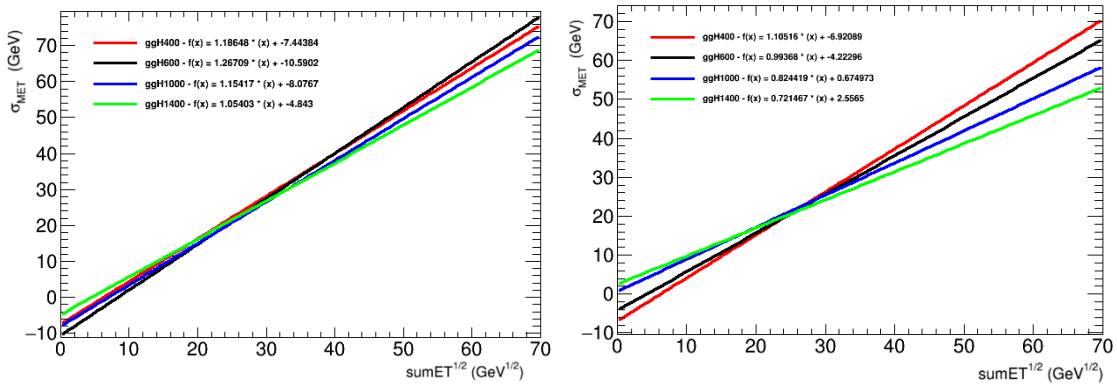

(a) events with jets (b) events without jets

Figure 7.6: Linear fits on the dependence of the $E_{\mathrm{T}}^{\mathrm{miss}}$ resolution (σ_{MET}) with $\sqrt{\Sigma E_{\mathrm{T}}}$ for each of the mass points for events (a) with jets and (b) without jets. The legend on each plot shows the fit values for each mass point, which are also summarized with the respective uncertainties in Table 7.1.

		Fit parameters	
Topology	**Mass point**	p_0 [GeV]	p_1[GeV$^{1/2}$]
with jets	400 GeV	-7.4 ± 1.6	1.19 ± 0.05
	600 GeV	-10.2 ± 1.2	1.27 ± 0.04
	1000 GeV	-8.1 ± 1.3	1.15 ± 0.04
	1400 GeV	-4.5 ± 1.5	1.05 ± 0.04
without jets	400 GeV	-7 ± 4	1.11 ± 0.16
	600 GeV	-4 ± 3	0.99 ± 0.12
	1000 GeV	1 ± 5	0.82 ± 0.17
	1400 GeV	3 ± 5	0.72 ± 0.14

Table 7.1: Fit parameters of the $E_{\mathrm{T}}^{\mathrm{miss}}$ resolution for the studied mass points of ggH production mode for events (a) with jets and (b) without jets. The parameters correspond to a linear function $y = p_0 + p_1 \cdot x$

resolution as a function of $\sqrt{\Sigma E_{\mathrm{T}}}$ are shown in Figure 7.7 for events (a) with jets and (b) without jets.

Finally, the changes in the definition of $E_{\mathrm{T}}^{\mathrm{miss}}$ and ΣE_{T} and the new fit parameters were implemented in the code, in addition to small tunings and corrections. The results of the new MMC significantly improved the reconstruction of high-mass signals, as shown in Figure 7.8. The new version was implemented in the analysis and was used for the studies of the final mass discriminant for the $H/A \to \tau\tau$ analysis described in Section 7.2.3.

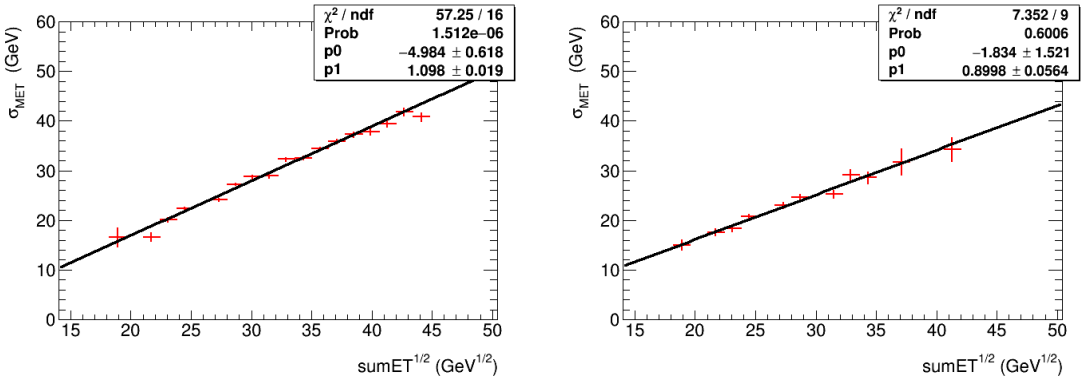

(a) events with jets $f(x) = (-5.0 \pm 0.6) + (1.098 \pm 0.018)\,x$

(b) events without jets $f(x) = (-1.8 \pm 1.5) + (-0.90 \pm 0.06)\,x$

Figure 7.7: Linear fits on the dependence of the $E_{\text{T}}^{\text{miss}}$ resolution (σ_{MET}) with $\sqrt{\Sigma E_{\text{T}}}$ for the combination of all mass points for events (a) with jets and (b) without jets.

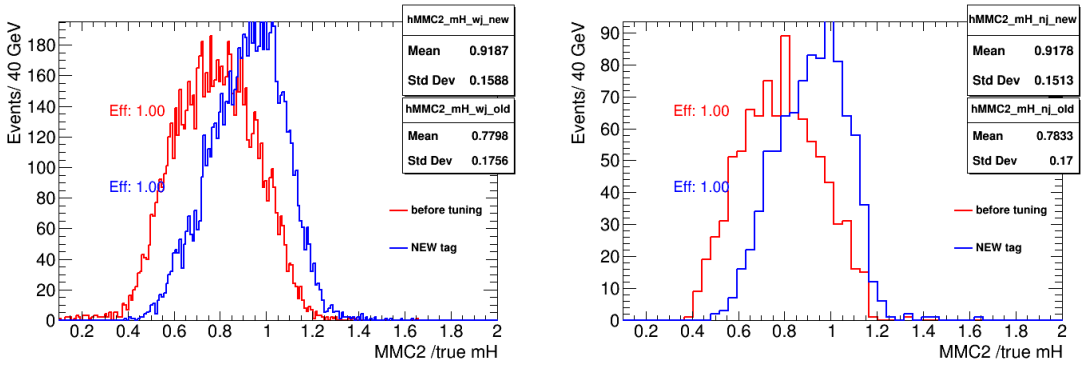

(a) events with jets

(b) events without jets

Figure 7.8: Accuracy of the reconstruction (reconstructed value divided by true value) of the mass of a Higgs boson of the ggH sample with $m_H = 600\,\text{GeV}$ for the new version of the MMC algorithm (labelled "NEW tag", in blue) and the previous version (labelled "before tuning", in red). Values close to 1 represent a better reconstruction. The mean and standard deviation of each distribution are shown in the boxes, for the new version (top) and the old version (bottom).

7.2.3 Final discriminant study

In order to choose the most adequate variable to act as the invariant mass discriminant, the performance of all $m_{\tau\tau}$ candidates was studied in the whole range of masses of the analysis. The candidates tested were the MMC, the MOSAIC, the $m_{\text{T}}^{\text{tot}}$ and, as a baseline, the visible mass, $m_{\tau\tau}^{\text{vis}}$. The figure of merit was the Asimov's significant, Z, defined as [214]:

$$Z \equiv \sqrt{2\left((s+b)\ln\left(1+\frac{s}{b}\right)-s\right)}, \tag{7.4}$$

where s and b are the signal and background expectation, respectively. The significance was computed bin by bin and summed in quadrature over the whole distribution

to get the final number. This was done for the four variables in the different mass points of the mass range of the analysis and at the end of the event selection for the inclusive category (defined in Section 7.6.3). The results are shown in Table 7.2. Plots of the mass distributions from the different algorithms are shown in Figure 7.9 for different mass points.

Mass point	$m_{\mathrm{T}}^{\mathrm{tot}}$	**MMC**	**MOSAIC**	$m_{\tau\tau}^{\mathrm{vis}}$
200 GeV	0.003	0.010	0.006	0.007
300 GeV	0.183	0.266	0.252	0.266
500 GeV	5.078	4.827	4.068	4.119
600 GeV	7.179	6.125	5.256	5.300
700 GeV	8.625	6.937	6.046	6.209
800 GeV	9.875	7.986	6.734	6.886
900 GeV	10.101	9.018	7.566	7.732

Table 7.2: Statistical significance of the different mass reconstruction algorithms as a function of the signal mass point. The numbers correspond to an integrated luminosity of $3.21\,\mathrm{fb}^{-1}$ and a conventional signal cross-section of $1\,\mathrm{pb}^{-1}$.

For lower mass signal samples, $m_{\mathrm{T}}^{\mathrm{tot}}$, MOSAIC and MMC algorithms have similar performance while for higher mass points, $m_{\mathrm{T}}^{\mathrm{tot}}$ performs slightly better. The MOSAIC and MMC algorithms are able to reconstruct with more accuracy the peak position of the signal but the $m_{\mathrm{T}}^{\mathrm{tot}}$ variable achieves a better separation between the multi-jet background and the signal. For this reason, the $m_{\mathrm{T}}^{\mathrm{tot}}$ was chosen as discriminant variable in the statistical analysis of this search.

7.3 Data and MC samples

7.3.1 Data samples

The dataset used in this analysis corresponds to $3.21\,\mathrm{fb}^{-1}$ collected in the first year (2015) of the Run 2 of the LHC, at $\sqrt{s} = 13\,\mathrm{TeV}$ and a bunch-spacing of 25 ns. The dataset undergoes a tight cleaning and selection to remove the events compromised by detector issues. The details of the luminosity delivered by LHC and the Data Quality checks were described in Section 3.4.8. In particular, data taken when the IBL detector was not fully operational have been discarded as the IBL is crucial for the identification of the b-jets. Also, the first set of data taken during the Run 2, with a bunch-spacing of 50 ns, was not used since they correspond to a small fraction of the data, without a noticeable impact in sensitivity.

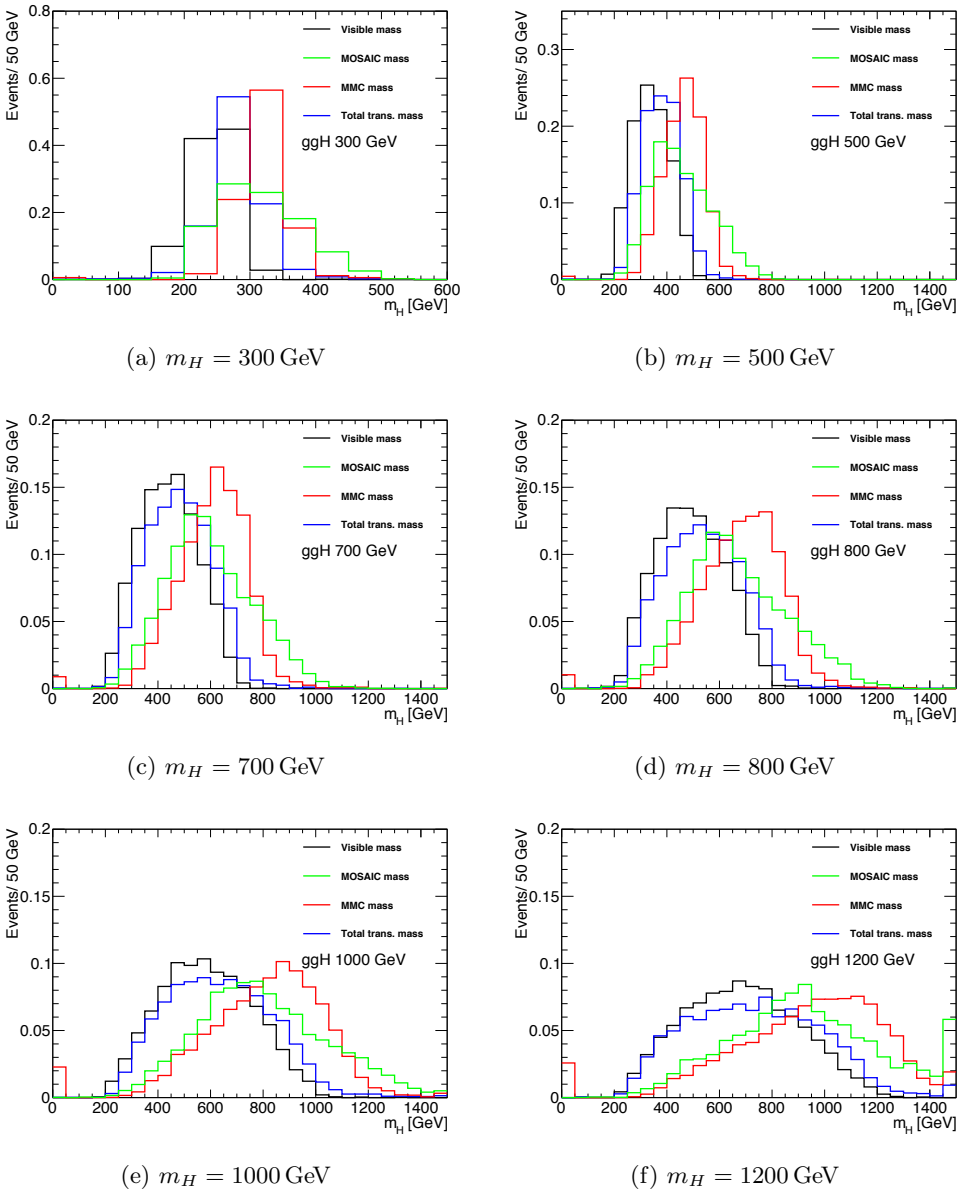

(a) $m_H = 300\,\text{GeV}$ (b) $m_H = 500\,\text{GeV}$

(c) $m_H = 700\,\text{GeV}$ (d) $m_H = 800\,\text{GeV}$

(e) $m_H = 1000\,\text{GeV}$ (f) $m_H = 1200\,\text{GeV}$

Figure 7.9: Normalized reconstruction of the invariant di-τ mass as a result of the different algorithms: visible mass, total transverse mass, MMC and the MOSAIC mass for different signal mass points.

7.3.2 Monte Carlo event samples

Simulated events of a heavy neutral MSSM Higgs boson produced via gluon fusion (ggH) and in association with b-quarks (bbH) are generated with the `POWHEG-BOX v2` [159–161] and `MADGRAPH5_aMC@NLO 2.1.2` [222, 223] programs, respectively. The CT10 [224] and CT10nlo_nf4 [225] sets of PDFs are used, respectively. `PYTHIA 8.210` [226] with the AZNLO [227] (A14 [228]) set of tuned parameters, or "tune", is used for the parton shower, underlying event and hadronization in the ggH (bbH) production. The production cross-sections for the various MSSM scenarios are calculated using `SusHi` [229] for ggH production [165–168, 230–238] and bbH production in the five-flavor scheme (5FS) [239];

bbH production in the four-flavor scheme (4FS) is calculated according to Ref. [240, 241]. The final bbH cross-section is obtained by using the method in Ref. [242] to match the 4FS and 5FS cross-sections. The masses and the couplings of the Higgs bosons are computed with `FeynHiggs` [83, 243–246], whereas the branching fraction calculation follows the procedure described in Ref. [83]. In the case of the hMSSM scenario, the method described in Ref. [74] is followed for the production cross-sections whereas `HDECAY` [247] is used for the branching fraction calculation.

The simulated backgrounds consist of the production of Z+jets, W+jets, $t\bar{t}$ pairs, single-top quarks and electroweak di-bosons ($WW/WZ/ZZ$). These are modeled with several event generators as described below, while contributions from multi-jet production are estimated with data, as described in Section 7.5.1.

Simulated samples of Z+jets and W+jets events are produced using `POWHEG-BOX v2` interfaced to `PYTHIA 8.186` with the AZNLO tune. In this sample, `PHOTOS++ v3.52` [248, 249] is used for final-state QED radiation. A dedicated W+jets sample binned in p_{T}^{W}, produced using the `SHERPA 2.1.1` generator [184], is used in the $\tau_{\mathrm{had}}\tau_{\mathrm{had}}$ channel in order to enhance the number of events with high invariant mass. For this sample, matrix elements are calculated for up to two partons at next-to-leading order (NLO) and four partons at leading order (LO), merged with the `SHERPA` parton shower model using the `ME+PS@NLO` prescription [250]. Spin correlation effects between the W boson and its decay products are simulated with the `TauSpinner` program [251]. All W/Z+jets samples use the CT10 PDF set and are normalized to the next-to-next-to-leading-order (NNLO) cross-sections calculated using `FEWZ` [167, 252, 253].

The `POWHEG-BOX v2` program with the CT10 PDF set is used for the generation of $t\bar{t}$ pairs and single-top quarks in the Wt and s-channels. Samples of t-channel single-top quark events are produced with the `POWHEG-BOX v1` generator employing the 4FS for the NLO matrix element calculations, together with the fixed 4FS PDF set CT10f4; the top-quark decay is simulated with `MadSpin` [254]. For all samples of top-quark production, the spin correlations are preserved and the parton shower, fragmentation and underlying event are simulated using `PYTHIA 6.428` [194] with the CTQ6L1 PDF set and the corresponding Perugia 2012 tune [255]. Final-state QED radiation is simulated using `PHOTOS + v3.52`. The top-quark mass is set to 172.5 GeV. The $t\bar{t}$ production sample is normalized to the NNLO cross-section, including soft-gluon resummation to next-to-next-to-leading-logarithm accuracy (Ref. [190] and references therein). The normalization of the single top quark event samples uses an approximate NNLO calculation from Refs. [191, 192, 195].

Finally, di-boson processes are simulated using the `SHERPA 2.1.1` program with the CT10 PDF. They are calculated for up to one additional parton at NLO, depending on the process, and up to three additional partons at LO. The di-boson samples use the NLO cross-sections that `SHERPA` calculates.

The simulation of b and c-hadron decays for all samples, excluding those generated with `SHERPA`, uses `EvtGen v1.2.0` [256]. All simulated samples include the effect of multiple pp interactions in the same and neighboring bunch-crossings (pile-up) by overlaying simulated minimum-bias events on each generated signal or background event. These minimum-bias events are generated with `PYTHIA 8.186` [169, 194], using the A2 tune [257] and the MSTW2008LO PDF [76]. Each sample is simulated using the full `GEANT4` [126, 258] simulation of the ATLAS detector, with the exception of the bbH MSSM Higgs boson signal, for which the `ATLFAST-II` [258, 259] fast simulation framework is used. This was motivated by the necessity of generating larger statistics for bbH due to the presence of large fraction of negative weight events in MC@NLO. Finally, the Monte Carlo samples are processed through the same reconstruction software as for the data.

7.4 Signal modeling in the MSSM framework

The $H/A \to \tau\tau$ analysis searches for an excess of di-τ events coming from the decay of heavy Higgs particles predicted by the MSSM framework. However, since the masses of the Higgs bosons are not fixed in the MSSM, several signal options, with mass values ranging from 200 GeV to 1400 GeV are tested in the analysis. For illustration purposes, the figures use a conventional cross-section of $1\,\text{pb}^{-1}$ for the signal distributions. The final results of the analysis allow to set upper limits on the cross-section times branching ratio of the different production modes and on the parameters m_A and $\tan\beta$ for different scenarios of the MSSM framework.

The production modes of the MSSM Higgs bosons in pp colliders were described in Section 2.3. The $H/A \to \tau\tau$ analysis searches for signal events of Higgs bosons produced by two main production modes: gluon fusion (ggH) and b-associated production (bbH), which are shown in Figure 7.10. The bbH production mode has a very small contribution in the SM but in the MSSM its cross-section depends on the $\tan\beta$ parameter. For high values of $\tan\beta$, the coupling of the b-quark to the Higgs bosons is enhanced and thus, the bbH contribution acquires more relevance, surpassing the ggH production rate for certain values. Additional modes as the VBF, VH or ttH were found to be small and are neglected. The signal models are estimated using MC simulation, described in Section 7.3.2.

7.5 Background estimation

This section describes the physics of the processes which can be a source of background of the $\tau_{\text{had}}\tau_{\text{had}}$ channel of the $H/A \to \tau\tau$ analysis, as well as any other information regarding their estimation or its validation.

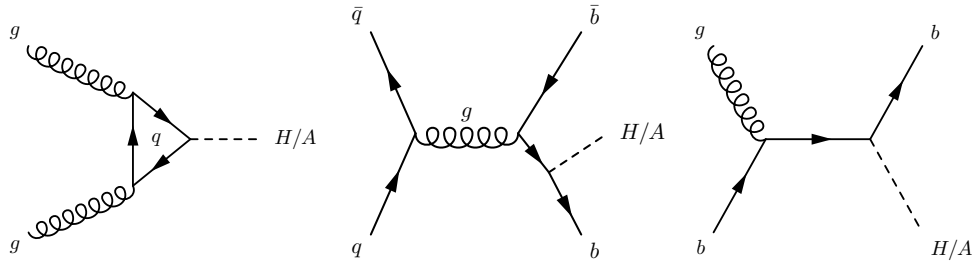

(a) ggH (b) bbH 4FS (c) bbH 5FS

Figure 7.10: Main production modes of a Higgs boson considered in the MSSM analysis, including (a) gluon fusion process (ggH) and b-associated production (bbH) in the (b) four-flavor scheme and (c) five-flavor scheme.

Two types of background can be observed in the $\tau_{\text{had}}\tau_{\text{had}}$ channel: backgrounds which are source of two real τ particles (the Z+jets, top-quark and di-boson processes), and backgrounds where at least one of the objects of the event is misreconstructed as a hadronic τ, such as the multi-jet and $W \to \tau\nu$ processes. The multi-jet process, which dominates the analysis, is modeled using a data-driven method. The rest of backgrounds are modeled using MC techniques, with the addition of a data-driven correction to correct for τ-misreconstruction effects.

7.5.1 Multi-jet processes

The main background of the analysis is the multi-jet process. Due to its extremely high production cross-section and the very low probability of passing the selection, the modeling of this background via MC methods is infeasible. Thus, a data-driven technique, the Fake Factor method (FF), is implemented to describe this background.

The FF technique derives a set of factors obtained in an enriched control region (CR) to estimate the background in the signal region (SR). This CR is defined so that the multi-jet processes dominate and no significant amount of signal is expected. This CR, labelled *di-jet CR*, is obtained by inverting the τ-identification (τ-ID) of the sub-leading τ. Then, using a tag-and-probe analysis, the fake factors are derived as the number of probe-jets in the di-jet CR that pass τ identification, $N^{\text{pass }\tau\text{-ID}}$, divided by the number of probe-jets failing it, $N^{\text{fail }\tau\text{-ID}}$, which is shown in Equation 7.5. These factors are parametrized as a function of p_{T} and number of the tracks of the τ_{had} (N_{track}) for the two analysis categories. The size of the p_{T} slices was chosen in such way that the amount of slices is maximized while keeping a reasonably low statistical error.

$$f_{\tau\text{-ID}}(p_{\text{T}}, N_{\text{track}}) \equiv \left.\frac{N^{\text{pass }\tau\text{-ID}}(p_{\text{T}}, N_{\text{track}})}{N^{\text{fail }\tau\text{-ID}}(p_{\text{T}}, N_{\text{track}})}\right|_{\text{di-jet CR}} \tag{7.5}$$

The estimation (shape and normalization) of the multi-jet contribution in the SR (where both τ candidates pass τ-ID), N_{mj}, is predicted by weighting the events where the sub-leading τ fails τ-ID by their Fake Factor:

$$N_{\text{mj}}(p_{\text{T}}, N_{\text{track}}) = f_{\tau\text{-ID}}(p_{\text{T}}, N_{\text{track}}) \times \left(N_{\text{data}}^{\text{fail } \tau\text{-ID}}(p_{\text{T}}, N_{\text{track}}) \right) \tag{7.6}$$

The di-jet CR is defined to be as similar to the SR as possible. However, the lack of statistics forced the loosening of several cuts. Tests were performed to confirm this had no significant impact on the value of the FF. The primary condition for this region is that the event had fired any of the single-jet triggers, which span a p_{T} range from 25 GeV to 460 GeV. The full selection of the di-jet CR is the following:

- Firing of any of the single-jet triggers.
- Two τ_{had} candidates with $p_{\text{T}} > 55$ GeV.
- Leading τ_{had} (tag object) with $p_{\text{T}} > 100$ GeV fails "medium" τ-ID and pass a tight electron veto.
- p_{T} of the sub-leading τ_{had} (probe object) at least 30% of the p_{T} of the leading τ_{had} (p_{T} balance).

In the preliminary studies of the FF, the values for the same-sign (SS) and opposite-sign (OS) events were computed separately. However, after observing that both sets of values were compatible within statistical uncertainties (Figure 7.11), their average was taken as a final result, benefiting from the increased statistics. The FF values were evaluated in both categories (b-tag and b-veto, whose definition is detailed in Section 7.6.3) and a small but significant difference between the two categories was observed, especially for 1-prong probe events (Figure 7.12 (a)). Therefore the FF were determined separately for the b-tag and b-veto categories. The final values for the FF, along with their uncertainty, are shown in Table 7.3.

		Range of $p_{\text{T}}^{\tau_2}$ [GeV]			
Category	**Prongs**	$50 - 110$	$110 - 160$	$160 - 210$	$210 - 1000$
b-tag	1-prong	0.110 ± 0.017	0.160 ± 0.019	0.19 ± 0.03	0.20 ± 0.03
	3-prong	0.0051 ± 0.0013	0.0073 ± 0.0012	0.009 ± 0.003	0.0107 ± 0.0013
b-veto	1-prong	0.077 ± 0.003	0.120 ± 0.005	0.151 ± 0.007	0.174 ± 0.004
	3-prong	0.0033 ± 0.0002	0.0065 ± 0.0005	0.0076 ± 0.0007	0.0103 ± 0.0008

Table 7.3: Fake Factors and their relative uncertainty for 1-prong and 3-prong events as a function of the sub-leading tau candidate p_{T} in the two categories.

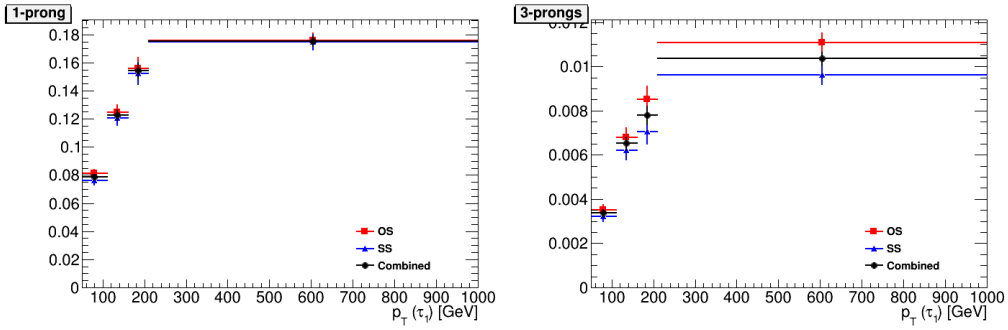

(a) 1-prong (b) 3-prong

Figure 7.11: Fake Factors $f_{\tau\text{-ID}}$ for (left) 1-prong and (right) 3-prong τ candidates, separated by the charge product of the two candidates, as measured in the di-jet CR.

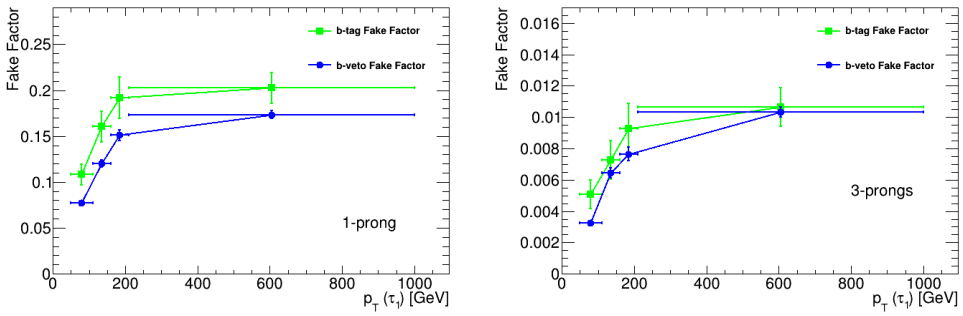

(a) 1-prong (b) 3-prong

Figure 7.12: Fake Factors $f_{\tau\text{-ID}}$ for (left) 1-prong and (right) 3-prong τ candidates, separated by category (passing or failing the b-tag requirement), as measured in the di-jet CR.

7.5.2 Other backgrounds

The rest of the backgrounds in the analysis –Z+jets (including $Z \to \tau\tau$ and $Z \to ll$), W+jets (including $W \to \tau\nu$ and $W \to l\nu$), top ($t\bar{t}$ and single-top processes) and di-boson– are modeled via MC methods, with the samples described in Section 7.3.2. However, these processes can contain events where at least one jet has been misidentified as a τ_{had}, which is especially relevant in the $W \to \tau\nu$ + jets and the $t\bar{t}$ processes. The τ-misidentification rate is not well modeled in the MC simulation, therefore their estimation is corrected with a data-driven method called *Fake Rate* (FR).

The FR are factors calculated from data in dedicated control regions defined by asking a single-muon trigger, an isolated muon with $p_{\text{T}} > 55\,\text{GeV}$, one τ_{had} with $p_{\text{T}} > 50\,\text{GeV}$ and $\delta\phi(\mu, \tau_{\text{had}}) > 2.4$ (for the b-veto category, an additional criterion is applied, $\sum_{\mu,\tau} \cos\delta\phi(l, E_{\text{T}}^{\text{miss}}) < 0$). The FR factors are then applied in the MC simulation for each misidentified τ, i.e. a reconstructed τ object not matched to a true τ. In addition to correcting the background yield, this also increases the statistical accuracy of these backgrounds, allowing for a more precise description, especially in the tails of the distributions. The FRs are parametrized in terms of p_{T} and number of prongs. In

addition, they are measured independently for OS and SS events, and depending on which τ (leading, sub-leading, or both) is misidentified. Also, the FR are derived independently in both categories, with different purposes: the ones obtained in the b-tag category are used for the $t\bar{t}$ and single-top events while the FR obtained in the b-veto category are applied to the remaining processes.

For the b-tag category, at least one b-tagged jet is required, which defines a CR with a 81% of purity of top events. This CR has a similar composition of top processes as the SR region, e.g. the fraction of $t\bar{t}$ is 89% in both cases. Regarding the other processes, the CR is composed of a 7% of Wt and 4% of single-top while the SR has 10% Wt and 1% single-top. The CR has also a significant contamination of true-τ processes, that is subtracted using MC prediction. For the b-veto category, in addition to the veto of any b-jet, two additional criteria are required: $\sum_{l=\mu,\tau} \cos\Delta\phi(l, E_{\text{T}}^{\text{miss}}) < 0$ and $\Delta\phi(\mu, \tau_{\text{had}}) > 2.4$, which reduce further the multi-jet contamination. The selection results in a purity of 88% of $W \to \mu\nu + \text{jets}$.

An additional weight is applied to $W \to \tau\nu$ events as a function of $m_{\text{T}}^{\text{tot}}$ to improve the modeling of the kinematics of the W+jets simulated events. The weight function is derived by fitting the ratio of the data to the simulation for the $W \to \mu\nu + \text{jets}$ process in a dedicated $W \to \mu\nu$ CR, defined in analogy with the SR selection as follow: pass single-muon trigger, one isolated muon with $p_{\text{T}}^{\mu} > 110\,\text{GeV}$ and one τ_{had} with $p_{\text{T}}^{\tau_{\text{had}}} > 55\,\text{GeV}$.

7.6 Event selection and categorization

7.6.1 Event cleaning

A first selection of events is performed by applying a Good Run List (GRL) selection of lumi-blocks to the dataset. In addition to the GRL, a primary vertex (PV) requirement is applied, asking for events that contain at least one PV with a minimum of two associated tracks, as well as removal of events containing jets whose energy is mismeasured.

7.6.2 Event selection

Once the dataset is ready for the physics analysis, the di-τ events are selected using a single-τ trigger that requires that the τ_{had} candidate has $p_{\text{T}} > 80\,\text{GeV}$ and that is matched to the object that fired the trigger. Then, a set of criteria are implemented to remove the largest amount of possible background and enhance any excess from a hypothetical di-τ signal. The selection criteria of the $\tau_{\text{had}}\tau_{\text{had}}$ channel requires:

- that at least 2 τ_{had} candidates are present in the event
- that the leading τ_{had} passes the "medium" identification criteria and satisfies $p_{\text{T}}^{\tau 1} > 110\,\text{GeV}$.

- that the sub-leading τ_{had} passes "loose" identification criteria and satisfies $p_{\text{T}}^{\tau 2} > 55\,\text{GeV}$.
- that the single-τ trigger is fired and the leading τ_{had} candidate matches to the trigger.
- a veto of any electron or muon passing the "loose" identification criteria.
- $\Delta\phi(\tau_1, \tau_2) > 2.7$.
- that the τ_1 and τ_2 candidates have opposite charge.

7.6.3 Categorization

Two categories are defined at the end of the selection to benefit from the different event topologies. As the coupling of b-quarks with the Higgs boson is enhanced for large $\tan\beta$ values in the MSSM, the bbH production mode could be greatly increased. Furthermore, the signal events produced by this mode have a very distinct signature, as the Higgs boson is produced along with two b-tagged jets.

Therefore a ***b*-tag** category is defined to collect the bbH events by requiring the presence of at least one b-tagged jet. On the other hand, a second category, orthogonal to the first, is defined by rejecting any event with a b-tagged jet. This category is labelled as ***b*-veto** category and aims to select events originated from the ggH production mode. The combination of both categories is called the **inclusive category** and it is used for the Z' boson search, as well as background studies.

In addition, the reversal of the opposite-sign requirement allows to define a same-sign region (SS), which acts as a validation region (VR), to control the background modeling. This VR can be split into the same categories as the signal region, b-tag and b-veto, allowing further checks of the background estimations. The distribution of the SS VR for both categories are shown in Figure 7.13.

7.7 Additional searches in the $H/A \to \tau\tau$ analysis

The $H/A \to \tau\tau$ analysis is divided in two orthogonal channels, the fully-hadronic $\tau_{\text{had}}\tau_{\text{had}}$ and the semi-leptonic $\tau_{\text{lep}}\tau_{\text{had}}$, which are combined to obtain the final result of the search. In addition, the analysis framework is used for the search of an additional heavy Z' boson. For completeness, a brief description of these searches is given below.

7.7.1 The $\tau_{\text{lep}}\tau_{\text{had}}$ channel

The $\tau_{\text{lep}}\tau_{\text{had}}$ channel aims to search for di-τ events in the semi-leptonic final state, where one τ decays leptonically and the other one hadronically. Hence, this channel benefits

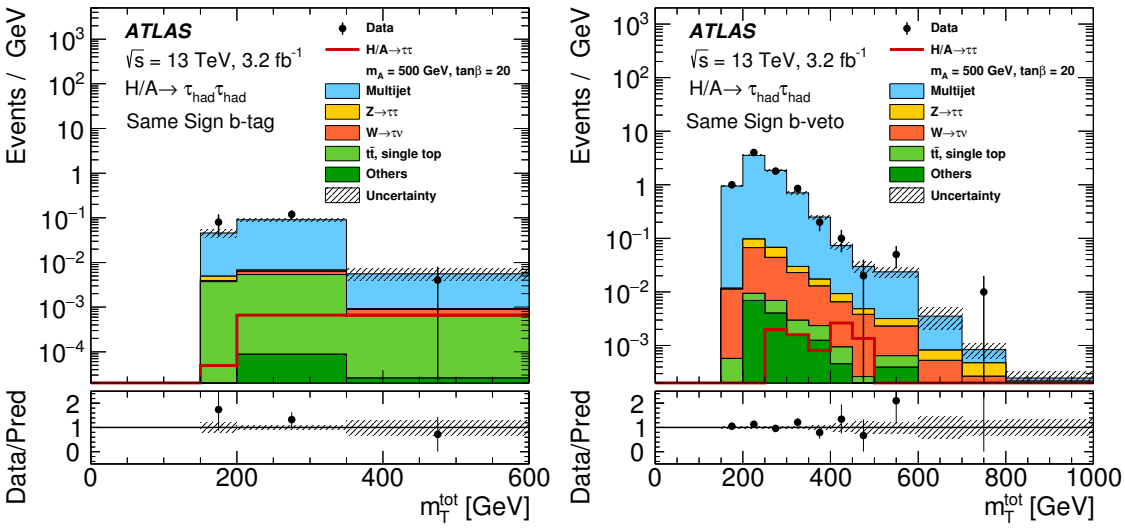

(a) b-tag category (b) b-veto category

Figure 7.13: Pre-fit distributions of $m_{\text{T}}^{\text{tot}}$ in the Same Sign validation region for the $\tau_{\text{had}}\tau_{\text{had}}$ channel in the (a) b-tag category and (b) b-veto category. The data are compared to the background prediction and a hypothetical MSSM $H/A \to \tau\tau$ signal ($m_A = 500\,\text{GeV}$ and $\tan\beta = 20$). The label "Others" refers to contributions due to di-boson, $Z \to ll$+jets and $W(\to l\nu)$+jets production. The background uncertainty includes statistical and systematic uncertainties. The bins have a varying size and overflows are included in the last bin of the distributions.

from the easy identification of the leptonic objects and the abundance of the hadronic decays of the τ.

The event selection of the $\tau_{\text{lep}}\tau_{\text{had}}$ channel requires the event to pass a single electron or muon trigger, in addition to at least one τ_{had} candidate with a $p_{\text{T}} > 25\,\text{GeV}$ and a "medium" τ-ID criteria. One reconstructed light lepton is needed and it has to be matched with the object that fired the trigger. The lepton and the τ_{had} are required to have opposite charges. Further kinematic criteria are applied: $\Delta\phi(l, \tau_{\text{had}}) > 2.4$ and $m_{\text{T}}(l, E_{\text{T}}^{\text{miss}}) < 40\,\text{GeV}$. For electrons, a veto is applied for events in the Z peak mass-window ($m_{e\tau} \in [80 - 110\,\text{GeV}]$). After the selection, the events are categorized in the same way as the $\tau_{\text{had}}\tau_{\text{had}}$ channel, with a b-tag category that requires at least a b-tagged jet and a complementary b-veto category, which rejects any b-tagged jet. A W+jets control region and a $t\bar{t}$ validation region are defined for the W+jets and $t\bar{t}$ backgrounds. Both of them reverse the m_{T} requirement while the latter also asks for a b-tag jet.

The main backgrounds in the $\tau_{\text{lep}}\tau_{\text{had}}$ channel arise from $Z \to \tau\tau$ production, followed by processes with a misidentified τ_{had} in the b-veto category, and $t\bar{t}$ (either with a true-τ lepton or a jet misidentified as a τ_{had}) in the b-tag category. Background processes where the τ_{had} candidate or both the lepton and τ_{had} candidates arise from misidentified jets are dominated by W+jets in the b-veto and by $t\bar{t}$ in the b-tag category. A data-driven Fake Factor technique is used to estimate the contribution of these processes to the signal region, analogous to what it is done in the $\tau_{\text{had}}\tau_{\text{had}}$ channel, but estimated separately

for the multi-jet background and the W+jets and $t\bar{t}$ contributions, and then combined. Background processes where the electron or the muon is identified as a τ_{had} object are modeled using simulation. To account for the modeling of electrons misidentified as τ_{had} objects in $Z \to ee$+jets events, the simulation is corrected using data-driven factors derived by reversing the mass-window criterion.

Distributions of $m_{\text{T}}^{\text{tot}}$ in the $\tau_{\text{lep}}\tau_{\text{had}}$ channel are shown in Figure 7.14 for the W+jets CR and the $t\bar{t}$ VR.

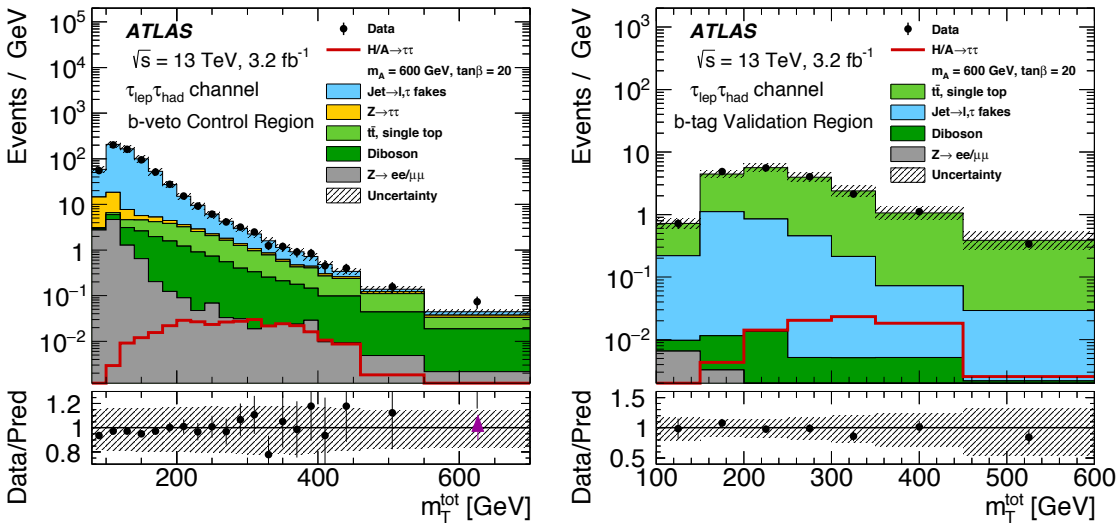

(a) W+jets CR (b) $t\bar{t}$ VR

Figure 7.14: Distributions of $m_{\text{T}}^{\text{tot}}$ in the $\tau_{\text{lep}}\tau_{\text{had}}$ channel for the (a) W+jets CR and (b) $t\bar{t}$ VR. The data are compared to the background prediction and a hypothetical MSSM $H/A \to \tau\tau$ signal ($m_A = 500\,\text{GeV}$ and $\tan\beta = 20$). The background uncertainty includes statistical and systematic uncertainties. The bins have a varying size and overflows are included in the last bin of the distributions.

7.7.2 The Z' boson search

Heavy Z bosons (labelled as Z') are present in several models beyond the SM. These bosons appear in theories extending the electroweak gauge group, where lepton universality is typically conserved. A frequently used benchmark is the Sequential Standard Model (SSM) [260], which contains a single additional Z' boson with the same couplings as the SM Z boson. Some models offering an explanation for the high mass of the top quark predict heavy gauge bosons that couple preferentially to third generation fermions [261–264]. A model predicting additional weak gauge bosons Z' and W' of this kind is the Strong Flavor Model (SFM) [262, 264].

One of the parameter of interest of the SFM model is the mixing angle between the light and heavy fermion parts of the $SU(2)$ gauge group of the model, $\sin^2\phi$. For small values of $\sin^2\phi$, the ratio starts increasing steeply as the production via b-quarks is becoming the dominant production mode. However, this effect was not properly accounted

for in this analysis, which caused an underestimation of the SFM production cross-section for small values of $\sin^2\phi$. It was corrected in a posterior publication [265].

The Z' decay to $\tau\tau$ gives essentially the same signal as $H/A \to \tau\tau$, therefore, the Z' boson search uses the same framework as the $H/A \to \tau\tau$ analysis, with the same object reconstruction and selection criteria. However, signal is expected to be produced by a Drell-Yan process (Figure 7.15). Therefore, the Z' analysis uses only an inclusive category (defined in Section 7.6.3), instead of the b-tag and b-veto regions.

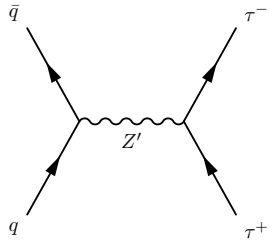

Figure 7.15: Feynman diagram of the production of a Z' boson via Drell-Yan process, and its decay in a pair of τ leptons.

7.8 Systematic uncertainties

The signal and background modeling is affected by a variety of systematic uncertainties, which are related with the detector simulation, the theoretical model and the data-driven background estimations. Table 7.4 shows the effect of the largest systematic deviations.

Regarding the detector simulation, the analysis is affected by the integrated luminosity measurement, which has an uncertainty of 5% and is used for all MC samples. Other detector-related systematics include:

- the τ_{had} reconstruction and identification efficiencies
- the τ_{had} trigger scale factor
- the τ_{had} electron veto
- the electron and muon trigger, reconstruction and identification efficiencies
- the energy scales for jet (JES), electron, muon and τ_{had} (TES) objects
- jet energy resolution (JER) and calibration
- calibration of the $E_{\text{T}}^{\text{miss}}$
- jet flavor tagging systematics

Any systematic effect on the overall normalization or shape of the $m_{\text{T}}^{\text{tot}}$ distribution in the signal region is considered, but the electron, muon, jet and $E_{\text{T}}^{\text{miss}}$ systematics are

Source of uncertainty	F_- (%)	F_+ (%)
$t\bar{t}$ and single top quark normalization	−13.0	+11.0
τ_{had} energy scale (TES)	− 3.0	+ 8.0
τ_{had} trigger	− 0.5	+10.0
Signal acceptance	− 6.0	+ 1.9
Jet-to-τ_{had} fake rate ($\tau_{\text{lep}}\tau_{\text{had}}$)	− 1.5	+ 2.4
Multi-jet background ($\tau_{\text{had}}\tau_{\text{had}}$)	− 0.4	+ 0.3
$t\bar{t}$ background modeling	− 0.1	+ 1.0
Jet-to-τ_{had} fake rate ($\tau_{\text{had}}\tau_{\text{had}}$)	− 0.2	+ 0.2
Jet-to-vertex association	− 0.1	+ 0.1
Statistics (data and simulation)	−75.0	+65.0

Table 7.4: Fractional impact of the most important sources of systematic uncertainty on the total uncertainty of the signal strength, for the MSSM signal hypothesis of $m_A = 500\,\text{GeV}$, $\tan\beta = 20$. For each source of uncertainty, $F_\pm = \pm\frac{\sigma^2_{\text{source}}}{\sigma^2_{\text{total}}}$ is defined as the positive (negative) fractional contribution to the signal strength uncertainty.

found to produce a negligible effect in the SR. The categorization implemented in this analysis (b-tag discrimination) introduces additional systematic uncertainties on the event selection and final distributions, that come from the flavor tagging of the jets and the jets themselves. These systematics were tested for normalization and shape effects, and found to be negligible.

Regarding the data-driven background estimations, the uncertainty on the FF measurement is obtained as the sum in quadrature of the statistical uncertainty of the measurement and the difference between the FF for SS and OS events, which were shown in Table 7.3 in Section 7.5.1. This effect is propagated to the multi-jet background in the statistical analysis. Regarding the FR, the main source of uncertainty is due to the statistical uncertainty of the FR measurement, which is a variation of ±30%.

Regarding the background modeling systematics, the uncertainty in the cross-section of the different processes is taken into account. The uncertainties for Z+jets and di-boson production are 5% and 6%, respectively while for $t\bar{t}$ and single top production the uncertainty is 6%. Uncertainties related to $t\bar{t}$ modeling include the systematics associated with the shower radiation and hadronization model. The estimation of systematic uncertainties is done by comparing different generators. Based on the available samples, no statistically significant shape effect is observed for these systematic variations, therefore only the effect on the normalization is considered. The quadratically combined systematic was determined to be $^{+15.0}_{-18.5}$% in b-veto and $^{+38.1}_{-32.5}$% in the b-tag category.

The signal modeling includes the uncertainties associated with the initial and final state radiation, the modeling of multi-parton interactions, the normalization and factorization scale, and the PDF uncertainties, which are summarized in Table 7.5.

		***b*-tag category**			***b*-veto category**		
Mode	**Variation**	400 GeV	700 GeV	1000 GeV	400 GeV	700 GeV	1000 GeV
bbH	Scales	$^{+19.2}_{-19.2}$	$^{+20.3}_{-20.1}$	$^{+22.3}_{-21.1}$	$^{+19.3}_{-18.1}$	$^{+21.4}_{-20.3}$	$^{+24.4}_{-21.7}$
	PDF	$^{+6.0}_{-5.5}$	$^{+13.1}_{-15.5}$	$^{+16.2}_{-9.5}$	$^{+6.5}_{-5.2}$	$^{+10.5}_{-9.0}$	$^{+15.1}_{-9.2}$
	Tune	±5	±4	±3	±4	±3	±3
	Total (+)	+20.7	+24.5	+27.7	+20.7	+24.5	+27.7
	Total (−)	−20.6	−25.7	−23.3	−20.6	−25.7	−23.3
ggH	Scales	$^{+19}_{-15}$	$^{+19}_{-16}$	$^{+18}_{-15}$	$^{+15}_{-13}$	$^{+15}_{-14}$	$^{+15}_{-14}$
	PDF	±4.9	±4.7	±4.1	±4.8	±4.7	±4.4
	Tune	±21.3	±17.4	±16.1	±3.1	±2.6	±1.2
	Total (+)	+29.0	+26.2	+24.5	+16.1	+16.0	+15.7
	Total (−)	−26.5	−24.1	−22.4	−14.2	−15.0	−14.7

Table 7.5: Signal acceptance uncertainties (in %) for *b*-associated production in both categories.

7.9 Results of the $H/A \to \tau\tau$ analysis

7.9.1 Signal extraction

The statistical framework used to extract the final result of the $H/A \to \tau\tau$ analysis is the same as for the SM $H \to \tau\tau$ analysis, described in Section 6.10.4. The framework is adapted to the features of the $H/A \to \tau\tau$ analysis, which are described below.

The parameter of interest of the $H/A \to \tau\tau$ analysis is the signal strength, μ, defined in Equation 6.13 as the ratio of the fitted signal cross-section times the branching fraction ($\sigma \times \text{BR}$) over the signal $\sigma \times \text{BR}$ predicted by a particular MSSM signal assumption. The value $\mu = 0$ corresponds to the absence of signal, whereas the value $\mu = 1$ suggests signal presence as predicted by the theoretical model under study. The statistical analysis of the data employs a binned likelihood function, constructed as the product of Poisson probability terms. Signal and background predictions depend on systematic uncertainties, which are parametrized as nuisance parameters (NP), and are constrained using gaussian functions. The binned likelihood function is constructed in bins of the discriminant variable, the total transverse mass, $m_{\text{T}}^{\text{tot}}$.

The distributions of $m_{\text{T}}^{\text{tot}}$ with post-fit systematic uncertainties in both categories are shown in Figure 7.16 for the $\tau_{\text{had}}\tau_{\text{had}}$ and $\tau_{\text{lep}}\tau_{\text{had}}$ channels. Yields of the $\tau_{\text{had}}\tau_{\text{had}}$ channel in the signal regions and their uncertainties are summarized in Table 7.6. The yields for the $\tau_{\text{lep}}\tau_{\text{had}}$ channel can be found in Appendix C.1.

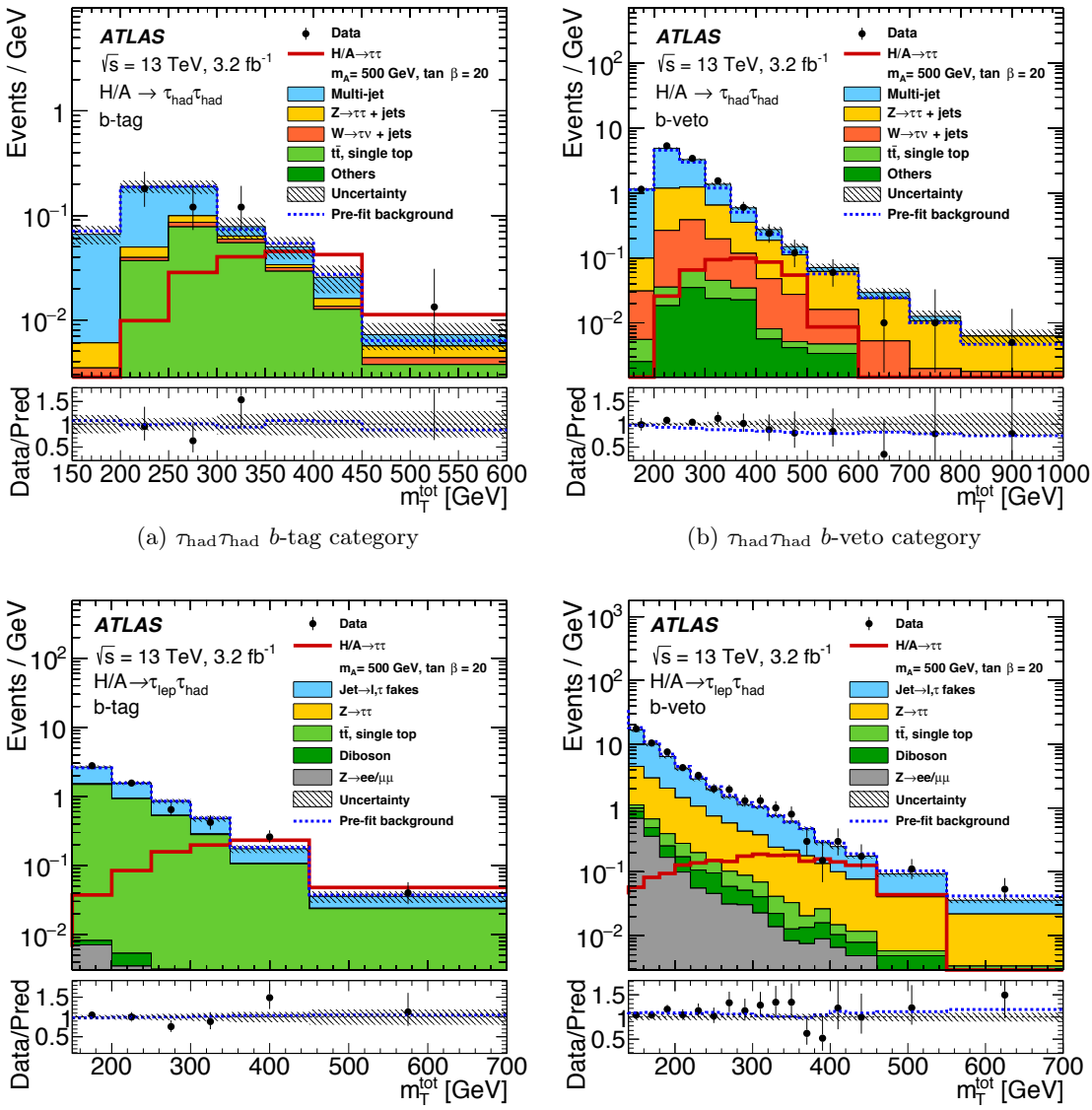

(a) $\tau_{\text{had}}\tau_{\text{had}}$ b-tag category

(b) $\tau_{\text{had}}\tau_{\text{had}}$ b-veto category

(c) $\tau_{\text{lep}}\tau_{\text{had}}$ b-tag SR

(d) $\tau_{\text{lep}}\tau_{\text{had}}$ b-veto SR

Figure 7.16: Distributions of $m_{\text{T}}^{\text{tot}}$ in the signal region of the (top) $\tau_{\text{had}}\tau_{\text{had}}$ and (bottom) $\tau_{\text{lep}}\tau_{\text{had}}$ channels for the (left) b-tag and (right) b-veto categories. The data are compared to the background prediction and a hypothetical MSSM $H/A \to \tau\tau$ signal with $m_A = 500\,\text{GeV}$ and $\tan\beta = 20$. The predictions and uncertainties for the background and signal processes are obtained from the fit under the hypothesis of no signal. The binning shown corresponds to the one used for the fit. The binning shown corresponds to the one used for the fit.

Process		***b*-tag category**	***b*-veto category**
Background	Multi-jet	17 ± 3	396 ± 16
	$Z \to \tau\tau$+jets	1.9 ± 0.3	146 ± 20
	$W \to \tau\nu$ + jets	1.1 ± 0.2	45 ± 7
	$t\bar{t}$ and single-top quark	11 ± 3	4.5 ± 0.9
	Others	0.13 ± 0.03	6.3 ± 0.8
Signal	ggH	0.034 ± 0.014	2.2 ± 0.7
	bbH	8 ± 3	15 ± 5
Total Background		31 ± 4	598 ± 21
Data		23	628

Table 7.6: Observed number of events and background predictions in the b-tag and b-veto categories for the $\tau_{\text{had}}\tau_{\text{had}}$ channel. The background predictions and uncertainties are obtained from the statistical procedure discussed in Section 7.9.1. The expected signal yields with $m_A = 500\,\text{GeV}$ and $\tan\beta = 20$ are shown for comparison.

The Z' search uses a cut-and-count technique in a discriminant distribution, where the events passing a certain $m_{\text{T}}^{\text{tot}}$ threshold are accounted. The discriminant variable is $m_{\text{T}}^{\text{tot}}$ in the inclusive category, as described before. The threshold is chosen for each Z' mass hypothesis to maximize the expected significance and ranges from 400 GeV at low Z' mass to 750 GeV at high Z' mass. Figure 7.17 shows the $m_{\text{T}}^{\text{tot}}$ distribution in the inclusive category of the $\tau_{\text{lep}}\tau_{\text{had}}$ and $\tau_{\text{had}}\tau_{\text{had}}$ channels of the Z' search.

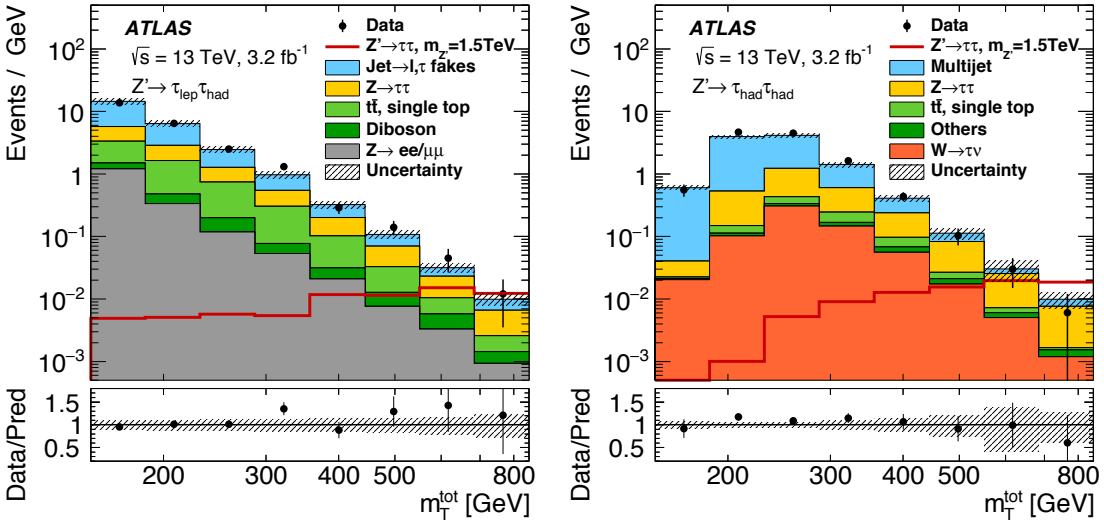

(a) $\tau_{\text{lep}}\tau_{\text{had}}$ (b) $\tau_{\text{had}}\tau_{\text{had}}$

Figure 7.17: Distributions of $m_{\text{T}}^{\text{tot}}$ in the (a) $\tau_{\text{lep}}\tau_{\text{had}}$ channel and (b) $\tau_{\text{had}}\tau_{\text{had}}$ channel of the Z' analysis. The label "Others" refers to contributions due to di-boson, $Z \to ll$ +jets and W+jets production. The distributions are shown before any statistical fit. Overflows are included in the last bin of the distributions.

7.9.2 Results

Since the data are in good agreement with the predicted background yields (i.e. no excess is observed), exclusion limits are set. Exclusion limits use the modified frequentist method known as CLs [266] and are calculated using the asymptotic approximation [214]. The test statistic used for the exclusion limits derivation is the $\widetilde{q}_\mu$ test statistic reviewed in Section 6.10.4. The 95% CL limits displayed belong to the combination of the two channels and represent the final result of the MSSM $H/A \to \tau\tau$ search.

Two interpretation of the results are given. First, a model-independent approach is adopted, where the 95% CL limits are calculated for both production modes, using the combination of the $\tau_{\text{lep}}\tau_{\text{had}}$ and $\tau_{\text{had}}\tau_{\text{had}}$ channels, and assuming the natural width of the boson to be negligible compared to the experimental resolution (as expected over the probed MSSM parameter space). The lowest excluded cross-section times branching fraction value, for a scalar boson produced via gluon fusion (Figure 7.18 (a)), ranges from $\sigma \times \text{BR} = 1.4\,\text{pb}$ at $m_{H/A} = 200\,\text{GeV}$ to $\sigma \times \text{BR} = 0.025\,\text{pb}$ at $m_{H/A} = 1.2\,\text{TeV}$. Similarly, for the b-associated production mechanism (Figure 7.18 (b)), the lowest excluded values range from $\sigma \times \text{BR} = 1.6\,\text{pb}$ at $m_{H/A} = 200\,\text{GeV}$ to $\sigma \times \text{BR} = 0.028\,\text{pb}$ at $m_{H/A} = 1.2\,\text{TeV}$. In both figures, the expected limits for the individual channels are shown as well. Tables with the exact values for the exclusion limits set for each of the production modes and their combination can be found in Appendix C.2.

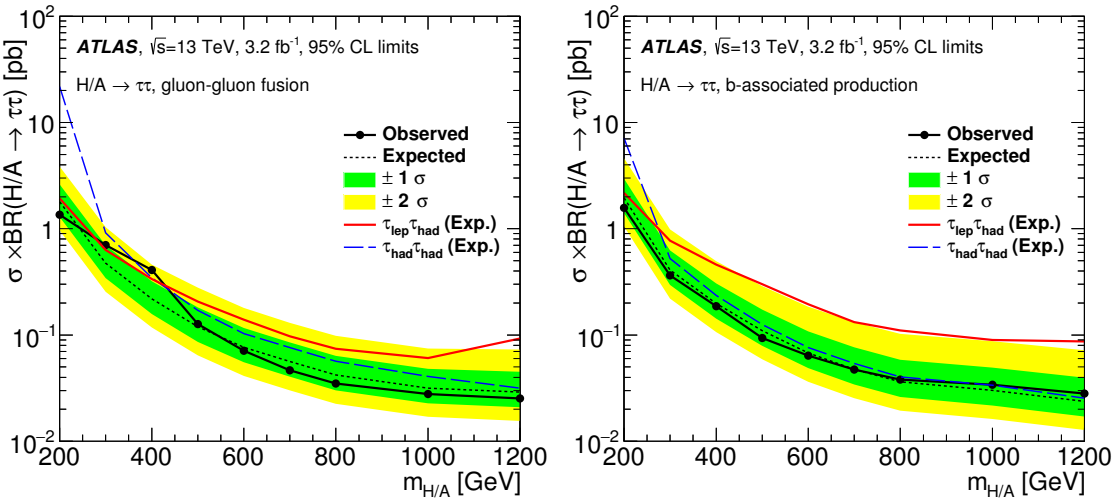

(a) gluon fusion production (b) b-associated production

Figure 7.18: Observed and expected 95% CL model-independent upper limits on the production cross-section times branching fraction of a scalar particles for the combination of the $\tau_{\text{lep}}\tau_{\text{had}}$ and the $\tau_{\text{had}}\tau_{\text{had}}$ channels. The production mechanism of $H/A \to \tau\tau$ is assumed to be (a) gluon fusion or (b) b-associated production. For comparison, the expected limits for the individual channels, are shown as well.

The second interpretation is the model-dependent approach, where the data is used to exclude a certain phase-space of a particular MSSM scenario. The observed and expected

95% CL limits of $\tan\beta$ as a function of m_A, for the combination of $\tau_{\text{lep}}\tau_{\text{had}}$ and $\tau_{\text{had}}\tau_{\text{had}}$ channels are shown in Figure 7.19 for the (a) MSSM $m_h^{\text{mod+}}$ scenario and (b) hMSSM scenario. Tables with the exact values for the exclusion limits set for each of the scenarios can be found in Appendix C.2. The expected limit in the $m_h^{\text{mod+}}$ scenario is compared in (a) to the expected limits from the individual $\tau_{\text{lep}}\tau_{\text{had}}$ and $\tau_{\text{had}}\tau_{\text{had}}$ channels and in (b) with the Run 1 result [87]. For the $m_h^{\text{mod+}}$ figure, lines of constant m_h and m_H are shown. For the hMSSM scenario in (b), the exclusion arising from the SM Higgs boson coupling measurements of Ref. [267] is also shown, in addition to the ATLAS Run 1 $H/A \to \tau\tau$ search result [87].

In the MSSM $m_h^{\text{mod+}}$ scenario, the 95% CL upper limits exclude $\tan\beta > 7.6$ for $m_A = 200\,\text{GeV}$ and $\tan\beta > 47$ for $m_A = 1\,\text{TeV}$. In the hMSSM scenario, the most stringent constraints on $\tan\beta$ for the combined search exclude $\tan\beta > 7.1$ for $m_A = 200\,\text{GeV}$ and $\tan\beta > 39$ for $m_A = 1\,\text{TeV}$ at the 95% CL. The feature of the expected limits in the hMSSM scenario exclusion plot at around $m_A = 350\,\text{GeV}$ is due to the behavior of the branching ratio for $A \to \tau\tau$ close to the $A \to t\bar{t}$ kinematic threshold. Some sensitivity of the search is also expected around $\tan\beta \sim 1$, $m_A \sim 200\,\text{GeV}$ due to the increase of the gluon fusion cross-section induced by the increased coupling to the top quark at low $\tan\beta$ values. The $\tan\beta$ constraints in the hMSSM scenario are stronger than those in the $m_h^{\text{mod+}}$ scenario due to the presence of low-mass neutralinos in the $m_h^{\text{mod+}}$ scenario that reduce the $H/A \to \tau\tau$ branching fraction, which are absent in the hMSSM scenario.

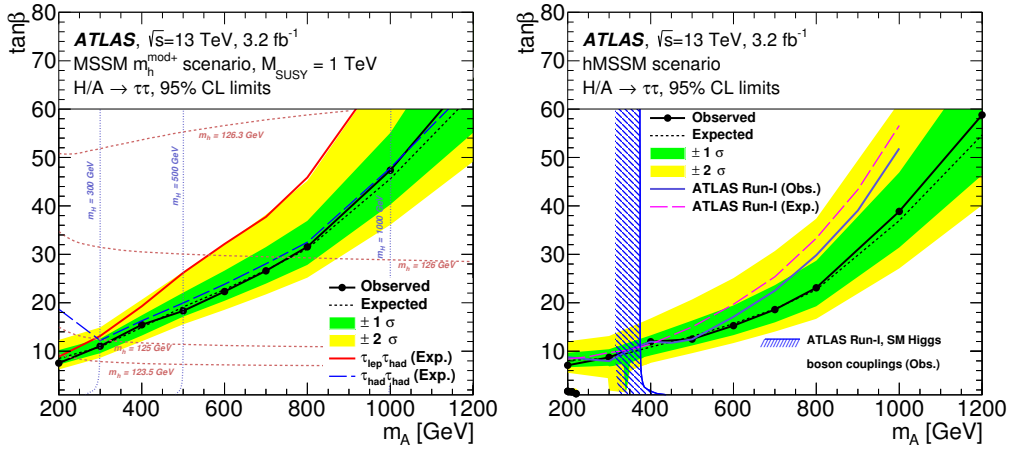

(a) $m_h^{\text{mod+}}$ scenario (b) hMSSM scenario

Figure 7.19: Observed and expected 95% CL model-dependent limits on $\tan\beta$ as a function of m_A for (a) the MSSM $m_h^{\text{mod+}}$ scenario and (b) the hMSSM scenario. For comparison, the expected limits from the individual channels, $\tau_{\text{lep}}\tau_{\text{had}}$ and $\tau_{\text{had}}\tau_{\text{had}}$, are given in (a). Dashed lines of constant m_h and m_H are shown in red and blue, respectively. In (b), the observed and expected limits from the ATLAS Run 1 analysis [87] are shown.

In addition, the results of the $H/A \to \tau\tau$ analysis are interpreted in the other MSSM benchmark scenarios described in Section 2.3.1. The 95% CL exclusion limits on the $m_A - \tan\beta$ plane computed for these models are shown in Figure 7.21, at the end of the chapter.

The $H/A \to \tau\tau$ analysis with the first Run 2 data is able to match the exclusion limits set using the full luminosity of Run 1 at low mass and it improves the limits of the previous searches for the mass range $m_A > 500\,\text{GeV}$.

In the case of the Z' search, no excess is observed in the inclusive region (Figure 7.17). Exclusion limits are set according to the SSM and SFM models. The resulting 95% CL upper limits are set on the cross-section times branching fraction as a function of the mass, which are shown in Figure 7.20. The resulting observed (expected) lower limit on the mass of the Z'_{SFM} boson is 1.90 (1.84) TeV. In the search for the Z'_{SFM} boson, results are presented as a function of $\sin^2\phi$. Masses below $1.82 - 2.17\,\text{TeV}$ are excluded in the range $0.1 < \sin^2\phi < 0.5$, assuming no $\mu - \tau$ mixing. For the value of $\sin^2\phi = 0.03$, the lower limit on the mass of a Z'_{SFM} boson is 2.12 TeV, extending the limits from previous direct and indirect searches by more than 200 GeV.

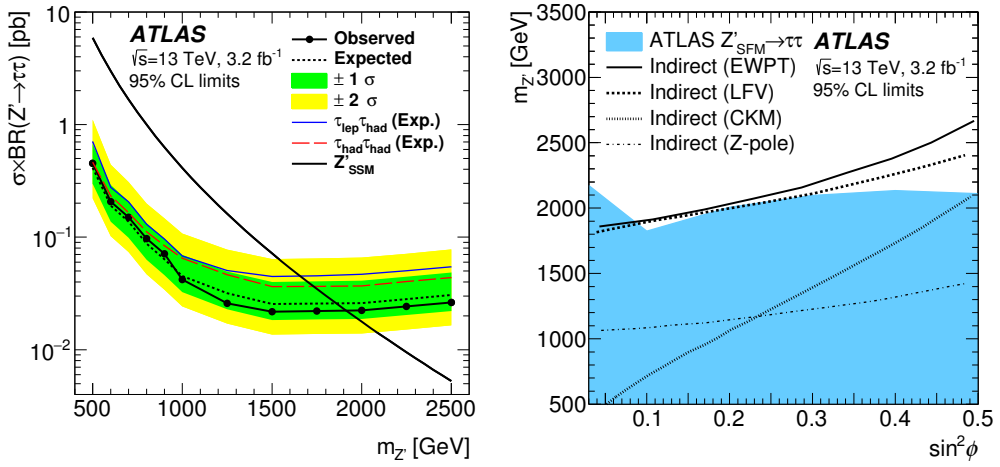

(a) SSM (b) SFM

Figure 7.20: Observed and expected 95% CL limits on the search of an $Z' \to \tau\tau$ in (a) the Sequential Standard Model and (b) the Strong Flavor Model. On (a) the limits are extracted on the cross-section times branching fraction while on (b) are extracted on the SFM parameter space, overlaid with indirect limits at 95% CL from fits to electroweak precision measurements [268], lepton flavor violation [269], CKM unitarity [270] and Z-pole measurements [262].

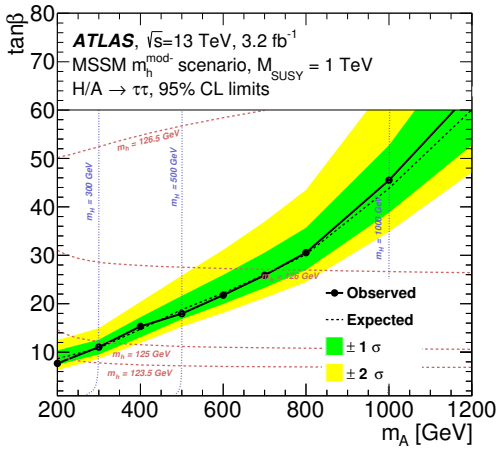

(a) $m_h^{\text{mod-}}$ scenario

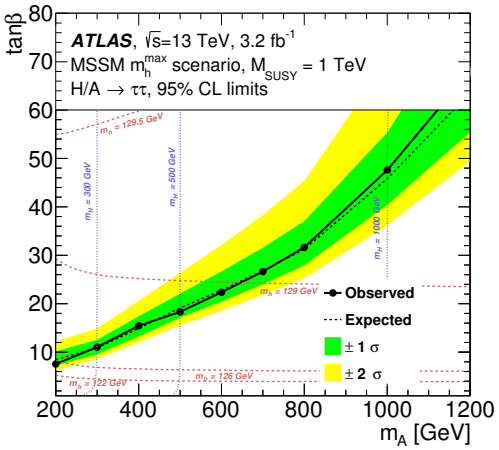

(b) m_h^{max} scenario

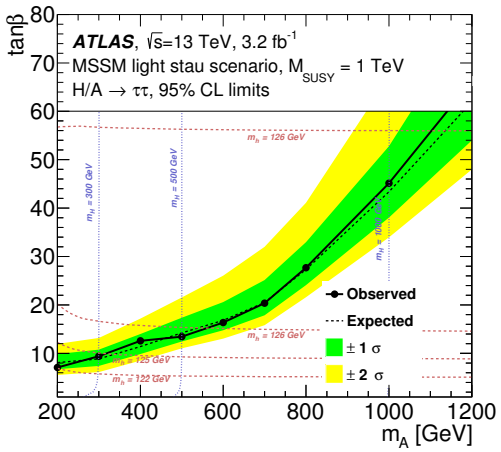

(c) light stau scenario

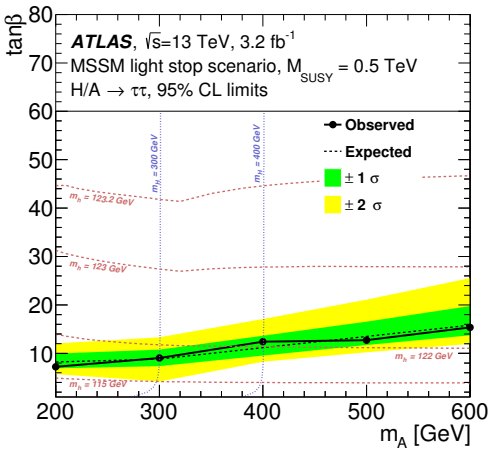

(d) light stop scenario

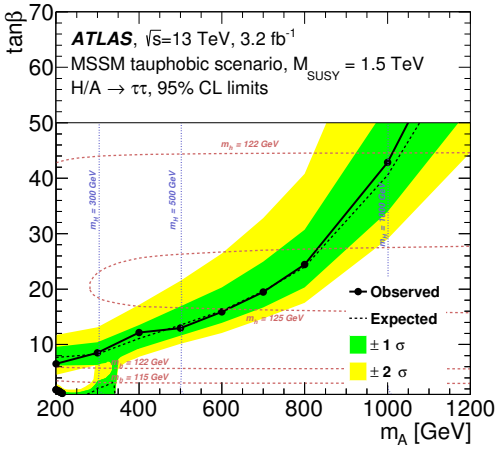

(e) tauphobic scenario

Figure 7.21: Observed and expected 95% CL model-dependent limits on $\tan\beta$ as a function of m_A for various MSSM scenarios. The description of the different scenarios is given in Section 2.3.1.

Chapter 8

Outlook and Conclusions

The aim of this thesis was the search for the Standard Model Higgs boson and for additional heavy MSSM Higgs bosons in the $\tau\tau$ channel. The analyses were performed with the data collected by the ATLAS detector. The SM analysis described in Chapter 6 used the data taken during Run 1: $4.5\,\text{fb}^{-1}$ of data collected at $\sqrt{s} = 7\,\text{TeV}$ and $20.3\,\text{fb}^{-1}$ collected at $\sqrt{s} = 8\,\text{TeV}$. The MSSM search described in Chapter 7 used the data taken during the first year of the Run 2: $3.21\,\text{fb}^{-1}$ of data collected at $\sqrt{s} = 13\,\text{TeV}$. Both analyses and their main results have been presented and discussed in their respective chapters, but further related studies have been performed, which will be documented in this chapter.

8.1 The SM $H \to \tau\tau$ analysis

The analysis shown in Chapter 6, corresponding to the search for the Higgs boson predicted by the SM in the $\tau\tau$ channel, was published in Ref. [155]. The analysis concluded with the following result in signal strength, for Higgs boson with a mass of $m_H = 125.36\,\text{GeV}$:

$$\mu^{\tau\tau}_{\text{ATLAS}} = 1.43\ ^{+0.43}_{-0.37} \tag{8.1}$$

with an observed (expected) significance of $4.5\,\sigma$ $(3.4\,\sigma)$.

This result has to be compared with the result of the same measurement from the CMS Experiment [271], which gave the following value for a mass of $m_H = 125\,\text{GeV}$:

$$\mu^{\tau\tau}_{\text{CMS}} = 0.86 \pm 0.29 \tag{8.2}$$

with an observed (expected) significance of $3.4\,\sigma$ $(3.6\,\sigma)$.

Both results are compatible with the SM expectation. The two independent results were combined by the ATLAS and CMS collaborations [45], as a part of the final result of the

Higgs measurements with the full luminosity of Run 1. The most relevant result of the combination for the purpose of this thesis is the combined $H \to \tau\tau$ signal strength which, for a mass[1] of $m_H = 125.09\,\text{GeV}$, yields the following result:

$$\mu^{\tau\tau}_{\text{ATLAS+CMS}} = 1.11^{+0.24}_{-0.22} \tag{8.3}$$

with an observed (expected) significance of $5.5\,\sigma$ $(5.0\,\sigma)$.

These values are shown in Figure 8.1, which also collects the signal strength measured by the LHC experiments, and their combination, for the rest of decay channels. The results are fully compatible with the SM prediction within uncertainty.

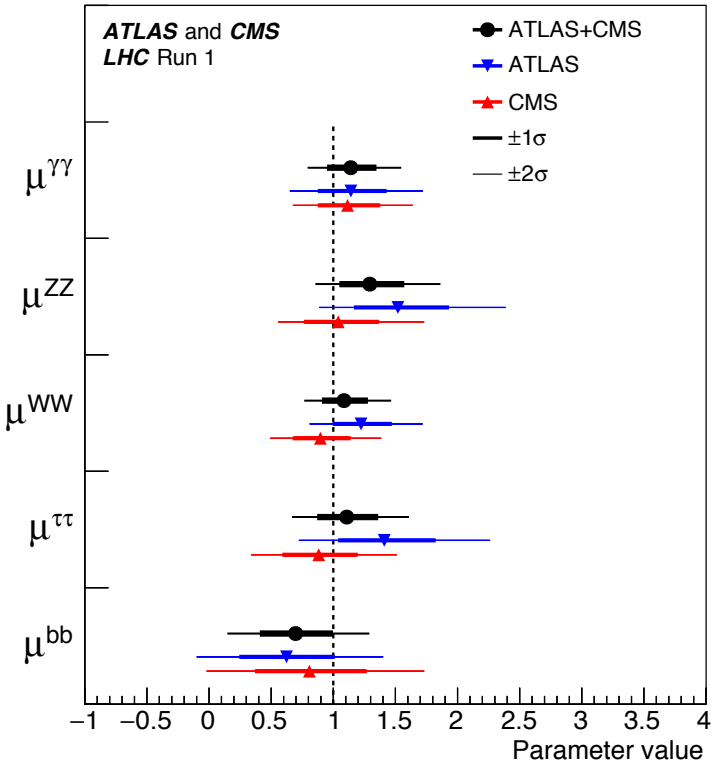

Figure 8.1: Best fit results for the decay signal strengths for ATLAS and CMS experiments for the different search channels. A value of $\mu = 1$ represents the SM prediction. The error bars indicate the $1\,\sigma$ (thick lines) and $2\,\sigma$ (thin lines) intervals [45].

The signal strength measured for the different productions modes (fermionic vs bosonic) is shown in Figure 8.2 in the form of $1\,\sigma$ likelihood contours for the different decay channels: $H \to ZZ$, $H \to WW$, $H \to \gamma\gamma$, $H \to \tau\tau$ and $H \to bb$. The distribution shows the best fit value for each channel, as well as the SM expectation (μ_i=1). Compatibility

[1]The choice is driven by the result of the combination of the Higgs boson mass measurement of the ATLAS and CMS experiments [45], yielding a value for the mass of the observed particle of $m_H = 125.09 \pm 0.21(\text{stat.}) \pm 0.11(\text{syst})\,\text{GeV}$.

of the results of the different channels as well as with the SM prediction (all within the $1\,\sigma$ contours) can be observed.

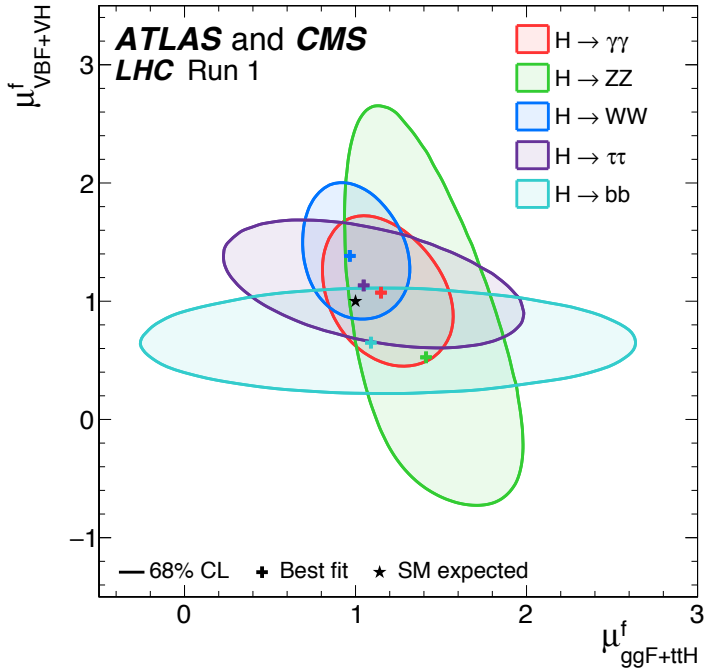

Figure 8.2: Contours of 68% CL in the ($\mu^f_{\mathrm{ggF+ttH}}$, $\mu^f_{\mathrm{VBF+VH}}$) plane for the combination of ATLAS and CMS, as obtained from the combined fit described in Ref. [45], for each of the five decay channels $H \to ZZ$, $H \to WW$, $H \to \gamma\gamma$, $H \to \tau\tau$ and $H \to bb$. The best fit values obtained for each of the five decay channels are also shown, together with the SM expectation [45].

As explained in Section 1.1.6, the Higgs mechanism predicts that the coupling of the Higgs boson with different particles has a dependence on the mass of these particles, which is linear for the Yukawa couplings to the fermions (Equation 1.52) and quadratic for the gauge couplings of the Higgs boson to the weak vector bosons. A parametrization to test this dependence is performed in Ref. [45]. The result, displayed in Figure 8.3, shows the compatibility of the measurements with the SM.

In addition, the compatibility of the results with the SM and BSM theories can be studied at leading order using the deviation of the observed coupling of the different particles, compared with the expectation from the SM. This is done by defining coupling modifiers, labelled κ. For a given production process or decay mode, denoted j, a coupling modifier κ_j is defined such that:

$$\kappa_j^2 \equiv \frac{\sigma_j}{\sigma_j^{SM}} = \frac{\Gamma^j}{\Gamma^j_{SM}} \tag{8.4}$$

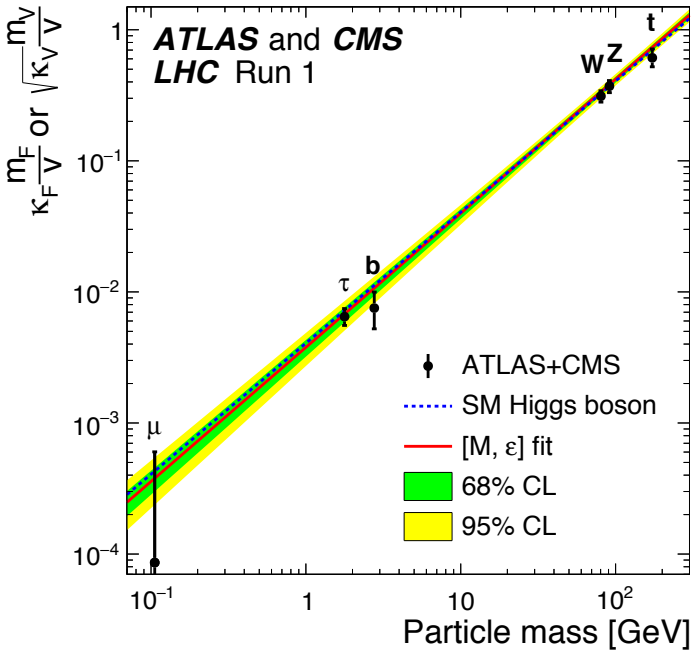

Figure 8.3: Best fit values as a function of particle mass for the combination of ATLAS and CMS data in the case of the parametrization described in Ref. [45]. The dashed (blue) line indicates the predicted dependence on the particle mass in the case of the SM Higgs boson. The solid (red) line indicates the best fit result to the $[M, \epsilon]$ phenomenological model with the corresponding 68% and 95% CL bands [45].

where values different from the unity implies a deviation from the SM. Further technical description of this approach, including the contributions of loops and the effects of interferences can be found in Ref. [45].

However, changes in the values of the couplings will result in a variation of the Higgs boson width. A new modifier, κ_H, defined as:

$$\kappa_H \equiv \sum_j B^j_{\mathrm{BSM}} \kappa_j^2 \tag{8.5}$$

is introduced to characterize this variation, where B_{BSM} indicates the total branching fraction into BSM decays, that accounts for the deviations from the SM. This relation can also be written as:

$$\Gamma_H \equiv \frac{\kappa_H^2 \cdot \Gamma_H^{SM}}{1 - B_{\mathrm{BSM}}} \tag{8.6}$$

The rates of Higgs boson production in the various decay modes are related to the Higgs boson width, which is sensitive to potential invisible or undetected decay modes predicted by BSM theories. To directly measure the individual coupling modifiers, an assumption about the Higgs boson width is necessary, which defines two possible scenarios: the first assumes $B_{\mathrm{BSM}} = 0$, the second one leaves B_{BSM} free, provided that $B_{\mathrm{BSM}} \geq 0$, but assumes that $|\kappa_W| \leq 1$ and $|\kappa_Z| \leq 1$ and that the signs of $|\kappa_W|$ and $|\kappa_Z|$ are the

same, assumptions denoted $|\kappa_V| \leq 1$. The constraints assumed in the second scenario are compatible with a wide range of BSM physics, which may become manifest, for example, in the loop-induced processes of the gluon fusion process. A further description of this framework, the scenarios and their implications of them, can be found in Ref. [45].

The parameters of interest, which are the seven independent coupling modifiers (κ_Z, κ_W, κ_t, κ_τ, κ_b, κ_g, and κ_γ), one for each SM particle involved in the production processes and decay modes studied, plus B_{BSM} in the case of the first scenario, are fit to data. The result of the fit is shown in Figure 8.4, where the second scenario is shown on the left. In the second scenario, an upper limit of $B_{\text{BSM}} = 0.34$ at 95% CL is obtained, compared to an expected limit of 0.39. The corresponding negative log-likelihood scan is shown in Figure 8.5.

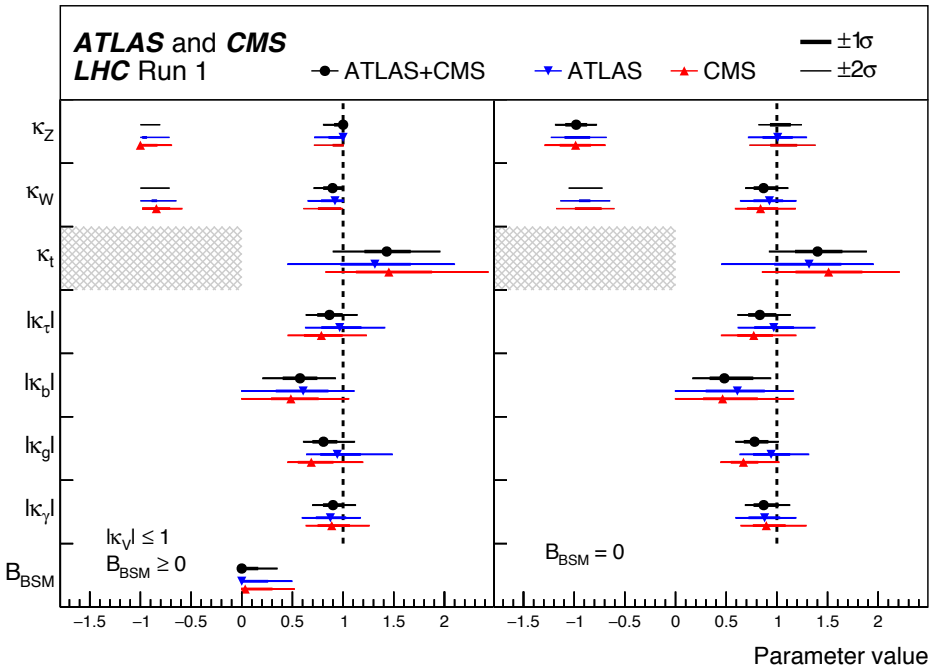

Figure 8.4: Fit results for two parametrizations allowing BSM loop couplings: the first one assumes that $B_{\text{BSM}} \geq 0$ and that $|\kappa_V| \leq 1$, where κ_V denotes κ_Z or κ_W, and the second one assumes that there are no additional BSM contributions to the Higgs boson width, i.e. $B_{\text{BSM}} = 0$. The measured results for the combination of ATLAS and CMS are reported together with their uncertainties, as well as the individual results from each experiment. The hatched areas show the non-allowed regions for the κ_t parameter, which is assumed to be positive without loss of generality. The error bars indicate the $1\,\sigma$ (thick lines) and $2\,\sigma$ (thin lines) intervals [45].

In summary, the work of this thesis contributed to the first observation of the SM $H \to \tau\tau$ decay at LHC. The value of the signal strength measured is fully compatible with the Standard Model prediction.

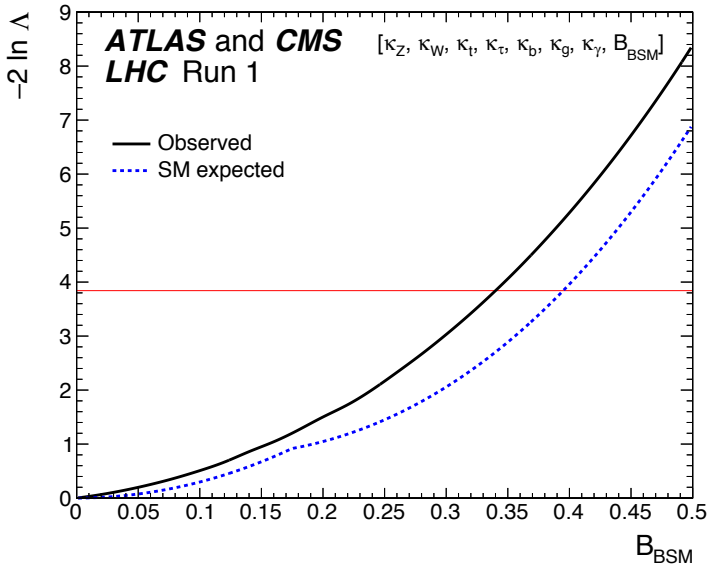

Figure 8.5: Observed (solid line) and expected (dashed line) negative log-likelihood scan of B_{BSM}, shown for the combination of ATLAS and CMS when allowing additional BSM contributions to the Higgs boson width. The results are shown for the parametrization with the assumptions that $|\kappa_V| \leq 1$ and $B_{\text{BSM}} \geq 0$ from Figure 8.4. All the other parameters of interest from the list in the legend are also varied in the minimization procedure. The red horizontal line at 3.84 indicates the log-likelihood variation corresponding to the 95% CL upper limit [45].

8.2 The MSSM $H/A \to \tau\tau$ analysis

The search for additional neutral Higgs bosons (H/A) described in Chapter 7 was done using the data collected during the first year of Run 2 of the LHC, accounting for 3.21 fb^{-1} taken at $\sqrt{s} = 13\,\text{TeV}$, which was published in Ref. [221]. The search found no indication of an excess over the expected background and thus, upper limits were extracted.

Model-independent upper limits on the production cross-section times branching fraction ($\sigma \times \text{BR}$) for the $\tau\tau$ final state of a scalar boson versus its mass, in both the gluon fusion and b-associated production modes, were presented. The 95% confidence level (CL) upper limits on $\sigma \times \text{BR}$ range from 1.4 (1.6) pb at $m_{H/A} = 200\,\text{GeV}$ to 0.025 (0.028) pb at $m_{H/A} = 1.2\,\text{TeV}$ for a scalar boson produced via ggH (bbH). For the model-dependent approach, several MSSM scenarios were tested. For the $m_h^{\text{mod+}}$ scenario, the most stringent 95% CL upper limit on $\tan\beta$ for the combined search is $\tan\beta < 7.6$ for $m_A = 200\,\text{GeV}$. This analysis improves the limits of the previous searches for the mass range $m_A > 500\,\text{GeV}$.

This work contributed to constrain the limits on the parameters for the existence of additional Higgs bosons in the $\tau\tau$ decay in one of the most popular extensions of the Standard Model. It was also one of the first publications with Run 2 data.

The main work of this thesis was done in the frame of the analysis published in Ref. [221], but an additional contribution was done in a subsequent update, which used up to $13.3\,\text{fb}^{-1}$ at $\sqrt{s} = 13\,\text{TeV}$, collected during the first part of the 2016 data-taking period, and which was preliminary released in Ref. [272].

The updated analysis followed the same procedure as the 2015 data paper described in Chapter 7, though optimizations and calibrations were performed using the new data, and a new high-$E_{\text{T}}^{\text{miss}}$ category was added in the $\tau_{\text{lep}}\tau_{\text{had}}$ channel. The increase in the instantaneous luminosity during the year 2016 forced to scale the trigger used in the 2015 data paper, therefore a combination of triggers depending on the p_{T} of the τ_{had} candidate had to be implemented. The definition of the two categories, b-tag and b-veto was kept but the selection criteria were further optimized for the new luminosity available. Figure 8.6 shows the $m_{\text{T}}^{\text{tot}}$ distributions in the $\tau_{\text{had}}\tau_{\text{had}}$ channel in both categories for this updated search.

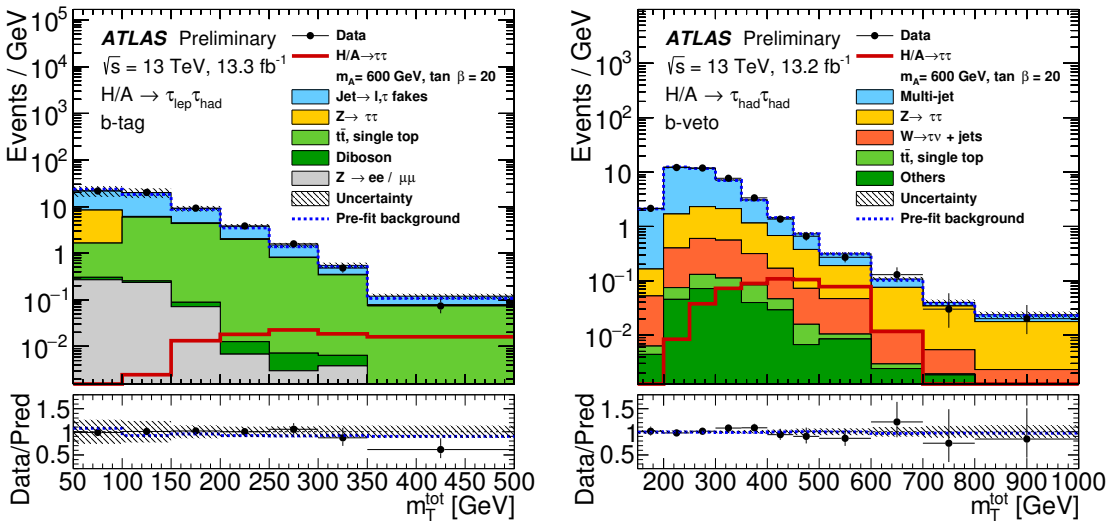

(a) $\tau_{\text{had}}\tau_{\text{had}}$ b-tag category (b) $\tau_{\text{had}}\tau_{\text{had}}$ b-tag category

Figure 8.6: Distributions of the final mass discriminant $m_{\text{T}}^{\text{tot}}$ with post-fit uncertainties in the (a) b-tag and (b) b-veto categories of the $\tau_{\text{had}}\tau_{\text{had}}$ channel of the updated MSSM analysis. The binning shown corresponds to the one used for the fit. A signal of $\tan\beta = 20$, $m_A = 600\,\text{GeV}$ is shown for reference [272].

The analysis found no indication of an excess over the expected SM background in the channels considered. Thus, 95% CL upper limits were set, to provide constraints in the cross-section of the production modes and in the MSSM parameter space. Model-independent upper limits are presented on the $\sigma \times \text{BR}$ in both production modes (Figure 8.7). They range from $\sigma \times \text{BR} = 2.0\,(2.1)\,\text{pb}$ at $m_{H/A} = 200\,\text{GeV}$ to $\sigma \times \text{BR} = 0.013\,(0.014)\,\text{pb}$ at $m_{H/A} = 1.2\,\text{TeV}$ for a scalar particle produced via ggH (bbH). For the model-dependent approach, in particular the $m_h^{\text{mod}+}$ scenario (Figure 8.8), the most stringent 95% upper limits on $\tan\beta$ for the combined search are $\tan\beta < 9$ for

$m_A = 200\,\text{GeV}$ and $\tan\beta < 50$ for $m_A = 1200\,\text{GeV}$. This analysis improves the limits set by the 2015 data paper for the mass range $m_A > 350\,\text{GeV}$.

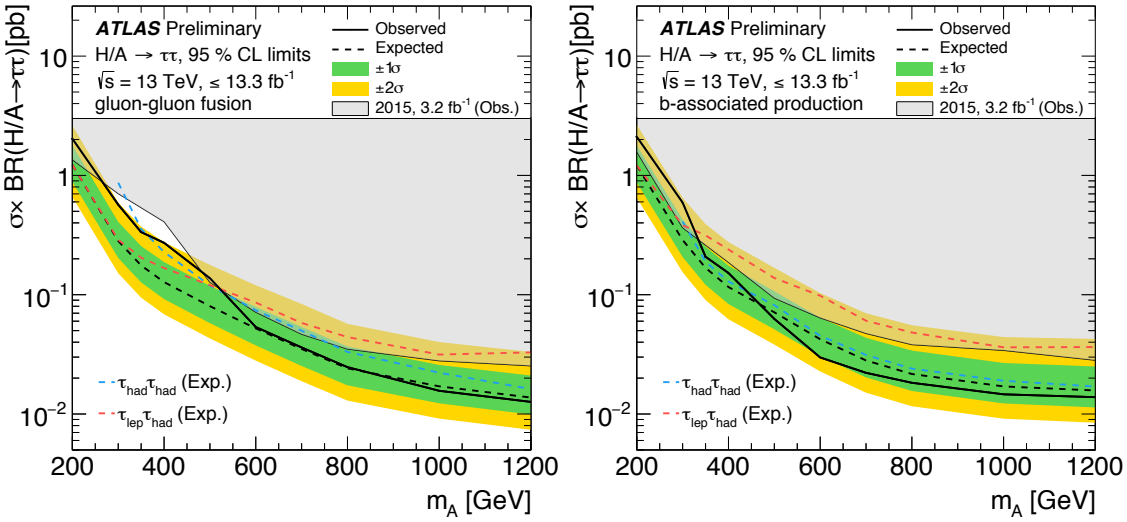

(a) gluon fusion (b) b-associated production

Figure 8.7: Observed and expected 95% CL upper limits on the production cross-section times branching fraction of a scalar particle for the ggH and bbH production modes for the combination of the $\tau_{\text{lep}}\tau_{\text{had}}$ and the $\tau_{\text{had}}\tau_{\text{had}}$ channels of the updated MSSM analysis. The production mechanism of $H/A \to \tau\tau$ is assumed to be (a) gluon fusion and (b) b-associated production. For comparison, the expected limits for the individual channels are shown as well [272].

Finally, at the end of 2017, the ATLAS Experiment released a preliminary result of the combination of several BSM searches, which is displayed in Figure 8.9. This plot shows the phase-space $\tan\beta$-m_A in the hMSSM scenario, marking the current exclusions set by the different BSM searches, including an updated $H/A \to \tau\tau$ analysis with the luminosity collected during the years 2015 and 2016 of Run 2 ($36.1\,\text{fb}^{-1}$) [265], and the BSM fit of the couplings modifiers performed in the combination of Run 1 analyses [45], which was reviewed in previous section. The $\tau\tau$ analyses contributed to the exclusion in a great extent, specially for high values of $\tan\beta$ and high m_A, since the enhanced τ (and b) coupling allows to set stricter exclusions.

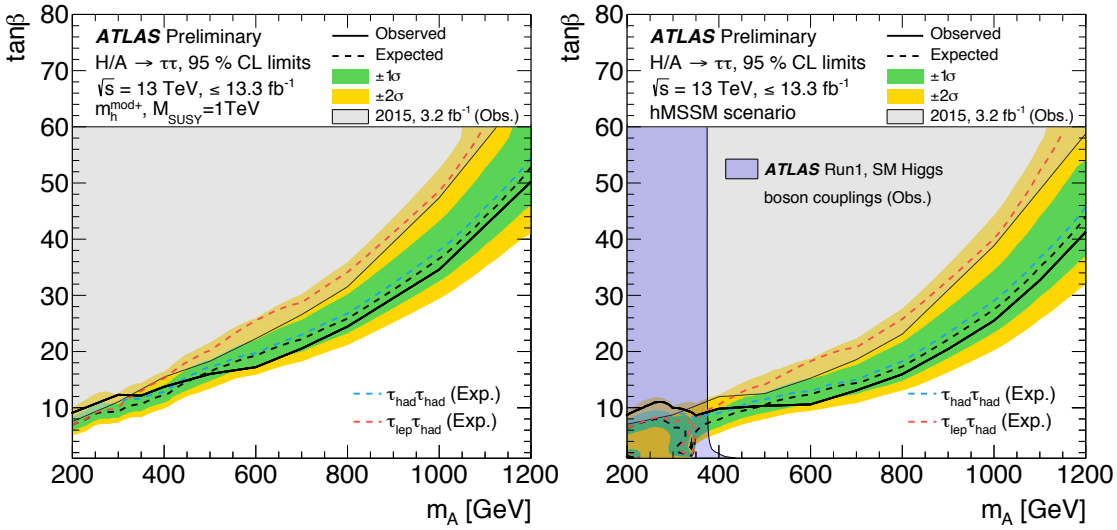

(a) $m_h^{\text{mod}+}$ scenario (b) hMSSM scenario

Figure 8.8: Observed and expected upper limits limits on $\tan\beta$ as a function of m_A for the model-dependent approach in the (a) $m_h^{\text{mod}+}$ and (b) hMSSM scenarios for the updated MSSM analysis [272]. For comparison, the expected limits from the individual channels, $\tau_{\text{lep}}\tau_{\text{had}}$ and $\tau_{\text{had}}\tau_{\text{had}}$, are also shown. The exclusion limits are compared to the ATLAS 2015 $H/A \to \tau\tau$ search result of [221]. For the hMSSM scenario in (b), the exclusion arising from the SM Higgs boson coupling measurements of the Run 1 analysis [87] is also shown [272].

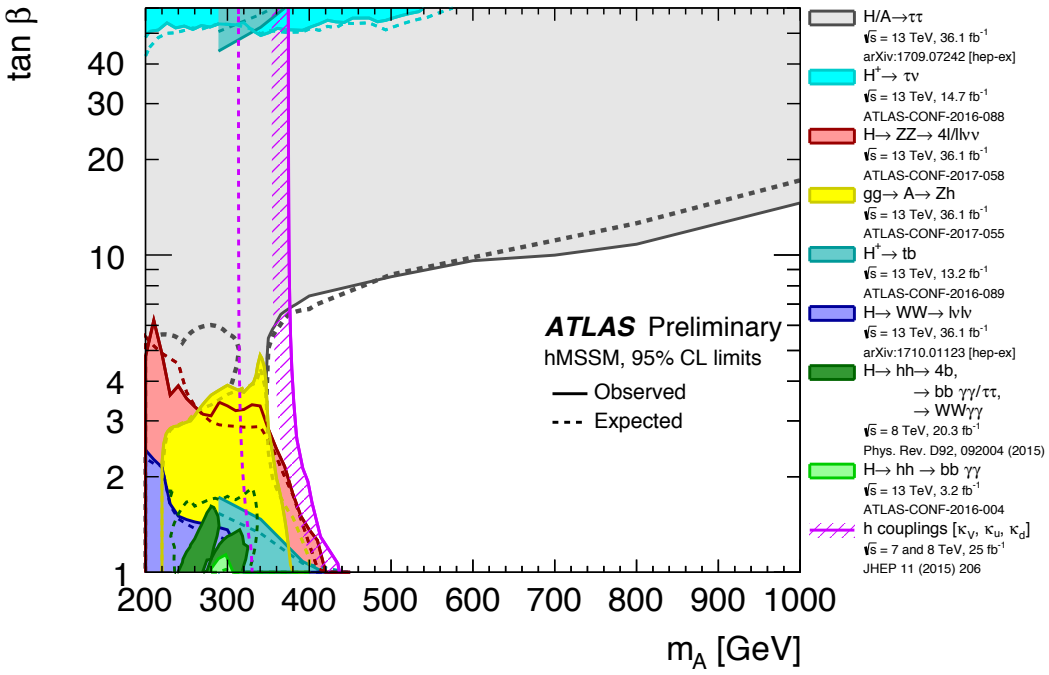

Figure 8.9: Regions of the $\tan\beta$-m_A phase-space excluded in the hMSSM model via direct searches for heavy Higgs bosons and fits to the measured rates of observed Higgs boson production and decays. Limits are quoted at 95% CL and are indicated for the data (solid lines) and the expectation for the SM Higgs sector (dashed lines). The light shaded or hashed regions indicate the observed exclusions. The procedure for the calculation of the cross sections and the branching ratios follows Ref. [81]. The summary plot was released in December 2017 [91].

8.3 Conclusions

The work of this thesis were performed during the period 2012-2016 in the scope of the high-energy physics program of the ATLAS Experiment. This time covers the last year of Run 1 (2012), the Long Shutdown (2013-2014) and the first two years of Run 2 (2015-2016). Contributions were done in the different phases, both in physics analysis and in technical tasks for the development and functioning of the Tile Calorimeter.

The results of the physics analyses contributed to expand the knowledge of the state-of-the-art physics. The first analysis, performed during Run 1, contributed to broaden the validity of the Standard Model of particle physics, providing evidence of the decay of the Higgs boson to τ fermions. The second analysis, performed with the first data of Run 2, contributed to the exploration of new physics, searching for predictions of a beyond-the-Standard-Model theory, the MSSM. This analysis did not find any excess, but constrained the parameters of the theory, improving to a large extent previous results.

This result opens the door to further research in the BSM field. The LHC and the ATLAS Experiment will keep working on these topics and it is expected that during the next years, with the following Runs of the LHC, new analyses based on the current results, to which this thesis contributed, will be able to provide a more precise answer to the concerns that the SM raises, and advance in the knowledge of the behavior of the subatomic world.

Resumen en español

Introducción

Esta tesis describe el estudio del acoplamiento con leptones τ del bosón de Higgs predicho por el Modelo Estándar y la búsqueda, en el mismo canal, de bosones de Higgs adicionales, predichos por una de las extensiones del Modelo Estándar, el Modelo Mínimamente Supersimétrico. Estos análisis fueron realizados con los datos obtenidos por el experimento ATLAS, como parte del programa de física del acelerador LHC del laboratorio CERN.

El Modelo Estándar de física de partículas (SM) es la teoría que describe el comportamiento de las partículas subatómicas. El modelo establece varios tipos de partículas: fermiones, con spin $1/2$, divididas en quarks (q) y leptones (l); y bosones, con spin entero: gluones (g), fotones (γ), los bosones débiles $W^{\pm}$ y Z y el bosón de Higgs (H). Además, el SM contiene dos tipos de interacciones entre estas partículas: la fuerza fuerte (cromodinámica cuántica o QCD), que describe la interacción entre quarks y gluones; y la fuerza electrodébil (EW), que describe la interacción entre todos los fermiones mediante los fotones y los bosones $W^{\pm}$ y Z. La Figura 8.10 muestra las diferentes partículas ordenadas por su tipo.

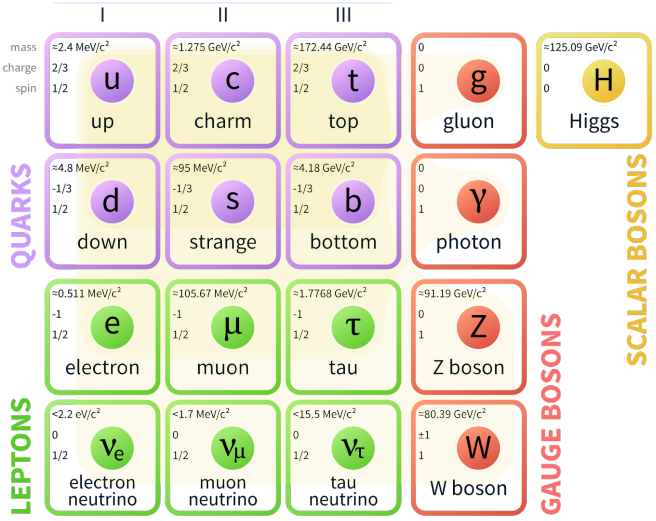

Figura 8.10: El Modelo Estándar de Física de Partículas, ordenando las partículas por tipo (quarks, leptones y bosones). Symmetry Magazine [1].

Las teorías gauge en las que están basadas las interacciones descritas exigen que los bosones mediadores sean partículas sin masa. Esto se cumple para el fotón y el gluón, pero no para los bosones $W^{\pm}$ y Z, que son masivos. Para solucionar el problema, la teoría electrodébil fue modificada añadiendo un campo nuevo, el campo de Higgs, un campo escalar con un máximo local para el vacío. Haciendo uso del mecanismo de ruptura espontánea de la simetría de este campo, los bosones débiles pueden adquirir masa sin violar las condiciones gauge, lo que se llama el **Mecanismo de Higgs**. La adición de este campo tiene, sin embargo, una consecuencia: la aparición de un nuevo bosón observable y masivo, el bosón de Higgs.

Esta hipotética partícula, predicción del Mecanismo de Higgs y, por ende, de la validez de la teoría electrodébil, fue buscada durante muchos años en las colisiones producidas por diferentes aceleradores de partículas, pero no fue hasta la construcción del LHC que se alcanzó la energía necesaria para estudiar el rango de masa favorecido por la teoría. En 2012, los experimentos ATLAS y CMS del LHC publicaron independientemente la observación de una partícula de masa $m_H \sim 125\,\text{GeV}$, compatible con el bosón de Higgs (Figura 8.11), siendo confirmado más adelante, conforme los nuevos datos permitían mejorar la precisión de las medidas.

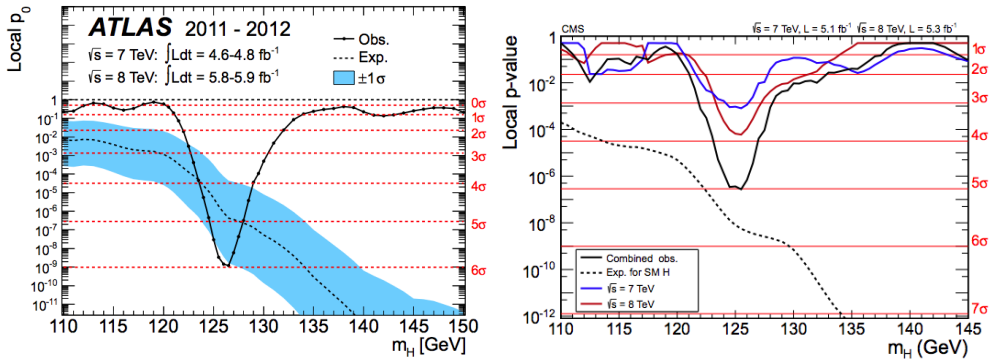

(a) ATLAS (b) CMS

Figura 8.11: Figuras de la significancia estadísitica del descubrimiento del bosón de Higgs que muestran excesos compatibles con un bosón escalar neutro de espín $s \neq 1$ en los experimentos (a) ATLAS [40] y (b) CMS [41].

El bosón de Higgs fue descubierto en los canales bosónicos, en análisis que estudiaban los decaimientos del bosón a pares de fotones, bosones $W^{\pm}$ y bosones Z. Teóricamente, el bosón de Higgs puede decaer también en fermiones, como pares de quarks b o de leptones τ pero, debido a la complejidad de encontrar rastro de esos decaimientos, no había estadística suficiente para confirmarlo. Los trabajos del primer análisis de esta tesis se enmarcan en la búsqueda de bosón del Higgs en el canal $\tau\tau$, en concreto, en el estado final di-leptónico, usando los datos del Run 1 del LHC. Como resultado del análisis, se reunió evidencia del decaimiento del bosón de Higgs a pares de partículas τ con una

significancia de $4{,}5\,\sigma$. El valor medido del acoplamiento entre fermiones τ y el bosón de Higgs es compatible con el SM.

A pesar de sus tremendos éxitos, el SM no está completo, ya que es incapaz de dar una explicación satisfactoria a varios fenómenos de la naturaleza como la gravedad, la masa de los neutrinos o el inexplicable pequeño valor de la masa del bosón de Higgs. Para solucionar estos problemas se han propuesto varias teorías que expanden el SM. Una de las más extendidas es la Supersimetría (SUSY), que plantea una simetría adicional fermión-bosón en la que todas las partículas conocidas tendrían una *super*-compañera del tipo opuesto y con una alta masa, que aún no habría sido descubierta. La mínima forma en la que SUSY puede implementarse en el SM es el Modelo Estándar Mínimamente Supersimétrico (MSSM). Este modelo, sin embargo, requiere una pequeña adición para poder reproducir correctamente los fenómenos observados, que consiste en un segundo campo de Higgs. La principal consecuencia del Mecanismo de Higgs modificado es que, tras la ruptura de la simetría, *cinco* bosones de Higgs observables aparecen en la naturaleza: dos escalares neutros, h y H, un pseudo-escalar neutro, A, y dos cargados $H^{\pm}$.

El descubrimento de cualquiera de estos bosones adicionales significaría la confirmación de unos de los requisitos del MSSM, dando un paso de gigante en la búsqueda de modelos más allá del SM. El segundo análisis de esta tesis consiste en la búsqueda de los bosones adicionales, H o A (considerando que h sería el bosón encontrado en 2012) en el canal $\tau\tau$ y el estado final hadrónico, en la región de alta masa $200 - 1200\,\text{GeV}$, usando para ello los datos del primer año del Run 2 del LHC. El análisis no encontró ningún exceso, así que se establecieron nuevos límites a la existencia de dichas partículas, tanto para la sección eficaz de los modos de producción como para los diferentes escenarios fenomenológicos del MSSM.

El LHC y el experimento ATLAS

El LHC (Gran Colisionador de Hadrones) es un colisionador circular de partículas de 27 km de longitud, situado en el Laboratorio Europeo para la Investigación Nuclear (CERN) en Ginebra, Suiza. Su propósito es acelerar y colisionar, principalmente, haces de protones a una energía de diseño de 14 TeV, que provee datos para la investigación en física de partículas de alta energía. El LHC es la última etapa del sistema de aceleradores del CERN, mostrado en la Figura 8.12, que ioniza y acelera átomos de hidrógeno en sucesivas etapas, empezando por el acelerador lineal LINAC2, y pasando por los aceleradores Booster, Protón-Sincrotón (PS), y Super-Protón-Sincrotón (SPS), antes de ser inyectados en el LHC.

El LHC funciona mediante una serie de imanes (dipolos, cuadripolos,...) cuya función es acelerar y colimar dos haces de protones en sentidos opuestos, para cruzarlos

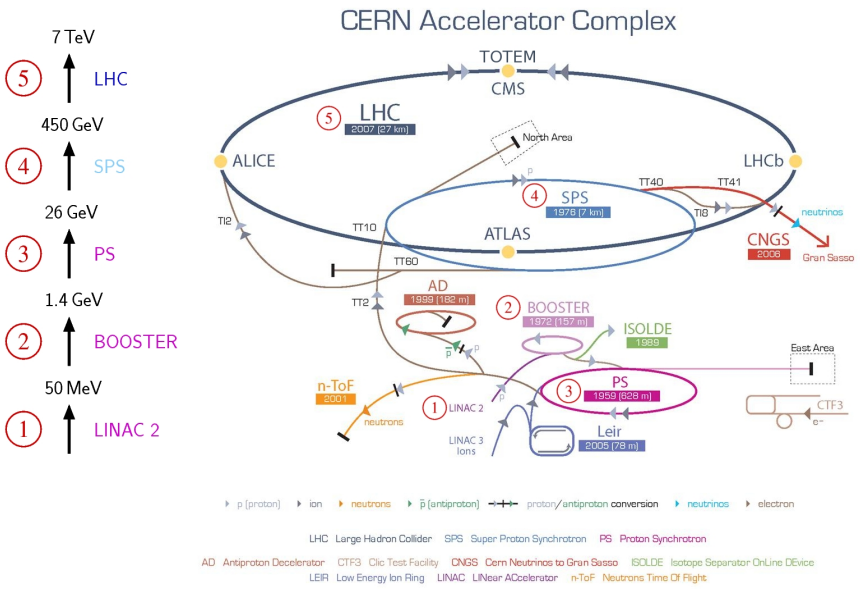

Figura 8.12: Diagrama del complejo de aceleradores del CERN, mostrando LINAC2, Booster, PS, SPS y el LHC con sus cuatro experimentos principales [105].

en los cuatro puntos donde se sitúan los experimentos ATLAS, CMS, LHCb y ALICE, haciendo que los protones colisionen a la energía y luminosidad instantánea requeridas. Por diseño, la energía en el centro de masas de la colisión iba a ser de 14 TeV, pero un grave incidente provocó el retraso de los planes, por lo que se empezó con una energía reducida (7 TeV) que ha sido aumentada hasta 13 TeV.

Los periodos de toma de datos del LHC están divididos en *Runs*, separados por paradas técnicas, cuyo propósito es la reparación y modernización del acelerador y los experimentos. La Figura 8.13 muestra la hoja de ruta del LHC y la previsión para los años futuros, incluyendo el futuro acelerador HL-LHC.

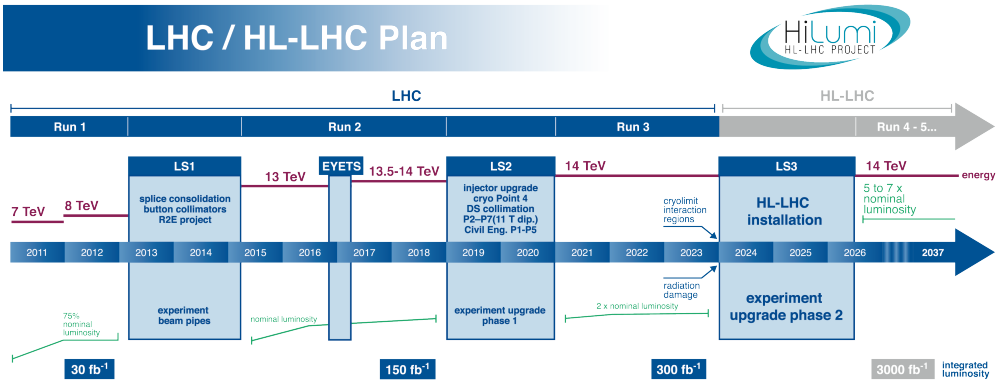

Figura 8.13: Hoja de ruta del programa del LHC mostrando los diferentes *Runs* y las paradas técnicas (LS), entre el inicio del experimento en 2011 y la preparación para la siguiente fase (el HL-LHC) [102].

El **Run 1** corresponde al primer periodo del experimento, entre 2010 y 2012. El año 2010 fue un año de comisión y no se tomó una cantidad significativa de datos. 2011 fue el primer año con datos recogidos, producidos con una energía en el centro de masas de 7 TeV y acumulando 4.5 fb^{-1} de datos. En 2012, la energía en el centro de masas fue aumentada a 8 TeV y se tomaron 20.3 fb^{-1} de datos. Tras dos años de parada técnica (2013-2014), empezó el **Run 2** (2015-2018), con una energía en el centro de masas de 13 TeV y tomando 3.21 fb^{-1} de datos en 2015 y 35.6 fb^{-1} en 2016. La Figura 8.14 muestra la comparación entre los datos obtenidos por el LHC durante los Runs 1 y 2. Los análisis de esta tesis fueron realizados con los datos del Run 1 y del año 2015 del Run 2.

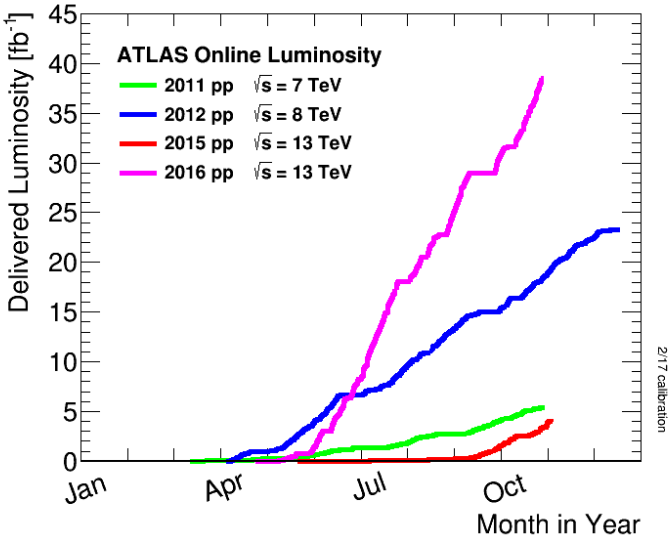

Figura 8.14: Comparación entre la luminosidad acumulada durante los años 2011 y 2012 del Run 1 y los años 2015 y 2016 del Run 2.

El experimento ATLAS (Figura 8.15) es un detector multipropósito de forma cilíndrica, de 44 m de longitud y 25 m de diámetro, situado a 100 m bajo tierra, en uno de los puntos donde se cruzan los haces del LHC y cuyo propósito es identificar y analizar los productos de las colisiones de protones. Para ello, el detector está dividido en varios subdetectores, cada uno de los cuales está enfocado en un tipo de detección.
Los principales componentes de ATLAS son:

- **El detector interno (ID)**. El ID es la parte más cercana al punto de colisión. Su propósito es la identificación precisa de la posición del punto de colisión, el reconocimiento de la traza de las partículas cargadas que salen de la colisión y la medida del momento y carga de esas partículas. El detector está compuesto de múltiples pares de chips de silicio dispuestos en cilindros alrededor del punto de colisión y en discos alrededor del tubo del haz.
- **Los calorímetros**. El sistema de calorímetros rodea al detector interno y su propósito es la medida de la energía de las partículas que son absorbidas en él. La parte más interna es el calorímetro de argón líquido (LAr), que se compone de un

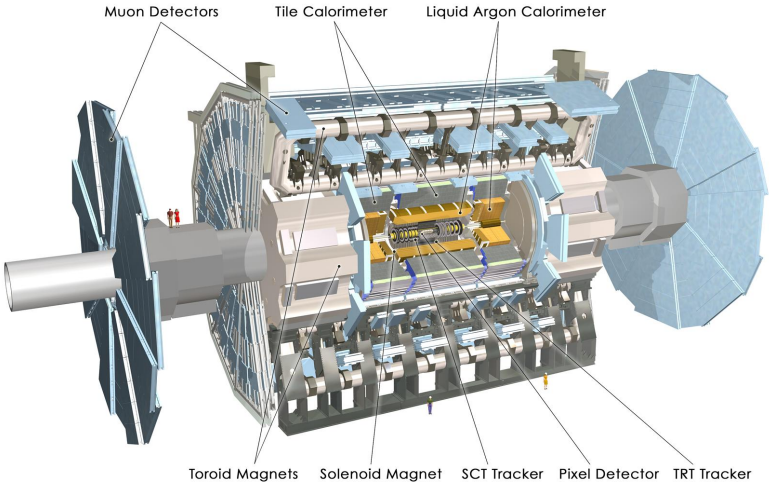

Figura 8.15: Diagrama del detector ATLAS y sus principales componentes.

cilindro alrededor del tubo del haz, que actúa como calorímetro electromagnético y unos tapones a los lados, que actúan de calorímetro hadrónico. Alrededor del cilindro se sitúa el TileCal, o calorímetro de tejas, que está formado por celdas de material centelleador y acero y actúa como calorímetro hadrónico.

- **El espectrómetro de muones**. Este subdetector está situado en la parte más externa de ATLAS y su propósito es la detección de muones y la medida de su momento. Está compuesto por varios sistemas, situados alrededor del TileCal y en discos alrededor del tubo del haz.
- Además de los tres sistema principales, hay otros sistemas que son indispensables para el funcionamiento del detector, como es el **sistema de imanes** (solenoide y toroides) que provocan la curvatura de la traza de las particulas; los **detectores delanteros**, que miden la luminosidad de la colisión; y **el sistema disparador (trigger)**, que analiza si la colisión es suficientemente interesante para el análisis, activando el sistema de almacenamiento de sus datos.

Búsqueda del bosón de Higgs del SM en canal $\tau_{\text{lep}}\tau_{\text{lep}}$

El primer análisis realizado durante esta tesis consistió en el estudio de evidencia del bosón de Higgs del SM, mediante la búsqueda de un exceso estadísticamente significativo de eventos di-τ respecto al fondo esperado por el SM ($H \to \tau\tau$). La comparación entre el exceso observado y el esperado da la medida del acoplamiento entre el bosón de Higgs y el leptón τ. Para este análisis se usaron los datos del Run 1 del LHC, que corresponden con una luminosidad integrada de $4.5\,\text{fb}^{-1}$ con datos tomados a 7 TeV y $20.3\,\text{fb}^{-1}$ a 8 TeV. El análisis fue publicado en la revista *Journal of High Energy Physics* en abril de 2015 [155].

Los procesos de señal y fondo

El canal de búsqueda considerado para este análisis es el canal $\tau\tau$, donde el bosón de Higgs decae en una pareja de leptones τ de cargas opuestas. Para una masa de $m_H = 125\,\text{GeV}$, este canal representa un 6 % del ancho de decaimiento del bosón de Higgs. A pesar de tener mucha menor abundancia que otro canal fermiónico, el bb, el canal $\tau\tau$ es más limpio ya que sus estados finales son más fácilmente identificables respecto al fondo. Debido a esto, el canal $\tau\tau$ está muy favorecido para el estudio del acoplamiento del bosón de Higgs con fermiones.

El leptón τ no es una partícula estable, decae en un neutrino-τ mediado por un bosón $W^{\pm}$. El bosón $W^{\pm}$ puede, a su vez, decaer de dos formas posibles: leptónicamente, si el $W^{\pm}$ decae en un leptón ligero (e, o μ) y su correspondiente neutrino; o hadrónicamente, si el $W^{\pm}$ decae en un par de de quarks que hadronizan. Ya que el bosón de Higgs se descompone en dos τ, el decaimento del bosón de Higgs en el canal $\tau\tau$ tiene tres estados finales: di-leptónico ($\tau_{\text{lep}}\tau_{\text{lep}}$), semi-leptónico ($\tau_{\text{lep}}\tau_{\text{had}}$) y hadrónico ($\tau_{\text{had}}\tau_{\text{had}}$).

Como estos estados finales tienen una topología muy diferente, el análisis se dividió en tres canales, que fueron optimizados de forma independiente, pero manteniendo un marco común que permitiera combinarlos para obtener el resultado final. Los trabajos de esta tesis se centraron principalmente en el canal $\tau_{\text{lep}}\tau_{\text{lep}}$. La Figura 8.16 muestra el diagrama de Feynman de un suceso del estado final $\tau_{\text{lep}}\tau_{\text{lep}}$.

Respecto a la producción del bosón de Higgs, según el SM, éste puede ser producido de tres modos en el LHC: fusión de gluones (ggH), fusión de bosones vectoriales (VBF) y producción asociada con un bosón vectorial (VH), mostrados en la Figura 8.17.

El modo ggH es el más dominante en el LHC, con una proporción del 87 %, lo que lo convierte en el principal modo de producción de las búsquedas del bosón de Higgs. El modo VBF tiene una abundancia mucho menor, del 7 %, sin embargo, la topología de estos eventos deja unas trazas fácilmente reconocibles en el detector, ya que los quarks salientes hadronizan, formando dos jets enfrentados, lo que facilita su identificación. Por último, el modo VH está formado por las componentes WH y ZH, y contribuye con alrededor de un 5 % de los eventos de señal. Otros modos de producción posibles como

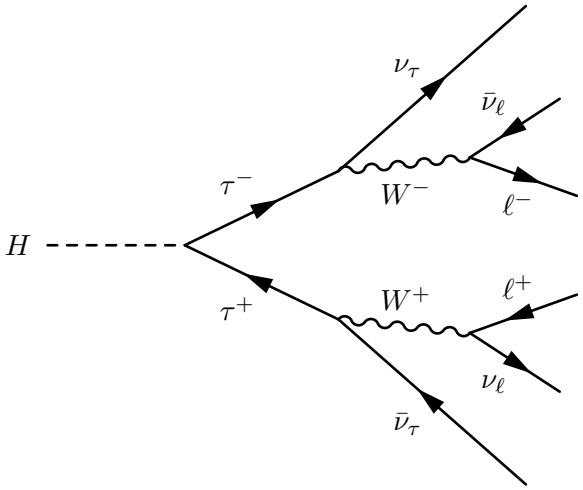

Figura 8.16: Diagrama de Feynman del decaimiento de un bosón de Higgs en el canal $\tau_{\text{lep}}\tau_{\text{lep}}$. El bosón de Higgs decae en un par de leptones τ que, a su vez, decaen leptónicamente en un leptón ligero (e o μ) y varios neutrinos.

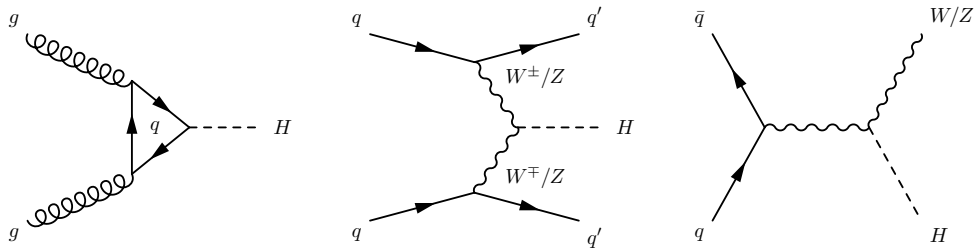

(a) ggH (b) VBF (c) VH

Figura 8.17: Principales modos de producción de un bosón de Higgs del SM en el LHC, incluyendo (a) la fusión de gluones, (b) la fusión de bosones vectoriales y (c) la producción asociada con un bosón vectorial.

la producción asociada con quarks top o bottom (ttH y bbH) no fueron considerados relevantes para este análisis.

Finalmente, debido a la presencia de hasta cuatro neutrinos en el decaimiento del leptón τ, que no pueden ser detectados, no es posible realizar una reconstrucción precisa de la masa del bosón de Higgs. Para estimar la masa, en varios estudios se utilizaron diversas aproximaciones, como son la masa del sistema di-leptónico (m_{ll}) o la aproximación colinear ($m_{\tau\tau}$) [157], que asume que los neutrinos son producidos en la misma dirección que el leptón ligero. Sin embargo, para el análsis $H \to \tau\tau$ se usó la masa calculada con el algoritmo Missing Mass Calculator (MMC o $m_{\tau\tau}^{\text{MMC}}$) [156], que da un valor de la masa del sistema tras escanear las diferentes direcciones en las que los neutrinos han podido decaer. Esto se consigue haciendo uso de información estadística (funciones de densidad de probabilidad) del decaimiento del τ, obtenidas directamente de datos reales.

Para poder afirmar con seguridad que se ha observado un posible exceso en la región de señal, el fondo del análisis tiene que estar completamente estudiado y controlado. Los posibles fondos se obtuvieron de las predicciones del SM para la zona analizada y se modelizaron usando principalmente técnicas de Monte Carlo (MC). Para los dos fondos más relevantes, debido a su relevancia o la dificultad de su modelización, se usaron estimaciones derivadas directamente de datos reales.

Donde fue posible, las contribuciones de fondo fueron controladas en regiones ortogonales a la región de la señal (SR), llamadas regiones de control (CR), donde el respectivo proceso de fondo domina y la contribución de la señal es despreciable. Para el resto de procesos, donde una CR no puede ser estrictamente definida, se construyeron regiones de validación (VR), donde se realza la contribución de un proceso en concreto para mostrar la validez de la modelización. Las CR, además, se usan para normalizar los respectivos fondos en el análisis estadístico.

El fondo más importante del análisis $H \to \tau\tau$ es el proceso $Z \to \tau\tau$, debido a la similitud entre los dos bosones, neutros y de masa cercana, que hace que este fondo sea irreducible (Figura 8.18 (a)). Para modelizarlo se recurrió a una compleja técnica mixta llamada *embedding* (incrustramiento) [198]. El embedding consiste en utilizar una muestra de datos reales del proceso $Z \to \mu\mu$ y substituir manualmente la partícula μ y la información concreta a su decaimiento por una partícula τ y su decaimento, obtenidos por MC. Con esto se consigue que toda la información colateral del evento, como es la energía perdida ($E_{\mathrm{T}}^{\mathrm{miss}}$), jets, y productos secundarios, con un gran impacto en el análisis, estén obtenidos directamente de los datos. La Figura 8.18 (b) muestra la comparación entre la reconstrucción del proceso $Z \to \tau\tau$ usando MC y la técnica embedding, mostrando que ésta es capaz de reproducir la distribución de masas.

Otro proceso de fondo del análisis es el decaimiento del bosón de Z a leptones ligeros e o μ ($Z \to ll$), que cobra relevancia en eventos donde los dos leptones son del mismo tipo (sabor). El requerimiento de que el evento tenga una alta energía perdida sirve para reducir la contribución de este fondo. Los procesos con quark top (especialmente $t\bar{t}$) son también parte del fondo, debido a la contribución de los estados finales leptónicos del mediador $W^{\pm}$ en el decaimiento del quark top. Ya que el quark top decae mayoritariamente en quarks bottom, la contribución de este proceso se puede reducir vetando eventos con jets marcados como b-jets. Finalmente, los procesos di-bosónicos (WW, ZZ y WH) también contribuyen al fondo de di-τ, aunque en mucha menor medida, debido a la reducida sección eficaz de producción de dichos procesos.

Los fondos $Z \to ll$ y top tienen unas CR asociadas, donde se asegura que la modelización del fondo es capaz de reproducir los datos medidos. Para el $Z \to \tau\tau$, al ser irreducible, no se puede obtener una CR, pero está controlado en los múltiples estudios del desarrollo del embedding y en una VR. El proceso di-bosónico, aunque tiene una contribución reducida, también está controlado en una VR.

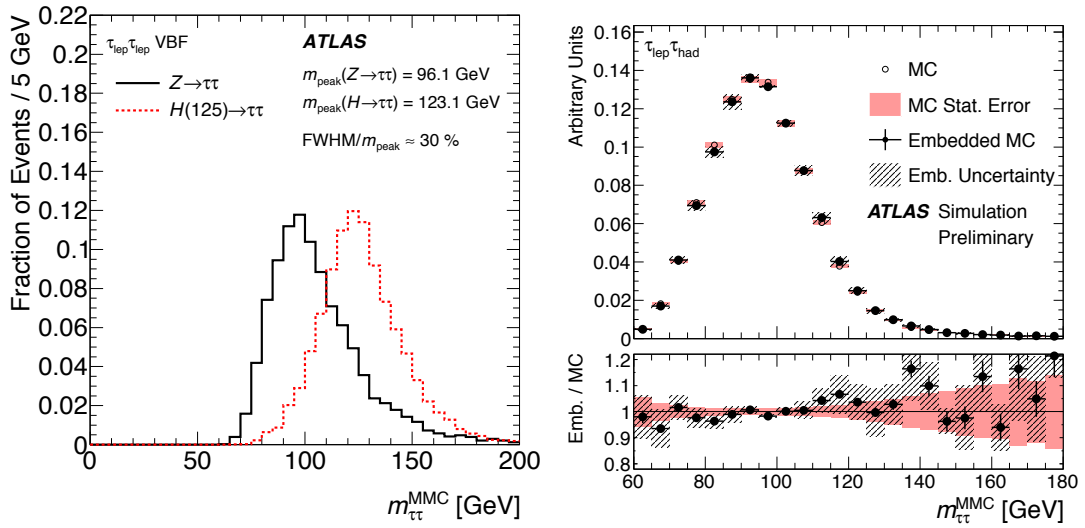

(a) (b)

Figura 8.18: Distribución de masa invariante $m_{\tau\tau}^{\mathrm{MMC}}$ para (a) los procesos $Z \to \tau\tau$ y $H \to \tau\tau$ en el canal $\tau_{\mathrm{lep}}\tau_{\mathrm{lep}}$ y (b) el proceso $Z \to \tau\tau$ en el canal $\tau_{\mathrm{lep}}\tau_{\mathrm{had}}$ comparando la estimación por MC y la técnica embedding [155].

Mención aparte merece el proceso $H \to WW$. Este proceso es un caso especial de contribución di-bosónica WW donde la partícula madre es un bosón de Higgs. Ya que este proceso fue confirmado en los análisis que participaron en el descubrimiento del bosón de Higgs en 2012, es considerado un fondo para el análisis del $H \to \tau\tau$ y tratado como tal. Además, debido a que el experimento ATLAS tiene en marcha varios análisis sobre este proceso y se pretende obtener una combinación de todos los análisis del Higgs para el final del Run 1, se aplica un corte que ortogonaliza los espacios de fase de ambos análisis, impidiendo que se solapen y permitiendo una futura combinación.

Las contribuciones de fondo descritas abarcan los procesos en los que los τ son reales. Sin embargo, debido a la precisión del experimento, puede haber casos en los que el detector reconstruya como τ partículas que no lo son. Este fondo de falsos positivos, llamado fondo *Fake*, tiene una contribución moderada en el canal di-leptónico, ya que los leptones son fácilmente identificables, sin embargo, sigue siendo una contribución relevante y, por tanto, fue modelizada usando una técnica basada en datos reales: *template fit* o ajuste de una plantilla. Esta técnica consiste en obtener una región de control donde estudiar el número de eventos que faltan para reproducir los datos, y extrapolarlo a la zona de señal, utilizando un ajuste. La región de control es obtenida invirtiendo el requerimiento en aislamiento del leptón secundario, mientras que todo el proceso es validado usando las mismas regiones pero invirtiendo, además, el requerimiento en carga, como muestra la Figura 8.19.

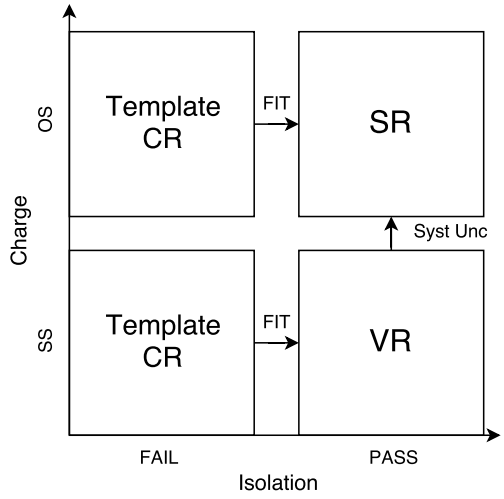

Figura 8.19: Diagrama de los espacios de fase del Template fit para la estimación del fondo Fake en el canal $\tau_{\text{lep}}\tau_{\text{lep}}$.

La selección de eventos

Debido al reducido número de eventos de señal en comparación con el fondo, se han de aplicar una serie de cortes y requisitos, que reduzcan la cantidad de eventos de fondo y aumenten la proporción de señal, de forma que la observación de un potencial exceso sea posible. Los criterios de selección son optimizados de manera independiente en cada canal, en función de los tipos de los procesos tratados. Además, debido a que los modos de producción del bosón de Higgs presentan una topología claramente diferenciada, se definen dos categorías, cuyo objetivo es potenciar cierto tipo de eventos.

La selección de eventos está divida en cuatro fases: la preselección, la selección principal, la categorización y la selección final, que dan lugar a las dos SR, además de las CR y VR.

La preseleción consiste en la preparación de la muestra de datos para su análisis, mediante la eliminación de eventos *defectuosos*, como pueden ser eventos donde los diferentes objetos no se han reconstruido correctamente, eventos tomados en momentos donde alguna parte del detector sufrió algún fallo o, incluso, eventos que no corresponden a una verdadera colisión (cósmicos). Para ello se utilizan una serie de recomendaciones desarrolladas por las diferentes comisiones de Calidad de Datos (Data Quality) correspondientes a cada subdetector.

La selección principal corresponde a los cortes aplicados con el propósito de reducir la cantidad de eventos de fondo y aumentar la proporción de señal. En el canal $\tau_{\text{lep}}\tau_{\text{lep}}$, la selección de eventos comienza con el requisito de que el evento contenga dos leptones ligeros (electrones o muones), para lo cual se utiliza la información proporcionada por los disparadores de eventos (triggers) mediante una lógica que optimiza la disponibilidad de

los diferentes triggers en función del momento transverso del leptón que lo ha activado. Además, se requiere que:

- el evento contenga exactamente dos leptones ligeros (e, μ) con carga opuesta (OS). Se vetan los eventos con τ hadrónicos.
- la masa invariante di-leptónica (m_{ll}) esté en el rango $30 - 75\,\text{GeV}$ para eventos del mismo sabor (SF: ee o $\mu\mu$) y en el rango $30 - 100\,\text{GeV}$ para eventos de diferente sabor (DF: $e\mu$). El requerimiento es más estricto en el canal SF para reducir la contribución del proceso $Z \to ll$.
- la suma del momento transverso de los dos leptones sea elevada ($p_{\text{T}}^{l1} + p_{\text{T}}^{l2} > 35\,\text{GeV}$) para eliminar procesos Fake.
- los eventos tengan al menos un jet con $p_{\text{T}} > 40\,\text{GeV}$.
- los eventos contengan alta energía perdida: $E_{\text{T}}^{\text{miss}} > 40\,\text{GeV}$ y $E_{\text{T}}^{\text{miss,HPTO}} > 40\,\text{GeV}$ para eventos SF y $E_{\text{T}}^{\text{miss}} > 20\,\text{GeV}$ para eventos DF, para eliminar la contribución del bosón Z y Fakes. La variable $E_{\text{T}}^{\text{miss,HPTO}}$ se define como la $E_{\text{T}}^{\text{miss}}$ calculada solo con objetos de alto p_{T}.
- la fracción del momento transportado por los objetos visibles del decaimiento esté entre 0.1 y 1, lo que se corresponde con la condición de la *aproximación colinear* del decaimiento del τ.
- la diferencia en el ángulo azimutal de los leptones sea pequeña ($\Delta\phi_{ll} < 2{,}5$), lo que permite suprimir eventos de $Z \to ll$ y $t\bar{t}$.

Tras esta selección, se divide la muestra de datos en dos categorías, que se definen de acuerdo con la topología de un modo de producción, para poder optimizar el análisis de esos eventos. Las dos categorías consideradas en el análisis, comunes a los tres canales son:

VBF optimizada para eventos producidos mediante el modo de producción del mismo nombre. Los eventos de señal provenientes de este modo suelen ir acompañados de dos jets energéticos, como resultado de la hadronización de los dos quarks salientes. La traza que forman estos jets es característica de estos eventos, lo que permite reconocerlos fácilmente a pesar de su relativamente poca abundancia. Los requisitos que definen esta categoría son:

- el evento contiene, al menos, dos jets.
- el momento transverso de estos jets satisface $p_{\text{T}}^{j1} > 40\,\text{GeV}$ y $p_{\text{T}}^{j2} > 30\,\text{GeV}$.
- su separación angular satisface $\left|\Delta\eta_{jj}\right| > 2{,}2$.

Boosted optimizada para eventos con un momento transverso alto, con una topología *boosted*. Esta categoría recoge principalmente los eventos de la producción mediante

el proceso *ggH*, que es el más abundante en el LHC. Los requisitos que definen esta categoría son:

- no ser parte de la categoría VBF.
- el momento transverso del candidato de señal satisface $p_{\mathrm{T}}^{\tau\tau} > 100\,\mathrm{GeV}$.

Tras la categorización, se aplica una selección final para definir las zonas de señal que consiste en:

- veto de los eventos con, al menos, un jet identificado como b-jet, que elimina drásticamente el fondo del $t\bar{t}$
- corte en la masa invariante $m_{\tau\tau}^{\mathrm{MMC}}$ para ortogonalizar los análisis $H \to \tau\tau$ y $H \to WW$, eliminando eventos que no cumplan la condición: $m_{\tau\tau} > m_Z - 25\,\mathrm{GeV}$

Análogamente, se definen las zonas de control invirtiendo ciertos cortes de la selección, que las ortogonaliza respecto a la SR. En concreto:

- **Top CR**, definida invirtiendo el veto en b-jets, es decir, requiriendo que el evento contenga al menos un b-jet. Así, el proceso $t\bar{t}$ domina la distribución, con una pequeña contribución de $Z \to \tau\tau$ y Fakes.
- **Zll CR**, definida modificando el corte en m_{ll} y requiriendo sólo eventos del mismo sabor. El nuevo corte en m_{ll} se define como $80\,\mathrm{GeV} < m_{ll} < 100\,\mathrm{GeV}$, lo que sitúa la CR en el pico del Z, y hace que el proceso $Z \to ll$ domine completamente la distribución.
- **Fake CR**, de donde se obtiene la plantilla usada en el Template fit para estimar el fondo de Fake en la SR. Los cortes que definen la CR requieren:
  - dos leptones aislados de cargas opuestas y veto de τ hadrónicos.
  - que la masa invariante del sistema leptónico esté entre $30 - 75\,\mathrm{GeV}$ para leptons del mismo sabor y entre $30 - 100\,\mathrm{GeV}$ para leptones de diferente sabor.
  - al menos un jet con $p_{\mathrm{T}} > 40\,\mathrm{GeV}$ y veto de b-jet
  - categorización:
    - VBF: al menos dos jets con $\left|\Delta\eta_{jj}\right| > 2.2$
    - Boosted: el evento no es VBF y $p_{\mathrm{T}}^{\tau\tau} > 100\,\mathrm{GeV}$.

Además, se definen varias VR, para comprobar la validez del resto de contribuciones de fondo, siendo los Fakes y el $Z \to \tau\tau$ los más relevantes.

- **Ztt VR**, debido a que el fondo de $Z \to \tau\tau$ es irreducible respecto a la señal por compartir espacio de fase, no se puede definir una CR completamente ortogonal a la zona de señal. Sin embargo, diversos estudios mostraron que hay una gran correlación entre la señal y los eventos con alto momento, por lo que se puede definir

una VR con poca cantidad de señal en la zona de bajo momento, reconstruyendo la masa usando la variable $E_{\mathrm{T}}^{\mathrm{miss,HPTO}}$, requiriendo $m_{\tau\tau}^{\mathrm{HPTO}} < 100\,\mathrm{GeV}$.

- **Di-bosón VR**, donde el proceso di-bosónico es controlado en una VR definida tras la preselección, con los siguientes criterios:
  - eventos OS $e\mu$ con $m_{ll} > 100\,\mathrm{GeV}$ y $p_{\mathrm{T}}^{l2} > 30\,\mathrm{GeV}$
  - veto de eventos con algún jet con $p_{\mathrm{T}} > 30\,\mathrm{GeV}$
  - $\cos\left(\Delta\phi(E_{\mathrm{T}}^{\mathrm{miss}}, l_2)\right) < -0{,}2$
- **Fake SS VR**, región que se usa para controlar la validez de la estimación del fondo Fake (Template fit), realizando el mismo procedimiento para eventos con mismo signo (SS). Debido a la falta de estadística, alguno de los cortes que definen la zona son relajados.

Discriminación de la señal: BDT

Para poder reconocer un posible exceso, la señal ha de ser separada del fondo. El método estándar es optimizar una serie de cortes secuenciales para aumentar la proporción de señal y reducir el fondo, pero, este método tiene una desventaja importante ya que, tras cada corte, parte de la señal se pierde. Para evitar esto, se pueden usar otros métodos alternativos, como son los algoritmos multivariantes (MVA).

Estos algoritmos estudian toda la información del evento al mismo tiempo, dando como resultado un valor de la probabilidad de que el evento estudiado pertenezca a uno de los patrones de referencia, en este caso señal o fondo. La mayor ventaja de estos algoritmos es que reducen drásticamente la pérdida de señal, aumentando la eficiencia de la selección. Por contra, la exactitud de su selección depende en gran medida del modelo usado para entrenarlo, por lo que su optimización ha de ser muy cuidadosa.

En el caso del análisis del $H \to \tau\tau$, se usó un Boosted Decision Tree, o BDT (árbol de decisión potenciado), cuya entrada de datos consiste en un conjunto de variables sobre la dinámica del evento, y el resultado, la probabilidad del evento de ser señal. Cada canal utilizó un tipo de diferente de BDT, optimizado para la topología de sus eventos, con diferentes variables y configuraciones. Diversos y exhaustivos estudios fueron realizados para seleccionar las variables de entrada al algoritmo y optimizar su funcionamiento. Además, se estudió minuciosamente que el algoritmo no sufriera ningún sesgo de selección. Las variables seleccionadas en el canal $\tau_{\mathrm{lep}}\tau_{\mathrm{lep}}$ fueron, en función de la categoría:

- Categoría VBF: $m_{\tau\tau}^{\mathrm{MMC}}$, ΔR_{ll}, $|\Delta\eta_{jj}|$, mín $(\Delta\eta_{l1l2,jets})$, m_{jj}, producto de las centralidades de los dos leptones, y $\Delta\eta_{j3;jj}$.
- Categoría Boosted: $m_{\tau\tau}^{\mathrm{MMC}}$, $m_{\tau\tau,j1}$, centralidad de la $E_{\mathrm{T}}^{\mathrm{miss}}$, m_{ll}, $\Delta\phi_{ll}$, esfericidad del evento, p_{T}^{l1}, p_{T}^{j1}, y $E_{\mathrm{T}}^{\mathrm{miss}}/p_{\mathrm{T}}^{l2}$

La centralidad y la esfericidad son variables angulares que miden la posición relativa de un objeto respecto a otros dos objetos (centralidad) o la distribución en la esfera angular (esfericidad).

El resultado de los BDT es una distribución en el rango $[-1, 1]$ que representa la compatibilidad de un evento con el patrón de fondo (valores negativos) o señal (valores positivos). La distribución de esta variable es el discriminante usado en el estudio estadístico del análisis.

Resultados del análisis

Los resultados del análisis en el canal $\tau_{\text{lep}}\tau_{\text{lep}}$ se exhiben en la Figura 8.20, donde se muestra la distribución del BDT y la masa $m_{\tau\tau}^{\text{MMC}}$ para cada categoría. La Figura 8.21 muestra la distribución del BDT para las Zll y Top CR en ambas categorías, enseñando que el modelo es capaz de reproducir los datos de las zonas de control dentro del error previsto.

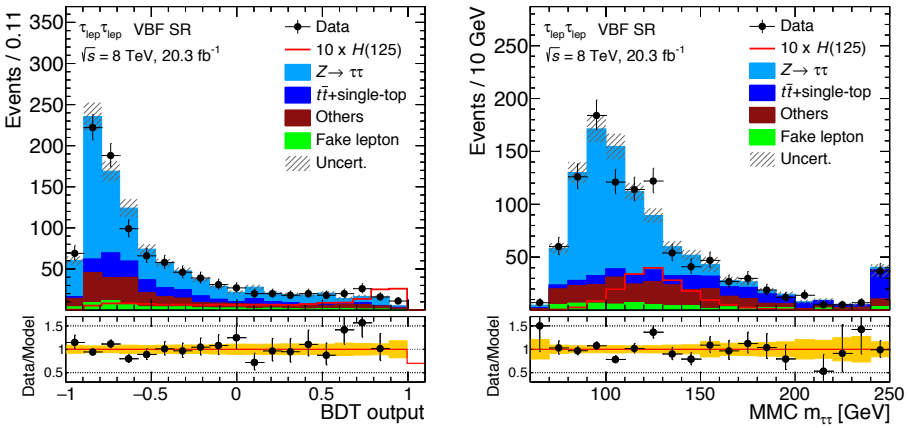

(a) VBF BDT

(b) VBF $m_{\tau\tau}^{\text{MMC}}$

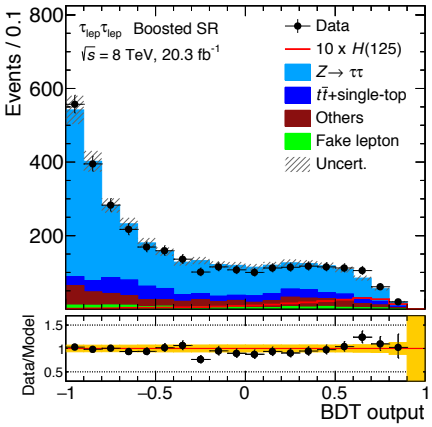

(c) Boosted BDT

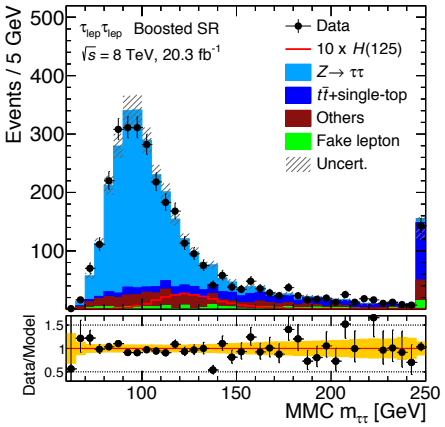

(d) Boosted $m_{\tau\tau}^{\text{MMC}}$

Figura 8.20: Distrución del BDT (izquierda) y $m_{\tau\tau}^{\text{MMC}}$ (derecha) en la región de señal para el canal $\tau_{\text{lep}}\tau_{\text{lep}}$ en las categorías VBF (arriba) y Boosted (abajo)

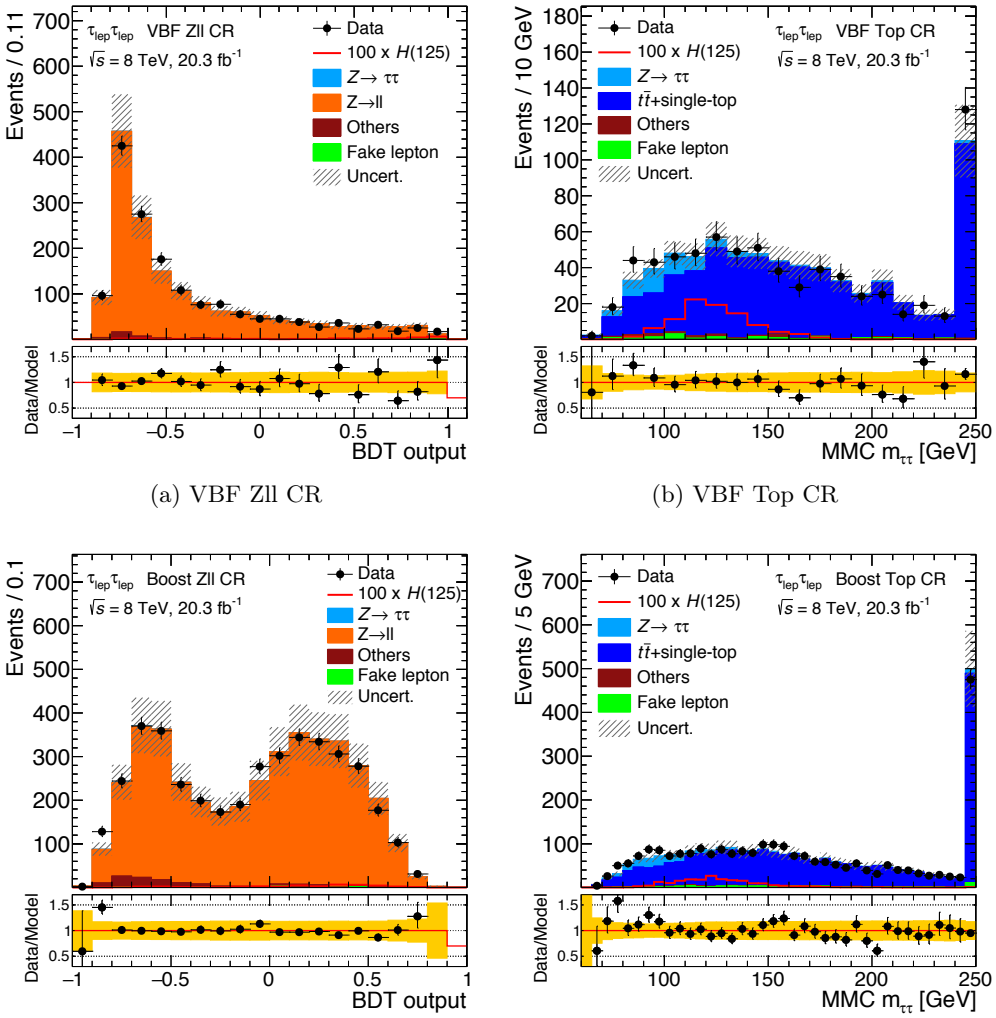

(a) VBF Zll CR

(b) VBF Top CR

(c) Boosted Zll CR

(d) Boosted Top CR

Figura 8.21: Distribución del en las regiones de control Zll (izquierda) y Top (derecha) en la región de señal para el canal $\tau_{\text{lep}}\tau_{\text{lep}}$ en las categorías VBF (arriba) y Boosted (abajo)

Como se puede observar en las distribuciones del BDT para la región de señal, en la zona donde se concentra la señal (valores altos del BDT) aparece un exceso de datos sobre el modelo de fondo. En las distribuciones de masa, este exceso aparece reflejado en los valores esperados para un bosón de Higgs del SM, alrededor de 125 GeV.

El resultado del análisis se obtiene mediante un estudio estadístico (un estimador de máxima verosimilitud o Maximum Likelihood Estimator) de las distribuciones del BDT en la zona de señal, combinando los resultados de los tres canales, usando las regiones de control como condiciones de contorno de las distribuciones del fondo y usando los errores sistemáticos como parámetros de perturbación de la regresión. La significancia del exceso observado sobre la hipótesis nula se calcula mediante un test estadístico estándar p_0. El resultado final del análisis se da en función de la fuerza de la señal (μ), parámetro

que resulta de dividir el valor del acoplamiento del bosón de Higgs medido entre el valor esperado por el SM. El resultado final del análisis del $H \to \tau\tau$ es de:

$$\mu = 1{,}43\,^{+0{,}27}_{-0{,}26}\,(\text{est.})\,^{+0{,}32}_{-0{,}25}\,(\text{sist.})\,\pm 0{,}09\,(\text{teo.}) \tag{8.7}$$

que corresponde a un exceso estadístico de 4,5 σ observadas frente a 3,4 σ esperadas para el SM. Este resultado es una fuerte evidencia del decaimiento del bosón de Higgs a leptones τ y la medida es totalmente compatible con lo esperado por el SM. La combinación final del resultado pesada para acentuar el exceso, y la compatibilidad con el SM se muestran en la Figura 8.22.

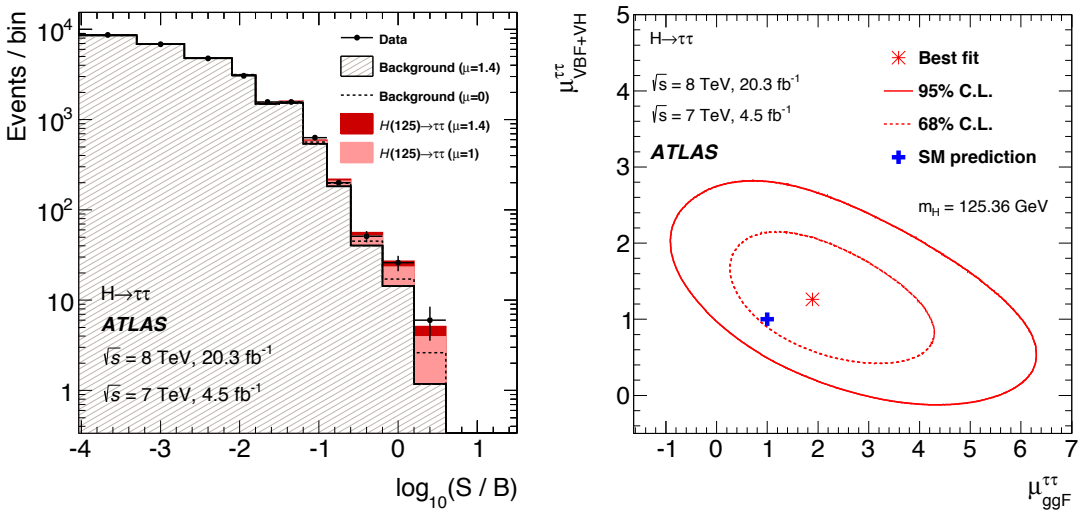

(a) (b)

Figura 8.22: Distribuciones de (a) eventos del análisis ponderados como función del ratio $\log_{10}(S/B)$, donde S y B son los eventos de señal y fondo respectivamente y (b) contornos de probabilidad de la fuerza de la señal medida de los modos de producción, mostrando la compatibilidad del resultado con el SM.

Búsqueda de bosones de Higgs adicionales del MSSM en el canal $\tau_{\text{had}}\tau_{\text{had}}$

El segundo análisis realizado durante esta tesis consistió en la búsqueda en el canal $\tau\tau$ de uno de los bosones adicionales (H, A) predichos por la teoría MSSM en el rango $200 - 1200\,\text{GeV}$ (análisis $H/A \to \tau\tau$). Para ello se usaron $3.21\,\text{fb}^{-1}$ de datos tomados a una energía del centro de masas de $13\,\text{TeV}$, que corresponde con el primer año del Run 2 del LHC (2015). El análisis fue publicado en la revista *European Physical Journal C* en noviembre de 2016 [221].

La teoría MSMM depende, a primer orden, de dos parámetros: la masa del bosón pseudo-scalar A (m_A) y el ratio entre los valores esperados de vacío de los dos campos de Higgs ($\tan\beta$). Además, en ella, los acoplamientos de los bosones de Higgs con las partículas son diferentes al SM. En concreto, para fermiones de tipo *down* (quarks d, s y b; y leptones e, μ y τ) el acoplamiento crece proporcionalmente con el valor de $\tan\beta$. Eso favorece al canal $\tau\tau$ en dos frentes, por un lado el acoplamiento directo $H/A \to \tau\tau$ y, por otro, aumenta la contribución del modo de producción asociada a quarks b (bbH); lo que convierte al $\tau\tau$ en uno de los canales principales en la búsqueda de evidencia del MSSM.

Aunque a primer orden la teoría MSSM depende de esos dos parámetros, al subir a mayores órdenes diferentes variables entran en escena. Una forma de poder estudiar la teoría es fijar estas variables adicionales de manera que se incentive un tipo de fenomenología que se pueda estudiar, lo que define ciertos *escenarios*. Los resultados de este análisis son interpretados en varios escenarios del MSSM, de entre los que destacan el hMSSM, donde la masa del bosón de Higgs más ligero del MSSM es definida como la masa del bosón medido en 2012 y el $m_h^{\text{mod}+}$, donde se modifica el acoplamiento de mezcla de la partícula stop para reproducir la masa del bosón de Higgs medido en 2012.

Los procesos de señal y fondo

Respecto a la producción de señal, dos modos de producción fueron considerados relevantes para el análisis, la fusión de gluones (ggH) y la producción asociada con quarks b (bbH), que depende del valor de $\tan\beta$. Los dos modos se muestran en la Figura 8.23.

Análogamente al análisis del SM, el análisis $H/A \to \tau\tau$ está dividido en canales de acuerdo con los estados finales del decaimiento del τ: el semi-leptónico y el hadrónico. El canal di-leptónico no fue considerado debido a su poca significancia esperada con los datos recogidos y a la poca sensitividad que tiene para el estudio en alta masa. Los trabajos de esta tesis se centraron principalmente en el canal hadrónico ($\tau_{\text{had}}\tau_{\text{had}}$).

Debido a que el decaimiento hadrónico de dos τ contiene dos neutrinos indetectables, la masa no puede ser reconstruida. Diferentes algoritmos y aproximaciones fueron exhaustivamente estudiados y, finalmente, la variable *masa total transversa* ($m_{\text{T}}^{\text{tot}}$) fue

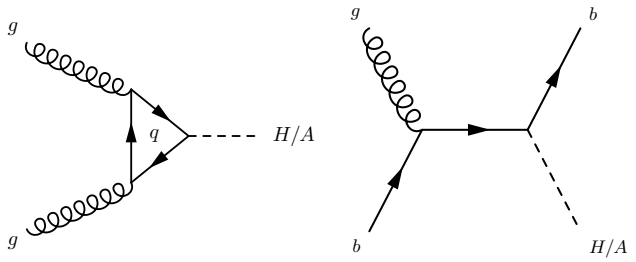

(a) *ggH* (b) *bbH*

Figura 8.23: Principales modos de producción del Higgs boson considerados en el análisis del MSSM, incluyendo (a) la fusión de gluones y (b) la producción asociada con quarks *b*.

escogida como el discriminante del análisis. Esta variable está definida como la suma cuadrática de las masas transversales de los diferentes sistemas del evento, como se puede observar en la siguiente ecuación:

$$m_{\mathrm{T}}^{\mathrm{tot}} = \sqrt{m_{\mathrm{T}}^2\left(\tau_1,\tau_2\right) + m_{\mathrm{T}}^2\left(\tau_1, E_{\mathrm{T}}^{\mathrm{miss}}\right) + m_{\mathrm{T}}^2\left(\tau_2, E_{\mathrm{T}}^{\mathrm{miss}}\right)} \tag{8.8}$$

donde la m_{T} entre dos objetos está definida como:

$$m_{\mathrm{T}}(1,2) = \sqrt{2\ p_{\mathrm{T}}^1\ p_{\mathrm{T}}^2\ \left(1-\cos(\Delta\phi_{12})\right)} \tag{8.9}$$

Respecto al fondo, dos tipos de contribuciones se pueden diferenciar, las debidas al fondo de τ *reales* y las contribuciones debidas a eventos sin ningún τ pero que el detector ha reconstruido como tales.

De estos últimos, llamados comúnmente fondo *Fake*, el más relevante es la contribución de eventos multi-jet, provenientes principalmente de procesos QCD, donde uno o dos jets son reconstruidos como τ taus hadrónicos (τ_{had}). Debido a la gran dificultad para estimar este fondo usando modelos teóricos, su contribución se estimó usando una técnica derivada de datos reales, los Factores Fake. Estos factores, parametrizados en p_{T}, son obtenidos en una zona de control de eventos di-jet, y calculados invirtiendo la identificación del segundo τ del evento. Tras ello, la estimación en la SR se obtiene multiplicando dichos factores por la distribución en la zona de señal pero invirtiendo la identificación de segundo τ.

Los otros fondos del análisis, con τ reales (W+jets, en particular el proceso $W \to \tau\nu$, Z+jets, top y di-bosónico) son modelados con métodos de MC. Sin embargo, en cada uno de esos fondos hay una pequeña contribución de eventos en los que uno de los τ ha sido identificado incorrectamente. Esta contribución es estimada con un factor de corrección derivado de datos (Fake Rate) y aplicado a los fondos de MC.

La selección de eventos

Los eventos del análisis son seleccionados para poder eliminar la mayor cantidad posible de fondo y realzar un posible exceso. La selección ocurre en tres fases, una primera

pre-selección, que actúa como limpieza de la muestra de datos, para eliminar eventos corruptos o afectados por fallos del detector en el momento de la toma de datos; la selección principal de eventos y la categorización.

El requisito básico de la muestra de datos en el canal $\tau_{\text{had}}\tau_{\text{had}}$ es que los eventos contengan al menos un τ hadrónico, τ_{had}, que haya disparado uno de los triggers de τ del detector. La selección de eventos se construye a partir de esta muestra, requiriendo que:

- el evento contenga al menos dos τ_{had}
- el τ_{had} principal haya sido identificado con un nivel "medio" y tenga un $p_{\text{T}} > 110\,\text{GeV}$
- el τ_{had} secundario haya sido identificado con un nivel "laxo" y tenga un $p_{\text{T}} > 55\,\text{GeV}$
- el objeto que ha disparado el trigger de τ se corresponda con el τ_{had} principal
- el evento no contenga ningún leptón ligero
- la diferencia en el ángulo azimutal entre los τ satisfaga $\Delta\phi(\tau_1, \tau_2) > 2{,}7$
- los dos τ_{had} tengan cargas opuestas

Tras la selección de eventos, la muestra restante es divida en dos categorías ortogonales, cuyo objetivo es optimizar la búsqueda de eventos de señal de los diferentes modos de producción (ggH y bbH) ya que tienen topologías diferentes. Las dos categorías del análisis, comunes a los dos canales, son:

- **Categoría b-tag**, definida requiriendo que al menos uno de los jets del evento provenga de un quark b (b-jet), que es la traza común del modo de producción bbH.
- **Categoría b-veto**, definida vetando cualquier b-jet, y que recoge los eventos del modo de producción ggH.

Además de las categorías en la región de señal (SR), se define una región de validación (VR) invirtiendo el corte de carga, es decir, pidiendo que los dos τ tengan la misma carga (Same Sign, SS). Las distribuciones en la SS VR para las dos categorías están mostrados en la Figura 8.24.

Resultados del análisis

Las distribuciones obtenidas para la SR (mostradas en la Figura 8.25 para el canal $\tau_{\text{had}}\tau_{\text{had}}$) son analizadas en busca de un exceso usando el mismo estudio estadístico del análisis $H \to \tau\tau$, combinando los dos canales ($\tau_{\text{lep}}\tau_{\text{had}}$ y $\tau_{\text{had}}\tau_{\text{had}}$). Con la luminosidad integrada recogida, los datos muestran un acuerdo con el modelo y no se observa ningún exceso. Por tanto, se extraen límites sobre la sección eficaz de los dos modos de producción así como restricciones a los parámetros de varios modelos MSSM.

Para los modos de producción (Figura 8.26) el límite inferior de la sección eficaz por el ancho de decaimiento ($\sigma \times \text{BR}$) para un bosón escalar y para el modo de producción ggH es de $\sigma \times \text{BR} = 1{,}4\,\text{pb}$ para una masa de $m_{H/A} = 200\,\text{GeV}$ y de $\sigma \times \text{BR} = 0{,}025\,\text{pb}$ para

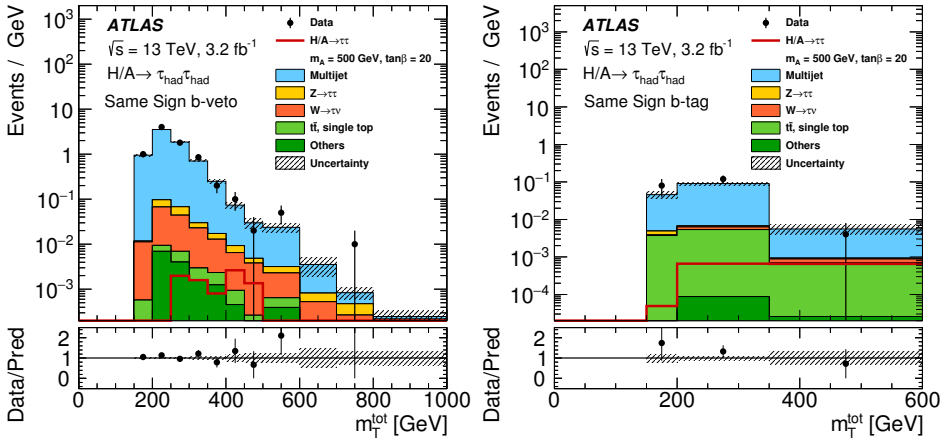

(a) b-veto category SS (b) b-tag category SS

Figura 8.24: Distribuciones antes del ajuste de la masa transversa total en la región de validación para el canal $\tau_{\text{had}}\tau_{\text{had}}$ para las categorías (a) b-veto y (b) b-tag. La etiqueta "Others" agrupa a las contribuciones de los fondos di-bosónico, $Z \to ll$+jets y $W(\to l\nu)$+jets. Como referencia, se muestra una señal de $\tan\beta = 20$, $m_A = 500\,\text{GeV}$.

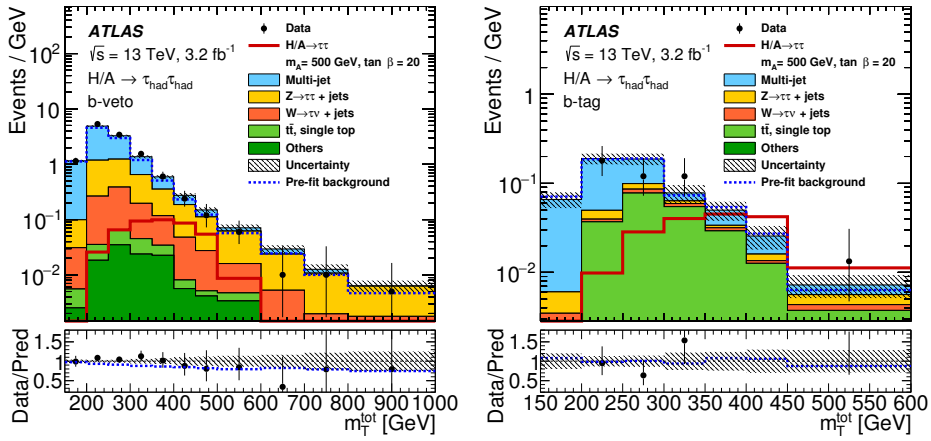

(a) b-veto category SR (b) b-tag category SR

Figura 8.25: Distribución de la masa total transversa con las incertidumbres del ajuste en la región de señal en el canal $\tau_{\text{had}}\tau_{\text{had}}$ para las categorías (a) b-veto y (b) b-tag. La etiqueta "Others"agrupa a las contribuciones de los fondos di-bosónico, $Z \to ll$+jets y $W(\to l\nu)$+jets. Como referencia, se muestra una señal de $\tan\beta = 20$, $m_A = 500\,\text{GeV}$.

$m_{H/A} = 1200\,\text{GeV}$. Para el modo bbH los valores mínimos se restringen a $\sigma \times \text{BR} = 1{,}6\,\text{pb}$ para una masa de $m_{H/A} = 200\,\text{GeV}$ y de $\sigma \times \text{BR} = 0{,}028\,\text{pb}$ para $m_{H/A} = 1200\,\text{GeV}$.

Los resultados en los diferentes escenarios del MSSM estudiados excluyen, para el escenario $m_h^{\text{mod}+}$, la región con $\tan\beta > 7{,}6$ para $m_A = 200\,\text{GeV}$ y $\tan\beta > 47$ para $m_A = 1000\,\text{GeV}$; para el hMSSM, se excluye la región con $\tan\beta > 7{,}1$ para $m_A = 200\,\text{GeV}$ y $\tan\beta > 39$ para $m_A = 1000\,\text{GeV}$. Estos límites están mostrados en la Figura 8.27.

El análisis $H/A \to \tau\tau$ con los primeros datos del Run 2 no ha encontrado ningún exceso sobre el SM en ninguna de las regiones consideradas. Sin embargo, el análisis es capaz de mejorar ligeramente los resultados obtenidos con los datos del Run 1.

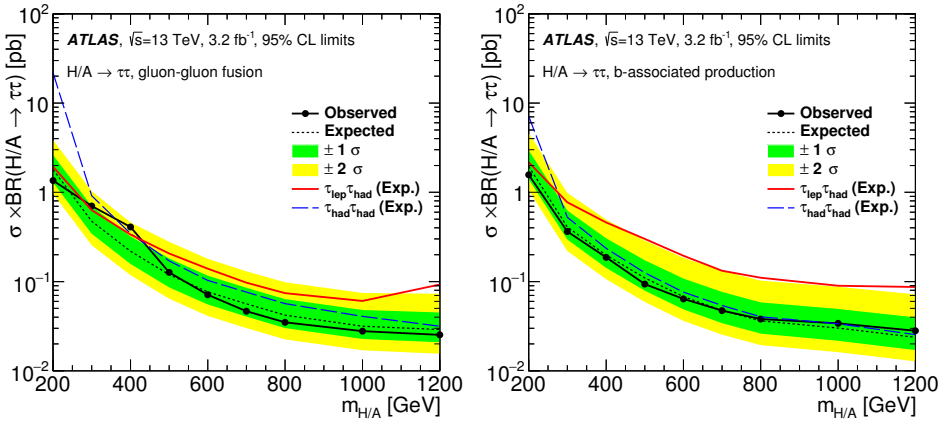

(a) ggH (b) bbH

Figura 8.26: Límites observados y esperados para la sección eficaz por el ancho de decaimiento para (a) fusión de gluones y (b) producción asociada con quarks b para el análisis $H/A \to \tau\tau$. Se muestran también los valores de los dos canales por separado.

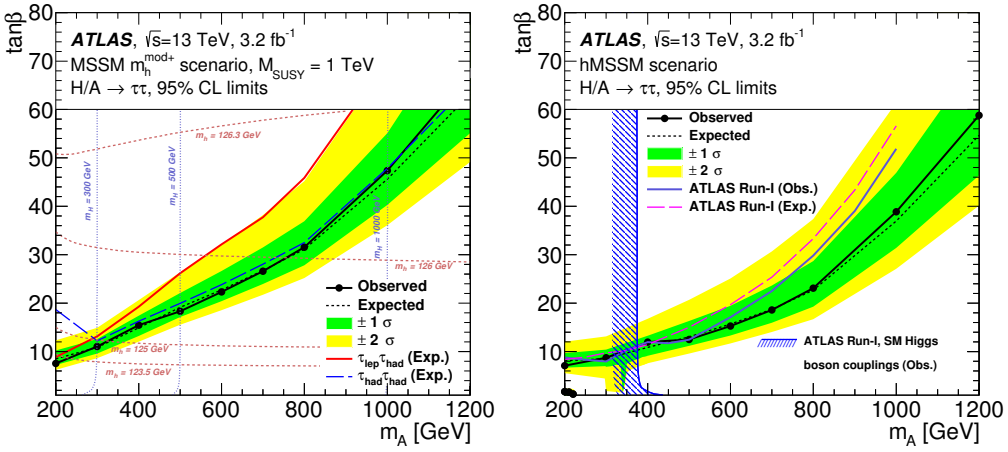

(a) $m_h^{\mathrm{mod}+}$ (b) hMSSM

Figura 8.27: Límites observados y esperados en el espacio $\tan\beta - m_A$ para los escenarios (a) $m_h^{\mathrm{mod}+}$ y (b) hMSSM del análisis $H/A \to \tau\tau$. Por comparación, se muestran los límites de los canales individuales y, en (b), el resultado del Run 1.

Appendix A

Mathematical extension

This appendix covers mathematical definitions not included in Chapter 1.

Gamma matrices - γ^i

$$\gamma^0 = \begin{pmatrix} 1 & 0 & 0 & 0 \\ 0 & 1 & 0 & 0 \\ 0 & 0 & -1 & 0 \\ 0 & 0 & 0 & -1 \end{pmatrix} \qquad \gamma^1 = \begin{pmatrix} 0 & 0 & 0 & 1 \\ 0 & 0 & 1 & 0 \\ 0 & -1 & 0 & 0 \\ -1 & 0 & 0 & 0 \end{pmatrix}$$

$$\gamma^2 = \begin{pmatrix} 0 & 0 & 0 & i \\ 0 & 0 & i & 0 \\ 0 & -i & 0 & 0 \\ -i & 0 & 0 & 0 \end{pmatrix} \qquad \gamma^3 = \begin{pmatrix} 0 & 0 & 1 & 0 \\ 0 & 0 & 0 & -1 \\ -1 & 0 & 0 & 0 \\ 0 & 1 & 0 & 0 \end{pmatrix}$$

Chiral projector - γ^5

$$\gamma^5 \equiv i\gamma^0\gamma^1\gamma^2\gamma^3 = \begin{pmatrix} 0 & 0 & 1 & 0 \\ 0 & 0 & 0 & 1 \\ 1 & 0 & 0 & 0 \\ 0 & 1 & 0 & 0 \end{pmatrix}$$

Pauli matrices

The generators of $SU(2)$ are the τ_i matrices, defined as $\tau_i \equiv \frac{1}{2}\sigma_i$, with σ_i:

$$\sigma_1 = \begin{pmatrix} 0 & 1 \\ 1 & 0 \end{pmatrix} \qquad \sigma_2 = \begin{pmatrix} 0 & -i \\ i & 0 \end{pmatrix} \qquad \sigma_3 = \begin{pmatrix} 1 & 0 \\ 0 & -1 \end{pmatrix}$$

Gell-Mann matrices - generators of $SU(3)$

The generators of $SU(3)$ are the T_i matrices, defined as $T_i \equiv \frac{1}{2}\lambda_i$, with λ_i:

$$\lambda_1 = \begin{pmatrix} 0 & 1 & 0 \\ 1 & 0 & 0 \\ 0 & 0 & 0 \end{pmatrix} \qquad \lambda_2 = \begin{pmatrix} 0 & -i & 0 \\ i & 0 & 0 \\ 0 & 0 & 0 \end{pmatrix} \qquad \lambda_3 = \begin{pmatrix} 1 & 0 & 0 \\ 0 & -1 & 0 \\ 0 & 0 & 0 \end{pmatrix}$$

$$\lambda_4 = \begin{pmatrix} 0 & 0 & 1 \\ 0 & 0 & 0 \\ 1 & 0 & 0 \end{pmatrix} \qquad \lambda_5 = \begin{pmatrix} 0 & 0 & -i \\ 0 & 0 & 0 \\ i & 0 & 0 \end{pmatrix}$$

$$\lambda_6 = \begin{pmatrix} 0 & 0 & 0 \\ 0 & 0 & 1 \\ 0 & 1 & 0 \end{pmatrix} \qquad \lambda_7 = \begin{pmatrix} 0 & 0 & 0 \\ 0 & 0 & -i \\ 0 & i & 0 \end{pmatrix} \qquad \lambda_8 = \frac{1}{\sqrt{3}} \begin{pmatrix} 1 & 0 & 0 \\ 0 & 1 & 0 \\ 0 & 0 & -2 \end{pmatrix}$$

Cabibbo–Kobayashi–Maskawa matrix - CKM matrix

The CKM matrix describes the flavour mixing in the quark sector, relating the mass and flavour eigenstates in the form:

$$\widetilde{d} = |V_{ud}|\, d + |V_{us}|\, s |V_{ub}|\, b \widetilde{s} \qquad = |V_{cd}|\, d + |V_{cs}|\, s |V_{cb}|\, b \widetilde{b} = |V_{td}|\, d + |V_{ts}|\, s |V_{tb}|\, b$$

The mixing parameters V_{ij} form the CKM matrix and can be written as [3]:

$$V_{\text{CKM}} = \begin{pmatrix} V_{ud} & V_{us} & V_{ub} \\ V_{cd} & V_{cs} & V_{cb} \\ V_{td} & V_{ts} & V_{tb} \end{pmatrix} = \begin{pmatrix} 0.97434(12) & 0.22506(50) & 0.00357(15) \\ 0.22492(50) & 0.97351(13) & 0.0411(13) \\ 0.00875(33) & 0.0403(13) & 0.99915(5) \end{pmatrix}$$

The matrix must follow certain constraints imposed by the SM as the unitarity of the flavours, that is, the sum of factors of each column/row, has to be equal to one.

With this constrains, the matrix parameters are not independent, hence the matrix can be parametrized, reducing the number of free terms to four.

Two main parametrizations are considered. First, the standard parametrization, which defines three angles that mix the different generations (θ_{12}, θ_{23} and θ_{13}) and one CP-violating phase, δ.

$$V_{\text{CKM}} = \begin{pmatrix} c_{12}c_{13} & s_{12}c_{13} & s_{13}e^{-i\delta_{13}} \\ -s_{12}c_{23} - c_{12}s_{23}s_{13}e^{i\delta} & c_{12}c_{23} - s_{12}s_{23}s_{13}e^{i\delta} & s_{23}c_{13} \\ s_{12}s_{23} - c_{12}c_{23}s_{13}e^{i\delta} & -c_{12}s_{23} - s_{12}c_{23}s_{13}e^{i\delta} & c_{23}c_{13} \end{pmatrix}$$

where c_{ij} stands for $\cos\theta_{ij}$ and s_{ij} for $\sin\theta_{ij}$

The second one is the Wolfestein parametrization, which defines four values of the order of the unit: λ, A, ρ and η. These values are related to the standard ones by the following relations:

$$\begin{aligned} s_{12} &= \lambda \\ s_{23} &= A\lambda^2 \\ s_{13}e^{-i\delta} &= A\lambda^3(\rho + i\eta) \end{aligned}$$

which defines the CKM matrix as:

$$V_{\text{CKM}} = \begin{pmatrix} 1 - \lambda^2/2 & \lambda & A\lambda^3(\rho - i\eta) \\ -\lambda & 1 - \lambda^2/2 & A\lambda^2 \\ A\lambda^3(1 - \rho - i\eta) & -A\lambda^2 & 1 \end{pmatrix}$$

The measured values for the respective parametrizations are [3]:

$$\begin{aligned} \theta_{12} &= (13.01 \pm 0.03)^\circ & A &= 0.811 \pm 0.026 \\ \theta_{23} &= (2.35 \pm 0.09)^\circ & \lambda &= 0.22506 \pm 0.0005 \\ \theta_{13} &= (0.20 \pm 0.04)^\circ & \rho &= 0.124 \pm 0.019 \\ \delta &= (70 \pm 3)^\circ & \eta &= 0.356 \pm 0.011 \end{aligned}$$

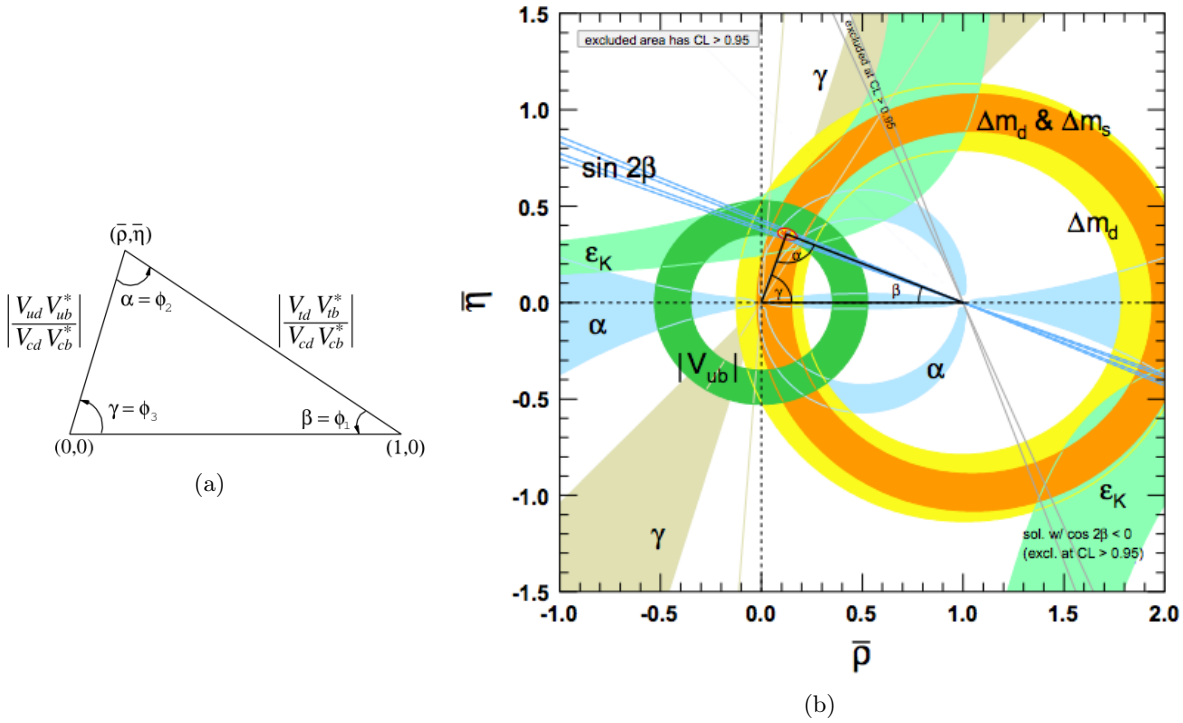

(a) (b)

Figure A.1: Diagram of the theoretical definition (a) and display of the experimental measurement with uncertainty (b) of the angles of the Cabbibo-Kobayashi-Maskawa matrix [3].

Pontecorvo–Maki–Nakagawa–Sakata matrix - PMNS matrix

The PMNS matrix describes the mixing of the neutrino flavours. Analogously to the CKM, the PMNS matrix can also be parametrized in three angles and a CP-violating phase. In contrast, the experimental measurement of this angles depends also on the -still unknown- hierarchy mass of the neutrinos, and thus, different values can be given, assuming one or other possible hierarchies.

$$V_{PMNS} = \begin{bmatrix} U_{e1} & U_{e2} & U_{e3} \\ U_{\mu 1} & U_{\mu 2} & U_{\mu 3} \\ U_{\tau 1} & U_{\tau 2} & U_{\tau 3} \end{bmatrix} = \begin{bmatrix} c_{12}c_{13} & s_{12}c_{13} & s_{13}e^{-i\delta} \\ -s_{12}c_{23} - c_{12}s_{23}s_{13}e^{i\delta} & c_{12}c_{23} - s_{12}s_{23}s_{13}e^{i\delta} & s_{23}c_{13} \\ s_{12}s_{23} - c_{12}c_{23}s_{13}e^{i\delta} & -c_{12}s_{23} - s_{12}c_{23}s_{13}e^{i\delta} & c_{23}c_{13} \end{bmatrix}$$

where c_{ij} stands for $\cos\theta_{ij}$ and s_{ij} for $\sin\theta_{ij}$

The values of the measured angles are [3]:

Angle	$m_1 < m_2 < m_3$	$m_3 < m_1 < m_2$
$\sin^2\theta_{12}$	0.297 ± 0.016	0.297 ± 0.016
$\sin^2\theta_{23}$	0.44 ± 0.03	0.57 ± 0.09
$\sin^2\theta_{13}$	0.0214 ± 0.0010	0.0218 ± 0.0016
δ/π	1.4 ± 0.2	1.3 ± 0.3

Appendix B

Additional results of the SM $H \to \tau\tau$ analysis

This appendix covers additional results of the SM $H \to \tau\tau$ analysis. The chapter is divided in three section: the first section shows additional information of the $\tau_{\text{lep}}\tau_{\text{had}}$ and $\tau_{\text{had}}\tau_{\text{had}}$ channels for the 8 TeV dataset. The second section shows the distributions of the 7 TeV dataset, collected during 2011. Finally, the last section displays the results of the cut-based analysis.

B.1 The $\tau_{\text{lep}}\tau_{\text{had}}$ and $\tau_{\text{had}}\tau_{\text{had}}$ channels

This section shows the event yields of the $\tau_{\text{lep}}\tau_{\text{had}}$ and $\tau_{\text{had}}\tau_{\text{had}}$ channels, shown in Tables B.1 and B.2

Process			**VBF** All bins	**VBF** Second to last bin	**VBF** Last bin	**Boosted** All bins	**Boosted** Second to last bin	**Boosted** Last bin
Background	Fake background		1680 ± 50	8.2 ± 0.9	5.2 ± 0.7	5640 ± 160	51.0 ± 2.5	22.3 ± 1.8
	$Z \to \tau\tau$		877 ± 29	7.6 ± 0.9	4.2 ± 0.7	6210 ± 170	57.5 ± 2.8	41.1 ± 3.2
	Top		82 ± 15	0.3 ± 0.4	0.5 ± 0.4	380 ± 50	12 ± 4	4.8 ± 1.5
	$Z \to ll$		54 ± 26	1.0 ± 0.7	0.30 ± 0.28	200 ± 50	13 ± 4	8.6 ± 3.5
	Di-boson		63 ± 11	1.0 ± 0.4	0.48 ± 0.20	430 ± 40	9.7 ± 2.2	4.7 ± 1.6
Signal	$H \to \tau\tau$	ggH	16 ± 6	1.0 ± 0.4	1.2 ± 0.6	60 ± 20	9.2 ± 3.2	10.1 ± 3.4
		VBF	31 ± 8	4.5 ± 1.1	9.1 ± 2.2	16 ± 4	2.5 ± 0.6	2.9 ± 0.7
		WH	0.6 ± 0.4	< 0.1	< 0.1	9.1 ± 2.3	1.3 ± 0.4	1.9 ± 0.5
		ZH	0.16 ± 0.07	< 0.1	< 0.1	4.6 ± 1.2	0.77 ± 0.20	0.93 ± 0.24
Total background			2760 ± 40	18.1 ± 2.3	10.7 ± 2.7	12 860 ± 110	143 ± 6	82 ± 6
Total signal			48 ± 12	5.5 ± 1.3	10.3 ± 2.5	89 ± 26	14 ± 4	16 ± 4
Data			2830	22	21	12 952	170	92

Table B.1: The predicted post-fit event yields in the $\tau_{\text{lep}}\tau_{\text{had}}$ channel for $m_H = 125\,\text{GeV}$ for the total number of events and for the two highest bins of the BDT distributions for the data taken at $\sqrt{s} = 8\,\text{TeV}$. The background normalizations, signal normalization, and their uncertainties represent the post-fit values. The uncertainties on the total background and total signal represent the full statistical and systematic uncertainty, while the uncertainties on the individual background components represent the full systematic uncertainty only [155].

Process			**VBF** All bins	**VBF** Second to last bin	**VBF** Last bin	**Boosted** All bins	**Boosted** Second to last bin	**Boosted** Last bin
Background	Fake background		370 ± 18	2.3 ± 0.9	0.57 ± 0.29	645 ± 26	35 ± 4	0.65 ± 0.33
	Others		37 ± 5	0.67 ± 0.22	< 0.1	89 ± 11	15.9 ± 2.0	0.92 ± 0.22
	$Z \to \tau\tau$		475 ± 16	0.6 ± 0.7	0.6 ± 0.4	2230 ± 70	93 ± 4	5.4 ± 1.6
Signal	$H \to \tau\tau$	ggH	8.0 ± 2.7	0.67 ± 0.23	0.53 ± 0.20	21 ± 8	9.1 ± 3.3	1.6 ± 0.6
		VBF	12.0 ± 3.1	1.8 ± 0.5	3.4 ± 0.9	6.3 ± 1.6	2.8 ± 0.7	0.52 ± 0.13
		WH	0.25 ± 0.07	< 0.1	< 0.1	4.0 ± 1.1	1.9 ± 0.5	0.41 ± 0.11
		ZH	0.16 ± 0.04	< 0.1	< 0.1	2.4 ± 0.6	1.13 ± 0.30	0.23 ± 0.06
Total background			883 ± 18	3.6 ± 1.3	1.2 ± 1.0	2960 ± 50	143 ± 6	7.0 ± 1.8
Total signal			20 ± 5	2.5 ± 0.6	3.9 ± 1.0	34 ± 10	15 ± 4	2.7 ± 0.8
Data			892	5	6	3020	161	10

Table B.2: The predicted post-fit event yields in the $\tau_{\text{had}}\tau_{\text{had}}$ channel for $m_H = 125\,\text{GeV}$ for the total number of events and for the two highest bins of the BDT distributions for the data taken at $\sqrt{s} = 8\,\text{TeV}$. The background normalizations, signal normalization, and their uncertainties represent the post-fit values. The uncertainties on the total background and total signal represent the full statistical and systematic uncertainty, while the uncertainties on the individual background components represent the full systematic uncertainty only [155].

B.2 The 7 TeV dataset

This section shows the distributions of the $m_{\tau\tau}^{\text{MMC}}$ and BDT Score for the two categories (VBF and Boosted), and for the three channelsm for the dataset collected at $\sqrt{s} = 7\,\text{TeV}$ during 2011.

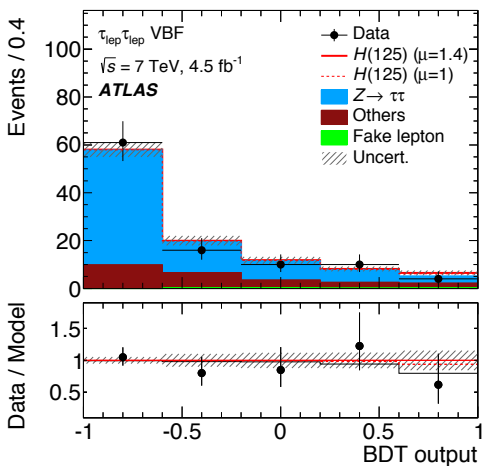

(a) VBF BDT

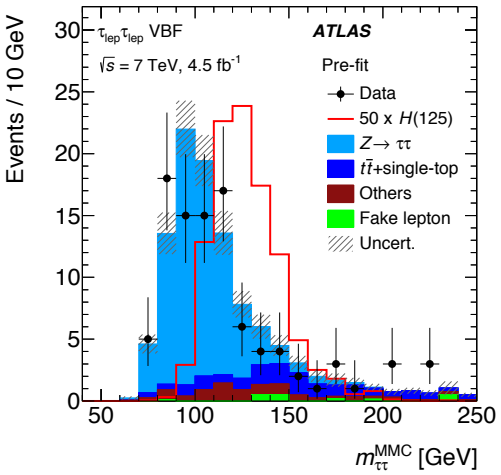

(b) VBF $m_{\tau\tau}^{\text{MMC}}$

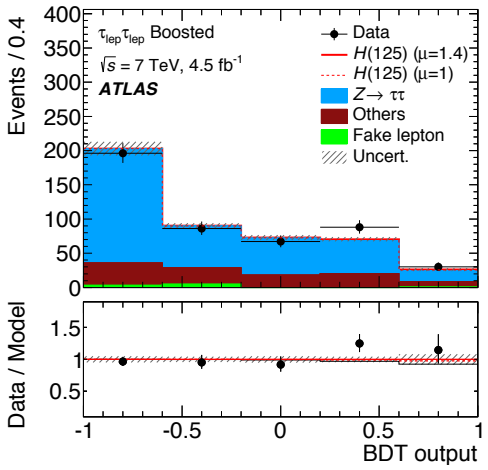

(c) Boosted BDT

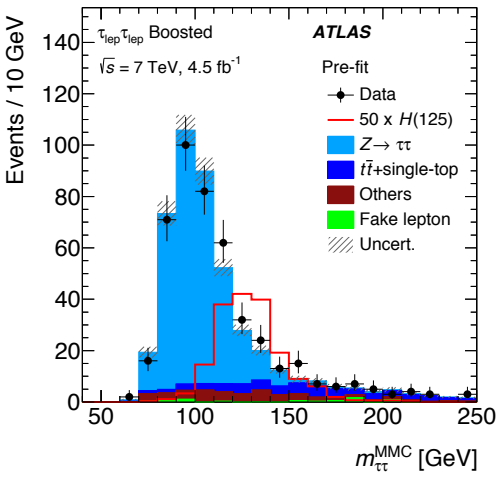

(d) Boosted $m_{\tau\tau}^{\text{MMC}}$

Figure B.1: Pre-fit distributions of the (left) BDT Score and (right) $m_{\tau\tau}^{\text{MMC}}$ in the (top) VBF and (bottom) Boosted categories, for the $\tau_{\text{lep}}\tau_{\text{lep}}$ channel, for the data collected at 7 TeV during 2011. The contributions from a SM Higgs boson with $m_H = 125\,\text{GeV}$ are superimposed, multiplied by a factor of 50. The error band includes statistical and pre-fit systematic uncertainties [155].

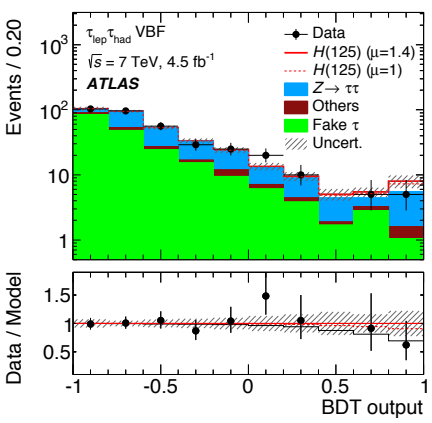

(a) $\tau_{\text{lep}}\tau_{\text{had}}$ VBF BDT

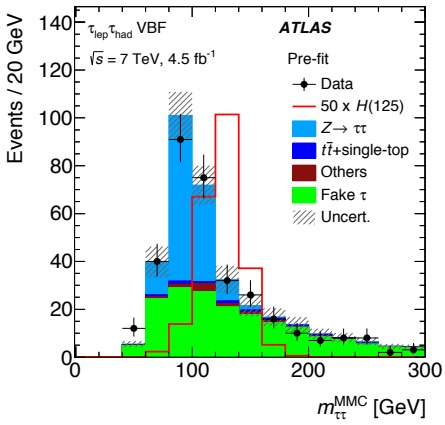

(b) $\tau_{\text{lep}}\tau_{\text{had}}$ VBF $m_{\tau\tau}^{\text{MMC}}$

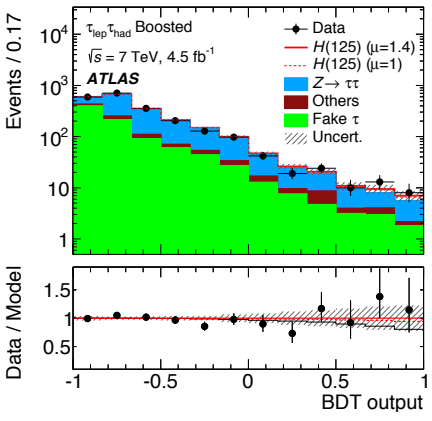

(c) $\tau_{\text{lep}}\tau_{\text{had}}$ Boosted BDT

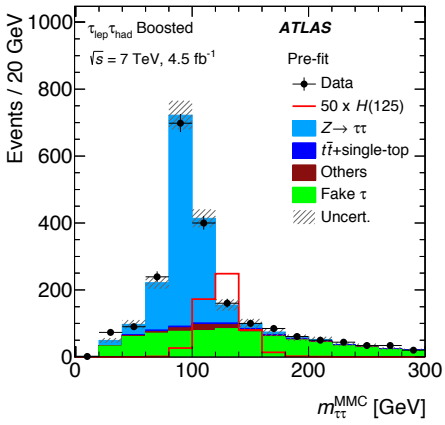

(d) $\tau_{\text{lep}}\tau_{\text{had}}$ Boosted $m_{\tau\tau}^{\text{MMC}}$

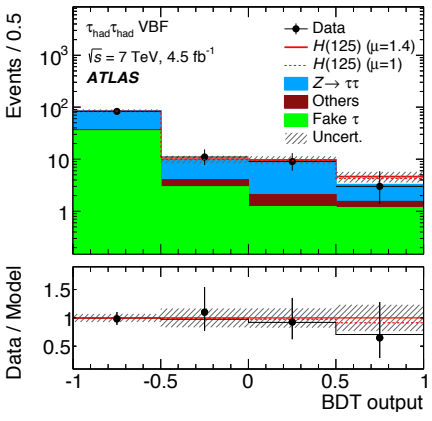

(e) $\tau_{\text{had}}\tau_{\text{had}}$ VBF BDT

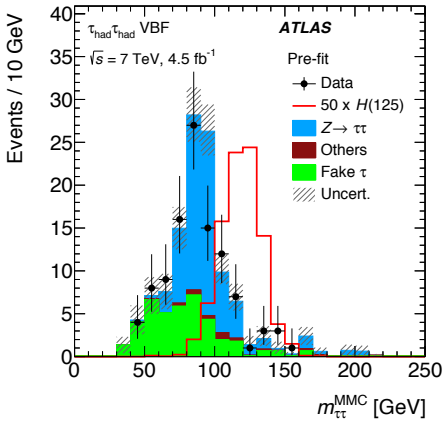

(f) $\tau_{\text{had}}\tau_{\text{had}}$ VBF $m_{\tau\tau}^{\text{MMC}}$

Figure B.2: Pre-fit distributions of the (left) BDT Score and (right) $m_{\tau\tau}^{\text{MMC}}$ in the VBF and Boosted categories, for the $\tau_{\text{lep}}\tau_{\text{had}}$ (top four) and $\tau_{\text{had}}\tau_{\text{had}}$ (bottom four) channels for the data collected at 7 TeV during 2011. The contributions from a SM Higgs boson with $m_H = 125\,\text{GeV}$ are superimposed, multiplied by a factor of 50. The error band includes statistical and pre-fit systematic uncertainties [155].

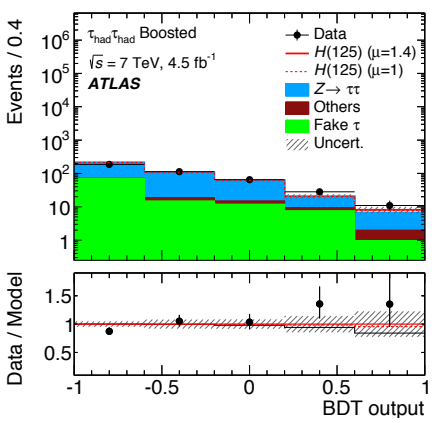

(g) $\tau_{\text{had}}\tau_{\text{had}}$ Boosted BDT

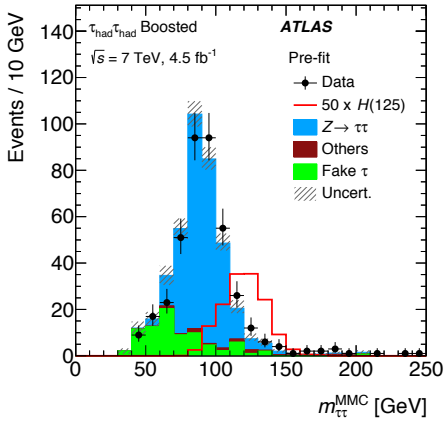

(h) $\tau_{\text{had}}\tau_{\text{had}}$ Boosted $m_{\tau\tau}^{\text{MMC}}$

Figure B.2: Pre-fit distributions of the (left) BDT Score and (right) $m_{\tau\tau}^{\text{MMC}}$ in the VBF and Boosted categories, for the $\tau_{\text{lep}}\tau_{\text{had}}$ (top four) and $\tau_{\text{had}}\tau_{\text{had}}$ (bottom four) channels for the data collected at 7 TeV during 2011. The contributions from a SM Higgs boson with $m_H = 125$ GeV are superimposed, multiplied by a factor of 50. The error band includes statistical and pre-fit systematic uncertainties [155].

B.3 The cut-based analysis

$\tau_{\text{lep}}\tau_{\text{lep}}$	**VBF**	**Boosted**
Signal	11 ± 4	38 ± 13
Background	130 ± 7	3400 ± 64
Data	152	3428

	VBF		
$\tau_{\text{lep}}\tau_{\text{had}}$	Tight	Loose VBF	**Boosted**
Signal	8.8 ± 3.0	17 ± 6	52 ± 17
Background	52 ± 4	398 ± 17	4399 ± 73
Data	62	407	4435

		VBF low $p_{\text{T}}^{\tau\tau}$		**Boosted**	
$\tau_{\text{had}}\tau_{\text{had}}$	**VBF high $p_{\text{T}}^{\tau\tau}$**	Tight	Loose	High $p_{\text{T}}^{\tau\tau}$	Low $p_{\text{T}}^{\tau\tau}$
Signal	5.7 ± 1.9	5.2 ± 1.9	3.7 ± 1.3	17 ± 6	20 ± 7
Background	59 ± 4	86 ± 5	156 ± 7	1155 ± 28	2130 ± 41
Data	65	94	157	1204	2121

Table B.3: The measured signal and background yields of the cut-based analysis at $\sqrt{s} = 8$ TeV in the $\tau_{\text{lep}}\tau_{\text{lep}}$, $\tau_{\text{lep}}\tau_{\text{had}}$ and $\tau_{\text{had}}\tau_{\text{had}}$ channels, for $m_H = 125$ GeV. The normalizations and uncertainties are taken from the global fit. The uncertainties on the predicted yields reflect the full statistical and systematic uncertainties [155].

Appendix C

Additional results of the MSSM $H/A \to \tau\tau$ analysis

This appendix covers additional results of the MSSM $H/A \to \tau\tau$ analysis.

C.1 The $\tau_{\mathbf{lep}}\tau_{\mathbf{had}}$ channel

This section covers the post-fit yields of the $\tau_{\text{lep}}\tau_{\text{had}}$ channel, separated in the e and μ subchannels.

Channel	Process	*b*-tag category		*b*-veto category	
$\tau_e\tau_{\text{had}}$	$Z \to \tau\tau$ +jets	42	± 7	4500	± 250
	Jet $\to l, \tau_{\text{had}}$ fakes	128	± 18	5400	± 350
	$Z \to ll$+jets	3.6	± 1.5	590	± 120
	$t\bar{t}$ and single-top	115	± 16	35	± 5
	Di-boson	0.33	± 0.07	44	± 4
	ggH	0.020	± 0.010	1.2	± 0.2
	bbH	6.4	± 1.7	7.4	± 1.9
	Total SM	289	± 24	10 600	± 360
	Data	275		10 619	
$\tau_\mu\tau_{\text{had}}$	$Z \to \tau\tau$ +jets	42	± 6	5500	± 300
	Jet $\to l, \tau_{\text{had}}$ fakes	109	± 14	2760	± 170
	$Z \to ll$ +jets	5.2	± 0.6	830	± 50
	$t\bar{t}$ and single-top	136	± 15	40	± 5
	Di-boson	0.34	± 0.07	55	± 5
	ggH	0.016	± 0.005	1.1	± 0.2
	bbH	3.3	± 1.3	6.4	± 1.7
	Total SM	293	± 19	9200	± 300
	Data	312		9163	

Table C.1: Observed number of events and background predictions in the b-tag and b-veto categories for the e and μ subchannels of the $\tau_{\text{lep}}\tau_{\text{had}}$ channel. The background predictions and uncertainties are obtained from the statistical procedure discussed in Section 7.9.1. The processes other than "Jet $\to l, \tau_{\text{had}}$ fakes" require a true hadronically decaying τ lepton or an electron or muon misidentified as a τ_{had}. The expected signal yields for the $m_h^{\text{mod+}}$ scenario with $m_A = 500\,\text{GeV}$ and $\tan\beta = 20$ are shown for comparison.

C.2 Tables of exclusion limits

In this section, there are collected the numerical results of the exclusion limits for the different interpretations. Table C.2 shows these values for the model-dependent approach, for the $m_h^{\text{mod+}}$ and hMSSM scenarios. Table C.3 shows the values for the model-independent approach, for the ggH and bbH production modes independently. The combination of both modes is shown in Tables C.4 to C.6. In all these tables, higher values than those quoted are excluded.

		Limit		**Uncertainty**			
Scenario	m_A [GeV]	observed	expected	$+2\,\sigma$	$+1\,\sigma$	$-1\,\sigma$	$-2\,\sigma$
$m_h^{\text{mod+}}$	200	7.6	8.5	12	10	7.3	6.2
	300	11	11	15	13	9.6	8.7
	400	15	15	21	17	13	12
	500	18	19	26	22	17	16
	600	22	23	32	27	20	19
	700	27	27	38	32	24	22
	800	32	31	45	37	28	25
	1000	47	46	> 60	55	40	36
	1200	> 60	> 60	> 60	> 60	> 60	49
hMSSM	200	7.1	8.1	12	9.7	6.7	5.6
	300	8.7	8.5	13	10	7.0	4.4
	400	12	11	17	13	9.1	7.6
	500	13	13	21	16	11	9.6
	600	15	16	25	19	13	12
	700	19	19	31	24	16	14
	800	23	23	37	29	19	17
	1000	39	37	> 60	47	31	27
	1200	59	55	> 60	> 60	46	40

Table C.2: The 95% CL upper limits in the $m_A - \tan\beta$ space in the $m_h^{\text{mod+}}$ and hMSSM scenarios. The quoted limits here are $\tan\beta$ values. Higher values than those quoted are excluded [221].

		Limit		**Uncertainty**			
Mode	m_A [GeV]	observed	expected	$+2\,\sigma$	$+1\,\sigma$	$-1\,\sigma$	$-2\,\sigma$
bbH	200	1.6	2.0	4.6	3.0	1.4	1.0
	300	0.36	0.41	0.99	0.63	0.30	0.22
	400	0.19	0.20	0.50	0.31	0.14	0.11
	500	0.094	0.11	0.29	0.17	0.079	0.059
	600	0.064	0.068	0.19	0.11	0.049	0.036
	700	0.047	0.048	0.13	0.077	0.034	0.025
	800	0.038	0.036	0.10	0.059	0.026	0.019
	1000	0.034	0.030	0.087	0.049	0.022	0.016
	1200	0.028	0.024	0.072	0.040	0.017	0.013
ggH	200	1.4	1.8	3.9	2.6	1.3	0.97
	300	0.70	0.48	1.0	0.70	0.34	0.26
	400	0.41	0.22	0.46	0.32	0.16	0.12
	500	0.13	0.12	0.28	0.18	0.086	0.064
	600	0.071	0.077	0.18	0.12	0.055	0.041
	700	0.047	0.056	0.13	0.085	0.041	0.030
	800	0.035	0.042	0.098	0.064	0.030	0.022
	1000	0.028	0.032	0.075	0.048	0.023	0.017
	1200	0.025	0.029	0.073	0.045	0.021	0.015

Table C.3: The 95% CL upper limits for the production cross-section times the branching ratio to a $\tau\tau$ pair of a scalar particle for the gluon fusion a b-associated production modes. The limit values are in pb and are valid under the assumption that the width of the particle is negligible with respect to the $m_{\mathrm{T}}^{\mathrm{tot}}$ mass resolution [221].

		Limit		**Uncertainty**			
$m_{H/A}$ [GeV]	f_b	observed	expected	$+2\,\sigma$	$+1\,\sigma$	$-1\,\sigma$	$-2\,\sigma$
200	0.00	1.4	1.8	3.9	2.6	1.3	0.97
200	0.10	1.4	1.8	3.8	2.6	1.3	0.98
200	0.20	1.4	1.8	3.8	2.6	1.3	0.98
200	0.30	1.4	1.8	3.8	2.7	1.3	0.99
200	0.40	1.4	1.9	3.8	2.7	1.3	1.00
200	0.50	1.5	1.9	3.9	2.7	1.3	1.0
200	0.60	1.5	1.9	4.0	2.7	1.4	1.0
200	0.70	1.5	1.9	4.1	2.8	1.4	1.0
200	0.80	1.5	1.9	4.2	2.8	1.4	1.0
200	0.90	1.5	1.9	4.4	2.9	1.4	1.0
200	1.00	1.6	2.0	4.6	3.0	1.4	1.0
300	0.00	0.70	0.48	1.0	0.70	0.34	0.26
300	0.10	0.67	0.48	1.0	0.71	0.35	0.26
300	0.20	0.64	0.49	1.0	0.71	0.35	0.26
300	0.30	0.62	0.49	1.0	0.71	0.35	0.26
300	0.40	0.58	0.48	1.0	0.70	0.35	0.26
300	0.50	0.55	0.47	1.0	0.70	0.34	0.25
300	0.60	0.51	0.47	1.0	0.69	0.34	0.25
300	0.70	0.47	0.45	1.0	0.68	0.33	0.24
300	0.80	0.44	0.44	1.0	0.66	0.32	0.24
300	0.90	0.40	0.43	1.00	0.65	0.31	0.23
300	1.00	0.36	0.41	0.99	0.63	0.30	0.22
400	0.00	0.41	0.22	0.46	0.32	0.16	0.12
400	0.10	0.41	0.23	0.48	0.33	0.16	0.12
400	0.20	0.40	0.23	0.49	0.34	0.17	0.13
400	0.30	0.38	0.24	0.50	0.35	0.17	0.13
400	0.40	0.36	0.24	0.51	0.35	0.17	0.13
400	0.50	0.34	0.24	0.51	0.35	0.17	0.13
400	0.60	0.31	0.23	0.52	0.35	0.17	0.12
400	0.70	0.27	0.23	0.52	0.34	0.16	0.12
400	0.80	0.24	0.22	0.52	0.33	0.16	0.12
400	0.90	0.21	0.21	0.51	0.32	0.15	0.11
400	1.00	0.19	0.20	0.50	0.31	0.14	0.11

Table C.4: The 95% CL upper limits for the production cross section times the branching ratio to a $\tau\tau$ pair of a scalar particle with a mass $[200 - 500\,\text{GeV}]$ produced both via b-associated production and gluon fusion. The columns show the Higgs boson mass, $m_{H/A}$, versus the fraction of the b-associated production of the total production cross-section, f_b. The limit values are in pb and they are valid under the assumption that the width of the particle is negligible with respect to the $m_{\text{T}}^{\text{tot}}$ mass resolution [221].

		Limit		**Uncertainty**			
$m_{H/A}$ [GeV]	f_b	observed	expected	$+2\,\sigma$	$+1\,\sigma$	$-1\,\sigma$	$-2\,\sigma$
500	0.00	0.13	0.12	0.28	0.18	0.086	0.064
500	0.10	0.13	0.12	0.29	0.19	0.089	0.066
500	0.20	0.13	0.13	0.29	0.19	0.091	0.068
500	0.30	0.12	0.13	0.29	0.19	0.091	0.068
500	0.40	0.12	0.13	0.29	0.19	0.091	0.068
500	0.50	0.12	0.13	0.29	0.19	0.090	0.067
500	0.60	0.11	0.12	0.29	0.19	0.089	0.066
500	0.70	0.11	0.12	0.29	0.19	0.087	0.065
500	0.80	0.10	0.12	0.29	0.18	0.085	0.063
500	0.90	0.099	0.11	0.29	0.18	0.082	0.061
500	1.00	0.094	0.11	0.29	0.17	0.079	0.059
600	0.00	0.071	0.077	0.18	0.12	0.055	0.041
600	0.10	0.074	0.078	0.18	0.12	0.057	0.042
600	0.20	0.075	0.079	0.18	0.12	0.057	0.042
600	0.30	0.075	0.079	0.18	0.12	0.057	0.042
600	0.40	0.075	0.078	0.18	0.12	0.057	0.042
600	0.50	0.074	0.077	0.18	0.12	0.056	0.042
600	0.60	0.072	0.076	0.18	0.12	0.055	0.041
600	0.70	0.071	0.074	0.18	0.12	0.054	0.040
600	0.80	0.069	0.072	0.19	0.11	0.052	0.039
600	0.90	0.066	0.070	0.19	0.11	0.051	0.038
600	1.00	0.064	0.068	0.19	0.11	0.049	0.036
700	0.00	0.047	0.056	0.13	0.085	0.041	0.030
700	0.10	0.049	0.057	0.13	0.086	0.041	0.031
700	0.20	0.051	0.057	0.13	0.086	0.041	0.031
700	0.30	0.051	0.057	0.13	0.086	0.041	0.030
700	0.40	0.052	0.056	0.13	0.085	0.040	0.030
700	0.50	0.051	0.055	0.13	0.084	0.040	0.030
700	0.60	0.051	0.054	0.13	0.083	0.039	0.029
700	0.70	0.051	0.053	0.13	0.082	0.038	0.028
700	0.80	0.050	0.051	0.13	0.080	0.037	0.027
700	0.90	0.049	0.049	0.13	0.079	0.036	0.026
700	1.00	0.047	0.048	0.13	0.077	0.034	0.025

Table C.5: The 95% CL upper limits for the production cross section times the branching ratio to a $\tau\tau$ pair of a scalar particle with a mass $[400 - 700\,\text{GeV}]$ produced both via b-associated production and gluon fusion. The columns show the Higgs boson mass, $m_{H/A}$, versus the fraction of the b-associated production of the total production cross-section, f_b. The limit values are in pb and they are valid under the assumption that the width of the particle is negligible with respect to the $m_{\text{T}}^{\text{tot}}$ mass resolution [221].

		Limit		**Uncertainty**			
$m_{H/A}$ [GeV]	f_b	observed	expected	$+2\,\sigma$	$+1\,\sigma$	$-1\,\sigma$	$-2\,\sigma$
800	0.00	0.035	0.042	0.098	0.064	0.030	0.022
800	0.10	0.037	0.043	0.098	0.064	0.031	0.023
800	0.20	0.038	0.043	0.098	0.064	0.031	0.023
800	0.30	0.039	0.042	0.098	0.064	0.030	0.023
800	0.40	0.040	0.042	0.098	0.063	0.030	0.022
800	0.50	0.040	0.041	0.098	0.062	0.029	0.022
800	0.60	0.040	0.040	0.099	0.062	0.029	0.022
800	0.70	0.040	0.039	0.10	0.061	0.028	0.021
800	0.80	0.039	0.038	0.10	0.061	0.028	0.021
800	0.90	0.039	0.037	0.10	0.060	0.027	0.020
800	1.00	0.038	0.036	0.10	0.059	0.026	0.019
1000	0.00	0.028	0.032	0.075	0.048	0.023	0.017
1000	0.10	0.030	0.032	0.075	0.049	0.023	0.017
1000	0.20	0.031	0.032	0.075	0.049	0.023	0.017
1000	0.30	0.032	0.032	0.076	0.049	0.023	0.017
1000	0.40	0.033	0.032	0.077	0.049	0.023	0.017
1000	0.50	0.033	0.032	0.078	0.049	0.023	0.017
1000	0.60	0.033	0.032	0.079	0.049	0.023	0.017
1000	0.70	0.034	0.032	0.081	0.050	0.023	0.017
1000	0.80	0.034	0.031	0.083	0.050	0.022	0.017
1000	0.90	0.034	0.031	0.085	0.050	0.022	0.017
1000	1.00	0.034	0.030	0.087	0.049	0.022	0.016
1200	0.00	0.025	0.029	0.073	0.045	0.021	0.015
1200	0.10	0.027	0.029	0.072	0.045	0.021	0.015
1200	0.20	0.027	0.028	0.070	0.044	0.020	0.015
1200	0.30	0.028	0.028	0.069	0.043	0.020	0.015
1200	0.40	0.028	0.027	0.069	0.042	0.020	0.015
1200	0.50	0.028	0.027	0.069	0.042	0.019	0.014
1200	0.60	0.028	0.026	0.069	0.041	0.019	0.014
1200	0.70	0.028	0.025	0.069	0.041	0.018	0.014
1200	0.80	0.028	0.025	0.070	0.040	0.018	0.013
1200	0.90	0.028	0.024	0.071	0.040	0.018	0.013
1200	1.00	0.028	0.024	0.072	0.040	0.017	0.013

Table C.6: The 95% CL upper limits for the production cross section times the branching ratio to a $\tau\tau$ pair of a scalar particle with a mass [$800 - 1200$ GeV] produced both via b-associated production and gluon fusion. The columns show the Higgs boson mass, $m_{H/A}$, versus the fraction of the b-associated production of the total production cross-section, f_b. The limit values are in pb and they are valid under the assumption that the width of the particle is negligible with respect to the $m_{\mathrm{T}}^{\mathrm{tot}}$ mass resolution [221].

References

[1] Fermilab Collaboration and SLAC Collaboration
Symmetry Magazine
2015, URL:
http://www.symmetrymagazine.org/article/july-2015/standard-model
(cit. on pp. 3, 231).

[2] Michael Peskin and Daniel Schroeder
An Introduction to quantum field theory
Addison-Wesley, URL: http://www.slac.stanford.edu/~mpeskin/QFT.html
(cit. on pp. 4, 6, 8).

[3] Particle Data Group
Review of Particle Physics
Chin. Phys. C **40** (2016) 100001
(cit. on pp. 5, 7, 22, 26, 27, 30, 34–36, 45–47, 193, 254–256).

[4] Sylvie Braibant, Giorgio Giacomelli, and Maurizio Spurio
Particles and Fundamental Interactions
Springer Netherlands, 2011 (cit. on pp. 6, 20).

[5] ALEPH Collaboration et al.
Precision electroweak measurements on the Z resonance
Phys. Rep. **427** (2006) 257 (cit. on p. 7).

[6] Chen Ning Yang and Robert L. Mills
Conservation of Isotopic Spin and Isotopic Gauge Invariance
Phys. Rev. **96** (1 1954) 191 (cit. on p. 9).

[7] Enrico Fermi
Tentativo di una Teoria Dei Raggi β
Il Nuovo Cimento (1924-1942) **11** (2008) 1 (cit. on p. 12).

[8] Sin-Itiro Tomonaga
On a Relativistically Invariant Formulation of the Quantum Theory of Wave Fields
Progress of Theoretical Physics **1** (1946) 27 (cit. on p. 12).

[9] Julian Schwinger
On Quantum-Electrodynamics and the Magnetic Moment of the Electron
Phys. Rev. **73** (1948) 416 (cit. on p. 12).

[10] Julian Schwinger
Quantum Electrodynamics. I. A Covariant Formulation
Phys. Rev. **74** (1948) 1439 (cit. on p. 12).

[11] Richard P. Feynman
Space-Time Approach to Quantum Electrodynamics
Phys. Rev. **76** (1949) 769 (cit. on p. 12).

[12] Richard P. Feynman
The Theory of Positrons
Phys. Rev. **76** (1949) 749 (cit. on p. 12).

[13] Richard P. Feynman
Mathematical Formulation of the Quantum Theory of Electromagnetic Interaction
Phys. Rev. **80** (1950) 440 (cit. on p. 12).

[14] Freeman John Dyson
The Radiation Theories of Tomonaga, Schwinger, and Feynman
Phys. Rev. **75** (1949) 486 (cit. on p. 12).

[15] Julian Schwinger
A theory of the fundamental interactions
Ann. Phys. **2** (1957) 407 (cit. on p. 12).

[16] Richard P. Feynman and Murray Gell-Mann
Theory of the Fermi Interaction
Phys. Rev. **109** (1 1958) 193 (cit. on p. 12).

[17] Ennackal C. G. Sudarshan and Robert E. Marshak
Chirality Invariance and the Universal Fermi Interaction
Phys. Rev. **109** (5 1958) 1860 (cit. on p. 12).

[18] Sheldon L. Glashow
Partial-symmetries of weak interactions
Nuclear Physics **22** (1961) 579 (cit. on pp. 12, 21).

[19] Abdus Salam and John C. Ward
Electromagnetic and weak interactions
Physics Letters **13** (1964) 168 (cit. on p. 13).

[20] Jeffrey Goldstone, Abdus Salam, and Steven Weinberg
Broken Symmetries
Phys. Rev. **127** (3 1962) 965 (cit. on p. 13).

[21] Phillip W. Anderson
Plasmons, Gauge Invariance, and Mass
Phys. Rev. **130** (1 1963) 439 (cit. on p. 13).

[22] François Englert and Robert Brout
Broken Symmetry and the Mass of Gauge Vector Mesons
Phys. Rev. Lett. **13** (9 1964) 321 (cit. on p. 13).

[23] Peter W. Higgs
Broken Symmetries and the Masses of Gauge Bosons
Phys. Rev. Lett. **13** (16 1964) 508 (cit. on pp. 13, 18).

[24] Peter W. Higgs
Broken symmetries, massless particles and gauge fields
Phys. Lett. **12** (1964) 132 (cit. on p. 13).

[25] Gerald S. Guralnik, Carl R. Hagen, and Tom W. B. Kibble
Global Conservation Laws and Massless Particles
Phys. Rev. Lett. **13** (20 1964) 585 (cit. on p. 13).

[26] Frank Close
The Infinity Puzzle: Quantum Field Theory and the Hunt for an Orderly Universe
Basic Books, 2011 (cit. on p. 13).

[27] Peter W. Higgs
Spontaneous Symmetry Breakdown without Massless Bosons
Phys. Rev. **145** (4 1966) 1156 (cit. on p. 13).

[28] Tom W. B. Kibble
Symmetry Breaking in Non-Abelian Gauge Theories
Phys. Rev. **155** (5 1967) 1554 (cit. on p. 14).

[29] Steven Weinberg
A Model of Leptons
Phys. Rev. Lett. **19** (21 1967) 1264 (cit. on p. 14).

[30] Gerard 't Hooft
Renormalizable Lagrangians for massive Yang-Mills fields
Nucl. Phys. B **35** (1971) 167 (cit. on p. 14).

[31] Gerard 't Hooft and Martinus Veltman
Regularization and renormalization of gauge fields
Nucl. Phys. B **44** (1972) 189 (cit. on p. 14).

[32] Gargamelle Neutrino Collaboration
Search for elastic muon-neutrino electron scattering
Phys. Lett. B **46** (1973) 121 (cit. on pp. 14, 54).

[33] Gargamelle Neutrino Collaboration
Observation of neutrino-like interactions without muon or electron in the Gargamelle neutrino experiment
Phys. Lett. B **46** (1973) 138 (cit. on pp. 14, 54).

[34] UA1 Collaboration
Experimental observation of isolated large transverse energy electrons with associated missing energy at s=540 GeV
Phys. Lett. B **122** (1983) 103 (cit. on pp. 14, 21, 54).

[35] UA2 Collaboration
Observation of single isolated electrons of high transverse momentum in events with missing transverse energy at the CERN pp collider
Phys. Lett. B **122** (1983) 476 (cit. on pp. 14, 21, 54).

[36] UA1 Collaboration
Experimental Observation of Lepton Pairs of Invariant Mass Around 95-GeV/c^2 at the CERN SPS Collider
Phys. Lett. B **126** (1983) 398 (cit. on pp. 14, 21, 54).

[37] UA2 Collaboration
Evidence for Z0 —> e+ e- at the CERN anti-p p Collider
Phys. Lett. B **129** (1983) 130 (cit. on pp. 14, 21, 54).

[38] TEVNPH Working Group, CDF Collaboration, and DØ Collaboration
Combined CDF and DØ Upper Limits on Standard Model Higgs-Boson Production with up to 2.4 fb^{-1} of data
2008, arXiv: 0804.3423 [hep-ex],
URL: https://inspirehep.net/record/783906 (cit. on p. 14).

[39] ALEPH Collaboration et al.
Search for the Standard Model Higgs boson at LEP
Phys. Lett. B **565** (2003) 61, URL:
http://www.sciencedirect.com/science/article/pii/S0370269303006142
(cit. on p. 14).

[40] ATLAS Collaboration
Observation of a new particle in the search for the Standard Model Higgs boson with the ATLAS detector at the LHC
Phys. Lett. B **716** (2012) 1, arXiv: 1207.7214 [hep-ex]
(cit. on pp. 14, 15, 54, 122, 232).

[41] CMS Collaboration
Observation of a new boson at a mass of 125 GeV with the CMS experiment at the LHC
Phys. Lett. B **716** (2012) 30, arXiv: 1207.7235 [hep-ex]
(cit. on pp. 14, 15, 54, 232).

[42] Yorikiyo Nagashima and Yoichiro Nambu
Elementary Particle Physics: Quantum Field Theory and Particles
Wiley, 2011, 964 pp. (cit. on pp. 20, 33).

[43] Alberto Aparici
Exotic properties of neutrinos using effective Lagrangians and specific models
PhD thesis: Valencia U., 2013, arXiv: 1312.0554 [hep-ph] (cit. on p. 20).

[44] Ling-Fong Li Ta-Pei Cheng
Gauge Theory of Elementary Particle Physics
Oxford science publications, Clarendon Press, 1988, 548 pp. (cit. on p. 20).

[45] ATLAS Collaboration and CMS Collaboration
Measurements of the Higgs boson production and decay rates and constraints on its couplings from a combined ATLAS and CMS analysis of the LHC pp collision data at $\sqrt{s} = 7$ and 8 TeV
J. High Energy Phys. **08** (2016) 70,
URL: https://cds.cern.ch/record/2158863 (cit. on pp. 22, 221–226, 228).

[46] Nicola Cabibbo
Unitary Symmetry and Leptonic Decays
Phys. Rev. Lett. **10** (12 1963) 531 (cit. on p. 24).

[47] Makoto Kobayashi and Toshihide Maskawa
CP-Violation in the Renormalizable Theory of Weak Interaction
Progress of Theoretical Physics **49** (1973) 652 (cit. on p. 24).

[48] Bruno Pontecorvo
Mesonium and anti-mesonium
Sov. Phys. JETP **6** (1957) 429, Zh. Eksp. Teor. Fiz.33,549(1957),
URL: http://www.jetp.ac.ru/cgi-bin/dn/e_006_02_0429.pdf (cit. on p. 24).

[49] Ziro Maki, Masami Nakagawa, and Shoichi Sakata
Remarks on the Unified Model of Elementary Particles
Progress of Theoretical Physics **28** (1962) 870 (cit. on p. 24).

[50] SNO Collaboration
Direct Evidence for Neutrino Flavor Transformation from Neutral-Current Interactions in the Sudbury Neutrino Observatory
Phys. Rev. Lett. **89** (1 2002) 011301 (cit. on pp. 24, 27).

[51] Super-Kamiokande Collaboration
Evidence for Oscillation of Atmospheric Neutrinos
Phys. Rev. Lett. **81** (8 1998) 1562 (cit. on pp. 24, 27).

[52] Sheldon Stone
New physics from flavour
Proceedings of Science: ICHEP2012 **ICHEP2012** (2012) 033,
arXiv: 1212.6374 [hep-ph] (cit. on p. 25).

[53] Peter Minkowski
$\mu \to e\gamma$ *at a Rate of One Out of* 10^9 *Muon Decays?*
Phys. Lett. B **67** (1977) 421 (cit. on p. 27).

[54] Murray Gell-Mann, Pierre Ramond, and Richard Slansky
Complex Spinors and Unified Theories
Conf. Proc. **C790927** (2013) 315, arXiv: 1306.4669 [hep-th] (cit. on p. 27).

[55] Rabindra N. Mohapatra and Goran Senjanovic
Neutrino Mass and Spontaneous Parity Violation
Phys. Rev. Lett. **44** (1980) 912, [,231(1979)] (cit. on p. 27).

[56] Rabindra N. Mohapatra and Goran Senjanovic
Neutrino Masses and Mixings in Gauge Models with Spontaneous Parity Violation
Physical Review D **23** (1981) 165 (cit. on p. 27).

[57] Aharon Davidson and Kameshwar C. Wali
Family mass hierarchy from universal seesaw mechanism
Phys. Rev. Lett. **60** (18 1988) 1813 (cit. on p. 27).

[58] Joseph Schechter and José W.F. Valle
Neutrino Masses in SU(2) x U(1) Theories
Phys. Rev. **D22** (1980) 2227 (cit. on p. 27).

[59] Giuseppe Degrassi et al.
Higgs mass and vacuum stability in the Standard Model at NNLO
J. High Energy Phys. **08** (2012) 098, arXiv: 1205.6497 [hep-ph] (cit. on p. 29).

[60] Anders Andreassen, William Frost, and Matthew Schwartz
Scale Invariant Instantons and the Complete Lifetime of the Standard Model
2017, arXiv: 1707.08124 [hep-ph] (cit. on p. 29).

[61] Marco Fabbrichesi and Alfredo Urbano
Naturalness redux: The case of the neutrino seesaw mechanism
Phys. Rev. **92** (2015) 015028, arXiv: 1504.05403 [hep-ph] (cit. on p. 29).

[62] Yorikiyo Nagashima
Beyond the Standard Model of Elementary Particle Physics
Wiley, 2014 (cit. on pp. 30, 35, 36, 38).

[63] Michael J. Dugan, Howard Georgi, and David B. Kaplan
Anatomy of a Composite Higgs Model
Nucl. Phys. **B254** (1985) 299 (cit. on p. 31).

[64] Stephen P. Martin
A Supersymmetry Primer
[Adv. Ser. Direct. High Energy Phys.18,1(1998)], 1997,
arXiv: 9709356v [hep-ph] (cit. on pp. 31, 33, 38, 48).

[65] Glennys R. Farrar and Pierre Fayet
Phenomenology of the Production, Decay, and Detection of New Hadronic States Associated with Supersymmetry
Phys.Lett. **B76** (1978) 575 (cit. on p. 33).

[66] Pierre Fayet
Relations Between the Masses of the Superpartners of Leptons and Quarks, the Goldstino Couplings and the Neutral Currents
Phys.Lett. **B84** (1979) 416 (cit. on p. 33).

[67] Savas Dimopoulos and Howard Georgi
Softly Broken Supersymmetry and SU(5)
Nucl.Phys. **B193** (1981) 150 (cit. on p. 33).

[68] Pierre Fayet
Spontaneously Broken Supersymmetric Theories of Weak, Electromagnetic and Strong Interactions
Phys.Lett. **B69** (1977) 489 (cit. on p. 33).

[69] Pierre Fayet
Supersymmetry and Weak, Electromagnetic and Strong Interactions
Phys.Lett. **B64** (1976) 159 (cit. on p. 33).

[70] Tsung-Dao Lee
A Theory of Spontaneous T Violation
Phys. Rev. D **8** (4 1973) 1226 (cit. on p. 35).

[71] Gustavo Castello-Branco et al.
Theory and phenomenology of two-Higgs-doublet models
Phys. Rept. **516** (2011) 1, arXiv: 1106.0034 [hep-ph] (cit. on p. 35).

[72] John F Gunion et al.
The Higgs hunter's guide
Vol. 80, Brookhaven Nat. Lab., 1989,
URL: https://cds.cern.ch/record/425736 (cit. on p. 35).

[73] Vernon Barger, JoAnne L. Hewett, and Roger J. N. Phillips
New constraints on the charged Higgs sector in two-Higgs-doublet models
Phys. Rev. D **41** (11 1990) 3421 (cit. on p. 35).

[74] Emanuele Bagnaschi et al.
Benchmark scenarios for low $\tan\beta$ *in the MSSM*
Tech. rep. LHCHXSWG-2015-002, CERN, 2015,
URL: https://cds.cern.ch/record/2039911 (cit. on pp. 38, 49, 51, 52, 203).

[75] Jonathan Pumplin et al.
New generation of parton distributions with uncertainties from global QCD analysis
J. High Energy Phys. **07** (2002) 012, arXiv: hep-ph/0201195 [hep-ph]
(cit. on p. 40).

[76] Alan D. Martin et al.
Parton distributions for the LHC
Eur. Phys. J. C **63** (2009) 189, arXiv: 0901.0002 [hep-ph]
(cit. on pp. 40, 173, 204).

[77] Richard D. Ball et al.
A determination of parton distributions with faithful uncertainty estimation
Nucl. Phys. B **809** (2008) 1, [Erratum: Nucl. Phys.B816,293(2009)],
arXiv: 0808.1231 [hep-ph] (cit. on p. 40).

[78] Jonathan M. Butterworth, Guenther Dissertori, and Gavin P. Salam
Hard Processes in Proton-Proton Collisions at the Large Hadron Collider
Annu. Rev. Nucl. Part. Sci. **62** (2012) 387, arXiv: 1202.0583 [hep-ex]
(cit. on p. 40).

[79] Josh McFayden
Third generation SUSY and tt + Z production: Searches using the ATLAS detector at the CERN Large Hadron Collider
Springer Theses, Springer International Publishing, 2014, 178 pp. (cit. on p. 41).

[80] LHC Higgs Cross Section Working Group
Handbook of LHC Higgs Cross Sections: 1. Inclusive Observables
2011, arXiv: 1101.0593 [hep-ph], URL: https://cds.cern.ch/record/1318996
(cit. on pp. 42, 172).

[81] LHC Higgs Cross Section Working Group
Handbook of LHC Higgs Cross Sections: 4. Deciphering the Nature of the Higgs Sector
2016, arXiv: 1610.07922 [hep-ph], URL: http://cds.cern.ch/record/2227475 (cit. on pp. 42–46, 229).

[82] Paolo Bolzoni et al.
Vector boson fusion at NNLO in QCD: SM Higgs and beyond
Phys. Rev. D: Part. Fields **85** (2011) 035002, arXiv: 1109.3717 [hep-ph] (cit. on p. 43).

[83] LHC Higgs Cross Section Working Group
Handbook of LHC Higgs Cross Sections: 3. Higgs Properties
2013, arXiv: 1307.1347 [hep-ph], URL: https://cds.cern.ch/record/1559921 (cit. on pp. 46, 47, 49, 51, 117, 203).

[84] Marcela Carena et al.
MSSM Higgs Boson Searches at the LHC: Benchmark Scenarios after the Discovery of a Higgs-like Particle
Eur. Phys. J. **C73** (2013) 2552, arXiv: 1302.7033 [hep-ph] (cit. on p. 49).

[85] Abdelhak Djouadi et al.
The post-Higgs MSSM scenario: Habemus MSSM?
Eur. Phys. J. **C73** (2013) 2650, arXiv: 1307.5205 [hep-ph] (cit. on p. 49).

[86] Marcela Carena et al.
Suggestions for benchmark scenarios for MSSM Higgs boson searches at hadron colliders
Eur. Phys. J. C **26** (2002) 601, arXiv: hep-ph/0202167 [hep-ph] (cit. on p. 49).

[87] ATLAS Collaboration
Search for neutral Higgs bosons of the minimal supersymmetric standard model in pp collisions at $\sqrt{s}$ = 8 TeV with the ATLAS detector
J. High Energy Phys. **11** (2014) 32, arXiv: 1409.6064 [hep-ex], URL: https://cds.cern.ch/record/1756956 (cit. on pp. 50, 193, 218, 229).

[88] CMS Collaboration
Search for neutral MSSM Higgs bosons decaying to a pair of tau leptons in pp collisions
J. High Energy Phys. **10** (2014) 160, arXiv: 1408.3316 [hep-ex] (cit. on p. 50).

[89] ATLAS Collaboration
Search for charged Higgs bosons decaying via $H^{\pm} \to \tau^{\pm}\nu$ in fully hadronic final states using pp collision data at $\sqrt{s} = 8$ TeV with the ATLAS detector
JHEP03 (2015) 088 **03** (2014) 088, arXiv: 1412.6663 [hep-ex] (cit. on p. 50).

[90] CMS Collaboration
Search for charged Higgs bosons with the H+ to tau nu decay channel in the fully hadronic final state at sqrt s = 8 TeV
Tech. rep. CMS-PAS-HIG-14-020, CERN, 2014,
URL: https://cds.cern.ch/record/1950346 (cit. on p. 50).

[91] ATLAS Collaboration
BSM Higgs exclusion in the hMSSM (large m_A range)
2017, URL: https://atlas.web.cern.ch/Atlas/GROUPS/PHYSICS/CombinedSummaryPlots/HIGGS/ATLAS_HIGGS5101_BSM_hMSSM_tanb_vs_mA_Summary_LargeRange/history.html (cit. on pp. 52, 229).

[92] Wikimedia Commons
CERN Aerial Views
2012, URL: https://commons.wikimedia.org/wiki/Category:CERN_aerial_photographs#/media/File:CERN-aerial_1.jpg (visited on 2017) (cit. on p. 54).

[93] NA48 Collaboration
A new measurement of direct CP violation in two pion decays of the neutral kaon
Phys. Lett. B **465** (1999) 335 (cit. on p. 54).

[94] NA31 Collaboration
First Evidence for Direct CP Violation
Phys. Lett. B **206** (1988) 169 (cit. on p. 54).

[95] NA31 Collaboration
A new measurement of direct CP violation in the neutral kaon system
Phys. Lett. B **317** (1993) 233 (cit. on p. 54).

[96] Jean-Luc Caron
Aerial view of CERN with the LHC sites.. Vue aérienne du CERN avec implantation des sites LHC.
AC Collection. Legacy of AC. Pictures from 1992 to 2002.,
URL: https://cds.cern.ch/record/841513 (cit. on p. 55).

[97] Oliver Sim Brüning et al.
LHC Design Report V1
CERN, 2004, URL: https://cds.cern.ch/record/782076 (cit. on p. 55).

[98] Oliver Sim Brüning et al.
LHC Design Report V2
CERN, 2004, URL: https://cds.cern.ch/record/815187 (cit. on p. 55).

[99] Michael Benedikt et al.
LHC Design Report V3
CERN, 2004, URL: https://cds.cern.ch/record/823808 (cit. on p. 55).

[100] Lyndon Evans and Philip Bryant
LHC Machine
Vol. 3, 08, IOP Publishing, 2008, URL: https://cds.cern.ch/record/1129806 (cit. on pp. 55–57).

[101] Giorgio Apollinari et al.
High-Luminosity Large Hadron Collider (HL-LHC): Preliminary Design Report
CERN, 2015, URL: https://cds.cern.ch/record/2116337
(cit. on pp. 56, 58, 87).

[102] HL-LHC Collaboration
The HL-LHC Project
1999, URL: http://hilumilhc.web.cern.ch%a (visited on 02/22/2016)
(cit. on pp. 58, 234).

[103] Reyes Alemany-Fernandez et al.
Operation and Configuration of the LHC in Run 1
Tech. rep., CERN, 2013, URL: https://cds.cern.ch/record/1631030
(cit. on p. 59).

[104] *Operation of the LHC with Protons at High Luminosity and High Energy*
CERN-ACC-2016-229, 2016, URL: https://cds.cern.ch/record/2207396
(cit. on p. 59).

[105] Florent Fayette
Strategies for precision measurements of the charge asymmetry of the W boson mass at the LHC within the ATLAS experiment
PhD thesis: Paris U., VI-VII, 2009, arXiv: 0906.4260 [hep-ex],
URL: http://inspirehep.net/record/823897/files/arXiv:0906.4260.pdf
(cit. on pp. 59, 234).

[106] LHC Machine Outreach
Relative beam sizes around interaction point 1 (ATLAS) in collision
2008, URL: https://lhc-machine-outreach.web.cern.ch/lhc-machine-outreach/collisions.htm (cit. on p. 60).

[107] Marta Bajko et al.
Report of the Task Force on the Incident of 19th September 2008 at the LHC
Tech. rep. LHC-PROJECT-Report-1168. CERN-LHC-PROJECT-Report-1168,
CERN, 2009, URL: http://cds.cern.ch/record/1168025 (cit. on p. 60).

[108] ATLAS Collaboration
ATLAS Luminosity Public Results Run2
2016, URL: https://twiki.cern.ch/twiki/bin/view/AtlasPublic/LuminosityPublicResultsRun2 (cit. on p. 62).

[109] Timothy J Berners-Lee
Information management: a proposal
Tech. rep. CERN-DD-89-001-OC, CERN, 1989,
URL: https://cds.cern.ch/record/369245 (cit. on p. 63).

[110] The Worldwide LHC Computing Grid
WLCG-TiersJun14
2016, URL: https://espace.cern.ch/WLCG-document-repository/images1/WLCG/WLCG-TiersJun14_v9.png (visited on 2014)
(cit. on p. 64).

[111] Jean-Luc Caron
ATLAS detector in A4 format with English captions
URL: https://cds.cern.ch/record/841458 (cit. on p. 65).

[112] ATLAS Collaboration
The ATLAS Experiment at the CERN Large Hadron Collider
Journal of Instrumentation **3** (2008),
URL: http://stacks.iop.org/1748-0221/3/i=08/a=S08003
(cit. on pp. 64, 66, 67, 69, 70, 73, 74, 76, 78–80, 106).

[113] Joao Pequenao and Paul Schaffner
An computer generated image representing how ATLAS detects particles
2013, URL: https://cds.cern.ch/record/1505342 (cit. on p. 66).

[114] Maria Del Mar Capeans Garrido et al.
ATLAS Insertable B-Layer Technical Design Report
Tech. rep. CERN-LHCC-2010-013. ATLAS-TDR-19, CERN, 2010,
URL: https://cds.cern.ch/record/1291633 (cit. on pp. 67–69).

[115] Joao Pequenao
Computer generated image of the ATLAS Liquid Argon
2008, URL: https://cds.cern.ch/record/1095928 (cit. on p. 71).

[116] ATLAS Collaboration
ATLAS tile calorimeter: Technical Design Report
Technical Design Report ATLAS, CERN, 1996,
URL: https://cds.cern.ch/record/331062 (cit. on p. 71).

[117] Hannah Herde and ATLAS Collaboration
Muon reconstruction performance in ATLAS at Run-II
Tech. rep. ATL-PHYS-PROC-2015-121, CERN,
URL: https://cds.cern.ch/record/2059849 (cit. on p. 77).

[118] ATLAS Outreach
ATLAS Fact Sheet : To raise awareness of the ATLAS detector and collaboration on the LHC
2010, URL: https://cds.cern.ch/record/1457044 (cit. on p. 77).

[119] ATLAS Collaboration
ATLAS Phase-II Upgrade Scoping Document
Tech. rep. CERN-LHCC-2015-020. LHCC-G-166, CERN, 2015,
URL: https://cds.cern.ch/record/2055248 (cit. on p. 78).

[120] Peter Jenni et al.
ATLAS high-level trigger, data-acquisition and controls: Technical Design Report
Technical Design Report ATLAS, CERN, 2003,
URL: https://cds.cern.ch/record/616089 (cit. on p. 78).

[121] ATLAS Collaboration
Data Quality Information for Data
2017, URL: https://twiki.cern.ch/twiki/bin/view/AtlasPublic/RunStatsPublicResults2010 (cit. on p. 83).

[122] José Alberto Valero Biot
The Back-End Electronics for the ATLAS Hadronic Tile Calorimeter at the Large Hadron Collider
PhD thesis: Valencia U., IFIC, 2014,
URL: http://roderic.uv.es/handle/10550/40316 (cit. on pp. 85–87).

[123] ATLAS Collaboration
Expected pileup values at the HL-LHC
Tech. rep. ATL-UPGRADE-PUB-2013-014, CERN, 2013,
URL: https://cds.cern.ch/record/1604492 (cit. on p. 87).

[124] Esteban Fullana et al.
Optimal Filtering in the ATLAS Hadronic Tile Calorimeter
Tech. rep., CERN, 2005, URL: http://cds.cern.ch/record/816152 (cit. on p. 87).

[125] Giulio Usai
Signal Reconstruction of the ATLAS Hadronic Tile Calorimeter: implementation and performance
Journal of Physics: Conference Series **293** (2011) (cit. on p. 87).

[126] GEANT4 Collaboration
GEANT4 - a simulation toolkit
Nucl. Instrum. Methods Phys. Res., Sect. A **506** (2003) 250,
URL: http://cds.cern.ch/record/602040 (cit. on pp. 98, 204).

[127] ATLAS Collaboration
Performance of the ATLAS Inner Detector Track and Vertex Reconstruction in the High Pile-Up LHC Environment
Tech. rep. ATLAS-CONF-2012-042, CERN, 2012,
URL: https://cds.cern.ch/record/1435196 (cit. on p. 103).

[128] Thijs Cornelissen et al.
Concepts, Design and Implementation of the ATLAS New Tracking (NEWT)
Tech. rep. ATL-SOFT-PUB-2007-007. ATL-COM-SOFT-2007-002, CERN, 2007,
URL: https://cds.cern.ch/record/1020106 (cit. on p. 103).

[129] ATLAS Collaboration
Performance of primary vertex reconstruction in proton-proton collisions at $\sqrt{s}$ =7 TeV in the ATLAS experiment
Tech. rep. ATLAS-CONF-2010-069, CERN, 2010,
URL: https://cds.cern.ch/record/1281344 (cit. on p. 104).

[130] ATLAS Collaboration
Expected Performance of the ATLAS Experiment - Detector, Trigger and Physics
2008, arXiv: 0901.0512 [hep-ex], URL: https://cds.cern.ch/record/1125884 (cit. on pp. 104–107, 114).

[131] ATLAS Collaboration
Electron reconstruction and identification efficiency measurements with the ATLAS detector using the 2011 LHC proton-proton collision data.
Eur. Phys. J. C **74** (2014) 74. 38 p, URL: http://cds.cern.ch/record/1694142 (cit. on p. 105).

[132] Samira Hassani et al.
A muon identification and combined reconstruction procedure for the ATLAS detector at the LHC using the (MUONBOY, STACO, MuTag) reconstruction packages
Nucl. Instrum. Methods Phys. Res., Sect. A **572** (2007) 77 (cit. on p. 105).

[133] Theodota Lagouri et al.
A Muon Identification and Combined Reconstruction Procedure for the ATLAS Detector at the LHC at CERN
IEEE Transactions on Nuclear Science **51** (2003) 3030, revised version number 1

submitted on 2003-10-30 18:34:15, URL: https://cds.cern.ch/record/681410 (cit. on p. 105).

[134] David Adams et al.
Track reconstruction in the ATLAS Muon Spectrometer with MOORE 007
Tech. rep. ATL-SOFT-2003-007,
revised version number 1 submitted on 2003-10-13 13:51:39: CERN, 2003,
URL: http://cds.cern.ch/record/685500 (cit. on p. 105).

[135] Shlomit Tarem et al.
MuGirl – Muon identification in the ATLAS detector from the inside out
2006 IEEE Nuclear Science Symposium Conference Record, vol. 1, IEEE, 2006 617 (cit. on p. 105).

[136] Jovan Mitrevski and ATLAS Colalboration
Preparing ATLAS reconstruction software for LHC's Run 2
Tech. rep. ATL-SOFT-PROC-2015-028. 7, CERN,
URL: http://cds.cern.ch/record/2016146 (cit. on p. 106).

[137] Despoina Sampsonidou and ATLAS Collaboration
Precise determination of the muon reconstruction efficiency in ATLAS at Run-II
Tech. rep. ATL-MUON-PROC-2016-013, CERN,
URL: https://cds.cern.ch/record/2238623 (cit. on p. 106).

[138] Matteo Cacciari, Gavin P Salam, and Gregory Soyez
The Anti-k(t) jet clustering algorithm
J. High Energy Phys. **04** (2008) 063, arXiv: 0802.1189 [hep-ph] (cit. on p. 106).

[139] Ariel Schwartzman
Jet energy calibration at the LHC
Int. J. Mod. Phys. A **30** (2015), arXiv: 1509.05459 [hep-ex],
URL: https://cds.cern.ch/record/2053870 (cit. on p. 106).

[140] ATLAS Collaboration
Pile-up subtraction and suppression for jets in ATLAS
Tech. rep. ATLAS-CONF-2013-083, CERN, 2013,
URL: https://cds.cern.ch/record/1570994 (cit. on p. 107).

[141] ATLAS Collaboration
Tagging and suppression of pileup jets with the ATLAS detector
Tech. rep. ATLAS-CONF-2014-018, CERN,
URL: https://cds.cern.ch/record/1700870 (cit. on p. 107).

[142] ATLAS Collaboration
Commissioning of the ATLAS high-performance b-tagging algorithms in the 7 TeV collision data
Tech. rep. ATLAS-CONF-2011-102, CERN, 2011,
URL: https://cds.cern.ch/record/1369219 (cit. on pp. 107, 174).

[143] ATLAS Collaboration
Calibration of the performance of b-tagging for c and light-flavour jets in the 2012 ATLAS data
Tech. rep. ATLAS-CONF-2014-046, CERN, 2014,
URL: http://cds.cern.ch/record/1741020 (cit. on pp. 107, 108, 174).

[144] ATLAS Collaboration
Calibration of b-tagging using dileptonic top pair events in a combinatorial likelihood approach with the ATLAS experiment
Tech. rep. ATLAS-CONF-2014-004, CERN, 2014,
URL: http://cds.cern.ch/record/1664335 (cit. on pp. 107, 108, 174).

[145] ATLAS Collaboration
Expected performance of the ATLAS b-tagging algorithms in Run-2
Tech. rep. ATL-PHYS-PUB-2015-022, CERN, 2015,
URL: https://cds.cern.ch/record/2037697 (cit. on p. 108).

[146] ATLAS Collaboration
Identification and energy calibration of hadronically decaying tau leptons with the ATLAS experiment in pp collisions at $\sqrt{s}$=8 TeV
Eur. Phys. J. C **75** (2014) 303, arXiv: 1412.7086 [hep-ex] (cit. on pp. 108, 174).

[147] ATLAS Collaboration
Reconstruction, Energy Calibration, and Identification of Hadronically Decaying Tau Leptons in the ATLAS Experiment for Run-2 of the LHC
Tech. rep. ATL-PHYS-PUB-2015-045, CERN,
URL: https://cds.cern.ch/record/2064383 (cit. on p. 109).

[148] ATLAS Collaboration
Performance of missing transverse momentum reconstruction in proton-proton collisions at $\sqrt{s} = 7\,\text{TeV}$ with ATLAS
Eur. Phys. J. C **72** (2011), arXiv: 1108.5602 [hep-ex] (cit. on p. 110).

[149] ATLAS Collaboration
Performance of algorithms that reconstruct missing transverse momentum in $\sqrt{s}$= 8 TeV proton–proton collisions in the ATLAS detector.
Eur. Phys. J. C **77** () 241. 68 p, URL: https://cds.cern.ch/record/2220441 (cit. on p. 110).

[150] ATLAS Collaboration
Performance of missing transverse momentum reconstruction with the ATLAS detector using proton-proton collisions at $\sqrt{s}$ = 13 TeV
Tech. rep. CERN-EP-2017-274, CERN,
URL: https://cds.cern.ch/record/2305380 (cit. on p. 110).

[151] ATLAS Collaboration
Search for the Standard Model Higgs boson in the $H \to \tau^+\tau^-$ decay mode in $\sqrt{s}$ = 7 TeV pp collisions with ATLAS
J. High Energy Phys. **09** (2012) 52, arXiv: 1206.5971 [hep-ex],
URL: https://cds.cern.ch/record/1458053 (cit. on pp. 111, 169).

[152] ATLAS Collaboration
Search for the Standard Model Higgs boson in $H \to \tau^+\tau^-$ decays in proton-proton collisions with the ATLAS detector
Tech. rep. ATLAS-CONF-2012-160, CERN, 2012,
URL: https://cds.cern.ch/record/1493624 (cit. on pp. 111, 112).

[153] ATLAS Collaboration
Evidence for Higgs Boson Decays to the $\tau^+\tau^-$ Final State with the ATLAS Detector
Tech. rep. ATLAS-CONF-2013-108, CERN, 2013,
URL: https://cds.cern.ch/record/1632191 (cit. on p. 111).

[154] ATLAS Collaboration
Evidence for Higgs boson Yukawa couplings in the $H \to \tau\tau$ decay mode with the ATLAS detector
Tech. rep. ATLAS-CONF-2014-061, CERN, 2014,
URL: https://cds.cern.ch/record/1954724 (cit. on p. 111).

[155] ATLAS Collaboration
Evidence for the Higgs-boson Yukawa coupling to tau leptons with the ATLAS detector
J. High Energy Phys. **04** (2015) 117, arXiv: 1501.04943 [hep-ex]
(cit. on pp. 111, 119, 120, 166–169, 180, 182, 184, 186–188, 190–192, 221, 237, 240, 258–262).

[156] Andrey Elagin et al.
A New Mass Reconstruction Technique for Resonances Decaying to di-tau
Nucl. Instrum. Methods Phys. Res., Sect. A **654** (2010) 481,
arXiv: 1012.4686 [hep-ex] (cit. on pp. 114, 115, 196, 197, 238).

[157] Richard Keith Ellis et al.
Higgs decay to $\tau^+\tau^-$ A possible signature of intermediate mass Higgs bosons at high energy hadron colliders
Nuclear Physics B **297** (1988) 221 (cit. on pp. 114, 238).

[158] ATLAS Collaboration
ATLAS detector and physics performance: Technical Design Report
Technical Design Report ATLAS, CERN, 1999,
URL: https://cds.cern.ch/record/391176 (cit. on p. 114).

[159] Paolo Nason
A new method for combining NLO QCD with shower Monte Carlo algorithms
J. High Energy Phys. **11** (2004) 040, arXiv: hep-ph/0409146
(cit. on pp. 117, 202).

[160] Stefano Frixione, Paolo Nason, and Carlo Oleari
Matching NLO QCD computations with parton shower simulations: the POWHEG *method*
J. High Energy Phys. **11** (2007) 070, arXiv: 0709.2092 [hep-ph]
(cit. on pp. 117, 202).

[161] Simone Alioli et al.
A general framework for implementing NLO calculations in shower Monte Carlo programs: the POWHEG *BOX*
J. High Energy Phys. **06** (2010) 043, arXiv: 1002.2581 [hep-ph]
(cit. on pp. 117, 202).

[162] Emmanuele Bagnaschi et al.
Higgs production via gluon fusion in the POWHEG approach in the SM and in the MSSM
J. High Energy Phys. **02** (2011) 088, arXiv: 1111.2854 [hep-ph] (cit. on p. 117).

[163] Abdelhak Djouadi, Michael Spira, and Peter Michael Zerwas
Production of Higgs bosons in proton colliders: QCD corrections
Phys. Lett. B **264** (1991) 440 (cit. on p. 117).

[164] Sally Dawson
Radiative corrections to Higgs boson production
Nucl. Phys. B **359** (1991) 283 (cit. on p. 117).

[165] Michael Spira et al.
Higgs boson production at the LHC
Nucl. Phys. B **453** (1995) 17, arXiv: 9504378 [hep-ph],
URL: https://cds.cern.ch/record/280777 (cit. on pp. 117, 202).

[166] Robert V. Harlander and William B. Kilgore
Next-to-next-to-leading order Higgs production at hadron colliders
Phys. Rev. Lett. **88** (2002) 201801, arXiv: hep-ph/0201206 [hep-ph]
(cit. on pp. 117, 202).

[167] Charalampos Anastasiou and Kirill Melnikov
Higgs boson production at hadron colliders in NNLO QCD
Nucl. Phys. B **646** (2002) 220, arXiv: hep-ph/0207004 [hep-ph]
(cit. on pp. 117, 202, 203).

[168] Vajravelo. Ravindran, John Smith, and Wilhelmus L. van Neerven
NNLO corrections to the total cross-section for Higgs boson production in hadron hadron collisions
Nucl. Phys. B **665** (2003) 325, arXiv: hep-ph/0302135 [hep-ph]
(cit. on pp. 117, 202).

[169] Torbjörn Sjöstrand, Stephen Mrenna, and Peter Skands
A Brief Introduction to PYTHIA 8.1
Comput. Phys. Commun. **178** (2007) 852, arXiv: 0710.3820 [hep-ph]
(cit. on pp. 117, 204).

[170] Mariano Ciccolini, Ansgar Denner, and Stefan Dittmaier
Strong and electroweak corrections to the production of Higgs + 2-jets via weak interactions at the LHC
Phys. Rev. Lett. **99** (2007) 161803, arXiv: 0707.0381 [hep-ph] (cit. on p. 117).

[171] Mariano Ciccolini, Ansgar Denner, and Stefan Dittmaier
Electroweak and QCD corrections to Higgs production via vector-boson fusion at the LHC
Phys. Rev. D: Part. Fields **77** (2007) 013002, arXiv: 0710.4749 [hep-ph]
(cit. on p. 117).

[172] Ken Arnold et al.
VBFNLO: A parton level Monte Carlo for processes with electroweak bosons
Comput. Phys. Commun. **180** (2008) 1661, arXiv: 0811.4559 [hep-ph]
(cit. on p. 117).

[173] Oliver Brein, Abdelhak Djouadi, and Robert Harlander
NNLO QCD corrections to the Higgs-strahlung processes at hadron colliders
Phys. Lett. B **579** (2003) 149, arXiv: hep-ph/0307206 [hep-ph] (cit. on p. 117).

[174] Daniel de Florian et al.
Higgs boson production at the LHC: transverse momentum resummation effects in the $H \to 2\gamma, H \to WW \to \ell\nu\ell\nu$ and $H \to ZZ \to 4\ell$ decay modes
J. High Energy Phys. **06** (2012) 132, arXiv: 1203.6321 [hep-ph] (cit. on p. 117).

[175] Massimiliano Grazzini and Hayk Sargsyan
Heavy-quark mass effects in Higgs boson production at the LHC
J. High Energy Phys. **09** (2013) 129, arXiv: 1306.4581 [hep-ph] (cit. on p. 117).

[176] John M. Campbell et al.
NLO Higgs Boson Production Plus One and Two Jets Using the POWHEG BOX, MadGraph4 and MCFM
J. High Energy Phys. **07** (2012) 092, arXiv: 1202.5475 [hep-ph] (cit. on p. 117).

[177] Andrea Banfi et al.
Higgs and Z-boson production with a jet veto
Phys. Rev. Lett. **109** (2012) 202001, arXiv: 1206.4998 [hep-ph] (cit. on p. 117).

[178] Andrea Banfi, Gavin P. Salam, and Giulia Zanderighi
NLL+NNLO predictions for jet-veto efficiencies in Higgs-boson and Drell-Yan production
J. High rgy Phys. **06** (2012) 159, arXiv: 1203.5773 [hep-ph] (cit. on p. 117).

[179] Andrea Banfi, Pier Francesco Monni, and Giulia Zanderighi
Quark masses in Higgs production with a jet veto
J. High Energy Phys. **01** (2013) 097, arXiv: 1308.4634 [hep-ph] (cit. on p. 117).

[180] Michelangelo L. Mangano et al.
ALPGEN*, a generator for hard multiparton processes in hadronic collisions*
J. High Energy Phys. **07** (2002) 001, arXiv: hep-ph/0206293 (cit. on p. 118).

[181] Stefano Catani et al.
Vector boson production at hadron colliders: A fully exclusive QCD calculation at next-to-next-to-leading order
Phys. Rev. Lett. **103** (8 2009) 082001, arXiv: 0903.2120 [hep-ph]
(cit. on p. 118).

[182] Stefano Catani and Massimiliano Grazzini
Next-to-next-to-leading-order subtraction formalism in hadron collisions and its application to Higgs-boson production at the Large Hadron Collider
Phys. Rev. Lett. **98** (22 2007) 222002 (cit. on p. 118).

[183] Gennaro Corcella et al.
HERWIG 6.5 Release Note. HERWIG 6.5
Tech. rep. CAVENDISH-HEP-2002-17. CERN-TH-2002-270. DAMTP-2002-124. IPPP-2002-58, CERN, 2002, arXiv: hep-ph/0210213,
URL: http://cds.cern.ch/record/586836 (cit. on p. 118).

[184] Tanju Gleisberg et al.
Event generation with SHERPA 1.1
J. High Energy Phys. **02** (2008) 007, arXiv: 0811.4622 [hep-ph]
(cit. on pp. 118, 203).

[185] Matteo Cacciari et al.
Top-pair production at hadron colliders with next-to-next-to-leading logarithmic soft-gluon resummation
Phys. Lett. B **710** (2011) 612, arXiv: 1111.5869 [hep-ph] (cit. on p. 118).

[186] Peter Bärnreuther, Michal Czakon, and Alexander Mitov
Percent Level Precision Physics at the Tevatron: First Genuine NNLO QCD Corrections to $q\bar{q} \to t\bar{t} + X$
Phys. Rev. Lett. **109** (2012) 132001, arXiv: 1204.5201 [hep-ph] (cit. on p. 118).

[187] Michal Czakon and Alexander Mitov
NNLO corrections to top-pair production at hadron colliders: the all-fermionic scattering channels
J. High Energy Phys. **12** (2012) 054, arXiv: 1207.0236 [hep-ph] (cit. on p. 118).

[188] Michal Czakon and Alexander Mitov
NNLO corrections to top pair production at hadron colliders: the quark-gluon reaction
J. High Energy Phys. **01** (2012) 080, arXiv: 1210.6832 [hep-ph] (cit. on p. 118).

[189] Michał Czakon, Paul Fiedler, and Alexander Mitov
The total top quark pair production cross-section at hadron colliders through $\mathcal{O}(\alpha_S^4)$
Phys. Rev. Lett. **110** (2013) 252004, arXiv: 1303.6254 [hep-ph] (cit. on p. 118).

[190] Michal Czakon and Alexander Mitov
Top++: A Program for the Calculation of the Top-Pair Cross-Section at Hadron Colliders
Comput. Phys. Commun. **185** (2011) 2930, arXiv: 1112.5675 [hep-ph]
(cit. on pp. 118, 203).

[191] Nikolaos Kidonakis
Two-loop soft anomalous dimensions for single top quark associated production with a W^- or H^-
Phys. Rev. D: Part. Fields **82** (5 2010) 054018, arXiv: 1005.4451 [hep-ph]
(cit. on pp. 118, 203).

[192] Nikolaos Kidonakis
Next-to-next-to-leading logarithm resummation for s-channel single top quark production

Phys. Rev. D: Part. Fields **81** (5 2010) 054028, arXiv: 1001.5034 [hep-ph] (cit. on pp. 118, 203).

[193] Borut Paul Kersevan and Elzbieta Richter-Was
The Monte Carlo event generator AcerMC versions 2.0 to 3.8 with interfaces to PYTHIA 6.4, HERWIG 6.5 and ARIADNE 4.1
Comput. Phys. Commun. **184** (2004) 919, arXiv: hep-ph/0405247 [hep-ph] (cit. on p. 118).

[194] Torbjörn Sjöstrand, Stephen Mrenna, and Peter Skands
PYTHIA 6.4 Physics and Manual
J. High Energy Phys. **05** (2006) 026, arXiv: hep-ph/0603175 (cit. on pp. 118, 203, 204).

[195] Nikolaos Kidonakis
Next-to-next-to-leading-order collinear and soft gluon corrections for t-channel single top quark production
Phys. Rev. D: Part. Fields **83** (9 2011) 091503, arXiv: 1103.2792 [hep-ph] (cit. on pp. 118, 203).

[196] John M. Campbell, R. Keith Ellis, and Ciaran Williams
Vector boson pair production at the LHC
J. High Energy Phys. **07** (2011) 018, arXiv: 1105.0020 [hep-ph] (cit. on pp. 118, 172).

[197] Thomas Binoth et al.
Gluon-induced W-boson pair production at the LHC
J. High Energy Phys. **12** (2006) 046, arXiv: hep-ph/0611170 (cit. on p. 118).

[198] ATLAS Collaboration
Modelling $Z \to \tau\tau$ processes in ATLAS with τ-embedded $Z \to \mu\mu$ data
J. Instrum. **10** (2015), arXiv: 1506.05623 [hep-ex], URL: http://cds.cern.ch/record/2026125 (cit. on pp. 119, 120, 239).

[199] Stanislaw Jadach et al.
The τ decay library TAUOLA, version 2.4
Comput. Phys. Commun. **76** (1993) 361 (cit. on p. 119).

[200] Zbigniew Was
TAUOLA the library for tau lepton decay, and KKMC/KORALB/KORALZ/... status report
Nucl. Phys. B Proc. Suppl. **98** (2000) 96, arXiv: hep-ph/0011305 (cit. on p. 119).

[201] Leo Breiman et al.
Classification and Regression Trees
Chapman & Hall, New York, 1984, 368 pp. (cit. on p. 140).

[202] Yoav Freund and Robert E. Schapire
Experiments with a New Boosting Algorithm
Machine Learning: Proceedings of the Thirteenth International Conference on Machine Learning (ICML 1996), ed. by Lorenza Saitta, Morgan Kaufmann, 1996 148 (cit. on pp. 140, 141).

[203] Andreas Höcker et al.
TMVA - Toolkit for Multivariate Data Analysis with ROOT: Users guide
Tech. rep. CERN-OPEN-2007-007, CERN, 2007,
arXiv: physics/0703039 [physics.data-an],
URL: http://cds.cern.ch/record/1019880 (cit. on pp. 140, 142, 154, 156).

[204] Corrado Gini
Variabilita e mutabilita
Memorie di metodologia statistica, I: Variabilita e concentrazione (1912) 189 (cit. on p. 140).

[205] Michael Kearns and Leslie G. Valiant
Crytographic Limitations on Learning Boolean Formulae and Finite Automata
STOC '89, ACM, 1989 433 (cit. on p. 141).

[206] Jerome H. Friedman
Stochastic Gradient Boosting
Computational Statistics & Data Analysis **38** (1999) 367, URL:
http://www.sciencedirect.com/science/article/pii/S0167947301000652
(cit. on p. 141).

[207] Rene Brun and Fons Rademakers
ROOT - An Object Oriented Data Analysis Framework
AIHENP'96 Workshop, Lausane, vol. 389, 1-2, Elsevier BV, 1996 81
(cit. on p. 142).

[208] Gail Hanson et al.
Evidence for Jet Structure in Hadron Production by e^+e^- Annihilation
Phys. Rev. Lett. **35** (1975) 1609 (cit. on p. 146).

[209] Stefano Frixione and Bryan R Webber
Matching NLO QCD computations and parton shower simulations
J. High Energy Phys. **06** (2002) 029, arXiv: hep-ph/0204244 (cit. on p. 173).

[210] Richard D. Ball et al.
Impact of heavy quark masses on parton distributions and LHC phenomenology
Nucl. Phys. B **849** (2011) 296, arXiv: 1101.1300 [hep-ph] (cit. on p. 173).

[211] ATLAS Collaboration
Improved luminosity determination in pp collisions at $\sqrt{s} = 7$ TeV using the ATLAS detector at the LHC
Eur. Phys. J. C **73** (2013) 2518, arXiv: 1302.4393 [hep-ex] (cit. on p. 173).

[212] ATLAS Collaboration
Determination of the tau energy scale and the associated systematic uncertainty in proton-proton collisions at $\sqrt{s} = 8$ TeV with the ATLAS detector at the LHC in 2012
Tech. rep. ATLAS-CONF-2013-044, CERN, 2013,
URL: https://cds.cern.ch/record/1544036 (cit. on p. 174).

[213] ATLAS Collaboration
Jet energy resolution in proton-proton collisions at $\sqrt{s} = 7$ TeV recorded in 2010 with the ATLAS detector
Eur. Phys. J. C **73** (2012) 2306, arXiv: 1210.6210 [hep-ex] (cit. on p. 174).

[214] Glen Cowan et al.
Asymptotic formulae for likelihood-based tests of new physics
Eur. Phys. J. C **71** (2010) 1, arXiv: 1007.1727 [physics.data-an]
(cit. on pp. 177, 179, 200, 217).

[215] Jerome H. Friedman
Data analysis techniques for high energy particle physics
Proceedings of 3rd CERN School on Computing, 1974 (cit. on p. 178).

[216] ATLAS Collaboration
Measurement of the Higgs boson mass from the $H \to \gamma\gamma$ and $H \to ZZ^* \to 4\ell$ channels with the ATLAS detector using 25 fb^{-1} of pp collision data
Phys. Rev. D: Part. Fields **90** (2014) 052004, arXiv: 1406.3827 [hep-ex],
URL: http://cds.cern.ch/record/1709081 (cit. on p. 181).

[217] LHC Higgs Cross Section Working Group
LHC HXSWG interim recommendations to explore the coupling structure of a Higgs-like particle
Tech. rep., CERN, 2012, arXiv: 1209.0040 [hep-ph],
URL: http://cds.cern.ch/record/1475887 (cit. on p. 184).

[218] Bradley Efron and Charles Stein
The Jackknife Estimate of Variance
The Annals of Statistics **9** (1981) 586,
URL: http://www.jstor.org/stable/2240822 (cit. on p. 189).

[219] Gerhard Bohm and Guenter Zech
Introduction to statistics and data analysis for physicists
2014 (cit. on p. 189).

[220] ATLAS Collaboration
Search for Neutral Minimal Supersymmetric Standard Model Higgs Bosons $H/A \to \tau\tau$ produced in pp collisions at $\sqrt{s} = 13$ TeV with the ATLAS Detector
Tech. rep. ATLAS-CONF-2015-061, CERN, 2015,
URL: https://cds.cern.ch/record/2114827 (cit. on p. 193).

[221] ATLAS Collaboration
Search for Minimal Supersymmetric Standard Model Higgs bosons H/A and for a Z' boson in the $\tau\tau$ final state produced in pp collisions at $\sqrt{s} = 13$ TeV with the ATLAS Detector
Eur. Phys. J. C **76** (2016) 28, arXiv: 1608.00890 [hep-ex],
URL: https://cds.cern.ch/record/2203593
(cit. on pp. 193, 226, 227, 229, 248, 265–269).

[222] Johan Alwall et al.
The automated computation of tree-level and next-to-leading order differential cross sections, and their matching to parton shower simulations
J. High Energy Phys. **07** (2014) 079, arXiv: 1405.0301 [hep-ph] (cit. on p. 202).

[223] M. Wiesemann et al.
Higgs production in association with bottom quarks
J. High Energy Phys. **02** (2014) 132, arXiv: 1409.5301 [hep-ph] (cit. on p. 202).

[224] Hung-Liang Lai et al.
New parton distributions for collider physics
Phys. Rev. D: Part. Fields **82** (2010) 074024, arXiv: 1007.2241 [hep-ph]
(cit. on p. 202).

[225] Sayipjamal Dulat et al.
New parton distribution functions from a global analysis of quantum chromodynamics
Phys. Rev. D: Part. Fields **93** (2015) 033006, arXiv: 1506.07443 [hep-ph]
(cit. on p. 202).

[226] Torbjörn Sjöstrand et al.
An Introduction to PYTHIA 8.2
Comput. Phys. Commun. **191** (2014) 159, arXiv: 1410.3012 [hep-ph]
(cit. on p. 202).

[227] ATLAS Collaboration
Measurement of the Z/γ^* boson transverse momentum distribution in pp collisions at $\sqrt{s} = 7$ TeV with the ATLAS detector
J. High Energy Phys. **09** (2014) 55, arXiv: 1406.3660 [hep-ex] (cit. on p. 202).

[228] ATLAS Collaboration
ATLAS Run 1 Pythia8 tunes
Tech. rep., CERN, 2014, URL: http://cdsweb.cern.ch/record/1966419 (cit. on p. 202).

[229] Robert V. Harlander, Stefan Liebler, and Hendrik Mantler
SusHi: A program for the calculation of Higgs production in gluon fusion and bottom-quark annihilation in the Standard Model and the MSSM
Comput. Phys. Commun. **184** (2012) 1605, arXiv: 1212.3249 [hep-ph] (cit. on p. 202).

[230] Robert V Harlander and William B Kilgore
Production of a pseudoscalar Higgs boson at hadron colliders at next-to-next-to leading order
J. High Energy Phys. **10** (2002) 017, arXiv: hep-ph/0208096 (cit. on p. 202).

[231] Charalampos Anastasiou and Kirill Melnikov
Pseudoscalar Higgs boson production at hadron colliders in NNLO QCD
Phys. Rev. D: Part. Fields **67** (2002) 037501, arXiv: hep-ph/0208115 (cit. on p. 202).

[232] Ugo Aglietti et al.
Two loop light fermion contribution to Higgs production and decays
Phys. Lett. B **595** (2004) 432, arXiv: hep-ph/0404071 (cit. on p. 202).

[233] Roberto Bonciani, Giuseppe Degrassi, and Alessandro Vicini
On the Generalized Harmonic Polylogarithms of One Complex Variable
Comput. Phys. Commun. **182** (2010) 1253, arXiv: 1007.1891 [hep-ph] (cit. on p. 202).

[234] Robert V. Harlander and Matthias Steinhauser
Supersymmetric Higgs production in gluon fusion at next-to-leading order
J. High Energy Phys. **09** (2004) 066, arXiv: hep-ph/0409010 (cit. on p. 202).

[235] Robert V Harlander and Philipp Kant
Higgs production and decay: Analytic results at next-to-leading order QCD
J. High Energy Phys. **12** (2005) 015, arXiv: hep-ph/0509189 (cit. on p. 202).

[236] Giuseppe Degrassi and Pietro Slavich
NLO QCD bottom corrections to Higgs boson production in the MSSM
J. High Energy Phys. **11** (2010) 044, arXiv: 1007.3465 [hep-ph] (cit. on p. 202).

[237] Giuseppe Degrassi, Stefano Di Vita, and Pietro Slavich
NLO QCD corrections to pseudoscalar Higgs production in the MSSM
J. High Energy Phys. **08** (2011) 128, arXiv: 1107.0914 [hep-ph] (cit. on p. 202).

[238] Giuseppe Degrassi, Stefano Di Vita, and Pietro Slavich
On the NLO QCD Corrections to the Production of the Heaviest Neutral Higgs Scalar in the MSSM
Eur. Phys. J. C **72** (2012) 2032, arXiv: 1204.1016 [hep-ph] (cit. on p. 202).

[239] Robert V. Harlander and William B. Kilgore
Higgs boson production in bottom quark fusion at next-to-next-to-leading order
Phys. Rev. D: Part. Fields **68** (2003) 013001, arXiv: hep-ph/0304035
(cit. on p. 202).

[240] Stefan Dittmaier, Michael Krämer, and Michael Spira
Higgs radiation off bottom quarks at the Tevatron and the LHC
Phys. Rev. D: Part. Fields **70** (2003) 074010, arXiv: hep-ph/0309204
(cit. on p. 203).

[241] Sally Dawson, Laura Reina Christopher B. Jackson, and Doreen Wackeroth
Exclusive Higgs boson production with bottom quarks at hadron colliders
Phys. Rev. D: Part. Fields **69** (2003) 074027, arXiv: hep-ph/0311067
(cit. on p. 203).

[242] Robert Harlander, Michael Krämer, and Markus Schumacher
Bottom-quark associated Higgs-boson production: reconciling the four- and five-flavour scheme approach
Tech. rep., CERN, 2011, arXiv: 1112.3478 [hep-ph],
URL: http://cds.cern.ch/record/1407669 (cit. on p. 203).

[243] Sven Heinemeyer, Wolfgang Hollik, and Georg Weiglein
The Masses of the neutral CP-even Higgs bosons in the MSSM: Accurate analysis at the two loop level
Eur. Phys. J. C **9** (1998) 343, arXiv: 9812472 [hep-ph] (cit. on p. 203).

[244] Meikel Frank et al.
The Higgs Boson Masses and Mixings of the Complex MSSM in the Feynman-Diagrammatic Approach
J. High Energy Phys. **02** (2006) 047, arXiv: hep-ph/0611326 (cit. on p. 203).

[245] Giuseppe Degrassi et al.
Towards high precision predictions for the MSSM Higgs sector
Eur. Phys. J. C **28** (2002) 133, arXiv: hep-ph/0212020 (cit. on p. 203).

[246] Thomas Hahn et al.
High-Precision Predictions for the Light CP-even Higgs Boson Mass of the Minimal Supersymmetric Standard Model
Phys. Rev. Lett. **112** (2013) 141801, arXiv: 1312.4937 [hep-ph] (cit. on p. 203).

[247] Abdelhak Djouadi, Jan Kalinowski, and Michael Spira
HDECAY: A Program for Higgs boson decays in the standard model and its supersymmetric extension
Comput. Phys. Commun. **108** (1997) 56, arXiv: 9704448 [hep-ph]
(cit. on p. 203).

[248] Elisabetta Barberio, Bob van Eijk, and Zbigniew Was
PHOTOS - a universal Monte Carlo for QED radiative corrections in decays
Comput. Phys. Commun. **66** (1991) 115 (cit. on p. 203).

[249] Nadia Davidson, Tomasz Przedzinski, and Zbigniew Was
PHOTOS Interface in C++: Technical and Physics Documentation
Comput. Phys. Commun. **199** (2010) 86, arXiv: 1011.0937 [hep-ph]
(cit. on p. 203).

[250] Stefan Höche et al.
QCD matrix elements + parton showers: The NLO case
J. High Energy Phys. **04** (2012) 027, arXiv: 1207.5030 [hep-ph] (cit. on p. 203).

[251] Tomasz Przedzinski, Elzbieta Richter-Was, and Zbigniew Was
TauSpinner: a tool for simulating CP effects in $H \to \tau\tau$ decays at LHC
Eur. Phys. J. C **C74** (2014) 3177, arXiv: 1406.1647 [hep-ph] (cit. on p. 203).

[252] Kirill Melnikov and Frank Petriello
Electroweak gauge boson production at hadron colliders through $O(\alpha(s)^2)$
Phys. Rev. D: Part. Fields **74** (2006) 114017, arXiv: hep-ph/0609070
(cit. on p. 203).

[253] Ryan Gavin et al.
FEWZ 2.0: A code for hadronic Z production at next-to-next-to-leading order
Comput. Phys. Commun. **182** (2010) 2388, arXiv: 1011.3540 [hep-ph]
(cit. on p. 203).

[254] Pierre Artoisenet et al.
Automatic spin-entangled decays of heavy resonances in Monte Carlo simulations
J. High Energy Phys. **03** (2012) 015, arXiv: 1212.3460 [hep-ph] (cit. on p. 203).

[255] Peter Z. Skands
Tuning Monte Carlo Generators: The Perugia Tunes
Phys. Rev. D: Part. Fields **82** (2010) 074018, arXiv: 1005.3457 [hep-ph]
(cit. on p. 203).

[256] David J. Lange
The EvtGen particle decay simulation package
Nucl. Instrum. Methods Phys. Res., Sect. A **462** (2001) 152 (cit. on p. 204).

[257] ATLAS Collaboration
Summary of ATLAS Pythia 8 tunes
Tech. rep., CERN, 2012, URL: http://cdsweb.cern.ch/record/1474107 (cit. on p. 204).

[258] ATLAS Collaboration
The ATLAS simulation infrastructure
Eur. Phys. J. C **70** (2010) 823, arXiv: 1005.4568 [physics.ins-det] (cit. on p. 204).

[259] ATLAS Collaboration
The simulation principle and performance of the ATLAS fast calorimeter simulation FastCaloSim
Tech. rep. ATL-PHYS-PUB-2010-013, CERN, 2010, URL: http://cdsweb.cern.ch/record/1300517 (cit. on p. 204).

[260] Guido Altarelli, Barbara Mele, and Marti Ruiz-Altaba
Searching for New Heavy Vector Bosons in $p\bar{p}$ Colliders
Zeitschrift fur Physik C Particles and Fields **47** (1990) 676, [Erratum: Z. Phys.C47,676(1990)] (cit. on p. 211).

[261] Kevin R. Lynch et al.
Finding Z' bosons coupled preferentially to the third family at LEP and the Tevatron
Phys. Rev. D: Part. Fields **63** (2000) 035006, arXiv: hep-ph/0007286 (cit. on p. 211).

[262] Ehab Malkawi, Timothy Tait, and Chien Peng Yuan
A model of strong flavor dynamics for the top quark
Phys. Lett. B **385** (1996) 304, arXiv: 9603349 [hep-ph] (cit. on pp. 211, 219).

[263] Ken Hsieh et al.
Global analysis of general $SU(2) \times SU(2) \times U(1)$ models with precision data
Phys. Rev. D: Part. Fields **82** (2010) 035011, arXiv: 1003.3482 [hep-ph] (cit. on p. 211).

[264] David J Muller and Satyanarayan Nandi
Top flavor: A Separate SU(2) for the third family
Phys. Lett. B **383** (1996) 345, arXiv: 9602390 [hep-ph] (cit. on p. 211).

[265] ATLAS Collaboration
Search for additional heavy neutral Higgs and gauge bosons in the ditau final state produced in 36 fb-1 of pp collisions at sqrts = 13 TeV with the ATLAS detector
JHEP 01 (2018) 055 **2018** (2017), arXiv: 1709.07242 [hep-ex]
(cit. on pp. 212, 228).

[266] Alexander L. Read
Presentation of search results: the CL_s technique
J. Phys. G: Nucl. Part. Phys. **28** (2002) 2693 (cit. on p. 217).

[267] ATLAS Collaboration
Constraints on new phenomena via Higgs boson couplings and invisible decays with the ATLAS detector
J. High Energy Phys. **11** (2015) 206, arXiv: 1509.00672 [hep-ex]
(cit. on p. 218).

[268] Qing-Hong Cao et al.
Discovery and identification of W' and Z' in $SU(2)_1 \otimes SU(2)_2 \otimes U(1)_X$ models at the LHC
Phys. Rev. D: Part. Fields **86** (2012) 095010, arXiv: 1205.3769 [hep-ph]
(cit. on p. 219).

[269] Kang Young Lee
Lepton flavor violation in a nonuniversal gauge interaction model
Phys. Rev. D: Part. Fields **82** (2010) 097701, arXiv: 1009.0104 [hep-ph]
(cit. on p. 219).

[270] Kang Young Lee
Unitarity violation of the CKM matrix in a nonuniversal gauge interaction model
Phys. Rev. D: Part. Fields **71** (2004) 115008, arXiv: hep-ph/0410381
(cit. on p. 219).

[271] CMS Collaboration
Evidence for the 125 GeV Higgs boson decaying to a pair of τ leptons
J. High Energy Phys. **05** (2014), arXiv: 1401.5041 [hep-ex],
URL: https://cds.cern.ch/record/1643937 (cit. on p. 221).

[272] ATLAS Collaboration
Search for Minimal Supersymmetric Standard Model Higgs Bosons H/A in the $\tau\tau$ final state in up to 13.3 fb^{-1} of pp collisions at $\sqrt{s}$= 13 TeV with the ATLAS Detector
Tech. rep. ATLAS-CONF-2016-085, CERN, 2016,
URL: https://cds.cern.ch/record/2206278 (cit. on pp. 227–229).

List of Figures

List of Tables

Acknowledgments

En primer lugar, tengo que agradecer a Luca, mi supervisor, por haberme aguantado todos estos años, por su paciencia, por las horas compartidas en el despacho del 40 y por todas las palabras de apoyo en los momentos duros. Es uno de los mejores físicos que conozco y he aprendido muchísimo de él. Sin toda su ayuda, *¡yo no sabría nada!*

Al grupo de TileCal de Valencia, por haberme acogido. A Alberto, por demostrar que se puede vivir alegre y sin estrés en este trabajo. A Fernando, por ser la única persona que se queda más que yo en el IFIC y por darme la bienvenida en el CERN los meses que compartimos mansión en Ginebra. A Pablo, in memoriam. A Juano, por los laboratorios de primero y por aceptarme en el grupo. A Emilio, Toni, Victoria y Enrique. Y a Sergi, con lo que me ha costado de educar, por seguir con mi legado de 8 a 5.

Mención especial tienen mis maravillosas compañeras de despacho. Yesenia ha sido mi hermana mayor, dándome la perspectiva de la experiencia y un inagotable buen humor. Un ejemplo a seguir en la vida. Todo lo contrario a Leo, que no sabe cuántos TileCal tenemos y hubo que enseñarle que los códigos no se escriben a mano. Aún así, creo que he aprendido yo más de ella. Leo es la persona con la que más tiempo y conversaciones he compartido estos años. Y viajes, despachos, pisos, amigos, salchichas con patatas fritas y muchas, pero muchas, historias que contar. Y, aunque podría llenar dos páginas de quejas sobre ella, (en el fondo) le he cogido mucho cariño.

Mi trabajo estos años ha sido principalmente en el CERN, lo que era uno de mis sueños desde que supe de su existencia. El CERN es un sitio muy especial, que supera cualquier expectativa. Es viejo, feo, oscuro, frío. Y a la vez, es el centro de todo, la cumbre de la ciencia, los valores y la sociedad. Un micro-nación, llena de gente con ideas y con ganas de hacer todo lo que puedas imaginar. Hay pocos sitios en el mundo donde importe tan poco tu bandera o tu idioma, donde el único propósito sea el conocimiento, ayudar a la gente y hacer una mejor comunidad. Es fácil olvidarlo, oculto por la cantidad de trabajo del día a día, pero deja una huella muy profunda y el listón demasiado alto.

Allí he tenido la suerte de conocer el mundo de la investigación avanzada y trabajar con gente entregada, de la que sólo puedes aprender, que te hace vivir lo que haces. Gracias a los convernors de los análisis del Higgs, del tautau y del BSM: Lidia, Sinead, Elias, Stan Lai, Sasha Pranko, Michel J, Nikos, Allison, Carl, Arnaud, Marumi, Eilam, Pierre y Bruno, por su esfuerzo y su guía. Y a los compañeros de los análisis, con quien he tenido el placer de trabajar. En particular a Christian y Mark, con los que compartí muchas horas de frustración y el sueño de montar un chiringuito en la playa. También al grupo del TileCal, con mención a Sasha Solodkov, Giulio y el Maintenance group, por enseñarme que no todo el trabajo es análisis. A Carlos Solans, por su filosofía de café, a César, por sus paellas y a Bruce, por ser Bruce. A Irene, por el vacío que dejó en el despacho. Y a toda la colaboración de ATLAS y al CERN, por hacer esto posible.

Pero el CERN no sería la mitad de especial si no fuera por la gente con la que lo compartes. Que hace que compense pagar 45 € por tres chupitos. A Mario, Silvia, Stefano, Luis, Mar, Roger, Ceci, mi padre JA, la spanish gang, y la *siesta y fiesta*, que me han acompañado estos años. Pero sobre todo a Andrea, porque es muy majita, me prohibió quejarme y me enseñó que Ginebra no está tan mal.

Y la gente de Valencia, compañeros de despacho, de comida, de cine y de descansos. Muchos amigos (docto)random, o lo que sea, que pasaron, huyeron, se doctoraron o siguen sufriendo. Gente que hace que cada día sea *un poco menos miserable*. Los doctores Pablo, Nacho, Elena, Sebas, Marija, Nuria, Ane, Víctor, Erica. Los jóvenes Javi J, Carlos Astro, Davide, Álvaro, Javi Nano. La secta de Antares, con Javi Barrios a la cabeza. El grupo *empollón* de Pablo León. Mi catalán favorito, Miguel Ángel. Aparici, al que le he robado muchas horas de empáticas conversaciones sobre humanos. Y finalmente, Ana y Rosa, por los *cinco minutos* de cada tarde en los que compartíamos nuestras quejas en compañía. Al menos hasta que llegó el gato. Los que me faltan por nombrar y los nuevos que han venido. A todos, gracias por las comidas, las sobremesas y las horas fuera del trabajo.

Y de todos, a Dani, porque lo que lo he echado en falta este año solo rivaliza con lo que lo admiro. Desde el *taxi* de Oviedo a fotografiar el Mont Blanc bajo la luna. Su fuerza es inmensa y ha dejado una marca en todos nosotros. Se quedan cortas las palabras.

Del trabajo, a casa. A Ander, por cinco años de convivencia y diez de amistad. Hemos compartido mucho en este tiempo, donde él ha sido un contrapeso a mi vida y mi forma de ser, y cuya opinión valoro como la de poca gente. Los mismos años conozco a Jesús, al que me une un ritual semanal, y que fue la primera persona que conocí de mi vida en Valencia. Han (hemos) cambiado mucho en este tiempo y me alegro haber podido vivirlo a su lado. En Valencia se fundó el Consejo de Sabios: Fabián, Alberto y Abde, mis todólogos de cabecera. Y además, tengo a Jonathan, que pasaba por casa; a Patricia, porque tras tanto, sigue estando ahí; a Vicent y Álvaro, mis hermanos de una generación de oro y, en el exilio, a Myles, mi legítimo heredero.

Cambiando de ciudad tengo a Arturo, Silvia, Óscar y Elena, que son una constante en mi vida y mis amigos más cercanos. Son, además, mi nexo de unión con Albacete. Estar con ellos es sentirme en casa, como que nada hubiera cambiado en 13 años.

Finalmente, a mi familia, porque aunque no pueden elegir otra cosa, no he podido tener más suerte con ellos. Tengo que agradecerles todo lo que han hecho para que yo haya llegado aquí. Me han ayudado en todo lo que necesitaba y me han dado la libertad para hacer lo que quisiera. La confianza que tienen en mí y el apoyo que representan en mi vida es algo que nunca podré valorar ni agradecer suficiente. A mis padres, a mi hermano Sergio, a mi abuela Juanita, a Tachi y a todos mis tíos, a mis primos, en especial a Ángela, Javi, Rubén y Tania; a los que ya no están y a los nuevos que han venido.

Y дякую, Ольга, for being solution to the naturalness issue. Sometimes, against all odds, the most complicated path is the one that works. And there is never enough of it.